Transactions of the ASME®

Transactions of the ASME, Journal of Turbomachinery (ISSN 0889-504X) is published quarterly (Jan., Apr., July, Oct.) for $205.00 per year by The American Society of Mechanical Engineers, Three Park Avenue, New York, NY 10016. Periodicals postage paid at New York, NY and additional mailing offices. POSTMASTER: Send address changes to Transactions of the ASME, Journal of Turbomachinery, c/o THE AMERICAN SOCIETY OF MECHANICAL ENGINEERS, 22 Law Drive, Box 2300, Fairfield, NJ 07007-2300.
CHANGES OF ADDRESS must be received at Society headquarters seven weeks before they are to be effective. Please send old label and new address.
PRICES: To members, $40.00, annually; to nonmembers, $205.00.
To countries outside the United States and Canada, add $40.00 for surface postage and $60.00 for airmail postage.
STATEMENT from By-Laws. The Society shall not be responsible for statements or opinions advanced in papers or . . . printed in its publications (B7.1, Par. 3).

INDEXED by Applied Mechanics Reviews and Engineering Information, Inc.
Canadian Goods & Services Tax Registration #126148048

Journal of Turbomachinery

Published Quarterly by The American Society of Mechanical Engineers

VOLUME 121 • NUMBER 2 • APRIL 1999

TECHNICAL PAPERS

(Contents continued on p. 256)

This journal is printed on acid-free paper, which exceeds the ANSI Z39.48-1992 specification for permanence of paper and library materials.♾™

♻ 85% recycled content, including 10% post-consumer fibers.

(Contents continued)

ANNOUNCEMENTS

M. Woinowsky-Krieger

J.-P. Lavoie

E. P. Vlasic

S. H. Moustapha

Turbine Component Engineering,
Pratt & Whitney Canada, Inc.,
Longueuil, Québec, Canada

Off-Design Performance of a Single-Stage Transonic Turbine

This paper presents results of rig testing of a transonic, single-stage turbine at off-design conditions. Mapping of the 3.4 pressure ratio, 1.9 stage loading turbine ranged from 70 through 120 percent of design speed and 75 to 125 percent of design pressure ratio. Results show expansion efficiency dropping over 4 percent from 100 to 80 percent of design speed at design pressure ratio, while remaining within half a percent from 90 to 110 percent of design pressure ratio at design speed. Efficiency lapse rate from equivalent sea-level to cruise altitude Reynolds numbers at the design point was measured and found to be worth over 1.5 percent. Analyses of test results using a viscous three-dimensional solver showed very good agreement for the efficiency change with speed.

Introduction

Research and development on single-stage, high-work compressor turbines is readily justified by their light weight, low initial cost, and maintenance. The work requirement from the single-stage high-pressure turbine becomes excessive when attempting to achieve a low-cost, moderately high overall pressure ratio two-shaft engine with acceptable fuel consumption. To maximize engine life, thereby reducing overall maintenance costs, the turbine design will run at speeds and annulus areas resulting in reduced blade and disk stresses, but at the expense of elevated exit Mach numbers and small aspect ratios. Generally the turbine inlet temperature is also high, thus requiring cooling both vane and blade.

A number of detailed experimental studies have been carried out on single-stage high-pressure-ratio turbines (Table 1). Ewen et al. (1973) tested a lightly loaded ($\Delta H/U^2 = 1.2$) turbine. Okapuu (1974) investigated the effect of reaction (ratio of blade static pressure drop to stage static pressure drop), aspect ratio, tip clearance, and vane outer wall contouring on the performance of a turbine with a *PR* of 3.9 (DRB). Liu et al. (1979) described the design and testing of a low-aspect-ratio turbine. Crow et al. (1980) tested a turbine, with and without cooling, as part of the Energy Efficient Engine (E^3) program. Bryce et al. (1985) reported on a cooled, high-pressure-ratio, high-stage-loading turbine (RAE). Moustapha et al. (1987) described the performance of a highly loaded turbine (HLT), investigating the effects of vane outer wall contouring and rotor loading. All of these studies focused mainly on design point performance, cooling flow losses, and parametric studies around the design point. Some, as indicated, investigated performance enhancement concepts such as outer wall contouring to increase design point efficiency. Of the many papers reporting on single-stage transonic turbines, few studied the off-design performance and altitude lapse rate. One of the more recent papers to investigate the off-design performance characteristics was Vlasic et al. (1996), the HWRT in Table 1. This work focused on the effects of speed and pressure ratio on the performance of a cooled transonic turbine with a high pressure ratio of 5.0. Vlasic's results showed significant effects of off-design operation of the turbine on efficiency, and underlined the importance of achieving the correct design point condition. The limited data obtained were well predicted by meanline correlations. No measurements of Reynolds number effect were undertaken. Given that off-design performance characteristics are extremely important to engine starting and transient modeling as well as to calculate mission fuel burn, it is suggested that more data be made available in this area.

This paper describes the aerodynamic design and cold flow rig testing of a single-stage compressor turbine with transonic aerofoils and a low-Reynolds-number blade. The turbine was designed for an engine pressure ratio of 3.12 and a stage loading of 1.9. The vane is cooled while the blade is uncooled. The cold flow rig results include off-design performance at various speeds and pressure ratios, and altitude efficiency lapse from sea level take-off to cruise Reynolds numbers. Analyses of test results include a comparison with predictions from a viscous three-dimensional solver.

Turbine Stage Aerodynamic Design

Stage Design. The compressor turbine described herein is a realistic stage for a small turbofan engine. The inlet temperature was chosen such that blade cooling would not be required. Table 1 gives the stage design point (13.1 km altitude cruise) parameters as compared to previously published high pressure ratio turbines. The stage design pressure ratio in the rig is 3.4 versus 3.12 for engine application) due to the difference between engine and rig specific heat ratios.

The gas path of Fig. 1 shows a contoured outer diameter for the vane; a cylindrical one was introduced for the unshrouded blade to reduce tip leakage losses. Rotor hub flare was chosen to reduce stage exit Mach number, thereby improving turbine and interturbine duct performance. The axial gap (30 percent of vane true chord) between vane and blade was chosen to satisfy mechanical and rotor dynamics considerations rather than optimize unsteady aerodynamic interactions.

The mean reaction of 27 percent was chosen to balance vane and blade exit Mach numbers and to reduce blade metal temperatures to below levels that require cooling. Midspan design point velocity triangles are presented in Fig. 2, showing the transonic nature of both aerofoils.

The chosen radial work distribution unloaded both the hub and tip, thereby reducing endwall and leakage losses. The selection of the number of aerofoils, from an aerodynamic point of view, was based on a compromise, which included optimum loading (pitch-to-chord ratio), trailing edge blockage, and aspect ratio (secondary losses). Mechanical and rotor dynamics considerations also played a role in the final choice of 16 vanes and 70 blades. The resulting efficiency, based on the correlation of Kacker and Okapuu (1982), is predicted to be 84.5 percent, for a blade tip clearance of 1.2 percent of span.

Contributed by the International Gas Turbine Institute and presented at the 43rd International Gas Turbine and Aeroengine Congress and Exhibition, Stockholm, Sweden, June 2–5, 1998. Manuscript received by the International Gas Turbine Institute February 1998. Paper No. 98-GT-2. Associate Technical Editor: R. E. Kielb.

Table 1 Comparison of single-stage turbine parameters

Stage Parameters	DRB	E³	RAE	HLT	HWRT	Present Turbine
P.R.	3.9	4.0	4.5	3.8	5.0	3.4
$\Delta H/U^2$	1.5	1.6	2.1	2.5	2.2	1.83
Cx/U	0.56	0.3	0.65	0.63	0.48	0.64
Vane count	29	24	40	14	18	16
Blade count	54	54	89	51	43	70
Reaction	28	35 & 43	30	30	31	27
Exit swirl, degrees	4	41	37	37	39	16.8
Exit Mach number	0.6	0.5	0.62	0.65	0.62	0.53
Blade Re x 10^{-3}	220	769	884	215	253	63
$AN^{2*}10^{-10}$, rpmxcm²	13.9	25.8	5.2	8.4	10.3	7.9
Aspect ratio, vane	1.0	0.65	0.58	0.7	0.7	0.50
Aspect ratio, blade	1.66	1.4	1.29	1.44	1.4	2.00
% TE blockage: vane	16	9	10	20	14	6.8
% TE blockage: blade	16	11	11	13	28	9.3
Clearance/span, %	1.7	0.8	1.4	1.5	1.1	1.2

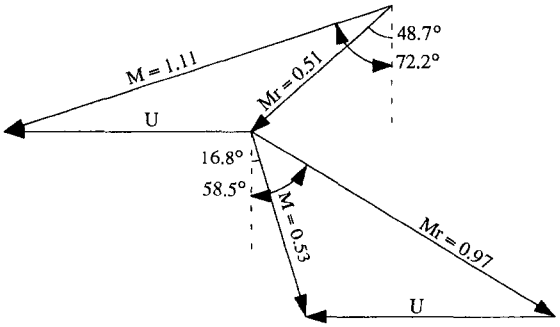

Fig. 2 Design point velocity triangles at midspan

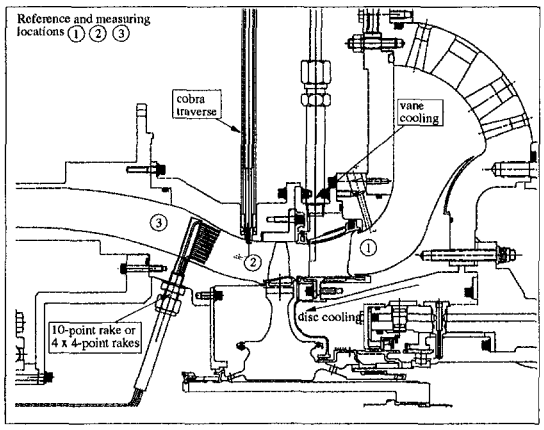

Fig. 1 Single-stage turbine rig

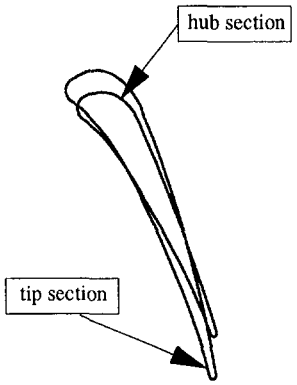

Fig. 3(*a*) Vane design sections

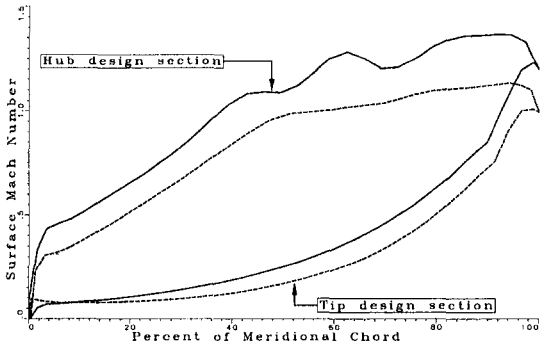

Fig. 3(*b*) Vane surface Mach number distribution

Vane Design. The number of vanes (16) was chosen primarily to satisfy rotor dynamics, while cooling considerations resulted in a thicker aerofoil than would be aerodynamically optimum. The 16-aerofoil design has an aspect ratio of 0.51, a pitch-to-chord ratio of 0.34, a turning angle of 57 deg, an exit Mach number of 1.15, and a Reynolds number of 435,000 based on mean true chord. The vane was designed such that a straight cooling insert could be used. The trailing edge has a pressure surface cutback cooling scheme. A 4.5 deg spanwise exit angle gradient was incorporated to help with the design of the downstream blade.

Figure 3(*a*) shows vane cross-sectional views at the two design radii (see Appendix I for geometry definition). The predicted surface Mach number distributions (Fig. 3(*b*)), as obtained by a three-dimensional inviscid solver (Ni and Bogoian, 1989), show the supersonic nature of the nozzle. They also show the rear loading of the vane with no pressure surface and low suction surface diffusion levels at both design sections. The hub shows evidence of a mild shock at approximately 65 percent of axial chord.

Blade Design. An uncooled, transonic, high work turbine usually poses a challenging design, requiring balancing stress and dynamics with aerodynamic considerations. This was especially true in this design due to the additional design parameter of hub flare introduced to reduce exit Mach number. The rotor has 70 aerofoils of 2.0 aspect ratio, a pitch-to-chord ratio of

Nomenclature

A = flow area, cm²
AR = aspect ratio = aerofoil height/chord
C_p = average specific heat at constant pressure, J/kg/K
C_x = axial velocity, m/s
H = stagnation enthalpy, J/kg
M = Mach number
N = rotational speed, rpm
P = total pressure, kPa
PR = pressure ratio
r = radius, mm
T = total temperature, K
T.E. = trailing edge
U = blade speed, m/s
W = mass flow, kg/s
Δ = change
η = total-to-total efficiency = $[(W*C_p*\Delta T)_{ms} + \Sigma(W*C_p*\Delta T)_{\text{cool}}]/[(W*C_{pi}*\Delta T_i)_{ms} + \Sigma(W*C_{pi}*\Delta T_i)_{\text{cool}}]$

Subscripts

cool = cooling flow
d = design
i = isentropic
ms = mainstream flow
r = relative

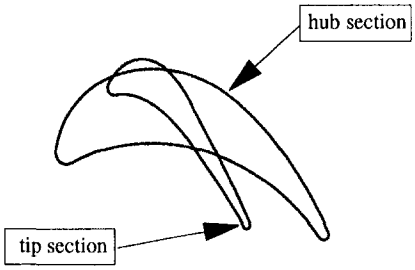

Fig. 4(*a*) Blade design sections

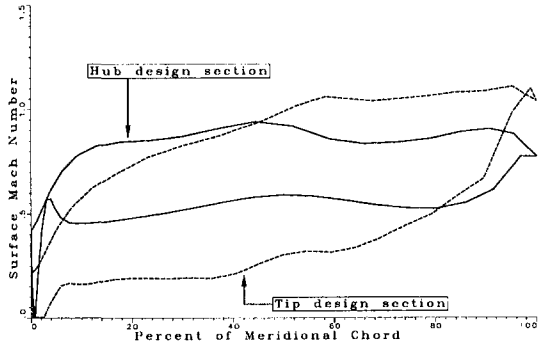

Fig. 4(*b*) Blade surface Mach number distribution

0.76, an exit Mach number of 0.97, and a Reynolds number of 63,000, also based on mean true chord. This is the lowest Reynolds number blade among the turbines shown in Table 1. The required hub to tip area ratio resulted in a highly loaded blade tip with a cavity. Figure 4(*a*) shows the cross-sectional views at two design radii (see Appendix I for the geometry).

The blade was designed with an average incidence of approximately 0 deg (at 13.1 km cruise). The upper portion of the span was designed with negative incidence to reduce losses at off-design conditions; this feature also lessens the impact of positive incidences at the lower radii resulting from blade fixing geometry constraints. The aerofoil was leaned toward the leading edge and suction surface to alleviate platform stresses. The predicted surface Mach number distributions, as obtained by the aforementioned three-dimensional inviscid solver, are shown in Fig. 4(*b*). It can be seen that again, much like the vane, the aerofoils are mid to rear loaded with low to mild surface Mach number diffusions.

Experimental Facility and Procedure

The general arrangement of the single-stage transonic turbine is shown in Fig. 1. The test section is fed by a plenum of air, which is pressurized by upstream compressors capable of reaching plenum pressures of 276 kPa. Prior to entering the plenum chamber, the air is heated by heat exchangers. Inlet turbulence is simulated by using a honeycomb screen between the plenum and inlet to the test section. An exhaust duct that reproduces an enginelike interturbine duct geometry is placed immediately downstream of the turbine up to the last measurement plane. Further downstream, the flow is diffused and then exhausted by two compressors, which can pull the exhaust pressure down to 13.8 kPa. This allows for the range of stage pressure ratios and Reynolds numbers necessary for mapping the turbine characteristics.

A water dynamometer is used as a means of absorbing the turbine power and controlling its speed. Mainstream and cooling mass flow rates are measured using upstream venturi flow meters. The vane cooling flow is fed via an outside plenum. Turbine disk cooling is provided by an inner feed system. Cooling flow temperature was set to ambient condition. Thermocouples and static pressure taps are located in each of the three cooling plenums. The mainstream flow plenum inlet temperature is sensed using 16 pairs of thermocouples equally spaced circumferentially inside the plenum chamber. Similarly, plenum pressure is sensed using eight static pressure taps. The temperature and pressure loss from the inlet of the test section to the vane leading edge were previously measured for several turbine stages, and a correlation was established that was used for the current turbine stage.

The rig inlet pressure was set to reproduce the engine equivalent sea-level or altitude stage Reynolds number. The plenum temperature was set as a function of the pressure ratio such that the turbine exit temperature was within 0.5 K of the test cell ambient temperature; this minimized the temperature change from the exit of the turbine to the turbine exit temperature measuring plane. A radial and circumferential traverse plane is provided one blade chord downstream. Exit total pressure measurement is accomplished using four shielded Kiel head rakes located four blade chords downstream. The rakes are made with four pressure heads spaced approximately at the centers of equal area; they are spaced circumferentially to cover one vane pitch at one quarter pitch intervals. A ten-point Pitot total pressure rake mounted in the same plane as the 4 Kiel rakes can be rotated over 360 deg at a continuous slow rate to provide detailed circumferential traversing of the flow field. Four exit temperature rakes of five heads each are installed 3 m downstream of the rotor to ensure a well mixed flow field.

Gas path, rotor disk (upstream and downstream) and shroud cavity static pressures are measured to provide information on stage reaction and boundary conditions for three-dimensional analysis. Blade tip clearances are determined using four capacitance probes located 90 deg apart with a demonstrated absolute uncertainty of less than ± 25 μm (i.e., ± 0.10 percent of blade tip clearance to span ratio) and 50 percent better uncertainty for variation of clearance within the same build test sequence.

The bulk of the data were obtained at sea-level conditions, where the higher power extraction levels ensured adequate rig stability. Measurements at high altitude conditions were limited to the minimum required to obtain off-design performance data of the turbine.

The uncertainty in the measured efficiency at off-design conditions is contained within an error band of less than ± 0.2 percent. This claim is supported in part by selective repeatability tests conducted throughout the current test program, as well as relying on a large body of previous test programs, which have demonstrated similar levels of uncertainty.

Effect of Pressure Ratio

The need often arises in aircraft engines to modify the pressure ratio split between the high and low-pressure turbines. One reason is to change the speed match of a twin-spool engine and

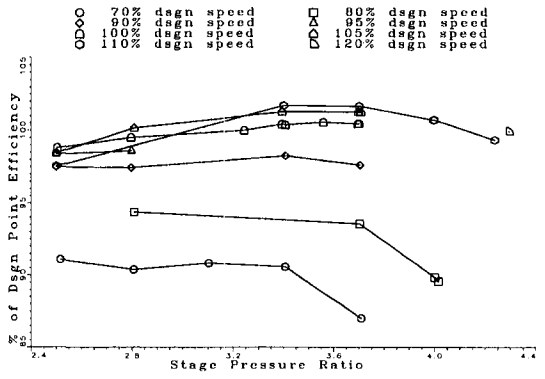

Fig. 5 Efficiency versus pressure ratio

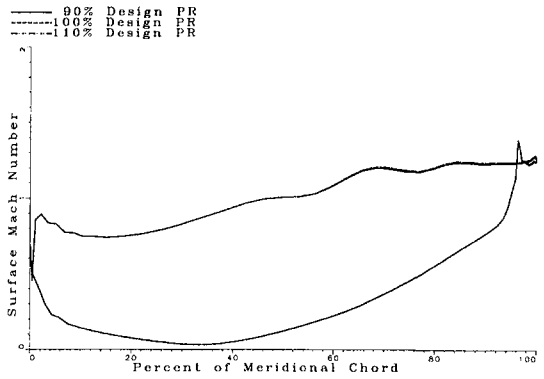

Fig. 6 Predicted vane midspan Mach number distribution

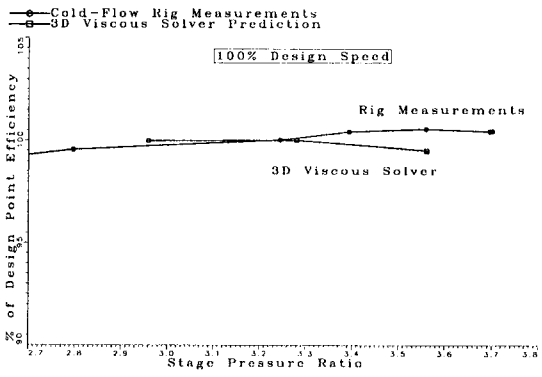

Fig. 8 Efficiency versus pressure ratio: three-dimensional viscous solver versus rig measurements

situate the compressor or turbine operating point at a more optimum speed. Another reason stems from the use of an existing design for a new application (sometimes termed an engine derivative). Use of existing hardware with aerofoil restaggers and change in pressure ratio will at times suffice to achieve customer requirements of power/thrust and engine performance. The impact of running the turbine at an off-design pressure ratio therefore needs to be well understood in order to better predict the engine overall performance.

Sea-level condition mapping was carried out at pressure ratios ranging over $PR_d \pm 20$ percent. Figure 5 presents the efficiencies normalized with respect to the design point for a family of constant speed lines. The results show a very flat characteristic of efficiency versus pressure ratio, with efficiency varying less than 2 percent over a 20 percent range in pressure ratio. The turbine does show signs of limit loading as it exceeds a pressure ratio of 4. This map is very similar in appearance to the one obtained by Vlasic et al. (1996).

A three-dimensional viscous solver (based on Ni and Bogoian, 1989, and Davis et al., 1996) was used to simulate the turbine running conditions. Figures 6 and 7 show Mach numbers for the vane and blade, respectively, at 90, 100, and 110 percent of design pressure ratio for the design speed. Figure 6 clearly shows the vane in choked condition, as the Mach number distribution hardly varies over the 20 percent range in pressure ratio. The inlet conditions to the blade thus remain unchanged as well, as seen in Fig. 7, and the additional loading resulting from the increase in pressure ratio is seen to take place entirely on the uncovered suction surface.

The three-dimensional viscous code predicts blade incidence changes of only +0.2 deg from 90 to 110 percent design pressure ratio, while average reaction is predicted to vary from 23 to 31 percent. The peak Mach number in the blade exit area is seen to vary from around 1.0 at 90 percent PR_d (around 84 percent meridional chord) to over 1.6 at 110 percent PR_d; the efficiency is predicted to vary only 0.4 percent over this range, as shown in Fig. 8.

Measured hub and tip reactions are shown in Fig. 9. The measured trend shows a typical (for a choked vane) rising reaction with pressure ratio. Results from the three-dimensional viscous code compare favorably with measurements, especially at the hub.

Effect of Speed

There are various reasons why a turbine, operating at the design thrust/power, will not be running at the design speed. The most obvious one is engine deterioration. A so-called throttle-push is required to maintain the required engine thrust/power, resulting in higher fuel consumption, higher turbine inlet temperature and thus lower normalized turbine speed ($N/\sqrt{T}$). Another cause is underachievement of component target efficiencies. There is therefore a need to understand how turbine efficiency varies with speed in order to better interpret engine performance data and to design aerofoils more tolerant to off-design operation.

Figure 10 plots efficiency normalized with respect to the design point value versus corrected speeds at constant pressure ratios. Testing covered a wide range in speed (±20 percent) and pressure ratios (±30 percent) around the design point value. The results show a pronounced decrease in efficiency for speeds below 100 percent design speed. The results also show that, at speeds exceeding the design value, expansion efficiency continues to rise for pressure ratios exceeding the design value by nearly 20 percent. Comparison of these results with those presented by Vlasic et al. (1996) shows similar trends, but covers a wider range in speed and pressure ratio. It is clear from these results how important it is to achieve target component efficiencies. Being 5 percent short of design speed will result in

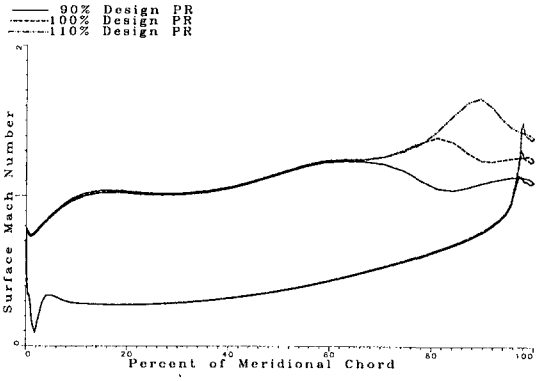

Fig. 7 Predicted blade midspan Mach number distribution

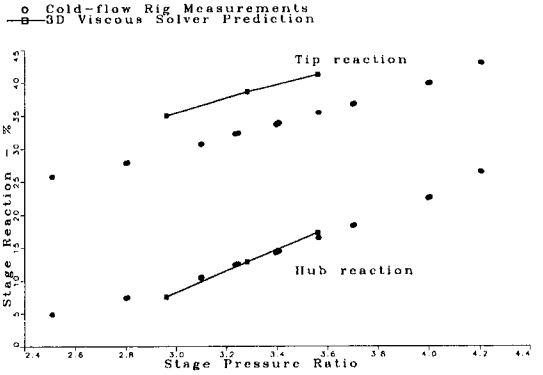

Fig. 9 Turbine stage reaction versus pressure ratio at design speed

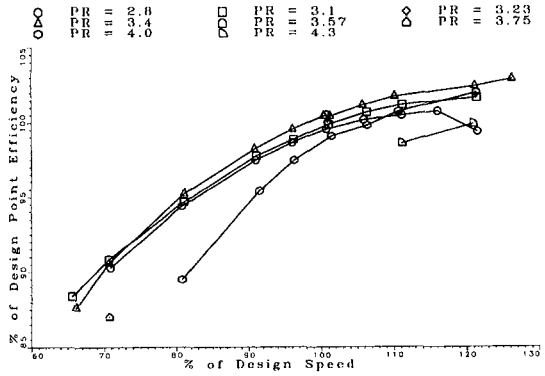

Fig. 10 Efficiency versus speed

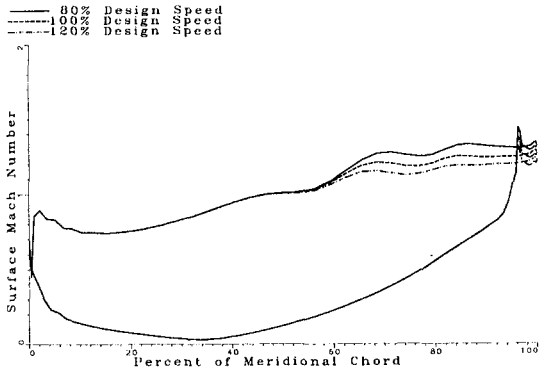

Fig. 11 Predicted vane midspan Mach number distribution

over 1 percent efficiency debit on the stage, roughly equivalent to one percent in specific fuel consumption on typical turbofan engines. The results also suggest it may be worth designing the blade with some negative incidence, situating the design point on a shallower part of the efficiency-versus-speed characteristic, thus retarding efficiency debits for cases of low operating speeds.

Figures 11 and 12 present the predicted three-dimensional viscous solver vane and blade Mach number distributions for various speeds at design pressure ratio. Note that speed is varied from 80 to 120 percent $N/\sqrt{T_d}$. The three-dimensional viscous solver predicts that the changing flow conditions on the blade, resulting from the varying operating speed, cause a variation in back-pressure on the vane and impact the Mach number profile in the vane exit area. Vane exit Mach number varies from 1.16 at 80 percent $N/\sqrt{T_d}$ down to 1.07 at 120 percent $N/\sqrt{T_d}$. The variation in speed is having a pronounced effect on the blade loading, as shown on Fig. 12. The leading edge area is seeing high excursions in incidence, which is predicted to increase by 8 deg from 100 to 80 percent $N/\sqrt{T_d}$, and to drop by 15 deg from 100 percent $N/\sqrt{T_d}$ to 120 percent $N/\sqrt{T_d}$. At the higher operating speeds, the peak exit Mach number is seen to decrease from some 1.5 at 80 percent $N/\sqrt{T_d}$ to less than 1.2 at 120 percent $N/\sqrt{T_d}$. The increase in expansion efficiency over the speed range is thus qualitatively substantiated by the Mach number distributions predicted by the three-dimensional viscous code.

Measured reaction versus speed is shown in Fig. 13. Results show reaction to fall to a minimum near 90 percent design speed, and thereafter rising on either side, with a steeper rising characteristic on the low-speed side. Such a characteristic is similar to an incidence loss distribution (albeit also including the effect of the variation in vane loss on the blade inlet conditions). The results shown in Figs. 11 and 12, telling of high incidence variations, suggest the two are indeed related.

To further discuss this suggestion, we consider a limiting case, where the high-pressure turbine is comprised of two choked nozzles in series, running at a constant overall pressure ratio.

On the low-speed side, a reduction in speed initially causes an increase in swallowing capacity of the blade, causing its inlet pressure to drop, thus yielding a lower reaction. As speed drops further, incidence losses increase to the point where, for a given exit pressure, the blade inlet pressure will have to begin to rise, thus yielding a higher reaction, as shown in Fig. 13.

On the high-speed side, the effect is that of a combination of reduced swallowing capacity of the blade and rising pressure loss in the blade passage, resulting in increased stage reaction, as shown on the same figure.

Figure 13 also shows results from the three-dimensional viscous solver. A similar difference in tip reaction is seen here, as was shown in Fig. 9. Furthermore, the viscous solver results suggest a leveling off in reaction at 80 percent of design speed, thus at a lower speed than shown by measurements.

Effect of Reynolds Number

Generally, the issue of turbine efficiency lapse with altitude concerns mainly the low-pressure turbines, as they are subjected to the lowest Reynolds numbers. However, recent applications have impacted the high-pressure turbine operation as well. Notably, with the drive toward lower cost and reduced engine weight and length, the aerodynamic designer is constrained toward shorter chord aerofoils. There arises the need to understand better the performance trade-off between short chord, low Reynolds numbers, lighter weight designs, and longer chord, higher Reynolds numbers, lower aspect ratio and heavier designs. The effect of low Reynolds number, combined with the transonic nature of a single-stage turbine, proves quite challenging for

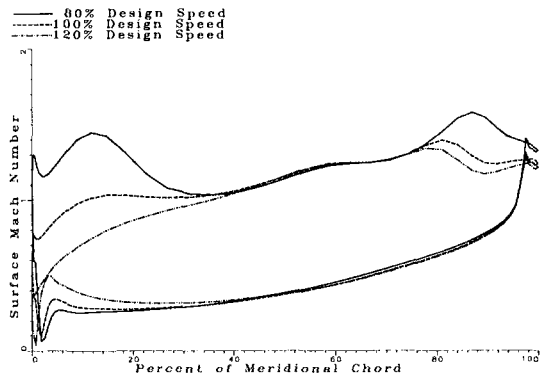

Fig. 12 Predicted blade midspan Mach number distribution

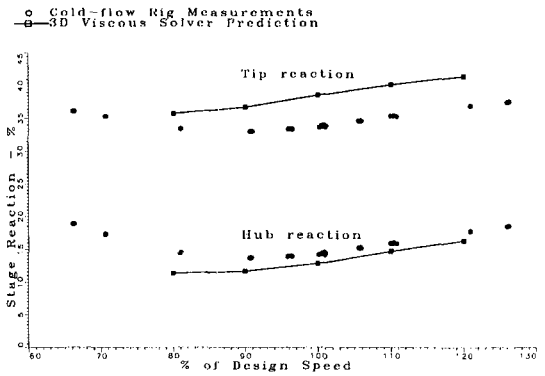

Fig. 13 Turbine stage reaction versus speed at design pressure ratio

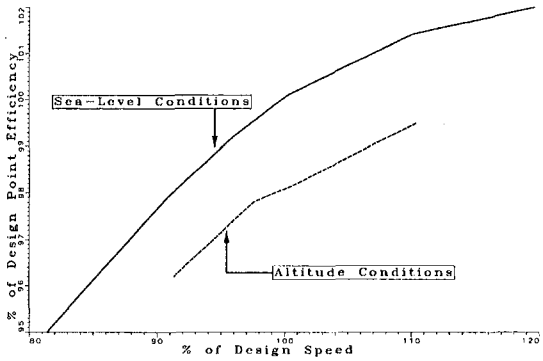

Fig. 14 Efficiency versus speed at design pressure ratio

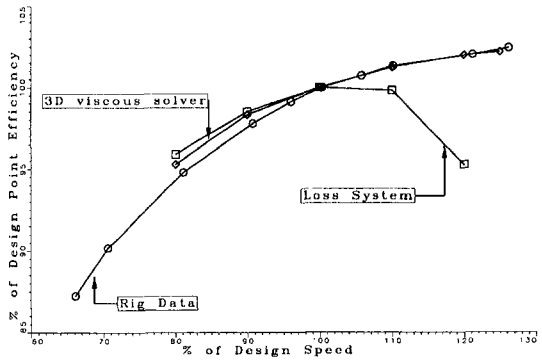

Fig. 16 Comparison with loss system and three-dimensional viscous solver

the design of an uncooled blade in order to ensure aerodynamic, structure, and dynamics design criteria are met.

After completing the turbine mapping exercise at sea level conditions, the rig was run at the altitude condition to measure the efficiency-versus-speed characteristic at the equivalent altitude cruise Reynolds number. Figure 14 compares the two characteristics, and shows that they are virtually identical, as the two curves are parallel. These results indicate that, for this series of tests, the Reynolds number effect can be disregarded when evaluating the efficiency-versus-speed characteristic.

The cold-flow rig was then used to measure the turbine efficiency lapse rate with Reynolds number. Figure 15 plots the measured efficiencies for blade Reynolds number ranging from as low as 32,000 to over 250,000. Recent trends in high-altitude cycles and turbofan engine designs have reached altitudes of 20,000 m, reducing the high-pressure turbine blade Reynolds number down to some 25,000. The need to validate the loss models to such low Reynolds numbers is therefore very much present. The results in Fig. 15 show the expected flat characteristic down to a Reynolds number of 100,000, below which there is then a pronounced fall in efficiency. Also shown on the figure is the result from a single-point run of the three-dimensional viscous solver at altitude, compared to the sea-level condition run. The predicted lapse is 1 percent, compared to a measured lapse of 1.6 percent.

Loss System and Three-Dimensional Viscous Validation

Stringent customer requirements can only be met with a more accurate component efficiency prediction. One purpose for the series of tests on single-stage transonic turbines is to obtain test data in order to calibrate loss systems further so as to improve aerofoil design methods.

Figure 16 presents efficiency versus speed as obtained from measurements, from predictions based on the design and off-design loss system of Kacker and Okapuu (1982), Moustapha et al. (1990), and Benner et al. (1997), and from the three-dimensional viscous solver.

There is excellent agreement between measurements and three-dimensional viscous prediction over the entire range of 80–125 percent speed. The mean-line correlation is seen to agree well for speeds below the design value, beyond which it tends to overpredict loss. It must be noted, however, that rig testing on other test sections has shown the efficiency versus speed lapse to vary considerably from one design to another. Nevertheless, it is clear that the loss system's prediction at off-design requires further improvement.

There has been much recent work on the effect of leading edge geometry on incidence losses (Walraevens and Cumpsty, 1995; Benner et al., 1997). The three-dimensional results shown in this paper indicate local leading edge flow varies significantly as the turbine operates at off-design conditions. There is also the effect of supersonic drag rise at the aerofoil exit, consequent to the varying exit Mach number shown on Figs. 11 and 12, all of which impact turbine efficiency, but whose correlation is currently limited in the turbine mean-line loss system. It is, however, encouraging to see the capability of the three-dimensional viscous solver to capture the sum of these effects. An additional application of the three-dimensional solver might now be to build a more robust meanline loss system.

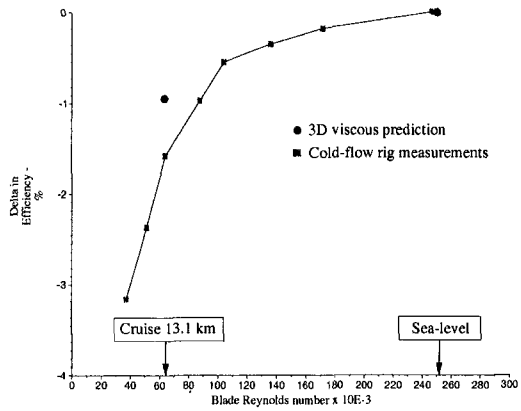

Fig. 15 Efficiency change with blade Reynolds number

Conclusions

The design of a typical single-stage transonic turbine with a low-Reynolds-number blade was described. The turbine was tested in a cold-flow rig to investigate its performance at off-design operating conditions. Investigation of the results has led to the following conclusions:

1 The turbine expansion efficiency was measured to vary mildly with pressure ratio, remaining within 1 percent over a 30 percent range in pressure ratio.

2 The expansion efficiency was shown to have a sharp roll-off of nearly 3 percent per 10 percent speed at speeds below design, while rising for speeds up to 15 percent above design value.

3 Turbine efficiency lapse rate with altitude was measured to be worth nearly 1.6 percent from sea level to cruise altitude Reynolds numbers. The results confirmed the mean-line loss system prediction. The three-dimensional viscous code predicted a lapse of 1 percent in expansion efficiency.

4 The efficiency versus speed characteristic was measured to be independent of altitude conditions for the turbine presented.

5 Three-dimensional viscous analysis showed very good agreement in efficiency lapse versus speed, pressure ratio and altitude. The mean-line loss system prediction at off-design performance was shown to agree well at speeds below design. Beyond design speed, the loss system prediction lapse is markedly steeper than measured.

Acknowledgments

The authors wish to thank the personnel from the Test Section Design and Aero Rig departments at Pratt & Whitney Canada for their support throughout the design and testing phases of the program. The authors wish to acknowledge as well the contributions of S. Girgis and P. Hemming in the analysis and interpretation of the cold-flow rig results.

References

Benner, M.W., Sjolander, S.A., and Moustapha, S.H., 1997, "Influence of Leading-Edge Geometry on Profile Losses in Turbines at Off-Design Incidence: Experimental Results and an Improved Correlation," ASME JOURNAL OF TURBOMACHINERY, Vol. 119, pp. 193–200.

Bryce, J.D., Litchfield, M.R., and Leversuch, N.P., 1985, "The Design, Performance and Analysis of a High Work Capacity Transonic Turbine," ASME *Journal of Engineering for Gas Turbines and Power,* Vol. 107, pp. 931–937.

Crow, D.E., Vanco, M.R., Welna, H., and Singer, I.D., 1980, "Results From Tests on a High Work Transonic Turbine for an Energy Efficient Engine," ASME Paper No. 80-GT-146.

Davis, R.L., Shang, T., Buteau, J., and Ni, R-H., 1996, "Prediction of 3D Unsteady Flow in Multi-stage Turbomachinery Using an Implicit Dual Time-Step Approach," AIAA Paper No. 96-2565.

Ewen, J.S., Huber, F.W., and Mitchell, J.P., 1973, "Investigation of the Aerodynamic Performance of Small Axial Turbines," ASME Paper No. 73-GT-3.

Kacker, S.C., and Okapuu, U., 1982, "A Mean Line Prediction Method for Axial Flow Turbine Efficiency," ASME *Journal of Engineering for Power,* Vol. 104, pp. 111–119.

Liu, H.C., Booth, T.C., and Tall, W.A., 1979, "An Application of 3D Viscous Flow Analysis to the Design of a Low Aspect Ratio Turbine," ASME Paper No. 79-GT-146.

Moustapha, S.H., Okapuu, U., and Williamson, R.G., 1987, "The Influence of Rotor Blade Aerodynamic Loading on the Performance of a Highly Loaded Turbine Stage," ASME JOURNAL OF TURBOMACHINERY, Vol. 109, pp. 155–162.

Moustapha, S.H., Kacker, S.C., and Tremblay, B., 1990, "An Improved Incidence Losses Prediction Method for Turbine Airfoils," ASME JOURNAL OF TURBOMACHINERY, Vol. 112, pp. 267–276.

Ni, R.H., and Bogoian, J., 1989, "Prediction of 3D Multi-stage Turbine Flow Field Using a Multiple-Grid Euler Solver," AIAA Paper No. 89-0203.

Okapuu, U., 1974, "Some Results From Tests on a High Work Axial Gas Generator Turbine," ASME Paper No. 74-GT-81.

Vlasic, E.P., Girgis, S., and Moustapha, S.H., 1996, "The Design and Performance of a High Work Research Turbine," ASME JOURNAL OF TURBOMACHINERY, Vol. 118, pp. 792–799.

Walraevens, R.E., and Cumpsty, N.A., 1995, "Leading Edge Separation Bubbles on Turbomachine Blades," ASME JOURNAL OF TURBOMACHINERY, Vol. 117, pp. 115–125.

APPENDIX I

Aerofoil Mean Section Geometries

All coordinates are in mm.

Vane geometry		
x	suction	pressure
-50.70	17.70	17.70
-50.37	19.08	16.40
-50.04	19.52	15.87
-49.05	20.30	15.02
-47.40	20.92	13.55
-45.75	21.21	11.84
-44.10	21.20	9.90
-42.45	20.88	7.74
-40.80	20.23	5.35
-39.15	19.19	2.75
-37.50	17.63	-0.04
-35.85	15.36	-2.97
-34.20	12.17	-5.99
-32.55	8.19	-9.07
-30.90	3.93	-12.21
-29.25	-0.56	-15.41
-27.60	-5.26	-18.70
-25.95	-10.18	-22.08
-24.30	-15.32	-25.60
-22.65	-20.68	-29.26
-21.00	-26.24	-33.16
-19.35	-31.98	-37.52
-18.86	-33.73	-38.55
-18.53	-34.90	-38.68
-18.20	-36.09	-38.65
-17.87	-37.27	-38.41
-17.70	-37.96	-37.96

Blade geometry		
x	suction	pressure
0.00	0.28	0.28
0.14	-0.16	0.65
0.29	-0.46	0.75
0.74	-1.15	0.73
1.50	-1.96	0.37
2.26	-2.51	0.14
3.01	-2.89	-0.00
3.77	-3.14	-0.06
4.53	-3.28	-0.04
5.28	-3.30	0.06
6.04	-3.22	0.22
6.80	-3.02	0.45
7.55	-2.70	0.76
8.31	-2.22	1.14
9.06	-1.57	1.58
9.82	-0.72	2.11
10.58	0.26	2.71
11.33	1.32	3.39
12.09	2.41	4.17
12.85	3.53	5.03
13.60	4.70	6.01
14.36	5.94	7.09
14.59	6.34	7.44
14.74	6.62	7.63
14.89	6.90	7.66
15.04	7.20	7.59
15.12	7.41	7.41

Gas-Path Geometry

All coordinates are in mm.

x	r-hub	x	r-shroud
-72.25	121.90	-11.38	148.46
-65.66	121.06	-6.85	148.47
-59.01	120.94	-2.32	148.48
-52.36	120.87	2.21	148.54
-45.75	120.24	6.75	148.53
-39.16	119.39	11.28	148.52
-32.54	118.80	15.81	148.55
-25.89	118.62	15.81	148.55
-19.25	118.71	15.81	148.55
-12.60	118.80	15.81	148.55
-5.95	118.79	15.81	148.55
0.69	118.54	15.81	148.55
7.26	117.58	15.81	148.55
17.92	115.34	18.67	148.76
29.06	114.99	30.35	149.79
40.11	116.37	41.86	152.03
50.90	119.19	53.03	155.61
56.18	120.95	58.45	157.87

N. W. Harvey
Turbine Engineering.

M. G. Rose
Turbine Engineering.

J. Coupland
Aerothermal Methods,
Rolls-Royce plc,
Derby, United Kingdom

T. V. Jones
University of Oxford,
Department of Engineering Science,
Derby, United Kingdom

Measurement and Calculation of Nozzle Guide Vane End Wall Heat Transfer

A three-dimensional steady viscous finite volume pressure correction method for the solution of the Reynolds-averaged Navier–Stokes equations has been used to calculate the heat transfer rates on the end walls of a modern High Pressure Turbine first-stage stator. Surface heat transfer rates have been calculated at three conditions and compared with measurements made on a model of the vane tested in annular cascade in the Isentropic Light Piston Facility at DERA, Pyestock. The NGV Mach numbers, Reynolds numbers, and geometry are fully representative of engine conditions. Design condition data have previously been presented by Harvey and Jones (1990). Off-design data are presented here for the first time. In the areas of highest heat transfer, the calculated heat transfer rates are shown to be within 20 percent of the measured values at all three conditions. Particular emphasis is placed on the use of wall functions in the calculations with which relatively coarse grids (of around 140,000 nodes) can be used to keep computational run times sufficiently low for engine design purposes.

Introduction

The aeroengine designer faces a constant drive to improve performance and reliability, typically at ever-increasing turbine entry temperatures. As a result the peripheral areas of turbine components such as platforms and shrouds now require the detailed attention that aerofoils have always received. This includes the need to predict accurately the heat transfer to the end walls of turbine components—made all the more difficult by the presence of highly complex, three-dimensional "secondary" flows in these regions.

Considerable research has been undertaken already into the secondary flow and heat transfer patterns experienced on turbine stator and rotor end walls. The review of secondary flows by Sieverding (1985) remains an excellent reference. There is no single review of the experimental investigations into end wall heat transfer, but a summary of some is given by Harvey and Jones (1990). More recently, Chana (1992) investigated the effects of end wall profiling on heat transfer and Spencer et al. (1996) presented very detailed measurements made using the liquid crystal technique.

In parallel with this, CFD codes have been developed for predicting heat transfer rates to all the surfaces of turbine components. Typical results have been those of Hah (1989) and Ameri and Steinthorsson (1996). Both obtained good results using grids with more than 600,000 nodes, resolving the boundary layers down to y^+ values of around 1. Although these tools are increasingly accurate, the need for large grids and complex turbulence models still makes them computationally demanding.

The work presented here has concentrated on providing the turbine designer with a tool for the prediction of end wall heat transfer of acceptable accuracy (target ± 20 percent, based on engine lifing requirements) but also sufficiently fast to be used in the design cycle. Typically an analysis could be completed on a workstation within a day, or even overnight. A three-dimensional viscous CFD code already much used within Rolls-Royce, see Chew et al. (1996), was used as the calculation method, but with a relatively coarse grid and wall functions, instead of modeling the laminar sublayer directly.

Key to the success of this approach is the need to validate such a tool against experiment, and over a range of operating conditions. For that purpose measurements of surface heat transfer rates have been made on the end walls of an NGV in annular cascade at three different conditions—a design point representative of a modern aero gas turbine, one condition at elevated Mach number ("M+") and one at elevated Reynolds number ("Re+"). Comparisons between calculation and measurement are only presented for the hub end wall.

Experimental Facility and Technique

Full details of the experimental facilities and the technique for acquiring the heat transfer measurements are given in Harvey (1991) and Harvey et al. (1989). The NGV was tested in an annular cascade in the Isentropic Light Piston Facility at DERA, Pyestock. The ILPF enables short-duration steady flow to be generated through a working section for up to one second at engine representative levels of M, Re, and Tg/Tw. The theory is given by Jones et al. (1973) and Schultz et al. (1977) and the facility is described by Brooks et al. (1985). A fast-acting plug valve allows the flow to be established in under 50 ms, giving a near step change in the external conditions of the vanes, which are initially at ambient temperature. Thin film gages painted onto machinable glass ceramic vanes measure their surface temperature response to the change in gas temperature. This is converted to heat transfer rate by an electrical analogue of the one-dimensional transient heat conduction process (Oldfield et al., 1982).

Figure 1 shows the working section of the ILPF, which included an inlet contraction to the NGV representative of an engine combustion chamber exit nozzle. Instrumented vanes, with pressure tappings or thin film gages, were held in removable cassettes at three positions around the annulus. Figure 2 shows the detailed locations of the pressure tapping and thin film gage centers on the hub end wall (104 gages in total). Typical gage dimensions were 4 × 0.5 mm.

Upstream of the inlet contraction, the annulus boundary layer was bled off through perforated walls. Inlet turbulence was generated by radial bars at the start of the contraction. The inlet

Contributed by the International Gas Turbine Institute and presented at the 43rd International Gas Turbine and Aeroengine Congress and Exhibition, Stockholm, Sweden, June 2–5, 1998. Manuscript received by the International Gas Turbine Institute February 1998. Paper No. 98-GT-66. Associate Technical Editor: R. E. Kielb.

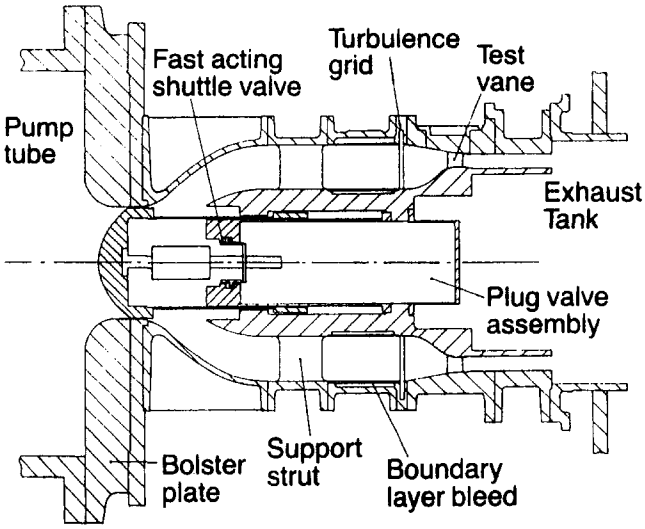

Fig. 1 General assembly of experimental working section

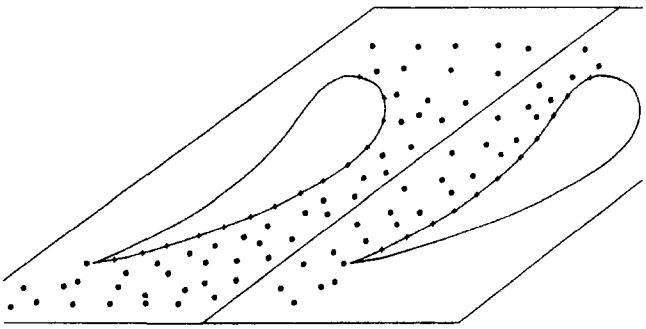

+ Fillet Radius Thin Film Gauges Centres
o Common Pressure Tapping and Thin Film Gauge Centres

Fig. 2 Hub end wall instrumentation locations

boundary layer was measured using pitot probes and thermocouples one axial chord upstream of the vane. The inlet temperature was measured using fast-response thermocouples and the turbulence intensity using a constant-temperature hot-wire anemometer.

The overall uncertainty on the experimental heat transfer results (h and Nu) was ±10 percent. The experimental details were as follows:

Blade dimensions	
True chord	70.1 mm
Axial chord	37.5 mm
Mean radius	277.0 mm
Span (at trailing edge)	37.4 mm
Pitch at hub trailing edge	50.7 mm
Test conditions	
Tg/Tw	1.29 ± 0.004
Hub inlet (design): δ	2.7 percent span
Momentum thickness Re	515
Casing inlet (design): δ	2.3 percent span
Momentum thickness Re	810
Inlet Tu (NGV leading edge plane)	6%
Design midheight exit M	0.885 ± 0.009
Design midheight exit Re	2.57 ± 0.03 × 10^6
"M+" midheight exit M	1.102 ± 0.007
"M+" midheight exit Re	2.58 ± 0.02 × 10^6
"Re+" midheight exit M	0.885 + 0.006
"Re+" midheight exit Re	3.52 ± 0.03 × 10^6

Calculation Method

The computational method was a standard turbomachinery CFD code used within Rolls-Royce. The code is a steady flow solver using a pressure correction method based on the algorithm of Moore (1985). The important feature of this algorithm is the use of upwinded control volumes for the momentum and rothalpy equations, thus allowing the equations to be discretized with second-order accuracy without the need to introduce smoothing to achieve numerical stability. A minimum of numerical mixing is essential for a code that is to be used for estimating aerodynamic losses and heat transfer. The iterative method used is based on the SIMPLER pressure correction scheme. Stability in transonic regions is achieved using an upwinded pressure in the calculation of density. The calculations use a structured "letter-box" type of body-fitted **H**-grid, which enables accurate representation of the full blade shape. Previous work has shown the capability of this numerical method for the prediction of turbomachinery aerodynamics and heat transfer, e.g., Moore and Gregory-Smith (1996) and Robinson et al. (1989).

Grid Details. The structured grids for the turbine NGV test case considered here were first created on the blade-to-blade axial-tangential plane. The midheight grid is illustrated in Fig. 3. These Q3D meshes are then stacked in the spanwise direction to produce the full three-dimensional grid. The grid used here consisted of 95 axial and 41 tangential points, and is stacked over 37 spanwise planes from hub to tip, giving a total of 144,115 points. The y^+ values were in the range 10–30 for the end walls and 10–45 for the aerofoil.

Nomenclature

c = true chord
c_p = gas specific heat capacity at constant pressure
CFD = Computational Fluid Dynamics
DERA = Defence Evaluation and Research Agency
E = turbulence model constant
F_{vd} = Van-Driest damping function
H^+ = normalized near-wall temperature
h = heat transfer coefficient (based on $[Tg - Tw]$)
ILPF = Isentropic Light Piston Facility
k = thermal conductivity
L = turbulence model length scale
M = Mach number
NGV = Nozzle Guide Vane
Nu = Nusselt number = hc/k_g
Re = Reynolds number = $\rho Vc/\mu$
S = mean flow strain rate
Tg = free-stream stagnation temperature
Tu = turbulence intensity
Tw = surface wall temperature
T = static temperature
U = mean flow velocity
U^+ = normalized near-wall velocity = U/U_τ
U_τ = skin friction velocity
V = cascade midheight exit velocity
y = distance from wall
y^+ = near-wall Reynolds number = $\rho U_\tau y/\mu$
δ = boundary layer thickness
κ = turbulence model constant
λ = turbulence model constant
μ = viscosity
μ_t = turbulent viscosity
ρ = gas density
σ = Prandtl number
σ_t = turbulent Prandtl number
τ_w = wall shear stress

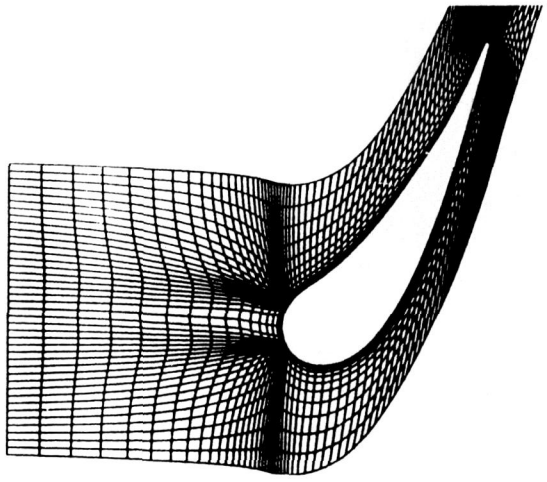

Fig. 3 Midheight blade-to-blade calculation grid

Boundary Conditions and Convergence Criteria. Uniform, free-stream inlet total pressure and temperature profiles were specified together with the measured velocity and total temperature boundary layers at both hub and casing inlet. These were measured at the design condition only and were deduced at the other two conditions, assuming constant inlet momentum thickness Reynolds number. An isothermal wall condition was specified with fully turbulent boundary layers on the end walls. The exit condition was a circumferentially averaged static pressure profile one axial chord downstream, interpolated between the measured end wall values assuming radial equilibrium.

Acceptable convergence was achieved when the residuals in all three velocity components, the static pressure and the total temperature had fallen by at least two orders of magnitude from their initial values. This was typically achieved after 100 iterations.

Turbulence Model. An algebraic mixing length model was used. Wall functions were adopted to represent the near-wall variation of the velocity and temperature boundary layers. The mixing length model is based on Prandtl's formulation for the length scale within a shear layer:

$$L = \min(\kappa y, \lambda\delta) \tag{1}$$

where $\kappa = 0.41$ and $\lambda = 0.08$ and δ is the overall thickness of the shear layer. Outside the shear layer the effect of the free-stream turbulence and mixing is represented by a free-stream length scale. For compressor blade calculations this length scale is generally set to be typically 3 percent of the blade chord, but for turbine blade calculations, such a value generates excessive shear stresses in the free-stream and resultant suppression of the secondary flows. Thus, as also reported by Moore and Gregory-Smith (1996), the free-stream length scale is here set to a reduced value corresponding to about 0.03 percent of the blade chord. This value is comparable with the blade trailing edge boundary layer length scales. The turbulent viscosity is then set using

$$\mu_t = \rho L^2 S F_{vd}^2 \tag{2}$$

where S is the magnitude of the strain rate and F_{vd} is the standard Van-Driest damping function, dependent on the wall shear stress, applicable in the near wall viscous and logarithmic region of the boundary layer.

Turbulence Model Wall Functions. The wall functions are based on a generalized expression for the law of the wall, see White (1991) or Spalding and Patankar (1967),

$$y^+ = U^+ + (1/E)\{\exp(\kappa U^+) - 1 - \kappa U^+ - \tfrac{1}{2}(\kappa U^+)^2 - \tfrac{1}{6}(\kappa U^+)^3\} \tag{3}$$

where U^+ and y^+ are the nondimensional velocity and Reynolds number at the near-wall grid point based on the distance from the wall and the skin friction velocity $U_\tau = (\tau_w/\rho)^{1/2}$, and $E = 8.8$, $\kappa = 0.41$.

This wall function blends the velocity profile smoothly between the linear region of the viscous sublayer and logarithmic region of the boundary layer, incorporating the buffer layer between these zones. The wall function is used to give the wall shear stress as a function of the near-wall grid point flow velocity and viscosity. The nonlinear equation (3) for the wall shear stress is solved at each iteration of the flow solver using a Newton–Raphson procedure, that converges reliably based on a good initial guess. This approach adds only a very small overhead to the whole flow calculation procedure.

A similar approach is used for the temperature boundary layer wall function. The temperature is nondimensionalized using

$$H^+ = \rho U_\tau c_p (T_{rw} - T_{rf})/E_w \tag{4}$$

where T_{rw} and T_{rf} are the recovery temperatures at the wall and flow points respectively and E_w is the total energy flux at the wall (heat plus work done). The recovery temperature is obtained using

$$T_r = T + HU^2/(2c_p) \tag{5}$$

where H is the recovery factor, set here equal to 0.9. The temperature wall function is then

$$y^+ = (1/\sigma)H^+ + (1/E')\{\exp(\kappa H^+/\sigma_t) - 1 - \kappa H^+/\sigma_t - \tfrac{1}{2}(\kappa H^+/\sigma_t)^2 - \tfrac{1}{6}(\kappa H^+/\sigma_t)^3\} \tag{6}$$

where

$$E' = E\exp(\kappa P_j) \tag{7}$$

and P_j is the so-called Jayatillaka term, see Spalding and Patankar (1967),

$$P_j = 9.24(\sigma/\sigma_t)^{-1/4}(\sigma/\sigma_t - 1) \tag{8}$$

Both these wall functions are valid for values of y^+ up to the edge of the logarithmic region, say 100 to 200 depending on the magnitude of the local pressure gradient. Of particular importance is the ability to apply the wall function model in the buffer layer region, say around $y^+ = 20$, and to give good results irrespective of the y^+ value itself, which inevitably varies substantially around all the surfaces in a three-dimensional turbine blade calculation. Although not reported in detail here, a grid dependency study found that the heat transfer results were not sensitive to near wall spacing for y^+ values up to 50.

Results: Static Pressure Field

The aerofoil and end wall static pressure fields are generally well calculated, especially in the regions of subsonic flow. An example is shown in Fig. 4, for the hub end wall at the design condition. The aerofoil is aft-loaded with the peak M at the geometric throat and diffusion on the back surface down to the trailing edge. The code slightly overestimates the peak M on the hub endwall on the late suction surface at 1.1, compared to 1.05 in the data. There is strong acceleration of the flow through the passage, typical of a first-stage stator.

The most significant difference between calculation and measurement is on the aerofoil at the M+ condition. Figure 5 compares the highest values of the measured and calculated M, which are at the hub section (10 percent span). The code calculates a shock late on the suction surface, up the whole of the vane span. There is some evidence of oscillations in the calcula-

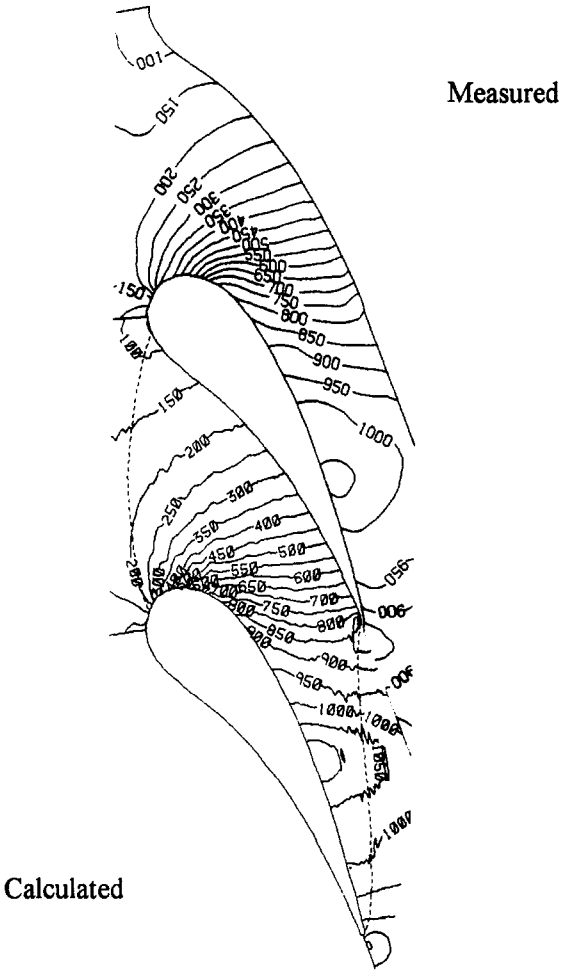

Fig. 4 Comparison of measured and calculated hub end wall Mach numbers (×1000): design condition

tion at these high M levels. This is not unexpected given the low level of smoothing in the calculation. The shock position is also sensitive to boundary layer development, and only a small error could cause the size of shift seen here. In addition the shock will have been moving in the experiment and thus its effect will have been smeared out in the measured surface static pressures.

Results: Surface Heat Transfer

Figure 6 compares contours of measured and calculated Nu on the hub end wall at the three conditions studied. It should

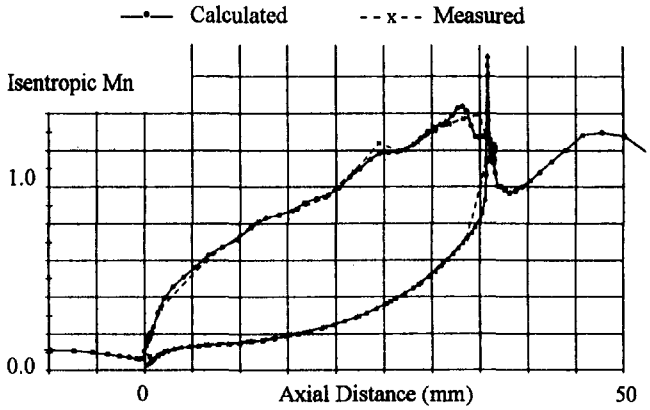

Fig. 5 10 percent aerofoil height Mach numbers; M+ condition

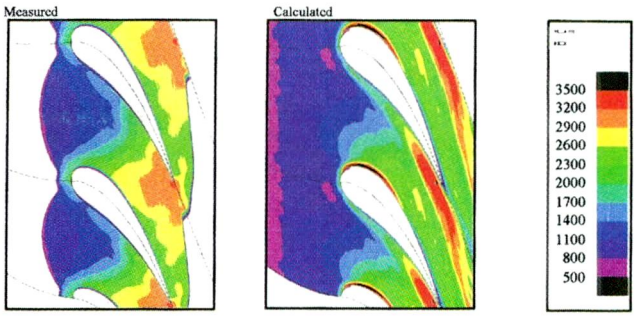

Fig. 6(*a*) Hub end wall Nusselt number: design condition

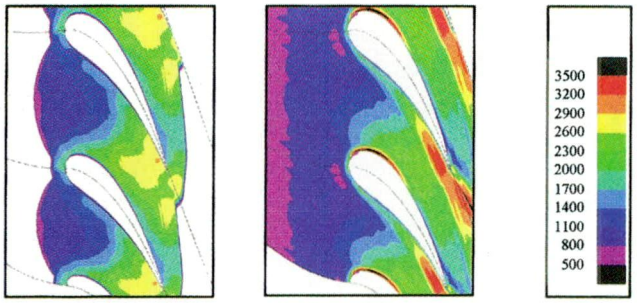

Fig. 6(*b*) Hub end wall Nusselt number: M+ condition

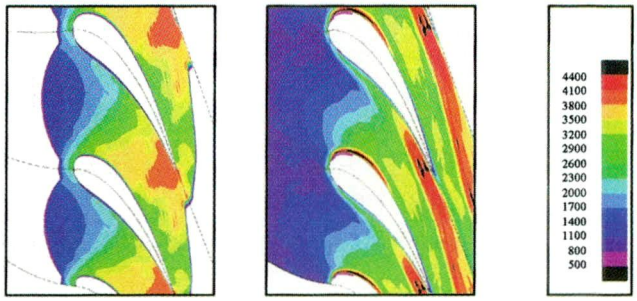

Fig. 6(*c*) Hub end wall Nusselt number: Re+ condition (note different scale)

be noted that the measured values are significantly smeared. The heat transfer rate measured by each thin film gage is averaged over its surface area, giving a "point" value, which is taken to apply at the gage center. These values are then interpolated using a quadratic surface fitting routine onto the calculation grid before contour plotting.

The general features of the measured end wall heat transfer patterns are as follows:

1 Increased heat transfer at the leading edge, not well resolved due to the relatively large size of the thin film gages.

2 A characteristic **V** shape in the contours at the inlet with a region of lower heat transfer intruding into the passage. After this the heat transfer rate increases in the passage up to the throat as the flow accelerates. A region of high heat transfer on the pressure side near the trailing edge extends into the passage, but falls markedly in the suction side back surface/end wall corner.

3 There is a strong effect of Reynolds number on the heat transfer rate. It roughly correlates with the Re ratio to the power of 0.8, rather than 0.5, supporting the assumption in the CFD model of fully turbulent end wall boundary layers.

Looking at the calculations it can be seen that:

(*a*) The leading edge heat transfer rate is elevated, but this is much more localized than in the interpolated measurements.

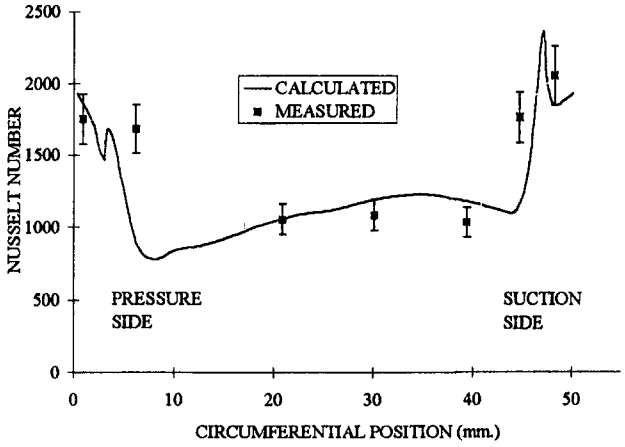

Fig. 7(*a*) Hub end wall Nusselt number at "Inlet" (0 percent axial chord): design condition

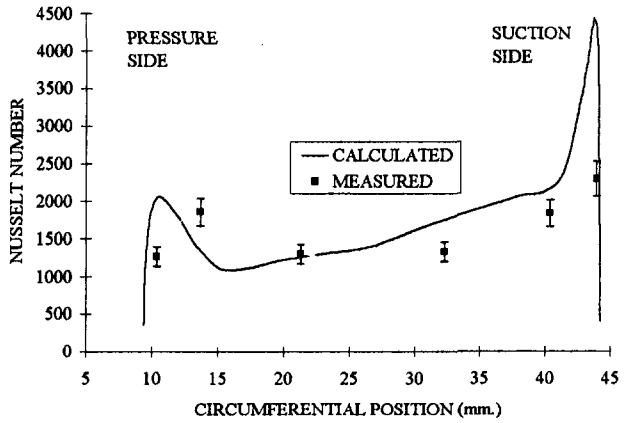

Fig. 7(*b*) Hub end wall Nusselt number at 24 percent axial chord: design condition

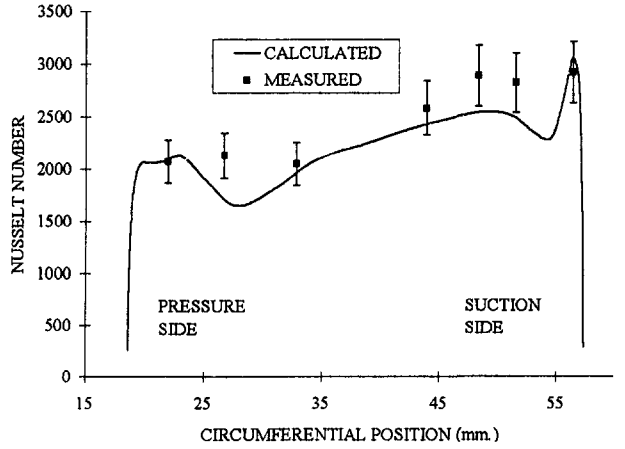

Fig. 7(*c*) Hub end wall Nusselt number at 55 percent axial chord: design condition

(*b*) The V shape in the contours at the inlet is present, but is closer to the pressure side than in the measurements.
(*c*) High heat transfer is calculated near the pressure side trailing edge corner, extending across the passage with a lower value in the suction side back surface/end wall corner.
(*d*) The strong effect of Re on heat transfer is reproduced.
(*e*) A region of very high, and highly localized, heat transfer is calculated on the suction surface shoulder.

Discussion. The biggest difference between calculation and measurement is the region of high heat transfer calculated near the suction side shoulder. Although there is no evidence for this

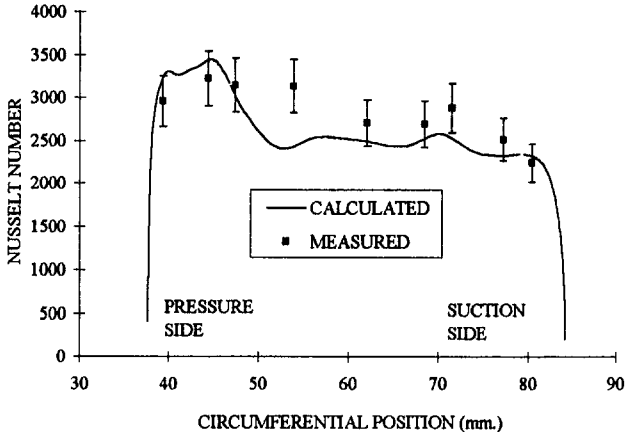

Fig. 7(*d*) Hub end wall Nusselt number at 87 percent axial chord: design condition

in the measured data, the thin film gage technique is very limited for capturing such features. Spencer et al. (1996), using the full-coverage liquid crystal technique on a similar NGV, did find such a region in their data on the casing end wall. In addition, the NGV geometry had a 2 mm fillet radius in the aerofoil end wall corner, whereas the CFD model had a sharp corner. It is thus inconclusive as to whether this discrepancy is due to limitations in the CFD model or the experimental data.

To help quantify the errors in the calculated end wall heat transfer rates, the values on the hub at the design condition have been plotted along approximately circumferential grid lines at four axial locations (Inlet, 24, 55, and 87 percent axial chord). Also shown are the measured "point" values of the gages that intersect these lines together with ±10 percent error bars. The Nu values are plotted in Figs. 7(*a–d*) respectively, and the locations of the lines in Fig. 8.

At Inlet and at 24 percent chord there is a reasonable match between measurement and calculation, but the largest errors are outside the ±20 percent target. The discrepancies are as much due to the uncertainties in the gage location as to the uncertainties in the measured values. However, the high heat transfer rate on the suction surface shoulder is certainly not found in the measured data.

At 55 percent axial chord calculation and measurement are well matched, with the code generally under estimating the heat transfer.

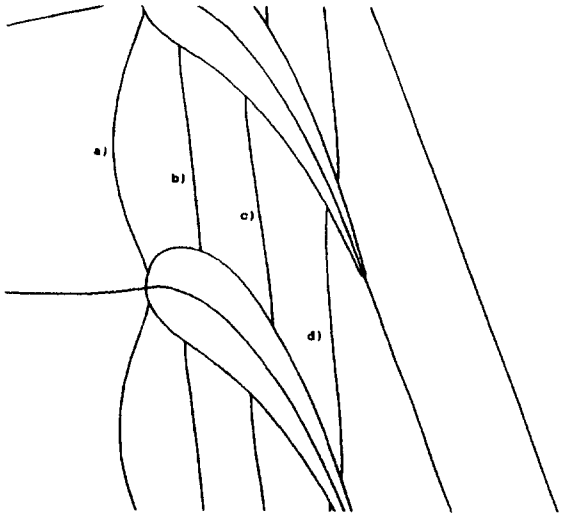

Fig. 8 Location of hub end wall line plots of Fig. 7

At 87 percent axial chord the area of high heat transfer extends farther from the pressure side in the measurements than is calculated. The general conclusion is that the heat transfer levels are well calculated with some detailed differences in the patterns. These can be explained by considering the effects of the secondary flows.

Downstream of the 24 percent axial chord location, in the region of highest heat transfer, measurement, and calculation are within 20 percent of each other. Accuracy in this region is of key interest to the designer, while the larger errors in the low heat transfer inlet region are of much less importance.

Effect of Secondary Flows. Referring to the simple model of the end wall secondary flows of Fig. 9, taken from Takeishi et al. (1990), their effects on the end wall heat transfer are as follows:

(*a*) The inlet boundary layer rolls up at the leading edge into a horseshoe vortex. The high heat transfer at the leading edge is at the saddle point of attachment of this vortex.

(*b*) There are two legs of the horseshoe vortex. That on the pressure side is overturned by the cross-passage pressure gradient, along with the rest of the inlet boundary layer, which then rolls up to form the passage vortex. A separation line on the end wall marks the limit of the penetration of the bottom of the inlet boundary layer into the passage. This separation line lies at the pressure side edge of the **V**-shaped region of the heat transfer contours in the inlet region.

(*c*) Upstream of the separation line, lateral convergence of the boundary layer results in its thickening, which has the effect of reducing the heat transfer rate, or at least mitigating the increase due to the thinning of the boundary layer as it accelerates in the passage.

(*d*) Downstream of the separation line, a new boundary layer forms in the pressure side end wall corner. Since the new boundary layer is thin, the heat transfer is high and it increases, getting nearer to the trailing edge as the free-stream flow velocities increase (see the M plots of Fig. 4).

(*e*) As this new boundary layer is swept toward the suction side, it grows, but also moves into a region of higher free-stream velocity. Thus overall the heat transfer remains high. In the suction side back surface/end wall corner the passage vortex above the boundary layer may act to additionally thicken the boundary layer, reducing the heat transfer further and giving the relatively low values locally.

(*f*) Downstream of the passage, the new end wall boundary layer continues growing, enhanced by a slight diffusion of the flow, with a corresponding drop in the heat transfer.

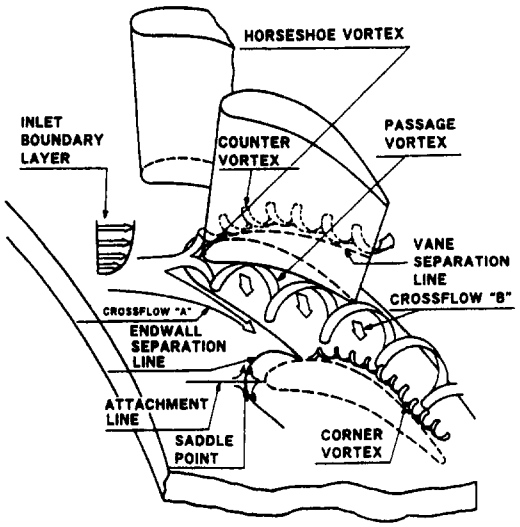

Fig. 9 End wall secondary flow model after Takeishi et al. (1990)

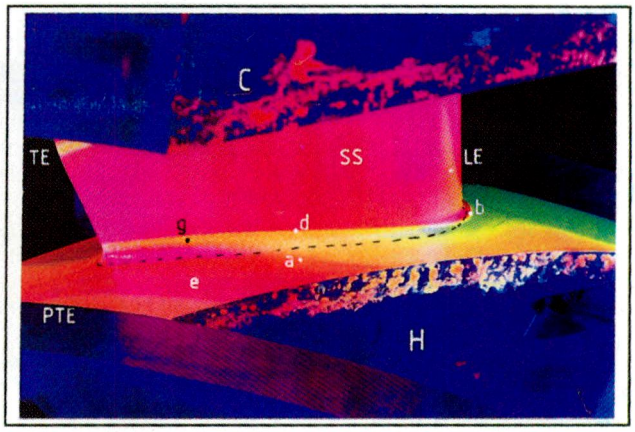

Fig. 10(*a*) Hub end wall and suction surface experimental flow visualization: design condition

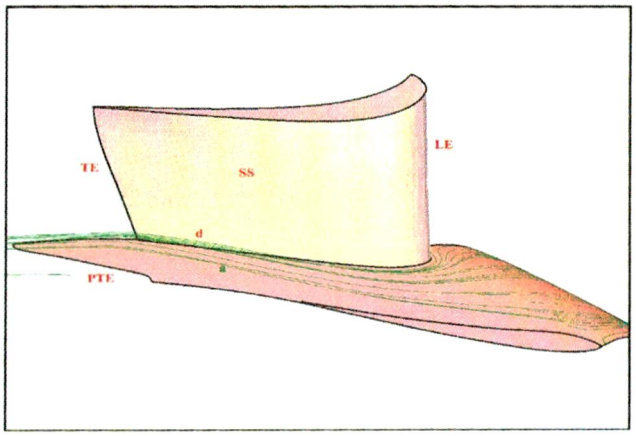

Fig. 10(*b*) Hub end wall and suction surface calculated flow streamlines: design condition

It is clear that a key difference between calculation and measurement is that the calculated secondary flow effects on the end wall are underestimated. In additional running of the experiment, end wall flow visualization was obtained at adiabatic design conditions and the calculation rerun at this condition. Results of the two are compared in Fig. 10.

Figure 10(*a*) shows an NGV, which initially had the platform upstream of the leading edge painted with a green fluorescent dye in a silicon oil and paraffin suspension. The rest of the aerofoil and end walls were similarly painted with a red dye. The movement of the green dye over the surfaces painted red during the run, which shows as yellow/orange areas, highlights the end wall secondary flows. Only half an end wall is shown in Fig. 10(*a*), together with the suction surface (labeled 'SS') of one aerofoil (with leading edge "LE"). The intersection of the fillet radius with the end wall is shown as a black dashed line. The separation line between the overturned inlet boundary layer and the new one (occupying region "*e*") is labeled "*a*." This can be seen to have moved fully onto the aerofoil suction surface well before the trailing edge ("TE"). The end wall boundary layer separates off the aerofoil surface along line "*d*."

By contrast, Fig. 10(*b*) shows that the calculated separation line only just reaches the aerofoil by the trailing edge. The cross-passage migration of the boundary layer is significantly underestimated by the code and, as a result, the extent of the region of high heat transfer starting at the pressure side near the trailing edge.

Some work was done to try to increase this migration by modifying the turbulence model, principally reducing the vis-

cosity in the near-wall region. However, although this was found to improve the secondary flows, it significantly reduced the heat transfer levels. The results shown here represent the best compromise found between calculation of the secondary flows and the heat transfer rates. It is likely that for components with stronger secondary flows (due to lower aspect ratio or higher turning) there would be larger errors in the calculated heat transfer due to the under estimate of these flows.

It appears that one way to further improve the calculation is to reduce the Reynolds stresses in the boundary layer in the cross-stream direction (increasing the secondary flow migration) while maintaining the Reynolds stresses in the direction normal to the surface (to maintain the heat transfer levels). This points in the direction of anisotropic turbulence models, as suggested by Rotta (1979) and Craft et al. (1995).

Conclusions

A method for the prediction of NGV end wall heat transfer rates using a steady viscous finite volume pressure correction CFD code with wall functions has been successfully demonstrated. In the areas of highest heat transfer it is accurate to within ± 20 percent of measurement over a range of operating conditions, notwithstanding the relatively unsophisticated form of turbulent boundary layer modeling used.

A calculation can be performed in one day on a workstation. The method is now ready for use by the turbine designer.

Further improvements to the modeling should be pursued. In particular the use of anisotropic turbulence models should be investigated. More experimental data are required to resolve very detailed features of the end wall heat transfer patterns.

Acknowledgments

This work has been carried out with the support of Rolls Royce plc and the Defence Research Agency (MoD and DTI), Pyestock. The authors would like to thank them for funding it and their permission to publish this paper. The technical assistance of Mr. K. J. Walton, Mr. I. J. Taylor and Mr. L. Philips are very much appreciated.

References

Ameri, A. A., and Steinthorsson, E., 1996, "Analysis of gas turbine rotor blade tip and shroud heat transfer," ASME Paper No. 96-GT-189.

Brooks, A. J., Colbourne, D. E., Wedlake, E. T., Jones, T. V., Oldfield, M. L. G., Schultz, D. L., and Loftus, P. J., 1985, "The isentropic light piston annular cascade facility at RAE Pyestock," AGARD CP 390, Paper 31.

Chana, K. S., 1992, "Heat transfer and aerodynamics of high rim speed turbine nozzle guide vane with profiled end-walls," ASME Paper No. 92-GT-243.

Chew, J. W., Taylor, I. J., and Bonsell, J. J., 1996, "CFD developments for turbine blade heat transfer," 3rd Int. Conf. Computers in Reciprocating Engines and Gas turbines, I.Mech.E. Paper No. C499-035.

Craft, T. J., Launder, B. E., and Suga, K., 1995, "Development and Application of a Cubic Eddy-Viscosity Model of Turbulence," *Int. J. Heat and Fluid Flow,* Vol. 17, pp. 108–115.

Hah, C., 1989, "Numerical study of three-dimensional flow and heat transfer near the endwall of a turbine blade row," Paper No. AIAA-89-1689.

Harvey, N. W., Wang, Z., Ireland, P. T., and Jones, T. V., 1989, "Detailed heat transfer measurements in linear and annular cascades in the presence of secondary flows," AGARD PEP 74B, Paper No. 24.

Harvey, N. W., and Jones, T. V., 1990, "Measurement and calculation of end wall heat transfer and aerodynamics on a nozzle guide vane in annular cascade," ASME Paper No. 90-GT-301.

Harvey, N. W., 1991, "Heat transfer on nozzle guide vane end walls," University of Oxford, DPhil Thesis.

Jones, T. V., Schultz, D. L., and Hendley, A., 1973, "On the Flow in an Isentropic Light Piston Tunnel," ARC R&M 3731.

Kato, M., and Launder, B. E., 1993, "The Modelling of Turbulent Flow Around Stationary and Vibrating Square Cylinders," *Proc. 9th Symp. Turbulent Shear Flows,* 10-4.

Oldfield, M. L. G., Jones, T. V., and Schultz, D. L., 1978, "On-line computer for transient turbine cascade instrumentation," *IEEE Trans. AES,* 14:738.

Moore, H., and Gregory-Smith, D. G., 1996, "Transition Effects on Secondary Flows in a Turbine Cascade," ASME Paper No. 96-GT-100.

Moore, J. G., 1985, "Calculation of 3D Flow without Numerical Mixing," AGARD-LS-140 on 3D Computation Techniques Applied to Internal Flows in Propulsion Systems, pp. 8.1–8.15.

Oldfield, M. L. G., Burd, H. J., and Doe, N. G., 1982, "Design of wide bandwidth analogue circuits for heat transfer instrumentation in transient tunnels," 16th Symposium of ICHMT, Hemisphere pub., Dubrovnik, I.

Robinson, C. J., Northall, J. D., and McFarlane, C. W. R., 1989, "Measurement and Calculation of the Three-Dimensional Flow in Axial Compressor Stators, With and Without End Bends," ASME Paper No. 89-GT-6.

Rotta, J. C., 1979, "A Family of Turbulence Models for Three-Dimensional Boundary Layers," Turbulent Shear Flows 1, pp. 267–278, Springer-Verlag.

Schultz, D. L., Jones, T. V., Oldfield, M. L. G., and Daniels, L. C., 1977, "A new transient cascade facility for the measurement of heat transfer rate," AGARD CP 229.

Sieverding, C. H., 1985, "Secondary flows in straight and annular turbine cascades. Ucer, Stow and Hirsch," *Thermodynamics & Fluids of Turbomachinery,* NATO, Vol. II, pp. 621–624.

Spalding, D. B., and Patankar, S. V., 1967, *Heat and Mass Transfer in Boundary Layers,* Morgan-Grampian.

Spencer, M. C., Jones, T. V., and Lock, G. D., 1996, "Endwall heat transfer measurements in an annular cascade of nozzle guide vanes at engine representative Reynolds and mach numbers," *Int. J. Heat and Fluid Flow 17,* pp. 139–147.

Takeishi, K., Matsuura, M., Aoki, S., and Sato, T., 1990, "An experimental study of heat transfer and film cooling on low aspect ratio turbine nozzles," ASME JOURNAL OF TURBOMACHINERY, Vol. 112, pp. 488–496.

White, F. M., 1991, *Viscous Fluid Flow,* McGraw-Hill, New York.

Controlling the Secondary Flow in a Turbine Cascade by Three-Dimensional Airfoil Design and Endwall Contouring

A. Duden
Institut für Strahlantriebe,
Universität der Bundeswehr München,
D-85577 Neubiberg,
Federal Republic of Germany

I. Raab
MTU München GmbH,
Daimler-Benz Aerospace,
D-80995 München,
Federal Republic of Germany

L. Fottner
Institut für Strahlantriebe,
Universität der Bundeswehr München,
D-85577 Neubiberg,
Federal Republic of Germany

A highly loaded turbine cascade has been redesigned with the objective to reduce the secondary flow by applying endwall contouring and three-dimensional airfoil design in the endwall regions. The overall loading and the axial area ratio of the cascade have been kept constant. With the tools of a three-dimensional design environment, a systematic study has been carried out regarding several features of the endwall pressure distribution and their influence on the secondary flow. Two optimized configurations have been investigated in a high-speed cascade wind tunnel. The flow field traverses showed improvements concerning the radial extent of the secondary flow and a decrease in secondary loss of 26 percent. Unfortunately this reduction was counterbalanced by increased profile losses and higher inlet losses due to increased blockage. The striking feature of the cascade with endwall contouring and three-dimensional airfoil design was a significant reduction of the exit flow angle deviations connected with the secondary flow. The predictions obtained by the three-dimensional Navier–Stokes solver TRACE_S showed a remarkable agreement with the experimental results.

Introduction

The continual development of advanced axial turbines toward a higher degree of stage loading increases the three-dimensional flow phenomena. Hence, a considerable portion of the efficiency debit is due to secondary flow not only in low-aspect-ratio high-pressure turbines but also in highly loaded low-pressure turbines. To account for and subsequently control the effects of secondary flow, the designer needs to have a detailed knowledge of the impact of aerodynamic and geometric parameters. A lot of publications focus on this subject. In the following some of the investigations concerning the shape of the airfoil and the meridional flowpath will be summarized.

Secondary flow in itself is a three-dimensional flow pattern. But nevertheless the two-dimensional shape of the airfoil has a strong influence. Weiß and Fottner (1995) tested two linear turbine cascades with the same overall loading but different load distributions. The cascade with a rear-loaded pressure distribution was observed to result in smaller secondary losses than the frontloaded cascade. As well, it is known from investigations regarding the influence of incidence (e.g., Hodson and Dominy, 1987) and from the authors' previous studies concerning the effect of endwall taper (Duden and Fottner, 1997) that an increased loading, especially in the front part of the cascade, strongly increases the secondary flow.

Investigations of Weiß (1993) with two linear turbine cascades, one with very thick airfoils and the second with extremely thin airfoils, featuring the same overall loading and load distribution, showed distinctly higher secondary losses for the latter cascade. The lack of a horseshoe vortex upstream of this cascade was suggested to be the main reason for the higher secondary losses, as the endwall cross-channel pressure gradient could directly affect the undisturbed and hence relatively thick inlet boundary layer. However, the overall velocity level in the cascade with thin airfoils was noticeably lower and was also considered as a possible cause for the observed difference in the secondary losses.

Concerning the radial stacking of turbine vanes, Filippow and Wang (1964) were the first to describe the application of tangential lean to control the spanwise distribution of the losses with a radial component of the airfoil force.

Wang and Han (1995) reported that bowed airfoils with compound positive lean (pressure side faces the endwalls at both ends of the airfoil) reduced the total loss in a turbine cascade with a low turning angle. This was explained by the reduction of the aerodynamic loading at the endwalls and the subsequent weakening of the secondary flow. In a cascade with a higher turning angle negative compound lean (suction side facing the endwalls) was found to reduce the total loss mainly by reducing a strong adverse axial pressure gradient in the inlet region of the cascade. This delayed the three-dimensional separation of the inlet boundary layer. In addition the increased loading at the endwalls in combination with a decreased loading at midspan built up a pressure gradient directed to the endwalls. Thus, the passage vortices did not merge at midspan as they did in the reference cascade with straight airfoils. As a consequence, the midspan loss was significantly decreased. However, the endwall loss of the bowed cascade was higher due to the increased pitchwise pressure gradient on the endwalls.

Endwall contouring was introduced by Deich et al. (1960) as a reduction of the airfoil span between leading edge and trailing edge at the tip. It was found that the meridional profiling reduced the losses, which was explained by a reduction of the velocity in the region of highest turning and by a shift of the diffusion part of the suction side pressure distribution toward the trailing edge. In addition, the more favorable pressure gradient due to the meridional contraction reduced the growth of the airfoil surface boundary layers and endwall boundary layers and was responsible for a major part of the benefit. The current study, however, was performed with a specific focus on low-pressure turbines, which are in general subject to a strong meridional divergence of the flow

Contributed by the International Gas Turbine Institute and presented at the 43rd International Gas Turbine and Aeroengine Congress and Exhibition, Stockholm, Sweden, June 2–5, 1998. Manuscript received by the International Gas Turbine Institute February 1998. Paper No. 98-GT-72. Associate Technical Editor: R. E. Kielb.

channel. A meridional shaping that results in channel convergence over the axial length of the airfoil row is not significant in this kind of turbine. Thus, only investigations in which the outlet-to-inlet area ratio of the cascade was not changed by the endwall contour are considered here.

Atkins (1987) tested several endwall contours in a linear turbine cascade. Four of the configurations had an outlet-to-inlet area ratio of one. The other four configurations had a converging outer endwall. Comparing the results with the straight endwalls and the best contoured endwall, a reduction of 4.8 percent in cascade loss (total loss minus inlet loss) was achieved concerning the cascades with a converging outer endwall. In this case the contour was similar to the one described by Deich et al. (1960). In the case of the cascades with the same span at the trailing edge and the leading edge, a reduction of 7.7 percent in cascade loss was reported. This was obtained by means of a bulge into the flow channel in the last third of the axial length.

Schnaus and Fottner (1997) investigated an endwall contour on an inclined outer wall of a linear turbine cascade. The contour resulted in a front-loaded pressure distribution at the endwall, which led to a reduced radial pressure gradient and hence to a slightly reduced radial movement of the secondary flow. Exit flow angle deviations were modestly decreased while the secondary losses were not affected.

Haas (1982) and Haas and Boyle (1984) incorporated a straight converging and an **S**-shaped converging outer wall in the lightly loaded stator of a test turbine. The **S**-shape was designed using the data of Deich et al. (1960). Comparing the two configurations, no significant change in the loss production was observed. The radial distribution of the stator exit flow angles showed a higher degree of overturning near the tip of the contoured stator. This led to slightly lowered local stage efficiencies in the tip region.

A similar investigation on a highly loaded stator was carried out by Moustapha and Williamson (1985, 1987). Without the rotor they observed hub flow separation at the stator with the straight converging outer wall. Consequently it showed a 7 percent higher loss than the contoured build. In contrast with the rotor operating, the hub separation was suppressed and the loss was up to 15 percent lower than downstream of the contoured stator. However, the stage efficiency was marginally higher using the contoured variant, which was supposed to be caused by a more favorable rotor incidence. The turning of the contoured nozzle was found to be higher, leading to less negative incidence on the rotor. Apart from that the radial distributions of the stator exit flow angles did not differ significantly. The authors concluded that the simple straight converging variant in combination with appropriate rotor design could be superior to the contoured endwall shape.

The current work is embedded in a research project with the aim of reducing secondary flows and their associated losses in highly loaded axial turbines. The investigations have been intended to study the possibilities of simultaneous endwall contouring and three-dimensional airfoil design. A linear turbine cascade with divergent outer walls and well-known aerodynamic properties has been chosen as the starting point of the investigations. With the tools of a three-dimensional design environment, the influence of various features of the endwall pressure distribution on the secondary flow has been analyzed in detail. An important aspect of the work has been the validation of the design studies in a cascade test.

Turbine Cascade

A highly loaded turbine cascade with a turning of more than 100 deg was chosen for the investigations. The design conditions and the profile shape representing the mid section of a low-pressure turbine rotor are given in Fig. 1. The so-called T106D cascade was fitted with symmetrically divergent endwalls of a taper angle of $\lambda = 15$ deg in order to obtain the acceleration ratio of a typical low pressure turbine. The airfoil heights of $h_{LE} = 227.2$ mm and $h_{TE} = 273.3$ mm, and an airfoil true chord length of $l = 100$ mm result in a large aspect ratio, which ensures two-dimensional flow at midspan. Therefore, the calculations could be based on a half-cascade, i.e., with a computational domain from midspan to one endwall. The three-dimensional flow field, the pressure distributions at midspan and at the endwalls, and the inlet boundary layer of the cascade T106D are well known from detailed measurements published by Duden and Fottner (1997). Figure 2 displays the half-cascade with one tapered endwall. The shape of a meridional endwall contour, which will be discussed later on, is also shown in the figure. The inflow plane of the computational domain was set at the position of the previously performed inlet boundary layer measurements upstream of the T106D. The outflow

Nomenclature

A = area normal to axial direction, m^2
h = airfoil height, m
h_{ref} = reference airfoil height = 0.3 m
H_{12} = shape factor $H_{12} = \delta_1/\delta_2$
l = true airfoil chord, m
Ma = Mach number
p, p_t = static pressure, total (stagnation) pressure, Pa
Re = Reynolds number
SVO = nondimensional streamwise vorticity = $(\Gamma_S * l)/w_{2is}$
t = pitch, m
T_t = total (stagnation) temperature, K
Tu = turbulence intensity, percent
w = flow velocity, m/s
x, u, z = axial, circumferential, spanwise coordinate, m
β = circumferential (pitchwise) flow angle, deg
β_S = stagger angle, deg
δ = boundary layer thickness, m
δ_1 = displacement thickness, m
δ_2 = momentum thickness, m
Γ_S = streamwise vorticity, s^{-1}
λ = taper angle, deg
ζ = loss coefficient; $\zeta = (p_{t1} - p_t)/(p_{t1} - p_K)$

Subscripts and Superscripts

1, 2 = cascade upstream and downstream conditions
ax = axial
g = mass-averaged in circumferential and spanwise direction
is = isentropic
K = wind tunnel pressure tank conditions
m = pitchwise mass-averaged
n = scaled to the reference airfoil height: $\zeta_{1,n} = \zeta_1 * (h_l/h_{ref})$; $\zeta_{g,n} = (\zeta_g - \zeta_P) * (h/h_{ref}) + \zeta_P$; $\zeta_{S,n} = \zeta_{g,n} - \zeta_{1,n} - \zeta_P$
P = profile
S = secondary

Abbreviations

EW = endwall
LE, le = leading edge
MS = midspan
NC, nc = negative curving
PS, SS = pressure side, suction side
TE, te = trailing edge
T106D = cascade with straight divergent endwalls
T106Cp = half-cascade with three-dimensional airfoil and straight divergent EW
T106Cc = half-cascade with three-dimensional airfoil and contoured divergent EW
3DE = three-dimensional Euler solver
3DNS = three-dimensional Navier–Stokes solver

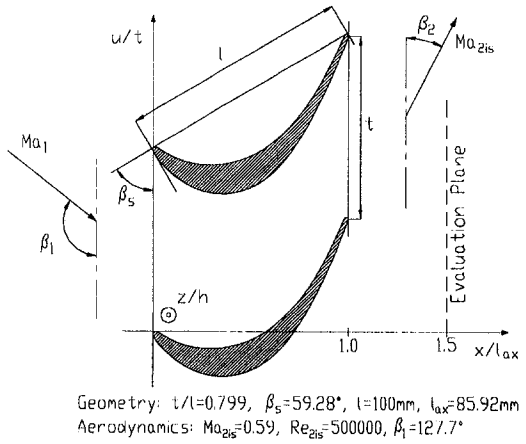

Fig. 1 Geometry and design conditions of turbine cascade T106

plane was identical with the downstream edge of the cascade endwalls.

Design Studies

Three-dimensional airfoil design and endwall contouring were supposed to be applied simultaneously to the turbine cascade T106D. The objective was to minimize the secondary losses and the strong deviations caused by the secondary flow. In order to obtain comparable results, it was attempted to retain the overall loading, in terms of the overall mass-averaged exit flow angle, and the massflow. With respect to an application in a turbine stage, the axial length of the airfoil was kept constant and the axial extent of the endwall contouring was confined between two planes, 15 percent of the axial airfoil length upstream and downstream of the airfoil bounds.

The means of three-dimensional airfoil design and endwall contouring were mainly intended to influence the endwall pressure distribution as the dominant feature on the development of the secondary flow. The following criteria were known from the literature or were assumed to be beneficial to the reduction of secondary flows:

- A lowered endwall pressure gradient, especially in the front part of the passage, moderates the development of the passage vortex.
- Building up a pressure gradient from midspan to the endwalls on the suction side or at least decreasing the usually strong gradient in the opposite direction should minimize the radial movement of the passage vortices towards the midspan.
- Despite the latter principle, the cross-channel pressure gradient at the endwalls should not be increased. Therefore, the pressure level at the pressure side should be lowered. This certainly causes an outwardly directed radial pressure gradient on the pressure side, which tends to reinforce the passage vortex, but because the boundary layers are thin on the airfoil pressure side, the positive effect of the lowered driving force in the circumferential direction is assumed to be dominating.
- Suppressing a deceleration of the suction side flow that is a common result of the secondary flow and is observed to be fairly strong in the reference cascade could reduce boundary layer growth and hence loss production in that area.

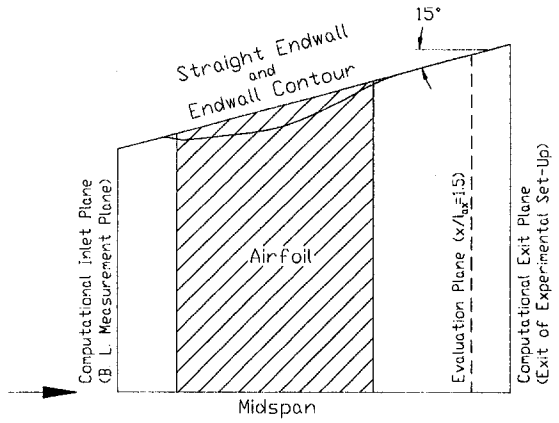

Fig. 2 Meridional view of half-cascade with straight endwall and with endwall contouring

The listed principles were applied in the design studies and their effects on the development of the secondary flow were analyzed.

Design Process. A combination of a quasi-three-dimensional and a fully three-dimensional approach was chosen for the investigations. Using the turbine cascade T106D as the starting point, with known measured and three-dimensional calculated flow properties, a quasi-three-dimensional inviscid streamsurface calculation was performed first. Modifications of the endwall contour were implemented into the quasi-three-dimensional calculation by means of two parametric cosine functions with a straight connecting line. The applied quasi-three-dimensional code could be run with an adequate number of calculating stations in the airfoil row providing a high resolution of the meridional shape. The assessment of the endwall contouring was made directly with the blade-to-blade results of the quasi-three-dimensional calculations. Due to a better resolution at the leading edge and the trailing edge, the airfoil section design was assessed with a two-dimensional Euler code whereby significant changes in the profile geometry required an extra quasi-three-dimensional calculation to provide the two-dimensional Euler code with a corrected stream tube thickness.

Quasi-three-dimensional calculations are not capable of predicting the secondary flow to its whole extent, e.g., the reduced airfoil loading near the endwalls that is caused by the deflection of the secondary flow can only be captured with a fully three-dimensional approach. Nevertheless, using the last fully three-dimensional solution a relative change can be superimposed in a quasi-three-dimensional design cycle. A fully three-dimensional Euler calculation was performed solely after a reasonable result was thought to be obtained in the quasi-three-dimensional cycle. This was mandatory because of the immense differences in CPU time. A single calculation with the quasi-three-dimensional and two-dimensional Euler code took about two minutes of CPU time on an SGI Power Challenge, whereas a three-dimensional Euler run consumed about three hours. Due to the required 25 hours of CPU time, a three-dimensional Navier–Stokes solver was only used as the last step of the design process to judge the effect of the design on the losses. Hence the assessment of the design variants was mainly done by evaluating the distributions of the pitchwise-averaged exit flow angle computed with the three-dimensional Euler solver. A minimum of deviation from the midspan flow angle and a secondary flow area with the least possible distance from the endwall was regarded as the optimum design. The positive effect of such a design on the losses was not yet certain, but it was supposed that less deviation resulting from weakened secondary flow should reduce secondary losses as well. With respect to a turbine stage, the described homogenization of the exit flow would reduce the stage losses due to decreased incidence on the downstream row.

The algorithm of the applied three-dimensional Euler code (Happel and Stubert, 1988) solves the three-dimensional Euler equations with an explicit time marching finite volume method.

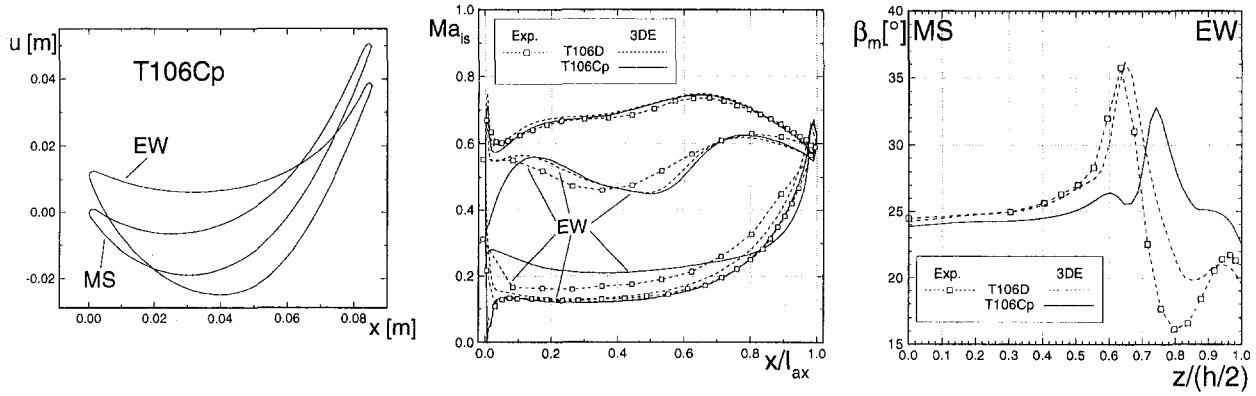

Fig. 3 Airfoil sections, midspan and endwall Mach number distributions, pitchwise mass-averaged exit flow angle at $x/l_{ax} = 1.5$

A $153(x)*29(u)*49(z)$ **H**-type grid was used for the computations. For the airfoil and endwall surfaces a distributed adjustable body force can be used to simulate viscous effects. In the present calculations the body forces were activated only at the endwalls. They were calibrated with the T106D experimental data. All of the applied codes were validated and, if possible, calibrated with this data prior to the use in the design process. The three-dimensional Navier–Stokes code TRACE_S (Vogel, 1997) that was developed by DLR Köln and MTU München was run on a $168(x)*55(u)*50(z)$ mesh of **H-O-H** topology. The basic algorithm time marches the fully three-dimensional unsteady equations of motion expressed in finite volume form with an explicit Runge–Kutta method. Turbulence modeling was performed by the standard $k-\varepsilon$ model. The measured fully turbulent inlet boundary layer of the T106D was input to the three-dimensional calculations. Nonreflecting boundary conditions are implemented in both of the applied three-dimensional codes. Thus, the previously mentioned inlet and outlet plane could be used without causing numerical instabilities.

Three-Dimensional Airfoil Design. As a first step, the airfoil geometry was changed without shaping the divergent endwall. The purpose was to isolate the possible benefit of an airfoil design in the endwall region that is adapted especially to the secondary flow. The changes to the airfoil should be restricted to the endwall region as far as possible. Hence, for all the investigated variants, the midspan profile was identical to that of the T106D. In order approximately to conserve the mass flow and overall loading, the throat was kept constant in the redesigned sections. Numerous approaches were attempted in order to obtain an endwall pressure distribution that matches the aforementioned criteria and that produces the lowest angle deviations. The midspan and endwall airfoil sections shown in Fig. 3 represent the achieved result, named T106Cp. Important changes were the increased airfoil thickness, the realization of negative incidence, and the increase in stagger angle. The transition from the endwall to the midspan profile was modeled with five sections that extended over a range of 30 percent of the half span of the cascade. Expressed alternatively, the airfoil was kept unchanged and prismatic from midspan up to 70 percent of the half airfoil height.

The midspan and endwall Mach number distributions plotted in Fig. 3 contain the results of the basic T106D measurements and the corresponding three-dimensional Euler calculations as well as the calculations of the T106Cp. The T106D computations reproduce the measured values at midspan very well. Near the endwalls differences can be observed but these can be attributed partly to the experiment, because the static pressure was determined with pressure tappings in the endwall with a distance of approximately 2 mm from the profile. The distribution of the pitchwise mass-averaged exit flow angle, evaluated in a plane 50 percent of the airfoil axial chord downstream of the cascade, is captured quite well. Only the degree of overturning near the endwall is underestimated. However, the radial position of the secondary flow system is almost exactly recognized. These results were taken as a proof that the code was sufficiently accurate to be used for the design studies.

The calculations of the modified cascade T106Cp show an unchanged midspan Mach number distribution. At the endwall the cross-channel pressure gradient in the front part of the cascade is significantly decreased. The level of the pressure side Mach number is raised, leading to a reduced loading. The exit flow angle distribution indicates that the secondary flow system is located remarkably closer to the endwall as in the case of the T106D. The peak of underturning is shifted radially by $\Delta(2z/h) = 0.09$ due to the three-dimensional profiling.

As can be seen in the plot of the airfoil sections in Fig. 3, the airfoil design leads to an obtuse angle between most of the airfoil surface and the endwall. The airfoil sections shown were stacked on a radial line, which passed through the center of gravity. Two further radial stacking methods with the same airfoil sections as the T106Cp were examined. In the cascade named T106Cple the sections were stacked along the leading edge resulting in an obtuse angle between the suction side and the endwall. The cascade T106Cpnc was stacked in a way that an acute angle appeared between the suction side and the endwall. In the following this is called negative curving. Figure 4 shows isoplots of the streamwise vorticity (SVO) for the three different stackings in the evaluation plane at $x/l_{ax} = 1.5$. The SVO represents the component of the vorticity vector that is parallel to the velocity vector at the same circumferential position at midspan and was calculated according to Niehuis et al. (1989). As can be seen from the isoplots, the stacking methods lead to distinctly different orientations of the secondary vortices, which mainly depend on the angle between the suction side and the endwall. Due to the increase in local velocity in between the passage vortex (SVO < 0) and the trailing shed vortex (SVO > 0), significant flow angle deviations are in-

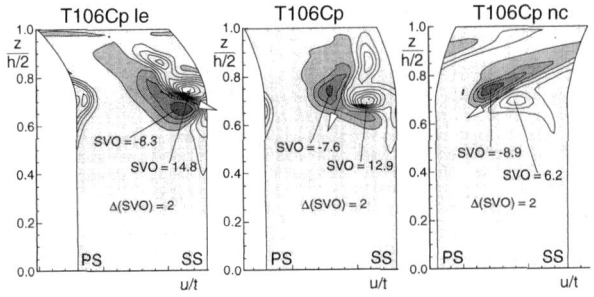

Fig. 4 Influence of radial stacking on streamwise vorticity at $x/l_{ax} = 1.5$ (3DE)

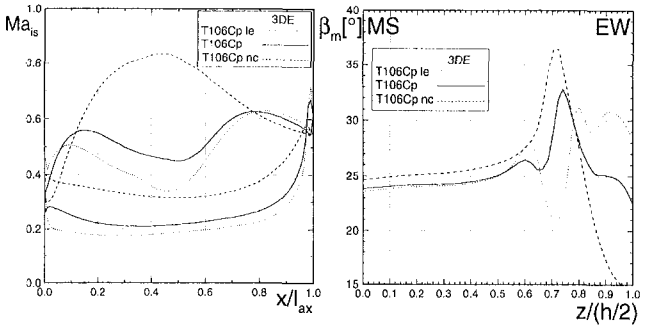

Fig. 5 Influence of radial stacking on endwall Mach number distribution and radial distribution of circumferentially averaged exit flow angle at $x/l_{ax} = 1.5$ (3DE)

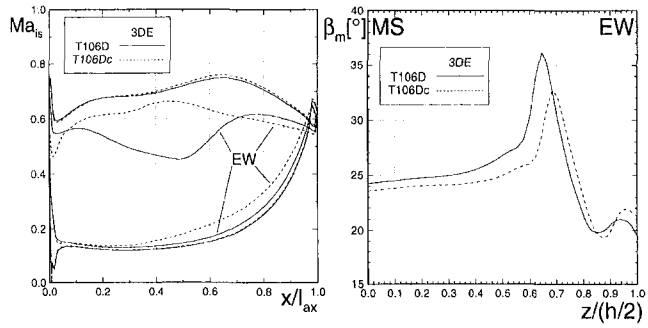

Fig. 6 Influence of endwall contouring on Mach number distribution and radial distribution of circumferentially averaged exit flow angle at $x/l_{ax} = 1.5$ (3DE)

duced in this area. The directions of the imposed velocities are marked in the plots. Looking at the matching radial positions in the angle distributions in Fig. 5, these deviations can be clearly identified. In the case of the stacking along the leading edge, the twisting of the vortices even leads to an inversion of the usual characteristic. The endwall Mach number distributions show an increased loading with airfoil negative curving and vice versa. This corresponds to the previously mentioned observations of other investigators. It is noteworthy that the endwall Mach number distribution obtained with the negative curved variant imposes the weakest trailing shed vortex ($SVO_{max} = 6.2$). Considering the midspan Mach number distribution (Fig. 3), which is unchanged for the configurations, this is caused by the imposed radial pressure gradient on the airfoil suction surface. Due to the lowered pressure level at the endwall, it is directed toward the significant velocities that are induced by the passage vortex on the suction surface. Hence, the differences between the spanwise velocities on the suction and pressure surfaces that form the trailing shed vorticity are reduced.

It shall be noted that attempts to prevent the deceleration (that is connected with the secondary flow) on the suction side of the endwall section with an appropriate airfoil shape in the endwall region have not been successful when using the "gravity stacking" method. The results of airfoil negative curving, however, show that it is possible to avoid such a diffusion by means of radial stacking. Of course the influence of negative curving on the location of the secondary vortices has to be considered simultaneously which complicates the optimization task. Regarding the variants designed during this investigation the "gravity stacking" method showed the most homogeneous distribution of the exit flow angle and therefore was chosen for further investigation.

Endwall Contouring. In the present studies, endwall contouring was restricted to the extension of the airfoil ±15 percent of the axial airfoil length. This led to an unchanged outlet-to-inlet area ratio of the cascades, which was an important constraint of the investigations. In order to confine the scope of the studies and also in order to reduce the costs of the subsequent cascade manufacturing, the endwall contours were restricted to be axisymmetric. In the first step the effects of endwall contouring were studied without simultaneously redesigning the airfoil, i.e., with the prismatic reference airfoil. As in the case of the three-dimensional airfoil shape many different configurations were designed, varying the axial extent, the direction (inward or outward), and the slope of the contour. It was learned that the airfoil pressure side was significantly less affected by the meridional profile than the suction side. The endwall contour plotted in Fig. 2 showed the best results in keeping the secondary flow system near the endwall and in realizing the objective of avoiding the strong deceleration at the suction side in the endwall section. Figure 6 displays the effect of the contour in comparison with the reference cascade T106D. As has already been mentioned, the airfoil was prismatic in both cascades. The convex meridional shape in the midregion of the passage eliminates the diffusion in this part of the suction side at the endwall section. In addition, it lowers the radial pressure gradient from the endwall toward the midspan on the airfoil suction side. At the cascade inlet, the incidence in the endwall region was decreased by a meridional acceleration of the flow that was also obtained by convex endwall curvature. On the pressure side, the velocity level was raised from 40 percent axial chord onward to the trailing edge. The contour reduces the radial extent of the secondary flow system as can be seen from the shift of the position of maximum underturning toward the endwall ($\Delta 2z/h = 0.04$). A small decrease in flow angle deviation, mainly concerning the underturning, can be observed.

Separation of Important Features of the Endwall Pressure Distribution. In the following some important features of the endwall pressure distribution are separated in order to analyze their influence on the secondary flow. The various features were distinguished by airfoil profiling and endwall contouring. As mentioned above, the gravity stacking method was applied and the midspan pressure distribution was kept constant throughout the variants. Starting with the reference cascade T106D, the features are added sequentially until the final design, which was chosen for the cascade test, is reached. As already discussed, the effect on the secondary flow is judged with the aid of the radial distribution of the exit flow angle.

Figure 7 clarifies the influence of the cross-channel pressure gradient at the cascade inlet and the influence of the airfoil pressure side velocity level. The two variants T106Cp1 and T106Cp were obtained by three-dimensional airfoil design without application of endwall contouring. The airfoil shape of the T106Cp has already been shown in Fig. 3. In order to separate the effects of the transition from the reference cascade to the T106Cp, the sections of the T106Cp near the endwall were redesigned with a significantly more concave pressure side while the suction side was

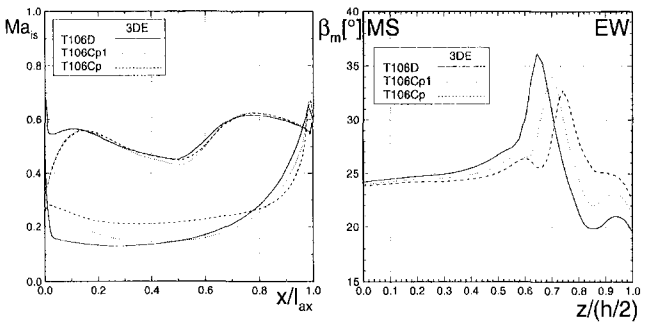

Fig. 7 Influence of cascade inlet loading and airfoil pressure side velocity level on endwall Mach number distribution and exit flow angle at $x/l_{ax} = 1.5$ (3DE)

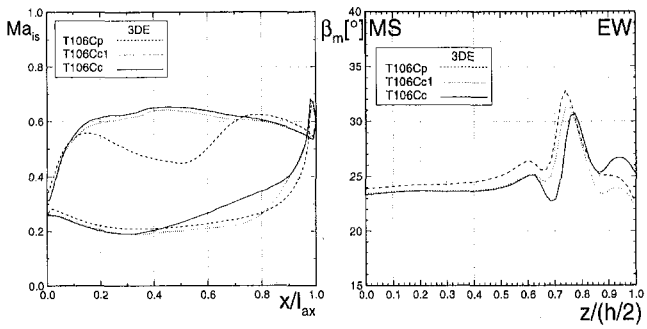

Fig. 8 Influence of airfoil suction side diffusion and airfoil pressure side acceleration on endwall Mach number distribution and exit flow angle at x/l_{ax} = 1.5 (3DE)

virtually unchanged. The resulting cascade was named T106Cp1. Compared with the reference case T106D, it shows a decidedly reduced loading of the endwall section in the inlet region. This leads to a diminished spanwise movement of the secondary flow as can be seen in the radial distributions of the exit flow angle. The location of the maximum underturning is displaced by $\Delta(2z/h) = 0.05$. A further reduction of $\Delta(2z/h) = 0.04$ in the radial shift is obtained by raising the Mach number level on almost 80 percent of the pressure side, thus reducing the cross-channel pressure gradient.

Endwall contouring can lead to additional improvements as was shown in the last section. A superposition of the already discussed meridional shape plotted in Fig. 2 and the variant T106Cp (see Fig. 3) resulted in a configuration named T106Cc. With this cascade the smallest radial extent of the secondary flow region was achieved (Fig. 8). In order to separate the corresponding changes in the endwall Mach number distribution, in the same way as described above, an intermediate version was designed. The resulting T106Cc1 had the meridional shape of the T106Cc but a modified airfoil profile near the wall. Hence the transition from the variant T106Cp to the variant T106Cc1 shows the influence of avoiding the strong diffusion on the suction side at the endwall (see Fig. 8). Only a small shift of the position of the maximum underturning ($\Delta(2z/h) = 0.01$) and minor changes in the magnitude of the deviations from the midspan flow angle can be observed. Due to eliminating the strong deceleration, however, reduced losses in the suction side boundary layer near the endwall and also of the endwall boundary layer were expected. The second part of the "evolution" from the T106Cp toward the T106Cc is an increased endwall Mach number level at the pressure side. This leads to a position of the peak of underturning at $2z/h = 0.77$, which is an additional shift of $\Delta(2z/h) = 0.02$. At the endwall two degrees of underturning can be observed, while at $2z/h = 0.69$ a region of slight overturning is predicted. Thus the radial distribution of the flow angle is a little more nonhomogeneous.

The development from the reference cascade T106D to the cascade T106Cc results in a significant decrease of the spanwise extent of the secondary flow field. Taking the radial position of the underturning maximum as the criterion, the three-dimensional Euler code predicted a total difference of $\Delta(2z/h) = 0.12$. According to their individual share of this shift, the aforementioned means influencing the endwall pressure distribution and thus the secondary flow field can be set in the following order:

- reducing the loading at the cascade inlet with an appropriate airfoil design ($\Delta(2z/h) = 0.05$)
- decreasing the cross-channel pressure gradient by raising the velocity level at the pressure side using significant profile thickening ($\Delta(2z/h) = 0.04$)
- increasing the velocity level at the rear part of the pressure side with endwall contouring ($\Delta(2z/h) = 0.02$)
- eliminating the strong deceleration on the suction side by a convex endwall curvature ($\Delta(2z/h) = 0.01$)

Experimental Setup

Turbine Cascade With Three-Dimensional Airfoil Design and Endwall Contouring. An important part of the investigations was to verify the predicted improvements in a cascade test. Because the aspect ratio of the cascade was sufficiently high and the midspan profiles were identical, two of the designed variants could be examined in one cascade setup. The T106Cc was chosen to be one half of the cascade because of the positive impact on the secondary flow described above. In order to separate the benefits due to three-dimensional airfoil design and due to endwall contouring, the opposite half of the setup represented the T106Cp. The comparison of these two variants could also be used to judge whether the endwall pressure distribution of the T106Cc (see Fig. 8) is desirable in terms of losses. The meridional view of the composite cascade is plotted in Fig. 9 together with the sectional view of the airfoil at midspan, at the straight endwall, and at the contoured endwall. The airfoil is symmetric to the midspan, but due to the intersection with the contoured endwall, the profile next to the contouring gets thinner than on the opposite side. A three-dimensional Euler calculation of the composite cascade was performed because of a small difference in the midspan exit flow angle of $\Delta\beta_m = 0.6$ deg between the two variants (see Fig. 8). The calculation (without figure) showed two-dimensional flow at midspan and almost the same radial distributions of the exit flow angle as the half-cascade calculations. This was mandatory because radial flow from one side to the other would have invalidated the results. It should be noted at this point that in terms of measurements of the radial flow angle and in terms of surface flow visualizations on the airfoil surfaces, the experiments verified the predicted two-dimensional flow at midspan.

In order to maintain the overall loading (in terms of the overall mass-averaged exit flow angle) and the mass flow rate of the reference cascade T106D the composite cascade was restaggered 0.4 deg open. A further three-dimensional Euler calculation demonstrated that the restaggering had no significant influence on the secondary flow field.

High-Speed Cascade Wind Tunnel. The experiments were carried out in the High-Speed Cascade Wind Tunnel of the "Universität der Bundeswehr München." This facility operates continuously in a large pressurized tank. Setting the compressor delivery pressure and the pressure level inside the tank allows

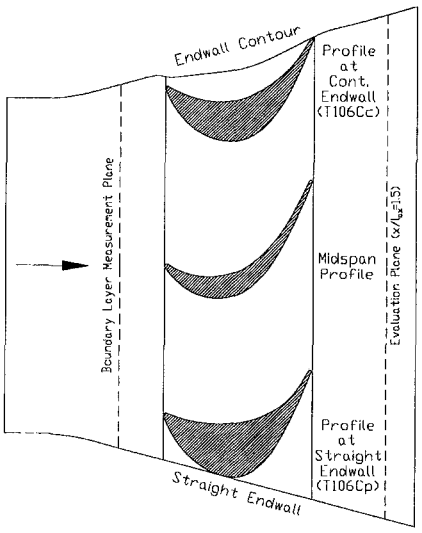

Fig. 9 Meridional view of experimental cascade setup

Table 1 Inlet boundary layers (experiment)

	T106D	T106Cp	T106Cc
δ [mm]	14.0	13.4	14.9
δ_1 [mm]	1.86	1.81	2.22
δ_2 [mm]	1.20	1.16	1.40
H_{12}	1.55	1.56	1.58
$\zeta_{1,in}$	0.0074	0.0083	0.0095

for the independent variation of Mach number and Reynolds number while the total temperature is kept constant. The turbulence intensity in the test section can be varied using different turbulence generators in front of the nozzle. The following data were used in order to monitor the flow conditions of the cascade main stream flow (Sturm and Fottner, 1985): the total temperature in the settling chamber, the static pressure in the tank (downstream conditions), the static pressure and the total pressure of the main stream flow upstream of the cascade.

The inlet turbulence intensity was surveyed on-line by a retractable single sensor hot-film probe. A value of $Tu_l = 3.3$ percent was measured for the present investigations. Inlet boundary layer measurements were carried out with a rake of pitots in the plane depicted in Fig. 9. The cascades were instrumented with static pressure tappings along the midspan section of the airfoils and in the endwalls. A five-hole spherical probe with a head diameter of 2.6 mm was used for the flow field traverses.

Experimental Results

Table 1 provides the parameters of the inlet boundary layers upstream of the three investigated variants. All parameters have been determined using the compressible form of the appropriate formulae. The shape factor H_{12} reveals that the boundary layers are fully turbulent. The increased blockage caused by the thicker endwall airfoil section led to slightly increased inlet boundary layer losses of the T106C variants. The highest value of the inlet loss coefficient was observed upstream the T106Cc-half. This is due to the additional blockage effect of the endwall contour.

The definitions of the loss coefficients have been adapted in order to make the loss coefficients of different axial planes comparable. This is necessary because the values of the secondary loss coefficients are calculated by subtracting the inlet and profile loss coefficients from the overall loss coefficient. As inlet and overall losses are determined by integrating over different channel heights, they have to be multiplied with the ratio of the channel height of the actual measuring plane and a constant reference height. The equations for the conversion are given in the nomenclature. Due to the fact that the channel height of the wind tunnel is $h = 300$ mm, this value was taken as the reference height h_{ref}. The channel height at the inlet boundary layer measurement plane was $h_1 = 213.2$ mm. The height at the evaluation plane at $x/l_{ax} = 1.5$ was $h_2 = 296.3$ mm.

The measured Mach number distributions shown in Fig. 10 demonstrate that the objectives of the design were achieved, with respect to the midspan and endwall pressure field. In comparison to the reference cascade, the midspan Mach number distribution of the T106C variants is slightly changed, resulting in a somewhat higher loading at midspan. This is caused by the above-mentioned restaggering of the whole T106C, which was done in order to keep the overall loading constant. The predictions of both three-dimensional CFD codes agree as well with the measurements as was shown and discussed already for the T106D (see Fig. 3). The calculations are not plotted in Fig. 10, as the capability of modern three-dimensional CFD solvers in predicting the static pressure field is widely known, and inclusion of this information would render the figure illegible.

The measured radial distributions of the pitchwise mass-averaged exit flow angle are disappointing when compared with the three-dimensional Euler predictions with respect to the reduction of the radial extent of the secondary flow system (compare Fig. 8). Taking again the radial position of the underturning maximum as criterion, the transition from the T106D to the T106Cp for example reduced this extent by only $\Delta(2z/h) = 0.04$ rather than the expected $\Delta(2z/h) = 0.09$. This leads to the assumption that the three-dimensional Euler solver overestimates the effects that are contained in the "evolution" from the T106D to the T106Cp. As discussed above, these were mainly driven by a reduced cross-channel pressure gradient. As a consequence the magnitude of the impact of the appropriate features of the endwall pressure distribution on the secondary flow is less than assumed at the discussion of these parameters. However, this is just a change in quantity. The trends that were figured out in the design studies with the three-dimensional Euler solver are assumed to be correct, as the measurements proved that the applied means successfully limit the radial movement of the secondary flow.

Regarding the deviations from the mean flow angle, especially downstream of the contoured half, the flow field is remarkably smooth. The maximum overturning is reduced from $(\beta_{m,\min} - \beta_{m,MS})_{T106D} = -8.4$ deg to $(\beta_{m,\min} - \beta_{m,MS})_{T106Cc} = -0.8$ deg while the underturning is reduced from $(\beta_{m,\max} - \beta_{m,MS})_{T106D} = 11.3$ deg to $(\beta_{m,\max} - \beta_{m,MS})_{T106Cc} = 2.6$ deg. Such a homogenization of the exit flow angle is of course highly desirable for a following rotor, all the more as the deviation is amplified in the moving frame of reference. For example Hourmouziadis and Hübner (1985) stated, that regarding a typical low-pressure turbine velocity triangle, a deviation of just ± 3 deg in the vane exit flow angle leads to an incidence of ± 11 deg to the following blade row.

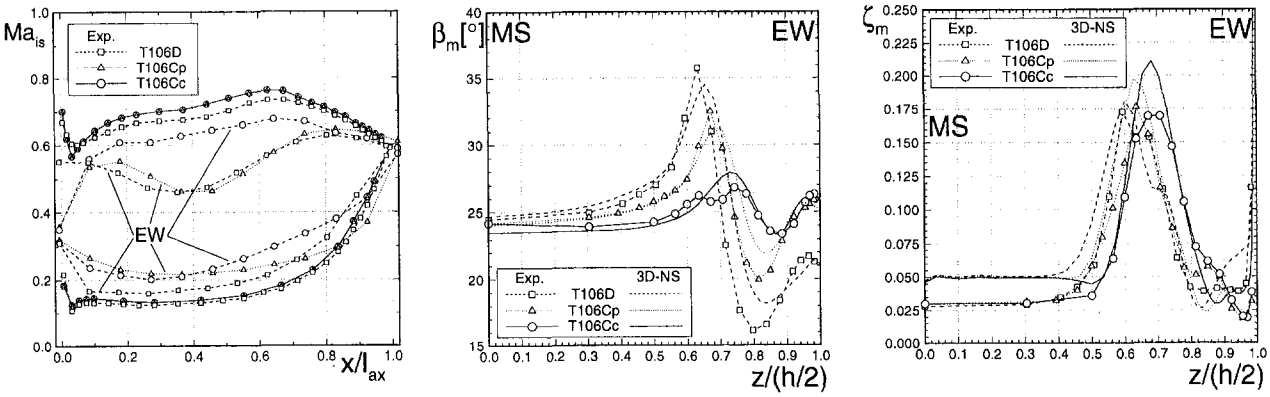

Fig. 10 Midspan and endwall Mach number distributions, pitchwise mass-averaged exit flow angle, and loss coefficient ($x/l_{ax} = 1.5$)

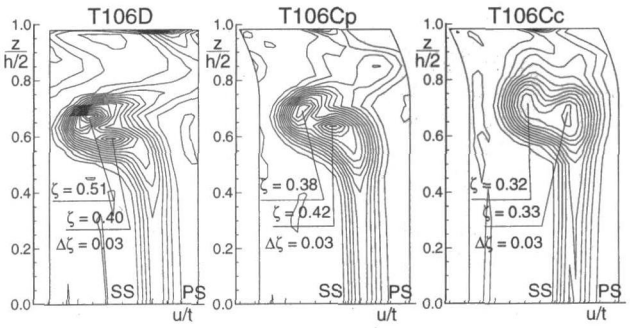

Fig. 11 Loss coefficient at traverse plane x/l_{ax} = 1.5 (experiment)

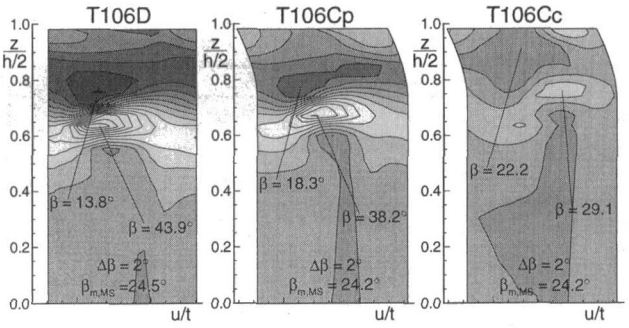

Fig. 12 Pitch flow angle at traverse plane x/l_{ax} = 1.5 (experiment)

In contrast to the three-dimensional Euler predictions, the three-dimensional Navier–Stokes calculations that have been performed as the last step of the design process pick up the radial distribution of the measured flow angles very well (Fig. 10). This is especially true for the contoured variant. Considerable discrepancies can only be observed concerning the radial position and magnitude of the overturning in case of the T106D and T106Cp.

The measured pitchwise mass-averaged total pressure loss coefficients are not influenced as significantly as the exit flow angles. The transition from the reference cascade T106D to the T106Cp leads to minor changes in the radial position of the secondary loss zone. The loss peak of the contoured variant T106Cc, however, is located $\Delta(2z/h) = 0.05$ closer to the endwall as the one of the T106D. Setting the T106C variants against each other it can be concluded that the avoidance of the strong suction side diffusion at the endwall does not improve the loss behavior of the T106Cc. However, it reduces the radial pressure gradient on the airfoil suction side and is assumed to be the main reason for the limited radial movement of the secondary losses of the T106Cc. For both redesigned variants, the quantities of the loss coefficient seem not to be significantly altered in comparison to the reference cascade. Only close to the endwall (minimum distance of 2.5 mm) could a distinct loss reduction be observed for both of the T106C variants. This is due to the reduction of the corner vortex in the more obtuse angle zone between the endwall and the suction surface. The effect can clearly be recognized in the isoplots of the loss coefficient in Fig. 11. The shape of the loss contours of the T106D and the T106Cp is very similar, while it is more diffuse downstream of the T106Cc. It is noteworthy that the maximum loss coefficient in the high-loss core that belongs to the passage vortex decreased from $\zeta_{T106D} = 0.51$ to $\zeta_{T106Cc} = 0.32$.

The three-dimensional Navier–Stokes predictions plotted in Fig. 10 show a remarkable agreement with the measurements. The profile loss (loss at midspan) is distinctly overestimated as a major part of the suction side flow is laminar and the calculation was performed fully turbulent. However, the position and the magnitude of the losses due to the secondary flow are reasonably well captured.

Table 2 contains the traverse results in terms of the overall mass-averaged loss coefficients, the profile loss coefficients (midspan loss), and the secondary loss coefficients. The latter are derived by subtracting the inlet and profile loss coefficients from the overall loss coefficient. As was mentioned at the discussion of the inlet boundary layer measurements, the loss coefficients are scaled to a reference height. With regard to the secondary loss coefficients, a significant reduction of 26 percent was achieved with the contoured half of the cascade. However, the overall values demonstrate only a slight loss reduction for the redesigned variants. A major part of the improvements in secondary loss is counterbalanced by increased profile losses due to the higher loading at midspan and due to thicker inlet boundary layers that are caused by the higher blockage of the T106C variants.

Table 2 Overall mass-averaged loss coefficients at x/l_{ax} = 1.5 (experiment)

	T106D	T106Cp	T106Cc
$\zeta_{g,n}$	0.062	0.059	0.060
ζ_P	0.028	0.030	0.030
$\zeta_{S,n}$	0.027	0.021	0.020

The aforementioned distinct improvements concerning the pitchwise-averaged exit flow angle needed to be verified with regard to the local values as well, because a smooth pitchwise-averaged distribution could also be obtained with an appropriate arrangement of regions with still high local deviations but reversed sign. Looking at the local values of the exit flow angle in Fig. 12, the improvements are impressively confirmed. The deviations are reduced by approximately 5 deg in case of the variant T106Cp. The additional endwall contouring of the T106Cc leads to a remarkable further reduction. As the consequence, the maximum value of underturning dropped from $(\beta_{max} - \beta_{m,MS})_{T106D} = 19.4$ deg to $(\beta_{max} - \beta_{m,MS})_{T106Cc} = 4.9$ deg. Overturning was diminished from $(\beta_{min} - \beta_{m,MS})_{T106D} = -10.7$ deg to $(\beta_{min} - \beta_{m,MS})_{T106Cc} = -2.0$ deg. The contours of the streamwise vorticity provided in Fig. 13 help to understand the reasons for the improvement. It has already been discussed that the relative position of the passage vortex and the trailing shed vortex has a strong effect on the exit flow angle in the secondary flow region. Downstream of the contoured variant T106Cc, the vortices are arranged in a manner that the induced velocities in between them have almost no circumferential component. Thus the pitchwise exit flow angle is not greatly affected by the vorticity. Of course this results in increased velocities in the radial direction towards midspan. However, this does not seem to have negative consequences as the radial extension of the disturbed flow angles and secondary losses was shown to be even less for the contoured variant.

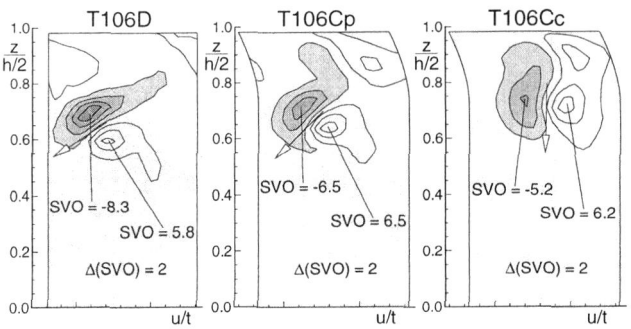

Fig. 13 Streamwise vorticity (SVO) at traverse plane x/l_{ax} = 1.5 (experiment)

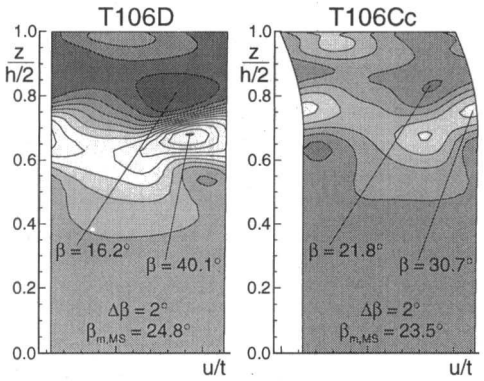

Fig. 14 Pitch flow angle at evaluation plane $x/l_{ax} = 1.5$ (3DNS)

Finally, Fig. 14 should emphasize the capability of the three-dimensional Navier–Stokes solver TRACE_S to predict the measured improvements. The differences of the midspan flow angle between calculation and measurement (Fig. 12) are due to the fact that the three-dimensional Navier–Stokes calculation was not repeated with the restaggered cascade. Hence, approximately 0.4 deg have to be added to the calculated value. The comparison with the measured angles demonstrates that the distributions and the magnitude of the local exit flow angles are captured extremely well.

Conclusions

A highly loaded linear turbine cascade with divergent outer walls has been redesigned, applying three-dimensional airfoil design and endwall contouring. The influence of the airfoil shape near the endwall, the radial stacking of the airfoil sections, and the effect of meridional shaping has been investigated in detail. A three-dimensional design environment has been used to analyze the influence of several features of the endwall pressure distribution on the secondary flow. In order to ascertain the computational results, the flow fields of two optimized variants of the former linear turbine cascade have been examined in a high-speed cascade wind tunnel. The following results should be pointed out:

- Decreasing the radial pressure gradient toward the midspan on the airfoil suction side obstructs the radial movement of the secondary flow. Lowering the pressure level at the endwall, e.g., by means of endwall contouring, can be used to achieve this effect.
- An increase of the velocity level on the airfoil pressure side near the endwall, combined with an unchanged suction side pressure distribution, reduces the airfoil loading and hence the driving factor of the secondary flow. Decreasing the loading at the endwall by lowering the velocity level at the suction side is not assumed to give comparable benefits because the radial pressure gradient toward midspan on the airfoil suction side is increased.
- The influence of the endwall section airfoil loading on the secondary flow is most significant at the cascade inlet. This loading should be modest in order to reduce secondary flows.
- A reduction of 26 percent of the secondary loss was achieved with the optimized cascade. However, a major part of the improvement was counterbalanced by increased inlet boundary layer losses due to a higher blockage of the thickened airfoil and the endwall contour and by a higher profile loss (midspan loss) due to a higher loading at midspan, which was caused by the retention of the overall loading.
- With regard to the flow angle deviations connected with the secondary flow, distinct improvements can be achieved by means of radial stacking and endwall contouring. It was found that, in order to achieve low pitchwise deviations, the passage vortex and the trailing shed vortex have to be arranged in such a way that the high velocities between them have no circumferential component.
- In a subsequent work within the national research cooperation "AG TURBO" the design insights acquired in the present study will be applied to redesigning the front 1.5 stages of a three-stage low-speed low-pressure turbine rig. As has been proven in the present cascade tests, it is possible to reduce the exit flow angle variation significantly. This will result in improvements throughout the downstream airfoil rows and will result in reduced overall losses for the whole turbine.
- The applied three-dimensional flow calculation methods were successfully used to design a cascade with reduced secondary flows. Especially the predictions of the three-dimensional Navier–Stokes solver TRACE_S showed a remarkable agreement with the experiments.

Acknowledgments

The work reported was performed within a research project that is part of the national research cooperation "AG TURBO." The project has been supported by the German Ministry of Education, Science, Research and Technology (BMBF) and the Daimler-Benz Aerospace (MTU München). The permission for publication is gratefully acknowledged.

References

Atkins, M. J., 1987, "Secondary losses and end-wall profiling in a turbine cascade," IMechE-Paper C255/87.

Deich, M. E., et al., 1960, "Method of increasing the efficiency of turbine stages with short blades," *Teploenergetika,* Feb.

Duden, A., and Fottner, L., 1997, "Influence of taper, Reynolds number, and Mach number on the secondary flow field of a highly loaded turbine cascade," *Proc. Instn. Mech. Engrs.,* Vol. 211, Part A.

Filippow, G. A., and Zhongqi Wang, 1964, "The effect of flow twisting on the characteristics of guide rows," *Teploenergetika,* May.

Haas, J. E., 1982, "Analytical and experimental investigation of stator endwall contouring in a small axial-flow turbine," NASA-TP-2023.

Haas, J. E., and Boyle, R. J., 1984, "Analytical and experimental investigation of stator endwall contouring in a small axial-flow turbine," NASA-TP-2309.

Happel, H. W., and Stubert, B., 1988, "Computation of transonic 3D cascade flow and comparison with experiments," AGARD CP 437.

Hodson, H. P., and Dominy, R. G., 1987, "The off-design performance of a low-pressure turbine cascade," ASME JOURNAL OF TURBOMACHINERY, Vol. 109, pp. 201–209.

Hourmouziadis, J., and Hübner, N., 1985, "3D-Design of turbine airfoils," ASME Paper No. 85-GT-188.

Moustapha, S. H., Okapuu, U., and Williamson, R. G., 1987, "Influence of rotor blade aerodynamic loading on the performance of a highly loaded turbine stage," ASME JOURNAL OF TURBOMACHINERY, Vol. 109, pp. 155–162.

Moustapha, S. H., and Williamson, R. G., 1985, "Investigation of the effect of two endwall contours on the performance of an annular nozzle cascade," AIAA Paper No. 85-1218.

Niehuis, R., Lücking, P., and Stubert, B., 1989, "Experimental and numerical study on basic phenomena of secondary flows in turbines," AGARD CP 469.

Schnaus, J., and Fottner, L., 1997, "Experimental and numerical investigations of the influence of endwall inclination and contouring on the flow field of a highly loaded turbine cascade," AIAA IS 123/GE3, Chattanooga.

Sturm, W., and Fottner, L., 1985, "The High Speed Cascade Wind Tunnel of the German Armed Forces University Munich," 8th Symposium on Measuring Techniques for Transonic and Supersonic Flows in Cascades and Turbomachines, Genoa.

Vogel, D. T., 1997, "Numerische Untersuchung des Mischungsverhaltens von Filmkühlstrahlen in Turbinenströmungen," DLR-Report 96-35, DLR Köln.

Wang Zhongqi and Han Wanjin, 1995, "The influence of blade negative curving on the endwall and blade surface flows," ASME Paper No. 95-GT-441.

Weiß, A. P., and Fottner, L., 1995, "The influence of load distribution on secondary flow in straight turbine cascades," ASME JOURNAL OF TURBOMACHINERY, Vol. 117, pp. 133–141.

Weiß, A. P., 1993, "Einfluß der Profildruckverteilung auf die Ausbildung der Sekundärströmungen in ebenen Turbinengittern," Dissertation, Universität der Bundeswehr München.

The Influence of Endwall Contouring on the Performance of a Turbine Nozzle Guide Vane

V. Dossena
Dipartimento di Energetica,
Politecnico di Milano,
Piazza Leonardo da Vinci 32,
20133 Milano, Italy

A. Perdichizzi

M. Savini

Facoltà di Ingegneria,
Università di Bergamo,
Viale G. Marconi 5,
24044 Dalmine (Bg), Italy

The paper presents the results of a detailed investigation of the flow field in a gas turbine linear cascade. A comparison between a contoured and a planar configuration of the same cascade has been performed, and differences in the three-dimensional flow field are here analyzed and discussed. The flow evolution downstream of the trailing edge was surveyed by means of probe traversing while a three-dimensional Navier–Stokes solver was employed to obtain information on flow structures inside the vaned passages. The experimental measurements and the numerical simulation of the three-dimensional flow field have been performed for two cascades; one with planar endwalls, and the other with one planar and one profiled endwall, so as to present a reduction of the nozzle height. The investigation was carried out at an isentropic downstream Mach number of 0.6. Airfoils of both cascades were scaled from the same high-pressure gas turbine inlet guide vane. Measurements of the three-dimensional flow field have been performed on five planes downstream of the cascades by means of a miniaturized five-hole pressure probe. The presence of endwall contouring strongly influences the secondary effects; the vortex generation and their development are inhibited by the stronger acceleration taking place throughout the cascade. The results show that the secondary effects on the contoured side of the passage are confined in the endwall region, while on the flat side the secondary vortices display characteristics similar to the ones occurring downstream of the planar cascade. The spanwise outlet angle distribution presents a linear variation for most of the nozzle height, with quite low values approaching the contoured endwall. The analysis of mass-averaged losses shows a significant performance improvement in the contoured cascade. This can be ascribed not only to lower secondary losses but also to a reduction of the profile losses.

Introduction

In the development of advanced gas turbines, one of the most effective methods to improve the turbine performance is the adoption of fully three-dimensional design both for stator vanes and rotor blades. Complex geometries, suggested by a better knowledge of the flow field, can often produce a reduction of aerodynamic losses. A very delicate task is the design of a high-pressure turbine vane, not only because of the well-known cooling problems, but also because of the high aerodynamic losses. In fact the first vane is characterized by low aspect ratios and, due to cooling requirements, the pitch–chord ratio is generally high. Both these features act to enhance the secondary flow intensity, so that secondary losses become of the same order of magnitude as the profile losses, or even predominant. A technique to lessen the losses is endwall contouring. In modern gas turbines, the transition between the combustion chamber and the turbine inlet requires a reduction of the flow passage area, and this may be accomplished by profiling the casing in the first vane.

Many authors have shown that endwall contouring is an effective tool to improve the vane efficiency. Dejc et al. (1965) proposed design rules for meridional tip endwall contouring, indicating the optimum contraction ratio for a given aspect ratio, and reported on efficiency increases in rotating rigs. The improvements were related to the major acceleration due to the greater channel convergence, which reduces profile losses and inhibits the secondary flow development. Ewen et al. (1973) investigated the aerodynamic performance of a small axial stage turbine, concluding that the efficiency increase was related mostly to improved rotor inlet conditions and to a higher degree of reaction. Morris and Hoare (1975) performed tests at low velocity on linear cascades with different endwall geometries; the correlation they developed on the basis of the results showed a significant loss reduction, even if its amount was much less than the one predicted by Dejc. Kopper et al. (1981) carried out an investigation on a cascade with one contoured endwall, at an exit Mach number of 0.85. Comparison with the planar endwall configuration surprisingly showed that most of the improvement occurred on the flat half span. Boletis (1985) performed a detailed analysis of the flow field in an annular cascade with meridional tip endwall contouring at low-velocity conditions. Besides the expected overall loss decrease, the whole flow field was found to be positively affected by tip contouring. Not only is the pitchwise pressure gradient in the front part of the cascade significantly reduced, thus causing lower secondary losses, but even in the rear part of the profile the endwall curvature is beneficial. In fact it produces a low-pressure region at the tip, counteracting the radial pressure gradient imposed by the annular configuration; as a result there is a minor inward migration of low-momentum fluid, which causes a contraction of the wake region. These findings were substantially confirmed by the work of Moustapha and Williamson (1986), where two different endwall shapes, with the same height contraction, were investigated. The nozzle characterized by a more rapid contraction and tip back curvature exhibited a better performance in the hub region; this was also related to the lower hub expansion ratio.

Due to the large number of geometric options in endwall profiling, even with regard to the profile features, it is difficult

Contributed by the International Gas Turbine Institute and presented at the 43rd International Gas Turbine and Aeroengine Congress and Exhibition, Stockholm, Sweden, June 2–5, 1998. Manuscript received by the International Gas Turbine Institute February 1998. Paper No. 98-GT-71. Associate Technical Editor: R. E. Kielb.

to make use of these investigations to optimize the design of a contoured vane. Moreover, the results of different authors are not in a complete agreement and the loss reduction for a particular vane cannot be predicted with reasonable accuracy. Therefore, according to Boletis, the only way to evaluate the potential benefits of a particular contouring is to support an analysis of the three-dimensional flow field, and to determine the actual losses by experimental testing.

Finally, in cooled gas turbines, a good knowledge of the three-dimensional flow field is a prerequisite for the design of an effective cooling system. The flow pattern close to the solid surfaces indeed determines the heat transfer coefficient distribution and, when film cooling is adopted, governs the interaction between the injected cooling air and the hot mainstream.

This paper presents the results of a detailed investigation of the flow field in contoured and planar cascades in linear configuration, by comparing the secondary flow development throughout the two cascades. The flow field inside the vane passages was analyzed by means of a three-dimensional Navier–Stokes code, while the flow evolution downstream of the trailing edge was surveyed by means of probe traversing.

The results presented aim to provide a contribution toward a better understanding of the complex three-dimensional flow configuration in contoured cascades, in order to give useful information to the designer of advanced gas turbines.

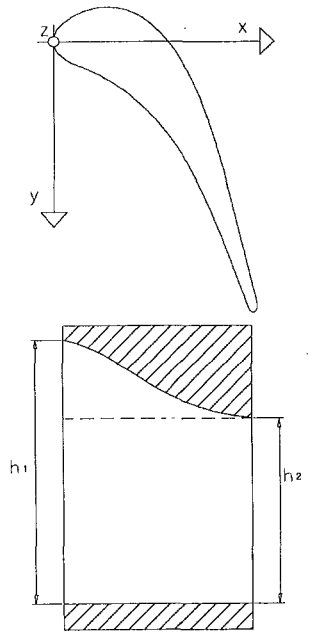

Fig. 1 Blade and meridional profile

Experimental Apparatus

Cascade Geometry. The investigation was carried out on two linear cascades formed with vanes scaled by the first stage of a large power gas turbine. One has a constant height with both endwalls flat, while the other presents a streamwise contraction of the span $h_2/h_1 = 0.70$, obtained by profiling the endwall at $z/h = 1.0$. Both the cascades have the same pitch–chord ratio $s/c = 0.812$ and the same outlet aspect ratio $h_2/c = 0.751$. No restaggering of the vane was performed in the contoured cascade. A qualitative picture of the airfoil section and meridional flow path is presented in Fig. 1. In both cascades two airfoils were instrumented by means of pressure tappings at midspan, to get the airfoil pressure distribution.

Wind Tunnel and Traversing System. Testing was performed in the high-speed wind tunnel for turbine cascades of the Politecnico di Milano; it is a blow-down type facility, equipped with large air storage, so that extensive three-dimensional flow surveys can be carried out. Downstream of the cascades, both composed of seven vanes, there are two adjustable tailboards permitting a fine tuning of the side boundary in order to get acceptable flow periodicity conditions.

The measurements have been carried out by means of a miniaturized five-hole probe, characterized by a probe head diameter of 1.5 mm. Since the outlet flow is highly three dimensional, the survey covered the whole flow field downstream of the trailing edge; the flow was traversed in five axial planes at $x/b = 1.10$, 1.2, 1.35, 1.50, and 1.65.

For this investigation a fully three-dimensional traversing system was developed, allowing the probe automatic positioning in a defined three-dimensional grid of measuring points. By means of a four-axis arrangement, based on stepping motors equipped with encoders, the probe can be displaced continuously not only along pitchwise and spanwise directions, but also in the axial direction. This is obtained by two eccentric rotations centered on parallel axis: the probe is mounted on a rotating probe-holder drum, and, at the same time, the probe can also be rotated around its stem. One of the advantages of this system is that the whole flow field can be investigated in a single run. The adopted measuring grid follows approximately the streamline pattern, in order to keep consistency between the results at different axial distances.

In high gradient zones, typically in the wake near the trailing edge, significant errors in yaw angle and static pressure may arise, due to the finite distance between the probe holes, notwithstanding the small probe head dimension. To minimize this error, a post-processing procedure is utilized to determine the five pressure values in the same identical point; this is obtained by means of a bilinear interpolation of the probe pressure data over the measuring grid. Further details about the experimental apparatus and the data reduction may be found in Osnaghi and Perdichizzi (1990) and Dossena et al. (1996).

Test Program and Test Conditions. The reference operating condition for this investigation corresponds to an outlet isentropic Mach number $M_{2is} = 0.6$ and to an outlet isentropic Reynolds number, based on chord, $Re_{2is} = 1.08 \times 10^6$; additional tests, not presented here, have been performed also at $M_{2is} = 0.4$ and $M_{2is} = 0.85$. The upstream flow was traversed

Nomenclature

b = axial chord
c = chord
Cps = static pressure coefficient = $(pt_1 - p)/(pt_1 - p_2)$
Cpt = total pressure coefficient = $(pt_1 - pt)/(pt_1 - p_2)$
h = height
M = Mach number
p = pressure
pt = total pressure
Re = Reynolds number
s = pitch
x, y, z = axial, pitchwise, and spanwise coordinates
β = flow angle with respect to tangential direction
ω = vorticity

Subscripts

1 = inlet
2 = exit
d = design
ov = overall
is = isentropic
s = streamwise
t = total

Table 1 Upstream flow characteristics

	z/h	δ^*	ϑ^*	H	Cpt_1/Cpt_d
CONT.	0-0.5	.0617	.0473	1.31	0.15
M_1=0.12	0.5-1	.0610	.0465	1.31	0.14
PLANAR	0-0.5	.076	.0532	1.44	0.27
M_1=0.16	0.5-1	.0775	.0542	1.43	0.27

by means of a flattened Pitot probe at $x/b = -0.8$. The inlet free-stream turbulence intensity was 0.5 percent in both tests. Table 1 reports on the integral boundary layer parameters and inlet conditions, where boundary layer thickness is made nondimensional with the channel half height. Note that, as expected, the integral value of the inlet loss is smaller for the contoured case; this is because the free-stream velocity in the inlet duct is significantly lower, thus producing lower energy dissipation.

Numerical Code

The code used in this work solves the full three-dimensional Reynolds-averaged Navier–Stokes equations by means of a finite volume explicit Runge–Kutta scheme. Acceleration to steady state is enhanced by the use of local time stepping, implicit residual smoothing and V-cycle multigrid. The $\kappa-\omega$ turbulence model is used in its standard formulation (Wilcox, 1988). More details about the numerical discretization and the implementation of the turbulence model can be found in Bassi and Savini (1995). Using the low-Reynolds-number version of the turbulence model (Wilcox, 1994), led in the contoured test case, due to the strong flow acceleration, to fully laminar boundary layers on the flat endwall and on the whole vane surface and to a fully laminar wake. It is quite difficult to presume that this latter result is correct, so the low-Reynolds formulation was discarded in favor of the standard one. As the inlet turbulence intensity in both cascades is rather low (around 0.5 percent), the imposed free-stream value of ω in the computations was prescribed setting the ratio of turbulent to laminar viscosity equal to 0.01. This choice guaranteed from any unphysical change in the turbulent kinetic energy values near the inlet boundary. The measured spanwise total pressure profile was imposed at the inlet while spanwise uniform static pressure was fixed at the outlet of the computational domain, which extends more than one axial chord downstream of the trailing edge. The computational meshes consist of 220 × 32 × 72 hexahedral cells and are obtained by stacking the same C-type grid (220 × 32) with a fixed function of the nondimensional height z/h. A plot of the grid used in the contoured case, showing half of the lines in each direction, can be seen in Fig. 2. Since the incoming boundary layer is not symmetric, the whole channel height was discretized in the flat cascade computation. The adopted clustering of mesh points near the solid walls resulted in y^+ values lower than 6 in the blade-to-blade planes and lower than 12 at the endwalls. All computations were performed in single precision on a workstation HP735 and convergence was fixed when the root mean square of the time derivative of density was brought down to 10^{-4}.

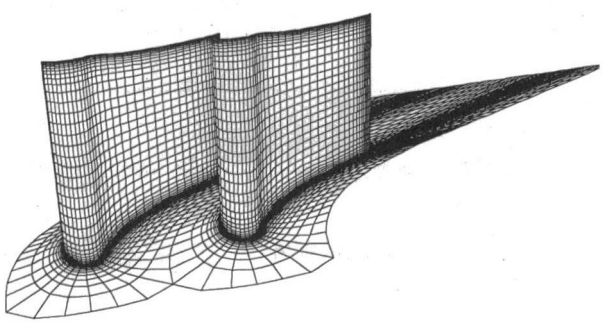

Fig. 2 Contoured cascade: computational grid

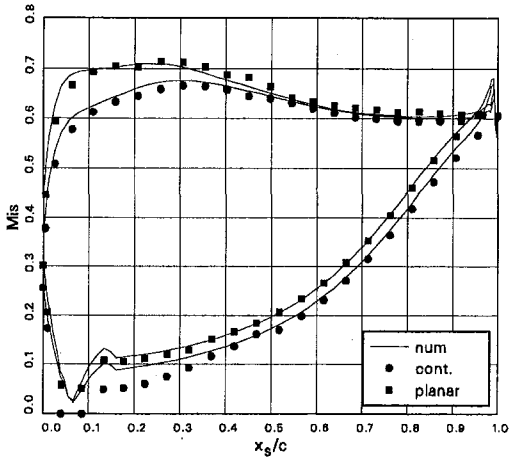

Fig. 3 Computed and experimental isentropic profile Mach number distribution at $z/h = 0.50$

Results and Discussion

Airfoil Pressure Distribution. The key effect of endwall contouring is the modification of the pressure distribution with respect to the planar configuration. In fact a proper endwall design permits the reduction of the pitchwise pressure gradients in the first part of the flow channel, so as to produce less intense secondary flow effects. The streamwise pressure distribution is also improved, leading to a lower inlet velocity and to a greater flow acceleration, so as to reduce vane and endwall boundary layers and the related losses.

Figure 3 presents the isentropic Mach number distributions measured and computed at midspan both for contoured and planar cascades. The major changes take place on the suction surface: lower velocities are found in the contoured case, being the major reduction in the front part of the profile; also the peak Mach number is reduced and its location is moved back, toward the trailing edge. As a result there is a lower diffusion rate over the whole rear suction surface, that is quite advantageous, relative to the profile loss. As can be observed, the computational results are in fairly good agreement with the experimental data. The computational code was used to determine the pressure field away from midspan, where pressure tappings were not available, and more generally to get the flow configuration inside the vane channel. Figure 4 shows the computed profile Mach number distribution at different percentages of span. Approaching the contoured endwall, the blade loading on the front part of the profile (up to 25 percent of the chord) is more and more decreased. This important unloading, occurring just where the flow undergoes the major turning, weakens the driving force responsible of the secondary flow development. Therefore, much less intense secondary effects have to be expected on this side. On the flat side no appreciable variation with respect to midspan is observed.

The computed static pressure distributions on the nozzle surfaces, presented in Fig. 5 in terms of Cps, provide a comprehensive picture of the pressure field inside the channel. On the suction surface clearly appear the stagnation effect caused by the contouring, then the subsequent acceleration occurring at the change of the endwall curvature, and the final recompression approaching the trailing edge.

Secondary Flow Analysis. The streamwise component of the vorticity vector ω_s, evaluated from the numerical results and made nondimensional with respect to the chord and the

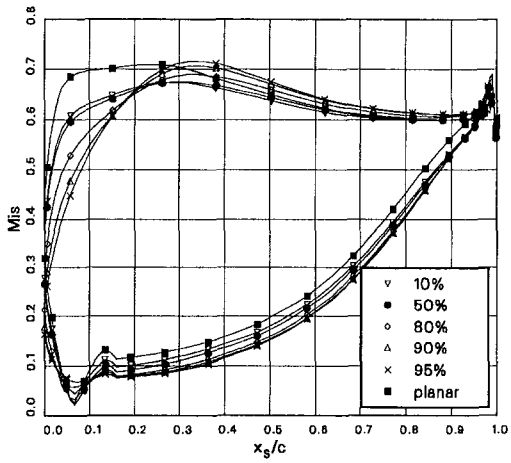

Fig. 4 Contoured cascade: computed isentropic profile Mach number distribution at different z/h

outlet velocity, has been plotted for different axial planes. The plots for the contoured cascade presented in Fig. 6 allow one to follow the development of the secondary flows. In the first plane ($x/b = 0.2$), at the hub there is a negative vorticity region across the passage, indicating the crossflow related to the formation of the passage vortex; a core with positive values, close to the suction surface, reveals the suction side leg of the horseshoe vortex.

At the tip only weak traces of negative vorticity are noticeable. Proceeding toward the trailing edge, at the hub one can observe the well-known secondary flow development, with the passage vortex core growing and moving toward the suction side. When the endwall crossflow impacts the suction surface, there is a rapid enlargement of the negative vorticity region, that rises along the span. The positive core, on the opposite, weakens and it is moved away from the corner.

At the contoured endwall a similar behavior is observed up to $x/b = 0.6$, but approaching the trailing edge a different configuration takes place. The vorticity core related to the passage vortex remains squeezed against the endwall, this being the combined effect of the spanwise pressure gradient and of the substantially higher acceleration, which affects the endwall flow inside the channel. The stronger acceleration occurring at the contoured side actually produces a vortex stretching, so that at the trailing edge there is not a passage vortex as well defined as usual. Further reduction of the intensity of the passage vortex is caused by the lower blade loading occurring at the tip. However, the most interesting feature reported in Fig. 6 is that in the rear part of the suction surface a negative vorticity region is developing, so that in the exit plane an uncommon vortex configuration takes place with two main cores, both with negative vorticity, in the two halves of the span. The cause of this unusual vortex is the deflection that the vane suction side boundary layer undergoes, due to the endwall back curvature occurring from $x/b = 0.6$ and $x/b = 1.0$. In fact, Fig. 5 shows that in this region a negative spanwise pressure gradient acts. Note also that here the flow is diffusing and the boundary layer is thickening. The net result is that there is a radial migration of low-momentum fluid over the vane suction surface toward the tip. It is worth noticing that this is a nonviscous effect, just like the one producing the passage vortex. On the pressure surface this phenomenon is much less significant as the mainflow is accelerating up to the trailing edge and the boundary layer remains very thin.

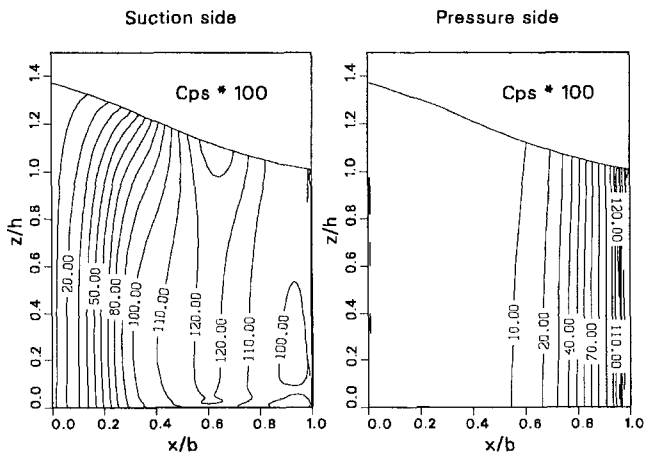

Fig. 5 Contoured cascade: computed pressure distribution on nozzle surfaces

In the planes downstream of the trailing edge, one can observe at the hub the presence of the trailing shed vortex and of the corner vortex, both with positive vorticity.

At the tip, the passage vortex remains confined close to the wall and it is swept away in tangential direction by the endwall crossflow. The negative vorticity core reduces rapidly and at $x/b = 1.5$ it has practically disappeared.

Figure 7 shows the evolution of the streamwise vorticity distribution in the planar cascade. The patterns on both sides appear quite similar one to the other and resemble those taking place at the hub of the contoured cascade; however, the vorticity levels are generally higher, indicating a larger intensity of the secondary vortices. Also the spanwise extent of the secondary effects is greater than in the contoured test case.

Downstream Flow. Figures 8 and 9 show the results of the area traversing in the measuring planes (located at $x/b = 1.1$, 1.2, 1.35, and 1.5) in terms of total pressure loss, respectively, for the planar and the profiled cascades. All loss coefficients are normalized with the profile loss of the contoured cascade, this being evaluated as the pitchwise mass-averaged value over 30 percent of nozzle height about midspan. The contour plots of the planar case show a two-dimensional wake and almost symmetric patterns with respect to midspan; differences noticeable in the endwall regions can be addressed to some leakage due to imperfect sealing at the nozzle hub. One can observe the typical secondary flow configuration, with the low-energy fluid region on the wake suction side and the loss core associated with the corner vortex close to the endwall. Moving downstream, the flow undergoes an overall mixing process with a reduction of loss peak values; the wake enlarges across the pitch and the secondary loss regions widen along the span.

The results of the contoured cascade in the same planes evidence, as expected, a non-symmetric loss distribution. At the flat side ($z/h = 0$), the loss contours resemble those of the planar case; the loss core related to the passage vortex is still present with roughly the same peak value, but its position is shifted toward the wall by approximately 10 percent of the span (e.g., $z/h = 0.15$ for $x/b = 1.50$); the same happens to the loss core associated with the corner vortex, which turns out to be more confined in the endwall region. These effects are related to the stronger acceleration that the flow undergoes throughout the vane passage.

The loss distribution on the contoured side is significantly different: The loss contours are concentrated in the endwall region and only traces of a loss core squeezed against the wall are present. The comparison between flat and contoured case reveals that the transport of low-energy fluid from the endwall boundary layer to the center of the channel is inhibited by the lower intensity of the secondary vortices. As a result, the total pressure loss distribution in the four planes resembles the one of a developing endwall boundary layer. This boundary layer

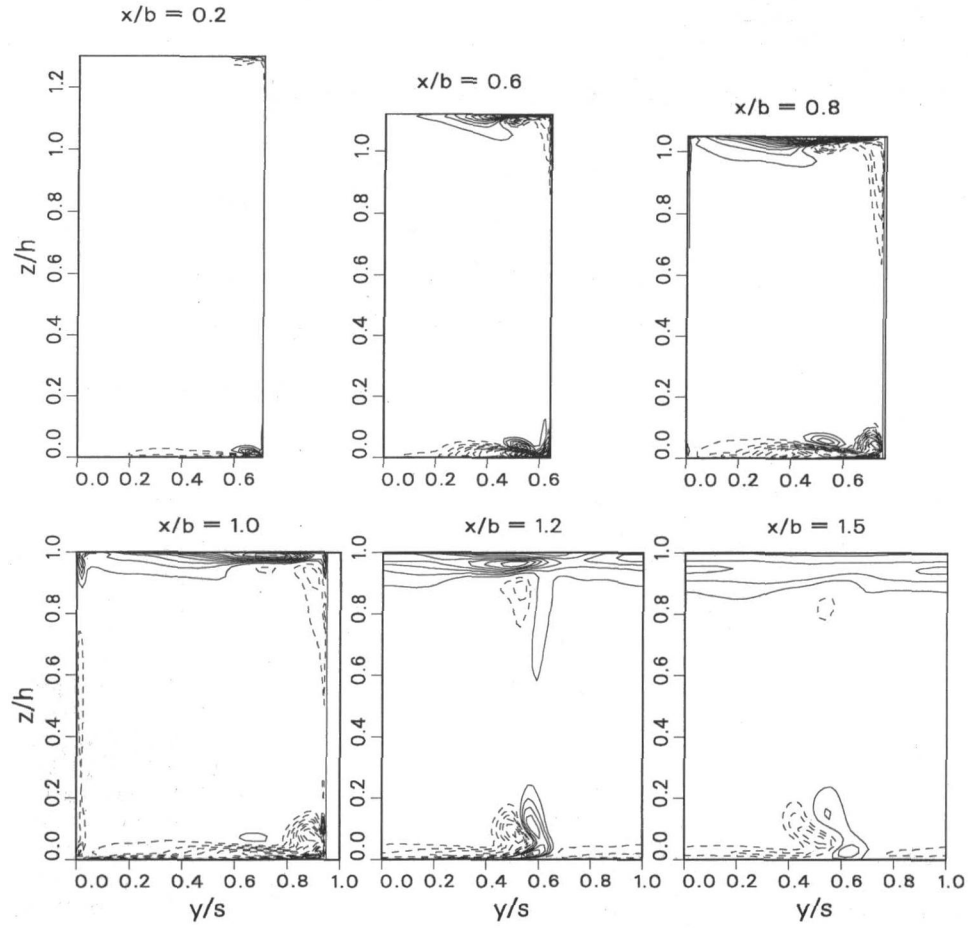

Fig. 6 Contoured cascade: computed streamwise vorticity contours (interval = 0.5; dashed = negative; channel pressure side = 0)

thickens considerably moving downstream under the influence of the recompression occurring at the tip.

Another important feature emerging by the comparison between Figs. 8 and 9 is the reduction of the wake width: In the contoured case the tangential extension of the wake is smaller (in the last plane by about 10 percent of the pitch). This is a consequence of the reduction of the blade loading and of the smaller diffusion rate over the suction surface, which produce a more favourable boundary layer development, thus reducing the profile loss.

For the purpose of comparison, the computed loss contours for both cascades at $x/b = 1.5$ are shown in Fig. 10. As can be noted, the simulation catches all the relevant features discussed above. The main differences with the experiments concern the position of the vortex cores (shifted toward midspan in the numerical results) and the wake, which appears to be thinner and with a greater energy deficit, as if it experienced a lower diffusion downstream of the trailing edge. This latter outcome is typical in the computation of turbine flows and is probably related to the inability of a steady-state computation to repro-

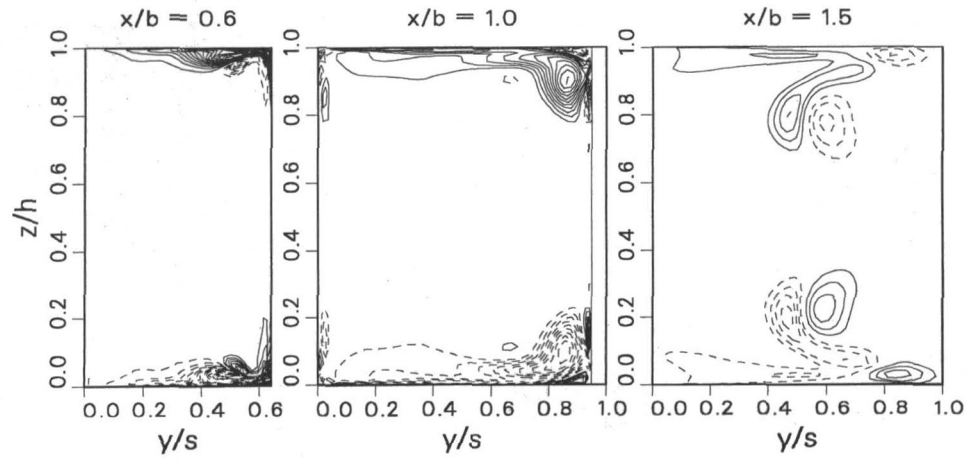

Fig. 7 Planar cascade: computed streamwise vorticity contours (interval = 0.5; dashed = negative; channel pressure side = 0)

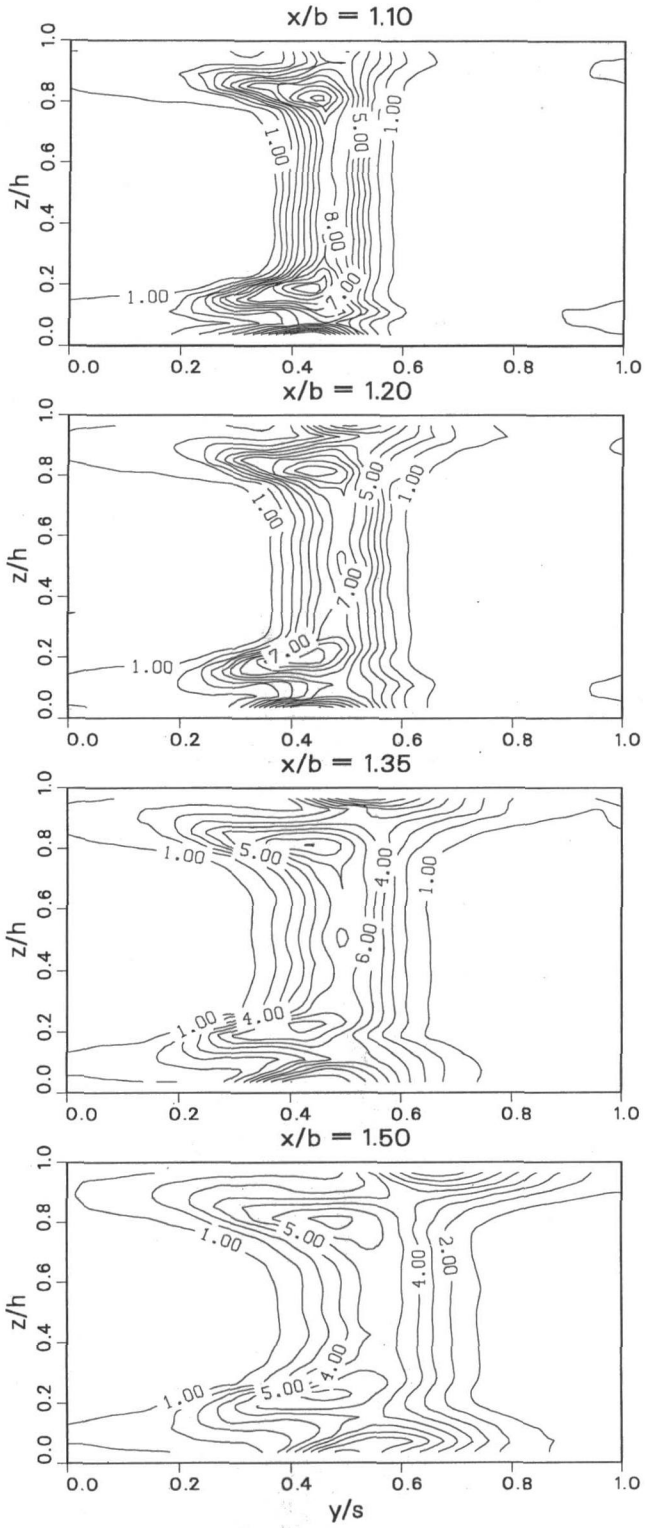

Fig. 8 Planar cascade: experimental total pressure loss contours on four downstream measuring planes

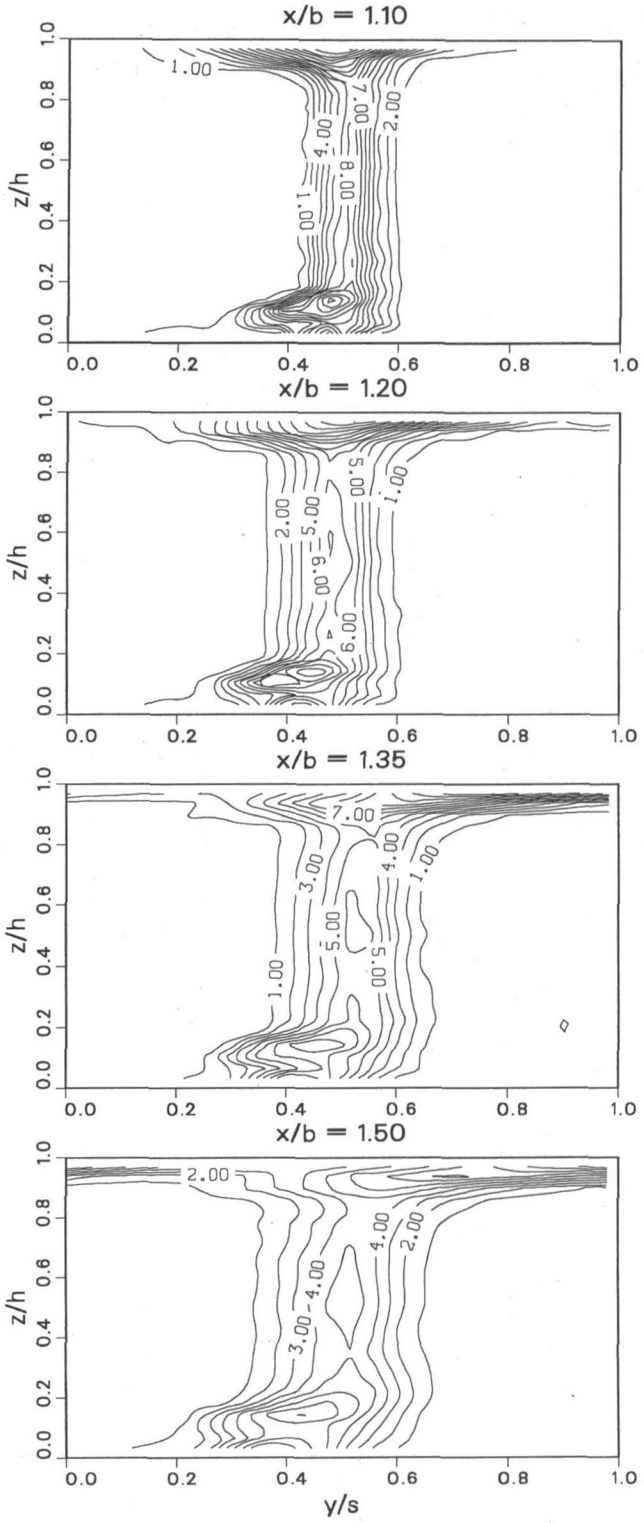

Fig. 9 Contoured cascade: experimental total pressure loss contours on four downstream measuring planes

duce the enhancement in mixing caused by the actual unsteady vortex shedding. Anyway, the simulations can be judged satisfactory, and this confirms the usefulness of their use as a predictive tool for the field inside the vane passage.

Another consequence of the confinement of the secondary vortices induced by the contouring is the larger extension of the two-dimensional region in all the planes. This appears also from Figs. 11 and 12, showing the spanwise distribution of the pitch-averaged loss coefficient, respectively, for the planar and the contoured case. The planar case reveals the typical secondary distribution of the mass-averaged losses versus span, characterized by a two-dimensional region in the middle and by peaks near the endwalls. The contoured case shows a quite different loss distribution with a wider two-dimensional region (60 percent of z/h, instead of 30 percent) and a lower level of the profile loss. Even on the flat side there is a lower loss level,

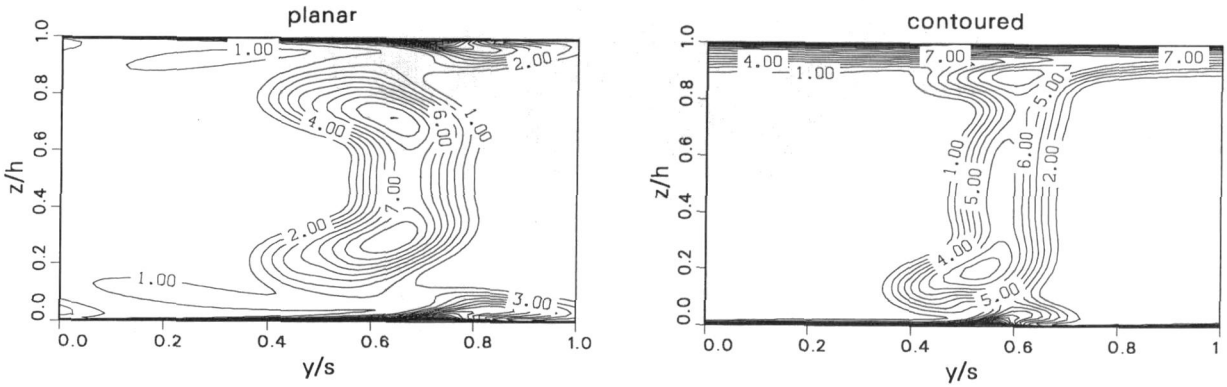

Fig. 10 Computed total pressure loss at $x/b = 1.5$

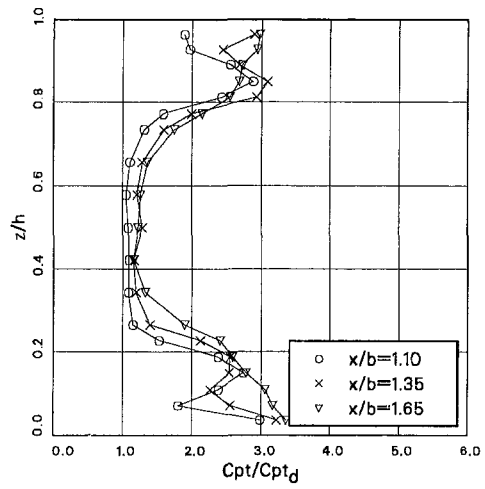

Fig. 11 Planar cascade: experimental pitchwise mass-averaged total pressure loss

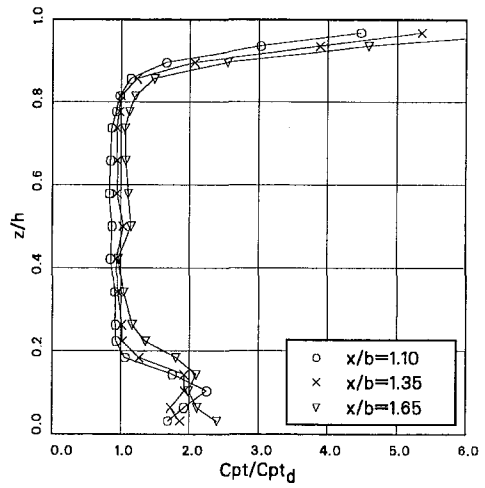

Fig. 12 Contoured cascade: experimental pitchwise mass-averaged total pressure loss

meaning that the stronger acceleration of the flow through the cascade produces lower secondary losses. At the tip a very sharp increase of the loss coefficient takes place, so that the loss distribution looks like the one of an endwall boundary layer.

Tables 2 and 3 present the loss share for the two cascades, in the plane at $x/b = 1.50$ for each half span. As already mentioned, the profile loss is defined as the (mass-averaged)

Table 2 Planar endwalls: mass-averaged loss measurements at $x/b = 1.5$

PLANAR ENDWALLS			
	z/h		
Cpt/Cpt$_d$	0 - 100 %	0 - 50%	50 - 100%
Overall	1.87	1.88	1.86
Profile	1.22	1.22	1.22
Net secondary	0.37	0.39	0.36

Table 3 Contoured endwall: mass-averaged loss measurements at $x/b = 1.5$

CONTOURED ENDWALL			
	z/h		
Cpt/Cpt$_d$	0 - 100 %	0 - 50%	50 - 100%
Overall	1.38	1.33	1.45
Profile	1.00	1.00	1.00
Net secondary	0.24	0.18	0.30

loss over 30 percent of the nozzle height about midspan. The net secondary loss is obtained by subtracting the profile loss and the inlet loss (see Table 1) from the overall loss. The most relevant result shown in the tables is the significant reduction of the overall loss obtained for the contoured cascade. The overall loss reduction (−0.49) comes from the profile loss (−0.22), and in a minor part from to the inlet loss (−0.14) and from the net secondary loss (−0.13). The lower level of inlet and profile losses is clearly due to the lower velocity throughout the cascade and hence it can be considered a two-dimensional effect. Moreover, the net secondary loss includes the endwall boundary layer dissipation. Therefore, it can be concluded that the better cascade performance cannot be related specifically only to a minor intensity or to a different structure of the secondary flows, but it is rather a global result connected to the substantial modification of the whole flow field.

In the planar cascade, the two halves of the span exhibit nearly the same amount of secondary losses, while, in the contoured cascade, the flat side performs considerably better, as also found by Kopper et al. (1981). This is mainly to be ascribed to two effects: One is the wider extension of the contoured wetted surface, the other is the adverse compression occurring at the tip downstream of the throat. Figure 13, showing the computed isolines of pitchwise-averaged static pressure coefficient in the $x-z$ plane, illustrates how, downstream of the

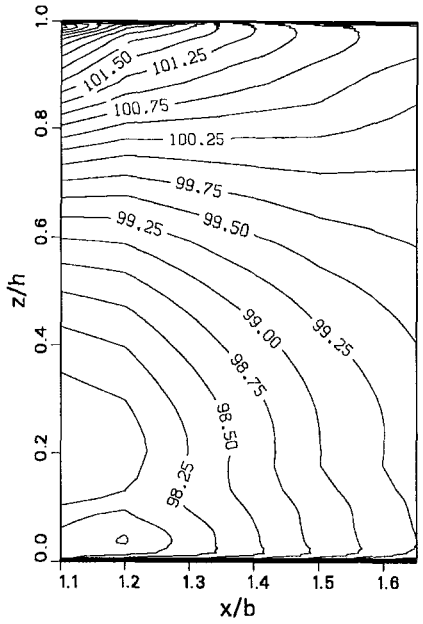

Fig. 13 Contoured cascade: computed pitchwise mass-averaged pressure contours (Cps*100)

trailing edge, the flow near the hub undergoes an acceleration and the flow near the tip a marked deceleration.

Spanwise Distribution of Averaged Flow Angle. The radial distribution in the measuring planes of the averaged outlet angle is presented for the two cascades in Figs. 14 and 15. The first feature emerging from the comparison between the two cascades is the increase of about one degree of the tangential flow angle at midspan for the contoured case.

The planar cascade exhibits the usual distribution connected to secondary flows with a substantial symmetry about midspan. In the first plane the maximum underturning angle is about 2 deg while the overturning at the endwall is 4–5 deg.

In the contoured cascade, only in the first plane is there a distribution resembling the one of the planar case with underturning and overturning regions. On the flat side there is a peak of underturning of about 2 deg, but the three-dimensional effects are confined close to the endwall, so that no overturning was found. On the opposite side the flow angle is practically constant up to $z/h = 0.85$ with only a slight underturning, but approaching the wall a significant overturning takes place. This

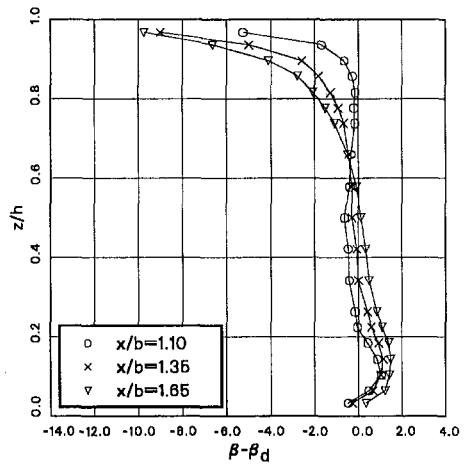

Fig. 15 Contoured cascade: experimental pitchwise mass-averaged outlet angle

is not a stable distribution, as in the following planes the outlet angle in the upper half channel decreases progressively, causing a substantial overturning angle (up to 9 deg). Finally, in the last plane there is a quasi-linear distribution over most of the span; this is confirmed also by the computational results presented in Fig. 16. This kind of distribution is quite beneficial in the real engine; in fact, due to the increase of the peripheral velocity from hub to tip, it produces an improvement of the uniformity of the inlet flow angle to the following rotor.

The explanation for this uncommon decrease of the exit angle at the tip lies in the pressure field taking place downstream of the trailing edge (see Fig. 13). The pressure rise at the contoured endwall can in fact be obtained only at the expense of the axial velocity, being the tangential velocity fixed once outside of the vane, and therefore the flow angle decreases. Note that this is consistent with the axial velocity density ratio distribution, obtained by experimental data and shown in Fig. 17. As a result, there is an enlargement of the streamtubes located closer to the tip, which confirms the progressive reduction of the outlet angle.

Conclusions

The work presents the results of an experimental and numerical investigation carried out in order to clarify the effects of endwall contouring on the three-dimensional flow field in a gas turbine nozzle guide vane.

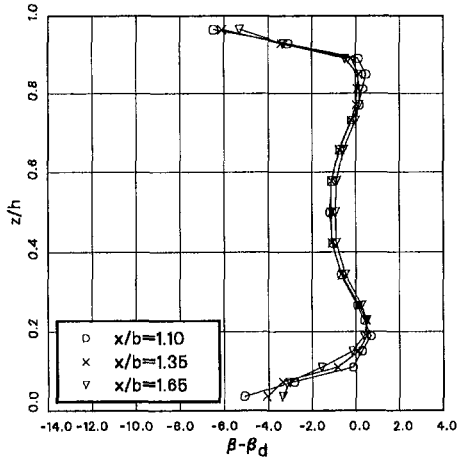

Fig. 14 Planar cascade: experimental pitchwise mass-averaged outlet angle

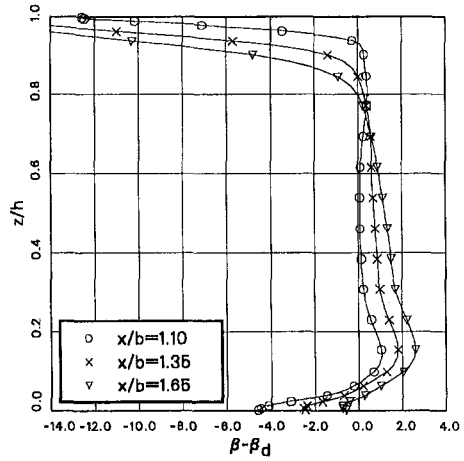

Fig. 16 Contoured cascade: computed pitchwise mass-averaged outlet angle

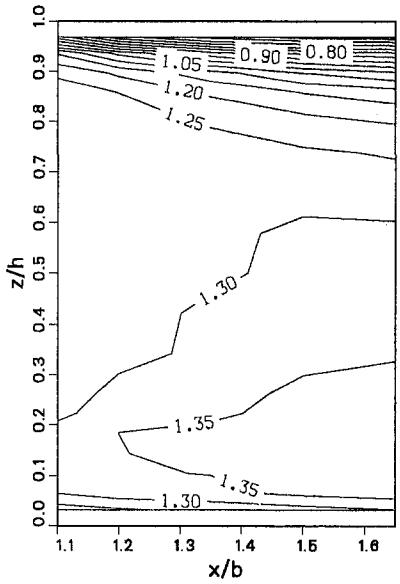

Fig. 17 Contoured cascade: experimental pitchwise mass-averaged axial velocity density ratio contours

The comparison gives evidence that the streamwise contraction of the channel produces a substantially lower loss level, affecting secondary, profile, and overall losses. The main cause of this reduction is the lower velocity inside the vane passage. In the contoured cascade, the flat side takes advantage of a stronger decrease of secondary losses, compared to the contoured side. This difference can be related to a poorer behavior of the endwall boundary layer, which on the contoured side undergoes a non-negligible diffusion.

The secondary vortex structures are strongly affected by the endwall contouring: On the flat side the structure is similar to the typical configuration of straight cascades, but characterized by lower vortex intensity. On the profiled endwall, the contraction inhibits the formation of a proper passage vortex and its migration toward midspan; this is the result of an intense vortex stretching due to the local acceleration and of the deflection of the suction side boundary layer under the influence of the radial pressure gradient. It is felt that the endwall backward curvature near the trailing edge plays an important role in the vortex configuration and in the amount of tip overturning.

Another important consequence of the different flow field is the quasi-linear spanwise distribution of the outlet angle. This produces a more favorable inlet condition for the following rotor.

The resulting three-dimensional flow field, basically different from the one commonly found in planar cascade, is believed to have a strong impact on the design of an effective cooling system.

Acknowledgments

The authors wish to thank ABB Power Generation Ltd. for the permission to publish this paper.

References

Bassi, F., and Savini, M., 1995, "Secondary Flows in a Turbine Cascade at Off-Design Conditions," AGARD CP-517, *Loss Mechanism and Unsteady Flows in Turbomachinery.*

Boletis, E., 1985, "Effects of Tip Endwall Contouring on the Three-Dimensional Flow Field in an Annular Turbine Nozzle Guide Vane: Part 1—Experimental Investigation," ASME *Journal of Engineering for Gas Turbines and Power,* Vol. 107, pp. 983–990.

Dejc, E., et al., 1965, *Atlas of Axial Turbine Blade Characteristic,* Machinostroenie Publishing House, Moscow CEGB Inf. Services, C. E. Trans. 4563.

Dossena, V., Osnaghi, C., Perdichizzi, A., and Savini, M., 1996, "On Testing the Aerodynamics of Film Cooled Blades," *Proc. XIII Symposium on Measuring Techniques on Transonic and Supersonic Flows in Cascades and Turbomachines,* Zurich.

Ewen, J. S., Huber, F. W., and Mitchell, J. P., 1973, "Investigation of the Aerodynamic Performance of a Small Axial Turbine," ASME Paper No. 73-GT-3.

Kopper, F. C., Milano, R., and Vanco, M., 1981, "Experimental Investigation of Endwall Profiling in a Turbine Blade Cascade," *AIAA Journal,* Vol. 19, No. 8, pp. 1033–1040.

Morris, A. W., and Hoare, R. G., 1975, "Secondary Loss Measurements in a Cascade of Turbine Blades With Meridional Wall Profiling," ASME Paper No. 75-WA/GT-13.

Moustapha, S. H., and Williamson, R. G., 1986, "Effect of Two Endwall Contours on the Performance of an Annular Nozzle Cascade," *AIAA Journal,* Vol. 84, No. 9.

Osnaghi, C., and Perdichizzi, A., 1990, "Aerodynamic Measurements in Turbine Cascades at High Mach Number," *Proc. X Symposium on Measuring Techniques on Transonic and Supersonic Flows in Cascades and Turbomachines,* Von Karman Institute, Bruxelles.

Wilcox, D. C., 1988, "Reassessment of the Scale-Determining Equation for Advanced Turbulence Models," *AIAA Journal,* Vol. 26, No. 11.

Wilcox, D. C., 1994, "Simulation of Transition With a Two-Equation Turbulence Model," *AIAA Journal,* Vol. 32, No. 2.

Influence of the Hole Length-to-Diameter Ratio on Film Cooling With Cylindrical Holes

E. Lutum

B. V. Johnson

ABB Corporate Research Ltd.,
CH-5405 Baden-Dättwil, Switzerland

Film cooling experiments were conducted to investigate the effects of coolant hole length-to-diameter ratio on the film cooling effectiveness. The results from these experiments offer an explanation for the differences between the film cooling results for cylindrical hole injection configurations previously reported by Goldstein et al. (1974), Pedersen et al. (1977), and Sinha et al. (1991). The previously reported injection configurations differed primarily in coolant hole length-to-diameter ratio. The present experiments were conducted with a row of cylindrical holes oriented at 35 deg to a constant-velocity external flow, systematically varying the hole length-to-diameter ratios (L/D = 1.75, 3.5, 5, 7, and 18), and blowing rates ($0.52 \leq M \leq 1.56$). Results from these experiments show in a region $5 \leq X/D \leq 50$ downstream of coolant injection that the coolant flow guiding capability in the cylindrical hole was apparently established after five hole diameters and no significant changes in the film cooling effectiveness distribution could be observed for the greater L/D. However, the film cooling effectiveness characteristics generally decreased with decreasing hole L/D ratio in the range of $1.75 \leq L/D \leq 5.0$. This decrease in film cooling performance was attributed to (1) the undeveloped character of the flow in the coolant channels and (2) the greater effective injection angle of the coolant flow with respect to the external flow direction and surface. The lowest values of film cooling effectiveness were measured for the smallest hole length-to-diameter ratio, L/D = 1.75.

Introduction

The review of film cooling technology by Goldstein (1971) delineates much of the physics of film cooling, especially the interactions between the free stream and the film cooling jets. Film cooling through discrete holes has been recognized as a three-dimensional phenomenon with complex interactions as the coolant and the external flow initially interact. Much of the early experimental work was focused on the effects of the coolant to external gas path velocity and density ratio using cylindrical holes at various angles to the external surface.

Geometric effects have also been investigated as the film cooling technology developed and as the manufacturers sought explanations for engine performance that was different from the laboratory data. Effects of geometry include coolant hole exit geometry with the shaping of the hole, the angles at which the coolant penetrates the gas path, the hole diameter to boundary layer thickness, the angle of coolant jet to the surface, the angle of the coolant jet to the gas stream, airfoil surface conditions including surface roughness, and curvature of the external wall. In addition to the conventional effects of coolant to free-stream blowing rate and density ratios, the effects of gas stream Mach number and free-stream scale and intensity of turbulence have also been investigated and reported. In addition to the published experimental studies on film cooling, additional film cooling technology is believed to have been developed experimentally by the industrial and aircraft gas turbine engine companies and not publicly published.

The numerical modeling of film cooling and some of the aforementioned effects have also been conducted for the past 20 years. Recent numerical modeling contributions include Leylek and Zerkle (1994), Vogel et al. (1995), and Walters and Leylek (1996, 1997).

As stated above, there have been extensive studies on film cooling. However, most of these studies have been focused on the gas path characteristics and the coolant flow ratios. The effects of the cooling hole inlet conditions and length and the control of the film cooling effectiveness through the variation of the hole inlet geometry and inlet flow conditions have not been systematically investigated in detail. Exceptions include: (1) the experimental studies from Papell et al. (1982) and Papell (1984), where efforts to control the vorticity from the coolant hole were made, (2) the numerical and experimental results from Vogel et al. (1995), which showed effects of coolant hole inlet conditions on the near jet film cooling aerodynamic, and (3) the experimental study from Burd and Simon (1997) who investigated the influence of coolant supply geometry and hole length on the film coolant exit flow and film cooling effectiveness.

However, there have been several experiments with coolant holes at the same angle to the flow with similar gas path and coolant flow conditions but with various values of coolant hole L/D that present different results. These include Goldstein et al. (1974) with a coolant hole L/D = 5.2, Pedersen et al. (1977) with L/D = 40, and Sinha et al. (1991) with L/D = 1.75. Table 1 summarizes the related geometric and experimental boundary conditions of the referred investigations, as far as available from the publications and those of the present study. Except for the experiments by Goldstein et al. (1974), all previous investigations mentioned were conducted at density ratios slightly above unity. A comparison of their results at two coolant blowing rates showed significant differences in both the centerline film effectiveness and the laterally averaged film effectiveness, especially at the higher blowing ratios. These significant differences in the results with moderate differences in the free-stream test conditions were the basis for pursuing the present study.

Contributed by the International Gas Turbine Institute and presented at the 43rd International Gas Turbine and Aeroengine Congress and Exhibition, Stockholm, Sweden, June 2–5, 1998. Manuscript received by the International Gas Turbine Institute February 1998. Paper No. 98-GT-10. Associate Technical Editor: R. E. Kielb.

Table 1 Comparison of the geometric and experimental conditions

Geometrical Parameter					
Reference	Channel width	Channel height	Number of holes	P/D	L/D
	[mm]	[mm]	[-]	[-]	[-]
Goldstein et al. (1974)	250	130	11	3.0	5.2
Pedersen et al. (1977)	610	305	15	3.0	40
Sinha et al. (1991)	610	610	7	3.0	1.75
Present Study	80	60	7	2.86	1.75-18
Fluid Boundary Condition					
Reference	Tu_∞	U_∞	**DR**	T_∞	T_c
	[%]	[m/s]	[-]	[°C]	[°C]
Goldstein et al. (1974)	low	20-55	0.90	25	-
Pedersen et al. (1977)	0.4	15-27	1.18	heat-mass transfer	
Sinha et al. (1991)	0.2	20	1.20	27	-23
Present Study	3.5	115	1.15	64	20

Objectives

The principle purposes of this investigation and paper are to show the effects of coolant hole L/D on the experimental film cooling performance, to compare results of the present experiments with the results of previous, and to discuss possible mechanisms for the differences in the performance of the various length coolant holes.

Experimental Apparatus

The adiabatic film cooling experiments were conducted in a subsonic open-circuit wind tunnel with a straight channel test section shown in Fig. 1. Ambient air was compressed by an electrical blower. The free-stream mass flow was determined by a calibrated orifice with a measurement uncertainty of 2.5 percent. Free-stream air was heated in a range of 60°C to 70°C by an electrical heater before it entered into the settling chamber. The hot air path and the settling chamber were insulated in order to minimize temperature differences of the incoming flow. An assembly of honeycomb and a series of screens homogenized the flow inside the settling chamber. The flow accelerated through the nozzle with a 10:1 contraction ratio into the test section.

A turbulence grid was placed at the test section entrance to increase the free-stream turbulence intensity. This turbulence grid consisted of 3 × 3 mm rectangular holes that were spaced, from hole center to hole center, 4 mm in width and height. The streamwise decay of the free-stream turbulence intensity was determined in previous measurements on this test facility (Tu_∞ = 5.0 percent at $X/D = -18$, Tu_∞ = 3.5 percent at $X/D = 0$ and Tu_∞ = 2.0 percent at $X/D = 40$). The approaching boundary layer was turbulent with a boundary layer thickness of about 4 mm at the injection location. The displacement thickness at this location was determined to be 0.5 mm. The free-stream velocity level was about U_∞ = 115 m/s.

A second pressurized air supply system of the lab delivered the cooling mass flow at ambient temperature level of about 20°C. The cooling mass flow was accurately determined by means of a turbine wheel meter (1 percent measurement uncertainty) and piped into the cooling air settling chamber, where the air passed through a set of flow straightening devices to minimize flow disturbances. The cooling air was finally injected into the heated free-stream flow through a single row of cylindrical holes at selected blowing rates in the range of $0.52 \leq M \leq 1.56$. The typical density ratio for all experiments conducted was $DR = 1.15$.

The dimensions of the straight test section were 80 mm in width and 60 mm in height with top and side walls constructed of polycarbonate material. The polycarbonate walls allowed optical access to the test surface. A color CCD camera was arranged to observe the test surface through the top wall of the test section. Secondary air was injected after 100 mm of the total length of 600 mm. The bottom wall of the straight channel, the actual test surface, held the different injection configurations investigated. The use of low conductivity material (Necurom, k = 0.1 W/m/K) and additional thermal insulation applied below this test surface kept the heat losses to low values. Temperature measurements errors due to heat losses were determined by a two-dimensional heat conduction analysis to be less than 0.05°C.

Figure 2 shows the top and side view of the removable test plate and illustrates the injection configurations. All configurations consisted of a single row of seven cylindrical holes with diameter, D, equal 4 mm. The hole spacing in lateral direction was P = 11.43 mm and corresponded to a pitch-to-diameter ratio of P/D = 2.86. The hole channels were inclined at α = 35 deg to the free-stream flow direction. The hole length-to-diameter ratio of the injection channels was systematically varied, L/D = 1.75, 3.5, 5, 7, 18, by variation of the test plate thickness as shown in Fig. 2.

Data Analysis

Adiabatic film cooling data were obtained by use of the well-established thermochromic liquid crystal (TLC) technique to measure the adiabatic wall temperature distribution. Isothermal temperature patterns due to film cooling on the adiabatic test plate were indicated by a mixture of up to six narrow-banded thermochromic liquid crystals and were recorded by a color CCD camera in conjunction with a color image processing sys-

Nomenclature

D = coolant hole diameter, m
DR = density ratio = ρ_c/ρ_∞
I = momentum flux ratio = $\rho_c U_c^2/\rho_\infty U_\infty^2$
L = length of coolant passage, m
M = blowing rate = $\rho_c U_c/\rho_\infty U_\infty$
P = hole pitch, distance between holes in lateral direction, m
P/D = dimensionless lateral spacing, pitch-to-diameter ratio
T = temperature, °C
Tu = turbulence intensity, percent
U = mean velocity, m/s
X = streamwise coordinate, origin at film hole center, m
X/D = dimensionless streamwise coordinate
Z = lateral coordinate, m
Z/D = dimensionless coordinate in lateral direction
k = thermal conductivity, W/m/K
α = injection angle of the fluid, deg
ρ = fluid density, kg/m^3
$\eta_{ad,cl}$ = centerline adiabatic film cooling effectiveness
$\eta_{ad,la}$ = lateral averaged adiabatic film cooling effectiveness

Subscripts

c = coolant fluid
∞ = free-stream fluid
TLC = thermochromic liquid crystal indication

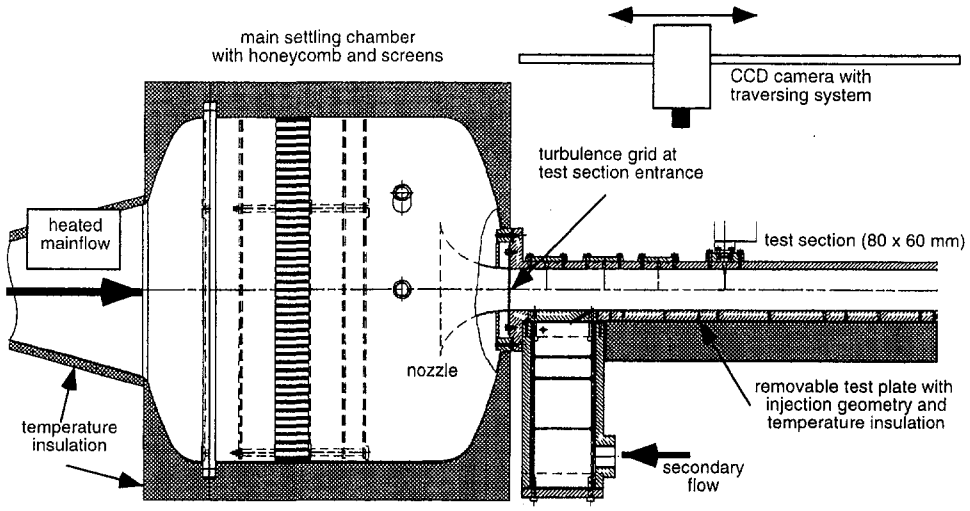

Fig. 1 Straight channel test facility

tem. All additional experimental data, i.e., temperature, pressure, and mass flow information of the main and secondary flow, were stored by a separate data acquisition system for later data reduction purposes.

To achieve accurate measurement of the wall temperature using the TLC's, a special apparatus was built to conduct the temperature calibration of the TLC indication temperatures inside the film cooling test section. The calibration was conducted by interchanging the test plate with a copper calibration plate. A linear temperature distribution was achieved by heating at one end of this plate and cooling at the other end. Determination of the TLC temperature indications on the copper surface was obtained with the same color image processing system used later for the film cooling measurements. Thermocouples, embedded in the copper surface, were used to measure the temperature distribution over the plate length. The experimental uncertainty of the local film cooling effectiveness values was determined by an uncertainty analysis to be not higher than 0.008.

During the experiments, the TLC data were captured using a color CCD camera in conjunction with a color image processing system. A complete data set was compiled using up to six adjacent smaller images. The camera was mounted above the experimental apparatus on a traverse system controlled by a step motor, allowing all pictures to be taken with the same reference points. Using multiple images to build up the final picture allowed higher resolution and better isotherm definition of the adiabatic wall temperature distributions. The temperature indications of the TLC's were assumed to be the adiabatic wall temperatures. The free-stream temperature was measured by a total temperature probe at $X/D = -10$ upstream of the injection location. The coolant temperature was measured by a thermocouple in the coolant settling chamber. With the additional information of the coolant and free-stream temperatures, these isothermal contour lines were recalculated to adiabatic film cooling effectiveness contours as shown in Fig. 3 by

$$\eta_{ad} = (T_\infty - T_{TLC})/(T_\infty - T_c). \quad (1)$$

For the calculation of the lateral averaged film cooling effectiveness values, a special interpolation technique was used. The field of interpolation was determined in lateral direction over a range of two pitches (three holes) and in the streamwise direction, dependent on the input data set, respectively. The interpolation was done by a stepwise interpolation technique using the following steps:

1 Interpolation in the streamwise direction with a power fit ($Y = AX^B$) based on the detected effectiveness contour lines. This interpolation was performed to form skeleton lines, that define the shape of the effectiveness hills and produce more input data for the following interpolation in lateral direction.

2 Interpolation in the lateral direction using a cubic spline for each streamwise position, based on both the detected effectiveness contour lines and the results of the streamwise interpo-

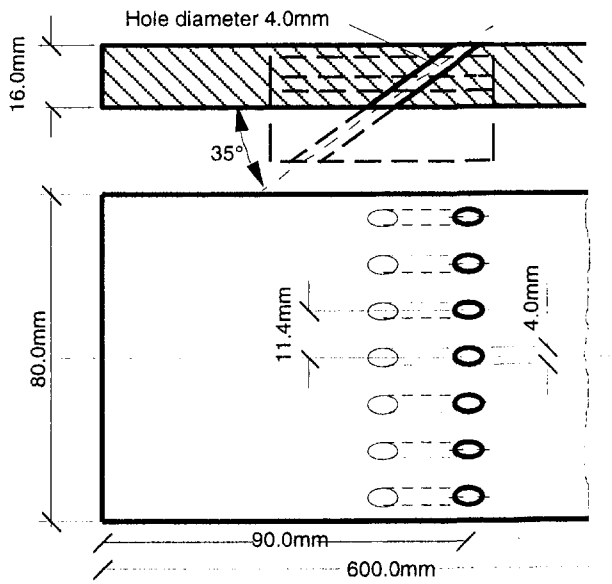

Fig. 2 Injection configurations ($P/D = 2.86$)

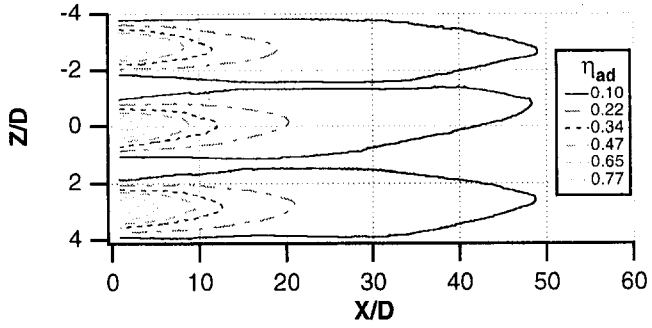

Fig. 3 Typical TLC contours of film cooling effectiveness values at low blowing rate

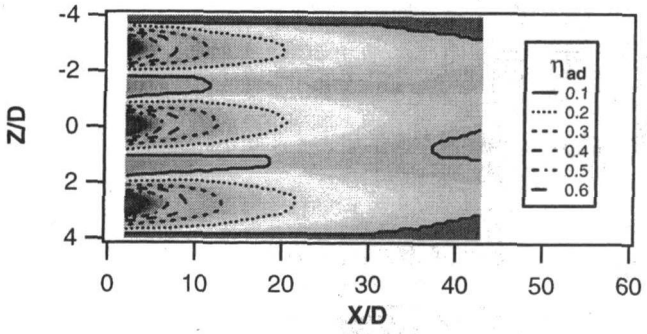

Fig. 4 Typical interpolated film cooling effectiveness data at low blowing rate

lation carried out just before. This interpolation was continued in the streamwise direction downstream of the injection location as far as sufficient input data was available. These results were also stored for the final interpolation step.

3 To obtain smooth contours, the data were again interpolated in the streamwise direction, similar to the first interpolation step for all lateral positions based on the results of the two previous interpolation steps. Because of the additional created effectiveness values, continuous interpolation was possible for the desired range of two pitches in lateral direction (Fig. 4).

The typical interpolation accuracy was within 2.5 percent of the local effectiveness values. Finally, an integration in lateral direction was performed to determine the lateral averaged film cooling effectiveness data at each streamwise position. The estimated integration error based on the experimental and interpolation uncertainty was about 1 to 3 percent of the streamwise local lateral averaged film cooling effectiveness. The uncertainty depended on the effectiveness level, with the higher uncertainty related to lower effectiveness values.

Present Results

Measurements of adiabatic film cooling effectiveness values at selected length-to-diameter ratios, L/D = 1.75, 3.5, 5, 7, and 18, are presented in the Figs. 5(a)–8(b). Centerline (a) and laterally averaged (b) film cooling results are shown, as a variation with the dimensionless streamwise coordinate, X/D, at four blowing rates, M = 0.52, 0.81, 1.15, and 1.56.

The centerline film cooling effectiveness distributions at a low blowing rate (M = 0.52) with the long holes (L/D = 5, 7, and 18) show small differences along the streamwise distance shown in Fig. 5(a). The film cooling effectiveness distribution obtained close to the injection location for L/D = 3.5 was similar to that obtained for longer injection holes. With increasing distance downstream, a larger decrease in film cooling effectiveness was measured for the L/D = 3.5 holes, compared to the effectiveness results for the longer holes. The results with L/D = 1.75 indicate about 20 to 25 percent lower film cooling effectiveness compared to the results of the long holes. The corresponding distributions of the lateral averaged film cooling effectiveness are shown in Fig. 5(b). Highest lateral averaged film cooling effectiveness values are achieved with the long injection holes, L/D = 5 and 7. However, for holes with the longest length, L/D = 18, slightly lower values of film cooling effectiveness are obtained in the near injection region (X/D < 35). Lower lateral averaged film cooling effectiveness values are generally obtained with the shorter injection holes compared to the long injection holes. The decrease of film cooling effectiveness is about 10 percent with L/D = 3.5 and about 20 percent with L/D = 1.75.

Figures 6(a) and 6(b) present the film cooling effectiveness values for the different hole length-to-diameter ratios at a blowing rate of M = 0.81. The centerline and lateral averaged film cooling effectiveness distributions with the injection holes, L/D = 5, 7, and 18, indicated very little variation in the effectiveness and are higher than the film cooling performance with the shorter injection holes. The decrease of film cooling performance with the L/D = 3.5 injection holes is about 20 percent and about 40 percent with the L/D = 1.75 injection holes compared to the longer holes.

The centerline film cooling effectiveness distributions, at a moderate blowing rate, M = 1.15, indicate the same trends as seen at the lower blowing rate, M = 0.81 (Fig. 7(a)). Compared to the film cooling effectiveness values obtained at the lower blowing rate, the decreases in the film cooling effectiveness values are attributed to a strong jet separation with the L/D = 1.75 hole at M = 1.15. The lateral averaged results shown in Fig. 7(b) indicate again higher levels of film cooling effectiveness for the longer injection holes. However, the distribution for holes with L/D = 5 shows a 10 to 15 percent decrease in film cooling performance compared to holes with L/D = 7 and 18 for X/D > 15. With the shorter injection holes, approximately 25 to 35 percent less film cooling effectiveness with L/D = 3.5 and about 30 to 50 percent less film cooling effectiveness with L/D = 1.75 is obtained compared to the values with L/D = 7 and 18.

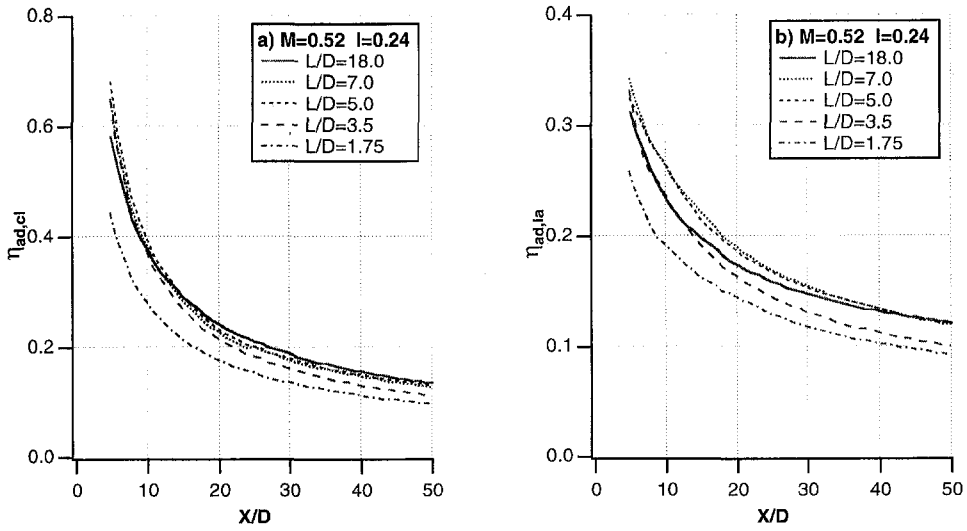

Fig. 5 (a) Centerline and (b) lateral averaged adiabatic film cooling effectiveness distributions at various length-to-diameter ratios obtained with M = 0.52

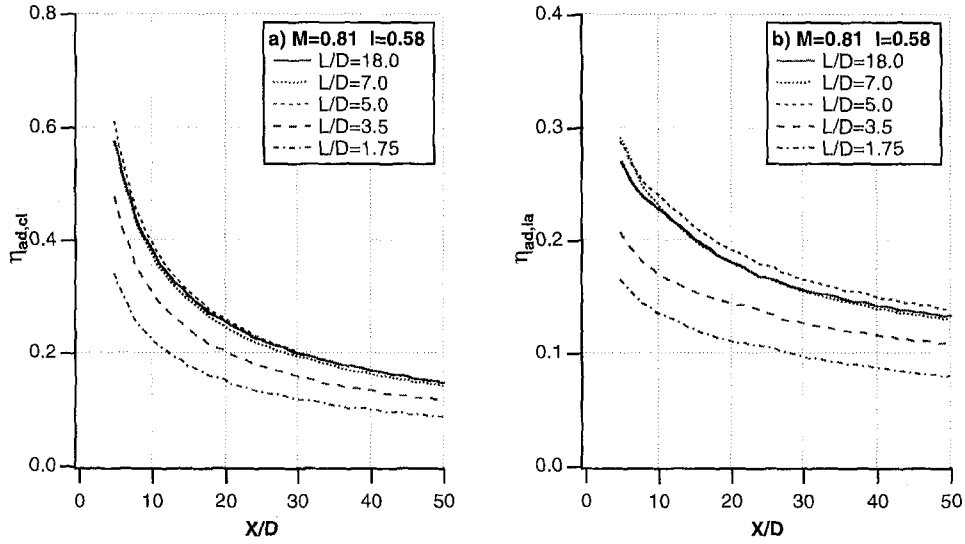

Fig. 6 (*a*) Centerline and (*b*) lateral averaged adiabatic film cooling effectiveness distributions at various length-to-diameter ratios obtained with $M = 0.81$

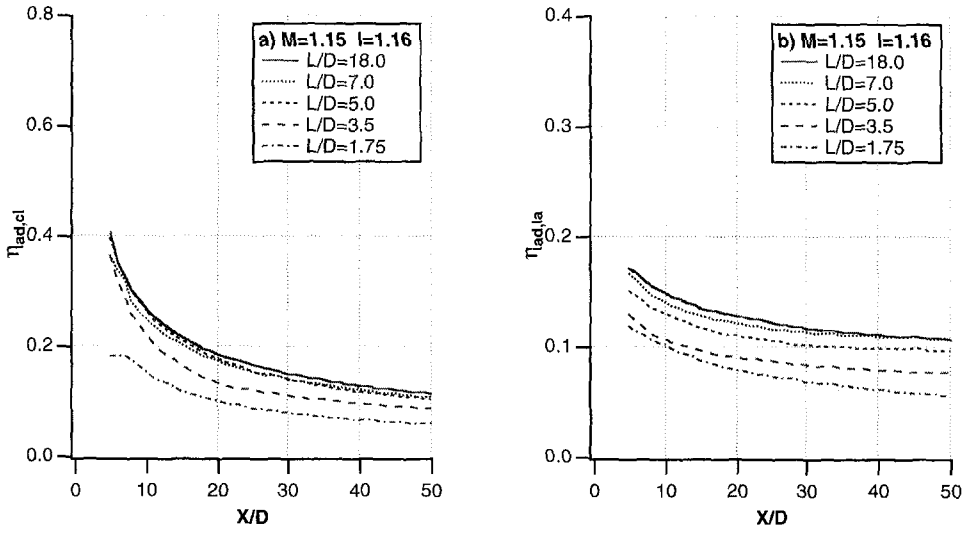

Fig. 7 (*a*) Centerline and (*b*) lateral averaged adiabatic film cooling effectiveness distributions at various length-to-diameter ratios obtained with $M = 1.15$

Figures 8(a) and 8(b) show the results for the highest blowing rate ($M = 1.56$) investigated during this film cooling study. All film cooling effectiveness distributions shown in Fig. 8(a) indicate that a strong jet separation from the test plate occurred at this high blowing rate. The highest film cooling performance obtained with $M = 1.56$ was with the longest injection hole ($L/D = 18$). The two other long hole injection configurations, $L/D = 7$ and 5, resulted in 10 percent lower lateral film cooling effectiveness values compared to the values with $L/D = 18$. The shorter injection holes caused about 35 to 45 percent less film cooling effectiveness with $L/D = 3.5$ and about 45 percent less film cooling effectiveness with $L/D = 1.75$ compared to the values with $L/D = 18$.

The lateral film cooling effectiveness values from Figs. 5–8 for selected values of X/D are re-plotted in Fig. 9 to show the influence of hole length-to-diameter ratio on the film cooling performance. The variations of lateral averaged film cooling effectiveness values with the hole length-to-diameter ratio, L/D, are shown for four streamwise locations, $X/D = 10$, 20, 30, and 40. At each streamwise location, the results are presented for the four blowing rates investigated, $M = 0.52$, 0.81, 1.15, and 1.56. Small effects of hole length-to-diameter ratio on the film cooling performance are measured for the well-developed coolant flows in the longer holes (i.e., $L/D = 7$ and 18). Small to moderate effects of hole length-to-diameter ratio on the film cooling performance are obtained with a $L/D = 5$ hole. For $M = 0.81$, a small (0.01) increase in effectiveness was measured compared to $L/D = 7$ and 18 holes. This is attributed to an unknown but beneficial interaction of the coolant jet and cross-flow for those conditions. The film cooling effectiveness decreases clearly with decreasing hole length-to-diameter ratio in the range of $1.75 \leq L/D \leq 5$. This decrease in film cooling effectiveness is attributed to: (1) the undeveloped character of the coolant flow and (2) the greater effective injection angle of the coolant flow, with respect to the external flow direction and surface, due to jetting of the coolant flow on the upstream edge of the film cooling holes (Burd and Simon, 1997).

The minimum film cooling effectiveness values are obtained for the coolant hole length-to-diameter ratio, $L/D = 1.75$. The decreases in film cooling performance are about 25 percent for the low blowing rate results ($M = 0.52$), about 40 percent for the moderate blowing rate results ($M = 0.81$) and about 30 to

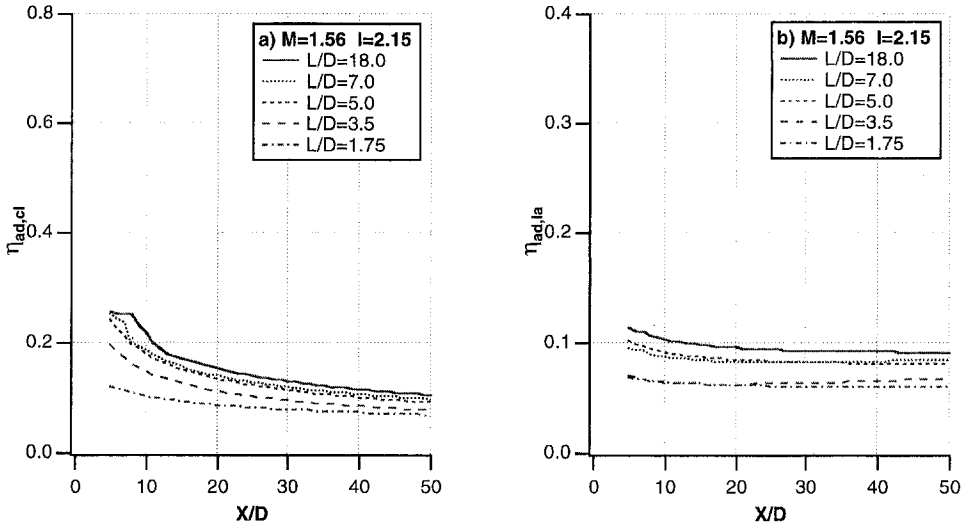

Fig. 8 (*a*) Centerline and (*b*) lateral averaged adiabatic film cooling effectiveness distributions at various length-to-diameter ratios obtained with $M = 1.56$

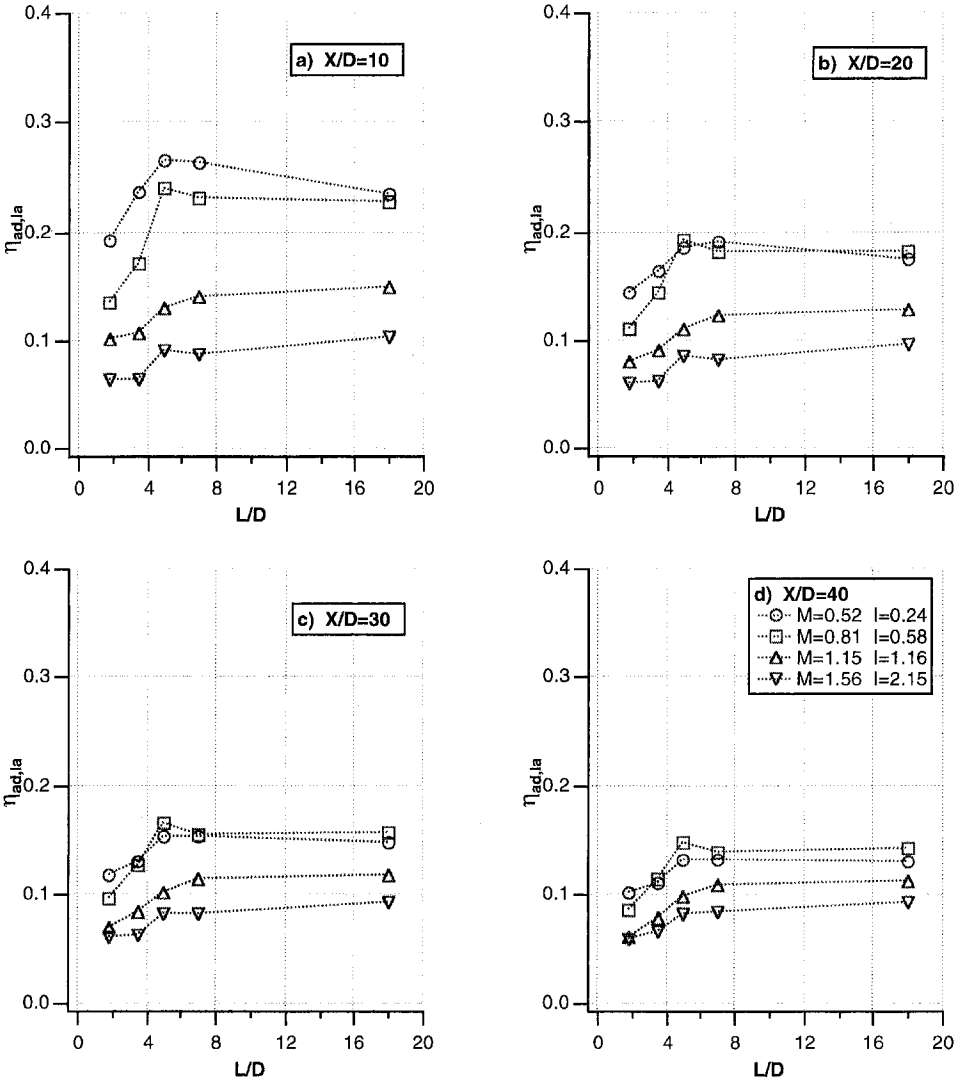

Fig. 9 Lateral averaged adiabatic film cooling effectiveness distributions versus length-to-diameter ratio at four streamwise locations, X/D: (*a*) = 10, (*b*) = 20, (*c*) = 30 and (*d*) = 40

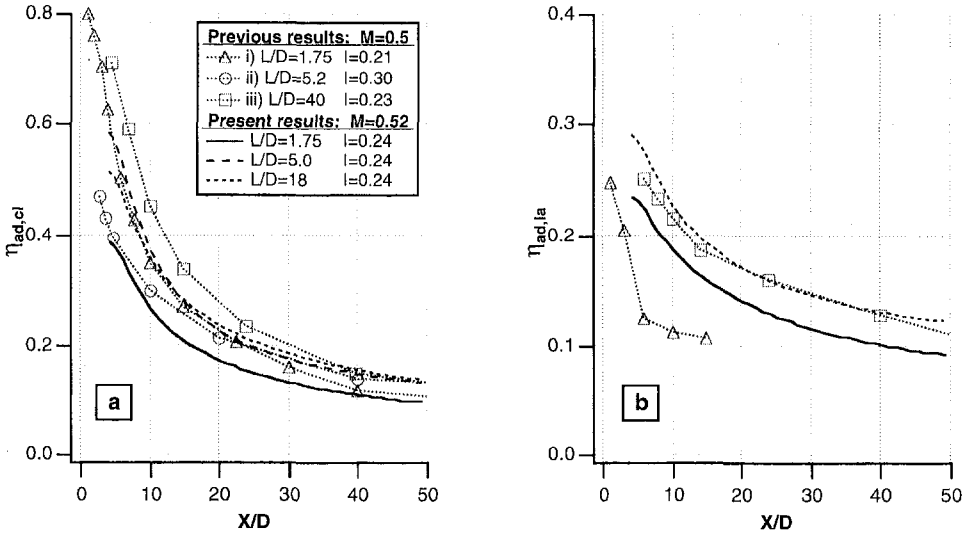

Fig. 10 Comparison of present (*a*) centerline and (*b*) lateral averaged adiabatic film cooling results with previous results from (*i*) Sinha et al. (1991), (*ii*) Goldstein et al. (1974), and (*iii*) Pedersen et al. (1977)

45 percent for the high blowing rate results (M = 1.15 and 1.56), compared to the corresponding results measured with the longer coolant channels. These results show that for injection configurations with the short coolant hole lengths, significant decreases in the film cooling effectiveness can occur and that the coolant hole L/D must be added to the long list of geometric and flow characteristics that influence film cooling performance.

Comparison With Previous Results

The comparison of the present results with data from Goldstein et al. (1974) at a blowing rate M = 0.5 indicates higher film effectiveness values from the present experiment in the near injection region and identical values farther downstream (Fig. 10*a*). These differences are attributed to the higher momentum flux ratio due to the lower density ratio of the experiments conducted by Goldstein et al. (1974). Results from Pedersen et al. (1977) and Sinha et al. (1991) indicate higher values of centerline film cooling effectiveness for $X/D < 40$ and identical values farther downstream, compared to the present results. The agreement between the present lateral averaged results for a blowing rate M = 0.5 shown in Fig. 10(*b*) with results from Pedersen et al. (1977) is good. Results from Sinha et al. (1991) indicate significantly lower lateral averaged film cooling effectiveness values in the near injection region, compared to the present results. These differences between these two measurements decrease with downstream distance, if the data from Sinha et al. (1991) are extrapolated to higher X/D values.

The agreement between the present results and data from Pedersen et al. (1977) at the higher blowing rate M = 1.0 is reasonably good for the centerline film cooling effectiveness (Fig. 11(*a*)). The centerline values from Goldstein et al. (1974) indicate lower values close to the injection holes and similar values for $X/D > 30$ compared to the corresponding present results. The centerline values from Sinha et al. (1991) indicate lower values compared to the corresponding present results. The lateral averaged film cooling effectiveness values from Pedersen et al. (1977) are less compared to the comparable present data (Fig. 11(*b*)).

The results from the present experiments do not identically repeat the aforementioned experiments. These differences are mainly attributed to higher free-stream turbulence intensity at

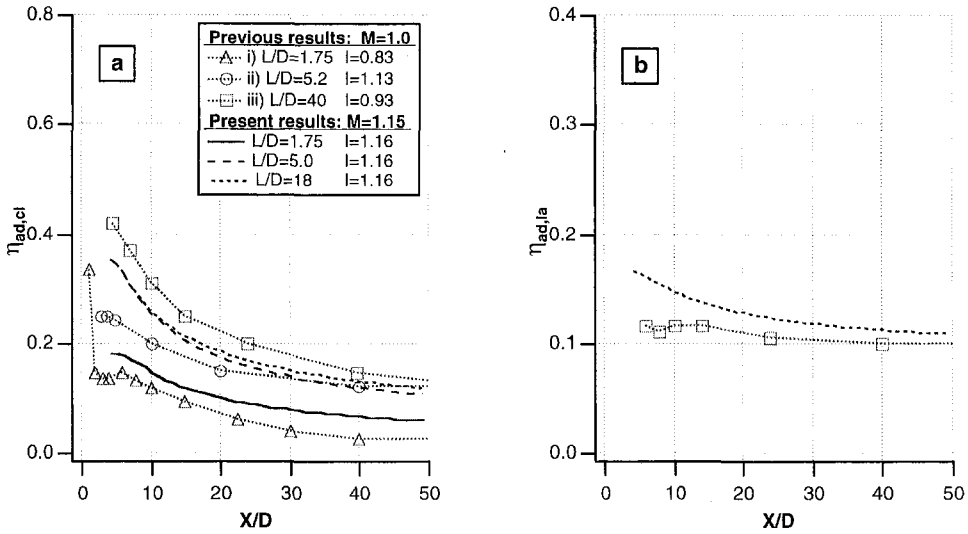

Fig. 11 Comparison of present (*a*) centerline and (*b*) lateral averaged adiabatic film cooling results with previous results from (*i*) Sinha et al. (1991), (*ii*) Goldstein et al. (1974), and (*iii*) Pedersen et al. (1977)

which the present experiments were conducted. However, the results show the significant effects of L/D ratios with the same trends as the previous experiments. In addition, the physical insight obtained from the experiments is useful in understanding some of the physical mechanisms governing film cooling.

Conclusions

Adiabatic film cooling experiments were conducted with a row of cylindrical holes oriented at 35 deg to the external flow direction. The hole length-to-diameter ratios were systematically varied in the range of L/D = 1.75, 3.5, 5, 7, and 18. The adiabatic film cooling effectiveness was determined for a range of blowing rates at a fixed free-stream velocity level (U_∞ = 115 m/s). The purpose of these experiments was to investigate systematically the effects of coolant hole length-to-diameter ratio and explain the diverse film cooling results previously obtained by several investigators with different ratios of coolant hole L/D.

Small to moderate effects of hole length-to-diameter ratio on film cooling performance was measured for the long injection hole configurations (i.e., L/D = 5, 7, and 18). The coolant flow characteristics in the cylindrical holes were apparently sufficiently established after seven hole diameters so as to not significantly alter the film cooling effectiveness distribution for the greater value of hole L/D.

The film cooling effectiveness decreased with decreasing hole L/D ratio in the range of $1.75 \leq L/D \leq 5.0$. This decrease in film cooling effectiveness was attributed to: (1) the undeveloped character of the flow in the coolant channels and (2) the greater effective injection angle of the coolant flow, with respect to the external flow direction and surface.

The lowest values of the film cooling effectiveness were measured for the smallest hole length-to-diameter ratio, L/D = 1.75. The decrease in film cooling performance was about 25 percent for the low blowing rate results (M = 0.52), about 40 percent for the moderate blowing rate results (M = 0.81), and about 30 to 45 percent for the high blowing rate results (M = 1.15 and 1.56), compared to the corresponding results achieved with the longer coolant channels.

Acknowledgments

The authors wish to acknowledge the help of Mr. S. Wolff and Mr. J. Wiegelmann for conducting the film cooling experiments described in this paper.

References

Burd, S. W., and Simon, T. W., 1997, "The influence of coolant supply geometry on film coolant exit flow and surface adiabatic effectiveness," ASME Paper No. 97-GT-25.

Goldstein, R. J., Eckert, E. R. G., and Burggraf, F., 1974, "Effects of hole geometry and density on three-dimensional film cooling," *Int. J. Heat Mass Transfer,* Vol. 17, pp. 595–607.

Goldstein, R. J., 1971, "Film Cooling," *Advances in Heat Transfer,* Vol. 7, Hartnett, J. P., Irving, T. F., eds., Academic Press.

Leylek, J. H., and Zerkle, R. D., 1994, "Discrete-Jet Film Cooling: A Comparison of Computational Results With Experiments," ASME JOURNAL OF TURBOMACHINERY, Vol. 116, pp. 358–368.

Papell, S. S., Wang, C. R., and Graham, R. W., 1982, "Film-Cooling Effectiveness With Developing Coolant Flow Through Straight and Curved Tubular Passages," NASA Technical Paper 2062.

Papell, S. S., 1984, "Vortex Generating Flow Passage Design for Increased Film-Cooling Effectiveness and Surface Coverage," NASA Technical Memorandum 83617, prepared for National Heat Transfer Conference, Aug. 5–8.

Pedersen, D. R., Eckert, E. R. G., and Goldstein, R. J., 1977, "Film cooling with large density differences between the free-stream and the secondary fluid measured by the heat-mass transfer analogy," ASME *Journal of Heat Transfer,* Vol. 99, pp. 620–627.

Sinha, A. K., Bogard, D. G., and Crawford, M. E., 1991, "Film-Cooling Effectiveness Downstream of a Single Row of Holes With Variable Density Ratio," ASME JOURNAL OF TURBOMACHINERY, Vol. 113, pp. 442–449.

Vogel, D. T., Wilfert, G., and Fottner, L., 1995, "Numerical and Experimental Investigation of Film Cooling From a Row of Holes at the Suction Side of a Highly Loaded Turbine Blade," *ISABE Paper,* Vol. 2, p. 1121.

Walters, D. K., and Leylek, J. H., 1996, "A Systematic Computational Methodology Applied to a Three-Dimensional Film-Cooling Flowfield," ASME Paper No. 96-GT-351; ASME JOURNAL OF TURBOMACHINERY, Vol. 119, 1997, pp. 777–785.

Walters, D. K., and Leylek, J. H., 1997, "A Detailed Analysis of Film Cooling Physics. Part I: Streamwise Injection With Cylindrical Holes," ASME Paper No. 97-GT-269.

Effect of High Free-Stream Turbulence With Large Length Scale on Blade Heat/Mass Transfer

H. P. Wang

R. J. Goldstein

S. J. Olson

Department of Mechanical Engineering,
University of Minnesota,
Minneapolis, MN 55455

The naphthalene sublimation technique is used to investigate the influence of high free-stream turbulence with large length scale on the heat/mass transfer from a turbine blade in a highly accelerated linear cascade. The experiments are conducted at four exit Reynolds numbers, ranging from 2.4 × 10^5 to 7.8 × 10^5, with free-stream turbulence of 3, 8.5, and 18 percent and corresponding integral length scales of 0.9 cm, 2.6 cm, and 8 cm, respectively. On the suction surface, the heat/mass transfer rate is significantly enhanced by high free-stream turbulence due to an early boundary layer transition. By contrast, the transition occurs very late, and may not occur at very low Reynolds numbers with low free-stream turbulence. In the turbulent boundary layer, lower heat/mass transfer rates are found for the highest free-stream turbulence level with large length scale than for the moderate turbulence levels with relatively small scales. Similar phenomena also occur at the leading edge. However, the effect of turbulence is not as pronounced in the laminar boundary layer.

Introduction

Developing more efficient and powerful gas turbines has been a goal of both designers and researchers for decades. This can be accomplished by running at higher operating temperatures, but care must be taken to account for potential heat transfer problems on surfaces within the turbine. Following the combustor, the turbulence level entering a blade row is high and causes early boundary layer transition along the blade surfaces and enhances heat transfer there. The role of the turbulence length scale, another important parameter in a turbulent field, however, is not yet well understood. Most of the experiments related to elevated free-stream turbulence have been conducted in a turbulent field generated by grids. These grids generate relatively small scales of turbulence in which the effect of scale on a blade surface has been generally ignored. Goldstein et al. (1983) found turbulence intensity of about 15–20 percent at the exit of can-type combustors. They found the profiles of the velocity, turbulence intensity, and temperature are fairly flat at the exit of the combustor. They did not measure the length scale for those flows.

Flow across cylinders under the influence of elevated free-stream turbulence is similar to leading edge flow over a turbine blade. The correlation, given by Kestin and Wood (1971), for cylinder stagnation heat transfer in the presence of free-stream turbulence does not include the influence of turbulence length scale. It works well for small turbulence length scales, but fails for larger length scales. Ames and Moffat (1990) and Ames (1997) used the combination of Reynolds number, turbulence intensity, and an energy length scale to correlate their data, which seems to give a satisfactory fit. The correlation implies that a larger length scale would diminish heat transfer, but not as significantly as the turbulence intensity augments heat transfer. Dullenkopf and Mayle (1995) used von Karman's energy spectrum theory of the inertial subrange of turbulence to develop a semi-empirical correlation of Nusselt number, which combines Reynolds number, integral length scale, and local acceleration factor into an "effective" turbulence intensity. The relation is linear and has the advantage that it applies not only to the stagnation region, but also to laminar boundary layers.

Grid turbulence generators are often used to increase the free-stream turbulence. Baines and Peterson (1951) reported that approximately 10 percent, nearly isotropic turbulence, could be reached with grid turbulence generators at about 30 bar diameters downstream of the grid. Some attempts have been made to generate much higher free-stream turbulence to approach the real turbine conditions. Young et al. (1992) used a jet grid, with jets directed upwind or downwind, to generate high free-stream turbulence. Thole et al. (1994) generated nearly 20 percent relatively large-scale turbulence using opposing wall jets separated by a splitter plate in the center of their flow passage.

Combustor simulators have also been used to generate high turbulence with large scale (Ames and Moffat, 1990; Chung and Simon, 1993). The main concern with these high-turbulence generators is the uniformity of the incoming velocity, turbulence intensity, and length scale. Ames and Moffat (1990) used the simulator to generate high free-stream turbulence intensity and large length scale to investigate their effect on heat transfer from a cylinder and to a flat plate turbulent boundary layer. They found that large length scale reduced heat transfer near the cylinder stagnation line and to the turbulent boundary layer. Later Ames (1997) used a similar combustor simulator and a grid to generate different length scales of turbulence to investigate the effect of high turbulence on turbine vane surfaces. He found there is no significant variation of Stanton number for a turbulent boundary layer where a slightly adverse pressure gradient prevails in all the high turbulence tests, in contrast to the augmentation of heat transfer in the accelerated laminar boundary layer. His data also showed that near the leading edge of his vane, the heat transfer rate with lower turbulence intensity and smaller scale is actually slightly higher than that with higher turbulence intensity and larger length scale for the two Reynolds numbers studied. Unlike many investigators, he found that the location of boundary layer transition is almost unchanged with increasing high free-stream turbulence.

Contributed by the International Gas Turbine Institute and presented at the 43rd International Gas Turbine and Aeroengine Congress and Exhibition, Stockholm, Sweden, June 2–5, 1998. Manuscript received by the International Gas Turbine Institute February 1998. Paper No. 98-GT-107. Associate Technical Editor: R. E. Kielb.

In the present study, a high turbulence generator, similar to a combustor simulator, along with conventional grids, are used to generate high turbulence with large length scales. The naphthalene sublimation technique is used to investigate the effect of the turbulence on transfer coefficients on simulated blade surfaces. This method has a well-defined boundary condition and the results can be readily converted through the heat and mass transfer analogy (Eckert, 1976). The mass transfer technique produces very detailed local measurements and the result represents purely the fluid transport phenomena, without extraneous conduction and radiation effects that are present in heat transfer studies. A detailed description of the mass transfer technique using naphthalene sublimation, including its advantages and disadvantages, is given by Goldstein and Cho (1995).

Experimental Apparatus

Wind Tunnel and Test Section. The wind tunnel is the same as used for the flow visualization experiments by Wang et al. (1997). It is a multi-purpose blowing type wind tunnel, powered by a 22.4 kW blower. The air flow enters the test section through a square contraction with an area ratio of 6.25 and with exit dimensions of 45.7×45.7 cm^2.

The test section after the contraction is shown in Fig. 1. All the walls of the test section are made of 1.9-cm-thick Plexiglas so that the flow in and around the cascade can be viewed to permit flow visualization experiments. The cascade contains four blades plus two bypass flexible walls. The two central blades are interchangeable to accomplish the experiments on either the pressure side or the suction side of the blades. Blade position 2 (see Fig. 1) is used for suction side tests and position 3 for pressure side tests. The other two outside blades are fixed in position in the cascade. The two tailboards behind the two outside blades and the flexible walls can be adjusted while monitoring the static pressure to balance the flow distribution in the central passage with the neighboring passages. This produces uniform flows through the three passages. The geometry of the central passage of the cascade is illustrated in Fig. 2. The cascade dimensions and flow conditions are listed in Table 1.

One of the two straight sections ahead of the cascade has two slots, which can be used to insert turbulence grids to generate free-stream turbulence. The straight and grid sections are interchangeable and with the grids can be used to provide different turbulence levels at the entrance of the cascade. Several slots and holes are cut into the walls ahead of and behind the cascade to insert probes to measure pressure, velocity and temperature.

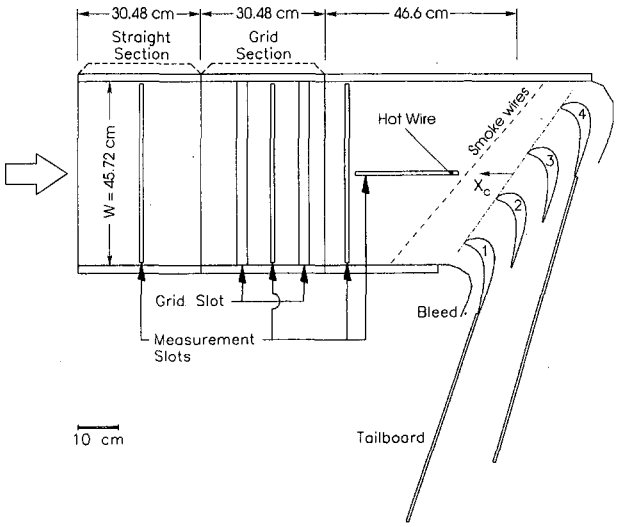

Fig. 1 Schematic top view of the test section

Test Blades. There are two test blades: One is a pressure measurement blade used to determine the static pressure distribution on the blade surface and the other is a naphthalene blade used for mass transfer measurements. The blade profile, supplied by General Electric Co., is given by Wang et al. (1997).

The pressure measurement blade is a hollowed-out aluminum blade. There are 30 pressure taps, of which 25 are used during flow balancing measurements. The static pressure distribution is measured at midspan with the pressure measurement blade in position 2 and position 3, as shown in Fig. 1. The tailboards and bleeds are adjusted so that the measurements at the two

Nomenclature

A_1 = inlet area of one flow passage, see Fig. 2, $= PH \cos \beta_1$
A_2 = outlet area of one flow passage, see Fig. 2, $= PH \cos \beta_2$
a_1 = dimensionless strain rate, $U_\infty = a_1 U_{in} x/D$ for flow near the leading edge of a circular cylinder, =4 for potential flow
C = chord length of blade = 18.4 cm
C_{Ps} = static pressure coefficient
C_x = axial chord of blade = 13.0 cm
D = diffusion coefficient of naphthalene in air or, diameter of a circular cylinder
H = height of test section =45.7 cm
h_m = mass transfer coefficient
L = distance from turbulence generator to cascade entrance
L_a = dimensionless length scale = $(L_x/D)\sqrt{a_1\ \mathrm{Re_D}}$
L_x = longitudinal integral length scale
M = mesh size of turbulence generators, see Table 2
Nu = Nusselt number based on chord length
$\mathrm{Nu_a}$ = effective stagnation Nusselt number = $\mathrm{Nu_D}/\sqrt{a_1\ \mathrm{Re_D}}$
$\mathrm{Nu_D}$ = Nusselt number based on cylinder diameter
n = power index used in heat/mass transfer analogy
P = pitch of cascade = 13.8 cm
Pr = Prandtl number
Re = Reynolds number based on chord length = UC/ν
$\mathrm{Re_D}$ = cylinder Reynolds number based on diameter and incoming velocity = $U_{in}D/\nu$
S_p = surface distance on pressure side starting at blade leading edge
S_s = surface distance on suction side starting at blade leading edge
Sc = Schmidt number = ν/D, taken to be ~2.285 for naphthalene
Sh = Sherwood number based on blade chord = $h_m C/D$
Tu = turbulence intensity
Tu_a = modified turbulence intensity = $Tu\sqrt{\mathrm{Re_D}/a_1}$
U = average free-stream velocity
U_c = average free-stream velocity measured at midspan
W = width of test section = 45.7 cm, see Fig. 1
X_c = distance upstream from the cascade entrance, see Fig. 1
X_M = distance from turbulence grids, or from the center of the second row of wall jets for high turbulence generator
X_n = longitudinal axial coordinate, see Fig. 2
x = surface distance from stagnation line, in equation for a_1
Y_n = transverse axial coordinate, see Fig. 2
β_1 = inlet flow angle = 35 deg
β_2 = exit flow angle = −72.49 deg
ν = kinematic viscosity of air

Subscripts

in = inlet condition
ex = exit condition
∞ = local main flow condition along surface distance

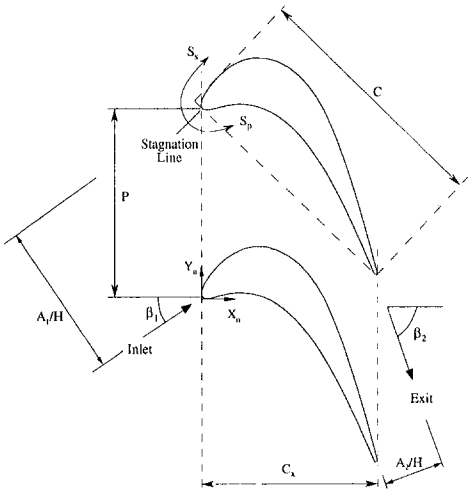

Fig. 2 Central passage of the cascade and dimensions

blade locations match one another and match a potential flow calculation for the blade passage.

The second test blade, the naphthalene blade, is also made from aluminum and has two metal caps on each end, which border the cast naphthalene in between. The middle part of the test blade is depressed about 2.5 mm. Melted naphthalene is cast, using a well-polished mold, into this gap to provide the same profile as the metal caps.

The pressure measurement and naphthalene blade segments are each 19.7 cm in length. The balance of the total blade length (and tunnel height) of 45.7 cm is made of two 13-cm-long blade segments. When conducting a two-dimensional test, the two solid segments are positioned at the top and bottom endwalls sandwiching the test blade in between. The total length of the three blade pieces has the same height as the wind tunnel. The three blades are held in place by two rods passing through the blades to the top and bottom walls. Two pin holes near the leading and trailing edge are drilled into the bottom endwall and the blade top and bottom caps to align the three blade pieces in position.

Turbulence Generators. Two grid turbulence generators are used to generate free-stream turbulence. They can be inserted into the slots ahead of the cascade. One is an expanded metal sheet and the other is a conventional cross-bar grid made from wood. Their open area ratios are 0.56 and 0.60, respectively. The original squared bar grids are routed to a relatively round bar with two different radii. The side with larger radius faces the oncoming flow and the other side with smaller radius faces downstream. More detailed information is available in the dissertation by Wang (1997).

Table 1 Cascade and test section data

Number of blades	4
Chord length of blade - C	18.4 cm
Axial chord of blade - C_x	13.0 cm
Pitch of cascade - P	13.8 cm
Height of cascade - H	45.7 cm
Width of wind tunnel - W	45.7 cm
Aspect ratio (Span/Chord) - H/C	2.48
Blade inlet angle - β_1	35°
Blade outlet angle - β_2	−72.49°
Inlet/Exit area ratio of the cascade	2.72
Area ratio of the contraction	6.25
Highest exit Reynolds number - Re_{ex}	7.8×10^5

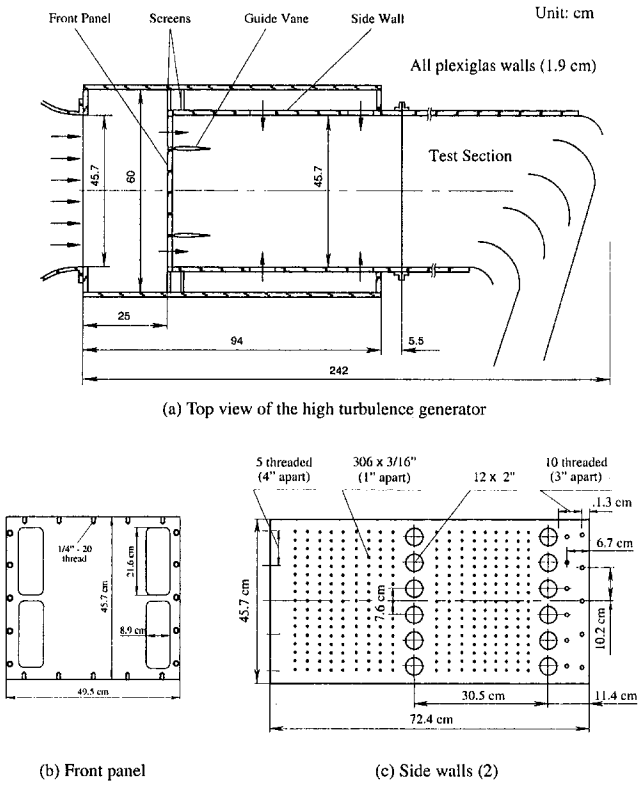

Fig. 3 Large-scale high-turbulence generator

The third turbulence generator, shown in Fig. 3, simulates the flow from a turbine combustor. The prototype of this simulator comes from Ames and Moffat (1990) and Chung and Simon (1993). In their designs, the simulators are followed by a small contraction to get a more uniform incoming turbulent flow. To simplify the design, the current high turbulence generator does not have that contraction.

Figure 3(a) is the top view of the high-turbulence generator. Its main components are the front panel and two side walls, shown in Figs. 3(b, c), respectively. The front panel has four slots, two along each side in parallel. The combination of the solid block in the middle and the slots along the sides will produce a large swirling flow. Each of the two side walls has two rows of holes, which inject air into the main stream to further enhance the flow circulation. The rows of small holes on the side walls were originally designed to simulate film cooling flow. However, in these tests the holes are blocked with tape and no flow comes out from the small holes. This high-turbulence generator is placed ahead of the test section, Fig. 1. Two guide vanes are added at the exit of the front slots to force the flow to move along the sides. In addition, several screens are added to reduce the wall jet flows at the place where the air flow enters the side wall gaps. Relatively uniform velocity and turbulence distributions are obtained in both the vertical and horizontal directions with this system (Wang, 1997).

Data Acquisition Systems. The turbulent field is measured using a TSI Model 1210 single-sensor, hot-wire probe, and TSI IFA 100 system. The flow and blade temperatures are measured using copper-constantan (Type T) thermocouples. The integral length scale of turbulence is computed from Taylor's hypothesis by averaging 30 sets of power spectrum sampling data, acquired at a 20 kHz sampling rate with a cutoff frequency of 10 kHz, and using an autocorrelation function.

The data acquisition system used in the naphthalene mass transfer experiments is generally the same as described in the paper by Goldstein et al. (1995). The measurement tables have

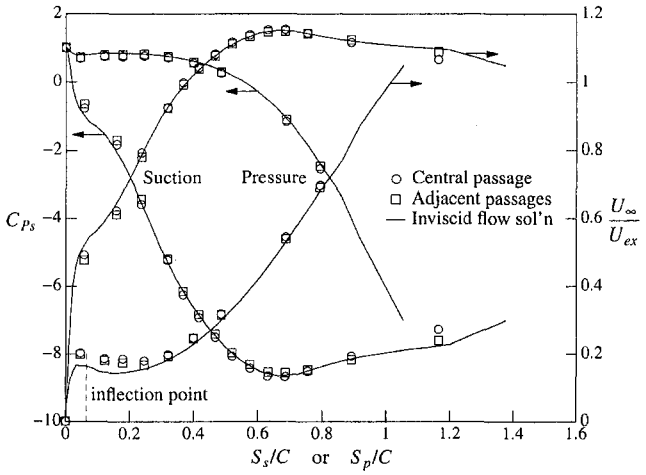

Fig. 4 Static pressure coefficient and velocity profiles along blade surfaces at $Re_{ex} = 5.2 \times 10^5$, $U_{ex}/U_{in} = 2.7$

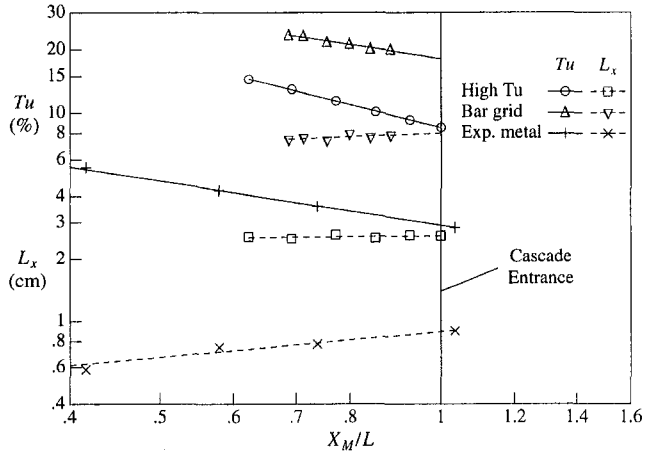

Fig. 6 Decay/growth of turbulence/scales of different turbulence generators

been refurbished to meet the need of scores of tests and the computer has been upgraded. Nearly 3000 data points can be taken in an hour. The uncertainty of the results, at 95 percent confidence using the methods described by Kline and McClintock (1953), is about 7 percent in Sherwood number measurement, of which 5 ~ 6 percent comes from the uncertainty in property correlations. As a result, the relative error would be much smaller.

A typical naphthalene sublimation wind tunnel test takes about 40 to 60 minutes during which about 0.08 mm naphthalene in average depth is sublimed. This amount of naphthalene sublimation generally does not affect the flow field around the blade.

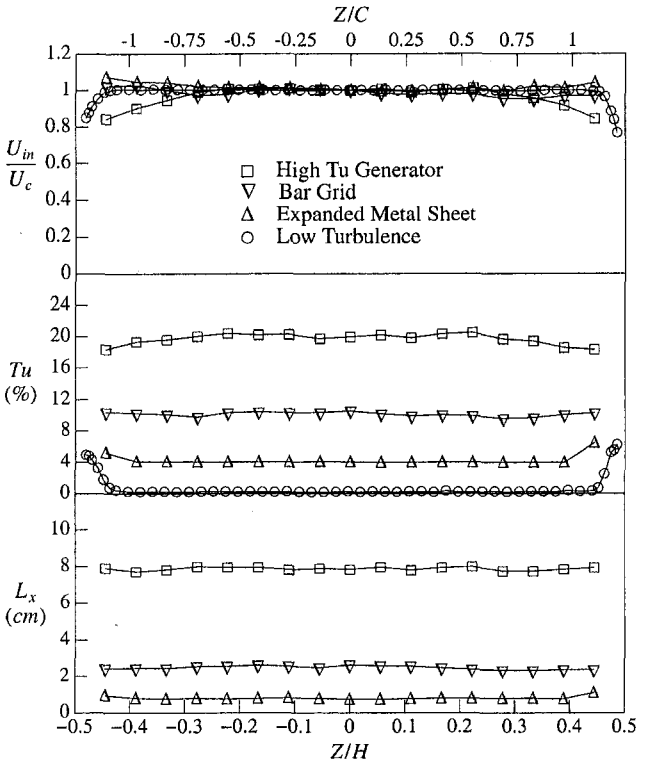

Fig. 5 Spanwise incoming velocity profiles measured at $X_c/C = 0.8$ with and without turbulence generators ($Re_{ex} = 5.2 \times 10^5$)

Results of Flow Field Measurement

Static Pressure Distribution in the Passage. The static pressure is measured along the suction and pressure surfaces at the midspan inside the central passage of the cascade using a special blade section with 25 pressure taps. The measured distribution is shown in Fig. 4. The static pressure distributions along the two adjacent passages are also measured to compare with the central passage measurement. It is seen from the figure that the neighboring passages have almost the same pressure distributions as the central passage. The solid lines in the figure are the results calculated from potential flow theory and match quite well with the measurements. The three passages between the two tailboards have almost the same volumetric flows. The flow inside the central passage is expected to represent the flow in a continuous blade cascade.

Based on the pressure distribution along the blade surfaces, a corresponding velocity distribution can be calculated using the Bernoulli equation. Figure 4 also shows the local free-stream velocity distribution along the surface distance, normalized by the exit velocity. The velocity profile computed from the potential flow theory can be used to define a local similarity variable, m, which is used to solve the local laminar wedge-flow similarity equations of momentum, heat, and mass transfer. The approximate analytical method is described by Goldstein et al. (1995).

Incoming Flow Profiles. The spanwise distributions of the incoming velocity, turbulence intensity, and integral length scale for each of the three turbulence generators as well as for the low turbulence case, are shown in Fig. 5. These are measured at $X_c/C = 0.8$. All the distributions are quite uniform along the span of the cascade. The turbulence decay and the length scale growth are plotted in Fig. 6. The decay/growth of turbulence/length scale are measured by moving the grids upstream to obtain the turbulent field for the corresponding cascade position. For the high-turbulence generator, the flow condition at the cascade entrance is extrapolated from its decay/growth curve. The data are summarized in Table 2. The values represent the

Table 2 Cascade-entrance free-stream turbulence parameters, $X_c = 0$

Generator	Tu(%)	L_x(cm)	M(cm)	L(cm)
No grid	0.2	-	-	-
Expanded Metal Sheet	3.0	0.9	1.27	51.0
Bar Grid of 2 cm	8.5	2.6	9.00	102.2
High Tu Generator	18.0	8.0	7.62	119.1

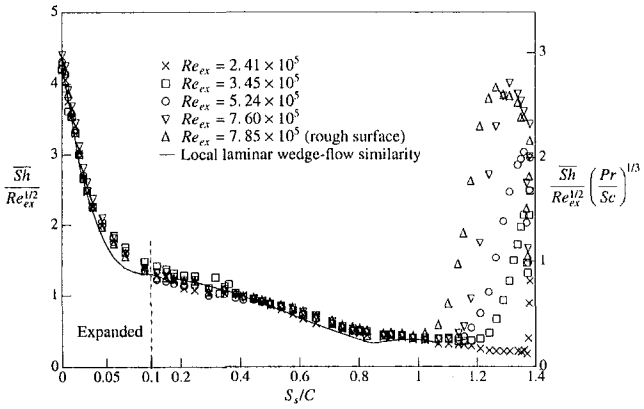

Fig. 7 Comparison of $\overline{Sh}/Re_{ex}^{1/2}$ along the suction surface at different Re_{ex}s (low turbulence)

flow conditions at a distance equal to the center of the cascade and would be slightly different at blade positions 2 and 3. No measurable difference in mass transfer was found at the stagnation points for the two blade positions, however.

Producing uniform velocity and turbulence profiles for the high turbulence generator is difficult. Before installing the guide vanes at the exit of the front panel slots (Fig. 3(*a*)), the measurement in the lateral direction showed a parabolic velocity profile, with the highest velocity in the middle. After installing the guide vanes and adjusting the wall jets, a relatively uniform velocity profile in the lateral direction is obtained at $X_c/C = 2.3$ ($X_M/M = 10.2$) with 4.5 percent variation in velocity and less than 10 percent variation in turbulence and length scale. The lateral distributions of velocity and turbulence parameters are very similar to the vertical distributions of Fig. 5. For detailed upstream information about power spectra, autocorrelation, and flow uniformity of the flow parameters on these turbulence generators, readers should refer to Wang (1997).

Mass Transfer Results and Discussion

Reynolds Effect at Low Free-Stream Turbulence. Tests are performed at four Reynolds numbers over the range $2.4 \times 10^5 < Re_{ex} < 7.8 \times 10^5$. The mass transfer results along the suction surface are shown in Fig. 7 using the dimensionless laminar flow parameter $Sh/Re^{1/2}$. Also shown in the figure are the local laminar wedge-flow similarity solutions for comparison. The mass transfer results on the pressure side in the absence of free-stream turbulence vary due to the development of Taylor–Görtler vortices. This issue is discussed in a forthcoming paper.

It is seen (Fig. 7) that in the region from $S_s/C < 1.05$, all the data fall on one curve and match well with the local laminar wedge-flow similarity solution. It appears that the flow regime is laminar over most of the suction surface for the Reynolds number range studied. Higher transfer rates are found both near the leading edge ($S_s/C \approx 0$) and near the trailing edge ($S_s/C > 1$) where boundary layer transition occurs for higher Reynolds numbers. When the Reynolds number is small ($Re_{ex} = 2.4 \times 10^5$) it appears that boundary layer transition does not occur until very near the trailing edge. The rapid rise in Sherwood number at the trailing edge indicates the vortex shedding behind the blade. With increasing Reynolds numbers, the start of boundary layer transition gradually moves upstream, but the transition is not complete by the trailing edge for $Re_{ex} < 7.6 \times 10^5$.

Also included in Fig. 7 is a second test at $Re_{ex} = 7.85 \times 10^5$. A rather rough surface finish due to poor casting near the trailing edge ($S_s/C > 1$) in the test is the main difference from the other run at this Reynolds number. These two tests are very repeatable except for the location of transition. As indicated by the mass transfer Sherwood number, the boundary layer flow with the rough surface has an earlier boundary layer transition than that with a relatively smooth surface.

Effect of Turbulence. Two Reynolds numbers (3.6×10^5 and 5.2×10^5) tests are performed with high incoming free-stream turbulence in the central passage of the cascade. Figures 8 and 9 show the distributions of mass transfer Sherwood number along the suction and the pressure surfaces when the test blade is exposed to different incoming free-stream turbulence.

On the suction surface at $Re_{ex} = 3.6 \times 10^5$, there is almost no effect of high free-stream turbulence on the mass transfer in the laminar boundary layer region. The Sherwood number matches well with the local laminar similarity solution even though the free-stream turbulence intensity is raised as high as 18 percent. When the Reynolds number reaches 5.2×10^5, a slightly higher mass transfer rate is observed around $S_s/C = 0.18$ with increasing turbulence level, but the boundary layer is still laminar.

An interesting impact of elevated turbulence is the bypass-type, early-boundary-layer transition. The start of transition shifts upstream with increasing turbulence level. When the turbulence level reaches $\approx$ 18 percent, the region with transition or a turbulent boundary layer covers about half of the blade suction surface. In addition, higher Reynolds numbers would move the start of transition even farther upstream and more blade surface would be exposed to a turbulent boundary layer.

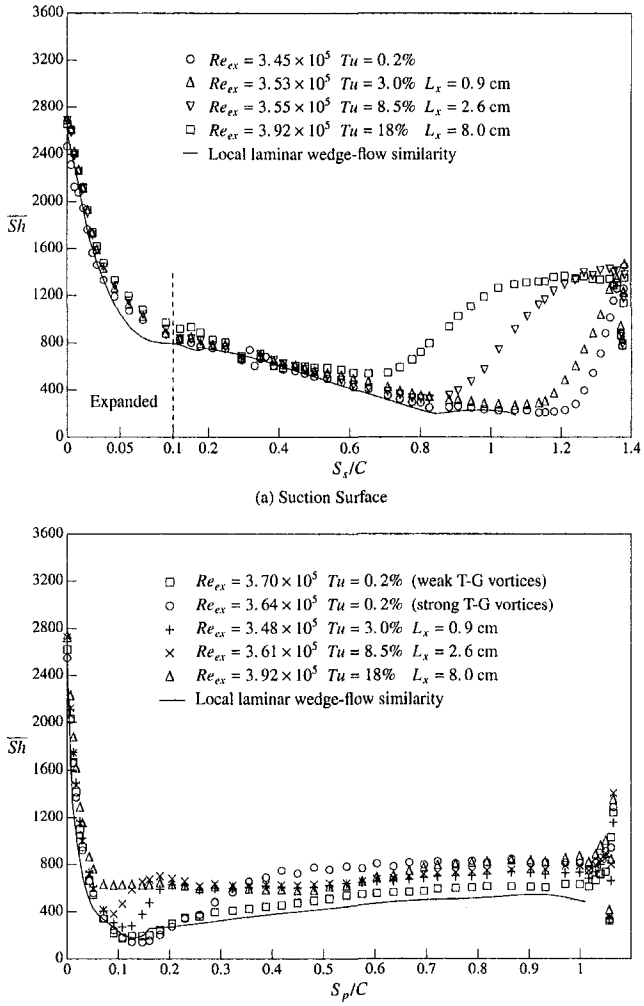

Fig. 8 Sherwood number distribution for elevated turbulence levels at $Re_{ex} = 3.6 \times 10^5$

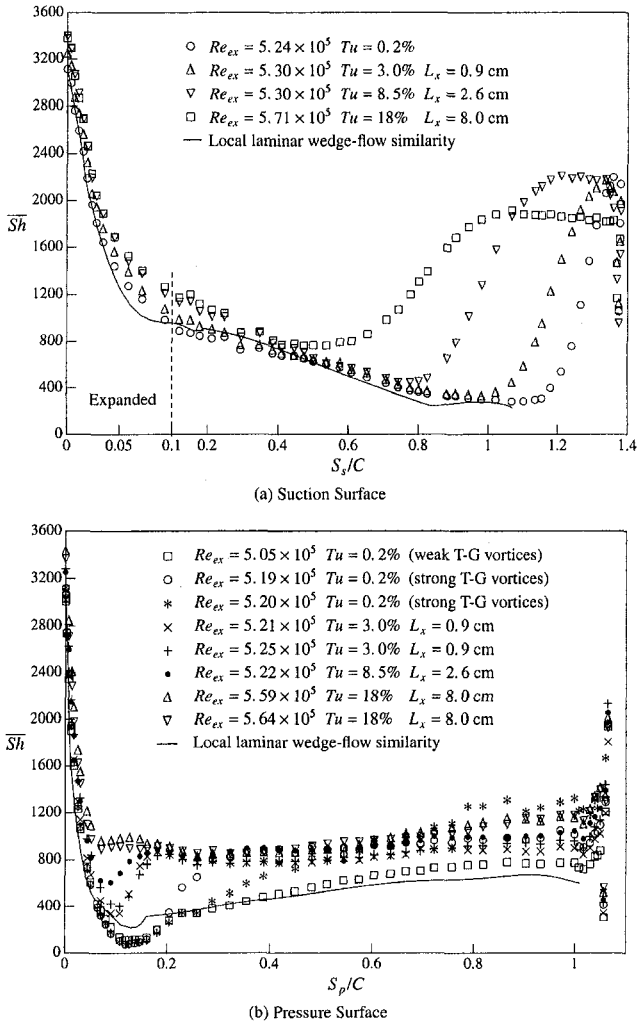

Fig. 9 Sherwood number distribution for elevated turbulence levels at $Re_{ex} = 5.2 \times 10^5$

This transition and the subsequent turbulent boundary layer significantly increase the mass transfer rate, compared to the results in the same area with a laminar boundary layer.

It is hard to determine from these limited tests how the length scale affects the boundary layer transition. It is seen from Fig. 8 and 9 that when the free-stream turbulence is less than 8.5 percent, the boundary layer transition starts in the decelerated region ($S_s/C > 0.8$, cf. Fig. 4) while for the case of the high-turbulence generator ($Tu = 18$ percent), it starts near the narrowest width (highest acceleration at $S_s/C \approx 0.65$) of the channel. Interestingly, the integral length scale of the latter ($L_x = 8$ cm) is roughly equivalent to the size of the blade passage. Actually, the narrowest width of the channel (~6 cm) is even smaller than the length scale. Also a longer length of boundary layer transition is found with increasing turbulence level, as indicated by the mass transfer results. More studies are needed to explore the effect of length scale on the boundary layer transition in this complicated accelerated/decelerated flow.

For $Re_{ex} = 3.6 \times 10^5$ (Fig. 8(a)), the mass transfer rates in the turbulent boundary layer region after transition are almost independent of free-stream flow conditions. For $Re_{ex} = 5.2 \times 10^5$ with 18 percent free-stream turbulence (Fig. 9(a)), however, a lower mass transfer rate close to the trailing edge has been found than occurs for 3 and 8.5 percent turbulence at large S_s/C. The reduction of mass transfer is about 15 percent. This suggests that, except for an early boundary layer transition, elevated free-stream turbulence may not necessarily produce higher mass transfer in the turbulent boundary layer. On the other hand, the large length scale may play a role in reducing the mass transfer rate in the turbulent boundary layer.

On the pressure surface, the mass transfer rate reaches a minimum near $S_p/C = 0.12$ after the blade inflection point ($S_p/C = 0.065$) with low free-stream turbulence. With increasing turbulence levels, the minimum gradually moves upstream and almost vanishes when the turbulence level reaches 18 percent with an integral length scale of about 8 cm. The incoming turbulence significantly enhances the mass transfer rate locally around $S_p/C = 0.1$, compared to the extremely low mass transfer rate with low free-stream turbulence.

For low free-stream turbulence intensity tests, Taylor–Görtler vortices develop on the pressure surface and can significantly enhance the mass transfer rate. In the presence of elevated free-stream turbulence, no Taylor–Görtler vortices have been observed on the pressure surface in any of the mass transfer tests. It is interesting to see from the figures that the mass transfer rate is not as strongly enhanced by the free-stream turbulence as it is by Taylor–Görtler vortices in the low-turbulence case. This issue will be discussed in a forthcoming paper.

It is believed that the pressure-side boundary layer remains laminar due to the strong acceleration in the cascade. However, the mass transfer rate in the presence of high free-stream turbulence over the entire pressure surface is higher than predicted using the local similarity analysis. It is interesting to see that the mass transfer rates in the tests do not vary significantly with turbulence level ($Tu = 3 \sim 18$ percent) except in the area immediately after the inflection point.

Comparison With Heat Transfer Results. Figure 10 shows a comparison with the heat transfer results of Mehendale et al. (1994). The geometry data reported in their paper and the present blade profile are very similar, and both profiles are acquired from General Electric Co. The main difference between the two cascades is the aspect ratio. They have a relatively short cascade with the aspect ratio (height/chord) about 1.1 while the present aspect ratio is about 2.5. A slightly different pitch/chord ratio accounts for another difference. Hence the velocity ratio is about 2.4 in their cases and is about 2.7 in the present work. A constant heat flux method was used in their experiments and their data are averaged over the whole span. Clearly their Nusselt numbers include the influence of the secondary flows from both endwalls.

In the conversion of Sherwood number to Nusselt number, the power index of $n = \frac{1}{3}$ and $n = 0.4$ are used in Eq. (1) for the laminar and turbulent boundary layers, respectively,

$$\frac{\mathrm{Nu}}{\mathrm{Sh}} = \left(\frac{\mathrm{Pr}}{\mathrm{Sc}}\right)^n \tag{1}$$

A linear interpolation between 0.33 and 0.4 is used in estimating the Nusselt number in the transition zone. The present mass transfer experiment with a constant surface concentration actually represents a constant-temperature case in heat transfer, which accounts for another difference from a constant heat flux experiment.

Since they used inlet velocity to calculate Reynolds number, a corresponding change of the current exit Reynolds number is made to match their definition. The inlet Reynolds number of the current primary turbulence tests is a little lower than theirs and only one test condition with no free-stream turbulence matches their flow condition. It is seen from the figure that the general trend for these tests is basically the same, but there are some differences that need to be addressed.

The present tests have much higher Nusselt numbers near the leading edge than the data presented by Mehendale et al. (1994). This is probably due to conduction inside their small nose. The mass transfer has no error equivalent to conduction. The peak value is probably smoothed out by the conduction. In

addition, an endwall horseshoe vortex flow around the stagnation region would affect the heat transfer from the blade surface.

On the suction side, the main feature is the early boundary layer transition caused by free-stream turbulence. In addition, much earlier transition found in Mehendale et al. (1994) could be attributed to the cascade secondary flows. It is interesting to note that for $Re_{in} = 3 \times 10^5$ with no free-stream turbulence, the boundary layer transition in the current case is later compared to theirs, but the transfer rate is much higher in the present tests in the turbulent boundary layer farther downstream. This phenomenon implies that the secondary flows in their cascade may considerably thicken the turbulent boundary layer and hence reduce the heat transfer downstream.

On the pressure side in the case of $Re_{in} = 3 \times 10^5$ with low free-stream turbulence, the present results clearly show the processes of transition and relaminarization at the location around $S_p/C = 0.2$. There is no valley or peak found in their Nusselt number distribution, probably due to the effect of conduction and secondary flows. In the presence of high free-stream turbulence ($Re_{in} = 2 \times 10^5$), very similar distributions of Nusselt number are obtained from both cascades.

Leading Edge Mass Transfer. The test blade has a very small leading edge nose. The flow around the stagnation line of a turbine blade is related to the flow around a circular cylinder in crossflow, but they are not exactly the same. A cylinder in crossflow usually has a laminar or turbulent boundary layer separation before the wake region, which a turbine blade near the stagnation line does not have. The boundary layer around the stagnation line of a blade is actually a little thicker than the boundary layer of a cylinder even though they may have the same nose size. In other words the stagnation flow around a cylinder with an effective nose size, larger than the real size of blade nose, could be adopted to simulate the flow around the stagnation line of blade. If the blade nose is large the effective size may be close to the real size. Since the current test blade has a very small nose, about 3 mm in diameter, caution must be taken when comparing to measurements on circular cylinders. Choosing a cylinder with calculated flow acceleration data and the local similarity solution, indicates an effective cylinder of 9 mm diameter.

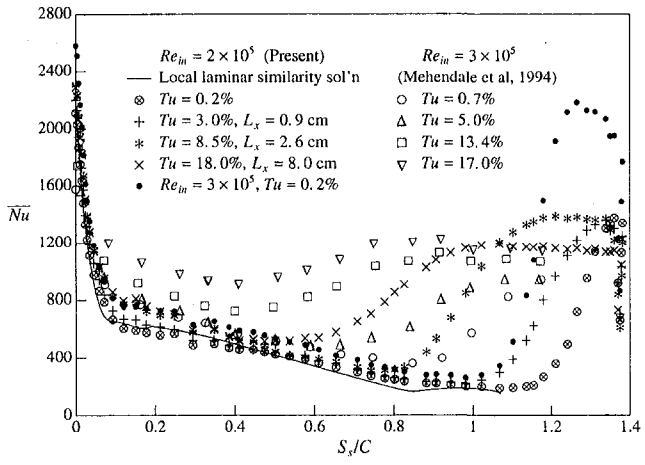

(a) Suction side

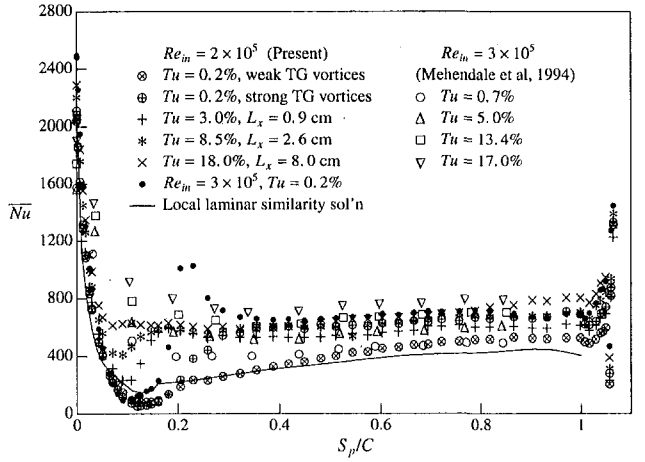

Fig. 10 Present investigation compared with heat transfer results of Mehendale et al. (1994)

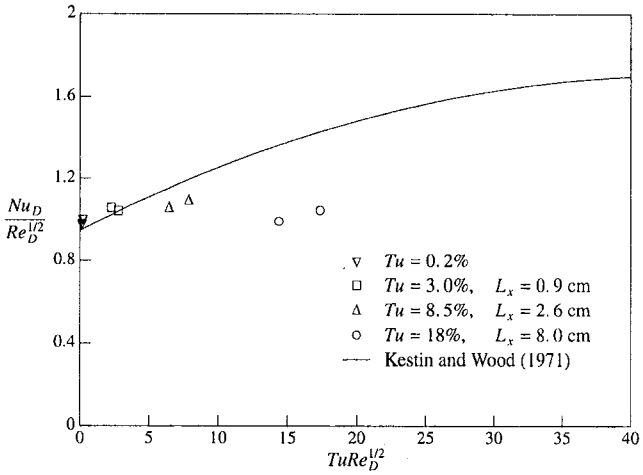

Fig. 11 Nusselt number at the leading edge of turbine blade, compared to the cylinder correlation of Kestin and Wood (1971)

Kestin and Wood (1971) suggested a correlation of Nusselt number for stagnation flow around a cylinder in the presence of high free-stream turbulence.

$$\frac{\mathrm{Nu}}{\mathrm{Re}_D^{1/2}} = 0.945 + 3.48\left(\frac{Tu\ \mathrm{Re}_D^{1/2}}{100}\right) + 3.99\left(\frac{Tu\ \mathrm{Re}_D^{1/2}}{100}\right)^2 \quad (2)$$

The correlation and the effective nose Nusselt number with elevated turbulence are shown in Fig. 11. It is seen from the figure that for relatively low free-stream turbulence the data match reasonably well with the correlation. For higher free-stream turbulence with large length scale the data are well off the correlation line; Kestin's correlation does not consider the effect of length scale.

The correlation suggested by Dullenkopf and Mayle (1995) includes both effect of turbulence intensity and integral length scale:

$$\mathrm{Nu}_a\ \mathrm{Pr}^{-0.37} = 0.571 + 0.01 Tu_\lambda \quad (3)$$

where

$$Tu_\lambda = \frac{Tu_a L_a^{1/2}}{(1 + 0.004 L_a^2)^{5/12}}$$

They used a more general acceleration parameter as a characteristic length and combined turbulence and length scale into an effective turbulence intensity. The comparison of the current experimental nose Nusselt numbers with the correlation is shown in Fig. 12. The data fit well with the correlation for moderately high turbulence and length scales. The data with large length scales are a bit off probably because the correlation may not fit well with extremely large scales, as indicated by the authors.

It must be mentioned that the dimensionless acceleration parameter a_1 in the equation may vary from 2.4 to 4, with the latter number a potential flow parameter. These stagnation data are obtained using $a_1 = 3.8$. As pointed out by the authors, the

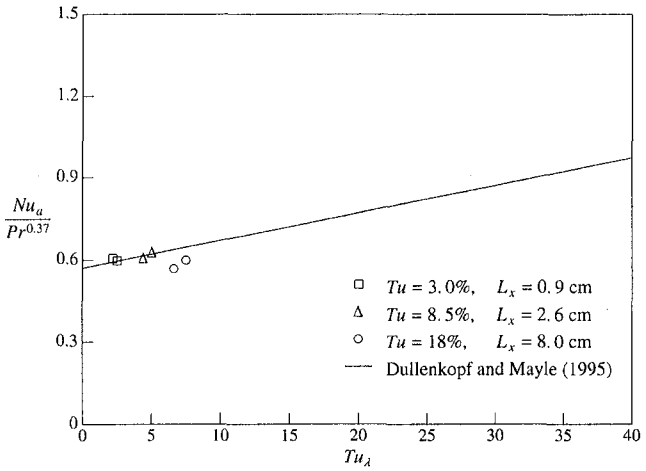

Fig. 12 Nusselt number at the leading edge of turbine blade, compared to the cylinder correlation of Dullenkopf and Mayle (1995)

parameter a_1 is a function of many factors including the length scale. It is worth mentioning that the current data would fit well with the correlation if a_1 is reduced for high turbulence and large length scale or if a_1 increases for relatively low turbulence and small length scale.

Conclusions

1 High free-stream turbulence with large length scale can be produced using a high turbulence generator (combustor simulator). A quite uniform incoming velocity and turbulent field has been obtained for the subsequent tests involving high free-stream turbulence.

2 Due to the strong acceleration of the passage flow, most of the suction and pressure surfaces are dominated by a laminar boundary layer for low free-stream turbulence. When Reynolds number is extremely low, $Re_{ex} < 2.4 \times 10^5$, essentially no transition has been observed on the suction surface.

3 The free-stream turbulence, by contrast, has little effect on the laminar boundary layer on the suction surface. The main contribution of free-stream turbulence is to cause an early boundary layer transition to turbulence, leading to a severalfold increase in mass transfer compared to the corresponding laminar boundary layer.

4 In the turbulent boundary layer on the suction surface, high turbulence intensity may not necessarily produce higher mass transfer rate. The length scale may have a considerable impact on mass transfer in reducing the transport rate. Attention to length scale should be paid at least equally with turbulence intensity to understand better the effect of free-stream turbulence.

5 Caution should be taken when comparing the blade leading edge data to cylinder data. The flows are not exactly the same for the two geometries, especially for a blade with a small nose at the leading edge. The correlation presented by Dullenkopf and Mayle (1995) includes the effect of both turbulence level and length scale and correlates the present data relatively well. More experiments are needed to document the information, particularly on large length scale, together with turbulence intensity.

Acknowledgments

We wish to thank the Advanced Gas Turbine Systems Research (AGTSR) Program funded by the United States Department of Energy and the Industrial Review Board Membership for their support and contract monitor Dr. Daniel Fant for his continued interest in our research. This paper was prepared with the support of the U.S. Department of Energy, Morgantown Energy Technology Center, Cooperative Agreement No. DE-FC21-92MC29061.

References

Ames, F. E., and Moffat, R. J., 1990, "Heat Transfer With High Intensity, Large Scale Turbulence: The Flat Plate Turbulent Boundary Layer and the Cylindrical Stagnation Point," in: NASA Report No. HMT-44. Department of Mechanical Engineering, Stanford University, Stanford, CA.

Ames, F. E., 1997, "The Influence of Large-Scale High-Intensity Turbulence on Vane Heat Transfer," ASME JOURNAL OF TURBOMACHINERY, Vol. 119, pp. 23–30.

Baines, W. D., and Peterson, E. G., 1951, "An Investigation of Flow Through Screens," *Trans. ASME,* Vol. 73, pp. 467–480.

Chung, J. T., and Simon, T. W., 1993, "Effectiveness of the Gas Turbine Endwall Fences in Secondary Flow Control at Elevated Freestream Turbulence Levels," ASME Paper No. 93-GT-51.

Dullenkopf, K., and Mayle, R. E., 1995, "An Account of Free-Stream-Turbulence Length Scale on Laminar Heat Transfer," ASME JOURNAL OF TURBOMACHINERY, Vol. 117, pp. 401–406.

Eckert, E. R. G., 1976, "Analogies to Heat Transfer Processes," in: E. R. G. Eckert and R. J. Goldstein, eds., *Measurement in Heat Transfer,* Hemisphere, New York, pp. 397–423.

Goldstein, R. J., Lau, K. Y., and Leung, C. C., 1983, "Velocity and Turbulence Measurements in Combustion Systems," *Experiments in Fluids,* Vol. 1, pp. 93–99.

Goldstein, R. J., and Cho, H. H., 1995, "A Review of Mass Transfer Measurements Using Naphthalene Sublimation," *Experimental Thermal and Fluid Science,* Vol. 10, pp. 416–434.

Goldstein, R. J., Wang, H. P., and Jabbari, M. Y., 1995, "The Influence of Secondary Flows Near the Endwall and Boundary Layer Disturbance on Convective Transport From a Turbine Blade," ASME JOURNAL OF TURBOMACHINERY, Vol. 117, pp. 657–665.

Kestin, J., and Wood, R. T., 1971, "The Influence of Turbulence on Mass Transfer From Cylinders," ASME *Journal of Heat Transfer,* Vol. 93, pp. 321–327.

Kline, S. J., and McClintock, F. A., 1953, "Describing Uncertainties in Single Sample Experiments," *Mechanical Engineering,* Vol. 75, Jan., pp. 3–8.

Mehendale, A. B., Ekkad, S. V., and Han, J. C., 1994, "Mainstream Turbulence Effect on Film Effectiveness and Heat Transfer Coefficient of a Gas Turbine Blade With Air and CO_2 Film Injection," *International Journal of Heat and Mass Transfer,* Vol. 37, No. 17, pp. 2707–2714.

Thole, K. A., Bogard, D. G., and Whan-Tong, J. L., 1994, "Generating High Freesteam Turbulence Levels," *Experiments in Fluids,* Vol. 17, pp. 375–380.

Wang, H. P., 1997, "Local Mass Transfer Measurement From a Turbine Blade: Influence of High Turbulence With Large Length Scale on Heat/Mass Transfer," Ph.D. dissertation, University of Minnesota, Minneapolis, MN.

Wang, H. P., Olson, S. J., Goldstein, R. J., and Eckert, E. R. G., 1997, "Flow Visualization in Linear Turbine Cascade of High Performance Turbine Blades," ASME JOURNAL OF TURBOMACHINERY, Vol. 119, pp. 1–8.

Young, C. D., Han, J. C., Huang, Y., and Rivir, R. B., 1992, "Influence of Jet-Grid Turbulence on Flat Plate Turbulent Boundary Layer Flow and Heat Transfer," ASME *Journal of Heat Transfer,* Vol. 114, pp. 65–72.

Film Cooling Effectiveness and Mass/Heat Transfer Coefficient Downstream of One Row of Discrete Holes

R. J. Goldstein

P. Jin

R. L. Olson[1]

Department of Mechanical Engineering,
University of Minnesota,
Minneapolis, MN 55455

A special naphthalene sublimation technique is used to study the film cooling performance downstream of one row of holes of 35 deg inclination angle with 3d hole spacing and relatively small hole length to diameter ratio (L/d = 6.3). Both film cooling effectiveness and mass/heat transfer coefficient are determined for blowing rates from 0.5 to 2.0 with density ratio of 1.0. The mass transfer coefficient is measured using pure air film injection, while the film cooling effectiveness is derived from comparison of mass transfer coefficients obtained following injection of naphthalene-vapor-saturated air with those from pure air injection. This technique enables one to obtain detailed local information on film cooling performance. The laterally averaged and local film cooling effectiveness agree with previous experiments. The difference between mass/heat transfer coefficients and previous heat transfer results indicates that conduction error may play an important role in the earlier heat transfer measurements.

Introduction

To increase the efficiency of gas turbine systems, the inlet temperatures of first-stage turbines have been raised significantly over the last decade. One of the consequences of this is the potential failure of components in the turbine section due to large thermal stresses. As the inlet temperature increases, material limits such as the creep and failure of turbine components are of great concern. Film cooling is one of the cooling schemes being used to reduce these problems. Air is bypassed from the compressor (often after the last stage) into the high-performance blade or vane, where it is used for internal cooling and then is ejected through the blade surface into the external boundary layer to reduce the temperature in the boundary layer and protect the surface over which the hot combustion gas flows.

Due to manufacturing and stress-related reasons, discrete-hole film cooling is preferred rather than slot injection film cooling. The discrete-hole geometry leads to three-dimensional flow and temperature fields downstream of injection. Jet liftoff, high turbulence intensity in the shear layer, and double counter-rotating vortices are important features of film cooling cited by many researchers.

The performance of film cooling is usually characterized by two figures of merit: the adiabatic wall effectiveness and heat transfer coefficient. Various geometric and fluid dynamics parameters can affect the performance of discrete hole film cooling. To name a few, hole spacing (s/d), length of hole (L/d), shape of hole, inclination angle (IA), compound angle (CA), surface curvature, and smoothness of the surface are common geometric factors while the fluid dynamics parameters include blowing rate (M), momentum flux ratio (I), density ratio ($D.R.$), velocity ratio ($V.R.$), free-stream turbulence intensity (Tu) and length scale, and mainstream pressure gradient.

Many studies have been conducted on the performance of discrete hole film cooling. While in most studies heat transfer measurements were made (e.g., Eriksen and Goldstein, 1974; Sinha et al., 1991), mass transfer and the heat/mass transfer analogy method were used by Pedersen et al. (1977) and Foster and Lampard (1980). In most studies, the detailed local values of film cooling effectiveness and heat transfer coefficient were not available due to the measurement methodology and averaged values were usually presented. Wall conduction errors in heat transfer experiments are often problematic. On the other hand, the modern development of gas turbine technology demands detailed information on film cooling effectiveness and heat transfer coefficient, especially immediately downstream of injection holes. In this study, the naphthalene sublimation technique is used to obtain detailed local information on film cooling effectiveness and mass/heat transfer coefficient downstream of one row of inclined holes.

Recently, the effects of hole geometry on the fluid dynamics and film cooling performance have been actively investigated by many researchers. Sinha et al. (1991) studied the adiabatic effectiveness downstream of one row of inclined holes with short length (L/d = 1.75) under various density ratios and blowing rates. They showed that short injection-hole length can cause early jet detachment at a small momentum flux ratio. In heat transfer measurements, Sen et al. (1996) and Schmidt et al. (1996) investigated the adiabatic wall effectiveness and heat transfer coefficient using a single row of inclined holes with different shapes, compound angles, and a hole length of $4d$. They found the geometry could influence the film cooling performance greatly. Ekkad et al. (1997a, b) presented film cooling effectiveness and heat transfer coefficient distributions over a flat surface with one row of inclined holes for different compound angle and density ratios at an elevated free-stream turbulence intensity (Tu = 8.5 percent) using a transient liquid crystal technique proposed by Vendula and Metzger (1991), which can determine local effectiveness and heat transfer coefficient distribution simultaneously. A hole length-to-diameter ratio (L/d) of 4.6 was used in their study.

In the present study, one row of discrete film cooling holes on a flat plate with inclination angle of 35 deg and a length-to-diameter ratio of 6.3 is investigated using the naphthalene sublimation technique and mass/heat transfer analogy, by which

[1] Current address: Lockheed Martin Corp., St. Paul, MN.

Contributed by the International Gas Turbine Institute and presented at the 43rd International Gas Turbine and Aeroengine Congress and Exhibition, Stockholm, Sweden, June 2–5, 1998. Manuscript received by the International Gas Turbine Institute February 1998. Paper No. 98-GT-174. Associate Technical Editor: R. E. Kielb.

the detailed local information of effectiveness and mass transfer coefficient can be attained. The blowing rate varies from 0.5 to 2.0 with the density ratio of 1.0.

Experimental Method and Naphthalene Sublimation Technique

Eckert (1984) analyzed two approaches used in film cooling experiments. The first uses the adiabatic wall temperature (effectiveness) and a heat transfer coefficient only dependent on the fluid mechanics, which is, arguably, the most prevalent method used in research and industry. The second approach uses a dimensionless temperature and hence a heat transfer coefficient varying linearly with the dimensionless temperature. Both methods utilize the linear energy equation under the condition of constant fluid properties to enable the superposition of temperature field. Eckert (1984) showed that the results of the two approaches are convertible under conditions of small temperature gradients on the film cooled wall.

The naphthalene sublimation method and the heat/mass transfer analogy were reviewed by Goldstein and Cho (1995); the advantages as well as the measurement technique were analyzed and compared to heat transfer results. Cho and Goldstein (1995a, b) measured film cooling effectiveness and mass/heat transfer coefficient for full coverage film cooling on a flat plate using naphthalene sublimation.

In summary, naphthalene sublimation can be used to determine the convective component of heat transfer with the absence of wall conduction and radiation errors. A mass transfer problem can be converted to a heat transfer problem under the same boundary conditions by mass/heat transfer analogy. Following Cho and Goldstein (1995a), using the naphthalene sublimation technique and the isothermal conditions, the mass/heat transfer coefficient for film cooling on a flat plate downstream of one row of holes can be obtained by measuring the mass transfer coefficient on the naphthalene wall with pure air injection,

$$h_m = h'_{m0} = \frac{\dot{m}_0}{\rho_{v,w} - \rho_{v,\infty}} \quad \text{when } \rho_{v,2} = \rho_{v,\infty}$$

$$= \frac{\dot{m}_0}{\rho_{v,w}} \quad \text{since } \rho_{v,\infty} = 0 \text{ in present study} \qquad (1)$$

The dimensionless mass transfer coefficient defined as the Sherwood number is used and often normalized by the mass transfer coefficient on the same surface without injection of secondary flow to cancel the effects of unheated starting length and Sherwood (Prandtl) number, making it comparable to the normalized heat transfer coefficient (h/h_o).

$$\frac{\mathrm{Sh}'_0}{\mathrm{Sh}_0} = \frac{h_m}{h_{mo}} = \frac{h'_{m0}}{h_{mo}} \qquad (2)$$

The isothermal (iso-concentration) wall film cooling effectiveness, which is shown by Eckert (1984) to be convertible to the adiabatic (impermeable) wall effectiveness, can be attained by comparing the mass transfer coefficient measured with injection of naphthalene-vapor-saturated air at the ambient temperature with the mass transfer coefficient measured with pure air injection,

$$h'_{m1} = \frac{\dot{m}_1}{\rho_{v,w} - \rho_{v,\infty}} \quad \text{when } \rho_{v,2} = \rho_{v,w}$$

$$= \frac{\dot{m}_1}{\rho_{v,w}} \quad \text{since } \rho_{v,\infty} = 0 \text{ in present study} \qquad (3)$$

$$\eta_{iw} = \frac{\rho_{v,iw} - \rho_{v,\infty}}{\rho_{v,2} - \rho_{v,\infty}} = 1 - \frac{h'_{m1}}{h'_{m0}} = 1 - \frac{\mathrm{Sh}'_1}{\mathrm{Sh}'_0} \qquad (4)$$

This method is used in the data reduction of the present investigation to get the effectiveness.

Experimental Facility and Qualification Test

A large open-cycle, suction-type wind tunnel in the Heat Transfer Laboratory at the University of Minnesota is used to

Nomenclature

$\dot{m}$ = mass transfer rate per unit area = $\rho_s(\delta y/\delta\tau)$
$\dot{m}_0$ = mass transfer rate per unit area for $\rho_{v,2} = \rho_{v,\infty}$
$\dot{m}_1$ = mass transfer rate per unit area for $\rho_{v,2} = \rho_{v,w}$
CA = compound angle of injection hole = 0 deg in present study
d = diameter of injection hole = 6.35 mm in present study
$D.R.$ = density ratio, = ρ_2/ρ_∞ = 1.0 in present study
D_{naph} = naphthalene vapor diffusivity in air
h = heat transfer coefficient
h'_{m0} = mass transfer coefficient for $\rho_{v,2} = \rho_{v,\infty}$
h'_{m1} = mass transfer coefficient for $\rho_{v,2} = \rho_{v,w}$
$\overline{h}$ = lateral average (over z) of h
h_m = impermeable wall mass transfer coefficient
h_o = heat transfer coefficient without injection
h_{mo} = mass transfer coefficient without injection
I = momentum ratio = $(\rho_2 U_2^2)/(\rho_\infty U_\infty^2)$
IA = inclination angle of injection hole, = 35 deg in present study
L = length of injection hole
M = blowing rate = $(\rho_2 U_2)/(\rho_\infty U_\infty)$
Re_d = Reynolds number based on U_∞ and d, = $\rho U_\infty d/\mu$
s = space between the injection holes = $3d$ in present study
Sc = Schmidt number = $\mu/\rho D_{\mathrm{naph}} \approx$ 2.29 in present study
Sh'_0 = Sherwood number for $\rho_{v,2} = \rho_{v,\infty}$
$\overline{\mathrm{Sh}'_0}$ = lateral average (over z) of Sh'_0
Sh'_1 = Sherwood number for $\rho_{v,2} = \rho_{v,w}$
Sh_0 = Sherwood number based on h_{mo}, = $h_{mo}d/D_{\mathrm{naph}}$
t = thickness of the injection plate
Tu = free-stream turbulence intensity, $\approx$ 0.54 percent in present study
U_2 = secondary flow velocity
U_∞ = mainstream velocity
$V.R.$ = velocity ratio = U_2/U_∞
x = streamwise distance from the center of injection hole
y = distance normal to film cooling wall
z = spanwise distance from the center of the injection hole
$\delta\tau$ = time interval for naphthalene sublimation in forced convection
δ^* = boundary layer displacement thickness
δy = local naphthalene sublimation depth in forced convection
η_{iw} = impermeable wall film cooling effectiveness
$\overline{\eta_{iw}}$ = laterally averaged impermeable wall film cooling effectiveness
ρ_2 = secondary flow density
ρ_s = density of solid naphthalene
ρ_∞ = mainstream density
$\rho_{v,2}$ = naphthalene vapor density in the secondary flow
$\rho_{v,\infty}$ = naphthalene vapor density in the mainstream
$\rho_{v,iw}$ = naphthalene vapor density at the impermeable wall
$\rho_{v,w}$ = naphthalene vapor density at the wall

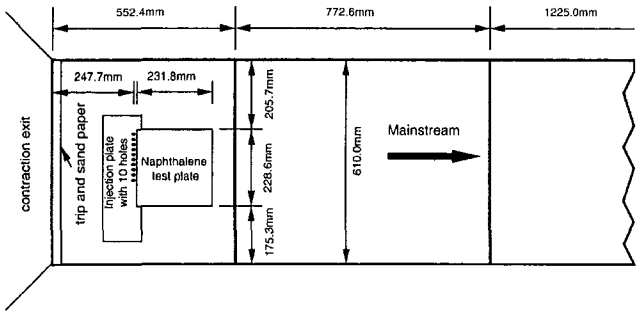

Fig. 1 Planview of test section

supply the mainstream for the film cooling test. Flow to the 2500-mm-long, 305.0-mm-high, and 610.0-mm-wide test section is preceded by a flow straightener and a 15:1 area contraction. The side and top walls of the test section are made of Plexiglas. The film cooling injection plate perforated with one row of holes and naphthalene test plate are installed in the bottom wall of the test section. The plan view of the test section is shown in Fig. 1. A 1.0-mm-dia trip followed by a 25.4 mm strip of sandpaper is set up at the exit of the contraction to trip and smooth the turbulent boundary layer developed on the flat wall. The center of the holes is 247.7 mm downstream of the trip.

The details of the injection hole are shown in Fig. 2. The one row of holes of 6.35 mm diameter is inclined at 35 deg to the direction of main-stream with a $3d$ hole spacing. The injection plate is 22.9 mm thick and made of aluminum, providing a hole length of $6.3d$. The coordinate directions are also shown in the same figure. In many previous studies, the origin of the coordinate system is often placed at the downstream tip of the hole. It is not a major issue when dealing with straight holes without compound angle. However, it is more appropriate to

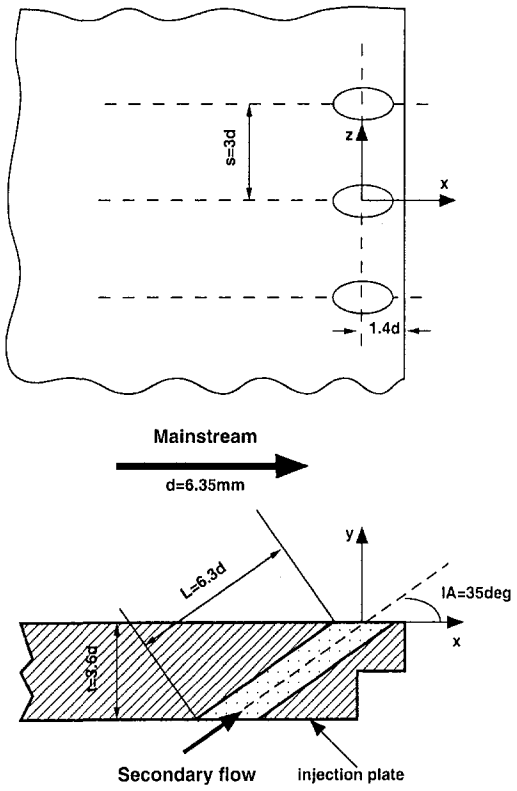

Fig. 2 Film cooling hole geometry

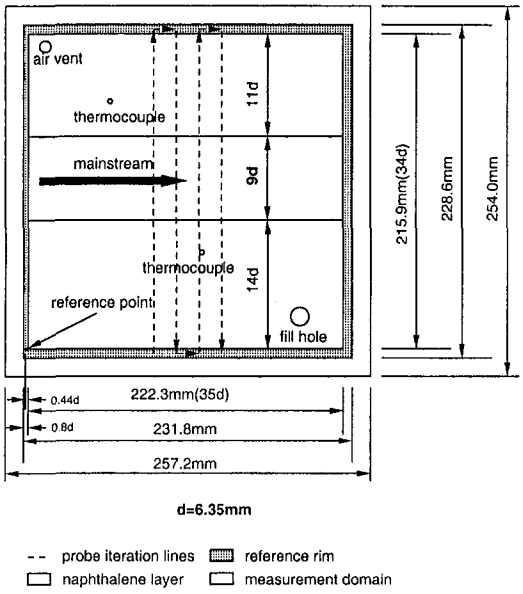

Fig. 3 Naphthalene sublimation test plate

put the origin of the coordinate at the center of the injection holes when compound angle geometry is used. To comply with later investigations of compound angle injection, the origin of the coordinates is placed at the center of hole in this study. Results from other studies are corrected for this definition of x.

The naphthalene test plate is located immediately downstream of the holes to facilitate the investigation of film cooling performance near the hole. Figure 3 shows the geometry of the plate. The naphthalene casting layer is $35d$ long, $34d$ wide, and 2.54 mm thick, of which only a $9d$ wide strip around the centerline of the test section (covering three holes) is used to measure the mass transfer coefficient. Two thermocouples are placed from the back into the naphthalene layer to monitor the surface temperature. The fill hole and air vent are used in naphthalene casting. The reference point and aluminum rim around the naphthalene layer are used as the references in the naphthalene sublimation profile measurement.

Figure 4 shows the secondary air injection system. Compressed air from the building supply passes through a 50.8-mm-dia piping system equipped with valve, flow regulating orifice, tape heater, and thermocouple, which provide control of the secondary air flow rate and temperature. At the end of the pipe, the secondary air goes into a plenum chamber 133.4 mm wide,

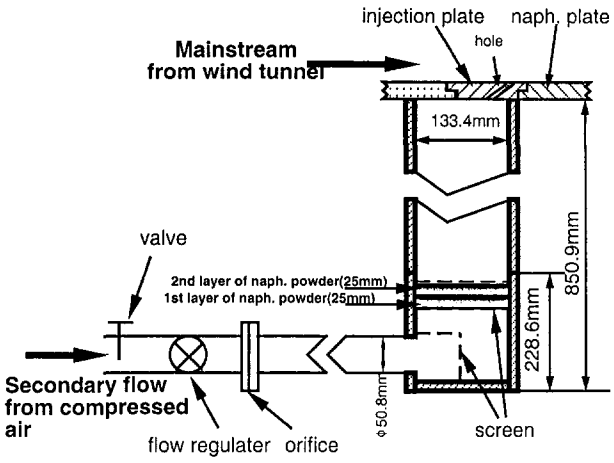

Fig. 4 Secondary flow injection system

Table 1 Film cooling geometry and operating conditions

$d(mm)$	s/d	L/d	IA(deg)	CA(deg)	x/d range
6.35	3	6.3	35	0	2-36
$U_\infty(m/s)$	$Tu(\%)$	δ^*/d	Re_d	M	D.R.
15.7	0.54	0.238	6300	0.5-2.0	1.0

414.7 mm long, and 850.9 mm high. The air first passes through a screen at the inlet of the plenum and then a flat screen for pure air injection or two layers of naphthalene powder in the naphthalene-vapor-saturated air injection case. Then the flow goes along the plenum passage and out through the injection holes into the mainstream. Thermocouples are installed to monitor the temperature of the flow in the mainstream, plenum and surrounding air.

The T-type thermocouples and orifice meter used in the experiment were previously calibrated by Cho (1992). The thermocouples are integrated with a GPIB board enabled Linux work station to facilitate the temperature measurement of the film cooling system. The total pressure is measured with a total pressure tube located 300 mm downstream of the holes and a static pressure tap is 20 mm upstream of the total pressure tube. Both of these are connected to a micromanometer with a reading precision of 0.01 mm H_2O to give the mainstream velocity. The secondary air flow is determined by measuring the pressure drop across the calibrated orifice in the pipe with a manometer system and is adjusted by the valve. The depth change of the naphthalene layer during the film cooling test is measured with an automated XY-table surface profile measuring system developed in the Heat Transfer Laboratory at the University of Minnesota. The details of the system and calibration procedure can be found from Cho (1992) and Olson (1996).

The uncertainty in naphthalene wall temperature measurement is 0.09 percent with 95 percent confidence level. The uncertainty in mainstream and secondary flow velocity is 1.4 and 2.5 percent, respectively. The uncertainty in blowing rate is 2.7 percent while in the naphthalene sublimation depth change it is within 0.80 percent, which includes the error of repositioning. The uncertainties in mass transfer coefficient and Sherwood number are 5.4 and 7.4 percent at 95 percent confidence level respectively. The relative uncertainty in effectiveness is local-effectiveness dependent in this method and is 6.2 percent for higher effectiveness of 0.5 and less than 27 percent for low effectiveness of 0.2. The naphthalene loss due to natural convection is estimated and included in this uncertainty analysis. The experimental procedure is described by Olson (1996) in detail.

The turbulent boundary layer established downstream of the trip without secondary air injection is described in Table 1. The mass transfer Stanton numbers downstream of (taped) holes without injection are measured and compared with heat transfer Stanton numbers with unheated starting length calculated from empirical equations. Good agreement is obtained. For a typical sublimation depth of 50 μm, the effect of thinner naphthalene wall on boundary layer thickness (of order of 10 mm) is neglected. Since the pressure of saturated naphthalene vapor is four orders of magnitude less than the atmospheric pressure, the fluid properties for saturated-naphthalene-vapor injection are considered to be constant. Thus, the density ratio is essentially unity. The saturation of naphthalene vapor in the air is assured by comparing results for two different thicknesses of the naphthalene layers used to add vapor to the injected flow and is confirmed by the repeatability of the results. The repeatability of mass transfer coefficient for both pure air film injection and naphthalene-vapor-saturated air injection is demonstrated in Olson (1996) and considered in the experimental uncertainty analysis.

Experimental Results and Discussion

Film Cooling Effectiveness. The laterally averaged film cooling effectiveness is compared with previous results for blowing rates of 0.5, 1.0, and 2.0 in Fig. 5. General agreement with heat transfer data of Goldstein et al. (1969) and mass transfer data of Pedersen et al. (1977) can be found for the three blowing rates. The effect of the relatively short hole (L/d = 6.3) used in the present case on the effectiveness is not obvious for low and high blowing rates of 0.5 and 2.0 when compared with the results of long tubes used in the experiments of Pedersen et al. (1977) and Goldstein et al. (1969). For the moderate blowing rate of 1.0, the relatively low effectiveness immediately downstream of the injection holes is apparently due to the short hole effect. At low blowing rate the secondary

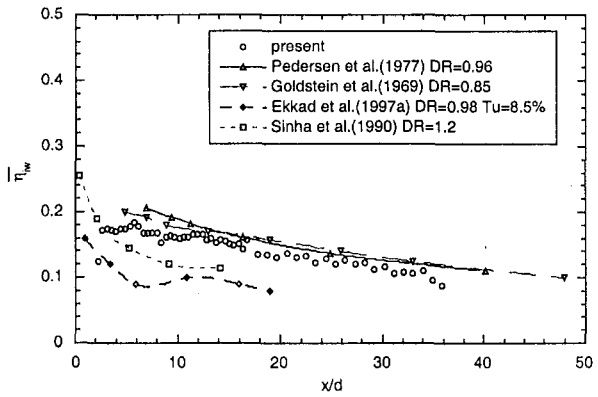

(a) M=0.5

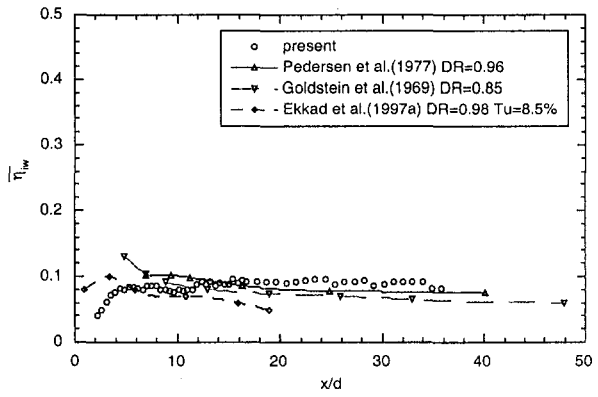

(b) M=1.0

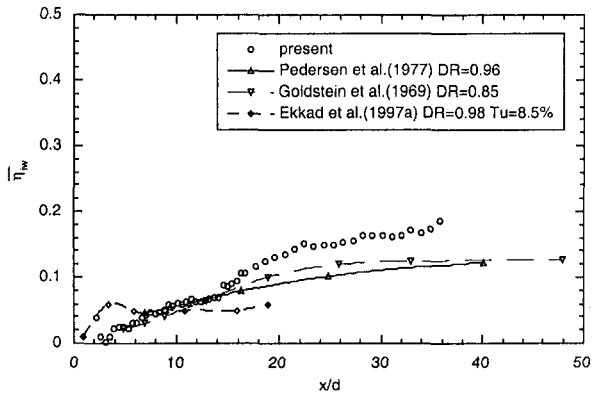

(c) M=2.0

Fig. 5 Comparison of $\overline{\eta_{iw}}$

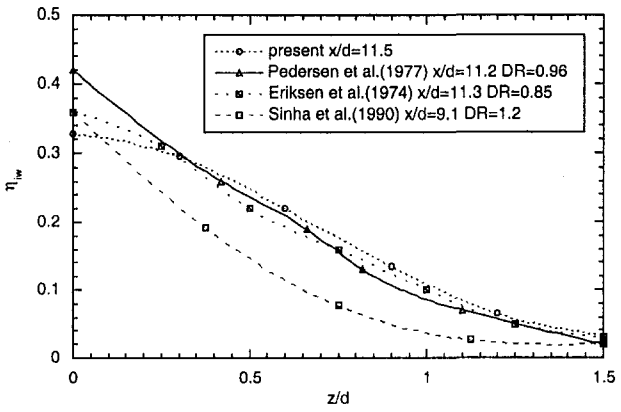

(a) M=0.5

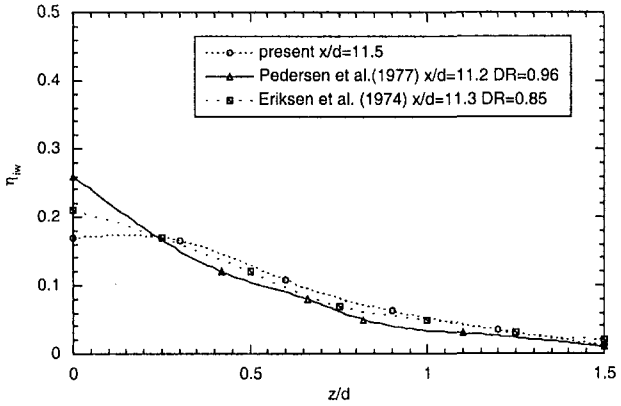

(b) M=1.0

Fig. 6 Comparison of local η_{iw}

flow velocity distribution is relatively uniform and similar to that of the long-tube case, while the high momentum flux caused liftoff of the secondary flow, which strongly affects the film cooling at the high blowing rate. At a blowing rate of 1.0, however, the nonuniformity of velocity of secondary flow due to the jetting effect of short holes apparently increases the possibility of liftoff and causes low effectiveness near the hole. The much higher film cooling effectiveness $20d$ downstream of the holes at a blowing rate of 2.0 may be due to the increased turbulent mixing induced by strong interaction of the mainstream with the injected jets.

The low effectiveness Sinha et al. (1991) found at $M = 0.5$ may be due to the much shorter hole length-to-diameter ratio ($L/d = 1.75$) used. For the case of Ekkad et al. (1997b), the high free-stream turbulence intensity of 8.5 percent causes strong mixing of coolant and mainstream, hence the even lower film cooling effectiveness at low blowing rate. With an increase of blowing rate, the turbulent mixing decelerates the liftoff of secondary flow and provides better coverage of film on the film cooled wall. Therefore, the effectiveness is relatively high in the near-hole region and more uniform further downstream with large Tu.

The local film cooling effectiveness $11d$ downstream of injection holes for blowing rates of 0.5 and 1.0 is shown in Fig. 6. The general agreement with data of Pedersen et al. (1977) and Goldstein et al. (1969) can be observed. Thus, it seems at this position, not very close to the injection holes, the relatively short holes used in the present study provides effectiveness similar to that found with long holes. The results of Sinha et al. (1991), also shown for $M = 0.5$, are consistently lower than other results apparently owing to the much smaller hole length to diameter ratio used.

Contour plots of effectiveness for $M = 0.5$, 1.0, and 2.0 are provided in Fig. 7. At $M = 0.5$, the effectiveness attains its highest value of 0.4 along the centerline of the holes near $x/d = 3$. The low effectiveness region midway between the holes is narrow compared with the width ($2d$) of the relatively high effectiveness area ($\eta_{iw} \geq 0.1$) downstream of holes. As the

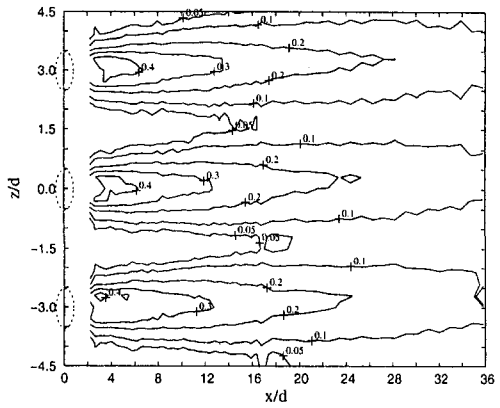

(a) M=0.5

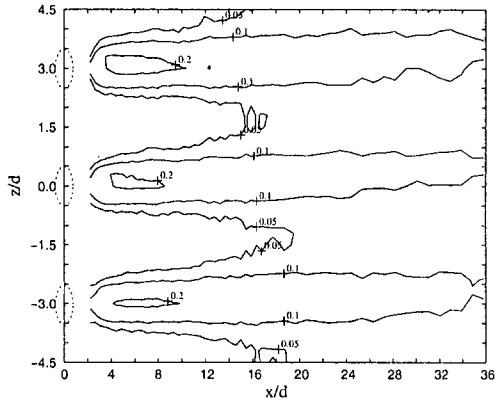

(b) M=1.0

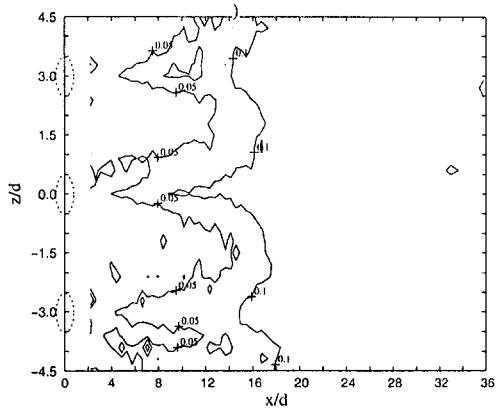

(c) M=2.0

Fig. 7 Local η_{iw} contour

blowing rate increases to 1.0, the peak of effectiveness is about 0.2 along the centerline of the hole at $x/d = 6$ while the low effectiveness region between the holes grows wide and the relatively high effectiveness area narrows to about $1d$. At blowing rate of 2.0, the above-mentioned two regions merge by $x/d = 16$ and form a uniform and moderate effectiveness region ($\eta_{lw} \geq 0.1$) after $x/d = 18$. These contour plots indicate that with an increase of blowing rate from 0.5 to 1.0, the coverage of the secondary flow decreases due to the liftoff effect. High effectiveness occurs when the secondary flow touches down on the wall. Further increasing blowing rate to 2.0, the increased interaction between the mainstream and the secondary flow spreads the secondary flow to midway between the holes and flattens the distribution of effectiveness in downstream areas.

Mass/Heat Transfer Coefficient. Comparisons of laterally averaged and normalized Sherwood number and heat transfer coefficient are plotted for $M = 0.5$, 1.0, and 2.0 in Fig. 8. The agreement with experiments of Eriksen and Goldstein (1974) becomes better at the near-hole region for blowing rate of 2.0 while the data appear collapsed to one curve farther downstream at the low blowing rate of 0.5 and 1.0. The difference among the data can't be explained by the effect of hole length-to-diameter ratio because the results of Sen et al. (1996) and Ekkad et al. (1997a) are for the short hole geometry while the data from Eriksen and Goldstein (1974) are for long-tube injection. The effect of Reynolds number may not be a large factor for these experimental results since the Reynolds number ranges from 6000 to 22,000. The different trend of data from Ekkad et al. (1997a) at blowing rate of 2.0 may be caused by the high free-stream turbulence level.

The comparisons of local normalized Sherwood number and heat transfer coefficient in Fig. 9 provides some insight. The present study and that of Goldstein and Taylor (1982) both used naphthalene sublimation though the latter used long tubes while the data of Eriksen and Goldstein (1974) and Sen et al. (1996) were from heat transfer measurements. The results from the different naphthalene sublimation measurements are relatively close. The variation of heat transfer results in the lateral direction (z) are small compared with that in the present study, especially for higher blowing rates. This suggests that heat conduction errors may play an important role in the heat transfer measurement.

Contour plots for normalized Sherwood number are shown in Fig. 10 for blowing rates of 0.5, 1.0, and 2.0, respectively. Regions of high and low mass transfer are shown in Fig. 11. Two regions of high mass transfer immediately downstream of the injection holes can be observed. At the low blowing rate of 0.5, the secondary flow remains attached to the naphthalene wall due to its low momentum flux ratio to the mainstream. Thus, the mass transfer rate at the centerline of the holes is even lower than without injection since the boundary layer becomes thicker. The area midway between the holes is not covered by the injected film so that the mass transfer rate remains almost the same as the case without injection. Immediately downstream of the holes, the mass transfer rate is higher at the edge of the secondary flow probably due to the interaction between the mainstream and secondary flow. This high mass transfer region is similar to region "D" described in Goldstein and Taylor (1982), resulting from large shear stresses and eddies created by mainstream and secondary flow interaction.

At the higher blowing rates of 1.0 and 2.0, the secondary flow lifts off from the wall. Due to the blockage of the mainstream by the secondary flow liftoff, the mainstream penetrates underneath the secondary flow by induced pressure deficit and sweeps toward the wall under the injected flow. Therefore, the mass transfer rate immediately downstream of the hole increases drastically at these blowing rates and forms a high mass transfer region similar to region "E" in Goldstein and Taylor (1982). The peak of the mass transfer coefficient stays at about $x/d = 4$ while this high mass transfer region, due to mainstream sweeping, extends farther downstream for higher blowing rates. The interaction between the mainstream and secondary flow is also greater at the edge of the secondary flow, extending the high mass transfer area observed at blowing rate of 0.5, but these Sh are smaller than those directly under the injected flow. The mass transfer coefficients farther downstream and midway between the holes are also higher than that at the centerline of

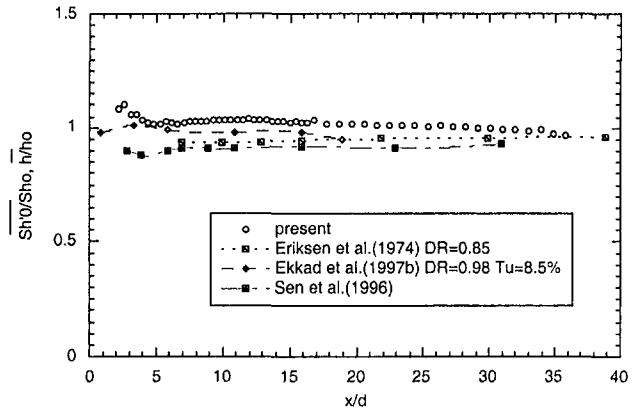

(a) M=0.5

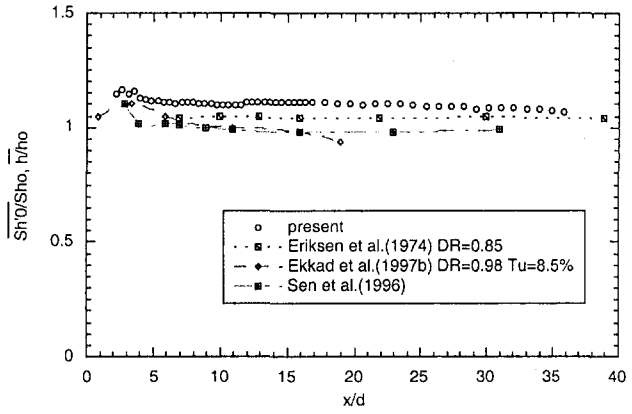

(b) M=1.0

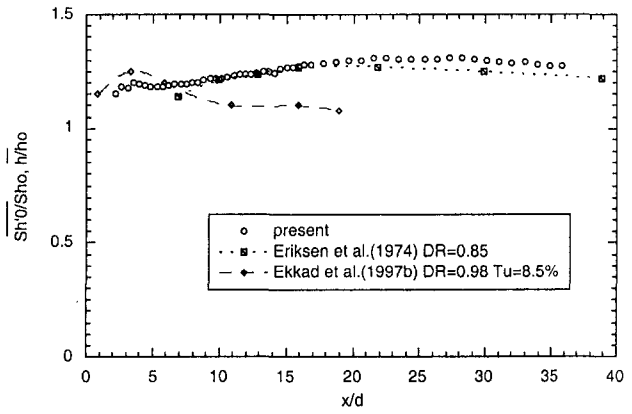

(c) M=2.0

Fig. 8 Comparison of $\overline{Sh_0'}/Sh_0$

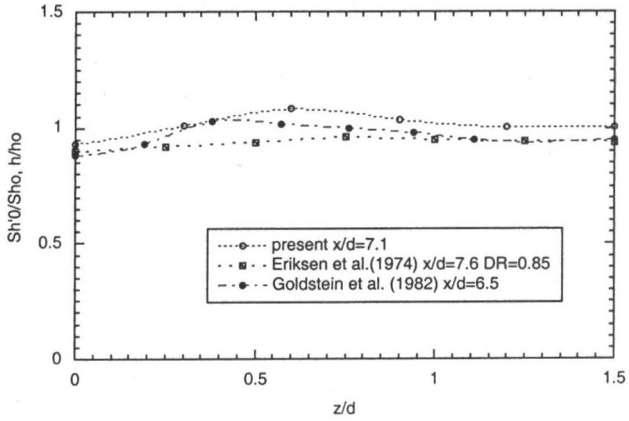

(a) M=0.5

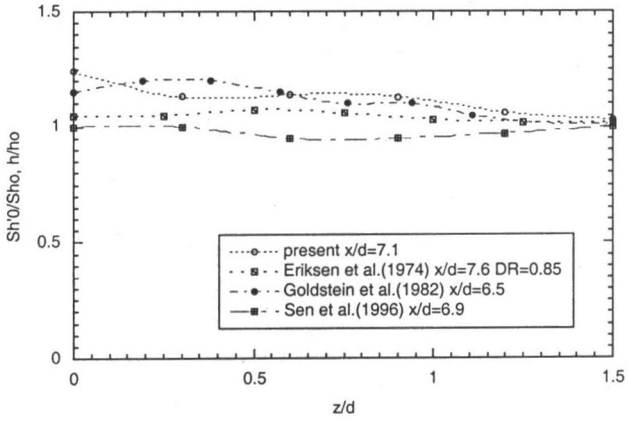

(b) M=1.0

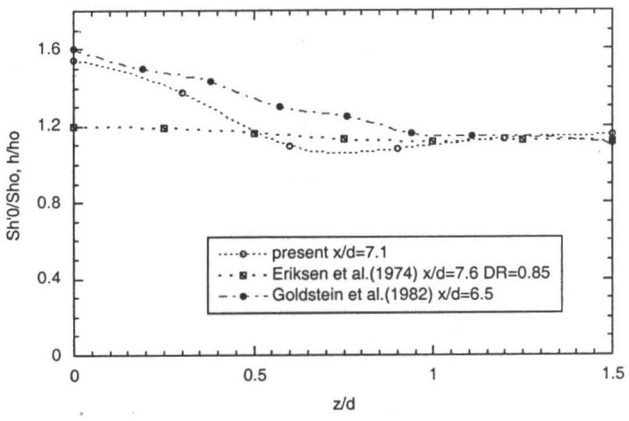

(c) M=2.0

Fig. 9 Comparison of local Sh_0'/Sh_0

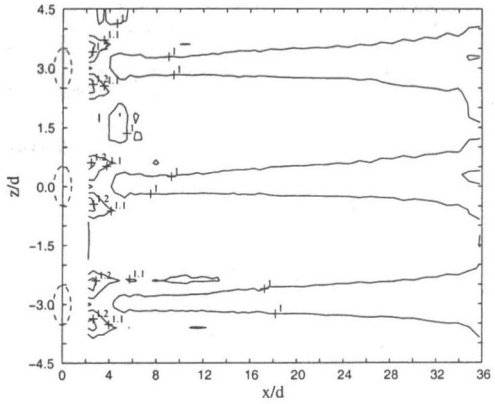

(a) M=0.5

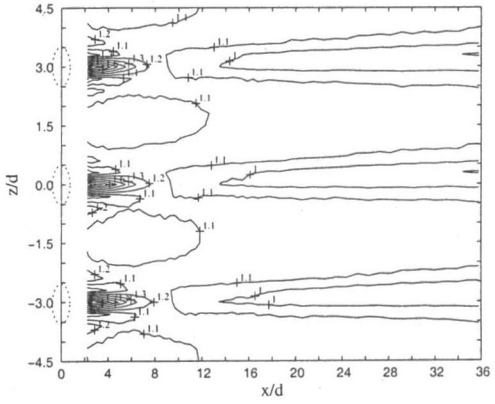

(b) M=1.0

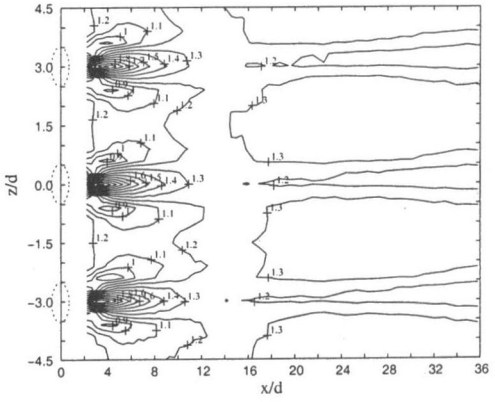

(c) M=2.0

Fig. 10 Local Sh_0'/Sh_0 contour

holes for the blowing rates. This is induced by the spreading and merging of two neighboring jets, and the interacting vortex structures, midway between the holes, and the increasing boundary layer thickness due to the re-attached flow along the centerline.

From these contour plots, we can see that the secondary flow from each hole remains separate until $x/d = 34$ for blowing rate of 0.5. At the blowing rate of 1.0, the secondary flow merges at about $x/d = 12$. For the highest blowing rate of 2.0, it seems the secondary flow from adjacent holes spreads and merges immediately after injection due to the strong interaction of the neighboring jets with each other and with the mainstream.

Conclusion

In the present study, the naphthalene sublimation technique and the heat/mass transfer analogy are used to measure the film

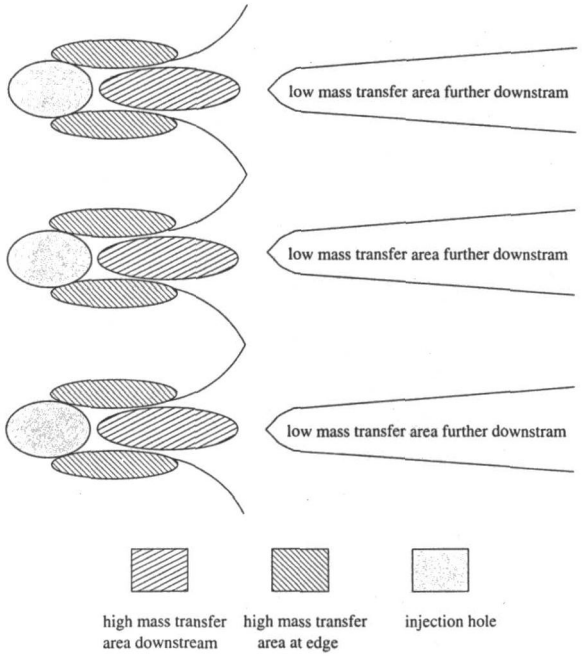

Fig. 11 Regions of high and low mass transfer

cooling performance for one row of holes with 35 deg inclination angle. The mass transfer coefficient is measured using pure air film injection while the film cooling effectiveness is derived from comparison of mass transfer coefficients obtained following injection of naphthalene-vapor-saturated air with that of pure air. The following conclusions can be drawn:

1 The local and the laterally averaged film cooling effectivenesses generally agree with previous results at blowing ratios of 0.5 and 1.0. The relatively short injection hole configuration used provides an effectiveness similar to that found with long injection holes at similar blowing rates.

2 The local and the laterally averaged mass transfer coefficients obtained in the present study do not agree as well with previous heat transfer results perhaps due to conduction effects in the region of large temperature gradient in the heat transfer measurements.

3 The naphthalene sublimation technique and the heat/mass transfer analogy used in the present experiment can be used to obtain detailed local and averaged information on film cooling performance.

References

Cho, H. H., 1992, "Experimental Study of Flow and Local Mass/Heat Transfer From Single Short Cylinders and Arrays of Short Pin-Fins in Crossflow," Ph.D. Thesis, University of Minnesota, Minneapolis, MN.

Cho, H. H., and Goldstein, R. J., 1995a, "Heat (Mass) Transfer and Film Cooling Effectiveness With Injection Through Discrete Holes: 1—Within Holes and on the Back Surface," ASME JOURNAL OF TURBOMACHINERY, Vol. 117, pp. 440–450.

Cho, H. H., and Goldstein, R. J., 1995b, "Heat (Mass) Transfer and Film Cooling Effectiveness With Injection Through Discrete Holes: 2—On the Exposed Surface," ASME JOURNAL OF TURBOMACHINERY, Vol. 117, pp. 451–460.

Eckert, E. R. G., 1984, "Analysis of Film Cooling and Full-Coverage Film Cooling of Gas Turbine Blades," ASME *Journal of Engineering for Gas Turbines and Power,* Vol. 106, pp. 206–213.

Ekkad, S. V., Zapata, D., and Han, J.-C., 1997a, "Film Effectiveness Over a Flat Surface With Air and CO_2 Injection Through Compound Angle Holes Using a Transient Liquid Crystal Image Method." ASME JOURNAL OF TURBOMACHINERY, Vol. 119, pp. 587–593.

Ekkad, S. V., Zapata, D., and Han, J.-C., 1997b, "Heat Transfer Coefficient Over a Flat Surface With Air and CO_2 Injection Through Compound Angle Holes Using a Transient Liquid Crystal Image Method," ASME JOURNAL OF TURBOMACHINERY, Vol. 119, pp. 580–586.

Eriksen, V. L., and Goldstein, R. J., 1974, "Heat Transfer and Film Cooling Following Injection Through Inclined Circular Tubes," ASME *Journal of Heat Transfer,* Vol. 96, pp. 239–245.

Foster, N. W., and Lampard, D., 1980, "The Flow and Film Cooling Effectiveness Following Injection Through a Row of Holes," ASME *Journal of Engineering for Power,* Vol. 102, pp. 584–588.

Goldstein, R. J., Eckert, E. R. G., Eriksen, V. L., and Ramsey, J. W., 1969, "Film Cooling Following Injection Through Inclined Circular Tubes," NASA Contract No. NAS 3-7904.

Goldstein, R. J., and Taylor, J. R., 1982, "Mass Transfer in the Neighborhood of Jets Entering Crossflow," ASME *Journal of Heat Transfer,* Vol. 104, pp. 715–721.

Goldstein, R. J., and Cho, H. H., 1995, "A Review of Mass Transfer Measurements Using Naphthalene Sublimation," *Experimental Thermal and Fluid Science,* Vol. 8, pp. 416–434.

Olson, R. L., 1996, "Film Cooling Effectiveness and Heat (Mass) Transfer Coefficient for a Single Row of Discrete Film Cooling Holes," Master's Thesis, University of Minnesota, Minneapolis, MN.

Pedersen, D. R., Eckert, E. R. G., and Goldstein, R. J., 1977, "Film Cooling With Large Density Differences Between the Mainstream and the Secondary Fluid Measured by the Heat-Mass Transfer Analogy," ASME *Journal of Heat Transfer,* Vol. 99, pp. 620–627.

Schmidt, D. L., Sen, B., and Bogard, D. G., 1996, "Film Cooling With Compound Angle Holes—Adiabatic Effectiveness," ASME JOURNAL OF TURBOMACHINERY, Vol. 118, pp. 807–813.

Sen, B., Schmidt, D. L., and Bogard, D. G., 1996, "Film Cooling With Compound Angle Holes—Heat Transfer," ASME JOURNAL OF TURBOMACHINERY, Vol. 118, pp. 800–806.

Sinha, A. K., Bogard, D. G., and Crawford, M. E., 1991, "Film-Cooling Effectiveness Downstream of a Single Row of Holes With Variable Density Ratio," ASME JOURNAL OF TURBOMACHINERY, Vol. 113, pp. 442–449.

Vendula, R. J., and Metzger, D. E., 1991, "A Method for the Simultaneous Determination of Local Effectiveness and Heat Transfer Distributions in Three-Temperature Convection Situations," ASME Paper No. 91-GT-345.

Investigation of Detailed Film Cooling Effectiveness and Heat Transfer Distributions on a Gas Turbine Airfoil

U. Drost

A. Bölcs

Swiss Federal Institute of Technology,
EPFL-LTT,
Lausanne, Switzerland

In the present study film cooling effectiveness and heat transfer were systematically investigated on a turbine NGV airfoil employing the transient liquid crystal technique and a multiple regression procedure. Tests were conducted in a linear cascade at exit Reynolds numbers of 0.52e6, 1.02e6 and 1.45e6 and exit Mach numbers of 0.33, 0.62 and 0.8, at two mainstream turbulence intensities of 5.5 and 10 percent. The film cooling geometry consisted of a single compound angle row on the pressure side (PS), and a single or a double row on the suction side (SS). Foreign gas injection was used to obtain a density ratio of approximately 1.65, while air injection yielded a density ratio of unity. Tests were conducted for blowing ratios of 0.25 to 2.3 on the SS, and 0.55 to 7.3 on the PS. In general film cooling injection into a laminar BL showed considerably higher effectiveness in the near-hole region, as compared to a turbulent BL. While mainstream turbulence had only a weak influence on SS cooling, higher effectiveness was noted on the PS at high turbulence due to increased lateral spreading of the coolant. Effects of mainstream Mach and Reynolds number were attributed to changes of the BL thickness and flow acceleration. Higher density coolant yielded higher effectiveness on both SS and PS, whereas heat transfer ratios were increased on the SS and decreased on the PS. Comparison of the single and double row cooling configurations on the SS revealed a better film cooling performance of the double row due to an improved film coverage and delayed jet separation.

Introduction

The power output and efficiency level of a gas turbine are improved by increasing the turbine inlet temperature. Since these temperatures exceed the highest allowable blade material temperature, the blades have to be cooled to guarantee safe operating conditions. Discrete hole film cooling is an effective way to achieve this objective, provided that the thermal boundary conditions are known accurately. As numerical predictions of three-temperature convection situations on complex geometries as turbine airfoils are not yet sufficiently reliable for design purposes, experimental information is urgently needed.

The objective of the present work is a systematic investigation of film cooling effectiveness (η) and heat transfer on a turbine airfoil at near engine flow conditions. On the suction side, streamwise single and double row injection are compared, while pressure side film cooling was conducted for one row of compound angle holes. A wide range of blowing ratios was investigated for several Mach and Reynolds numbers, different approach *Tu* levels and coolant densities (air or CO_2). For SS film cooling the upstream BL was either laminar or turbulent, as both situations can be encountered in an engine. First film cooling (FC) results on the same airfoil have already been reported by Drost et al. (1997).

CO_2 injection to simulate engine density ratios correctly has been validated by Teekaram et al. (1989) using air and CO_2 injection at the same densities by adequately adjusting the coolant temperatures. From basic flat plate FC heat transfer investigations conducted with both air and CO_2 as coolants as done by Ammari et al. (1990) for 35 deg streamwise injection and Ekkad et al. (1997) for compound angle injection, decreasing heat transfer enhancement with increasing DR can be observed, especially at high I. Recent FC investigations on turbine airfoils conducted with air and CO_2 injection by Du et al. (1998), Heidmann et al. (1997), and Ou et al. (1994) show, however, increased heat transfer for the denser coolant on the suction surfaces, whereas on the pressure surface decreased values were observed by Ou et al. Du et al. and Heidmann et al. noted, however, equally increased heat transfer on the pressure side, when using CO_2 as coolant.

An extensive FC study was done by Ames (1997), who conducted film cooling effectiveness and heat transfer measurements on a turbine blade at true chord Re_2 = 5e5 and 8e5 and M_2 = 0.17 and 0.27, applying SS, PS, and showerhead cooling at a DR of unity. Heat transfer augmentation due to injection was found to be higher when injecting into a laminar BL (PS) compared to injection into a turbulent BL (SS). Double row cooling produced higher heat transfer augmentation than a single row on the blade SS, however at equally higher η. High free-stream turbulence strongly decreased η on the PS, but affected η only moderately on the SS.

Goldstein and Yoshida (1982) performed flat-plate FC measurements with both laminar and turbulent upstream BL states at very similar BL thicknesses. Both η and heat transfer coefficients showed increased values for injection into a laminar BL at least close to injection. Liess (1975) conducted flat plate FC measurements with both laminar and turbulent upstream BL, but although η decreased for a turbulent BL state, this effect was rather attributed to the increased BL thickness, than to the BL state.

Camci and Arts (1990) studied overall heat transfer coefficients based on the free-stream recovery temperature on a film-cooled rotor blade at engine representative conditions, and did

Contributed by the International Gas Turbine Institute and presented at the 43rd International Gas Turbine and Aeroengine Congress and Exhibition, Stockholm, Sweden, June 2–5, 1998. Manuscript received by the International Gas Turbine Institute February 1998. Paper No. 98-GT-20. Associate Technical Editor: R. E. Kielb.

not find a significant effect of the approach Tu level, which was varied from $Tu = 0.8$ to 5.2 percent. Also, they noted that the existence of cooling holes without injection leads to an earlier BL transition.

Pressure side FC at engine representative conditions has been measured by Arts and Bourguignon (1990) for double row injection. Heat transfer increase was negligible and η was only weakly influenced by the approach Tu level (1 to 6 percent). Variations in η when changing the chord Re_2 from 1.5e6 to 3e6 were seen to be essentially related to modifications of the upstream BL state changing from transitional to turbulent.

Nirmalan and Hylton (1990) investigated film cooling at engine representative conditions, with particular attention to flow field variations. They observed that variations of exit Mach number from 0.6 to 1.05 did not significantly alter the FC performance for the major part of the data. Increasing the true chord Re_2 from 1.5e6 to 2.5e6 was shown to yield equally increasing FC performance.

Detailed FC results on turbine blades showing also the spanwise variations due to the three-dimensional film cooling phenomena have been reported by Du et al. (1998), as mentioned above, using a liquid crystal technique, as well as by Takeishi et al. (1992), who used a heat–mass transfer analogy to measure η, and presented results for three spanwise positions (centerline and between holes), obtained in a low-speed linear cascade.

Data Analysis. The local heat flux in the film cooling situation can be described by

$$q = \alpha_f(T_{aw} - T_w) \tag{1}$$

so that the convection coefficient is referred to the adiabatic wall temperature, being a function of the supply temperatures of the main and secondary streams and the degree of mixing. Rendered dimensionless, this temperature becomes the film cooling effectiveness, defined according to the superposition model of film cooling with viscous dissipation (Teekaram et al., 1991) as

$$\eta = \frac{T_{aw} - T_{rg}}{T_{tc} - T_{tg}} \tag{2}$$

Hence, the heat transfer coefficient, α_f, and the film cooling effectiveness, η, allow together to fully describe a film cooling situation.

The present measurements have been conducted with the transient liquid crystal technique using 30°C narrow band liquid crystals. The technique requires a uniform initial temperature of the model, which is rapidly exposed to a flow at a different temperature for a limited amount of time. The test duration is chosen short enough to guarantee that the penetration of the heating pulse into the model is small compared to the model wall thickness. Thus, the heat conduction can be considered to be transient and one-dimensional into a semi-infinite surface. An analytical modelization of the transient wall temperature rise allows us then to deduce the film cooling parameters α_f and η, based on a multiple test regression scheme. Five to six tests were carried out at identical blowing ratios, but different coolant temperatures varied in a range of $T_{tc}/T_{tg} = 0.88$ to 0.97. The free-stream temperature was held constant at 60°C, and the initial blade temperature was adapted for each test typically in a range of 0°C to −20°C to compensate for time variations of the liquid crystal color play due to different coolant temperatures. A detailed description of the evaluation methodology used in the presented study can be found from Drost et al. (1997).

Uncertainty in heat transfer coefficient has a rather constant value of ±6 percent, and in local effectiveness a value of ±10 percent at $\eta = 0.1$, decreasing to ±4 percent for $\eta = 0.3$. The uncertainty can be significantly higher in the immediate vicinity of the holes (about one diameter laterally and downstream and two to three diameters upstream) since the semi-infinite model assumption is not fully valid due to lateral conduction effects.

Test Facility/Measuring Equipment. The measurements were conducted in a linear turbine cascade facility with five airfoils and a contoured platform mounted onto a cylindrical disk in the 99 × 340 mm working section as shown in Fig. 1. The test facility is supplied from a continuously running air source delivering a mass flow up to 10 kg/s with a maximum pressure ratio of 3.5. The exit Reynolds and isentropic Mach number as well as the downstream flow periodicity are regulated by two tailboards and two bypass vanes. The periodicity was determined by means of surface pressure measurements on the center and the adjacent airfoils. The total pressure was measured 125 mm upstream of the airfoil leading edges behind the turbulence grid employing a multihole Pitot probe, pneumatically removable prior to transient tests, and the total temperature was measured in the settling chamber.

An insertion mechanism (Fig. 2) was used to create a step change in temperature for the transient experiments (Hoffs et al., 1996). For test initiation, a pneumatic cylinder pulls the center airfoil very rapidly (below 0.1 s) through the sidewalls of the linear cascade, which are equipped with inflatable seals so as not to harm the liquid crystal layer. The same pneumatic cylinder, by means of a closed-loop computer controlled positioning system, allows us to traverse a pressure tap equipped part of the center blade through the channel to survey the complete blade surface pressure field.

In order to obtain two distinct turbulence levels, a square array biplane grid constructed with rectangular bars was inserted

Nomenclature

d = cooling hole diameter, mm
DR = density ratio = ρ_c/ρ_g
G = blowing ratio = $\rho_c u_c/\rho_g u_g$
I = momentum flux ratio = $\rho_c u_c^2/\rho_g u_g^2$
l_h = hole length, mm
L = airfoil chord, mm
L_x = integral length scale, mm
m = mass flow rate, kg/s
M = Mach number
p = hole pitch, mm
Re = Reynolds number
R_a = arithmetic mean deviation of roughness profile DIN-ISO 1302, μm
R_z = 5 point peak roughness average DIN-ISO 1302, μm
s = surface distance from leading edge, mm
T = temperature, K
Tu = turbulence intensity, percent
x = streamwise distance along the airfoil, mm
α = heat transfer coefficient, W/m^2 K
γ = spanwise injection angle, deg
δ_1 = boundary layer displacement thickness
η = film cooling effectiveness = $(T_{aw} - T_{rg})/(T_{tc} - T_{tg})$
ρ = density, kg/m^3
φ = streamwise injection angle, deg

Subscripts

aw = adiabatic wall
c = coolant
f = with film cooling
g = free-stream
r = recovery
t = total
w = wall
0 = without film cooling
1 = inlet
2 = exit

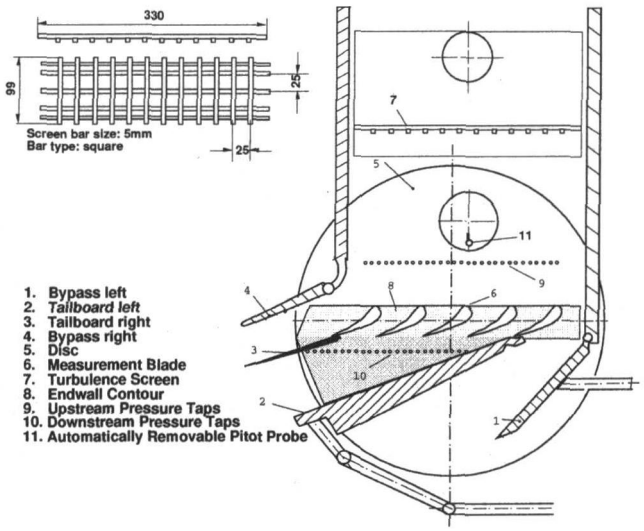

Fig. 1 Schematic view of the linear test facility

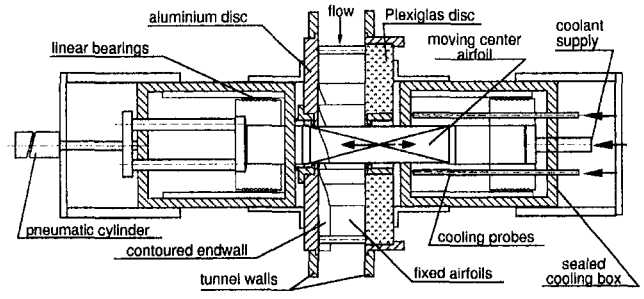

Fig. 2 Insertion mechanism

Table 1 Film cooling configuration airfoil

Geometry	s/L	φ [°]	γ [°]	p/d	l_h/d
single PS	-0.123	55	60	6.25	9.25
single SS	0.377	35	90	3.75	11.0
double SS	0.377	30	90	4.30	11.0

into the channel (Fig. 1). Turbulence intensity in the clear channel was $Tu = 5.5$ percent, accompanied by an high integral length scale of $L_x = 25$ mm. With the turbulence grid installed, the turbulence level yields a value of $Tu = 10$ percent at the blade leading edges, and a length scale of $L_x = 13$ mm. The turbulence intensities and the length scales with and without grid were independent of the Reynolds number within the tested range. A detailed description of the turbulence characteristics of the tunnel can be found in Hoffs et al. (1996).

Test Airfoil. The heat transfer measurements were conducted on the center airfoil of the cascade, which consists of an aluminum part equipped with 34 pressure taps and a Plexiglas part covered with narrow-band encapsulated liquid crystals. The initial temperature was measured with eight thermocouples in the plexi part and its uniformity was within ±2 K. Spline interpolation allowed us to obtain local initial temperature values within ±0.5 K. The chord length of the airfoil was 77 mm.

A first test blade was equipped with single film cooling rows on both pressure and suction sides, whereas a staggered double row was placed on the suction side of a second blade. The dimensionless positions of the film cooling holes with respect to the geometric leading edge are $s/L_{PS} = -0.123$ for the pressure side row and $s/L_{SS} = 0.377$ for the suction side rows (Table 1). The hole shape was cylindrical. The hole diameters of the double row were 15 percent less than those of the single row, yielding about 50 percent more coolant mass flow at identical blowing ratios since the hole number was doubled. The coolant was supplied from one side to a cylindrical plenum chamber in the blade, and the film holes were sharp entry.

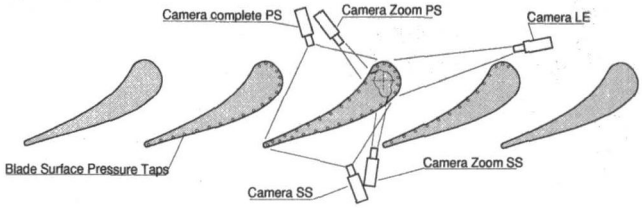

Fig. 3 Camera positions

The coolant properties were measured in the plenum chamber with two thermocouples and a pressure tapping. The coolant mass flow rate was regulated by means of interchangeable sonic orifices and metered with a Meriam Instruments laminar flow element.

FC Measurement Technique. The image processing system used to record the transient color change of the liquid crystals is based on a hue-capturing technique. Two camera signals can be simultaneously recorded at 25 Hz each. The cameras as well as the light sources are installed outside of the channel, observing the center-blade surface through Plexiglas windows in the platform. Three cameras allow us to cover the entire blade circumference and about 80 percent of the span (Fig. 3) with a spatial resolution of about 0.5 mm. Two additional cameras focus on the film cooling row locations on the suction and pressure surface, yielding a resolution of 0.07 mm. Since the color play of the liquid crystals is taken under a certain viewing angle, the surface coordinates are correlated numerically with the image coordinates to correct the image distortion by means of optical reference points painted onto the part of the blade, which resides in the tunnel prior to testing.

The liquid crystals were applied to the surface with an airbrush, and covered with a thin layer of binder to protect the capsules. Due to the spraying process, the surface always exhibits a certain roughness so that polishing of the surface with very fine sandpaper became inevitable to obtain smooth and repeatable surface conditions. The roughness was surveyed with a Mitutoyo Surftest 301 profilometer at various surface locations. An average roughness value of $R_z = 15$ μm ($R_a = 2.2$ μm) was obtained, with variations in R_z of ±2.5 μm and in R_a of ±0.2 μm, yielding roughness Reynolds numbers at $Re_2 = 1.45e6$ of up to 11 and at $Re_2 = 0.52e6$ of up to 6 on the airfoil suction side. The airfoil surface roughness can be therefore characterized as slightly transitional, according to Kays and Crawford (1993).

The liquid crystal calibration was performed in situ, heating the coated airfoil in a low-speed flow to steady-state conditions. Then, the liquid crystal color play was calibrated against the surface embedded thermocouples equally used for the initial temperature survey. The temperature calibration were repeatable within ±0.2 K.

Turbulence Measurement Technique. Turbulence intensity decay and length scale growth were measured with a Dantec 55M01 constant temperature anemometer and a single hot-wire probe at a sampling frequency of 40 kHz, low-pass filtered at 16 kHz to avoid aliasing errors. The probe was calibrated in a Laval nozzle for different velocities maintaining a constant static pressure corresponding to the linear cascade inlet static pressure. Via a Fast Fourier transform and the Wiener–Khinchin Theorem the autocorrelation was calculated, integration of which yielded the integral length scale. The uncertainties for the turbulence level and scale are 0.5 percent and 2 mm, respectively.

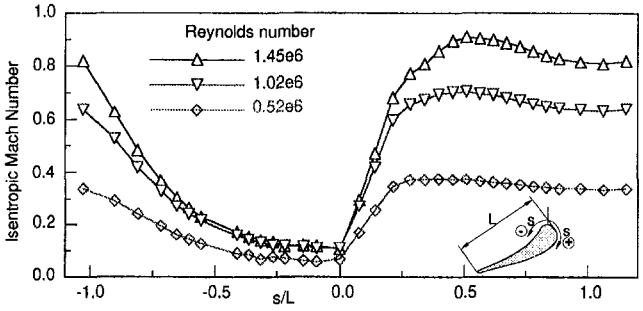

Fig. 4 Airfoil Mach number distribution

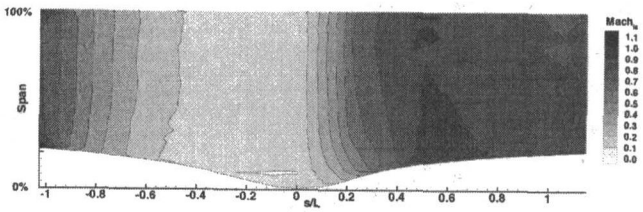

Fig. 5 Surface Mach number distribution at Re_2 = 1.45e6

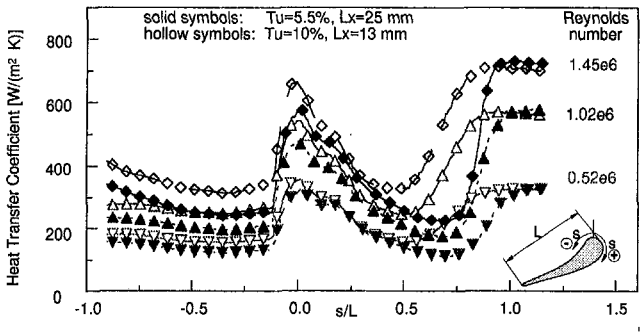

Fig. 6 Solid airfoil heat transfer at low and high *Tu*

Results and Discussion

Flowfield and Heat Transfer Baseline Measurements. Three different mainstream flow conditions have been investigated yielding exit Reynolds numbers of 0.52e6, 1.02e6, and 1.45e6 and exit Mach numbers of 0.33, 0.62, and 0.8 (Fig. 4). At all three conditions, the flow first strongly accelerates on the suction surface. For the lowest Reynolds number of 0.52e6, this acceleration ends at s/L = 0.4, going over into a mild adverse pressure gradient, which runs out toward the trailing edge. For the moderate (1.02e6) and the highest Reynolds numbers (1.45e6), the change from favorable to adverse pressure gradient is shifted downstream to s/L = 0.5, and the magnitude of the subsequent deceleration is less than for Re_2 = 0.52e6. On the airfoil pressure surface, continuous flow acceleration up to the trailing edge is observed at all flow conditions.

A contour plot of the surface Mach number distribution is shown in Fig. 5 for Re_2 = 1.45e6. Delayed flow acceleration in proximity to the contoured endwall is obvious, but in a span range of 50 to 80 percent the lateral variations are weak and the flow is approximately two dimensional. Hence, all subsequently presented results have been averaged within 60 and 70 percent of span.

Heat transfer distributions on a solid blade are presented in Fig. 6 for two mainstream *Tu* levels. One can clearly see the laminar heat transfer augmentation and the shift of transition toward the leading edge due to increased turbulence. Heat transfer in the fully turbulent region on the SS yields, however, slightly higher values at low *Tu* and high Reynolds numbers compared to the high *Tu* data, which is assumed to be due to a thinner BL thickness as a results of later transition. These measurement serve as reference cases for PS cooling investigations, but are not suited as SS references due to the natural transition region downstream of the injection locations.

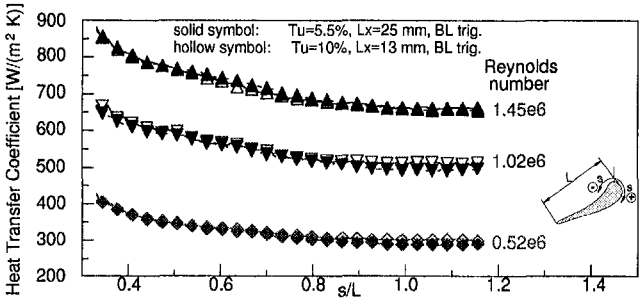

Fig. 7 SS heat transfer at 2 *Tu* levels and triggered BL

Table 2 Boundary displacement layer thickness upstream of injection

	δ_1/d, single row	δ_1/d, double row
SS, laminar BL 1.45e6	0.09	0.11
SS, laminar BL 0.52e6	0.17	0.20
SS, turbulent BL 1.45e6	0.13	0.15
PS, laminar BL 1.45e6	0.27	-

Hence, additional heat transfer measurements have been conducted with a BL trip wire of 0.5 mm diameter pasted onto the SS at s/L = 0.21 to serve as reference for FC tests, where the BL has equally been tripped. The position of the trip wire has been chosen far enough from the leading edge to avoid relaminarization. These wire-triggered cases yield a completely turbulent BL even at lowest Reynolds numbers and exhibit no significant mainstream turbulence influence (Fig. 7).

Film Cooling Measurements. Boundary layer displacement thicknesses at the upstream edge of the cooling holes have been derived from computations conducted with the TEXSTAN BL code (Crawford, 1986). To simulate the wire-triggered transition on the SS at s/L = 0.21, abrupt transition has been imposed at this location. Values for Reynolds numbers of 0.52e6 and 1.45e6 at a *Tu* level of 10 percent are given in Table 2.

Using air as coolant medium yielded a density ratio, ρ_{Tc}/ρ_{Tg}, of 1.05 based on total temperatures, whereas a value of ρ_{Tc}/ρ_{Tg} = 1.65 was achieved with CO_2.

FC results will be presented in the following sections first for the airfoil suction side, and then for the pressure side. For both SS and PS detailed distributions of η and heat transfer enhancement are presented revealing information of the three-dimensional character of the injection process. Heat flux ratio distributions are also shown to describe the overall performance of the different cooling geometries, followed by a detailed discussion of the η and heat transfer coefficient ratio variations under the influence of the different boundary conditions.

Suction Side Film Cooling Results

Detailed film cooling effectiveness and heat transfer coefficient ratio results are presented in Figs. 8–11 for a Reynolds number of 1.45e6 and *Tu* = 10 percent for both the single and double row configurations. The FC heat transfer coefficients are refered to uncooled measurements conducted with a wire BL trip (Fig. 7). These surface contour plots show results for blowing ratio variations at two density ratios (air and CO_2 injection) as well as laminar and turbulent upstream BL states. The holes shown on the plots are overscaled because data in immediate

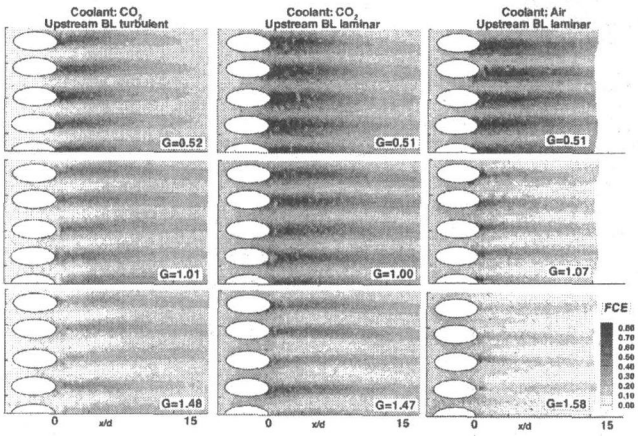

Fig. 8 SS single row η distributions at high Tu and Re_2 = 1.45e6

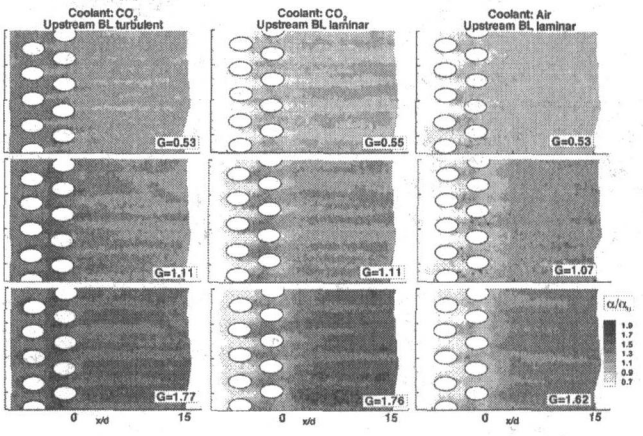

Fig. 11 SS double row heat transfer ratios at high Tu and Re_2 = 1.45e6

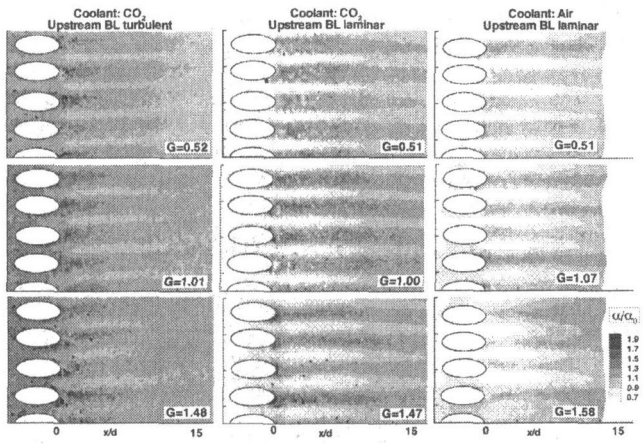

Fig. 9 SS single row heat transfer ratios at high Tu and Re_2 = 1.45e6

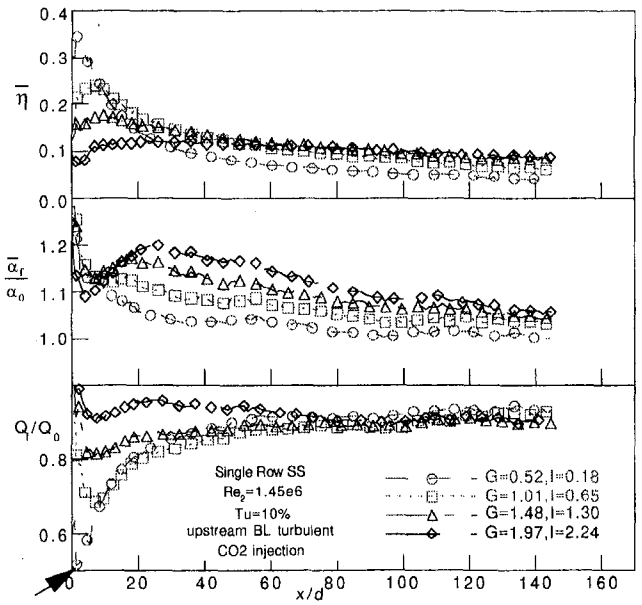

Fig. 12 η, $\bar{\alpha}_f/\alpha_0$, and heat flux ratio for the SS single row configuration referred to a turbulent BL reference case

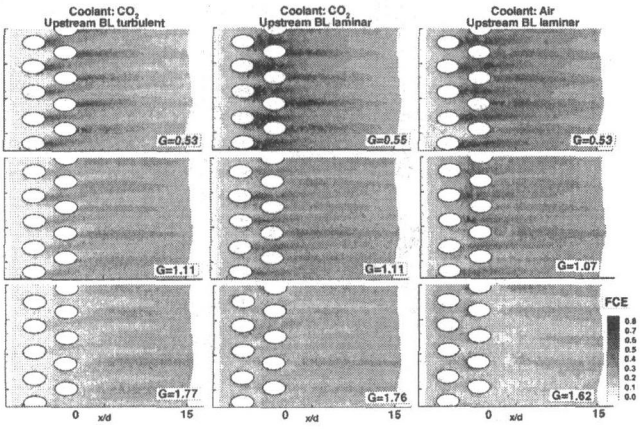

Fig. 10 SS double row η distributions at high Tu and Re_2 = 1.45e6

vicinity of the holes were strongly altered due to conduction effects. These plots will be referred to in subsequent sections.

Effect of Blowing Ratio. Since the object of film cooling is to reduce the heat load to a turbine blade, Mehendale et al. (1994) proposed to represent cooling results in terms of a heat flux ratio, referring the heat flux of the cooled surface to an uncooled case:

$$\frac{Q_f}{Q_0} = \frac{\bar{\alpha}_f}{\alpha_0}\left(1 - \frac{\bar{\eta}}{\Phi}\right) \quad \text{with } \Phi = \frac{T_w - T_g}{T_c - T_g} \tag{3}$$

where Φ is the overall cooling effectiveness, which, according to Mehendale et al., ranges usually from 0.5 to 0.7 for gas turbines. A constant value of 0.6 has been chosen for presentation of the results in this paper, although in real engines this value will be a function of surface location.

η, $\bar{\alpha}_f/\alpha_0$, and heat flux ratio variation with blowing ratio for the single row SS configuration at Tu = 10 percent, a Reynolds number of 1.45e6 and high density ratio are shown in Fig. 12 as a function of downstream distance divided by the hole diameters, counted from the downstream edge of the holes. Both FC and baseline tests have been conducted with the trip wire at s/L = 0.21 so that the BL was fully turbulent.

For the lowest shown blowing ratio of 0.52, a heat flux reduction of 50 percent is achieved immediately downstream of injection, where η has a value of 0.35. Thereafter, both η and $\bar{\alpha}_f/\alpha_0$ decay, but since the rate of heat transfer reduction is stronger, returning to values close to uncooled heat transfer after 20 hole diameters, heat flux reduction of 6 to 8 percent is still achieved in the range x/d = 60 to 145.

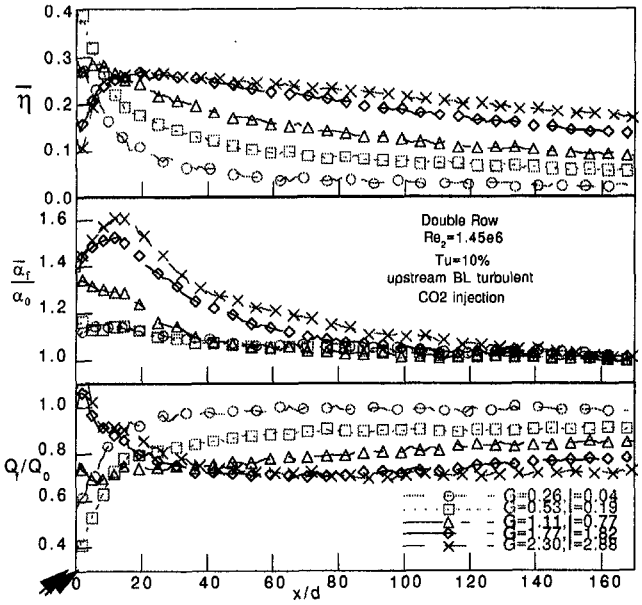

Fig. 13 η, $\bar{\alpha}_f/\alpha_0$, and heat flux ratio for the SS double row configuration refered to a turbulent BL reference case

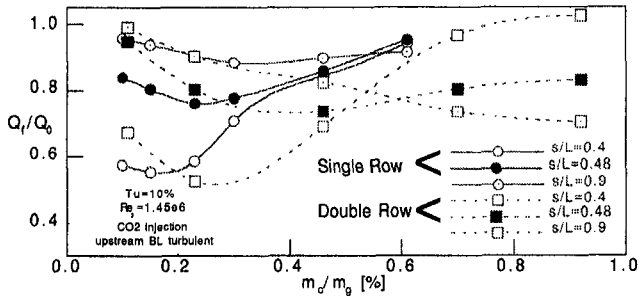

Fig. 14 Heat flux ratios for the SS single and double row configurations

Increase of blowing ratio has two effects: close to injection η decreases due to gradually detaching jets, whereas further downstream η increases even up to the highest blowing ratio of 1.97, because of the greater coolant mass introduced into the BL. On the other hand, heat transfer is enhanced with increasing G, showing peak values at the location where the coolant jets reattach to the wall. The impact on heat flux ratio is a reduction of the cooling performance close to the holes due to reduced η, which is worst at the location of jet reattachment. Further downstream at $x/d > 70$, however, the reduction is nearly independent of G and of the order of 8 percent, due to the balancing effect of both increasing η and heat transfer with increasing G.

A similar investigation has been performed for the suction side double row configuration (Fig. 13). The lowest blowing ratio ($G = 0.26$) yields substantial heat flux reduction only in the injection region, because the η decays rapidly from an initial value of 0.27 to 0.06 at $x/d = 40$. The effects with increasing G are generally the same as for the single row, but η decrease in vicinity of injection is now limited to the first 15 hole diameters, and η decay at higher blowing ratios is less steep. Heat transfer enhancement on the other hand yields values that reach 1.6 at the highest blowing ratio of 2.3 at the point of jet reattachment, compared to a highest observed value of 1.2 for the single row at $G = 1.97$. The combined effects of η and heat transfer enhancement on the heat load with increasing G indicate a worsening protection in proximity of injection, but significant increases at locations $x/d > 20$. Hence, at a blowing ratio as high as 1.77, a heat load reduction of 25 to 30 percent is achieved for $x/d > 20$. This blowing ratio seems, however, to be the limiting value, because the results for the highest tested blowing ratio of 2.3 does not differ significantly from $G = 1.77$.

Comparing the detailed η distributions for the single row (Fig. 8) and the double row (Fig. 10) shows that the film coverage is well improved for the double row. Strong centerline η streaks as observed for the single row are much less apparent for the double row. At high blowing ratios, the single row centerline effectiveness streaks become quite narrow due to lateral mainstream penetration, strongly reducing η, whereas for the double row η remains elevated because of the staggered hole arrangement. As observed in Fig. 10, the upstream row injects coolant into the lateral gaps of the downstream row, blocking this flowpath for the mainstream fluid.

Detailed heat transfer coefficients for the single row (Fig. 9) on the other hand show only strong increase in the hole centerlines, whereas for the double row (Fig. 11) increased heat transfer extends well over the span downstream of injection.

A direct comparison of the single and double row performance in function of the coolant-to-mainstream mass flow ratio is shown in Fig. 14 at three downstream locations ($s/L = 0.4$, 0.48, 0.9). At less than 0.25 percent coolant mass flow, the single row shows better protection, mainly due to less heat transfer enhancement, whereas at flow rates above this limit the double row behavior is increasingly superior. Hence, in spite of stronger heat transfer enhancement, the double row yields improved performance due to a better film coverage and delayed jet detachment at medium to high coolant mass flow rates.

Effect of Upstream Boundary Layer State. Laterally averaged η and heat transfer coefficient ratio of the SS single row configuration with laminar and turbulent upstream boundary layer states are presented in Fig. 15 for three downstream locations ($x/d = 5$, 20, 100) as a function of blowing ratio. To allow a comparison, all subsequently presented heat transfer coefficient ratios are referred to a turbulent uncooled BL state. η is higher with a laminar BL, and this increase is most pronounced close to the injection holes ($x/d = 5$), where η is increased up to 30 percent with respect to the turbulent BL case. At 20 and 100 hole diameters downstream, an increase is still obvious at moderate blowing ratios, but insignificant or even nonexistent at low and high blowing ratio ends. Hence, close to injection, greater fluctuations of the turbulent BL tend to dilute the coolant, as it can be clearly noted from the detailed η distributions in Fig. 8 (left and center column) where the downstream effectiveness streaks are much thinner and shorter for injection into a turbulent BL. Farther downstream at high G, however, the higher BL turbulence possibly increases the

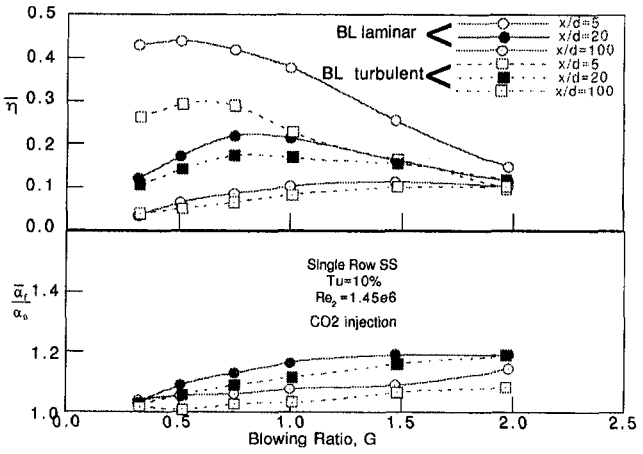

Fig. 15 SS single row η and heat transfer ratio for laminar and turbulent upstream BL states

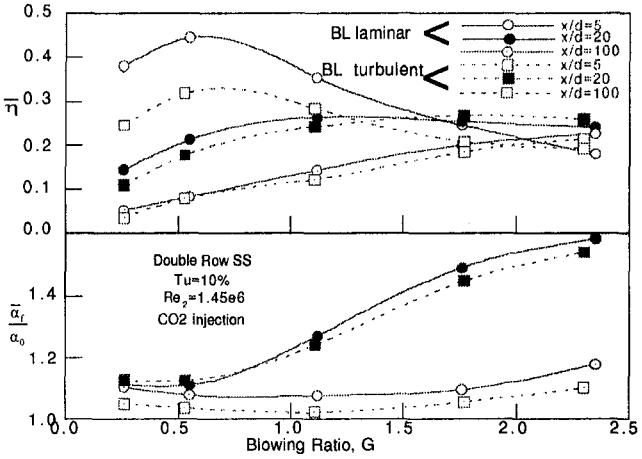

Fig. 16 SS double row η and heat transfer ratio for laminar and turbulent upstream BL states

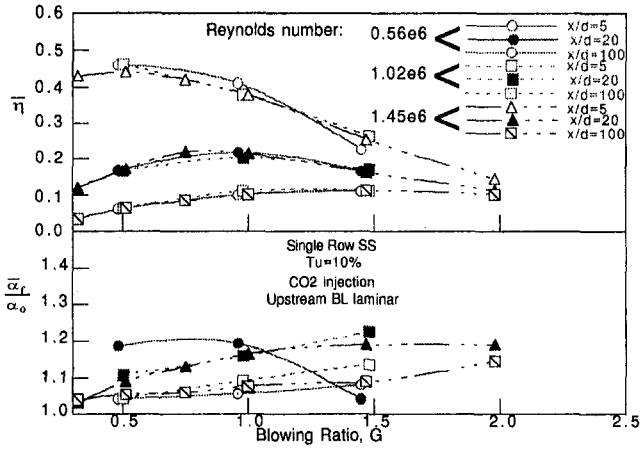

Fig. 17 SS single row η and heat transfer ratios for different Re_2

jet diffusion back to the wall, yielding similar values as obtained with injection into a laminar BL.

For the double row configuration, the situation is comparable (Fig. 16). Since even higher blowing ratios have been investigated (up to $G = 2.35$) one can state that at these high mass flow rates injection into a turbulent BL becomes slightly favorable at $x/d = 5$. A possible explanation is that the higher turbulence of a turbulent BL diffuses a greater portion of the detaching jets into the BL.

Heat transfer enhancements as functions of blowing ratio and boundary layer state are equally shown in Figs. 15 and 16 for two axial positions of $x/d = 20$ and 100. Values at $x/d = 5$ are not presented, because for injection into a laminar BL, transition is not completed at this position, rendering comparison difficult. Both configurations show a general tendency of increased heat transfer for injection into a laminar BL. The differences are rather weak and within the measurement uncertainty, but could be attributed to the fact that for injection into a laminar BL, a new and hence thinner turbulent BL is generated, yielding higher heat transfer rates as a turbulent BL, which has already started well upstream.

The detailed heat transfer coefficient distributions in Figs. 9 and 11 reveal that the centerline heat transfer is well increased for injection into a laminar BL close to the holes and the hole wakes of increased heat transfer extend farther downstream as for the turbulent BL case, possibly because the centerline BL becomes turbulent at the hole exit.

Effect of Mainstream Flow Condition. Essentially two parameters can produce an alteration of the film cooling performance in function of the flow condition. A slightly different flow field in terms of flow acceleration as well as a different BL displacement thickness, being a function of the Reynolds number, can have an impact on η. Teekaram et al. (1991) observed that high acceleration discourages jet detachment, causing the jets to stay closer to the wall, consequently increasing η, and according to Liess (1975), an augmentation of the BL displacement thickness-to-hole diameter ratio reduces η for $\delta_1/d > 0.2$. Since however δ_1/d ranges from 0.09 (Re_2 = 1.45e6) to 0.17 (Re_2 = 0.52e6) for the single row, only a little effect of BL thickness changes would be expected.

In terms of flow acceleration, the flow fields for Re_2 = 1.02e6 and 1.45e6 are very similar, whereas at the lowest Re_2 of 0.52e6 acceleration at the injection location is reduced by a factor 2, and the change from favorable to adverse pressure gradient is shifted upstream (Fig. 4).

In fact, the single row data show slight η reductions at Re_2 = 0.52e6 and high G (Fig. 17), as is expected from the acceleration parameters. For the medium and high Reynolds numbers, on the other hand, very good agreement of η at all locations and blowing ratios can be noted.

The present heat transfer data, again referred to fully turbulent solid blade data for consistency, show that far downstream at $x/d = 100$, heat transfer enhancement agrees well for all Reynolds numbers, whereas at $x/d = 20$ only the medium and high Reynolds numbers exhibit comparable increase (Fig. 17, lower part). At this location, stronger heat transfer increase occurs at low blowing ratios ($G = 0.5$) and reduced enhancement is encountered at high blowing ratios ($G = 1.5$) for Re_2 = 0.52e6, when compared to the higher Reynolds number flow conditions. Hence, at low blowing ratios and less acceleration (Re_2 = 0.52e6), increased BL turbulence could cause stronger mixing of the secondary fluid with the mainstream, whereas at high injection rates mixing is reduced at this flow condition, due to a jet trajectory further away from the wall.

Although not shown, double row data exhibited very similar trends for both η and $\bar{\alpha}_f/\alpha_0$, confirming the above observations.

Effect of Coolant Density. In order to assess the effect of different coolant-to-mainstream density ratios, measurements have been conducted with both air and CO_2 at Re_2 = 1.45e6, high Tu, and both laminar and turbulent upstream BL state. Results are only shown for the laminar BL state for the SS single row in Fig. 18 and for the double row in Fig. 19, plotted as a function of the momentum flux ratio. It can be noted that for both configurations lateral averaged effectiveness is not significantly influenced by the coolant density for $I < 0.3$. Strong discrepancies occur, however, at higher I, especially at the axial locations of $x/d = 5$ and 20, where η drops strongly for air injection compared to CO_2 injection. The detailed η distributions (Fig. 8 and 10, center and right columns)

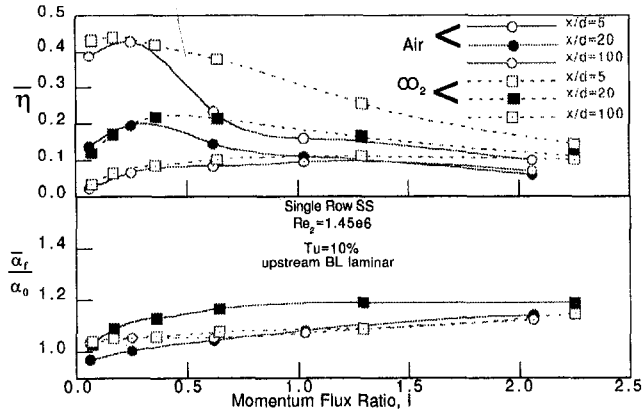

Fig. 18 SS single row η and heat transfer ratios for air and CO_2 injection

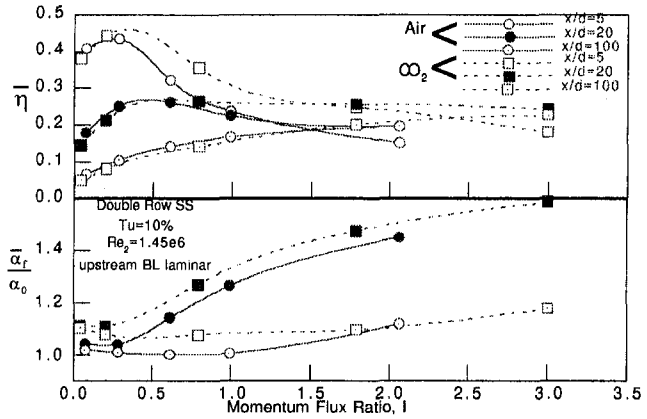

Fig. 19 SS double row η and heat transfer ratios for air and CO_2 injection

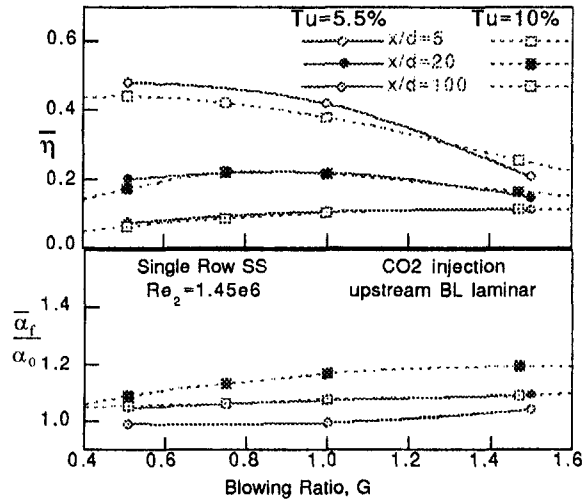

Fig. 20 SS single row η and heat transfer ratios for low and high *Tu*

show very similar pattern at low injection rates. At medium and high rates (G = 1 and 1.5), however, CO_2 injection produces larger lateral extensions of high η streaks downstream of the holes, indicating that the jets remain closer to the wall producing better coverage, when compared at constant G. Hence, for the same coolant mass flow rate, CO_2 as coolant has less momentum than air, reducing jet detachment, whereas at constant momentum flux ratio, more coolant mass is introduced at the higher DR increasing η.

The coolant density effect is more pronounced for the single row, where at I = 1 and x/d = 5, air injection yields about 50 percent reduced η values, whereas for the double row the reduction is only about 25 percent. Additionally, at x/d = 100, the *DR* has no noticeable influence on the double row performance, but still yields reduced η for the single row. This behavior confirms again that the double row is less sensitive to jet separation due to the blockage effect produced by the first of the two staggered rows.

Heat transfer enhancement for both *DR* are equally shown in Figs. 18 and 19, as previously referred to turbulent solid blade heat transfer. Although the general behavior with increasing I is the same for air and CO_2 injection, up to 10 percent higher values for CO_2 are obvious close to injection at x/d = 20. As pointed out in the introduction, such increased heat transfer for CO_2 was also noted by other researchers. The detailed heat transfer maps in Figs. 9 and 11 reveal that this increase is most pronounced in the hole centerlines, where the coolant concentration is highest. Hence, the local density of the BL is increased by the heavier coolant increasing also the local Reynolds number and consequently the local heat transfer. Although not shown here, the same behavior was noted for a fully turbulent approaching BL, so that a possible change of the transition character due to density differences was excluded as mechanism for the differences observed in this study.

Effect of Free-Stream Turbulence. FC performance at two distinct levels of mainstream turbulence, with and without a turbulence generating grid, has been investigated at Re_2 = 1.45e6, laminar upstream BL, and CO_2 injection. For the single row configuration (Fig. 20), η yields slightly increased values at low *Tu* close to injection (x/d = 5) and at low to moderate blowing ratios, whereas at a high G of 1.5 better η is observed at high *Tu*. At x/d = 20, differences are much less pronounced, although the tendency of increased η for low *Tu* and low G and decreased η at high G is still noticeable. This kind of behavior has also been observed in a FC flat plate investigation (Drost et al., 1997), and can be attributed to high mainstream *Tu* and increased BL turbulence, which sheds a part of the coolant mass flow from the jets, which detach at high G from the wall, improving the coolant dispersion into the boundary layer.

η double row results for the two *Tu* levels shown in Fig. 21 do not exhibit a significant influence of mainstream *Tu*. This is not surprising, since the sensibility of the double row to jet detachment phenomena is reduced with respect to the single row, as noted previously.

Heat transfer enhancement with respect to turbulent solid blade data is quite constantly increased with higher mainstream *Tu*, yielding values about 10 percent above those for low mainstream *Tu* for both cooling configurations (Figs. 20 and 21) and both axial positions shown in the plots.

Pressure Side Film Cooling Results

As on the suction surface film cooling measurements have been conducted on the pressure surface for various blowing ratios, air and CO_2 injection, as well as two free-stream turbulence levels. Due to the closeness of the pressure side row location to the leading edge and thus in a region of very strong flow acceleration, attempts to trigger the BL state from laminar to turbulent upstream of injection failed because of immediate relaminarization of the BL downstream of the trigger wire.

Hence, measurements were only conducted with a laminar upstream BL state. Detailed η, $\overline{\alpha}_f/\alpha_0$ distributions for low and high *Tu*, as well as CO_2 and air injection are shown in Figs. 22 and 23 for three blowing ratios. As for the detailed SS plots, the holes shown are not to scale.

Effect of Blowing Ratio. Heat flux ratios are presented for the PS in Fig. 24 together with η and $\overline{\alpha}_f/\alpha_0$ to give an impression of the overall cooling performance at Re_2 = 1.45e6, CO_2 injec-

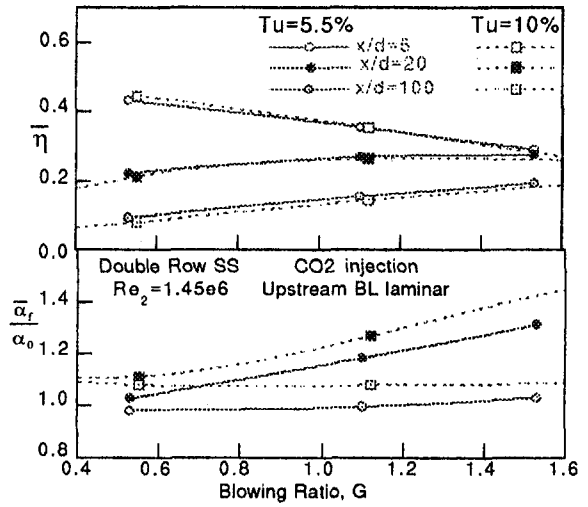

Fig. 21 SS double row η and heat transfer ratios for low and high *Tu*

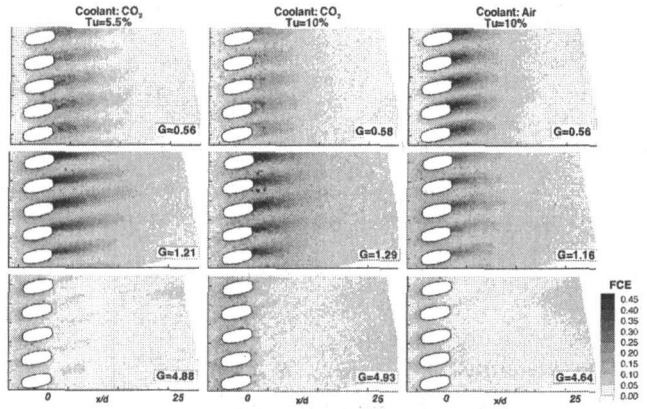

Fig. 22 Detailed PS single row η distributions at Re_2 = 1.45e6

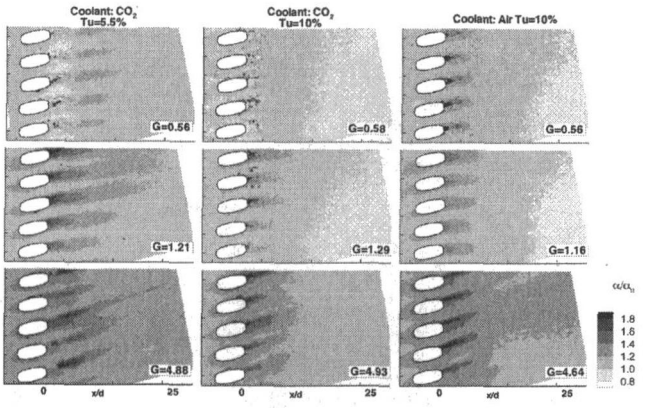

Fig. 23 Detailed PS single row heat transfer ratio distributions at Re_2 = 1.45e6

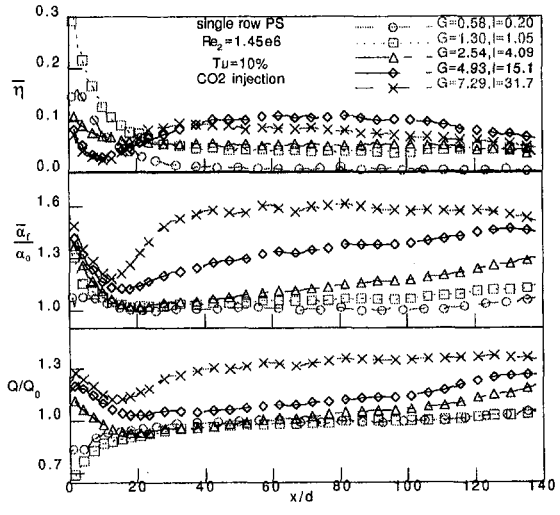

Fig. 24 PS single row η, $\bar{\alpha}_f/\alpha_0$, and heat flux ratios at Re_2 = 1.45e6

tion, and high Tu. The lowest tested blowing ratio of 0.58 yields a 19 percent heat flux reduction at the injection location, where η has a value of 0.15, which then decays very rapidly to zero reduction and zero η at x/d = 40. At this low blowing ratio, heat transfer is hardly affected by the FC injection, relaminarizing right after injection. An increase in blowing ratio to 1.3 improves the cooling performance at the injection location, where a 40 percent reduction is achieved, and also farther downstream, so that a positive heat flux ratio persists up to 80 hole

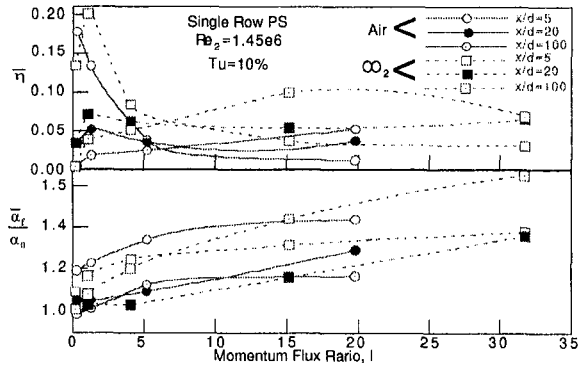

Fig. 25 PS single row η and heat transfer ratios for air and CO_2 injection

diameters downstream. According to the detailed η distribution (Fig. 22), the jets remain attached to the wall at this regime, so that a peak η of 0.3 is achieved immediately downstream of the holes, although accompanied by an $\bar{\alpha}_f/\alpha_0$ of 1.3 due to increased mixing. At G = 2.54 and higher, jet lift-off evidently occurs, since η now drops significantly in the near-hole region. At G = 2.54 the separation is, however, still weak, because $\bar{\alpha}_f/\alpha_0$ is not enhanced in the range x/d = 20 to 40. Slight enhancement occurs, however, farther downstream, possibly due to increased instabilities in the laminar BL. The highest two blowing ratios shown exhibit the behavior of strong jet detachment and reattachment, which occurs at these high blowing ratios, first due to the strong favorable pressure gradient, and second due to the concave nature of the PS. η is nearly nonexistent within the first 15 hole diameters downstream, then rising to a level of 0.1 at G = 4.93. At even higher G, η decreases again. Simultaneously, $\bar{\alpha}_f/\alpha_0$ is strongly increased at jet reattachment, provoking transition start at x/d = 15 for G = 4.93 and possibly complete transition in the range of x/d = 15 to 30 at G = 7.29. Due to this alteration of the BL state, heat flux ratios are unfavorable at high G on the entire surface.

Effect of Density Ratio. η and $\bar{\alpha}_f/\alpha_0$ for air and CO_2 injection are plotted versus the momentum ratio in Fig. 25 for three downstream locations (x/d = 5, 20, 100). At all locations and all but the lowest momentum flux ratios, the higher density coolant yields higher η values. This general tendency, as noted for the SS cases, is due to reduced air mass flow rates at maintained momentum flux ratios, reducing the η.

In contrast to the SS heat transfer behavior, where CO_2 injection yielded stronger enhancement, the effect is at least partly inversed on the PS (Fig. 25). Close to injection at x/d = 5 and 20, higher heat transfer is observed with air injection. Only at x/d = 100, CO_2 yields higher values, indicating a different transition behavior, which might be due to slight variations of surface roughness between the test series.

The effect of increased heat transfer on the SS and reduced heat transfer on the PS for CO_2 injection compared to air injection has equally been noted by Ou et al. (1994) in an airfoil study. They used compound angle injection on the PS, similar to the present configuration. Ekkad et al. (1997) conducted flat plate measurements with compound angles and both air and CO_2 and found that air injection produced much higher heat transfer than CO_2 injection, whereas at streamwise angles the influence was small.

Looking at the $\bar{\alpha}_f/\alpha_0$ maps (Fig. 23, center and left columns) reveals that increased heat transfer for air injection occur not only at constant momentum flux ratios, but also at constant blowing ratios, an observation also confirmed by the data of Ekkad et al. Only the volume flow rate remains higher for air injection at both constant G and constant I, so that it may be assumed that it is this increased volume of the secondary fluid

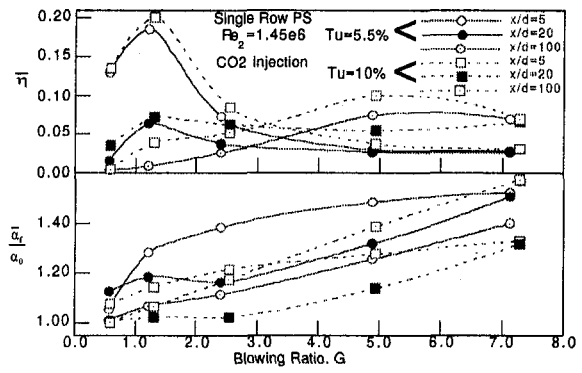

Fig. 26 PS single row η and heat transfer ratios for low and high *Tu*

that favors its lateral spread and hence its mainflow interaction, yielding increased heat transfer values.

Effect of Free-Stream Turbulence. At blowing ratios below 1.5, the influence of mainstream *Tu* on η is very weak and well within the measurement uncertainty (Fig. 26). Above this value, however, a quite noticeable increase of η with *Tu* becomes evident at all three axial locations presented, and disappears only at the highest tested blowing ratio of 7.3.

From the detailed η distributions in Fig. 22 it is obvious that for the blowing ratio of 4.9 more coolant is held back in the BL at high *Tu* so that the effect of high *Tu* is assumed to be an increased coolant diffusion into the BL increasing the η. At very high coolant momentum, however, the effect becomes negligible again, because the additional fluctuations introduced into the BL by high *Tu* do not have enough energy to make up for the strong momentum of the detaching jets.

Heat transfer enhancement equally shown in Fig. 26 has been referred to low and high *Tu* baseline tests, respectively. At x/d = 5 and 20, $\bar{\alpha}_f/\alpha_0$ is higher at low *Tu*, whereas at x/d = 100 differences are insignificant at low blowing ratios ($G \leq 1.3$) and reversed at high ones. The detailed $\bar{\alpha}_f/\alpha_0$ distributions in Fig. 23 show that the lateral jet spreading is less strong at low *Tu*, so that centerline streaks of high heat transfer are more pronounced.

An explanation of this behavior is possibly that the momentum surplus is preserved farther downstream at low *Tu* due to less mixing, thus increasing the heat transfer. Far downstream on the other hand, the BL goes earlier into transition at high *Tu*, explaining the reduced $\bar{\alpha}_f/\alpha_0$ values at x/d = 100 at low *Tu*.

Conclusions

Film cooling measurements on both pressure and suction surface of a gas turbine blade have been conducted for three flow conditions, Re_2 = 0.52e6, 1.02e6, 1.45e6, various blowing ratios, two *Tu* levels, laminar and turbulent approach BL states, as well as air and CO_2 injection.

- Detailed η and heat transfer ratios have been presented for the near-hole region.
- On the SS, a double row of film cooling holes provided superior heat load reduction over a single row at medium to high coolant mass flow rates, due to an improved film coverage and delayed jet lift-off at high blowing ratios. A compound angle cooling configuration on the PS showed very little heat load reduction at low blowing ratios, and an unfavorable cooling performance at blowing ratios above 1.3 due to strong heat transfer enhancement.
- η on the SS was significantly higher in the near-hole region with an approaching laminar BL.
- Variations in Mach and Reynolds number changed the film cooling performance on the SS, because the flow acceleration and/or the boundary layer thickness were changed.
- Higher density coolant improves the η on both suction and pressure side, and heat transfer is increased on the SS at higher density possibly due to increased local Reynolds numbers. On the PS, on the other hand, heat transfer decreased with increasing density ratio, an effect assumed to be related to the compound angle configuration, which produces stronger mixing at higher volume flow rates occurring at lower density ratios.
- Free-stream turbulence only weakly affects SS η, but heat transfer coefficient ratios increase with *Tu*. On the pressure side, η is increased at higher *Tu*, because of favored jet diffusion in the BL. Heat transfer ratios on the PS were observed to be lower at high *Tu*.

Acknowledgments

The research project is subsidized by ABB Power Generation Ltd., Switzerland and the "Nationaler Energie-Forschungs Fonds" (NEFF), Switzerland. The authors are very grateful to B. Weigand and A. Hoffs for their revision of the paper.

References

Ames, F. E., 1997, "Aspects of Vane Film Cooling With High Turbulence: Part I—Heat Transfer; Part II—Adiabatic Effectiveness," ASME JOURNAL OF TURBOMACHINERY, Vol. 120, pp. 768–784.

Ammari, H. D., Hay, N., and Lampard, D., 1990, "The Effect of Density Ratio on the Heat Transfer Coefficient From a Film-Cooled Flat Plate," ASME JOURNAL OF TURBOMACHINERY, Vol. 112, pp. 444–450.

Arts, T., and Bourguignon, A. E., 1990, "Behavior of a Coolant Film With Two Rows of Holes Along the Pressure Side of a High Pressure Nozzle Guide Vane," ASME JOURNAL OF TURBOMACHINERY, Vol. 112, pp. 512–520.

Camci, C., and Arts, T., 1990, "An Experimental Convective Heat Transfer Investigation Around a Film-Cooled Gas Turbine Blade," ASME JOURNAL OF TURBOMACHINERY, Vol. 112, pp. 497–503.

Crawford, M. E., 1986, "Simulation Codes for Calculation of Heat Transfer to Convectively Cooled Turbine Blades," *Convective Heat Transfer & Film Cooling in Turbomachinery,* VKI-LS 1986-06.

Drost, U., Hoffs, A., and Bölcs, A., 1997, "Utilization of the Transient Liquid Technique for Film Cooling Effectiveness and Heat Transfer Investigations on a Flat Plate and a Turbine Airfoil," ASME Paper No. 97-GT-26.

Du, H., Han, J. C., and Ekkad, S. V., 1998, "Effect of Unsteady Wake on Detailed Heat Transfer Coefficient and Film Effectiveness Distributions for a Gas Turbine Blade," ASME JOURNAL OF TURBOMACHINERY, Vol. 120, pp. 808–817.

Ekkad, S. V., Zapata, D., and Han, J. C., 1997, "Heat Transfer Coefficients Over a Flat Surface With Air and CO_2 Injection Through Compound Angle Holes Using a Transient Liquid Crystal Image Method," ASME JOURNAL OF TURBOMACHINERY, Vol. 119, pp. 580–586.

Goldstein, R. J., and Yoshida, T., 1982, "The Influence of a Laminar Boundary Layer and Laminar Injection on Film Cooling Performance," ASME *Journal of Heat Transfer,* Vol. 104, pp. 355–362.

Heidmann, J. D., Lucci, B. L., and Reshotko, E., 1997, "An Experimental Study of the Effect of Wake Passing on Turbine Blade Film Cooling," ASME Paper No. 97-GT-255.

Hoffs, A., Drost, U., and Bölcs, A., 1996, "Heat Transfer Measurements on a Turbine Airfoil at Various Reynolds Numbers and Turbulence Intensities Including Effects of Surface Roughness," ASME Paper No. 96-GT-169.

Kays, W. M., and Crawford, M. E., 1980, *Convective Heat and Mass Transfer,* 2nd ed., McGraw-Hill, New York.

Liess, C., 1975, "Experimental Investigation of Film Cooling With Ejection From a Row of Holes for the Application to Gas Turbine Blades," ASME *Journal of Engineering for Power,* Vol. 97, pp. 21–27.

Mehendale, A. B., Han, J. C., Lee, C. P. and Ou, S., 1994, "Unsteady Wake Over a Linear Turbine Blade Cascade With Air and CO_2 Film Injection: Part II—Effect on Film Effectiveness and Heat Transfer Distributions," ASME JOURNAL OF TURBOMACHINERY, Vol. 116, pp. 730–737.

Nirmalan, N. V., and Hylton, L. D., 1990, "An Experimental Study of Turbine Vane Heat Transfer With Leading Edge and Downstream Film Cooling," ASME JOURNAL OF TURBOMACHINERY, Vol. 112, pp. 477–487.

Ou, S., Han, J. C., Mehendale, A. B., and Lee, C. P., 1994, "Unsteady Wake Over a Linear Turbine Cascade With Air and CO_2 Film Injection: Part I—Effect on Heat Transfer Coefficients," ASME JOURNAL OF TURBOMACHINERY, Vol. 116, pp. 721–729.

Takeishi, K., Aoki, S., Sato, T., and Tsukagoshi, K., 1992, "Film Cooling on a Gas Turbine Rotor Blade," ASME JOURNAL OF TURBOMACHINERY, Vol. 114, pp. 828–834.

Teekaram, A. J. H., Forth, C. J. P., and Jones, T. V., 1989, "The Use of Foreign Gas to Simulate the Effects of Density Ratios in Film Cooling," ASME JOURNAL OF TURBOMACHINERY, Vol. 111, pp. 57–62.

Teekaram, A. J. H., Forth, C. J. P., and Jones, T. V., 1991, "Film Cooling in the Presence of Mainstream Pressure Gradients," ASME JOURNAL OF TURBOMACHINERY, Vol. 113, pp. 484–492.

Measurements of Discharge Coefficients in Film Cooling

S. W. Burd

T. W. Simon

Heat Transfer Laboratory,
University of Minnesota,
Minneapolis, MN 55455

Measurements of discharge coefficients for several film cooling configurations having hole length-to-diameter ratios of 2.3, 4.6, 6.6, and 7.0 are presented. Recently, it was documented that the velocity distributions over the hole exit plane vary significantly with changes in hole length-to-diameter ratio. This paper documents the effects of such variations on coolant discharge coefficients. Due to the short holes, injection in engines is with a substantial amount of coolant departing the upstream portions of the hole exit plane. This results in a higher rate of momentum exchange with the free stream at that location than for longer holes, which permits more uniform exit flows. Discharge coefficient measurements are discussed in terms of this distribution of velocity. This paper also documents the effects of the hole supply plenum geometry on discharge coefficients. When the coolant flow is delivered to the holes with significant momentum either in the direction of the free stream or opposite to that direction, significant changes in discharge coefficient values are observed.

Introduction

Discharge coefficients are a measure of the flow losses through the coolant supply plenum, hole, and the coolant–free-stream interaction zone. They are used to determine film cooling flow, given supply plenum total pressure and free-stream static pressure. Values depend on the geometry as well as the supply plenum and free-stream flow conditions.

Hay and Lampard (1998) published a review of data on discharge coefficients acknowledging measurements of Hay et al. (1983, 1994a, b) and Hay and Lampard (1995). Per these data, discharge coefficients scale on the coolant-total-to-mainstream-static pressure ratio, p_c^+/p_s, and vary with hole geometry. Haller and Camus (1984) noted that holes with a spanwise flare angle of 25 deg offer significant improvements in film cooling effectiveness without any additional loss. Hay and Lampard (1995) reported higher discharge coefficients for 25 deg flared holes than for cylindrical holes. Gritsch et al. (1998) documented higher discharge coefficients for fan-shaped and laidback-fan-shaped holes than for cylindrical holes and detailed effects of approach flow conditions. Byerley (1989) looked at approach flow effects with coolant delivered at acute and obtuse angles to the hole axes. Higher C_d values were observed with acute angles. Hay et al. (1994a) documented discharge coefficients for cylindrical, compound-angled, lateral, and radiused-entry injection. Hay and Spencer (1992) investigated the effects of radiused and chamfered inlets of short holes ($L/D = 0.25–2.0$). Both have increased discharge coefficients over sharp-edged holes. Hay et al. (1994b) noted increases in discharge coefficients with proper radiusing.

External crossflow changes the pressure drop needed to drive a given mass flow rate through a film cooling hole. Experiments (Abramovich, 1963) and computations (Walters and Leylek, 1997) show that the jets are deflected as they emerge, due to the stagnation pressure exerted by the free stream. Mixing and shearing with the free stream along the coolant jet periphery cause the flow in the outer regions of the jet to lose momentum and, thus, deflect. In addition, the coolant-to-free-stream momentum flux ratio influences jet penetration, trajectory, and the coolant static pressure distribution (Burd et al., 1996; Walters and Leylek, 1997). With square-edged orifices, Rogers and Hersh (1975) showed that external crossflows restrict the emerging flow as would a lid attached to the upstream edge of the orifice. Hay et al. (1983) and Gritsch et al. (1998) noted decreased discharge coefficients with external crossflows for streamwise-inclined holes. To the contrary, Rowbury et al. (1997) noted that, at high pressure ratios, depending on hole inclination, C_d may actually increase with external crossflows. They identified a "crossover" point beyond which the free-stream pumps the emerging flow. Khaldi (1987) documented this for normal injection.

Correlating changes in pressure due to crossflow interactions, Sasaki et al. (1976) defined additive loss coefficients at the hole entrance, δ_{in}, and exit, δ_{out}. For external crossflows, they found δ_{out} to correlate well with the momentum flux ratio, I; high at low I, decreasing monotonically to near zero for $I > 1$. Their data, however, show significant variability (200–300 percent) in δ_{out} for $I < 1.0$. Tillman and Jen (1984) and Hay et al. (1994b) adopted Sasaki's definition in describing discharge coefficients. Hay and Lampard (1998) noted that such data presented in terms of outlet additive losses scatter strongly for cases of various hole geometries. CFD predictions of losses by Khaldi (1987) show significant mismatch with correlations deduced from the data of Sasaki et al. and Tillman and Jen. A goal of the present study is to document the effects that hole and plenum geometry and flow conditions have on discharge coefficients.

Experimental Test Facility

The facility is shown in Fig. 1. It has two major systems: the mainstream and coolant supply systems. The mainstream flow is supplied via a high-turbulence wind tunnel constructed by Wang (1996). The tunnel is a combustor simulator that produces turbulence levels characteristic of those found downstream from the combustor in an actual engine. The mean velocity, turbulence level, and integral length scale in the free stream above the hole centerlines are nominally 10.8 m/s, 11.5 percent, and 7.7 cm, respectively. The boundary layer thicknesses at injection are $\delta_{99}/D = 1.13$, $\theta/D = 0.082$, and $\delta^*/D = 0.105$. The coolant flow is delivered by a blower through a large, unrestricted plenum (37.5 cm × 66 cm × 17.8 cm) to the film cooling hole test plate. Mass flow is monitored with laminar flow meters. Engine-representative Re's ($0 < \mathrm{Re} < 30{,}000$) and coolant-to-mainstream momentum flux ratios ($I < 2.3$) are tested. The nominal density ratio between the two streams is unity.

In engines, coolant-total-to-mainstream-static pressure ratios can vary significantly, depending upon location along the blade,

Contributed by the International Gas Turbine Institute and presented at the 43rd International Gas Turbine and Aeroengine Congress and Exhibition, Stockholm, Sweden, June 2–5, 1998. Manuscript received by the International Gas Turbine Institute February 1998. Paper No. 98-GT-9. Associate Technical Editor: R. E. Kielb.

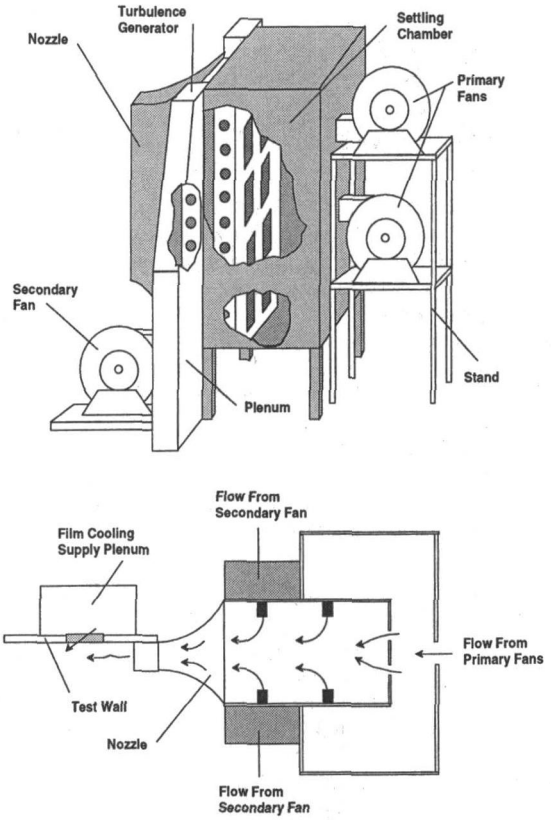

Fig. 1 Film cooling test facility

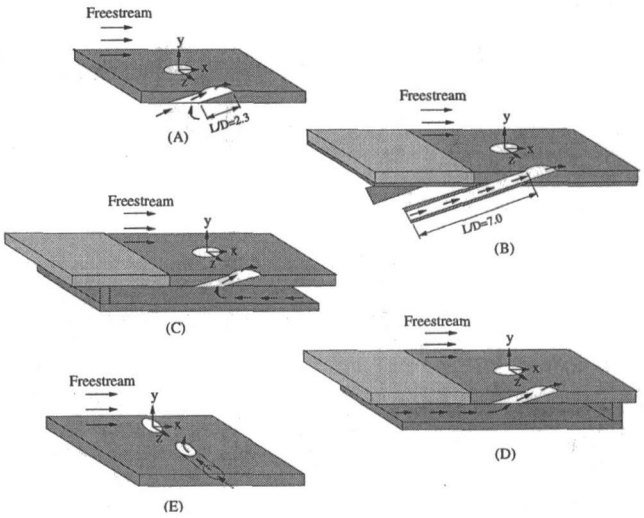

Fig. 2 Film cooling geometries

from low values near the blade stagnation region to high values along the suction surface near the throat. The latter values may be high enough that compressibility effects come into play. Coolant-total-to-free-stream-static pressure ratios are chosen in this experiment to achieve engine representative momentum flux ratios, I. Compressibility is not captured in this experiment. The objective of this paper is to document momentum flux ratio and geometry effects.

Film Cooling Geometries

Several film cooling configurations are investigated. Discharge coefficients are given for cases of streamwise injection through holes of differing lengths supplied by either a large, open plenum or one in which coolant with significant approach flow momentum is delivered to the holes. For the streamwise-oriented film cooling cases, the test plate consists of one row of eleven film cooling holes, 19.05 mm in diameter with 35 deg inclination, machined in a 2.54-cm-thick phenolic laminate plate (Fig. 1). The hole pitch-to-diameter ratio is 3.

To investigate the influence of hole length-to-diameter ratio, sets of tubes of different lengths were connected to the supply plenum side of the film cooling test plate such that no steps are created on the tube inner diameters (e.g., see Fig. 2(B)). The base case L/D is 2.3 (Fig. 2(A)) and, with the tubes, hole length-to-diameter ratios of 4.6, 6.6, and 7.0 (Fig. 2(B)) are achieved. The tubes have t/D equal to 0.18. In engines, of course, this t/D ratio would be very large. Entrance loss data of Fried and Idelchick (1989) indicate that the t/D used in this study is large enough that t influences on mean flow performance are insignificant. The L/D = 7.0 tube geometry is machined with its entrance normal to the tube centerline (Fig. 2(B)). The entrance is parallel to the hole exit plane with the L/D = 4.6 and 6.6 tubes. Coolant flow is delivered from a large, open plenum to these geometries (called "sink flow" cases).

Two additional geometries (Fig. 2(C) and 2(D)), in which flow of significant momentum is supplied to the holes, are added. For these geometries, a baffle was placed along the plenum side of the film cooling test plate to restrict the coolant supply, forcing it to enter with a counterflow (parallel but in the opposite direction, Fig. 2(C)) or coflow (parallel and in the same direction, Fig. 2(D)) relative to the mainstream. The total baffle length is 25.3 cm (13.3 D) with the entrance to the channel located 10.5 cm (5.5 D) upstream from the leading edge of the holes. The channel height is two hole diameters. The delivery channel cross-sectional area is eight times the total cross-sectional area to the film cooling holes. The three plenum geome-

Nomenclature

A = total cross-sectional area of film cooling holes
C_d = discharge coefficient
$C_{d,o}$ = discharge coefficient measured without free stream
D = film cooling hole diameter
L = film cooling hole length
I = coolant-to-mainstream momentum flux ratio
$\dot{m}_a$ = actual mass flow rate through film cooling holes
$\dot{m}_i$ = ideal mass flow rate through film cooling holes
p_c^+ = coolant supply total pressure
p_s = free-stream static pressure
Re = Reynolds number based on U_{hole} and D
t = wall thickness of hole extension tube
U = local mean effective velocity
U_{hole} = bulk mean film cooling hole velocity
U_∞ = free-stream velocity
VR = coolant-to-free-stream velocity ratio
u' = rms fluctuation about mean effective velocity
x = streamwise distance from hole center
y = wall-normal distance
z = lateral distance from hole center
δ^* = boundary layer displacement thickness
δ_{99} = boundary layer thickness (99 percent)
δ_{in} = inlet additive loss coefficient
δ_{out} = outlet additive loss coefficient
θ = boundary layer momentum thickness
ρ = density

tries will be referred to as "sink flow" (Figs. 2(*A*) and (*B*)), "counterflow" (Fig. 2(*C*)), and "coflow" (Fig. 2(*D*)). Both counterflow and coflow cases have $L/D = 2.3$. These supply geometries differ from the throughflow channels used by Hay et al. (1984) and Gritsch et al. (1998) in that the present channels carry only the coolant flow rate.

A lateral injection configuration, with $L/D = 2.3$ and flow delivered to the holes as a sink flow (Fig. 2(*E*)), is also investigated. The geometry is nearly identical to that of the streamwise-oriented geometry (Fig. 2(*A*)), but with the hole machined 90 deg relative to the streamwise direction.

All film cooling geometries are machined with sharp-edged entrances and exits. L/D's are representative of those found in actual engines, which range over $1.0 < L/D < 10$. Cases with restricted plenums are somewhat representative of actual engine geometries, although the complex approach flow of the engine geometry is replaced by the simpler "counter-" or "co-" flows described previously.

Experimental Procedure

Single-sensor, hot-wire anemometry (TSI 1218-T1.5 probe and TSI IFA-100 bridge) is used to measure instantaneous velocity over the exit plane of the film cooling holes. Measurements were with the hot-wire positioned normal to the free stream and parallel to the film-cooled surface. Thus, the measured velocities are effective cooling velocities, U, to the hot-wire sensor and, more precisely, the vector sum of the local streamwise and wall-normal components of velocity. Uncertainties in the mean effective velocities are 5 percent (95 percent confidence).

Discharge coefficients are useful for determining film cooling flow given the pressures of the coolant supply and free stream. A discharge coefficient is the fraction of the "ideal" mass flow rate which actually flows through the film cooling holes:

$$C_d = \frac{\dot{m}_a}{\dot{m}_i} \tag{1}$$

This ideal flow is based upon an isentropic, one-dimensional expansion of the coolant from the supply plenum total pressure, p_c^+, to the mainstream static pressure, p_s. For the present study, compressible effects can be ignored and this ideal mass flow was calculated using the Bernoulli equation:

$$\dot{m}_i = A\sqrt{2\rho(p_c^+ - p_s)} \tag{2}$$

The total pressure in the coolant supply plenum and the mainstream static pressure were measured using a pitot-static probe. For delivery from a large, open plenum (Figs. 2(*A*), 2(*B*), and 2(*E*)), total pressure measurements were taken sufficiently far from the hole that there was no perceptible velocity head. For the counterflow and coflow configurations (Figs. 2(*C*) and 2(*D*)), the coolant total pressure was measured along the channel centerline at the entrance plane to the channel, 6.3 D upstream from the centers of the film cooling hole inlets. Thus, the supply total pressure to the channel and hole is measured for these geometries. Surveys indicated negligible variations in total pressure along the channel centerline at the entrance plane. The static pressure is taken outside the boundary layer in the free stream at $x/D = 0.0$ and is nominally the ambient pressure. In the vicinity of the hole, static pressures vary significantly from point to point. Pressures are recorded using a Dwyer Microtector micromanometer. The mass flow to all film cooling holes was measured using laminar flow meters.

Uncertainties in $(p_c^+ - p_s)$ and ρ are ± 1.1 Pa and ± 0.004 kg/m^3, respectively. Machining tolerances result in negligible contributions to the uncertainty. The uncertainty in the mass flow rate is ± 2.3 percent. Discharge coefficients have nominal uncertainties of 2.5 percent (2.5–8 percent for lowest C_d values). Uncertainties are expressed with 95 percent confidence.

Losses associated with the external free-stream crossflow are quantified in terms of outlet additive loss coefficients. This loss, δ_{out}, relates the difference between measured pressures, with and without the external freestream, to the film cooling velocity head:

$$\delta_{\text{out}} = \frac{[(p_c^+ - p_s)_{U_\infty \neq 0} - (p_c^+ - p_s)_{U_\infty = 0}]_{U_{\text{hole}},\rho}}{1/2\rho(U_{\text{hole}})^2} \tag{3}$$

When the bulk mean velocity, density, and, thus, momentum flux of the coolant flow with and without an external free stream are matched, the net loss introduced exclusively by the external free-stream flow can be quantified. This expression can be simplified in terms of discharge coefficients with, C_d, and without, $C_{d,o}$, the free stream:

$$\delta_{\text{out}} = \frac{1}{(C_d)^2} - \frac{1}{(C_{d,o})^2} \tag{4}$$

Results and Discussion

The film cooling literature lacks documentation of the role of hole length-to-diameter ratio and of internal approach flow momentum on measured discharge coefficients. The present paper provides such documentation. Coolant velocity profiles at the hole exit plane and the interaction of the coolant and free-stream flows vary substantially from case to case. This is quantified in terms of measured discharge coefficients and outlet additive losses.

Hole-Exit Velocity Distributions. Hole exit mean velocity distributions measured along the hole centerlines ($y = z = 0$) with $VR = 1.0$ are presented in Fig. 3. Figure 3(*A*) shows that distributions differ with L/D. The coolant jet has increasingly higher momentum at the upstream side of the hole ("jetting") as hole L/D's are reduced. It is expected that the coolant flow will separate on the downstream (relative to the free-stream) side of the hole entrance. Short lengths allow shorter distances over which this separation zone effect may attenuate. More details on "jetting" are provided by Burd and Simon (1997) and Walters and Leylek (1997). Similar profiles are shown for coflow and counterflow configurations in Fig. 3(*B*). In general, the location and size of the separation zones at the entrance of the film cooling holes cause the coolant to distribute differently with coflow, counterflow, sink flow, and with differing L/D. The major observations are that co-flow and longer L/D cases are characterized by higher coolant momentum fluxes in the downstream portion of the jet exit while counterflow and shorter L/D cases have the most "jetting" in the upstream portion of the hole exit plane. Less can be said about the lateral injection case due to the complexity of the exit flow. The major flow patterns and expected separation zones for the streamwise-oriented geometries in this study are shown in Fig. 7.

It has been suggested that the interaction with the free stream modifies the pressure distribution over the film cooling hole. Walters and Leylek (1997), for instance, through computations, found that there is a high-pressure zone where the mainstream flow first meets the coolant flow upstream of the hole leading edge. The streamwise turning of the exiting coolant then results in a low-pressure region downstream of the hole. The present experiments document the net effect of this via measurements of discharge coefficients.

Effect of Hole L/D. The measured discharge coefficients, C_d, for cases with an unrestricted plenum are plotted against the ratio of the coolant total-pressure-to-free-stream-static pressure ratio, p_c^+/p_s, in Fig. 4. Figure 4(*A*) is without an external free-stream flow whereas Fig. 4(*B*) is with free-stream flow. Without the free-stream flow, the three shortest L/D geometries exhibit nominally the same magnitudes for all pressure ratios exceeding 1.001. All of these cases have the same inlet geometry so the

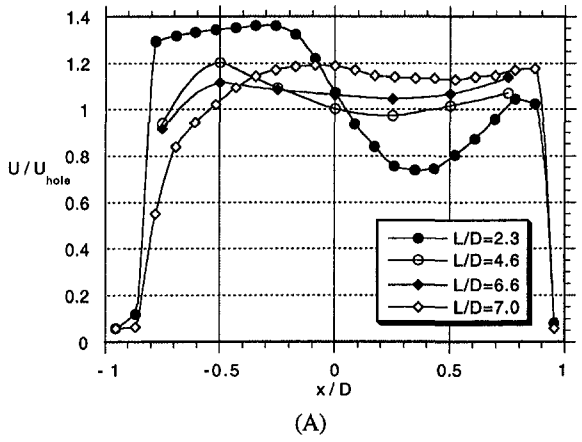

(A)

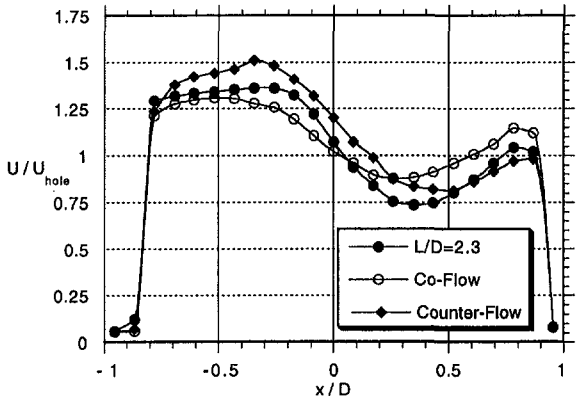

(B)

Fig. 3 Centerline mean velocities at hole exit: (*A*) holes of varying *L/D* and with sink flow delivery; (*B*) holes with and without approach flow momentum, *L/D* = 2.3

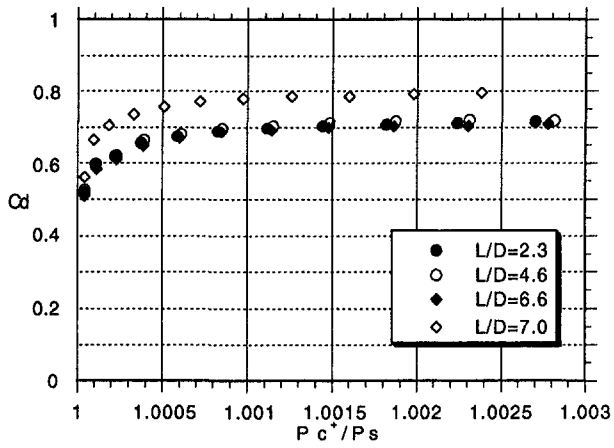

(A)

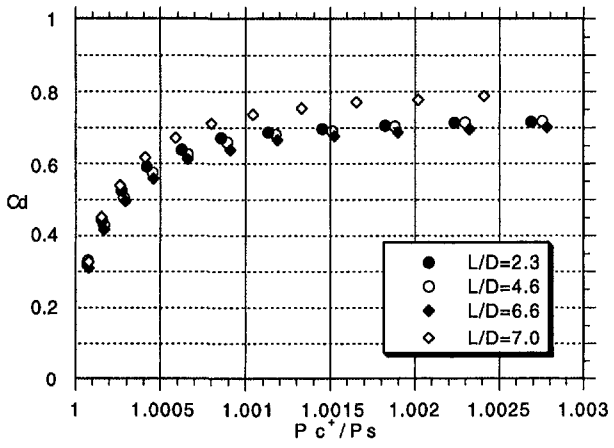

(B)

Fig. 4 Discharge coefficients for holes of varying *L/D*: (*A*) without the free stream; (*B*) with the free stream

only expected differences between these cases would be attributable to skin friction or experimental uncertainty. The data suggest that friction losses are negligible, corroborating the findings of Lichtarowicz et al. (1965), Andrews and Mkpadi (1984), and Hay and Lampard (1998). Due to the different inlet geometry, the $L/D = 7.0$ case has higher C_d values throughout. This is consistent with the results of Fried and Idelchik (1989). For all cases with free-stream flow, discharge coefficient magnitudes increase nearly monotonically as p_c^+/p_s increases, with the C_d values asymptotically approaching a near constant level at the highest p_c^+/p_s. Although no other 35 deg inclination data are available in the open literature, C_d values of 0.70–0.75 are anticipated for 35 deg inclination at high p_c^+/p_s based on 30 and 45 deg data of Gritsch et al. (1998), Hay et al. (1994b), and Byerley (1989).

A comparison of the curves with (Fig. 4(*B*)) and without (Fig. 4(*A*)) the external free stream shows that free-stream flow causes a reduction in C_d at each pressure ratio; significant at the low p_c^+/p_s, reducing to near zero at the highest p_c^+/p_s. The effect of the free stream varies with geometry. The "with" and "without" free-stream curves for $L/D = 2.3$ are relatively closer to one another than curves for the $L/D = 7.0$ case.

Outlet additive losses are presented in Fig. 5 for the different L/D configurations. The δ_{out} values increase with L/D; substantial values ($\delta_{out} > 1.00$) are measured at low momentum flux ratios but near-zero values are measured for large I. For $0.25 < I < 1.5$, there are considerable differences in δ_{out} among varying L/D cases (e.g., 0.15–0.20 higher for $L/D = 7.0$ than for $L/D = 2.3$, at $I = 0.7$). Since $\delta_{out} > 0$ for these cases, the free stream appears to restrict the emerging coolant flow.

A review of Figs. 3 and 5 shows that outlet additional losses are reduced for geometries with which more coolant is distrib-

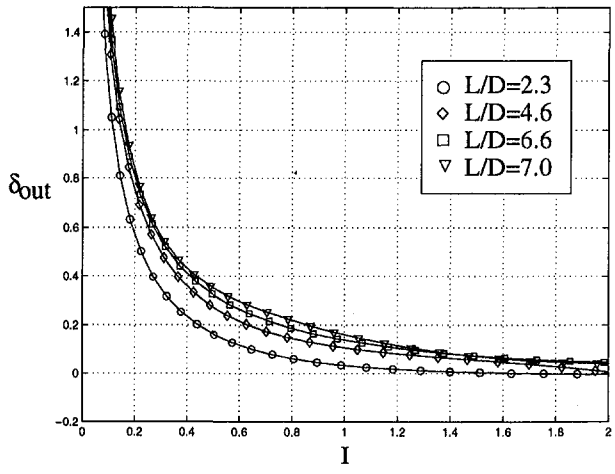

Fig. 5 Outlet additive losses for holes of varying *L/D*

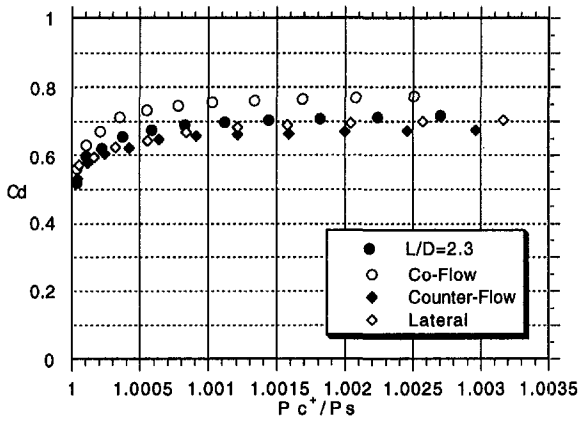

(A)

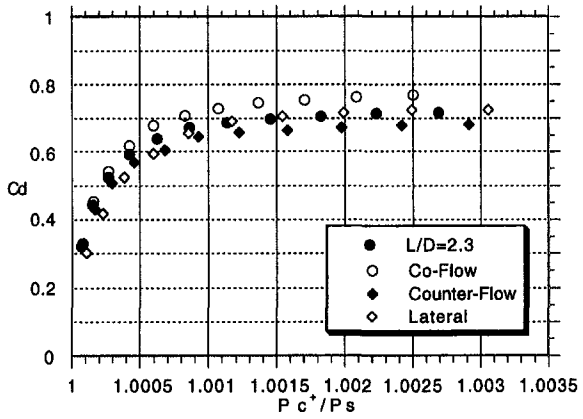

(B)

Fig. 6 Discharge coefficients for holes with and without approach flow momentum, L/D = 2.3; (A) without the free stream; (B) with the free stream

uted in the upstream portion of the hole exit plane (i.e., short holes). For such cases, interaction with the free stream is more active, pressures where the mainstream and coolant flows first meet are higher, and pressures over much of the hole exit plane are reduced as the coolant jet is turned. This is similar to a cylinder in crossflow in which high pressures are found near the stagnation point and low pressures are found downstream in the cylinder wake. The low downstream pressure increases the mass flux at the downstream portion of the hole exit. Configurations with more coolant distributed at the downstream portion of the hole exit (i.e., long holes) have higher δ_{out} values. A more passive momentum exchange where the mainstream and coolant flows first meet for these cases results in a downstream shift of the high-pressure region, a smaller low-pressure region in the downstream portion of the hole exit plane, and a higher effective static pressure at the hole exit.

Effect of Approach Flow Momentum. Figure 6 details discharge coefficients measured for the counterflow and coflow configurations with and without free-stream flow. Discharge coefficients for the L/D = 2.3 case with no internal approach flow momentum are presented for comparison. Approach flow momentum, though fairly small relative to the cooling flow momentum, has a significant influence on discharge coefficient magnitudes (Fig. 6(A)); with coflow, the highest discharge coefficients and, with counterflow, the lowest. With supply from a large, unrestricted plenum, a separation zone is expected at the downstream (relative to the mainstream) edge of the entrance to

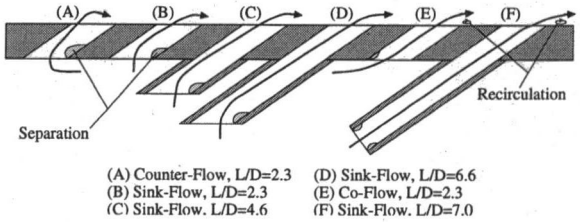

Fig. 7 Expected flow patterns of coolant through various hole geometries

the cooling hole (Fig. 7(B)). With coflow, this separation is apparently smaller and perhaps located at the upstream (relative to the mainstream) edge of the cooling hole (Fig. 7(E)). With counterflow, this separation is apparently larger (Fig. 7(A)).

As with the cases in Fig. 4, the presence of free-stream flow causes reductions in discharge coefficients. For all I, δ_{out} values are greatest for the coflow configuration and smallest for the counterflow configuration (Fig. 8). For the most part, the "sink" flow supply case falls between the two, but is closer to the counterflow case. The δ_{out} values suggest that coflow has the highest net exit static pressures of the three cases. In terms of hole-exit velocity distributions (Fig. 3), it appears that the smallest outlet losses are observed for the geometry with the most coolant at the upstream portion of the hole exit plane (counterflow) and largest for the configuration with the coolant velocity distribution most skewed toward the downstream portion of the hole exit plane (coflow). This is consistent with the trends with L/D. Also noteworthy in Fig. 8 are the negative loss values with counterflow for $I > 1.0$.

In all cases, the approach flow velocity is low. The flow area ratio between the cooling holes and the channel is 1:8, so approach velocities are on the order of 12 percent of in-hole velocities. That C_d and δ_{out} variations with approach geometry exist demonstrates the strong sensitivity.

Streamwise Versus Lateral Injection. The authors are aware of no outlet additive loss coefficients for lateral injection in the literature, though the use of lateral injection in film cooling applications is becoming common. Without free-stream flow (Fig. 6(A)), C_d values for lateral injection resemble those of the streamwise injection case, as anticipated, since both have L/D = 2.3 and both eject into the same ambient. With the addition of free-stream flow (Fig. 6(B)), C_d values for lateral injection drop more rapidly at low p_c^+/p_s than for the streamwise injection case. The opposite is true at high p_c^+/p_s.

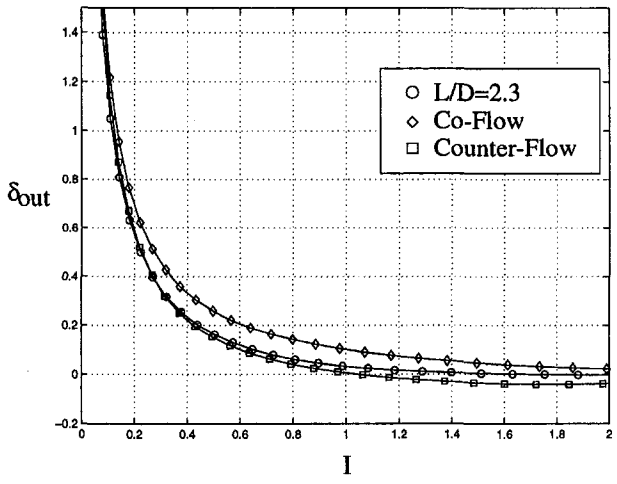

Fig. 8 Outlet additive loss for holes with and without approach flow momentum, L/D = 2.3

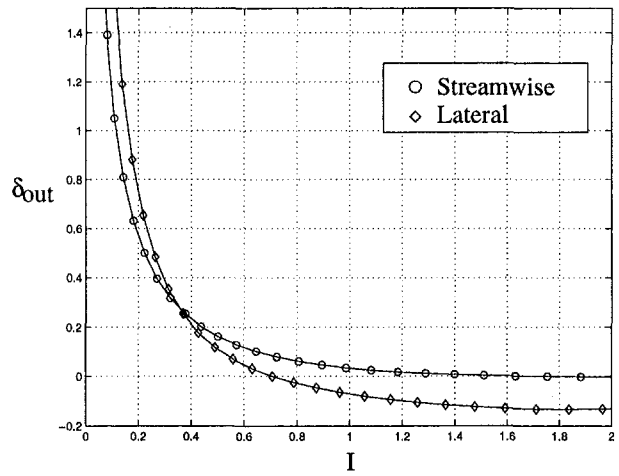

Fig. 9 Outlet additive loss for streamwise and lateral injection, L/D = 2.3

Outlet additive losses are plotted for the streamwise and lateral injection cases in Fig. 9. For $I \leq 0.4$, lateral injection has higher δ_{out} values, whereas for $I > 0.4$, they are lower, even assuming negative values ($\delta_{out} = -0.15$). This behavior is similar to that for normal injection, as described by Khaldi (1987), in which $\delta_{out} = -0.2$ for large I. The data are also consistent with the model of Rowbury et al. (1997), which contends that negative losses are more common and significant for film cooling holes with greater angles of orientation.

Conclusions

Discharge coefficients for a variety of film cooling geometries have been presented. The trends documented in this study provide insight into the influence that hole length and coolant supply geometry have on discharge coefficients. In general, shorter film cooling holes have higher discharge coefficient values due to interaction with free-stream flow. The skewing of coolant velocity distributions over the hole exit plane toward the upstream, with short holes, imposes a net effect of reducing static pressures over the hole exit plane. This, in turn, leads to higher flow rates. Similarly, discharge coefficient values for streamwise and lateral injection cases are discussed.

The results indicate that scaling of δ_{out} on I appears to be appropriate, although, since all measurements were taken with a density ratio of 1.0, the robustness of this scaling was not put to a rigorous test. In previous work, hole inclination angle and position effects were quantified. This study suggests that hole L/D and supply plenum geometry have significant impact on δ_{out} values.

Acknowledgments

This work is part of a combined study of film cooling with short film cooling holes and lateral injection sponsored by the NASA-Lewis Research Center and the Department of Energy, respectively. The NASA study project manager is Douglas Thurman. The DOE project is managed by Dr. Daniel Fant of the South Carolina R&D Center.

References

Abramovich, G. N., 1963, *The Theory of Turbulent Jets,* English Translation by M.I.T. Press, Boston, MA.

Andrews, G. E., and Mkpadi, M. C., 1984, "Full-Coverage Discrete Hole Wall Cooling: Discharge Coefficients," ASME *Journal of Engineering for Gas Turbines and Power,* Vol. 106, pp. 183–192.

Burd, S. W., Kaszeta, R. W., and Simon, T. W., 1996, "Measurements in Film Cooling Flows: Hole L/D and Turbulence Intensity Effects," ASME Paper No. 96-WA/HT-7; ASME JOURNAL OF TURBOMACHINERY, Vol. 120, 1998, pp. 791–798.

Burd, S. W., and Simon, T. W., 1997, "The Influence on Film Cooling Supply Geometry on Film Coolant Exit and Surface Adiabatic Effectiveness," ASME Paper No. 97-GT-25.

Byerley, A., 1989, "Heat Transfer Near the Entrance to a Film Cooling Hole in a Gas Turbine Blade," Ph.D. Thesis, Department of Engineering Science, University of Oxford, UK.

Fried, E., and Idelchik, I. E., 1989, *Flow Resistance: A Design Guide for Engineers,* Hemisphere Publishing Corp., New York.

Gritsch, M., Schulz, A., and Wittig, S., 1998, "Discharge Coefficient Measurements of Film Cooling Holes With Expanded Exits," ASME JOURNAL OF TURBOMACHINERY, Vol. 120, pp. 557–564.

Haller, B. R., and Camus, J., 1984, "Aerodynamic Loss Penalty Produced by Film Cooling in Transonic Turbine Blades," *ASME Journal of Engineering For Gas Turbines and Power,* Vol. 106, pp. 198–205.

Hay, N., Henshall, S. E., and Manning, A., 1994a, "Discharge Coefficients of Holes Angled to the Flow Direction," ASME JOURNAL OF TURBOMACHINERY, Vol. 116, pp. 92–96.

Hay, N., and Lampard, D., 1995, "The Discharge Coefficient of Flared Film Cooling Holes," ASME Paper No. 95-GT-15.

Hay, N., and Lampard, D., 1998, "Discharge Coefficient of Turbine Cooling Holes: A Review," ASME JOURNAL OF TURBOMACHINERY, Vol. 120, pp. 314–319.

Hay, N., Lampard, D., and Benmansour, S., 1983, "Effect of Crossflows on the Discharge Coefficient of Film Cooling Holes," ASME *Journal of Engineering for Gas Turbines and Power,* Vol. 105, pp. 243–248.

Hay, N., Lampard, D., and Khaldi, A., 1994b, "The Coefficient of Discharge of 30 Degree Inclined Film Cooling Holes With Rounded Entries or Exits," ASME Paper No. 94-GT-180.

Hay, N., and Spencer, A., 1992, "Discharge Coefficients of Cooling Holes With Radiused and Chambered Inlets," ASME JOURNAL OF TURBOMACHINERY, Vol. 114, pp. 701–706.

Khaldi, A., 1987, "Discharge Coefficients of Film Cooling Holes With Rounded Entries or Exits," Ph.D. Thesis, Univ. of Nottingham, UK.

Lichtarowicz, A., Duggins, R. K., and Markland, E., 1965, "Discharge Coefficients for Incompressible Non-cavitating Flow Through Long Orifices," *J. Mech. Eng. Science,* Vol. 7, No. 2, pp. 210–219.

Rogers, T., and Hersh, A. S., 1975, "The Effect of Grazing Flow on the Steady State Resistance of Square-Edged Orifices," AIAA Paper No. 75-493.

Rowbury, D. A., Oldfield, M. L. G., and Lock, G. D., 1997, "Engine Representative Discharge Coefficients Measured in an Annular Nozzle Guide Vane Cascade," ASME Paper No. 97-GT-99.

Sasaki, M., Takahara, K., Sakata, K., and Kumsgai, T., 1976, "Study on Film Cooling of Turbine Blades," *JSME Bulletin,* Vol. 19, No. 137, pp. 1344–1352.

Thole, K., Gritsch, M., Schulz, A., and Wittig, S., 1997, "Effect of a Crossflow at the Entrance to a Film-Cooling Hole," ASME *Journal of Fluids Engineering,* Vol. 119, pp. 537–540.

Tillman, E. S., and Jen, H. F., 1984, "Cooling Airflow Studies at the Leading Edge of a Film Cooled Airfoil," ASME *Journal of Engineering for Gas Turbines and Power,* Vol. 106, pp. 214–221.

Walters, D. K., and Leylek, J. H., 1997, "A Detailed Analysis of Film-Cooling Physics: Part 1—Streamwise Injection With Cylindrical Holes," ASME Paper No. 97-GT-269.

Wang, L., 1996, "A Study of Gas Turbine Flows, Turbulence Generation, and Film Cooling Flow Measurement," M.S. Thesis, Department of Mechanical Engineering, University of Minnesota.

Heat Transfer in a "Cover-Plate" Preswirl Rotating-Disk System

R. Pilbrow[1]

H. Karabay[2]

M. Wilson

J. M. Owen

Department of Mechanical Engineering,
Faculty of Engineering and Design,
University of Bath,
Bath BA2 7AY, United Kingdom

In most gas turbines, blade-cooling air is supplied from stationary preswirl nozzles that swirl the air in the direction of rotation of the turbine disk. In the "cover-plate" system, the preswirl nozzles are located radially inward of the blade-cooling holes in the disk, and the swirling air flows radially outward in the cavity between the disk and a cover-plate attached to it. In this combined computational and experimental paper, an axisymmetric elliptic solver, incorporating the Launder–Sharma and the Morse low-Reynolds-number $k-\epsilon$ turbulence models, is used to compute the flow and heat transfer. The computed Nusselt numbers for the heated "turbine disk" are compared with measured values obtained from a rotating-disk rig. Comparisons are presented, for a wide range of coolant flow rates, for rotational Reynolds numbers in the range 0.5×10^6 to 1.5×10^6, and for $0.9 < \beta_p < 3.1$, where β_p is the preswirl ratio (or ratio of the tangential component of velocity of the cooling air at inlet to the system to that of the disk). Agreement between the computed and measured Nusselt numbers is reasonably good, particularly at the larger Reynolds numbers. A simplified numerical simulation is also conducted to show the effect of the swirl ratio and the other flow parameters on the flow and heat transfer in the cover-plate system.

1 Introduction

Figure 1 shows a simplified diagram of a so-called cover-plate preswirl system that is used to supply the cooling air to the turbine blades in some gas turbine designs. Studies of these preswirl systems have been carried out by many research workers, and the reader is referred to Meierhofer and Franklin (1981), El-Oun and Owen (1989), Chen et al. (1993a, b), Popp et al. (1998), Wilson et al. (1997), and Karabay et al. (1999). Further details of these and other rotating-disk systems are given by Owen and Rogers (1989, 1995).

The cooling air is supplied from stationary preswirl nozzles, at a radial location of $r = r_p$, that swirl the air in the direction of rotation of the turbine disk, or rotor in Fig. 1. At $r = r_p$, the swirl ratio, β_p (which is the ratio of the tangential component of velocity of the air, $V_{\phi,p}$, to that of the disk, Ωr_p) is usually greater than unity. The swirling air then flows radially outward, in the space between the rotor and a cover-plate attached to it, to leave the system through blade-cooling passages in the disk at $r = r_b$. By swirling the cooling air, its temperature is reduced relative to the rotating passages, with consequent advantages for the blade-cooling system.

Some of the preswirl air is allowed to leak radially outward through the seal between the rotating cover-plate and the stator, as shown in Fig. 1. This sealing air helps to prevent or reduce the ingress of hot mainstream gas into the cooling system, and it also removes the "windage heating" that is generated by the rotating cover-plate.

The complete system shown in Fig. 1 can be considered as two subsystems: a rotor–stator system and a rotating cavity (see Owen and Rogers, 1989, 1995). A combined theoretical, computational and experimental study of the flow in an adiabatic cover-plate system was conducted by Karabay et al. (1999), who showed that the flow in the rotating cavity was not affected by that in the rotor–stator system. The flow in the rotating cavity is mainly controlled by two parameters: β_p and $\lambda_{T,b}$, where $\lambda_{T,b}$, is the turbulent flow parameter defined as

$$\lambda_{T,b} = C_{w,b}\,\mathrm{Re}_\phi^{-0.8} \tag{1.1}$$

$C_{w,b}$ is the nondimensional flow rate of the blade-cooling air and Re_ϕ is the rotational Reynolds number defined in the nomenclature.

The flow structure in a rotating cavity comprises a number of regions (see Owen and Rogers, 1995): There are boundary layers on the two disks and the outer shroud, between which there is a core of rotating fluid. For small values of $\lambda_{T,b}$, the core will comprise two regions: a source region at the smaller radii, in which flow is entrained into the boundary layers on the disks, and an inviscid core between the nonentraining Ekman-type boundary layers. The source region extends radially to the point where all superposed flow has been entrained into the boundary layers. For sufficiently large flow rates or, more precisely, for sufficiently large values of $\lambda_{T,b}$, the source region fills the entire space between the boundary layers in the cavity.

Inside the source region, angular momentum is conserved and a free vortex is formed outside the boundary layers such that

$$\frac{V_\phi}{\Omega r} = \beta_p \left(\frac{x_p}{x}\right)^2 \tag{1.2}$$

Owen and Rogers also suggested that, providing $\beta_p x_p^2 < 1$, the source region would fill the cavity when

$$\lambda_{T,b} = 0.437\,(1 - (\beta_p x_p^2)^{1.18})^{1.66} \tag{1.3}$$

For $\lambda_{T,b}$ greater than this value, or when $\beta_p x_p^2 > 1$, Eq. (1.2) should apply throughout the cavity, outside of the boundary layers; for smaller values of $\lambda_{T,b}$, Ekman-type layers will form on the disks and angular momentum will not be conserved in the core.

Karabay et al. (1999) computed the flow structure and compared the computed tangential components of velocity in the cover-plate system with measured values. They showed that, for sufficiently large values of $\lambda_{T,b}$, there is free-vortex flow between the cover-plate and the disk, and their computations were in good agreement with the measured velocities. As the

[1] Current address: Rolls-Royce plc, P O Box 3, Filton, Bristol BS34 7QE, United Kingdom.

[2] Current address: Department of Mechanical Engineering, Kocaeli Universitesi, Izmit, Turkey.

Contributed by the International Gas Turbine Institute and presented at the 43rd International Gas Turbine and Aeroengine Congress and Exhibition, Stockholm, Sweden, June 2–5, 1998. Manuscript received by the International Gas Turbine Institute February 1998. Paper No. 98-GT-113. Associate Technical Editor: R. E. Kielb.

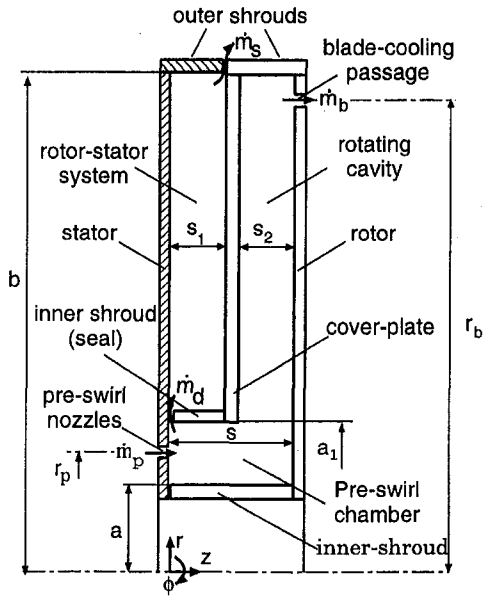

Fig. 1 Simplified diagram of cover-plate preswirl system

computations were made using an axisymmetric solver (see Section 2), the good agreement between the computed and measured velocities suggests that the three-dimensional effects associated with discrete preswirl nozzles have little influence on the flow between the cover-plate and the rotor.

In this paper, the adiabatic study of Karabay et al. is extended to include heat transfer from the disk to the cooling air, and measurements made in an experimental rig are compared with computations made with an elliptic solver. A separate "parametric study" is also carried out computationally for the rotating cavity, so that the effects of Re_ϕ, $C_{w,b}$, $\lambda_{T,b}$, and β_p on the flow structure and heat transfer can be examined. The computational method is outlined in Section 2, and the experimental rig is described in Section 3. In Section 4, the parametric study is discussed, in Section 5 the computed and measured Nusselt numbers are compared, and the conclusions are summarized in Section 6.

2 Computational Model

The steady-state, axisymmetric finite-volume solver used in this work is the same as that described by Karabay et al. (1999) for a study of the flow structure.

Turbulent flow computations were made using both the low-Reynolds-number $k-\epsilon$ models of Launder–Sharma (1974) and of Morse (1988), the latter incorporating modifications suggested by its author (Chen et al., 1996). Incompressible flow was assumed and turbulent heat transfer was represented using a turbulent Prandtl number Pr_t equal to 0.9.

A staggered grid was used with the axial and radial velocity components stored midway between the grid points where other solution variables were located (pressure, tangential velocity, turbulence kinetic energy and dissipation rate, and total enthalpy). The cover-plate and inner shroud (see Fig. 1) were represented by block obstructions within the computational grid and the equations were solved using the SIMPLEC pressure-correction algorithm.

The inlet nozzles and blade-cooling holes of the experimental rig were represented in the axisymmetric model by equivalent-area annular slots on the stator and rotor, with centerlines at $r = r_p$ and $r = r_b$ respectively. The axial velocity V_z of the preswirl air, which was assumed uniform at the inlet, was deduced from the prescribed mass flow rate $\dot{m}_p$. Similarly, the axial velocity at the blade-cooling slot and the radial velocity at the outer seal were calculated from mass flow rates $\dot{m}_b$ and $\dot{m}_s$ respectively; global mass balance was achieved by ensuring that $\dot{m}_p = \dot{m}_b + \dot{m}_s$. The inlet tangential velocity $V_{\phi,p}$ was fixed to give the required swirl ratio β_p, and Neumann (zero normal-derivative) boundary conditions for V_ϕ were used at the two outlets. The remaining velocity components at flow boundaries were taken to be zero, and no-slip conditions were applied at all solid surfaces. The temperatures of the preswirl air and the heated rotating disk were taken from the measured values, the other solid surfaces were assumed to be adiabatic, and zero-derivative conditions were used at both outlets.

The turbulence models required a very fine grid near the boundaries, with $y^+ < 0.5$ for the near-wall grid nodes, and the grid spacing increased geometrically away from walls (including the cover-plate and shroud) with expansion factors of about 1.2. A 223 × 223 axial by radial grid was used for the whole system, and for the simple cavity a 67 × 111 axial by radial grid was used (see Fig. 2). Eight points covered the inlet and blade-cooling slots. (Computations were also conducted with a

Nomenclature

a = inner radius of disk
a_1 = inner radius of cover-plate
b = outer radius of disk
C_p = specific heat at constant pressure
C_w = nondimensional flow rate = $\dot{m}/\mu b$
k = thermal conductivity
$\dot{m}$ = mass flow rate
Nu = Nusselt number = $rq_s/k(T_s - T_{s,ad})$
Pr = Prandtl number = $\mu C_p/k$
Pr_t = turbulent Prandtl number
q_s = convective heat flux from disk to air
r, ϕ, z = radial, tangential and axial coordinates
R = recovery factor
Re_ϕ = rotational Reynolds number = $\rho\Omega b^2/\mu$
s_1, s_2 = axial clearance in rotor–stator and rotating cavity, respectively
s = axial width of entire system
$T_{o,in}$ = total temperature at inlet
T_s = surface temperature
$T_{s,ad}$ = adiabatic-disk temperature
U_τ = friction velocity = $\sqrt{\tau_w/\rho}$
V_r, V_ϕ, V_Z = time-averaged radial, circumferential, axial velocity components
x = nondimensional radial coordinate = r/b
y = distance normal to the wall
y^+ = nondimensional distance = $\rho y U_\tau/\mu$
β = swirl ratio = $V_\phi/\Omega r$
β_p = preswirl ratio = $V_{\phi,p}/\Omega r_p$
ΔT = temperature difference = $T_S - T_{0,in}$
ϵ = turbulent energy dissipation rate
λ_T = turbulent flow parameter = $C_W/\mathrm{Re}_\phi^{0.8}$
μ = dynamic viscosity
ρ = density
τ_w = total wall shear stress
Ω = angular speed of disk

Subscripts

ad = adiabatic
b = blade-cooling air
d = disk-cooling air
in = inlet
p = preswirl air
o = total temperature in stationary frame
s = surface or sealing air
t = total temperature in rotating frame

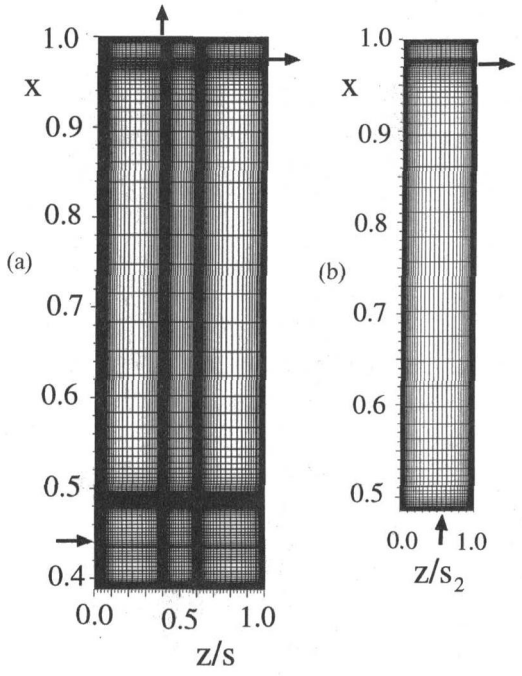

Fig. 2 Grid distribution used in computation: (*a*) complete system; (*b*) simple cavity

141 × 185 grid. This made no significant difference to the comparison between the computed and measured Nusselt numbers, which suggests that the results presented below are sensibly grid-independent.)

About 55 axial grid nodes were located within the cover-plate, with the remaining points divided equally between the rotor–stator system and the rotating cavity; about 70 grid points covered the annular preswirl chamber (see Fig. 1).

Convergence of the iterative method was improved using the Gosman distributive damping term and a fixed V-cycle multigrid algorithm. Computation times, using a Silicon Graphics R10000 processor, were typically around 12 hours for the complete system and two hours for the simple cavity.

3 Experimental Apparatus

The apparatus is the same as that used by Karabay et al. (1999) for their adiabatic study. A schematic diagram is shown in Fig. 1, and details of the rotating-disk rig are shown in Fig. 3.

The outer radius of the system, b, was approximately 207 mm, and the radial location of the preswirl nozzles and blade-cooling holes were r_p = 90 mm and r_b = 200 mm. There were 19 preswirl nozzles of 7.92 mm diameter, angled at 20 deg to the tangential direction, and 60 blade-cooling holes of 7.7 mm diameter, with their axes normal to the disk. The axial spacing between the cover-plate, which was 5 mm thick, and the stator, s_1, was 10 mm, and between the cover-plate and the rotor the spacing, s_2, was also 10 mm. The inner radius, a, and outer radius, a_1, of the annular preswirl chamber were 80 mm and 100 mm, and air entered the rotating cavity through the annular clearance at the center of the cover-plate.

The mass flow rates of the preswirl, blade-cooling, and sealing flow, $\dot{m}_p$, $\dot{m}_b$ and $\dot{m}_s$, respectively, could be independently controlled, and the flow rates were measured, with an uncertainty of ±3 percent, by orifice plates made to British Standards (BS1042). The rotor assembly could be rotated up to 7000 rpm by a variable-speed electric motor, and the speed could be measured with an uncertainty of ±1 rpm. (For the tests conducted on this rig, a speed of 7000 rpm corresponds to $Re_\phi \cong 2.4 \times 10^6$.)

The front (cavity-side) face of the heated rotor was covered in a fiberglass "mat," 1 mm thick, in which ten thermocouples and six fluxmeters were embedded. It should be pointed out that the instrumentation had been installed on the rotating disk for the earlier tests with a direct-transfer preswirl system (see Wilson et al., 1997). Three of the thermocouples were placed in the heated outer part of the disk, and one of the fluxmeters was located underneath the carbon-fiber ring that connected the outside of the cover-plate to this disk. Consequently, only seven thermocouples and five fluxmeters were located in the test section of the cover-plate system. Unfortunately, none of the fluxmeters was located at the radius of preswirl nozzles. Details of the RdF thermopile fluxmeters and their calibration are given by Wilson et al. (1997).

In addition, total-temperature thermocouple probes were located in two of the blade-cooling holes in the disk. (The measurements of the temperature of the blade-cooling air will be reported in a future paper.) The signals from all the rotating instrumentation were brought out through a 24-channel silver/silver-graphite slipring unit, and the voltages were measured with an uncertainty of ±1 μV by a computer-controlled Solartron data logger.

The outer part of the rotating disk was heated up to 150°C by means of stationary radiant electric heater units, with a maximum power output of 9.5 kW. The actual temperature distribution over the instrumented section of the disk depended on the rotational speed and on the flow rate of the cooling air, and the maximum temperature in this section was typically around 70°C. The temperature of the air at the preswirl nozzles, which was measured with two total-temperature probes, was controlled by a heat exchanger to between 10°C and 20°C. The outlet temperature of the cooling air in the rotor–stator system was measured by two total-temperature probes in the adiabatic collection chamber.

The cover-plate was made from transparent polycarbonate ($k \cong 0.2$ W/mK) giving optical access for LDA measurements. Segments of both surfaces of the cover-plate and the front surface of the heated disk were coated with thermochromic liquid crystal, which enabled the temperature to be estimated. The periphery of the cover-plate was attached to the disk by a carbon-fiber ring, the inner surface of which was insulated with a

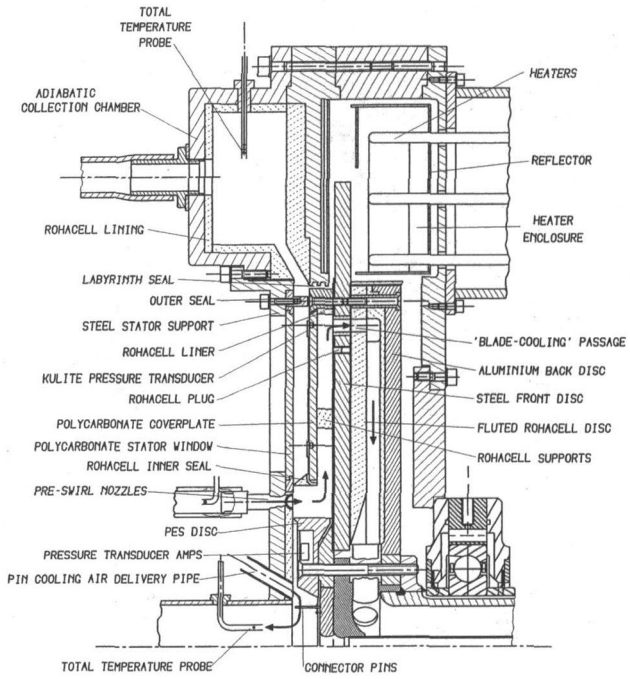

Fig. 3 Details of rotating-disk rig

Rohacell-foam liner ($k \cong 0.03$ W/m K); the cover-plate itself was quasi-adiabatic. The axial spacing between the cover-plate and the disk was maintained by six supports, made from Rohacell foam.

For a typical engine, $\mathrm{Re}_\phi \cong 10^7$, $\lambda_{T,b} \cong 0.3$, $\beta_p \cong 2.5$. For the heat transfer tests in the rig, the following range of parameters was tested: $0.5 \times 10^6 < \mathrm{Re}_\phi < 1.5 \times 10^6$, $0.16 < \lambda_{T,b} < 0.32$, $0.9 < \beta_p < 3.1$. It should be pointed out that, as $\beta_p \propto C_{w,p}/\mathrm{Re}_\phi$ and $C_{w,p} = C_{w,b} + C_{w,s}$, it is possible to keep $C_{w,b}$ and Re_ϕ constant and to vary β_p by varying $C_{w,s}$.

4 Parametric Study of Simple Rotating Cavity

For this computational study, which was made using the Morse turbulence model, the geometry was based on the rotating cavity between the cover-plate and rotor of the rotating-disk rig described in Section 3. The following range of parameters was used:

$s_2/b = 0.048$, $a/b = 0.48$, $r_b/b = 0.97$
$0.5 \times 10^6 < \mathrm{Re}_\phi < 3.6 \times 10^6$
$8730 < C_{w,b} < 26180$
$0.1 < \lambda_{T,b} < 0.3$
$0.75 < \beta_p < 3.0$

Unlike the rig, where the flow entered the cavity axially, the flow in this model entered radially at $r = a_1$ with $V_\phi = \beta_p \Omega a_1$, and left axially through an annular slot at $r = r_b$. Details of the computational model are given in Section 2, and the computational grid is shown in Fig. 2(*b*).

Figure 4 shows the computed streamlines for six different sets of flow parameters. Figures 4(*a*) and 4(*b*) show the effect of $\lambda_{T,b}$ (or $C_{w,b}$) when Re_ϕ and β_p are held constant; Figs. 4(*c*) and 4(*d*) show the effect of Re_ϕ (or $\lambda_{T,b}$) when $C_{w,b}$ and β_p are constant; Figs. 4(*e*) and 4(*f*) show the effect of β_p when Re_ϕ and $C_{w,b}$ (and consequently $\lambda_{T,b}$) are constant.

Referring to Fig. 4(*a*), the following points should be noted:

(*i*) Recirculation occurs in the separation zone on both disks up to $x \cong 0.58$. In source-sink flow in rotating cavities, radial outflow occurs in the boundary layers on the disks where $V_\phi/\Omega r < 1$, and inflow occurs where $V_\phi/\Omega r > 1$ (see Owen and Rogers, 1995). For $\beta_p = 1.5$, $V_\phi/\Omega r = 1$ at $x \cong 0.58$; this marks the border between inflow and outflow in the boundary layers.

(*ii*) According to Eq. (1.3), for $\beta_p = 1.5$ and $\mathrm{Re}_\phi = 1.5 \times 10^6$, the source region fills the cavity when $\lambda_{T,b} \geq 0.25$. This implies that, for $\lambda_{T,b} = 0.1$, Ekman-type layers will occur at the larger radii, as is indeed shown in Fig. 4(*a*) where the source region ends at $x \cong 0.83$.

(*iii*) Half the fluid flows up the left-hand disk and separates from the shroud, at $x = 1$, to form a free shear layer that flows axially out through the exit slot in the right-hand disk. The other half of the fluid flows up the right-hand disk to mix with that from the left-hand disk in the exit slot.

Figure 4(*b*) shows no sign of Ekman-type layers: for $\mathrm{Re}_\phi = 1.5 \times 10^6$ and $\beta_p = 1.5$, a value of $\lambda_{T,b} = 0.3$ ensures source flow throughout the cavity, which is consistent with Eq. (1.3).

The flow structure for Fig. 4(*c*) is virtually the same as for Fig. 4(*b*). For both these figures, $\beta_p = 1.5$ and $\lambda_{T,b} = 0.3$; even though the values of $C_{w,b}$ and Re_ϕ are different, the values of $\lambda_{T,b}$ are the same. The same observation about similar flow structures can be made for Figs. 4(*d*) and 4(*a*) where $\beta_p = 1.5$ and $\lambda_{T,b} = 0.1$. This supports the statement that, for a given value of β_p, the flow structure depends principally on $\lambda_{T,b}$.

Figures 4(*e*) and 4(*f*) show the effect of β_p on the flow structure for the case where $\lambda_{T,b} = 0.2$. For $\mathrm{Re}_\phi = 1.5 \times 10^6$, Eq. (1.3) gives $\lambda_{T,b} = 0.25$ for $\beta_p = 1.5$ and 0.078 for $\beta_p = 3$. These results are consistent with the fact that the source region shown in Fig. 4(*e*) does not fill the cavity and that in Fig. 4(*f*) does.

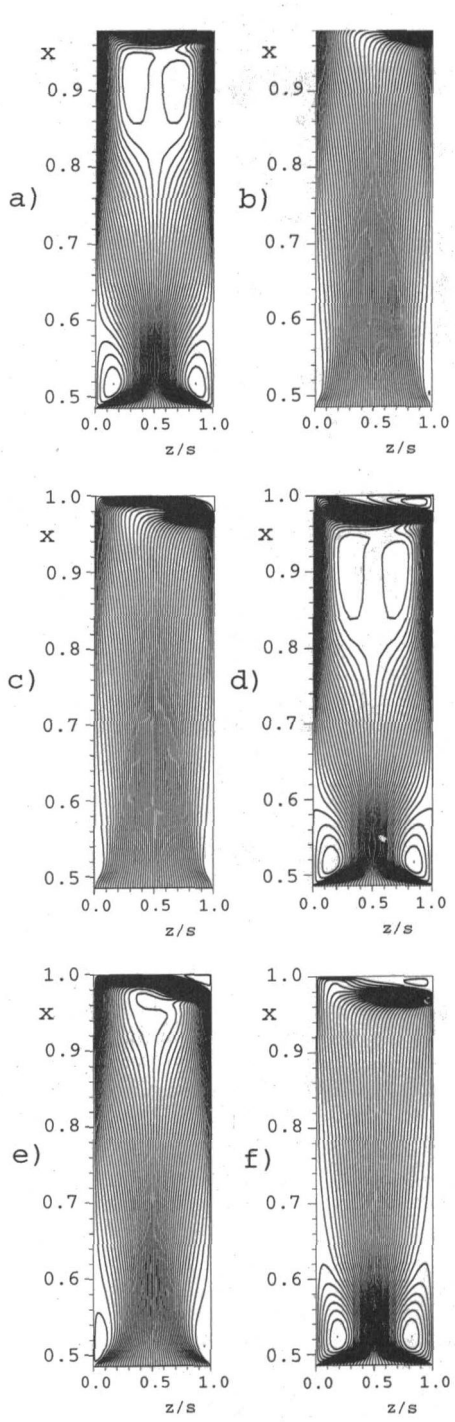

Fig. 4 Computed streamlines in simple cavity:
(*a*) $\mathrm{Re}_\phi = 1.5 \times 10^6$, $C_{w,b} = 8730$, $\lambda_{T,b} = 0.1$, $\beta_p = 1.5$
(*b*) $\mathrm{Re}_\phi = 1.5 \times 10^6$, $C_{w,b} = 26180$, $\lambda_{T,b} = 0.3$, $\beta_p = 1.5$
(*c*) $\mathrm{Re}_\phi = 0.9 \times 10^6$, $C_{w,b} = 17455$, $\lambda_{T,b} = 0.3$, $\beta_p = 1.5$
(*d*) $\mathrm{Re}_\phi = 3.56 \times 10^6$, $C_{w,b} = 17455$, $\lambda_{T,b} = 0.1$, $\beta_p = 1.5$
(*e*) $\mathrm{Re}_\phi = 1.5 \times 10^6$, $C_{w,b} = 17455$, $\lambda_{T,b} = 0.2$, $\beta_p = 1.5$
(*f*) $\mathrm{Re}_\phi = 1.5 \times 10^6$, $C_{w,b} = 17455$, $\lambda_{T,b} = 0.2$, $\beta_p = 3.0$

Figures 5(*a*), 5(*b*), and 5(*c*) show the effects of $\lambda_{T,b}$ and β_p on the computed Nusselt numbers for the heated disk. (For the Nusselt numbers presented in this paper, the adiabatic-disk temperature was derived from Owen and Rogers, 1995.)

Referring to Fig. 5(*a*), it can be seen that there are large peaks in Nu near the inlet at $x = 0.48$, near the edge of the separation zone at $x \cong 0.58$ and near the outlet at $x \cong 0.97$.

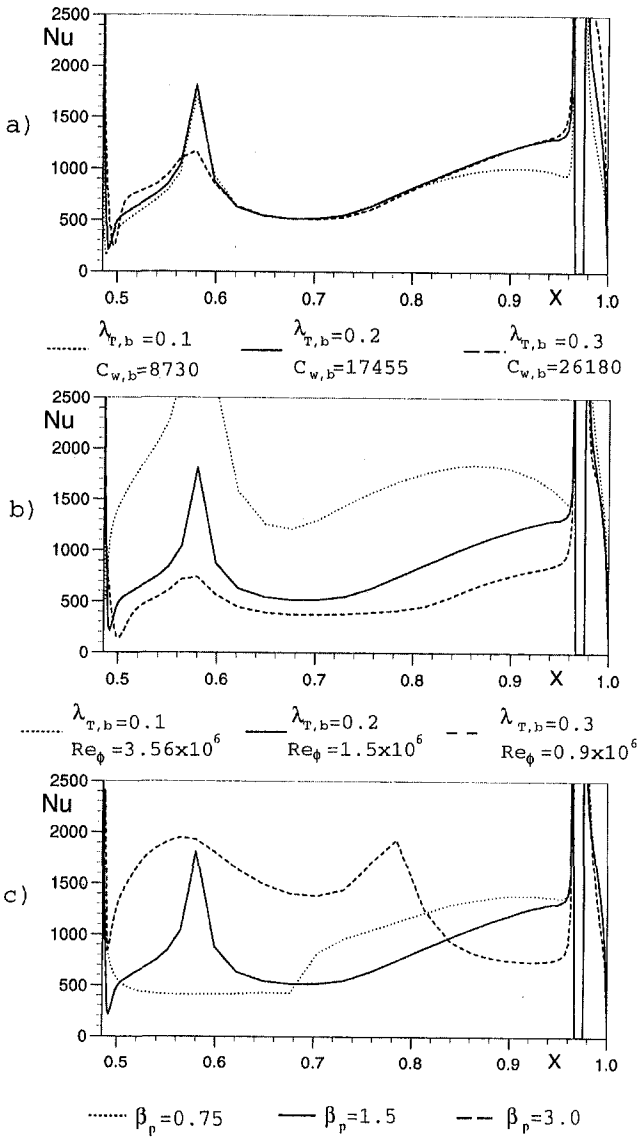

Fig. 5 Computed Nusselt numbers in simple cavity:
(*a*) Effect of $\lambda_{T,b}$ for $Re_\phi = 1.5 \times 10^6$ and $\beta_p = 1.5$
(*b*) Effect of Re_ϕ for $C_{w,b} = 17455$ and $\beta_p = 1.5$
(*c*) Effect of β_p for $Re_\phi = 1.5 \times 10^6$, $C_{w,b} = 17455$ ($\lambda_{T,b} = 0.2$)

Large values of Nu are expected in these regions, where the boundary layers are very thin, but the computed magnitudes, which depend on the turbulence model, are unlikely to be correct. For $\lambda_{T,b} = 0.2$ and 0.3, Nu increases with x for $0.7 \leq x \leq 0.97$. This is in the source region where cold fluid is entrained into the boundary layers on the disks: the heated disk behaves in a similar way to a free disk where Nu increases as x increases. The curve for $\lambda_{T,b} = 0.1$ departs from those for $\lambda_{T,b} = 0.2$ and 0.3 at $x \cong 0.82$, which is the start of the Ekman-type layers shown in Fig. 4(a): In these nonentraining layers, the fluid heats up as it flows radially outward, and the heat transfer drops below that in the entraining layers.

Figure 5(b) shows the three peaks in Nu referred to above but there is a significant effect of Re_ϕ: Nu increases as Re_ϕ increases. In particular, for $\lambda_{T,b} = 0.1$ and $\beta_p = 1.5$, comparison between Figs. 5(a) and 5(b) shows that Re_ϕ is much more significant than $C_{w,b}$ in its effect on Nu: For a given value of β_p, $\lambda_{T,b}$ has the most significant effect on flow structure but Re_ϕ has the most significant effect on Nu. Again, for $\lambda_{T,b} = 0.1$ and $Re_\phi = 3.56 \times 10^6$, the decay in Nu for $x \cong 0.85$ is associated with the formation of Ekman-type layers on the heated disk.

Figure 5(c) shows the effect of β_p on Nu. For $\beta_p = 0.75$, where the flow in the boundary layers is radially outward and there is no recirculation zone near the center, there appears to be transition from laminar to turbulent flow at $x \cong 0.68$ where $x^2\ Re_\phi = 6.9 \times 10^5$. For $\beta_p = 1.5$ and 3.0, the reattachment points occur at $x \cong 0.58$ and 0.78, respectively; these mark the points where the respective maxima in Nu occur in Fig. 5(c). It can be seen that, for a given value of $\lambda_{T,b}$, β_p has a significant effect on the distribution of Nu.

The following tentative conclusions are drawn about the flow and heat transfer in the simple rotating cavity:

(*i*) The flow structure depends strongly on $\lambda_{T,b}$ and β_p.
(*ii*) For $\lambda_{T,b}$ large enough to ensure that the source region fills the entire cavity, Nu is virtually independent of $\lambda_{T,b}$ but depends strongly on Re_ϕ and β_p.
(*iii*) There are peaks in Nu near the inlet, near the reattachment point (for $\beta_p > 1$), and near the exit.

5 Comparison Between Computed and Measured Nusselt Numbers

In Section 4, the computed flow streamlines and Nusselt numbers were presented for the simple cavity where the flow enters radially. In the experiments, the swirling flow leaves the preswirl nozzles axially and enters the rotating cavity as shown in Fig. 6, where $Re_\phi = 1.52 \times 10^6$, $C_{w,b} = 1.55 \times 10^4$, $\lambda_{T,b} = 0.17$, and $\beta_p = 1.65$; this corresponds to one of the test cases discussed below. (Karabay et al., 1999, include details of the computed flow structures for a range of conditions.)

Referring to Fig. 6, the rotor–stator system (which is not discussed here) is on the left and the rotating cavity on the right. A swirling jet of fluid (with $\beta_p = 1.65$) flows axially from the preswirl nozzles at $x_p = 0.44$ and impinges on the rotor at $x \cong 0.5$; for $x < 0.5$ the flow on the rotor is radially inward, and for $x > 0.5$ it is radially outward. The flow separates from the edge of the cover plate, forming a recirculation zone, and reattaches at $x \cong 0.6$. For these conditions, the source region does not fill the cavity, and there are signs of Ekman-type layers for $x > 0.85$.

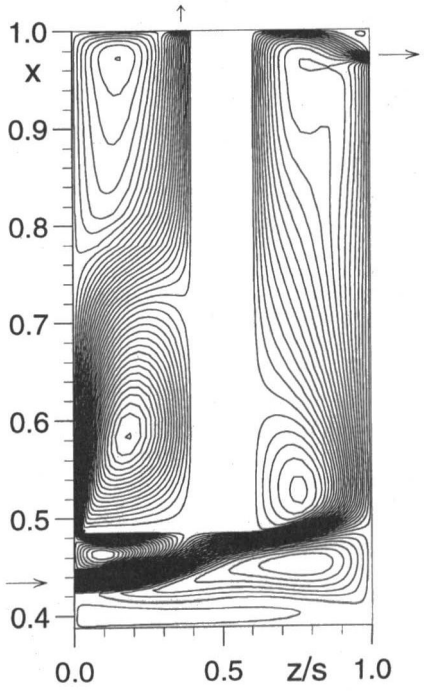

Fig. 6 Computed streamlines for cover-plate preswirl system: $Re_\phi = 1.52 \times 10^6$, $C_{w,b} = 1.55 \times 10^4$, $\lambda_{T,b} = 0.17$, and $\beta_p = 1.65$

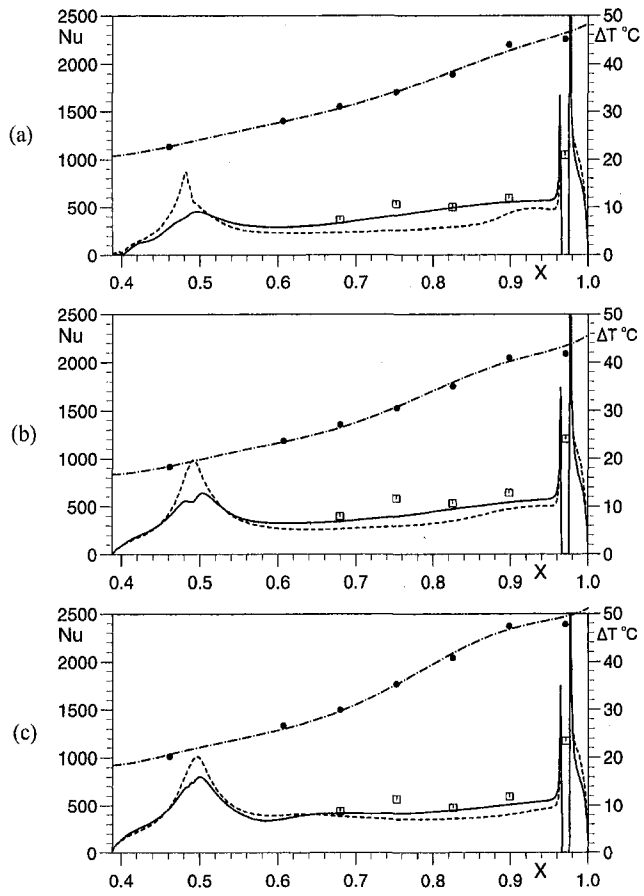

Fig. 7 Comparison between computed and measured Nusselt numbers for $Re_\phi \cong 0.5 \times 10^6$ and $\lambda_{T,b} \cong 0.17$: □ measured Nu, ● measured ΔT, - · - fitted ΔT, - - - - computed Nu (LS model), — computed Nu (Morse model):

(a) $Re_\phi = 0.535 \times 10^6$, $C_{w,b} = 6636$, $\lambda_{T,b} = 0.173$, $\beta_b = 1.11$
(b) $Re_\phi = 0.542 \times 10^6$, $C_{w,b} = 6785$, $\lambda_{T,b} = 0.176$, $\beta_p = 1.54$
(c) $Re_\phi = 0.559 \times 10^6$, $C_{w,b} = 7005$, $\lambda_{T,b} = 0.177$, $\beta_p = 2.01$

Compared with the simple cavity, the flow is similar at the larger radii (see, for example, Fig. 4(*e*)) but differs significantly at the smaller radii. In particular, the flow near the impingement point on the rotor is significantly different from that in the simple cavity; the computed radial location of this impingement point is virtually invariant with $\lambda_{T,b}$ and β_p.

Comparisons between the computed and measured Nusselt numbers are shown in Figs. 7 to 10. Also shown are the measured values of ΔT (where $\Delta T = T_S - T_{0,in}$), and the fitted curve, which was used to provide the thermal boundary conditions for the rotor surface in the computations; the other surfaces were assumed to be adiabatic. For the computations, both the Launder–Sharma and Morse turbulence models were used, as described in Section 2.

Figure 7 shows the effect of β_p on Nu for $Re_\phi \cong 0.5 \times 10^6$ and $\lambda_{T,b} \cong 0.17$; as discussed in Section 3, β_p was varied by varying $C_{w,s}$ while keeping $\lambda_{T,b}$ approximately constant. The following observations can be made:

(*i*) There is a peak in the computed Nusselt numbers at $x \cong 0.5$ for all cases, which corresponds to the impingement region referred to above. Unlike the results for the simple cavity shown in Fig. 5, there is no peak in Nu at $x = 0.4$; this is a direct result of the difference between the radial and axial inlets for these two configurations. (Unfortunately, as stated in Section 3, there are no fluxmeters in this inner region.)

(*ii*) There are computed peaks near the outlet at $x \cong 0.97$, as also observed in the simple cavity. In the axisymmetric computations, the blade-cooling holes were modeled as an equivalent-area annular slot, and so the heat transfer in this region is not directly comparable with the measurements, which were obtained in the area between the blade-cooling holes. However, the measurements do show a significant increase in Nu in this region, and the magnitude is approximately double that of the measured values at the other radii. The flow and heat transfer in the region around the holes is highly three dimensional and cannot be simulated by an axisymmetric solver.

(*iii*) Between these two peaks, the computed Nusselt numbers show similar trends to the measured values. Both turbulence models tend to underestimate the measurements, although the Morse model shows much closer agreement than the Launder–Sharma model. As there are no experimental data in the impingement region, it is not possible to comment on the relative performance of the two models in this area. (As the Morse model shows better agreement with all the data presented here, only that model will be mentioned in the following discussion.)

Figure 8 shows the effect of β_p for $Re_\phi \cong 1.5 \times 10^6$ and $\lambda_{T,b} \cong 0.17$. As stated above, the value of β_p does not significantly affect the radial location of the impingement region, but it does affect the magnitude of Nu in this region. It can be seen that, for the larger value of Re_ϕ, the agreement between the measured

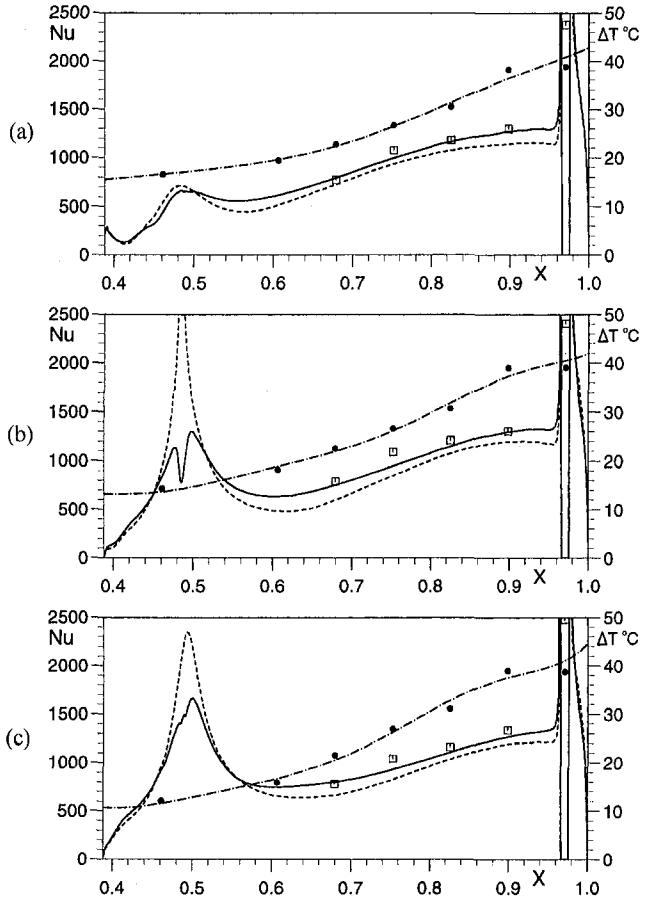

Fig. 8 Comparison between computed and measured Nusselt numbers for $Re_\phi \cong 1.5 \times 10^6$ and $\lambda_{T,b} \cong 0.17$ (for legend, see Fig. 7):

(a) $Re_\phi = 1.41 \times 10^6$, $C_{w,b} = 14411$, $\lambda_{T,b} = 0.174$, $\beta_p = 0.91$
(b) $Re_\phi = 1.41 \times 10^6$, $C_{w,b} = 14411$, $\lambda_{T,b} = 0.174$, $\beta_p = 0.91$
(c) $Re_\phi = 1.52 \times 10^6$, $C_{w,b} = 15514$, $\lambda_{T,b} = 0.176$, $\beta_p = 1.65$

and computed Nusselt numbers, using the Morse model, is good. Comparison between Figs. 7 and 8 shows that Nu increases as Re_ϕ increases, as was found for the simple cavity.

Figure 9 shows the effect of β_p for $Re_\phi \cong 0.5 \times 10^6$ and $\lambda_{T,b} \cong 0.35$; the value of Re_ϕ is similar to that in Fig. 7 but the value of $\lambda_{T,b}$ is double. The computations show little effect of β_p and are in reasonable agreement with the experimental data, except for the case shown in Fig. 9(*c*), where $\beta_p = 3.06$; for this case, the measured Nusselt numbers are significantly higher than the computed values.

Figure 10 shows the effect of β_p for $Re_\phi \cong 1.2 \times 10^6$ and $\lambda_{T,b} \cong 0.35$; the value of Re_ϕ is similar to that in Fig. 8 but the value of $\lambda_{T,b}$ is double. Again the agreement between the computed and measured values of Nu is reasonable. Comparison between Figs. 9 and 10 shows that increasing Re_ϕ has, as noted above, a significant effect on the magnitude of Nu.

6 Conclusions

(*i*) A computational parametric study of the effects of Re_ϕ, $C_{w,b}$, $\lambda_{T,b}$, and β_p on the flow and heat transfer in a simple rotating cavity with a radial inlet shows conventional source-sink flow where the size of the source region depends on $\lambda_{T,b}$ and β_p. For large values of $\lambda_{T,b}$, the source region can fill the entire cavity outside the (entraining) boundary layers on the discs and shroud. For small values of $\lambda_{T,b}$, where the source region does not fill the cavity, (nonentraining) Ekman-type layers form on the rotating disks. Owing to the fact that the fluid in the nonentraining layers heats up as it flows radially outward, the Nusselt numbers in these layers tend to be lower than those in the entraining layers.

(*ii*) The computations show that the Nusselt numbers on the heated rotor depend principally on Re_ϕ, $\lambda_{T,b}$, and β_p.

(*iii*) The agreement between the measured Nusselt numbers and the axisymmetric computations using the Morse turbulence model is reasonably good, particularly at the larger values of Re_ϕ. The Launder–Sharma model tends to underpredict the measured data.

(*iv*) The computations show peaks in Nu in the region where the preswirl flow impinges on the rotor and in the region around the blade-cooling slot; measurements of Nu were not made in the impingement region, but those made near the blade-cooling holes in the rig showed a peak value approximately double that of the measurements at smaller radii.

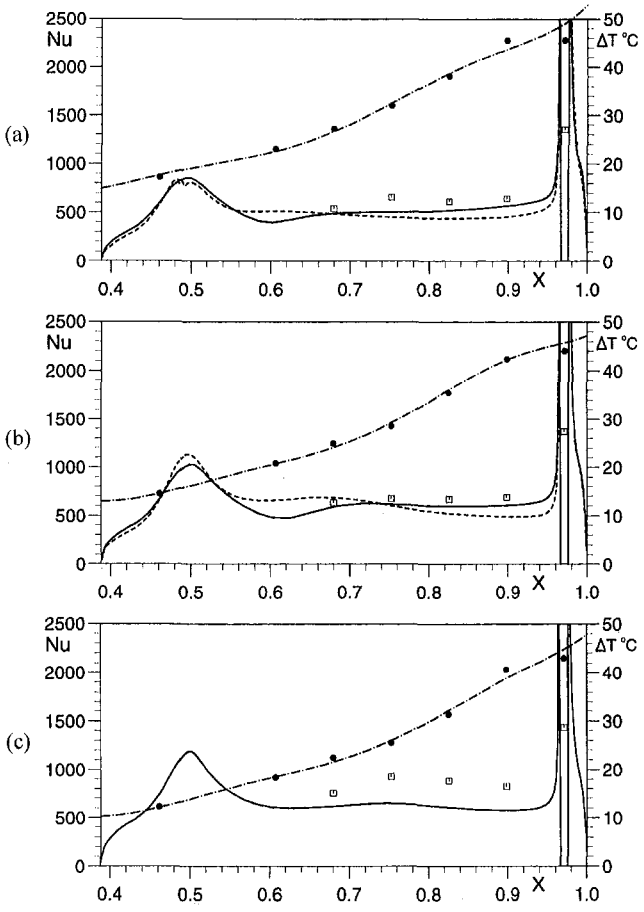

Fig. 9 Comparison between computed and measured Nusselt numbers for $Re_\phi \cong 0.5 \times 10^6$ and $\lambda_{T,b} \cong 0.35$ (for legend, see Fig. 7):
(*a*) $Re_\phi = 0.569 \times 10^6$, $C_{w,b} = 14068$, $\lambda_{T,b} = 0.350$, $\beta_p = 2.24$
(*b*) $Re_\phi = 0.569 \times 10^6$, $C_{w,b} = 14162$, $\lambda_{T,b} = 0.352$, $\beta_p = 2.53$
(*c*) $Re_\phi = 0.588 \times 10^6$, $C_{w,b} = 14562$, $\lambda_{T,b} = 0.353$, $\beta_p = 3.06$

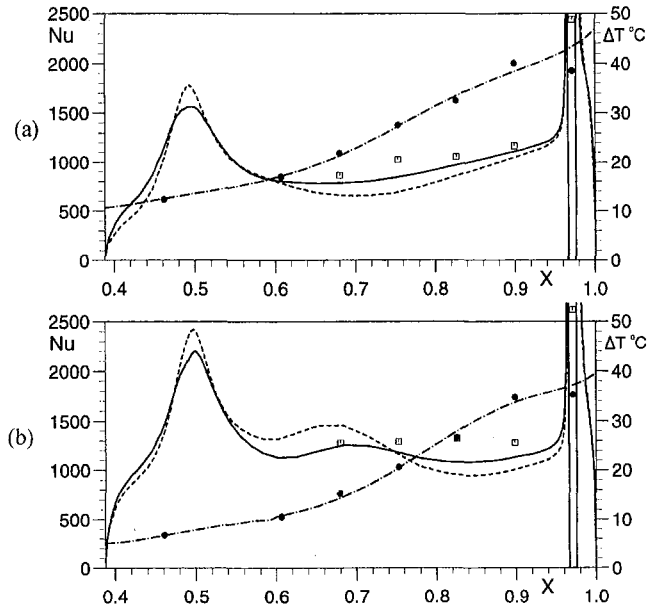

Fig. 10 Comparison between computed and measured Nusselt numbers for $Re_\phi \cong 1.2 \times 10^6$ and $\lambda_{T,b} \cong 0.35$ (for legend, see Fig. 7):
(*a*) $Re_\phi = 1.22 \times 10^6$, $C_{w,b} = 25953$, $\lambda_{T,b} = 0.351$, $\beta_p = 1.90$
(*b*) $Re_\phi = 1.37 \times 10^6$, $C_{w,b} = 28354$, $\lambda_{T,b} = 0.349$, $\beta_p = 2.61$

The study reported in this paper has concentrated principally on the local Nusselt numbers. These obviously have a significant effect on the temperature of the blade-cooling air, and this will be the subject of a future paper on the cover-plate preswirl system.

Acknowledgments

The authors thank the Engineering and Physical Sciences Research Council and European Gas Turbines Ltd. for funding the research described in this paper, and the Turkish Government and Kocaeli University for providing the financial support for Hasan Karabay.

References

Chen, J., Owen, J. M., and Wilson, M., 1993a, "Parallel-computing techniques applied to rotor–stator systems: fluid dynamics computations," in: *Numerical Methods in Laminar and Turbulent Flow*, Vol. 8, pp. 899–911, Pineridge Press, Swansea.

Chen, J., Owen, J. M., and Wilson, M., 1993b, "Parallel-computing techniques applied to rotor–stator systems: thermal computations," in: *Numerical Methods in Thermal Problems*, Vol. 8, pp. 1212–1226, Pineridge Press, Swansea.

Chen, J.-X., Gan, X., and Owen, J. M., 1996, "Heat transfer in an air-cooled rotor–stator system," ASME JOURNAL OF TURBOMACHINERY, Vol. 118, pp. 444–451.

El-Oun, Z., and Owen, J. M., 1989, "Pre-swirl blade-cooling effectiveness in an adiabatic rotor–stator system," ASME JOURNAL OF TURBOMACHINERY, Vol. 111, pp. 522–529.

Karabay, H., Chen, J.-X., Pilbrow, R., Wilson, M., and Owen, J. M., 1999, "Flow in a cover-plate preswirl rotor–stator system," ASME JOURNAL OF TURBOMACHINERY, Vol. 121, pp. 160–166.

Launder, B. E., and Sharma, B. I., 1974, "Application of the energy dissipation model of turbulence to flow near a spinning disc," *Letters in Heat and Mass Transfer,* Vol. 1, pp. 131–138.

Meierhofer, B., and Franklin, C. J., 1981, "An investigation of a preswirled cooling airflow to a gas turbine disk by measuring the air temperature in the rotating channels," ASME Paper No. 81-GT-132.

Morse, A. P., 1988, "Numerical prediction of turbulent flow in cavities," ASME JOURNAL OF TURBOMACHINERY, Vol. 110, pp. 202–215.

Owen, J. M., and Rogers, R. H., 1989, *Flow and heat transfer in rotating-disc systems, Vol. 1: Rotor-stator systems,* Research Studies Press, Taunton; Wiley, New York.

Owen, J. M., and Rogers, R. H., 1995, *Flow and heat transfer in rotating-disc systems, Vol. 2: Rotating Cavities,* Research Studies Press, Taunton; Wiley, New York.

Popp, O., Zimmermann, H., and Kutz, J., 1998, "CFD analysis of coverplate receiver flow," ASME JOURNAL OF TURBOMACHINERY, Vol. 120, pp. 43–49.

Wilson, M., Pilbrow, R. G., and Owen, J. M., 1997, "Flow and heat transfer in a preswirl rotor–stator system," ASME JOURNAL OF TURBOMACHINERY, Vol. 119, pp. 364–373.

Heat Transfer Contributions of Pins and Endwall in Pin-Fin Arrays: Effects of Thermal Boundary Condition Modeling

M. K. Chyu

Y. C. Hsing

T. I.-P. Shih

Department of Mechanical Engineering,
Carnegie Mellon University,
Pittsburgh, PA 15213

V. Natarajan
The BOC Group Technical Center,
Murray Hill, NJ 07947

Short pin-fin arrays are often used for cooling turbine airfoils, particularly near the trailing edge. An accurate heat transfer estimation from a pin-fin array should account for the total heat transfer over the entire wetted surface, which includes the pin surfaces and uncovered endwalls. One design question frequently raised is the actual magnitudes of heat transfer coefficients on both pins and endwalls. Results from earlier studies have led to different and often contradicting conclusions. This variation, in part, is caused by imperfect or unrealistic thermal boundary conditions prescribed in the individual test models. Either pins or endwalls, but generally not both, were heated in those previous studies. Using a mass transfer analogy based on the naphthalene sublimation technique, the present experiment is capable of revealing the individual heat transfer contributions from pins and endwalls with the entire wetted surface thermally active. The particular pin-fin geometry investigated, $S/D = X/D = 2.5$ and $H/D = 1.0$, is considered to be one of the optimal array arrangement for turbine airfoil cooling. Both inline and staggered arrays with the identical geometric parameters are studied for $5000 \leq Re \leq 25{,}000$. The present results reveal that the general trends of the row-resolved heat transfer coefficients on either pins or endwalls are somewhat insensitive to the nature of thermal boundary conditions prescribed on the test surface. However, the actual magnitudes of heat transfer coefficients can be substantially different, due to variations in the flow bulk temperature. The present study also concludes that the pins have consistently 10 to 20 percent higher heat transfer coefficient than the endwalls. However, such a difference in heat transfer coefficient imposes very insignificant influence on the overall array-averaged heat transfer, since the wetted area of the uncovered endwalls is nearly four times greater than that of the pins.

Introduction

Heat transfer with flow over an array of circular pin-fins has been the subject of extensive research in the past because of its importance in a wide variety of engineering applications. Pin-fins with small height-to-diameter ratios, on the order of unity, are often used as heat transfer augmentation devices for cooling of turbine airfoils. They are especially effective for internal cooling passage near the blade trailing section where the pin-fins (the so-called pedestals) also serve a structural purpose in bridging the narrow span between the pressure and suction surfaces. Under this context, heat transfer and pressure loss for short, circular pin-fin arrays have been studied extensively since the early 1980's. Substantial contributions were made by groups at NASA-Lewis (VanFossen, 1982; Simoneau and VanFossen, 1984; Brigham and VanFossen, 1984) and Arizona State University (Metzger et al., 1982a, b, c, 1984, 1986). Their findings collectively suggest that the transport phenomena associated with short pin-fins are considerably different from that of the conventional "cylinders in crossflow" problem (Zukauskas, 1972) where the cylinders are much longer, say $H/D > 8$, and without endwalls present. Important results concerning staggered pin-fin arrays from these studies were compiled in a review article by Armstrong and Winstanley (1988). Using a heat/mass transfer analogous system, Chyu (1990) later reported that the presence of fillets at the cylinder–endwall junction reduces the heat transfer from a pin-fin array. Without fillets, his mass transfer results agree favorably with those using direct heat transfer measurements. Recently, Chyu et al. (1996) found that square or diamond-shaped pin elements may be more effective for heat transfer augmentation than circular pins. However, actual manufacturing of sharp-edged pins may be difficult.

One issue concerning the total heat transfer from a pin-fin array as well as the actual split of heat transfer between the pins and uncovered endwalls is of great importance for the thermal design of turbine airfoils. In reality, both pins and endwalls participate in the process of cooling the component. However, to ease the experimental setup and heat transfer measurements, virtually all the previous studies have in one way or another involved certain approximations of thermal boundary conditions in the laboratory models. Either the pins or the endwalls, but generally not both, are heated or thermally active. The well-known correlations obtained by Metzger and his associates (1982a, b, c) are based on heat transfer measurements on the uncovered portion of the endwall, while the pins are made of nonconductive basswood. On the other hand, Simoneau and VanFossen (1984) used a single, heated pin and tested it in different positions within the array to determine the row-resolved heat transfer coefficient. The mass transfer work by Chyu et al. (1990, 1996) and Natarajan and Chyu (1994) had the surface of all the pin elements coated with a thin layer of naphthalene and the pins were situated on an aluminum tooling plate without naphthalene coating. This setup is analogous to a heat

Contributed by the International Gas Turbine Institute and presented at the 43rd International Gas Turbine and Aeroengine Congress and Exhibition, Stockholm, Sweden, June 2–5, 1998. Manuscript received by the International Gas Turbine Institute February 1998. Paper No. 98-GT-175. Associate Technical Editor: R. E. Kielb.

transfer situation in which each pin is isothermally maintained, i.e., the pin has a fin efficiency of unity, and the endwall is adiabatic. Using the same mass transfer technique, Chyu and Goldstein (1991) examined the detailed distribution of mass (heat) transfer coefficient on a naphthalene-coated endwall while the pins were kept mass transfer inactive.

Only a few studies in the pin-fin literature are focused explicitly on the difference of heat transfer between the pins and endwall. VanFossen (1982) reported that, for $S/D = X/D = 3.46$ and $0.5 \leq H/D \leq 2$, the heat transfer coefficient on the pin surface is approximately 35 percent higher than that of the endwall. His conclusion is drawn by comparing the overall heat transfer from pins made of highly conductive material with that of nonconductive wooden pins. Using the same approach, Metzger et al. (1984) reported that, for $2.5 \leq S/D \leq 3.5$, $1.5 \leq X/D \leq 3.5$, and $H/D = 1.0$, the pin surface heat transfer coefficient is approximately double the endwall value. In a separate study Metzger et al. (1982b) suggested that the heat transfer coefficient measured on the endwall is somewhat insensitive to whether the pin is conductive or nonconductive. Using the mass transfer analogy, Chyu (1990) reported comparable heat transfer coefficients on the surface of the pins and endwall for both in-line and staggered arrays, $S/D = X/D = 2.5$, $H/D = 1$. While all pins were made mass transfer active in his study, only one row of the endwall was active during the experiment, so the boundary condition is not a perfect representation of the real situation. Al Dabagh and Andrews (1992) later employed a transient heating technique to evaluate the heat transfer contributions from the pins and the endwall for three staggered arrays, $S/D = 2.0$, $X/D = 1.5$ and $H/D = 0.7$, 1.0 and 2.2. Contradicting all the previous findings, their results indicated that the endwall heat transfer coefficient is 15 to 35 percent higher than the pins.

The present study is an attempt to resolve the aforementioned controversy. It is speculated that the inconsistent results among the earlier studies may be attributable to the limitation as well as the uncertainty involved in the experimental systems. The convective transport with the flow passing through a pin-fin array is so complex that it can result in highly nonuniform local heat transfer coefficients distributed over the entire wetted surface. Conventional thermal methods based on thermocouple measurements of several selected points over a heat transfer surface may not be representative of the overall system behavior. In addition, heat loss is always a concern and is virtually unavoidable. Finally, individual studies have used different ways of prescribing thermal boundary conditions in their test rigs, which may lead to different results.

Given the priority to quantifying the heat transfer difference between the pins and endwalls, the mass transfer analogous approach based on naphthalene sublimation emerges as one of the most effective choices for the present use. Since the surfaces of all pins and endwalls can be separately coated with naphthalene, the concern of overall system "mass loss" as well as "internal mass leakage" between pins and endwall is virtually nonexistent. In an unprecedented attempt, the entire test section, which includes all the pin wetted surface and the uncovered endwalls attached to both ends of the pins, is coated with naphthalene, and hence is mass transfer active. By analogy, the mass transfer system as such is equivalent to a heat transfer system whose wetted surface is entirely isothermal. Mass transfer of individual pins and row-resolved endwall segments can be determined by weighing the amount of naphthalene sublimed during the test period. The weighing approach has been well documented and proven to be a highly accurate method for determining regional average data by numerous studies in the past.

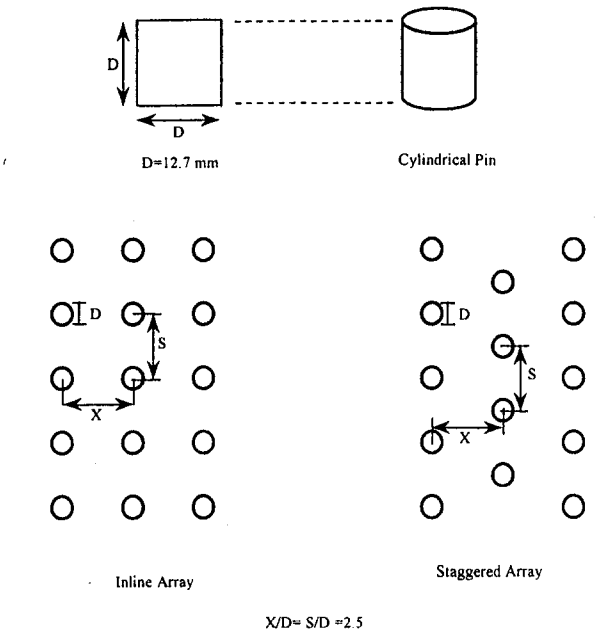

Fig. 1 Pin-fin geometry

Experimental Apparatus and Procedures

The geometry of pin-fin arrays as well as the housed channel is the same as that of an earlier study performed by one of the present authors (Chyu, 1990). The pin-fin elements are perfectly cylindrical in shape and made of aluminum rods approximately 12.5 mm in diameter. To facilitate a rational comparison, the two arrays studied here, an in-line array and a staggered array, have identical geometric parameters: $H/D = 1$, $S/D = X/D = 2.5$. Figure 1 shows the geometry of the two arrays. The staggered array with these array parameters is deemed to

Nomenclature

D = pin diameter
H = pin height
h = heat transfer coefficient, Eq. (2)
h_m = naphthalene mass transfer coefficient, Eq. (1)
k = thermal conductivity of air
m = mass transfer flux of naphthalene from pin-fin surface
n = power index
Nu = Nusselt number = hD/k
Pr = Prandtl number = ν/α
q = heat flux from pin-fin surface
Re = Reynolds number = U_mD/ν
S = pin spacing in spanwise direction
Sc = naphthalene–air Schmidt number = ν/K
Sh = pin-resolved naphthalene mass transfer Sherwood number = h_mD/K
T = temperature
U_m = mean flow in the minimum flow area
X = pin spacing in streamwise direction
α = thermal diffusivity
K = naphthalene–air diffusion coefficient
ν = kinematic viscosity of air
$\rho_{v,w}$ = vapor mass concentration or density of naphthalene on pin-fin surface
$\rho_{n,b}$ = vapor mass concentration or density of naphthalene in flow bulk
ρ_s = density of solid naphthalene

Subscripts

A = array-averaged
b = bulk
C = column-averaged
N = normalized by mean value
R = row-averaged
w = wall, fin surface

be the most optimal configuration for turbine blade cooling. There are seven rows for both arrays, but the total number of pins is different. For the inline array, each row has five pins, giving a total of 35 pins. On the other hand, the number of pins per row in the staggered array alternates with five in the odd number row and four in the even number row, a total of 32 pins.

The test channel that houses the pin-fin arrays is made of aluminum tooling plate and has a rectangular cross section, 159 mm wide × 12.7 mm high. Downstream of the test section is a 230-mm-long discharge duct, which is approximately ten times the hydraulic diameter of the test section. Inlet flow to the array is introduced through a rectangular opening (25.4 mm wide × 12.5 mm high) on one side of the test channel. The center of the first row of pins is about a two-pin spacing from the furthest edge of the test section. Attached to the opening is an approximate 455-mm-long aluminum duct, which serves as the entrance section. Airflow is supplied by a 50 hp compressor and is monitored by a pressure regulator, a control valve, and an orifice before reaching the test section.

Each experiment starts with preparation of naphthalene coating on the pin-fin surface. This coating is achieved by dipping the cylinder, with both ends taped, into a pool of nearly boiling, molten naphthalene. During the dip, the cylinder is held by tweezers at both ends and immersed in the liquid naphthalene for about one second. The naphthalene solidifies 1 mm thick layer on the cylinder surface. Such a coating process generally results in a quality surface, so no additional polishing or machining procedure is necessary. A similar coating process also applies to preparing the endwall samples. The endwall on either top or bottom surface of the test channel is comprised of seven separated segments. Each segment, which represents the endwall of a given row, extends one-half pitch upstream as well as downstream to the pin axis of that row and spans across the entire width of the array. After the coating process, the pins and endwall segments are stored in a tightly sealed plastic box for at least 15 hours to ensure that they attain thermal equilibrium with the surrounding air.

Before a test run, all pins and endwall segments are separately weighed using an electronic balance with an accuracy of 10^{-2} mg in a 166 g range. They are then screw-mounted together, forming the test section of the desired array geometry. After the test section is assembled, the compressed air is induced and flows through the channel for about 30 minutes. During the test run, the system temperature is determined from the average readings of four thermocouples embedded in the inner surface of the two endwalls. The system temperature is used to evaluate the naphthalene vapor concentration, $\rho_{v,w}$, on the fin surface. Since the value of $\rho_{v,w}$ is very temperature sensitive, an isothermal system is highly desirable. A test is considered to be a failure and discarded if any two of the four thermocouple readings differ more than 0.2°C. After the test run, all pins and endwall segments are unscrewed and removed from the channel and each is weighed again. The weight difference for each individual component yields the amount of naphthalene sublimed during the test run. The average naphthalene mass sublimed is approximately 20 mg. The repeatability for all the test runs is within 8 percent.

Heat/Mass Transfer Analogy and Data Reduction

The convective heat transfer coefficient, h, of each participating element is given by

$$h = q/(T_w - T_b) \tag{1}$$

where T_w and T_b are the element wall temperature and the bulk mean temperature in the channel, respectively. By analogy (Eckert, 1976), the mass transfer coefficient, h_m, of each cubic fin is

$$h_m = m/(\rho_{v,w} - \rho_{n,b}) \tag{2}$$

where m is the mass transfer rate per unit area, which can be calculated from the weight change of the coated pin or endwall segment before and after the experiment. The naphthalene concentration at the wall, $\rho_{v,w}$, is obtained by evaluating the time-averaged naphthalene vapor pressure using the pressure-temperature correlation of Ambrose et al. (1975) in conjunction with the ideal gas law.

The value of naphthalene concentration in the bulk flow at a given row is determined by the total mass transfer upstream. The increase in bulk concentration naphthalene vapor within the domain of a specific row j can be expressed as

$$\Delta\rho_{n,b} = M_j/Q \tag{3}$$

where M_j is the mass transfer per unit time from all participating surfaces of the entire row j, and Q is the volumetric air flow rate through the channel. Since the air flow at the channel inlet is naphthalene free, it leads to

$$\rho_{n,b} = \sum_{1}^{j-1} M_j/Q \tag{4}$$

As the mass transfer system is essentially isothermal, the naphthalene vapor pressure and vapor concentration at the wall are constant. As mentioned earlier, this is equivalent to a wall boundary condition of constant temperature in heat transfer, and the pins thus can be regarded to have an ideal 100 percent efficiency.

The dimensionless local mass transfer coefficient, Sherwood number, Sh, is defined by

$$\mathrm{Sh} = h_m D/\mathrm{K} \tag{5}$$

where K is the naphthalene–air diffusion coefficient, which is determined by taking the Schmidt number equal to 2.5; i.e.,

$$\mathrm{Sc} = \nu/\mathrm{K} \tag{6}$$

Since the naphthalene concentration in the boundary layer is extremely small, the kinematic viscosity, ν, uses the value of air under the operating conditions. By analogy, Sherwood number can be transformed to its heat transfer counterpart, Nusselt number (Nu), using the relation

$$\mathrm{Nu}/\mathrm{Sh} = (\mathrm{Pr}/\mathrm{Sc})^n \tag{7}$$

where Pr is the Prandtl number and the power index n is approximately equal to 0.4, according to Sparrow and Ramsey (1978). Using air (Pr = 0.7) as the coolant, a direct conversion relationship can be obtained,

$$\mathrm{Nu} = 0.6\mathrm{Sh} \tag{8}$$

Results and Discussion

To illustrate the quality of the present experiment, Fig. 2 shows the relative magnitude of mass transfer among all individual pins. Here both pins and endwalls are mass transfer active. The numerical value marked atop each pin is the ratio of its individual pin-resolved Sherwood number, Sh, to the Sherwood number averaged over all pins in the array. The value marked outside the figure border are the row-average ($\mathrm{Sh_{RN}}$, top border) and column-average ($\mathrm{Sh_{CN}}$, right border) of the normalized Sherwood number. By analogy, these normalized values are equal to the ratios of corresponding Nusselt number in heat transfer. One significant feature revealed in Fig. 2 is the excellent data symmetry for both arrays, as the value of $\mathrm{Sh_{CN}}$ varies less than ±1 percent across the array span. Although Fig. 1 displays the results for Reynolds number about 16,800 only, the same observation prevails over the entire range of the Reynolds number tested.

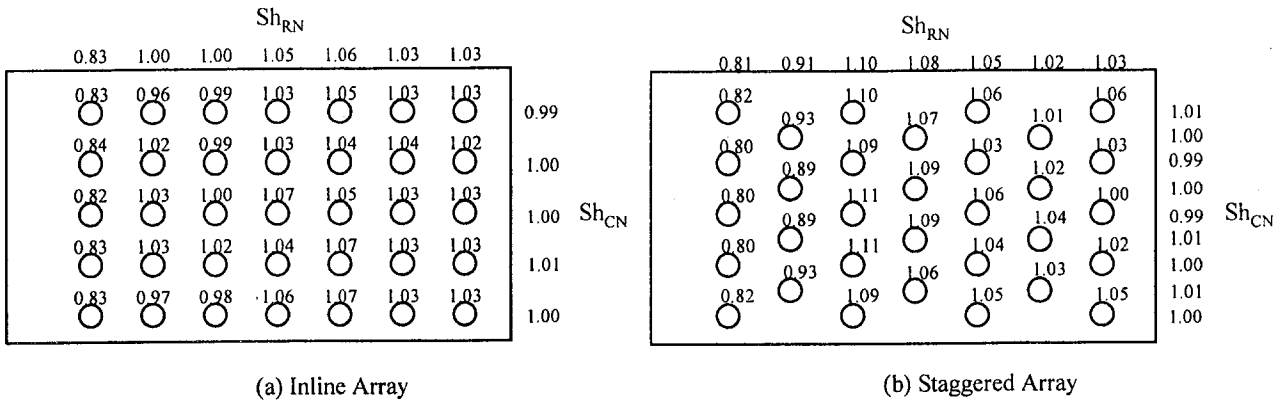

Fig. 2 Relative heat transfer coefficient on pin elements, Re = 16,800

As a contrast to the invariant nature of Sh_C, the row-averaged mass transfer, Sh_R, varies relatively significantly along the streamwise direction, as shown in Fig. 3. In addition, the magnitudes of Sh_R depend also on the Reynolds number, the array geometry, as well as the participating boundary layer. According to Metzger et al. (1982a) and Chyu (1990), the maximum Sh_R exists at the second row and the third row for the inline and staggered array, respectively, provided that the Reynolds number is sufficiently high, say $Re \geq 10{,}000$. The maxima become less obvious when Re decreases. Despite such similar findings, their conclusions, in fact, are based on quite different tests and both with partially active boundary conditions. Metzger et al. (1982a) measured the row-averaged heat transfer over the endwall while the pins are made of basswood and thus are heat transfer inactive. Chyu (1990), on the other hand, measured the mass transfer from the pins and kept the endwall inactive. Since the array geometry of the latter is identical to that of the present study, the effects of mass transfer (thermal) boundary condition on the pin mass (heat) transfer can be realized by comparing the corresponding results between the two studies, as exhibited in Fig. 3. While the general trend of Sh_R versus row number and Re is by and large uninfluenced by the difference in boundary condition, the value of Sh_R is consistently higher, by approximately 10–20 percent, for the present study in which both pins and endwalls are mass transfer active. Such a difference is a result of simple interpolation, since the corresponding cases shown in Fig. 3 do not have identical Reynolds numbers.

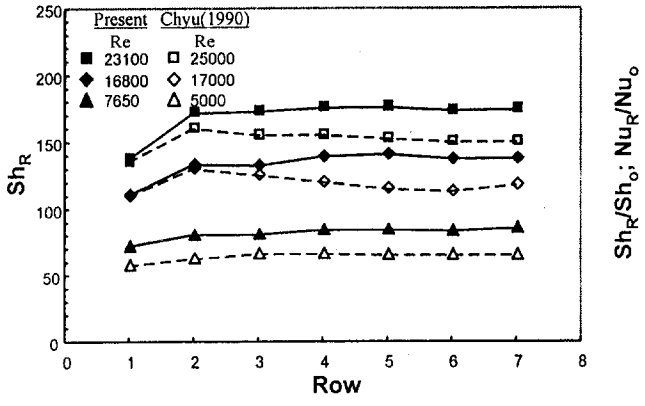

(a) Inline Array

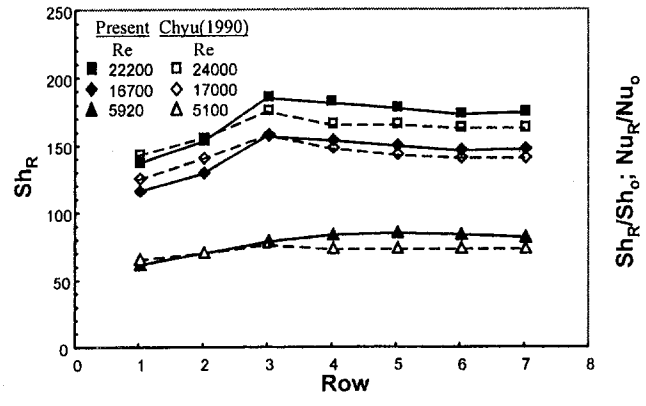

(b) Staggered Array

Fig. 3 Heat transfer coefficient on pin surface

Based on the same data shown in Fig. 3, Fig. 4 gives a different perspective of the results by presenting the enhancement factor relative to a smooth channel without pin array. The ordinate of Fig. 4 has dual meaning: Sh_R/Sh_o and Nu_R/Nu_o, where Sh_o and Nu_o are the Sherwood and Nusselt number, respectively, for the corresponding smooth channel case without pin array. The value of Sh_o is determined from the Dittus–Boelter equation for heat transfer (Kays and Crawford, 1980)

$$Nu_{Do}/Pr^{0.4} = 0.023\ Re_D^{0.8} \tag{9}$$

where Re_D is the channel Reynolds number and Nu_{Do} is the fully developed Nusselt number based on the channel hydraulic diameter, D_h. To be compatible with the characteristic length used for Sh, Sh_o can be expressed by

$$Sh_o/Sc^{0.4} = Nu_o/Pr^{0.4} = (D/D_h)(Nu_{Do}/Pr^{0.4}) = 0.0124\ Re_D^{0.8} \tag{10}$$

Mass transfer results obtained from the present test channel without pins agree favorably with this correlation with an average error about 8 percent over the entire range of Reynolds number. In addition to the effects of boundary condition, the results shown in Fig. 4 also implies that the enhancement factor decreases with Reynolds number. While more detailed discussion and quantitative correlations are to be given later, the enhancement factor for the pin surface alone is roughly about 4 for $Re \sim 5000$ and 3 for $Re \sim 20{,}000$.

One significant effect of thermal boundary conditions on the convective transport is to alter the nature of temperature distribution in the flow bulk. For given channel geometry and Reynolds number, the change of bulk temperature in a channel is expected to be greater with a fully active channel wall than without. By analogy, such a notion is equally applicable to mass transfer, as evidenced by Eqs. (3) and (4). Figure 5 reveals a

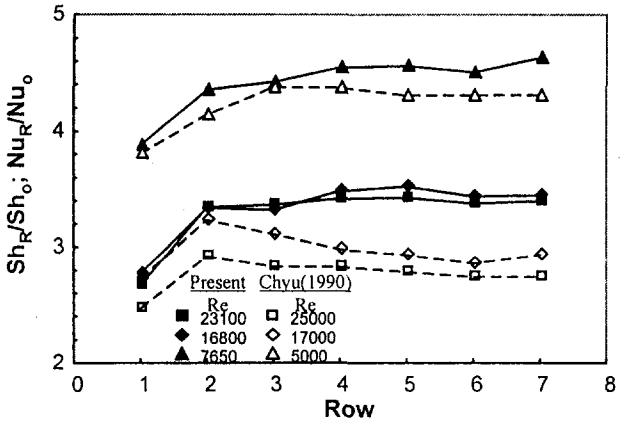

(a) Inline Array

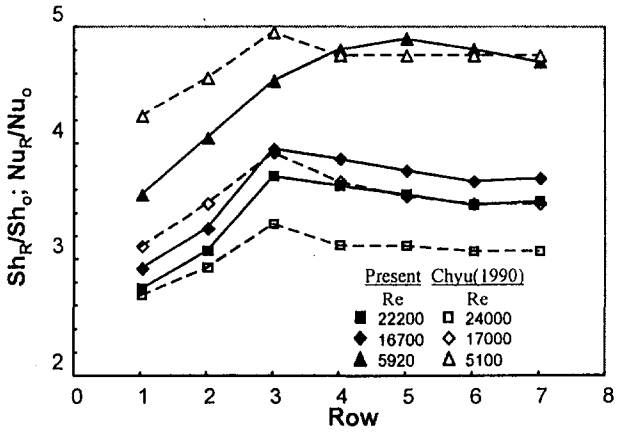

(b) Staggered Array

Fig. 4 Normalized heat/mass transfer coefficients

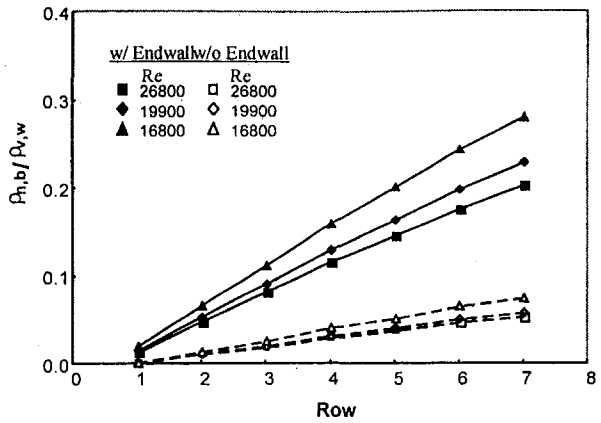

Fig. 5 Variation of bulk concentration in staggered array

comparison of the streamwise variation of naphthalene vapor concentration in the flow bulk with or without active uncovered endwall for the staggered array. The abscissa of the figure marked as "row" includes the pins in the row and the uncovered endwall ranging one-half longitudinal pitch upstream and downstream to the pin axis. The ordinate represents the magnitude of bulk mass concentration of naphthalene, ρ_{nb}, normalized by its counterpart near the wall, ρ_{vw}. Since ρ_{vw} is constant in the present naphthalene sublimation system, the ratio ρ_{nb}/ρ_{vw} is equivalent to the value of $T_b - T_i/T_w - T_i$ in heat transfer.

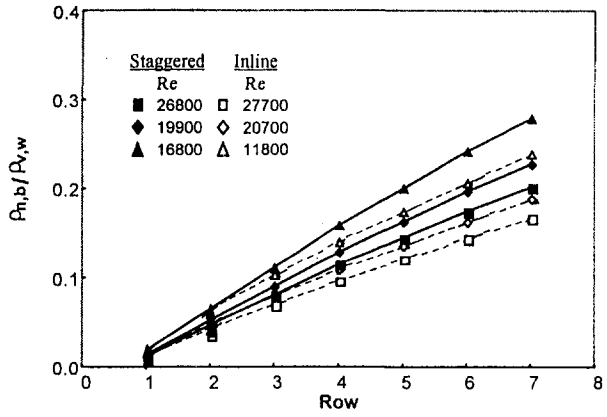

Fig. 6 Variation of bulk concentration

Most evident in Fig. 5 is the substantial contribution of the mass transfer from the endwall toward the increase in bulk concentration. The difference in ρ_{nb} with endwall inclusion is nearly 4 to 5 times higher than without. Because the area of uncovered endwall over the entire pin-fin array accounts for nearly 80 percent of the total wetted area in the channel, complete negligence of the endwall heat transfer not only is unrealistic but may also be inaccurate in presenting a sensible heat transfer coefficient based on bulk temperature. Although the level of surface mass transfer rate under a highly turbulent flow is dominated primarily by the local hydrodynamics, rather than the details of thermal boundary condition, the corresponding local mass transfer coefficient, however, can vary significantly with the boundary condition via the change in bulk concentration in the test channel. Since $\rho_{vw} - \rho_{nb}$ is smaller downstream for the case of fully active boundary than that of only the pins active, the resulting heat transfer coefficient is higher for the former, provided that m is either a constant or decreases with a lesser extent than that of $\rho_{vw} - \rho_{nb}$ downstream. This notion substantiates the finding displayed in Fig. 4, where the row-averaged mass transfer coefficient is consistently higher for the case with the entire test surface active. Regardless of the nature of the boundary condition, the change of bulk mass concentration decreases with the Reynolds number. In addition, the staggered array tends to have a stronger increase in bulk concentration than the in-line array for a given Reynolds number, as illustrated in Fig. 6. Such a difference between the two arrays appears to be widened downstream.

As a major finding from the present study, Fig. 7 shows the comparison of heat transfer coefficient on the pin surface and the uncovered endwall region. Similar to Fig. 4, the data shown in Fig. 7 are presented as enhancement factors relative to the corresponding values of fully developed smooth channel, Sh_R/Sh_o or Nu_R/Nu_o. Note that Sh_R or Nu_R here represents the row-averaged Sherwood number or Nusselt number for either the pins or the endwall. The difference in the row-average transfer coefficient between the pins and endwalls varies to a certain extent with the Reynolds number, the array configuration, and the row position. Except for the first one or two rows, the heat transfer coefficient on the pin surface for both arrays is consistently higher than that of the endwall, by 10 to 20 percent. The difference widens with a decrease in Reynolds number. Although the overall trend that a pin has a higher heat transfer coefficient than the endwall agrees favorably with most of the earlier findings, the margin of difference observed here is relatively low. VanFossen (1982) reported a 35 percent differential, while Metzger et al. (1984) cautiously claimed that the difference is nearly 100 percent. On the other hand, the present finding contradicts the observation by Al Dabagh and Andrews (1992) who reported that the heat transfer coefficient on the pin surface is lower instead, by approximately 15 to 35 percent.

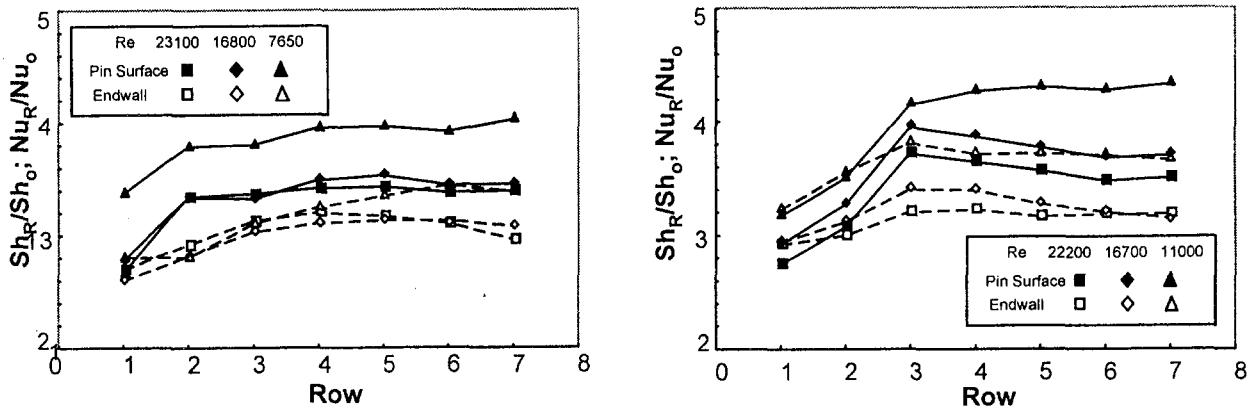

Fig. 7 Heat transfer coefficient on pin surface and endwall

Further examination of Figs. 7(*a*) and 7(*b*) reveals that one of the most significant differences between the two arrays lies in the entrance region. With an exception for the case of the in-line array with the lowest Reynolds number (Re = 7650), the pins and uncovered endwall have very comparable magnitude of heat transfer coefficient in the first row for the inline array and the first two rows for the staggered array. This difference, on the other hand, may be fundamentally insignificant, since the second row of the staggered array is effectively part of the first row, as no pins are situated directly in front of the row.

The most useful information for turbine designers probably is the area-averaged heat transfer coefficient over the entire array. Figure 8 shows such area-averaged data, in the form of $Sh_A/Sc^{0.4}$ or $Nu_A/Pr^{0.4}$, varying with the Reynolds number for both arrays. As expected, the staggered array overall has a higher average heat or mass transfer coefficient than the inline array. The difference is about 10 to 20 percent for Re $\geq$ 20,000 and becomes less significant when the Reynolds number gets higher. Also included in the figure are the corresponding area-averaged data, respectively, for pins and endwalls. Largely because the endwall accounts for nearly 80 percent of total wetted area for either array, the array-averaged results are virtually equal to the corresponding endwall averages, rather than the pin averages. In other words, the 10 to 20 percent higher heat transfer coefficient on the pin surface has a marginal effect on the overall array heat transfer. However, this notion may change for different arrays in which pin surface accounts for a large portion of the array wetted area. Such a situation happens when an array has dense pin arrangements, i.e., smaller pitches, or taller pins.

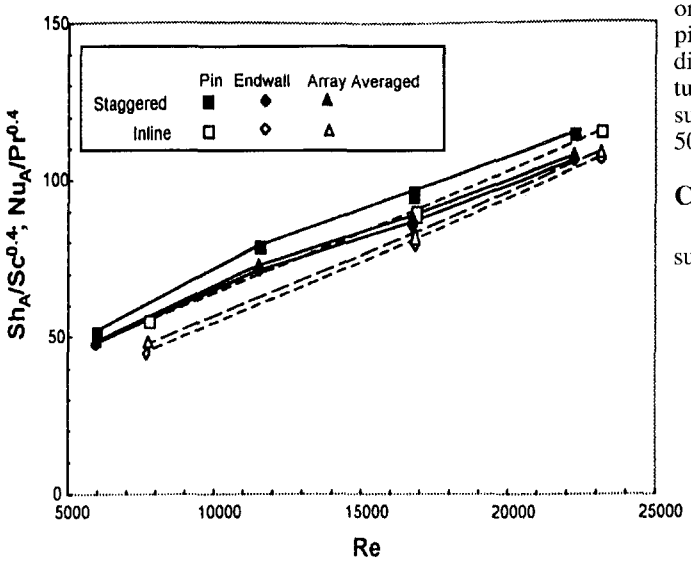

Fig. 8 Array-averaged heat transfer coefficient

Table 1 gives the power correlations between the average Nusselt number and Reynolds number. The in-line array shows a stronger Reynolds number dependence than the staggered array, $b = 0.733$ versus 0.583. From the geometric standpoint, this trend is not surprising. The inline array is expected to preserve more channel flow characteristics as the pins in adjacent rows form two virtual walls for a channel. On the other hand, flow passing through the staggered array should experience stronger separation and stagnation effects. In the limiting case, the turbulent Nu–Re correlation should reveal a power index nearly 0.8 for smooth channel flow and 0.5 for separated flow over stagnant obstacles.

Compared to the well-known correlation reported by Metzger et al. (1982a) for the staggered array, i.e.,

$$Nu/Pr^{0.4} = 0.080\ Re^{0.728}$$

for $H/D = 1$, $S/D = X/D = 2.5$, $1000 \leq Re \leq 100{,}000$,

the present correlation shows a relatively weaker dependence on Re, 0.583 versus 0.728. A combination of different test range in Reynolds number and thermal boundary condition may be responsible for such a deviation. Metzger's correlation is based on heat transfer data measured over the endwall only, while the pins are virtually adiabatic. Despite this seemingly apparent disparity in Reynolds number dependence, the actual magnitudes of Nu derived from the two correlations, in fact, agree surprisingly well (<10 percent) within the present test range, $5000 < Re < 25{,}000$.

Concluding Remarks

The information revealed from the present mass transfer measurements is expected to provide important guidelines for re-

Table 1 Nu–Re correlations

Array Configuration		a	b
Inline	Pin Surface	0.155	0.658
	Fin Surface	0.052	0.759
	Averaged Pin & Fin	0.068	0.733
Staggered	Pin Surface	0.337	0.585
	Fin Surface	0.315	0.582
	Averaged Pin & Fin	0.320	0.583

solving a long-standing issue concerning the heat transfer contribution from different participating segments in a pin-fin array. The present study inherits two distinct features that may make its results more reasonable and reliable than those in the past. The first feature has to do with the implementation of an equivalent isothermal boundary condition over the entire test channel. This feature provides a baseline to quantify the effects of partially active or imperfect boundary conditions on the data accuracy of heat transfer coefficient. The second feature is the attainment of a true row-averaged data, which includes all the nonuniformity existing in the domain of a measured segment. Further affirming the general observation of VanFossen (1982) and Metzger et al. (1984), the present data collectively indicate that the heat transfer coefficient on the pin surface is higher than that on the uncovered endwall, by approximately 10 to 20 percent. However, the two earlier studies reported differences higher than the present finding. The primary cause of such disagreement is deemed to be a combination of imperfect boundary conditions and measurement techniques that may be insufficient for resolving the highly complex heat transfer characteristics inherited in pin-fin arrays. In more practical perspective, the 10 to 20 percent difference in heat transfer coefficient may have little impact on the overall array-averaged heat transfer. This result is mainly because the endwall accounts for nearly 80 percent of the wetted area for the present array configuration, $H/D = 1$, $S/D = X/D = 2.5$. Hence, an experimental approach focused solely on the endwall measurement is expected to be more representative than one focused on the pins.

References

Al Dabagh, A. M., and Andrews, G. E., 1992, "Pin-Fin Heat Transfer: Contribution of the Wall and the Pin to the Overall Heat Transfer," ASME Paper No. 92-GT-242.

Ambrose, D., Lawenson, I. J., and Sprake, C. H. S., 1975, "The Vapor Pressure of Naphthalene," *J. Chem. Thermo.*, pp. 1173–1176.

Armstrong, J., and Winstanley, D., 1988, "A Review of Staggered Array Pin Fin Heat Transfer for Turbine Cooling Applications," ASME JOURNAL OF TURBOMACHINERY, Vol. 110, pp. 94–103.

Brigham, B. A., and VanFossen, G. J., 1984, "Length-to-Diameter Ratio and Row Number Effects in Short Pin Fin Heat Transfer," ASME *Journal of Engineering for Gas Turbines and Power,* Vol. 106, pp. 241–246.

Chyu, M. K., 1990, "Heat Transfer and Pressure Drop for Short Pin-Fin Arrays With Pin-Endwall," ASME *Journal of Heat Transfer,* Vol. 112, pp. 926–932.

Chyu, M. K., and Goldstein, R. J., 1991, "Influence of Cylindrical Elements on Local Mass Transfer From a Flat Surface," *Int. J. Heat Mass Transfer,* Vol. 34, pp. 2175–2186.

Chyu, M. K., Hsing, Y. C., and Natarajan, V., 1998, "Convective Heat Transfer of Cubic Fin Array in a Narrow Channel," ASME JOURNAL OF TURBOMACHINERY, Vol. 120, pp. 362–367.

Eckert, E. R. G., 1976, "Analogies to Heat Transfer Processes," *Measurements in Heat Transfer,* Eckert, E. R. G., and Goldstein, R. J., eds., Hemisphere Publishing Corp., New York.

Metzger, D. E., Berry, R. A., and Benson, J. P., 1982a, "Developing Heat Transfer in Rectangular Ducts With Staggered Arrays of Short Pin Fins," ASME *Journal of Heat Transfer,* Vol. 104, pp. 700–706.

Metzger, D. E., and Haley, S. W., 1982b, "Heat Transfer Experiments and Flow Visualization of Arrays of Short Pin Fins," ASME Paper No. 82-GT-138.

Metzger, D. E., Fan, Z. X., and Sheppard, W. B., 1982c, "Pressure Loss and Heat Transfer Through Multiple Rows of Short Pin Fins," *Heat Transfer 1982,* Vol. 3, Hemisphere Publishing Corp., pp. 137–142.

Metzger, D. E., Fan, C. S., and Haley, S. W., 1984, "Effects if Pin Shape and Array Orientation on Heat Transfer and Pressure Loss in Pin Fin Arrays," ASME *Journal of Engineering for Gas Turbines and Power,* Vol. 106, pp. 252–257.

Metzger, D. E. and Sheppard, W. B., 1986, "Row Resolved Heat Transfer Variations in Pin Fin Arrays Including Effects of Non-uniform Arrays and Flow Convergence," ASME Paper No. 86-GT-132.

Natarajan, V., and Chyu, M. K., 1994, "Convective Heat Transfer From Finite Cylinders Mounted on a Plane Wall," Paper No. 4-EC-15, Vol. 3, pp. 71–77, 10th International Heat Transfer Conference, Brighton, UK, Aug. 14–18.

Simoneau, R. J., and VanFossen, G. J., 1984, "Effect of Location in an Array on Heat Transfer to a Short Cylinder in Crossflow," ASME *Journal of Heat Transfer,* Vol. 106, pp. 42–48.

Sparrow, E. M., and Ramsey, J. M., 1978, "Heat Transfer and Pressure Drop for a Staggered Wall-Attached Array of Cylinders With Tip Clearance," *Int. J. Heat Mass Transfer,* Vol. 21, pp. 44–50.

VanFossen, G. J., 1982, "Heat Transfer Coefficient for Staggered Arrays of Short Pin Fins," ASME *Journal of Engineering for Power,* Vol. 104, pp. 268–274.

Zukauskas, A. A., 1972, "Heat Transfer From Tubes in Cross Flow," *Advances in Heat Transfer,* Vol. 8, pp. 116–133.

Heat Transfer and Pressure Drop in Pin-Fin Trapezoidal Ducts

J.-J. Hwang
Professor.
email: jjhwang@chu.edu.tw

D.-Y. Lai

Y.-P. Tsia

Department of Mechanical Engineering,
Chung-Hua University,
Hsinchu, Taiwan 300

Experiments are conducted to determine the log-mean averaged Nusselt number and overall pressure-drop coefficient in a pin-fin trapezoidal duct that models the cooling passages in modern gas turbine blades. The effects of pin arrangement (in-line and staggered), flow Reynolds number ($6{,}000 \leqq Re \leqq 40{,}000$) and ratio of lateral-to-total flow rate ($0 \leqq \varepsilon \leqq 1.0$) are examined. The results of smooth trapezoidal ducts without pin arrays are also obtained for comparison. It is found that, for the single-outlet-flow duct, the log-mean averaged Nusselt number in the pin-fin trapezoidal duct with lateral outlet is insensitive to the pin arrangement, which is higher than that in straight-outlet-flow duct with the corresponding pin array. As for the trapezoidal ducts having both outlets, the log-mean averaged Nusselt number has a local minimum value at about $\varepsilon = 0.3$. After about $\varepsilon \geqq 0.8$, the log-mean averaged Nusselt number is nearly independent of the pin configuration. Moreover, the staggered pin array pays more pressure-drop penalty as compared with the in-line pin array in the straight-outlet-flow duct; however, in the lateral-outlet-flow duct, the in-line and staggered pin arrays yield almost the same overall pressure drop.

Introduction

It is well known that the gas turbine thermal efficiency can be improved by increasing the turbine inlet gas temperature, which unavoidably will increase the heat load to the turbine components. Therefore, highly sophisticated internal and external cooling techniques for turbine blades have been developed over the years in order to maintain an acceptable safety requirement below the extreme operating conditions. This study focuses on the internal cooling channels at the trailing edge of turbine blade. Figure 1 shows a cross-cut view of an advanced gas turbine blade. In the trailing edge region of blade, aerodynamic considerations demand a small wedge angle for the blade profile. As a result, the internal cooling passages become so narrow that the choice of the cooling method is limited. Pin fins are one augmentation device that can be used to increase heat transfer in this region. The pin fins of circular cross section span the distance between the suction and pressure surfaces that form the endwalls of the cooling passage. Some of the coolant from the blade base exits through bleed slots at the blade tip; the remainder passes through the pin-fin channel and then is ejected from the slots along the trailing edge of the airfoil. Heat from the hot gas stream is convected from not only the endwalls but also the pin-fin surfaces. Also, the pin fins promote turbulence that enhances heat transfer.

VanFossen (1982) measured the overall heat transfer coefficients in large-aspect-ratio rectangular ducts ($AR = 10$ and 20) with staggered arrays of short pin fins ($0.5 < l/d < 2.0$). Heat transfer rates were averaged over the four-row pin array. It was found that the overall heat transfer coefficients for short pins were lower than those for long pin fins ($l/d = 8.0$). Then, by using the same flow path as that in VanFossen (1982), Brigham and VanFossen (1984) investigated the effects of the pin row number in streamwise direction and pin length (height) on the array-averaged heat transfer. Results showed that the array-averaged heat transfer coefficients for the eight-row configuration were slightly higher than those for the four-row configuration. In addition, for an l/d less than 2, the array-averaged heat transfer was not affected by the pin length; while, as $l/d > 2$, the heat transfer increased significantly with an increase of l/d.

Metzger et al. (1982) studied experimentally the local heat transfer variation in a rectangular duct ($AR = 10$) with staggered short pin array ($l/d = 1.0$). Results showed that the local heat transfer increased in the first few rows, reached a peak value and then slowly decreased to a fully developed value. The overall heat transfer correlations were also developed in their work in terms of the Reynolds number for two pin configurations (i.e., $S_T/d = S_L/d = 2.5$, and $S_T/d = 2.5$, and $S_L/d = 1.5$). Later, Metzger and Haley (1982) conducted experiments to examine the effect of replacing the thermally active (copper) pins with the thermally inactive (wooden) pins on the heat transfer in rectangular ducts ($AR = 10$) with a staggered pin array. It was found that the streamwise development of the row-averaged Nusselt number in these two kinds of pins showed the same rapidly increasing then gradually decreasing trend. The overall heat transfer in the copper-pin case was higher than that in the wooden-pin case at high Reynolds numbers but was lower at low Reynolds numbers. Metzger et al. (1984) further experimentally investigated the effect of varying the orientation of flattened pins with respect to the main flow direction on the heat transfer and pressure drops in pin-fin rectangular channels. They found that, by varying the orientation of the pin-fin array, it was possible to increase the heat transfer and, in the meantime, reduce the pressure drop. Moreover, the use of flattened pins increased the heat transfer slightly but doubled the pressure loss.

Lau et al. (1987) employed the naphthalene sublimation technique to measure the distributions of local endwall heat transfer coefficient in rectangular channels ($AR = 10$) with in-line and staggered pin-fin arrays. The effects of Reynolds number, pin configuration, and entrance length on the local endwall heat transfer coefficient distribution were examined. Overall, and row-averaged Nusselt numbers compared well with the previous published data (Metzger et al., 1982). Lau et al. (1989) further experimentally studied the overall heat transfer and friction factor in pin-fin rectangular channels ($AR = 10$) with lateral ejection. It was found that the overall heat transfer for a rectangular pin-fin channel with lateral ejection was lower than that for a rectangular channel with no ejection holes.

As noted in the discussion above, the available data concerning the pin-fin heat transfer in open literature are mostly for *rectangular* channels with or without lateral ejection. As de-

Contributed by the International Gas Turbine Institute and presented at the 43rd International Gas Turbine and Aeroengine Congress and Exhibition, Stockholm, Sweden, June 2–5, 1998. Manuscript received by the International Gas Turbine Institute February 1998. Paper No. 98-GT-110. Associate Technical Editor: R. E. Kielb.

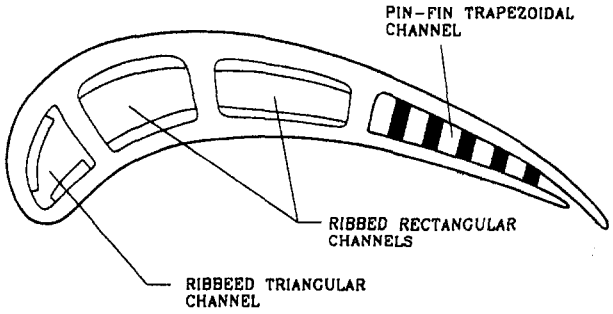

Fig. 1 Cross-sectional view of the modern internally cooled turbine blade

tailed by the external shape of the blade trailing edges (Fig. 1), however, the cooling cavities in this region often have very a narrow *trapezoidal* shape with characteristically small passage aspect ratios. In this circumstance, the pin fins spanning the distance between two principal walls of the trapezoidal passage have different lengths. The heat transfer and friction characteristics in such a channel, especially with lateral outlet flow, should be different from those in rectangular channels. However, to the author's best knowledge, the related studies so far have not considered the overall heat transfer and pressure-drop characteristics in pin-fin trapezoidal ducts. Therefore, the present study experimentally investigates the overall heat transfer and pressure drop in pin-fin trapezoidal ducts with straight and/or lateral outlets. During this work, the log-mean averaged heat transfer and overall pressure drop across the pin-fin duct are obtained for various pin configurations (in-line and staggered), ratios of lateral-to-total flow rate ($0 \leqq \varepsilon \leqq 1.0$), and Reynolds numbers ($6000 \leqq \mathrm{Re} \leqq 40{,}000$) typical of gas turbine airfoil application.

Experimental Apparatus

Figure 2 shows schematically the layout of the experimental apparatus and the detailed construction of the test section. Air from the laboratory room flows through a honeycomb straightener, a bell-mouth inlet, the entrance (unheated) section, and then into the test section. Subsequently, part of the air is drawn laterally by a 3 hp blower; the remainder traverses the test section, then exits through the straight outlet, and is finally pulled downstream by another blower (5 hp). Both streams exit to the outside of building via an exhaust system. The lateral and straight flow rates are controlled by varying the motor speed of the blowers via PWM (Pulse Wave Modulation) inverters, and are measured by the rotameters (with an accuracy of 5 percent) situated downstream of the lateral and straight exits.

The test section is a wide symmetric trapezoidal duct with a array of various length pin fins that models the pin-fin cooling passage in a gas turbine blade. As shown in Fig. 2, the upper and lower walls (i.e., the endwalls) of the test section are heat transfer surfaces, while the left (long) side wall is adiabatic. The right (short) side wall of the test section is either blocked or open depending the test conditions. The heat transfer surface having area of 160 by 160 mm^2 ($W \times L$, Fig. 3(a)) is constructed of a 5-mm-thick aluminum plate associated with a 0.18-mm-thick foil heater. The foil heater is flatly and uniformly adhered on the backside surface of the aluminum plate by using thermal epoxy to ensure good contact. The heated aluminum plate is then mounted flush on a 10-mm-thick bakelite holder. The longer (left) channel side wall, 40 mm in height (H_l, Fig. 3(a)), is machined from a 10-mm-thick bakelite plate, which is held in place by bolts extending through two principal walls and bakelite material. The blockages for the straight and lateral exits are made of balsa wood. These blockages are not attached permanently to the test section. Rather, they are screwed in place from the top and bottom channel walls. The assembly is sealed from air leakage with petrolatum sealant. All outer surfaces of the test section are well surrounded by the glassfiber to prevent the possible heat losses. Twenty-five (5 by 5) aluminum pins with a diameter of 12 mm (d) are well fitted between two heated walls with thermal epoxy in a required arrangement. The aluminum pins are adopted because of their high conductivity and machinability. The length of the aluminum pins varies

Nomenclature

A = total heat transfer area, including the end walls and the pin surfaces, m^2
A_c = cross-sectional area at the test section inlet, m^2
A_l = cross-sectional area at lateral outlet, m^2
AR = aspect ratio the rectangular duct
c_p = specific heat at constant pressure, kJ/kg-K
De = equivalent hydraulic diameter at the trapezoidal duct inlet $= 4A_c/(2W + H_1 + H_2)$, m
d = pin diameter, m
f = Darcy friction factor
G = total mass flux, kg/m^2-s
G_l = mass flux in the lateral duct, kg/m^2-s
H_1 = height of the longer side wall of the trapezoidal duct, m
H_2 = height of the short side wall of the trapezoidal duct, m
K_L = pressure-drop coefficient $= 2\Delta P/(G^2/\rho)$
k_f = air thermal conductivity, W/m-K
L = trapezoidal duct length along streamwise direction, m
l = fin length (or height), m
$\overline{\mathrm{Nu}}$ = log-mean averaged Nusselt number $= Q_c \cdot De/(A \cdot \Delta T_{lm} \cdot k_f)$
$\overline{\mathrm{Nu}}_s$ = log-mean averaged Nusselt number for the developing smooth trapezoidal duct
Pr = Prandtl number
ΔP = pressure drop across the test section, kPa
Q_c = net convective heat from the test section to the coolan, W
Q_e = electrical power dissipated by the foil heater, W
Q_l = total heat losses from the test section, W
Re = Reynolds number $= G \cdot De/\mu$
S_L = longitude spacing between the pins, m
S_T = transverse spacing between the pins, m
T_{bi} = air bulk mean temperature at the test section inlet, K
T_{bl} = bulk mean temperature of air at the lateral exit, K
T_{bo} = average bulk mean temperature of air at the test section exits, K
T_{bs} = bulk mean temperature of air at the straight exit, K
$\bar{T}_w$ = average temperature on the end wall, K
ΔT_{lm} = log-mean temperature difference, Eq. (3), K
W = width of the heated plate, Fig. 3, m
ε = ratio of lateral-to-total flow rate $= G_l A_l / G A_c$
μ = viscosity of the air, kg/s-m^2
ρ = air density, kg/m^3

Subscripts

b = bulk mean
c = cross section or convection
l = lateral or loss
s = smooth or straight
w = wall

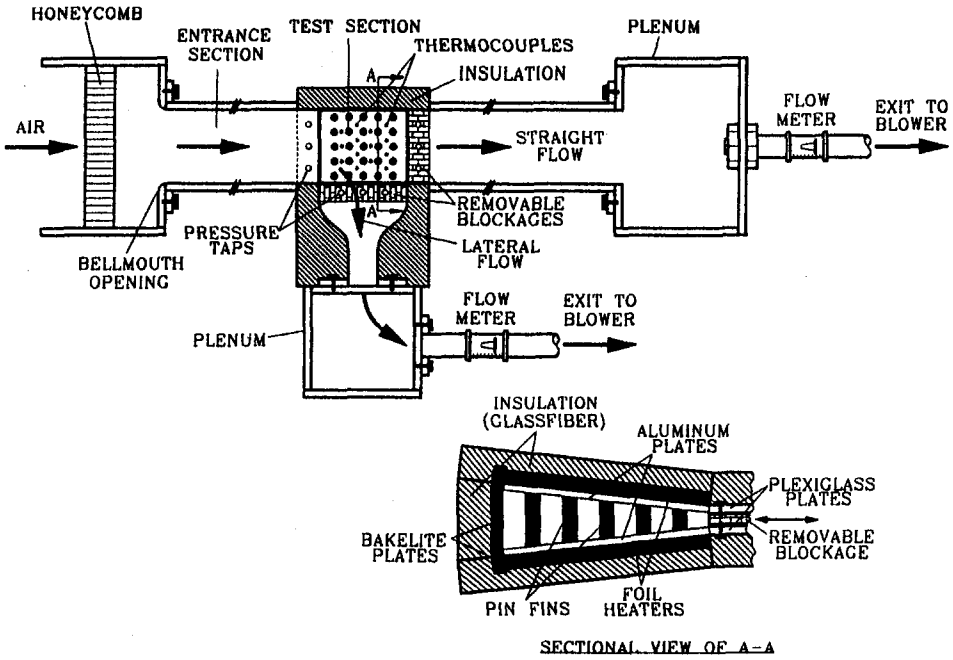

Fig. 2 Sketch of the experimental apparatus and the construction of the test section

from $1.3 \leqq l/d \leqq 3.6$ depending on the location within the trapezoidal duct. The pin spacings both in the longitude (S_L) and in the transverse (S_T) directions are fixed 30 mm (Fig. 3(a)). Note that the thickness of epoxy used at each of the above-mentioned interfaces is less than 0.12 mm. The heat transfer flux to the portion of plate under the pin is reduced by less than 2 percent; thus the thermal resistance of the epoxy is negligible (Hwang, 1997).

As shown in Fig. 2, 14 copper-constantan thermocouples are distributed over the heated plate for wall temperature measurements. The junction-beads of thermocouple (about 0.15 mm in diameter) are carefully embedded in the wall, and then ground flat to ensure that they are flush with the surface. An additional seven thermocouples (one at the duct inlet, three at the straight outlet, and three at the lateral outlet, respectively) are used to measure the air temperature. All temperature signals are first sent to a hybrid recorder (Yokogawa, DA100) for pre-processing, and then are transmitted to a Pentium computer via a Multi-I/O interface for the calculation of the nondimensional parameter. As shown in Fig. 2, on the entrance and two exits of the test section are respectively installed three pressure taps for the static-pressure-drop measurement. They are connected to a micro-differential transducer and a conditioner to amplify the pressure signals, which are subsequently transferred to a digital readout.

A total of eight trapezoidal ducts are tested in the present work. Two of them are smooth, cases A and B; three are inserted with staggered pins (not an equilateral triangular array), cases C, E, and G; and the remaining three are inserted with in-line pins, cases D, F, and H. As for the duct outlet conditions, cases C and D have a single duct exit, while cases G and H have both exits in the straight and lateral directions. The ratio of lateral-to-total flow rate in cases G and H varies from 0.2 to 0.8. Detailed configurations of the investigated pin-fin channels and associated parameters varied are provided by Fig. 3(b) as well as Table 1.

Data Reduction and Uncertainty

Heat Transfer Coefficient. The log-mean averaged heat transfer coefficient of the pin-fin channel is presented customarily in terms of the Nusselt number and is defined as

$$\overline{\mathrm{Nu}} = Q_c \cdot De/(A \cdot \Delta T_{lm} \cdot k_f) \tag{1}$$

where Q_c is the net heat transfer rate from the test section to the coolant, and is calculated by subtracting the heat loss from the supplied electrical power, i.e., $Q_c = Q_e - Q_l$. The electrical power generated from the foil heater is determined from the measured heater resistance and the current through the heater. It is also checked by measuring voltage drop across the heater. The total heat loss can be estimated by the following equation:

$$Q_l = Q_{bl} + Q_{sl} + Q_{al} \tag{2}$$

Q_{bl} represents the conduction loss from the backside of the heated plate to the environment, Q_{sl}, the lateral conduction loss through the two adiabatic side plates to the environment, and Q_{al}, the axial conduction loss through upstream and downstream ends of the heated plates. By using one-dimensional heat conduction analysis, they are estimated to be less than 6.0, 3.0, and 3.0 percent, respectively. To confirm energy conservation during the experiment, the total net heat transfer rate from the test duct to the cooling air is further checked with the cooling air enthalpy rise along the test duct, and a very good agreement is achieved. The log-mean temperature difference, ΔT_{lm}, in Eq. (1) is in terms of $\bar{T}_w$, T_{bi}, and T_{bo}, i.e.,

$$\Delta T_{lm} = \frac{(\bar{T}_w - T_{bi}) - (\bar{T}_w - T_{bo})}{\ln\left[(\bar{T}_w - \bar{T}_{bi})/(\bar{T}_w - \bar{T}_{bo})\right]} \tag{3}$$

The inlet bulk mean air temperature, T_{bi}, is measured by a thermocouple positioned at the test section entrance, typically about 25–27°C. The wall temperature, $\bar{T}_w$, is an averaged value of the 14 thermocouple readings on the heated plate, and is read directly from the hybrid recorder. Note that since the end wall is made of highly conductive aluminum, the 14 thermocouples measure the average wall temperature rather than the local wall temperature. Therefore, in all test runs, the uniformity of the wall temperature is very good, with a maximum variation less than 2.2°C. To further check the temperature uniformity of the entire end wall, an additional thermocouple is instrumented in the region near the remote corner where the heat transfer coefficients are expected to be localized. This temperature reading, however, is only 0.8°C higher than the average wall temperature. Therefore, we should recognize here that, by using the

present test rig, only the average heat transfer coefficients could be obtained. In addition, since the total heat transfer area (A, including the end walls and the pin surfaces) is employed to determine the log-mean average heat transfer coefficients (Eq. (1)), the pin surface temperature should not be too different from the end wall temperature. A simple calculation is done to check the validity of this assumption by using the heat transfer coefficients from a cylinder-in-crossflow correlation by Zhukauskas (1972). It is found that the maximum deviation of the temperature between the pin surface and the end wall is less than 3 percent. The typical difference between the averaged wall temperature and the inlet air temperature is fixed 30 ± 2°C by adjusting the power input the heater. The common outlet bulk-mean air temperature based on the two streams, T_{bo}, is evaluated as

$$T_{bo} = (1 - \varepsilon)T_{bs} + \varepsilon T_{bl} \tag{4}$$

where ε is the ratio of lateral-to-total flow rate. T_{bs} and T_{bl} are the bulk mean temperatures of the exiting air, and are respectively measured by three thermocouples positioned at the straight and lateral outlets of the test section. Also, by using an energy balance, the common outlet bulk mean air temperature can be readily calculated as $T_{bo} = T_{bi} + Q_c/(Gc_p)$. It is found that the agreement of T_{bo} obtained from these two methods is very good, typically within approximately 5 percent in discrepancy.

UNIT:mm

W	L	S_L	S_T	H_1	H_2	d
160	160	30	30	48	12	12

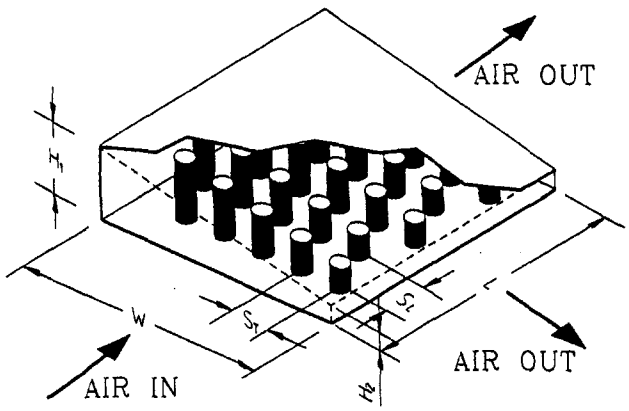

Fig. 3(*a*) Dimensions of the pin-fin trapezoidal duct investigated

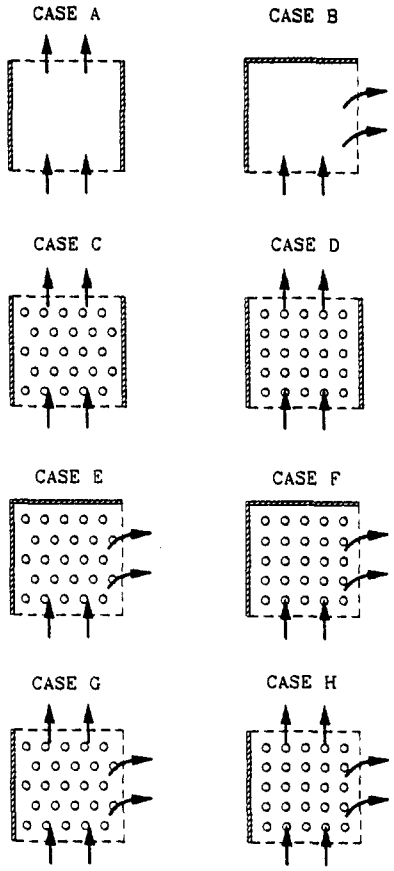

Fig. 3(*b*) Schematic of top view of pin-fin channels from cases A to H

Table 1 Test section configuration

Case	Pin Arrangement	Number of Pins	Straight Exit	Lateral Exit	ε
A	SMOOTH	0	OPEN	BLOCKED	0
B	SMOOTH	0	BLOCKED	OPEN	1.0
C	STAGGERED	5×5	OPEN	BLOCKED	0
D	IN LINE	5×5	OPEN	BLOCKED	0
E	STAGGERED	5×5	BLOCKED	OPEN	1.0
F	IN LINE	5×5	BLOCKED	OPEN	1.0
G	STAGGERED	5×5	OPEN	OPEN	0.2-0.8
H	IN LINE	5×5	OPEN	OPEN	0.2-0.8

Pressure-Drop Coefficient. The pressure drop across the finite-length duct of trapezoidal cross section can be made dimensionless as

$$K_L = 2\Delta P/(G^2/\rho) \tag{5}$$

This nondimensional pressure-drop parameter can be represented by multiplying the Darcy friction factor by the dimensionless length L/De, i.e.,

$$K_L = f \cdot (L/De) \tag{6}$$

The pressure-drop coefficient obtained is based on adiabatic conditions (i.e., test without heating).

Reynolds Number. The Reynolds number used herein is based on the average velocity, i.e.,

$$\mathrm{Re} = G \cdot De/\mu \tag{7}$$

where De is the equivalent hydraulic of the trapezoidal duct, i.e., $4A_c/(2W + H_1 + H_2)$. This reduction is similar to that in VanFossen (1982), but is different from that in Mezeger et al. (1982) and Kumaran et al. (1991), in which the Reynolds number is based on the pin diameter and the maximum velocity in the duct. This is not peculiar because the overall heat transfer in trapezoidal ducts, either with or without pin-fin enhancement, is interesting in the present study; while the previous works were devoted to pin-fin heat transfer. The Reynolds number ranges from 6000 to 40000, which is similar to the range of interest for the turbine cooling application (VanFossen, 1982).

Uncertainty. The individual contributions to the uncertainties of the nondimensional parameters for each of the measured physical properties are summarized in Table 2. By using the estimation method of Kline and McClintock (1953), the maximum uncertainties of the investigated nondimensional parameters are as follows: Re, 6.5 percent; $\overline{\mathrm{Nu}}$, 8.4 percent; and K_L, 7.6 percent.

Table 2 Typical nondimensional interval for the relevant variables

Variables	Uncertainty
Air density, ρ	± 1.3 %
Specific heat of air, c_p	± 3.0 %
Dynamic viscosity of air, ν	± 2.9 %
Air thermal conductivity, k_f	± 1.5 %
Equivalent duct hydraulic diameter, De	± 0.5 %
Air mass flux, G	± 5.4 %
Log-mean temperature difference, $\triangle T_{lm}$	± 3.0 %
Net heat flux, Q_c	± 7.6 %
Pressure difference, $\triangle P$	± 5.1 %

Results and Discussion

Log-Mean Averaged Heat Transfer Coefficient

Smooth Duct. It is important to validate the present experimental procedure and results by comparing the present data with previous works. Figure 4 shows the comparison of overall heat transfer between the present smooth-trapezoidal-duct results and a correlation (dashed line, McAdams, 1954) of length-mean heat transfer for developing turbulent pipe flow. The circular and triangular symbols here pertain to the results of cases A and B, respectively (i.e., ducts with straight exit and lateral exit, respectively). Since the present trapezoidal test section has only about 3.7 times the duct hydraulic diameter in streamwise distance, the entrance-length effect on the overall heat transfer in this finite-length test section should be significant. To make the comparison fairly, the correlation selected in Fig. 4, which was modified from the Dittus–Boelter equation (Dittus and Bolter, 1930), has considered the entrance-length effect. It is observed from this figure that, within the range of Reynolds number investigated, the agreement between the modified correlation and the present experimental data of case A is very good. This good agreement gives confidence that the present measurement technique and the data analysis are working well. Further observing Fig. 4 has that the log-mean averaged Nusselt number for case B is higher than that for case A. The higher heat transfer for the lateral-outlet-flow duct may be attributed to the acceleration of coolant through the convergent lateral exit and, partly, the significant flow turning effects.

Effect of Outlet-Flow Direction. Figures 5–7 show the overall heat transfer in the present trapezoidal ducts with pin arrays. Attention is first focused on Fig. 5 for the results that ducts have a single exit (i.e., cases C to F). In this figure, the log-mean averaged Nusselt numbers are shown as a function of Reynolds number. The corresponding smooth-walled results are also included for comparison. The symbols represent the actual experiments and the solid lines passing through these symbols are curve fits of the forms

$$\overline{\mathrm{Nu}} = a\,\mathrm{Re}^{b} \tag{8}$$

where the values of a and b are listed in Table 3. The maximum deviation between the equation above and the experimental data shown in Fig. 5 is less than 5 percent. From Fig. 5 and Table 3, the log-mean averaged Nusselt number in the pin-fin trapezoidal duct increases with increasing Reynolds number. In the trapezoidal duct with straight outlet flow, the staggered pin arrangement (case C) has higher overall heat transfer than the in-line pin arrangement (case D). Physically, heat transfer enhancement is favored by the more tortuous flow of a staggered arrangement (Incropera and DeWitt, 1994). As for the lateral-outlet-flow ducts (cases E and F), interestingly, the log-mean averaged heat transfer coefficient is insensitive to the pin arrangements investigated. This is very reasonable because, in these two cases, the main flow has to turn to the lateral exit totally; in such a way, the pin array for case F appears to be staggered relative to the turning flow. Therefore, with respect to the turning main flow, the pin arrangements for cases E and

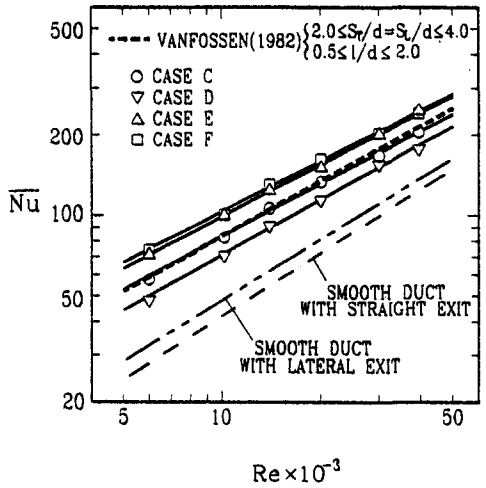

Fig. 5 Reynolds number dependence of log-mean-averaged Nusselt number for cases C to F

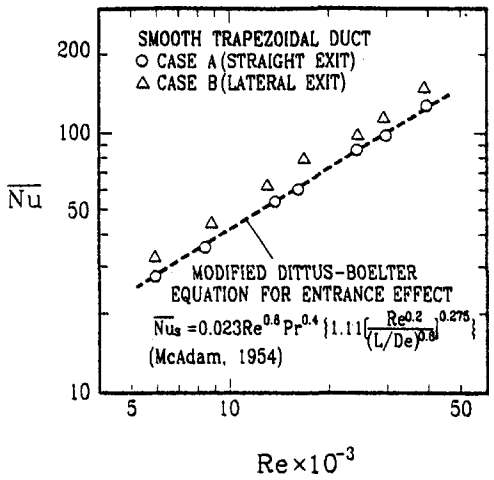

Fig. 4 Comparison of average heat transfer of the present smooth trapezoidal duct and the previous correlation

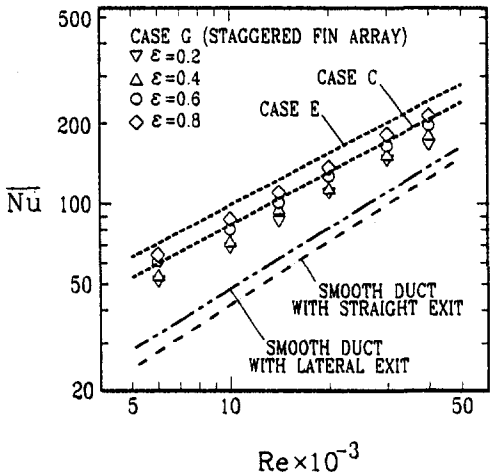

Fig. 6 Reynolds number dependence of log-mean-averaged Nusselt number for case G

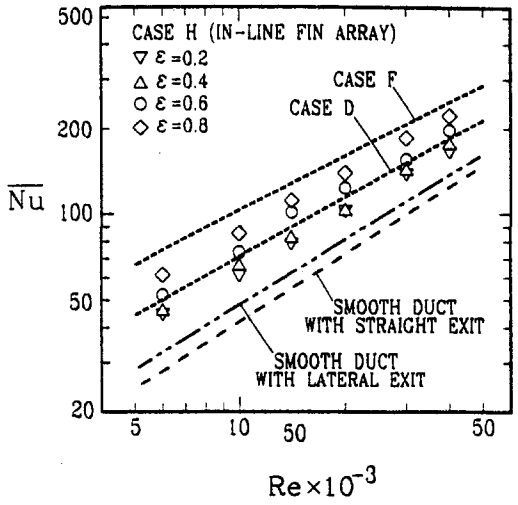

Fig. 7 Reynolds number dependence of log-mean-averaged Nusselt number for case H

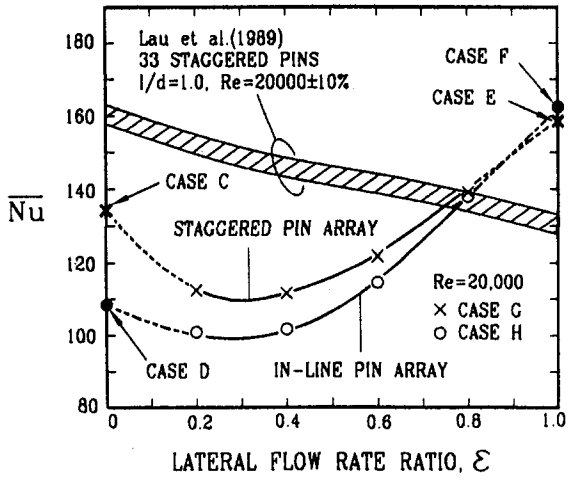

Fig. 8 Effect of the ratio of lateral-to-total flow rate on log-mean-averaged Nusselt number for staggered and in-line pin arrays

F do not differ from each other too much. It is further observed from this figure that, for both the staggered and the in-line fashions, the lateral-outlet-flow ducts (cases E and F) perform better as heat transfer coefficients than the corresponding straight-outlet-flow ducts (cases C and D). In comparison of the smooth-duct results with straight outlet flow (centerline), the enhancement in the overall heat transfer is up to about 120, 70, 160, and 160 percent for cases C, D, E, and F, respectively, in the range of Reynolds number investigated.

It is worthwhile to make a comparison of the log-mean averaged heat transfer coefficients in the present pin-fin trapezoidal duct and those in previous pin-fin rectangular ducts. The dashed line shown in Fig. 5 is the VanFossen correlation (VanFossen, 1982) for a straight-outlet-flow channel with staggered pin array. His data were obtained in a rectangular test section with four rows of copper and wooden short pins (l/d = 0.5, and 2.0); while the present data of case C are obtained in a trapezoidal duct with five rows of aluminum pins of an averaged pin length l/d = 2.0. Figure 5 shows that the present data of case C compare well with his correlation.

Effect of Lateral Flow Rate Ratio. The overall heat transfer in the trapezoidal ducts with straight as well as lateral exits (i.e., both exits are open) is shown in Figs. 6 and 7, respectively, for the staggered (case G) and in-line (case H) pin arrangements. Experimental data for the ratios of lateral-to-total flow rate (ε) from 0.2 to 0.8 are shown in these figures. For convenience, the results that pin-fin ducts have only a single exit (cases C to F, dashed lines) are also plotted on these figures. It is found in Figs. 6 and 7 that the log-mean averaged Nusselt number for the small lateral flow rates (ε = 0.2 and 0.4) is lower than that without lateral outlet flow (cases C and D). But at high-lateral-flow conditions, say ε = 0.8, the $\overline{Nu}$ is higher than that without lateral outlet flow (cases C and D). The explanation of this fact is as follows. When both the straight exit and the lateral exit are open, the fluid either flows straight downstream or turns laterally; therefore the apparent cross-sectional area for the throughflow is higher than that with a single exit only. The increase in the duct cross-sectional area reduces the averaged throughflow velocity, hence overall heat transfer. However, further increasing the lateral flow rate ($\varepsilon \geqq 0.6$ or 0.8) adds the effect of flow acceleration through the convergent lateral exit as well as the flow turning effect that, in turn, augments the overall heat transfer.

Table 3 Coefficients and exponents of heat transfer correlation

CASE	$\overline{Nu} = a\,Re^{b}$	
	a	b
C	0.188	0.662
D	0.118	0.690
E	0.254	0.651
F	0.288	0.636

For clarity, the effects of the ratio of lateral-to-total flow rate on the log-mean-averaged Nusselt number in trapezoidal ducts are further shown in Fig. 8 for a fixed Reynolds number of Re = 20,000. Results of the single-outlet ducts, i.e., cases C to F, are also provided for extrapolation. The symbols are actual experiments and the solid lines passing through these symbols are curve-fitting results. Both the staggered and the in-line pin configurations reveal a general trend, namely, the log-mean-averaged Nusselt number starts with a decrease with increasing ε, then sharply increases with increasing ε after about $\varepsilon \geqq 0.4$, and finally approaches a maximum value at ε = 1.0. The log-mean-averaged heat transfer coefficient in the trapezoidal duct with staggered pin array has a local minimum at approximately ε = 0.3. However, for the in-line pin array, the rate of decrease in the log-mean-averaged Nusselt number in the low ε range is not as significant as that for the staggered pin array. This is because the in-line pin configuration looks like a staggered pin configuration relative to the turning flow, which positively enhances the log-mean-averaged heat transfer. Consequently, the decrease in overall heat transfer due to the reduction in the throughflow velocity mentioned above is somewhat compensated by this effect. Another notable feature is that at high lateral flow conditions, say $\varepsilon \geqq 0.8$, the log-mean-averaged Nusselt number seems to be unaffected by the pin arrangement. The previous results in a rectangular pin-fin duct by Lau et al. (1989) are shown by a data band in this figure for comparison. Their data showed that the log-mean-averaged Nusselt number is decreased monotonically with the increase in the ratio of lateral-to-total flow rate from ε = 0 to 1.0. The disagreement in the ε dependence of the log-mean-averaged Nusselt number between the present and previous data may be due to the difference in the cross-sectional area of the test duct investigated. Further investigation is need to examine in detail the effect of ε on the heat transfer characteristics in ducts of different cross sections.

Pressure Drops

Smooth Duct. Figure 9 shows the overall pressure-drop coefficient of the present smooth trapezoidal ducts as a function of Reynolds number. First, the present pressure-drop results

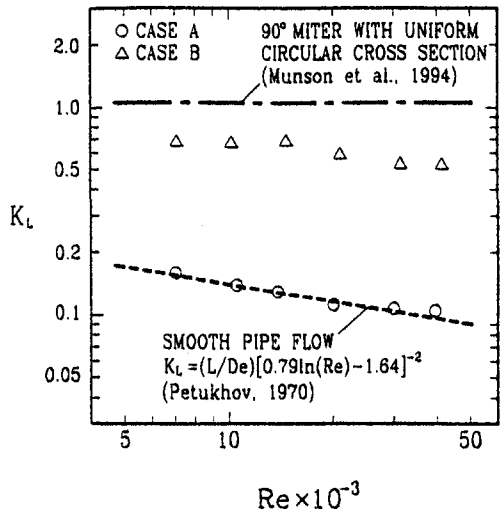

Fig. 9 Comparison of overall friction coefficient present smooth trapezoidal ducts with previous correlation

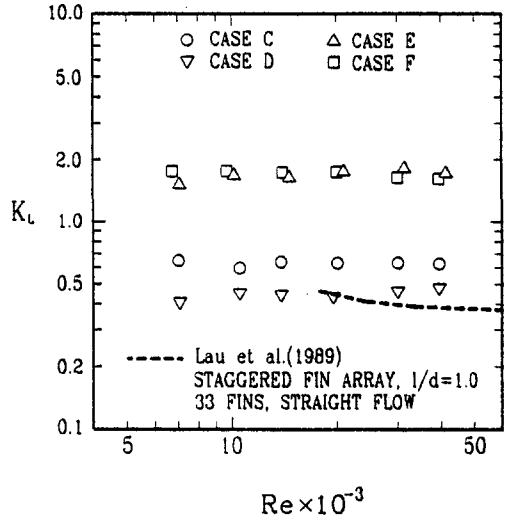

Fig. 10 Reynolds number dependence of overall pressure-drop coefficient of the present pin-fin trapezoidal ducts for cases C to F

for the trapezoidal duct with straight outlet flow (case A) are compared with the previous correlation (Petukhov, 1970) for the smooth pipe flow, and a good agreement is achieved. This comparison confirms again the reliability of the present data and the validation of the present experimental procedure. As for the trapezoidal duct with lateral exit (case B), physically, the flow in this situation is largely similar to that the fluid flows though a 90 deg sharp bend. Therefore, the previous results of pressure drop across a 90 deg miter with uniform cross section at duct entrance and exit (Munson et al., 1994) is plotted for comparison. It is observed from this figure that the overall pressure-drop coefficients for case B are significantly higher than those in the straight-outlet-flow duct (case A), but lower than those across the 90 deg miter. This may be because case B results in the separated region of the flow near the concave corner formed between the longer side wall and the blocked straight exit, and the swirling secondary flow that occurs due to the imbalance of the centripetal forces as a result of the curvature of the duct centerline. The reason for the later fact may be explained as that in the present trapezoidal duct the convergence in the flow cross-sectional area from the duct entrance to the lateral exit reduces the pressure drops.

Pin-Fin Duct. The pressure drops across the present trapezoidal ducts with staggered and in-line pin arrays are shown in Fig. 10 as a function of Reynolds number. In this figure, the previous experimental results (Lau et al., 1989) for the straight-outlet-flow duct are also plotted for comparison. The results of Lau et al. (1989) were obtained from a 15:1 rectangular channel with 33 pins. The pin length-to-diameter ratio and pin spacing-to-diameter ratio were fixed at $l/d = 1.0$ and $S_L/d = S_T/d = 2.5$, respectively. The Reynolds number was developed in terms of the pin diameter and the maximum flow velocity in the duct in their work. Accordingly, the data of Lau et al. (1989) shown in Fig. 10 have been recast for the common basis. It is seen that the present data of case C (circular symbols) are higher than Lau's data. This may be attributed to the taller pins employed in the present work. Qualitatively, the data of the present and previous works reveal that the overall pressure-drop coefficients are nearly independent of the Reynolds number and stay almost at a constant value as the Reynolds number varies. Similar trends were observed by several investigators (Metzger et al., 1982; Lau et al., 1989).

It is further shown in Fig. 10 that the pin-fin trapezoidal ducts with lateral exit (cases E and F) have much higher pressure-drop coefficients than those with straight exit (cases C and D). Comparing to the results of the smooth duct with a straight outlet flow (case A), the pressure-drop coefficients are about 12 to 15-fold, and 3 to 5-fold, respectively, for the trapezoidal duct with lateral exit (cases E and F) and that with straight exit (cases C and D). As for the effect of pin arrangement, the staggered pin array pays more pressure-drop penalties than the in-line pin array in the trapezoidal duct with straight exit. In the trapezoidal duct with lateral exit, however, the in-line and staggered pin arrays have almost the same overall pressure-drop coefficients.

Concluding Remarks

Overall heat transfer and pressure drop in pin-fin trapezoidal ducts, simulating the trailing edge cooling cavities of turbine blades, have been performed experimentally. This study has extended the rectangular-duct works originated by Metzger et al. (1982) and VanFossen (1982) to a more realistic geometry. In addition, the effect of the lateral-to-total flow rate ratio on heat transfer and pressure drop in a trapezoidal duct, which has not been considered before, has been examined. Main findings based on the experiment are:

1 The log-mean-averaged Nusselt number for the smooth trapezoidal duct with lateral exit (case B) is higher than that with straight exit (case A), which may be attributed to the acceleration of coolant through the convergent lateral exit as well as the significant flow turning effects for the lateral-outlet-flow case.

2 In the trapezoidal duct with lateral exit only, the log-mean-averaged Nusselt numbers for the in-line pin array are largely identical to those for the staggered pin array. This trend is different from that in the trapezoidal duct with straight outlet flow, in which the staggered pin array has higher heat transfer than the in-line pin array.

3 For the duct with straight as well as lateral outlets, the effect of ε on the log-mean averaged Nusselt number in previous rectangular ducts is significantly different from that in the present trapezoidal ducts. In previous rectangular ducts, the log-mean-averaged Nusselt number decreases monotonically with increasing ε. In the present trapezoidal duct, the staggered pin array has a local minimum log-mean-averaged Nusselt number at about $\varepsilon = 0.3$, while the log-mean-averaged Nusselt number is relatively unaltered before $\varepsilon \leqq 0.4$ for the in-line pin array. For both pin configurations, the log-mean-averaged Nusselt number increases with increasing lateral flow rate ($\varepsilon \geqq 0.4$). After $\varepsilon \geqq 0.8$, the log-mean-averaged Nusselt number is nearly independent of the pin configuration.

4 As for the duct with a straight exit, the staggered pin array pays more pressure-drop penalty as compared with the in-line pin array. In the trapezoidal duct with a lateral exit, however, the in-line and staggered pin arrays have almost the same overall pressure-drop coefficients.

5 Future efforts are required for the investigation of local heat transfer coefficient distributions on the endwall as well as the pin-fin surfaces in a pin-fin trapezoidal duct.

Acknowledgments

This work was sponsored by the National Science Council of the Republic of China under contract No. NSC 85-2212-E-216-003.

References

Brigham, B. A., and VanFossen, G. J., 1984, "Length to Diameter Ratio and Row Number Effects in Short Pin Fin Heat Transfer," ASME *Journal of Engineering for Gas Turbines and Power,* Vol. 106, pp. 241–245.

Dittus, F. W., and Boelter, L. M. K., 1930, University of California at Berkeley, *Publications in Engineering,* Vol. 2, p. 443.

Hwang, J. J., 1997, "Turbulent Heat Transfer and Fluid Flow a Porous-Baffled Channel," *AIAA J. Thermophysics and Heat Transfer,* Vol. 11, pp. 429–436.

Incropera, F. P., and DeWitt, D. P., 1994, *Introduction to Heat Transfer,* 3rd ed., Wiley, New York.

Kline, S. J., and McClintock, F. A., 1953, "Describing Uncertainties on Single-Sample Experiments," *Mechanical Engineering,* Vol. 75, Jan., pp. 3–8.

Kumaran, T. K., Han, J. C., and Lau, S. C., 1991, "Augmented Heat Transfer in a Pin Fin Channel With Short and Long Ejection Holes," *Int. J. Heat Mass Transfer,* Vol. 34, pp. 2617–2628.

Lau, S. C., Kim, Y. S., and Han, J. C., 1987, "Local Endwall Heat/Mass Transfer Distributions in Pin Fin Channels," *AIAA J. Thermophysics and Heat Transfer,* Vol. 1, pp. 365–372.

Lau, S. C., Han, J. C., and Kim, Y. S., 1989, "Turbulent Heat Transfer and Friction in Pin Fin Channels With Lateral Flow Injection," ASME *Journal of Heat Transfer,* Vol. 111, pp. 51–58.

McAdams, W. H., 1954, *Heat Transmission,* 3rd ed., McGraw-Hill, New York.

Metzger, D. E., Berry, R. A., and Bronson, J. P., 1982, "Developing Heat Transfer in Rectangular Ducts With Staggered Pin Fins," ASME *Journal of Heat Transfer,* Vol. 104, pp. 700–706.

Metzger, D. E., and Haley, W. W. P., 1982, "Heat Transfer Experiments and Flow Visualization for Arrays of Short Pin Fins," ASME Paper No. 82-GT-138.

Metzger, D. E., Fan, C. S., and Haley, S. W., 1984, "Effects of Pin Shape and Array Orientation on Heat Transfer and Pressure Loss in Pin Fin Arrays," ASME *Journal of Heat Transfer,* Vol. 106, pp. 252–257.

Munson, B. R., Young, D. F., and Okiishi, T. H., 1994, *Fundamentals of Fluid Mechanics,* 2nd ed., Wiley, New York.

Petukhov, B. S., 1970, *Advances in Heat Transfer,* Vol. 6, pp. 503–504, Academic Press, New York.

VanFossen, G. J., 1982, "Heat-Transfer Coefficients for Staggered Arrays of Short Pin Fins," ASME *Journal of Heat Transfer,* Vol. 104, pp. 268–274.

Zhukauskas, A., 1972, "Heat Transfer From Tubes in Cross Flow," *Advances in Heat Transfer,* Vol. 8, Academic Press, New York.

45 deg Round-Corner Rib Heat Transfer Coefficient Measurements in a Square Channel

M. E. Taslim

A. Lengkong

Department of Mechanical, Industrial, and Manufacturing Engineering, Northeastern University, Boston, MA 02115

Cooling channels, roughened with repeated ribs, are commonly employed as a means of cooling turbine blades. The increased level of mixing induced by these ribs enhances the convective heat transfer in the blade cooling cavities. Many previous investigations have focused on the heat transfer coefficient on the surfaces between these ribs and only a few studies report the heat transfer coefficient on the rib surfaces themselves. The present study investigated the heat transfer coefficient on the surfaces of 45 deg, round-corner ribs. Three staggered rib geometries corresponding to blockage ratios of 0.133, 0.167, and 0.25 were tested in a square channel for pitch-to-height ratios of 5, 8.5, and 10, and for two distinct thermal boundary conditions of heated and unheated channel wall. Comparisons were made between the surface-averaged heat transfer coefficients and channel friction factors for sharp- and round-corner ribs and 45 versus 90 deg ribs, reported previously. Heat transfer coefficients of the furthest upstream rib and that of a typical rib located in the middle of the rib-roughened region were also compared. It was concluded that: (a) For the geometries tested, the rib average heat transfer coefficient was much higher than that for the area between the ribs. (b) The general effect of rounding the rib corners was a decrease in both rib heat transfer coefficient and channel pressure drop. (c) For the highest blockage ratio ribs ($e/D_h = 0.25$), 90 deg ribs performed superior to 45 deg ribs. However, this trend reversed for smaller rib blockage ratios. (d) Heat transfer coefficients for the two smaller rib geometries ($e/D_h = 0.133$ and 0.167) did not vary significantly with the pitch-to-height ratio in the range tested. However, the heat transfer coefficient for the high blockage rib geometry increased significantly as the ribs were brought closer to each other. (e) Under otherwise identical conditions, ribs in the furthest upstream position produced lower heat transfer coefficients than those in the midstream position. (f) Rib thermal performance decreased with the rib blockage ratio. The smallest rib geometry ($e/D_h = 0.133$) at a pitch-to-height ratio of 10 and the largest rib geometry ($e/D_h = 0.25$) at a pitch-to-height ratio of 5, both in midstream position, produced the highest and the lowest thermal performances, respectively.

Introduction

Various cooling methods have been developed over the years to ensure that gas turbine blade metal temperatures are maintained at a level consistent with airfoil design life. The objective in turbine blade cooling is to achieve maximum internal heat transfer coefficients while minimizing the coolant flow rate. One such method is to route coolant air through serpentine channels within the airfoil and remove heat convectively from the blade. The coolant is then ejected either at the tip of the blade, through the cooling slots along the trailing edge or film holes on the airfoil surface. Heat transfer coefficients in the cooling passages can be increased by roughening their walls. One such method, used over the past 25 years in gas turbine blade and nozzle internal cooling, is to cast ribs on the walls of the cooling passages. These ribs, also called turbulators, increase the level of mixing of the cooler core air with the warmer air close to the channel wall and restart the boundary layer after flow reattachment between ribs resulting in enhanced heat transfer coefficients.

Geometric parameters such as channel aspect ratio (AR), rib height-to-passage hydraulic diameter (e/D_h) or blockage ratio, rib angle of attack (α), the manner in which the ribs are positioned relative to one another (in-line, staggered, criss-cross, etc.), rib pitch-to-height ratio (S/e) and rib shape (round versus sharp corners, fillets, rib aspect ratio (AR_r), and skewness toward the flow direction) have pronounced effects on both local and overall heat transfer coefficients. Some of these effects were studied by different investigators, such as Abuaf et al. (1986), Burggraf (1970), Chandra et al. (1988), Chandra and Han (1989), Han (1984), Han et al. (1978, 1985, 1992), Metzger et al. (1983, 1988, 1990), Taslim et al. (1988a, b, 1991, 1994, 1996), Webb et al. (1971). Considerable data are available on the heat transfer coefficient on the passage surface between the ribs. However, the heat transfer coefficients on the surface of the ribs themselves have not been investigated to the same extent.

Several investigators have studied the flow and heat transfer associated with the ribs in rib-roughened channels. Solntsev et al. (1973) conducted an experimental investigation on heat transfer in the vicinity of sudden two- and three-dimensional steps of circular and square cross-sectional areas mounted on a flat surface in an open channel. They reported enhancements in heat transfer coefficient for a range of Reynolds numbers between 10^4 to 10^5.

Contributed by the International Gas Turbine Institute and presented at the 43rd International Gas Turbine and Aeroengine Congress and Exhibition, Stockholm, Sweden, June 2–5, 1998. Manuscript received by the International Gas Turbine Institute February 1998. Paper No. 98-GT-176. Associate Technical Editor: R. E. Kielb.

Berger and Hau (1979) used an electrochemical analogue technique to measure mass/heat transfer on square ribs as well as on the wall surface between the ribs in a pipe. For a blockage ratio (e/d) of 0.0364 and a range of Reynolds numbers between 10,000 and 25,000, they varied the rib pitch-to-height ratio from 3 to 10. At the Reynolds number of 10^4, they showed enhancements, compared to smooth channels, in mass (heat) transfer on the ribs in the order of 4.4 and 5.2 for pitch-to-height ratios of 10 and 7, respectively.

Metzger et al. (1988) used a thermal transient technique to examine the contribution of the rib heat transfer to the overall heat transfer of a rib-roughened wall with variations in rib angle of attack and pitch. Square ribs representing a blockage ratio of 0.14 were mounted on only one wider side of a 0.154 aspect ratio rectangular channel. The main conclusions were that heat transfer on the rib surface significantly contributed to the overall rib-roughened wall heat transfer and this contribution mainly depended on the rib pitch-to-height spacing, with very little effect from the rib angle.

Lockett and Collins (1990) used a holographic interferometry technique to measure heat transfer coefficient in a 0.25 aspect ratio rectangular channel. Square ribs with sharp as well as round top corners representing a blockage ratio, e/D_h, of 0.067 and a pitch-to-height ratio of 7.2 were mounted on one of the wider sides of the channel, perpendicular to the flow direction. They reported overall enhancements in heat transfer of up to 2.24 for the Reynolds number of 7400.

Liou et al. (1991) performed numerical as well as experimental investigation of turbulent flow in a 4:1 aspect ratio rectangular channel roughened on two opposite wider sides with square ribs in an in-line arrangement perpendicular to the flow direction. The rib blockage ratio, e/D_h, was 0.081 and four pitch-to-height ratios of 5, 10, 15, and 20 were examined at a fixed Reynolds number of 33,000. Two-dimensional Navier–Stokes equations in elliptic form in conjunction with the $k-\epsilon$ turbulence model were solved numerically and a holographic interferometry technique was used in the experimental part. They reported an enhancement in heat transfer on the rib surface of 3.1.

Sato et al. (1992) investigated the flow characteristics and heat transfer in a rectangular channel with a total of 20 square ribs on two opposite walls in staggered, in-line, and quarter-pitch-shift arrangements. The channel aspect ratio was 0.2 and the ribs, mounted on the two wider sides of the channel, had a blockage ratio of 0.12. Details of the flow and heat transfer over a typical rib-roughened section (including the rib surface) well downstream of the first rib were presented. They concluded that the staggered arrangement had a better heat transfer performance than the other two arrangements.

Dawes (1993) solved the three-dimensional Navier–Stokes equations in a rotating serpentine coolant passage of cylindrical geometry roughened with square ribs. Rib blockage, e/d, and pitch-to-height ratios were 0.2 and 10, respectively. Results of this work were compared with other numerical and experimental works.

Liou and Hwang (1993) also used the holographic interferometry technique to measure the heat transfer coefficient and friction factor in a 0.25 aspect ratio rectangular channel with three rib shapes including a square rib geometry mounted on two opposite wider sides in an in-line arrangement perpendicular to the flow direction. For a blockage ratio of 0.08, they tested four rib pitch-to-height ratios of 8, 10, 15, and 20 for a range of Reynolds numbers between 7800 and 50,000. The heat transfer coefficient was measured over the ribs as well as the wall surfaces between the ribs. They reported overall heat transfer coefficient enhancements, with respect to an all-smooth-wall-channel, in the order of 2.2 and 2.7 for semi-cylindrical and square ribs, respectively.

Taslim and Wadsworth (1997) reported on the rib surface-averaged heat transfer coefficients in a square channel. Thirteen rib geometries including three blockage ratios and four pitch-to-height ratios were tested. Sharp corner ribs were mounted on two opposite walls of the channel at a 90 deg angle with respect to the flow direction in a staggered arrangement. A major conclusion of their study was that the rib surface-average heat transfer coefficient was much higher than that for the area between the ribs (h_{floor}). Therefore, the contribution of the ribs to the overall heat transfer in a rib-roughened passage is significant. They showed that for a typical rib arrangement the $h_{\text{rib}}A_{\text{rib}}$ can be as high as 33 to 53 percent of $h_{\text{overall}}A_{\text{total}}$. Other conclusions were that (a) for sharp-edged ribs, a pitch-to-height ratio of 8.5 produced the highest heat transfer coefficient, and (b) heat transfer coefficient on ribs in the furthest upstream position was lower than that on the midchannel ribs.

Korotky and Taslim (1998) and Taslim and Korotky (1998) tested two sets of rib geometries with rib aspect ratios of 1 and 0.667. All ribs had round top corners and made a 90 deg angle

Nomenclature

a = channel height (Fig. 1)
b = channel width (Fig. 1)
A = channel cross-sectional area without ribs = ab
A_{floor} = wall heat transfer area between two ribs
A_{rib} = rib total heat transfer area (three sides)
A_{total} = total heat transfer area = $A_{\text{rib}} + A_{\text{floor}}$
AR = channel aspect ratio = b/a
AR_r = rib aspect ratio = e/w
D_h = hydraulic diameter based on the smooth cross section = $4A/P = a$
e = rib height
$\bar{f}$ = Darcy friction factor = $\Delta P(D_h/L)/(1/2\rho U_m^2)$
$\bar{f}_s$ = Darcy friction factor in an all-smooth-wall channel
h_{floor} = average heat transfer coefficient on the wall surface between a pair of ribs
h_{overall} = overall average heat transfer coefficient on a rib and on the wall surface between a pair of ribs
h_{rib} = rib average heat transfer coefficient = $q/(T_s - T_m)$
i = current through the heater inside the copper rib
k = air thermal conductivity
L = length of the rib-roughened portion of the test section (Fig. 1)
$\dot{m}$ = air mass flow rate
$\overline{\text{Nu}}$ = rib average Nusselt number = $h_{\text{rib}}D_h/k$
$\overline{\text{Nu}}_s$ = average Nusselt number in a smooth channel
P = channel perimeter without ribs
Pr = Prandtl number
q = net heat flux from the copper rib three surfaces = $(vi - Q_{\text{loss}})/A_{\text{rib}}$
Q_{loss} = heat losses from the copper rib by radiation and conduction
r = Rib corner radius
Re = Reynolds number = $\rho U_m D_h/\mu$
S = rib pitch (center-to-center)
T_f = film temperature = $0.5(T_s + T_m)$
T_m = air mixed mean temperature at copper rib location
T_s = copper rib surface temperature
U_m = air mean velocity
v = voltage drop across the heater inside the copper rib
w = rib width
X = distance between the instrumented rib and test section entrance (Fig. 1)
α = rib angle of attack
ΔP = pressure drop across the rib-roughened portion of the test section
μ = air dynamic viscosity
ρ = air density

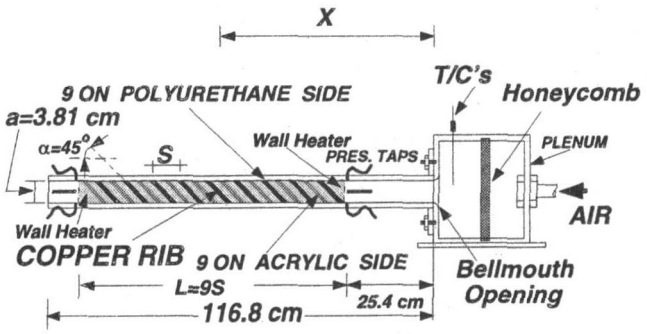

(1a) Test Section Layout

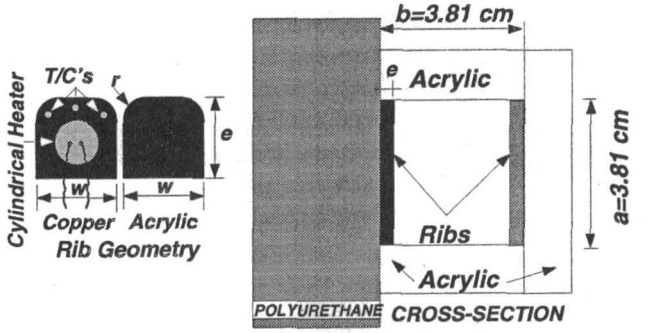

(1b) Channel Cross-Section and Rib Geometry

Fig. 1 Schematic of a typical test section

with the flow direction. They concluded that the general effect of rounding was a decrease in midstream rib heat transfer coefficient and an increase for the ribs in the furthest upstream position. The effects of low-aspect-ratio ribs were a decrease in channel friction factor for all rib geometries, a decrease in the rib heat transfer coefficient for the highest rib blockage ratio ($e/D_h = 0.25$) and a heat transfer increase for the medium ($e/D_h = 0.167$) and smallest ($e/D_h = 0.133$) blockage ratios.

Taslim and Lengkong (1998) reported rib heat transfer coefficients on 45 deg sharp-cornered ribs and compared the results with those of 90 deg sharp-cornered ribs under otherwise identical conditions. They concluded that, for their highest blockage ratio (0.25), 45 deg rib heat transfer results were close to those of 90 deg ribs. However, as the blockage ratio decreased, 45 deg ribs produced higher heat transfer coefficients.

In small gas turbine blades and nozzle airfoils with small cooling passages and relatively large ribs, the rib surfaces comprise a large portion of the passage heat transfer area. Therefore, an accurate account of the heat transfer coefficient on the rib surfaces is critical in the overall design of the blade and nozzle cooling systems. The objective of this investigation, which is the continuation of an extensive program on the measurement of heat transfer coefficient on the rib surfaces was, while isolating the ribs from the wall surface thermally, (a) to measure the overall heat transfer coefficient on the rib surface, (b) to study the effects of pitch-to-height ratio (S/e) and blockage ratio (e/D_h), (c) to study the effects rib orientation (furthest upstream position or in the middle of the channel rib-roughened portion) have on the rib surface heat transfer coefficient, (d) to compare 45 deg round-cornered rib results with with those of 45 deg sharp-cornered ribs, and (e) to compare 45 deg rib results with previously reported 90 deg rib results.

Test Sections

Figure 1 shows schematically the layout and cross-sectional area of a typical test section. Rib geometry details are shown in Table 1. All test sections, with a length of 116.84 cm, had a square of 3.81 cm by 3.81 cm cross-sectional area. Three walls of these channels were made of 1.27-cm-thick clear acrylic plastic. The fourth wall, on which the surface heaters and instrumented copper rib were mounted and all measurements were taken, was made of a 7.62-cm-thick machinable polyurethane slab. Eighteen ribs of square cross section with round corners were symmetrically staggered on the polyurethane wall and its opposite acrylic wall (nine on each) at 45 deg angle of attack to the air flow. The entrance region of all test sections was left smooth to simulate the cooling passage in the dovetail region of a gas turbine blade. All ribs but one were machined out of acrylic plastic and were glued to the channel walls. The instrumented rib on which all measurements were taken was machined out of copper. Inside this copper rib, a 60 Ohm cylindrical electric heater was installed using a highly conductive silver glue. The heater, which ran the full length of the rib, was mounted as centrally as possible. Also installed in the copper rib were three calibrated thermocouples to measure the surface temperature. These three thermocouples were equally spaced over the length of the rib with their beads close to the rib surface. Their temperature readings were found to be the same within a fraction of a degree. For data reduction, the average of the three temperatures was used. Copper rib surfaces were polished to minimize the radiational heat losses from the copper rib to the unheated wall. Radiational heat flux was calculated to be insignificant (0.05 percent of total surface heat flux). Rib heat transfer coefficient measurements were performed for two distinct rib locations. First, the copper rib was mounted in the middle of the rib-roughened portion of the channel (fifth rib) and other eight acrylic plastic ribs were arranged on each side with the desired rib pitch-to-height ratio. Second, the copper rib was moved to the furthest upstream position and the other eight ribs were mounted downstream of it. Table 1 shows the rib location from the channel entrance, X, for each geometry. Two 3.81 cm × 30.48 cm × 5.39 cm × 26.67 cm trapezoidal custom-made etched-foil heaters with a thickness of 0.15 mm were glued on the polyurethane wall abutting both sides of the copper rib. With a 45 deg side, these heaters were laid snuggly on both sides of the copper rib and were turned on in those tests termed as "Heated Wall" in Fig. 2. The air mixed mean temperature, T_m, was calculated from an energy balance between the channel inlet and copper rib location. Air inlet temperature, T_i, was measured at the channel inlet as shown in Fig. 1. The test section was covered on all sides by 5-cm-thick styrofoam sheets to minimize the heat losses to the environment. Surface heat flux in the test section was generated by the heaters through a custom-designed power supply unit. Each heater was individually controlled by a variable transformer. Thermocou-

Table 1 Specifications

Test	e(mm)	e/Dh	r/e	S/e	X (cm)	X/Dh	Remarks
1	9.525	0.25	0.25	5	60.96	16	Midstream
2	9.525	0.25	0.25	8.5	60.96	16	Midstream
3	9.525	0.25	0.25	10	60.96	16	Midstream
4	9.525	0.25	0.25	8.5	28.58	7.5	Upstream
5	6.35	0.167	0.25	5	59.06	15.5	Midstream
6	6.35	0.167	0.25	8.5	59.06	15.5	Midstream
7	6.35	0.167	0.25	10	59.06	15.5	Midstream
8	6.35	0.167	0.25	8.5	37.47	9.83	Upstream
9	5.08	0.133	0.197	5	60.96	16	Midstream
10	5.08	0.133	0.197	8.5	60.96	16	Midstream
11	5.08	0.133	0.197	10	60.96	16	Midstream
12	5.08	0.133	0.197	8.5	43.69	11.47	Upstream
Dh=3.81 cm, AR = 1, ARt = e/w = 1, α = 45°, 9 Ribs on Each Side							
Staggered Ribs for all Geometries							

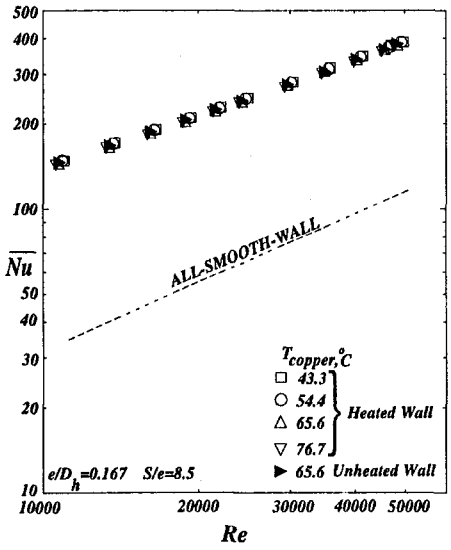

Fig. 2 Rib-average Nusselt number for a range of rib surface temperature

ples were calibrated using ice water and boiling water reference points prior to testing. For a typical test run, the Reynolds number was set by precisely fixing the mass flow rate. The heat flux was induced by adjusting heater power until the copper rib reached the desired temperature. Enough time was given so that the system came to thermal equilibrium at which time data was recorded. Power to the copper rib was then increased to gather data at a higher surface temperature. This procedure was repeated for all copper temperatures and flow rates.

Static pressure taps were mounted on all three acrylic plastic walls of the test section to measure the pressure drop across the rib-roughened portion of the test section. A contact micromanometer with an accuracy of 0.025 mm of water column measured the pressure differences between the static pressure taps. A critical venturimeter, with choked flow for all cases tested, measured the total mass flow rate entering the test section. The reported friction factor, $\overline{f}$, is based on the pressure drop across the rib-roughened segment of the test section. Details of the experimental apparatus and test procedures are reported by Lengkong (1996).

The radiational heat loss from the heated rib (and wall) to the unheated walls as well as losses to ambient air were taken into consideration when heat transfer coefficients were calculated. The reported heat transfer coefficients are the averages over the rib surfaces and not that of wall surfaces between the ribs. The heat transfer coefficients on the resurface between the ribs, h_{floor}, for various geometries are reported by those investigators mentioned in the introduction. Experimental uncertainties, following the method of Kline and McClintock (1953), were determined to be ±8 percent and ±6 percent for the heat transfer coefficient and friction factor, respectively.

Results and Discussion

Heat transfer and friction factor results for the twelve 45 deg round-cornered rib geometries are compared with those of 45 deg sharp-cornered ribs and 90 deg round-cornered ribs in Figs. 3–6. The Dittus–Boelter (1930) correlation for an all-smooth-wall channel ($\overline{Nu}_s = 0.023\ Re^{0.8}\ Pr^{0.4}$) is plotted in Fig. 2. With this correlation, the enhancement (relative to smooth walls) in rib-roughened heat transfer coefficients is readily evaluated. The thermal performance based on the same pumping power was derived by Gee and Webb (1980) as $(\overline{Nu}/\overline{Nu}_s)/(\overline{f}/\overline{f}_s)^{1/3}$, where $\overline{f}_s$ is the all-smooth-wall friction factor from Moody (1944). Air properties for Nusselt and Reynolds number calculations are based on the local film temperature, T_f, for all cases.

Figure 2 shows the Nusselt versus Reynolds numbers for the medium rib geometry corresponding to a blockage ratio, e/D_h, of 0.167 and a pitch-to-height ratio, S/e, of 8.5. Copper rib temperature is varied from 43.3°C to 76.7°C with no change in the measured heat transfer coefficient. This lack of effect of the copper surface temperature on heat transfer coefficient continued for all geometries examined. Furthermore, this insensitivity of the measured heat transfer coefficient to the rib surface temperature supports the accuracy of our accounting for the heat losses to the ambient air and radiational losses from the heated copper rib to the unheated surrounding walls. Shown in Fig. 2 are also the results of two tests of identical geometries for which the foil heaters were on and off, respectively. The difference in the Nusselt number was well below the experimental uncertain-

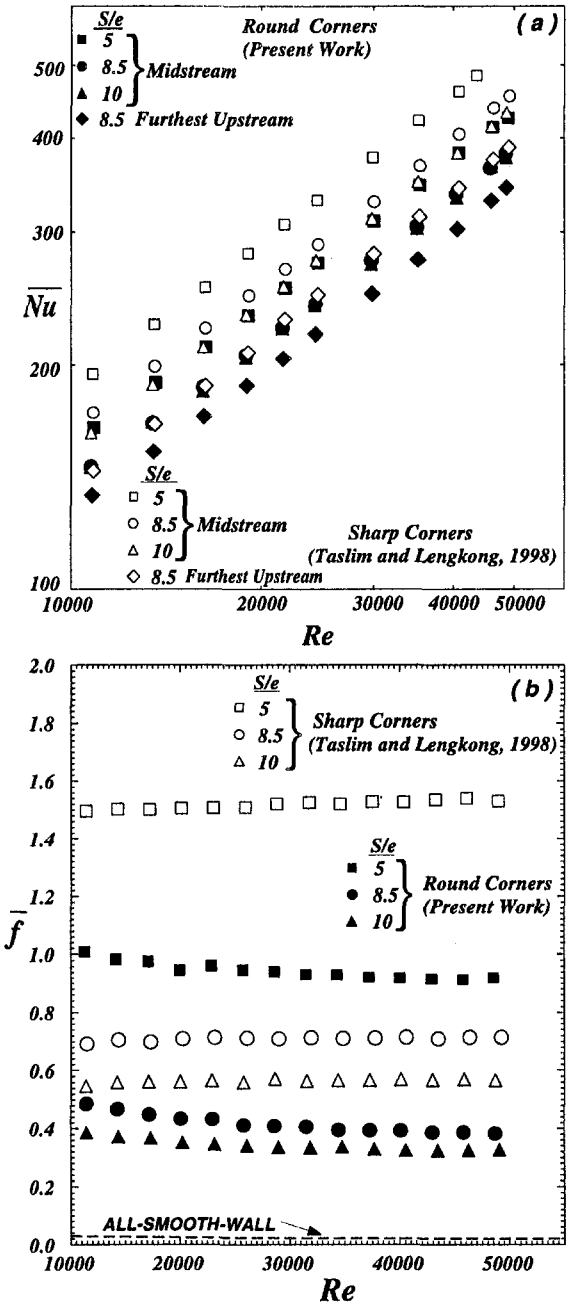

Fig. 3 Rib-average Nusselt number and channel-average friction factor for a range of pitch-to-height ratios, $e/D_h = 0.25$

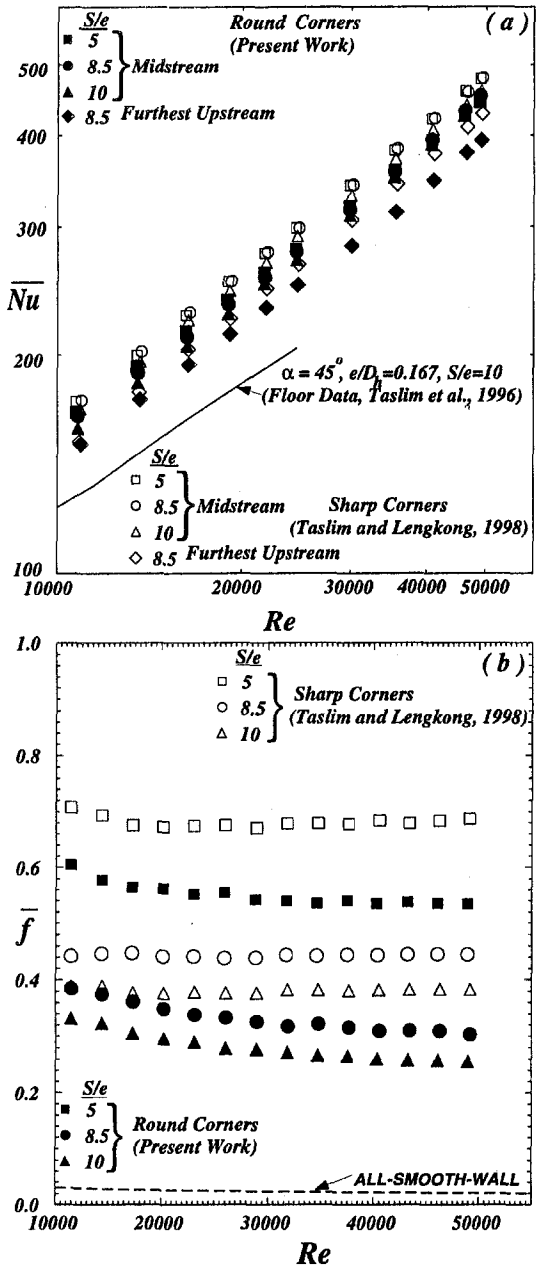

Fig. 4 Rib-average Nusselt number and channel average friction factor for a range of pitch-to-height ratios, e/D_h = 0.167

ties, indicating that the thermal boundary layer, being interrupted repeatedly by the ribs, did not affect the heat transfer. It would appear that the mixing phenomenon was the dominant driving force for the high levels of heat transfer coefficient. All rib geometries were tested for the above-mentioned range of copper temperature and with the surface foil heaters on and off. However, since no appreciable difference was observed between the results, the reported data in this paper are for the case of adiabatic channel walls with the copper rib temperature set at 65.6°C. As for having only one heated wall, it is noted that an experimental investigation by El-Husayni et al. (1994) on heat transfer in a rib-roughened channel with one, two, and four heated walls showed that, in a stationary roughened channel, the heat transfer coefficient was not significantly sensitive to the number of heated walls, i.e., the variation in heat transfer coefficient was within the reported experimental uncertainty of ±8 percent.

To investigate the effects pitch-to-height ratio have on rib heat transfer and channel overall friction factor, a 9.525 mm by 9.525 mm rib with round top corners was tested for three pitch-to-height ratios of 5, 8.5, and 10 (geometries 1–3 in Table 1). The heat transfer results, compared with those of sharp-cornered ribs (Taslim and Lengkong, 1998) are shown in Fig. 3(*a*). Also shown in Fig. 3(*a*) are the rib heat transfer results for an *S/e* of 8.5 when the instrumented copper rib was mounted in the furthest upstream position (geometry 4 in Table 1). Several observations are made. First, the heat transfer coefficient for the furthest upstream rib was considerably lower than that for the rib in the middle of the rib-roughened region, indicating that upstream ribs and those staggered on the opposite wall contribute significantly to the very high level of heat transfer enhancement of downstream ribs by interrupting the flow and diverting its direction, thus promoting high levels of mixing. Second, for these ribs of high blockage ratio, the pitch-to-height

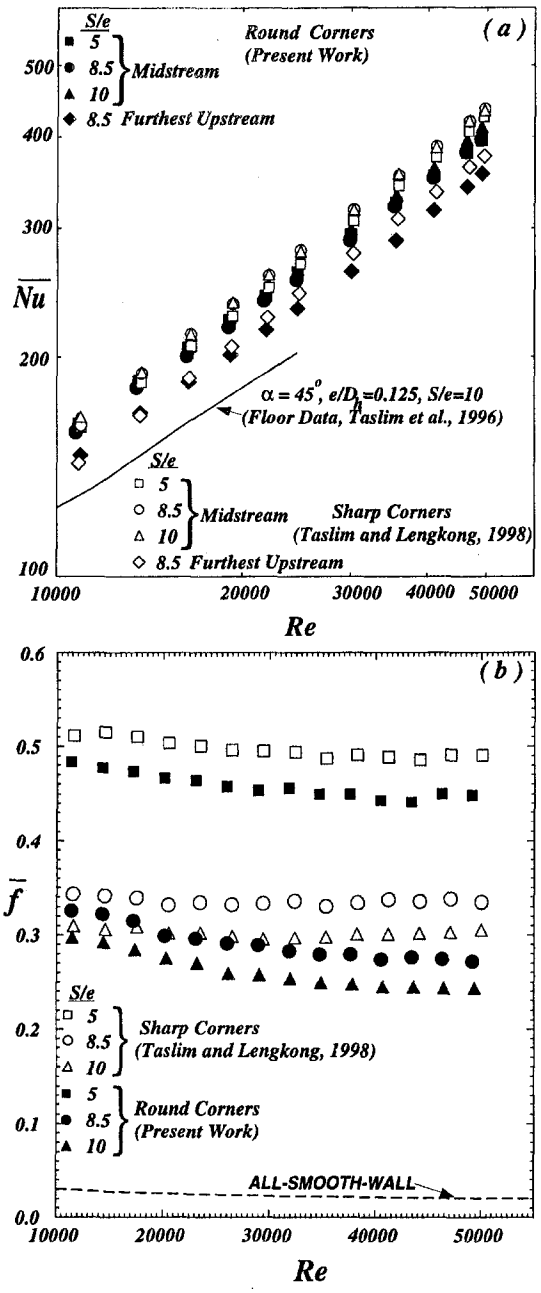

Fig. 5 Rib-average Nusselt number and channel average friction factor for a range of pitch-to-height ratios, e/D_h = 0.133

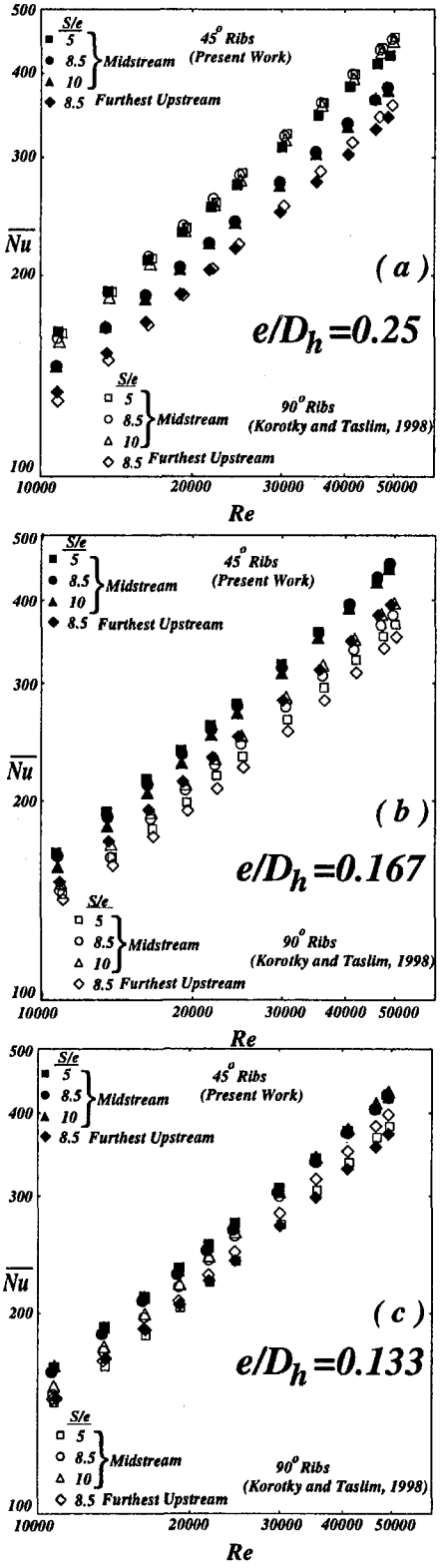

Fig. 6 Comparison of 45 and 90 deg rib-average Nusselt numbers

ratio of 5 produced the highest heat transfer coefficient and as the pitch-to-height ratio increased, the heat transfer coefficient decreased. Secondary flows in the form of swirls along the angled ribs, especially for these relatively big ribs, are believed to be responsible for high levels of heat transfer coefficients. These secondary flows are stronger when angled ribs are brought closer to each other, as is seen for both sharp- and round-cornered ribs at the pitch-to-height ratio of 5. Third, round-cornered ribs in midstream as well as furthest upstream position produce lower heat transfer coefficients than sharp-cornered ribs. The average reductions in heat transfer coefficients are 17.5, 16, 12, and 10 percent for S/e of 5, 8.5, and 10, and for the furthest upstream position, respectively. This behavior is consistent with the friction factor behavior shown in Fig. 3(b) (reduction in the amounts of 38, 41 and 15 percent for S/e of 5, 8.5, and 10, respectively) and is also observed for 90 deg ribs and for heat transfer coefficient on the area between the ribs (h_{floor}) by these and other investigators. It is also consistent with the Colburn analogy of heat transfer coefficient and friction factor. That is, the more streamlined round-cornered ribs do not promote as much mixing of the near-wall higher temperature air with the lower temperature core air when compared with the sharp-cornered ribs.

The next series of four tests, shown in Fig. 4, correspond to a rib blockage ratio of 0.167, three of which (test geometries 5–7 in Table 1) were performed for pitch-to-height ratios of 10, 8.5, and 5 with the instrumented copper rib mounted in the middle of the rib-roughened region. The fourth test represents the heat transfer results when the copper rib was mounted in the furthest upstream position (geometry 8 in Table 1). Also shown in Fig. 4 are the heat transfer results for the area between the ribs (called floor heat transfer coefficient by some investigators) reported by Taslim et al. (1996). It can be seen that the rib-average heat transfer coefficient is much higher than that for the area between the ribs (h_{floor}). The difference increases from 19 percent at the lowest Reynolds number to 42 percent at the highest Reynolds number. Therefore, the contribution of the ribs to the overall heat transfer in a rib-roughened passage is significant. As for the comparison between the round- and sharp-cornered rib results, the same behavior as the case of higher blockage ratio ribs is observed, i.e., the general effect of rounding the rib corners is a 5.5 percent decrease in heat transfer coefficient and reduction in the amounts of 19, 25, and 26 percent in friction factor for S/e of 5, 8.5, and 10, respectively. This trend is repeated once again for the next rib geometry of still lower blockage ratio to be discussed shortly. Similar to the rib geometry discussed previously, the midstream ribs produced higher Nusselt numbers than that in the furthest upstream position. A comparison of Figs. 3 and 4 shows that the Nusselt number is much less dependent on the pitch-to-height ratio for these smaller ribs, and this will continue to be the case for the next rib geometry of lower blockage ratio. The pitch-to-height ratio of 10 produced the lowest midstream heat transfer coefficient for both round- and sharp-cornered ribs indicating that the optimum spacing for rib heat transfer coefficient is generally lower than that for the heat transfer coefficient on the area between the ribs. This trend is observed for several rib geometries tested and reported previously (Taslim and Wadsworth, 1997; Korotky and Taslim, 1998).

The next four tests, shown in Fig. 5, correspond to a yet smaller rib blockage ratio of 0.133. The first three tests (geometries 9–11 in Table 1) were performed for pitch-to-height ratios of 5, 8.5, and 10 with the instrumented copper rib mounted in the middle of the rib-roughened region. The fourth test represents the heat transfer results for the copper rib mounted in the furthest upstream position (geometry 12 in Table 1). Floor heat transfer results (Taslim et al., 1996) for a blockage ratio of 0.125, the closest geometry that could be found in open literature, are also shown for comparison. Several observations are made. Rib heat transfer coefficient is greater than floor heat transfer coefficient by 11 percent at the lowest Reynolds number to 37 percent at the highest Reynolds number. Similar to the previously discussed rib geometry, round-cornered rib results for this small blockage ratio are lower than those for the sharp-cornered ribs by 2.5, 6.5, 3.8, and 3 percent for the midstream ribs at S/e of 5, 8.5, and 10, and the furthest upstream rib, respectively. Again, the rib in the furthest upstream position

produced a lower heat transfer coefficient than those in the midstream position. The corresponding friction factors for this rib geometry are shown in Fig. 5(*b*). The trend is similar to those of higher blockage ratio ribs. A pitch-to-height ratio of 5 has consistently produced the highest pressure drop, which is not always accompanied with higher heat transfer coefficients, indicating high levels of form drag when ribs are brought too close to each other. Friction factors for the round-cornered ribs are 8, 13, and 13 percent less than those for the sharp-cornered ribs for *S/e* of 5, 8.5, and 10, respectively.

45 deg rib heat transfer results are compared with those of 90 deg ribs of otherwise identical geometry in Fig. 6. Several observations are made: (*a*) As the rib blockage ratio reduces, the heat transfer coefficients of 45 and 90 deg ribs are getting closer to each other. (*b*) *The highest blockage ratio ribs (e/D_h = 0.25)*: In midstream position, 90 deg ribs produce much higher heat transfer coefficients for S/e = 8.5 and 10. However, when ribs are brought too close to each other at S/e = 5, 90 deg ribs perform similar to 45 deg ribs at the lower end of the Reynolds number range and superior to 45 deg ribs at the higher Reynolds numbers. In the furthest upstream position, the results of both sets of ribs are comparable. (*c*) *The medium blockage ratio ribs (e/D_h = 0.167)*: 45 deg ribs perform superior to their 90 deg counterparts for all pitch-to-height ratios, and both in midstream and furthest upstream positions. Secondary flows associated with the angled ribs are believed to be responsible for this difference. (*d*) *The smallest blockage ratio ribs (e/D_h = 0.133)*: 45 deg ribs in midstream position perform superior to their 90 deg counterparts for all pitch-to-height ratios. In the furthest upstream position, however, 90 deg ribs produced higher heat transfer coefficients especially at higher Reynolds numbers. The reason for such behavior in the furthest upstream position is that the angled rib does not benefit from the secondary flows in that position.

Figure 7 combines the results of all round-cornered rib geometries for all pitch-to-height ratios. First, it is observed that the rib heat transfer coefficients for the medium size rib (e/D_h = 0.167) in midstream position, represented by circle symbols (hollow, solid, and half solid), are generally higher than those of other two rib geometries, especially in the higher range of Reynolds number. The same is true for the furthest upstream position. This suggests an optimum rib size for the highest on-rib heat transfer coefficient when ribs are positioned at an angle 45 deg with the flow direction. We attribute this behavior to two phenomena acting against each other: first, the formation of secondary flows along the angled ribs and, second, tripping of the flow over the ribs. While the former enhances the rib heat transfer, the latter may not always do the same. It appears that, for the high-blockage ribs, strong recirculating bubbles formed behind the ribs and possibly on the rib top prevent the direct contact between the core air and the rib surfaces, thus reducing the heat transfer coefficient. In other words, when the ribs are angled, a combination exists of the secondary flows and the recirculating bubbles, mentioned above, that act in opposite ways and, depending on the strength of each phenomenon, the overall rib heat transfer coefficient varies. There is a better flow adherence to the smaller ribs but the secondary flows are not as strong as those for higher blockage ratio ribs. On the other hand, high blockage ribs produce strong secondary flows, which are accompanied with the separation of the main flow from the top and back surfaces. This combination results in a lower heat transfer coefficient than that for the medium size rib for which a proper combination of the two effects produces the highest heat transfer coefficient. Pitch-to-height ratio of 5 was the least desirable spacing from both friction factor (as evidenced by Fig. 7(*b*)) and heat transfer point of views. Only for the largest blockage ratio was the heat transfer coefficient for the pitch-to-height ratio of 5 higher than those for the other two rib spacings. But it was, however, accompanied by the highest friction factor measured for all these geometries. Several

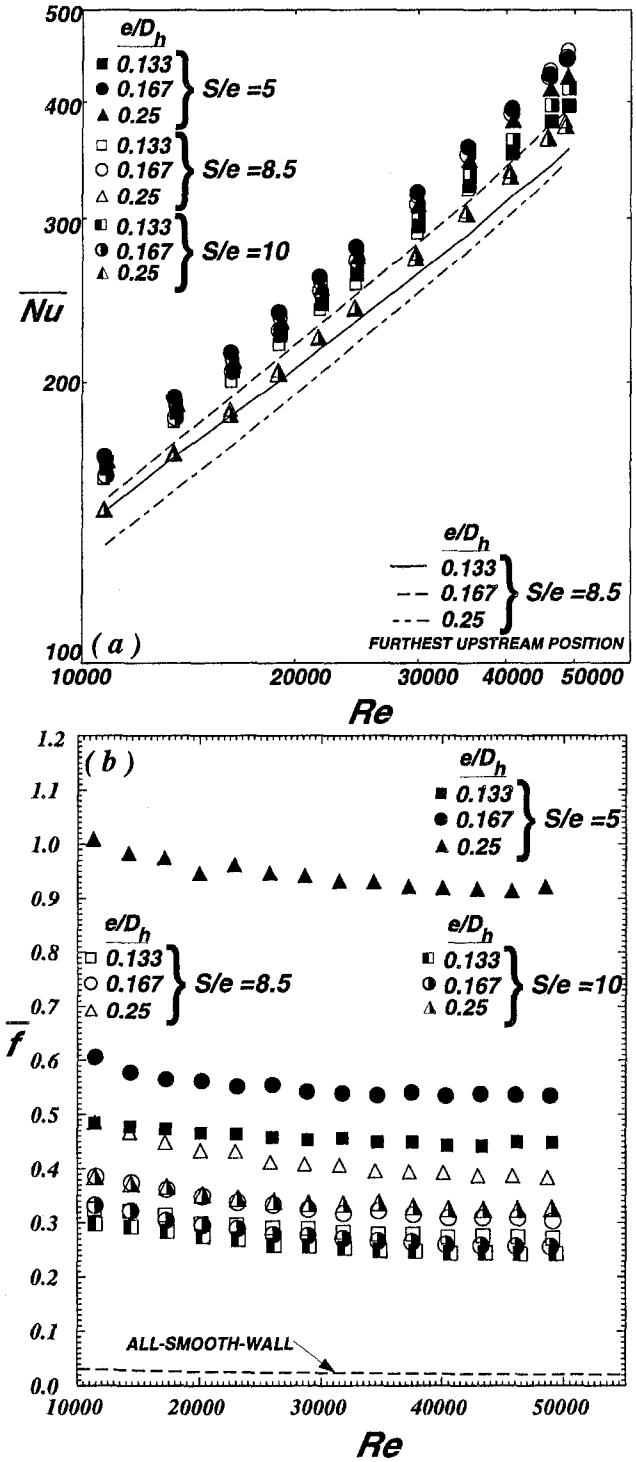

Fig. 7 Rib-average Nusselt number and channel-average friction factor for all blockage and pitch-to-height ratios

observations are made of Fig. 7(*b*). First, ribs positioned too close to each other produced the highest friction factor with the highest blockage ratio producing a friction factor almost three times that of the smallest rib geometry. A lower pitch-to-height ratio corresponds to more ribs per channel length, which results in a higher pressure drop. A high level of form drag contributes to the very high friction factor for the biggest rib. Second, channel friction factor increases with rib blockage ratio and decreases with rib spacing, a known behavior documented by many investigators.

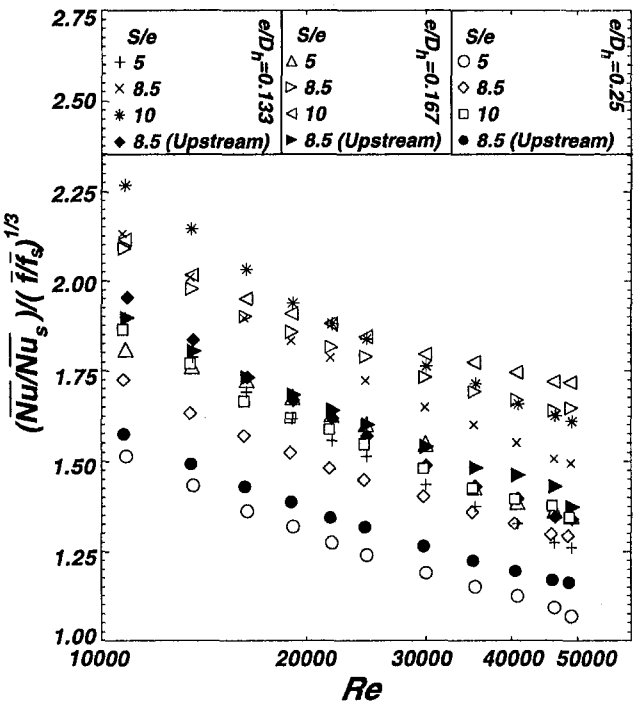

Fig. 8 Rib thermal performances of the twelve geometries

Finally, the thermal performances of all geometries tested are compared in Fig. 8. It should be noted that the thermal performances reported here do not include the contribution of the heat transfer coefficient on the surface area between the ribs, h_{floor}. Thermal performance data for the surface area between the ribs are reported by the first author (Taslim et al., 1996) and can be combined with the present data to determine the overall thermal performances. It is seen that as the blockage ratio increases, the rib thermal performance decreases. For all geometries tested, the maximum and minimum thermal performances corresponded to the smallest rib ($e/D_h = 0.133$) with a pitch-to-height ratio of 10 and the biggest rib ($e/D_h = 0.25$) at a pitch-to-height ratio of 5, respectively. For all blockage ratios, pitch-to-height ratios of 5 and 10 produced the lowest and the highest thermal performances, respectively. Low thermal performances for the pitch-to-height ratio of 5 is an indication that the high pressure drops for those geometries (Figs. 3(b), 4(b), and 5(b)) were mainly due to form drag, and not skin friction, which is responsible for high levels of heat transfer coefficients.

Conclusions

Twelve 45 deg round-cornered rib geometries representing three blockage ratios in a practical range for small aircraft engine turbine blades and at three pitch-to-height ratios were tested for heat transfer and pressure loss variations. The results were compared with those of sharp-cornered ribs as well as round-cornered 90 deg ribs reported previously. From this study, it was concluded that:

1 For the geometries tested, the rib-average heat transfer coefficient was much higher than that for the area between the ribs. For high blockage ribs with large heat transfer areas, commonly used in small gas turbines, the rib heat transfer is a significant portion of the overall heat transfer in the cooling passages.

2 For all rib geometries tested, both on-rib heat transfer coefficient and channel friction factor decreased when the rib corners were rounded.

3 Highest blockage ratio ($e/D_h = 0.25$) ribs produced higher heat transfer coefficient when they were positioned at an angle of 90 deg with the flow direction. This trend reversed for the lower blockage ratio ($e/D_h = 0.167$ and 0.133) ribs.

4 Under otherwise identical conditions, ribs in the furthest upstream position produced lower heat transfer coefficients than those in the midstream position.

5 Heat transfer coefficients for the two smaller rib geometries ($e/D_h \approx 0.133$ and 0.167) did not vary significantly with the pitch-to-height ratio in the range tested. However, the heat transfer coefficient for the high-blockage rib geometry increased significantly as the ribs were brought closer to each other.

6 Rib thermal performance decreased with the rib blockage ratio. The smallest rib geometry ($e/D_h = 0.133$) at a pitch-to-height ratio of 10 and the largest rib geometry ($e/D_h = 0.25$) at a pitch-to-height ratio of 5, both in midstream position, produced the highest and the lowest thermal performances, respectively.

References

Abuaf, N., Gibbs, R., and Baum, R., 1986, "Pressure Drop and Heat Transfer Coefficient Distributions in Serpentine Passages With and Without Turbulence Promoters," *The Eighth International Heat Transfer Conference*, C. L. Tien, V. P. Carey, and J. K. Ferrel, eds., pp. 2837–2845.

Berger, F. P., and Hau, K. F., 1979, "Local Mass/Heat Transfer Distribution on Surfaces Roughened With Small Square Ribs," *International Journal of Heat and Mass Transfer*, Vol. 22, pp. 1645–1656.

Burggraf, F., 1970, "Experimental Heat Transfer and Pressure Drop With Two Dimensional Turbulence Promoters Applied to Two Opposite Walls of a Square Tube," *Augmentation of Convective Heat and Mass Transfer*, A. E. Bergles and R. L. Webb, eds., ASME, pp. 70–79.

Chandra, P. R., Han, J. C., and Lau, S. C., 1988, "Effect of Rib Angle on Local Heat/Mass Transfer Distribution in a Two-Pass Rib-Roughened Channel," ASME JOURNAL OF TURBOMACHINERY, Vol. 119, pp. 233–241.

Chandra, P. R., and Han, J. C., 1989, "Pressure Drop and Mass Transfer in Two-Pass Ribbed Channels," AIAA *Journal of Thermophysics*, Vol. 3, No. 3, pp. 315–319.

Colburn, A. P., 1933, "A Method of Correlating Forced Convection Heat Transfer Data and a Comparison With Fluid Friction," *Trans. AIChE*, Vol. 29, pp. 174–210.

Dawes, W. N., 1993, "The Solution-Adaptive Numerical Simulation of the Three-Dimensional Viscous Flow in the Serpentine Coolant Passage of a Radial Inflow Turbine Blade," ASME JOURNAL OF TURBOMACHINERY, Vol. 116, pp. 141–148.

Dittus, F. W., and Boelter, L. M. K., 1930, University of California, Berkeley, CA, *Publications in Engineering*, Vol. 2, p. 443.

El-Husayni, H. A., Taslim, M. E., and Kercher, D. M., 1994, "An Experimental Investigation of Heat Transfer Coefficients in a Spanwise Rotating Channel With Two Opposite Rib-Roughened Walls," ASME JOURNAL OF TURBOMACHINERY, Vol. 113, pp. 75–82.

Gee, D. L., and Webb, R. L., 1980, "Forced Convection Heat Transfer in Helically Rib-Roughened Tubes," *Int. J. Heat Mass Transfer*, Vol. 23, pp. 1127–1136.

Han, J. C., Glicksman, L. R., and Rohsenow, W. M., 1978, "An Investigation of Heat Transfer and Friction for Rib Roughened Surfaces," *Int. J. Heat Mass Transfer*, Vol. 21, pp. 1143–1156.

Han, J. C., 1984, "Heat Transfer and Friction in Channels With Two Opposite Rib-Roughened Walls," ASME *Journal of Heat Transfer*, Vol. 106, No. 4, pp. 774–781.

Han, J. C., Park, J. S., and Lei, C. K., 1985, "Heat Transfer Enhancement in Channels With Turbulence Promoters," ASME *Journal of Engineering for Gas Turbines and Power*, Vol. 107, pp. 628–635.

Han, J. C., Zhang, Y. M., and Lee, C. P., 1992, "Influence of Surface Heat Flux Ratio on Heat Transfer Augmentation in Square Channels With Parallel, Crossed, and V-Shaped Angled Ribs," ASME JOURNAL OF TURBOMACHINERY, Vol. 114, pp. 872–880.

Kline, S. J., and McClintock, F. A., 1953, "Describing Uncertainty in Single-Sample Experiments," *Mechanical Engineering*, Vol. 75, Jan., pp. 3–8.

Korotky, G. J., and Taslim, M. E., 1998, "Rib Heat Transfer Coefficient Measurements in a Rib-Roughened Square Passage," ASME JOURNAL OF TURBOMACHINERY, Vol. 120, No. 2.

Lengkong, A., 1996, "An Experimental Investigation of Surface-Averaged Rib Heat Transfer Coefficient in a Square Passage Roughened With 45° Ribs," M.S. Thesis, Department of Mechanical, Industrial and Manufacturing Engineering, Northeastern University, Boston, MA.

Liou, T. M., Hwang, J. J., and Chen, S. H., 1991, "Turbulent Heat Transfer and Fluid Flow in a Channel With Repeated Rib Pairs," *Proc. ASME/JSME Thermal Eng.*, Vol. 3, pp. 205–212.

Liou, T. M., and Hwang, J. J., 1993, "Effects of Ridge Shapes on Turbulent Heat Transfer and Friction in a Rectangular Channel," *Int. J. Heat Mass Transfer*, Vol. 36, pp. 931–940.

Lockett, J. F., and Collins, M. W., 1990, "Holographic Interferometry Applied to Rib-Roughness Heat Transfer in Turbulent Flow," *Int. J. Heat Mass Transfer*, Vol. 33, pp. 2439–2449.

Metzger, D. E., Fan, C. S., and Pennington, J. W., 1983, "Heat Transfer and Flow Friction Characteristics of Very Rough Transverse Ribbed Surfaces With and Without Pin Fins," *Proc. ASME–JSME Thermal Engineering Joint Conference,* Vol. 1, pp. 429–436.

Metzger, D. E., Chyu, M. K., and Bunker, R. S., 1988, "The Contribution of On-Rib Heat Transfer Coefficients to Total Heat Transfer From Rib-Roughened Surfaces," *Transport Phenomena in Rotating Machinery,* J. H. Kim, ed., Hemisphere Publishing Co.

Metzger, D. E., Fan, C. S., and Yu, Y., 1990, "Effects of Rib Angle and Orientation on Local Heat Transfer in Square Channels With Angled Roughness Ribs," *Compact Heat Exchangers: A Festschrift for A. L. London,* Hemisphere Publishing Co., pp. 151–167.

Moody, L. F., 1944, "Friction Factors for Pipe Flow," *Trans. ASME,* Vol. 66, p. 671.

Sato, H., Hishida, K., and Maeda, M., 1992, "Characteristics of Turbulent Flow and Heat Transfer in a Rectangular Channel With Repeated Rib Roughness," *Exp. Heat Transfer,* Vol. 5, pp. 1–16.

Solntsev, V. P., Luzhanskii, B. E., and Kryukov V. N., 1973, "An Investigation of Heat Transfer in the Turbulent Separation Zones in the Vicinity of Sudden Steps," *Heat Transfer—Soviet Research,* Vol. 5, No. 2, pp. 122–128.

Taslim, M. E., and Spring, S. D., 1988a, "An Experimental Investigation of Heat Transfer Coefficients and Friction Factors in Passages of Different Aspect Ratio Roughened With 45° Turbulators," *Proc. ASME National Heat Conference,* Houston, TX.

Taslim, M. E., and Spring, S. D., 1988b, "Experimental Heat Transfer and Friction Factors in Turbulated Cooling Passages of Different Aspect Ratios, Where Turbulators Are Staggered," Paper No. AIAA-88-3014.

Taslim, M. E., Bondi, L. A., and Kercher, D. M., 1991, "An Experimental Investigation of Heat Transfer in an Orthogonally Rotating Channel Roughened With 45 deg Criss-Cross Ribs on Two Opposite Walls," ASME JOURNAL OF TURBOMACHINERY, Vol. 113, pp. 346–353.

Taslim, M. E., and Spring, S. D., 1994, "Effects of Turbulator Profile and Spacing on Heat Transfer and Friction in a Channel," *AIAA J. Thermophysics and Heat Transfer,* Vol. 8, No. 3, pp. 555–562.

Taslim, M. E., Li, T., and Kercher, D. M., 1996, "Experimental Heat Transfer and Friction in Channels Roughened With Angled, V-Shaped, and Discrete Ribs on Two Opposite Walls," ASME JOURNAL OF TURBOMACHINERY, Vol. 118, pp. 20–28.

Taslim, M. E., and Wadsworth, C. M., 1997, "An Experimental Investigation of the Rib Surface-Averaged Heat Transfer Coefficient in a Rib-Roughened Square Passage," ASME JOURNAL OF TURBOMACHINERY, Vol. 119, pp. 381–389.

Taslim, M. E., and Korotky, G. J., 1998, "Low-Aspect-Ratio Rib Heat Transfer Coefficient Measurements in a Square Channel," ASME JOURNAL OF TURBOMACHINERY, Vol. 120, pp. 831–838.

Taslim, M. E., and Lengkong, A., 1998, "45 deg Staggered Rib Heat Transfer Coefficient Measurements in a Square Channel," ASME JOURNAL OF TURBOMACHINERY, Vol. 120, pp. 571–580.

Webb, R. L., Eckert, E. R. G., and Goldstein, R. J., 1971, "Heat Transfer and Friction in Tubes With Repeated-Rib-Roughness," *Int. J. Heat Mass Transfer,* Vol. 14, pp. 601–617.

Heat Transfer in a Rotating Cavity With a Stationary Stepped Casing

I. Mirzaee[1]

P. Quinn[2]

M. Wilson

J. M. Owen

Department of Mechanical Engineering,
Faculty of Engineering and Design,
University of Bath,
Bath BA2 7AY, United Kingdom

In the system considered here, corotating "turbine" disks are cooled by air supplied at the periphery of the system. The system comprises two corotating disks, connected by a rotating cylindrical hub and shrouded by a stepped, stationary cylindrical outer casing. Cooling air enters the system through holes in the periphery of one disk, and leaves through the clearances between the outer casing and the disks. The paper describes a combined computational and experimental study of the heat transfer in the above-described system. In the experiments, one rotating disk is heated, the hub and outer casing are insulated, and the other disk is quasi-adiabatic. Thermocouples and fluxmeters attached to the heated disc enable the Nusselt numbers, Nu, to be determined for a wide range of rotational speeds and coolant flow rates. Computations are carried out using an axisymmetric elliptic solver incorporating the Launder–Sharma low-Reynolds-number $k-\epsilon$ turbulence model. The flow structure is shown to be complex and depends strongly on the so-called turbulent flow parameter, λ_T, which incorporates both rotational speed and flow rate. For a given value of λ_T, the computations show that Nu increases as Re_ϕ, the rotational Reynolds number, increases. Despite the complexity of the flow, the agreement between the computed and measured Nusselt numbers is reasonably good.

1 Introduction

Rotating-disk systems can be used to model the flow and heat transfer that occurs in the internal cooling-air systems of gas turbines (see Owen and Rogers, 1989, 1995). In some cases, the turbine disk rotates close to a stationary casing: the so-called rotor–stator system. In other cases, two corotating turbine disks are usually cooled by a radial outflow of air: the rotating cavity.

A less common case is where corotating disks are cooled by peripheral inflow and outflow of air, as shown in Fig. 1. In this system, which was studied by Gan et al. (1996) and Mirzaee et al. (1998), the cavity is bounded by two rotating disks, an inner rotating cylinder and an outer stationary cylindrical casing. Air enters the system through radial nozzles in the stationary casing and leaves through the annular clearances between the casing and the disks.

The combined computational and experimental study of Gan et al. showed that the stationary casing creates two recirculation regions, as shown in Fig. 1. The strength and extent of the recirculation increases as the flow rate increases and decreases as the rotational speed increases. Outside the boundary layers on the disks and casing, the core of fluid rotates as a combined free and forced vortex: the so-called Rankine vortex. An axisymmetric elliptic solver, incorporating the Launder–Sharma (1974) low-Reynolds-number $k-\epsilon$ turbulence model, was used to compute the velocity, but the agreement between the computations and measurements was not as good as that found for other rotating-disk systems (see Wilson et al., 1996).

For the heat transfer study reported in this paper, the rig used for the previous experiments in the peripheral flow system was modified as shown in Fig. 2. The rig models a turbine cooling system where the air enters through holes in the periphery of one of the rotating disks and leaves through the annular clearances between the stationary stepped casing and the two disks. Details of the rig and experimental apparatus are given in Section 2, and the computational method is described in Section 3. In Section 4, the computed flow structure is discussed, comparisons between computed and measured Nusselt numbers are made in Section 5, and the principal conclusions are given in Section 6.

2 Experimental Apparatus

2.1 Rotating-Disk Rig. Details of the apparatus used in the previous studies are given by Gan et al. (1996) and Mirzaee et al. (1998). The modified rig used in the current study is shown in Fig. 2, and the salient features are described below.

The rig comprised two steel disks of 782 mm diameter, a cylindrical hub of 410 mm diameter made from Rohacell foam, and a stationary stepped casing made from steel and insulated with Rohacell foam. A carbon-fiber nozzle ring, with 74 holes of 8.6 mm diameter, was attached to the periphery of each disk. The holes were inclined at an angle $\theta = 24$ deg to the radial direction in the $r-z$ plane, as can be seen in Fig. 2; there was no inclination to the radial direction in the $r-\phi$ plane.

The axial spacing between the two disks was 120 mm, the axial spacing between the radial surface of the stepped casing and the upstream disk was 60 mm, and the radial locations of the inner and outer cylindrical surfaces of the stepped casing were 335 mm and 411 mm, respectively. The central clearance, between the nozzle ring and the stepped casing, was 3 mm, and the downstream clearance was 2 mm.

The disk assembly and cylindrical hub could be rotated at speeds up to 3000 rpm by means of a thyristor-controlled DC motor. The upstream disk could be heated up to a maximum temperature of around 100°C by a stationary thyristor-controlled radiant-heater unit.

Up to 0.2 kg/s of compressed air was introduced into a stationary annular cavity surrounding the upstream nozzle ring. The air entered the annular cavity through six tubes of

[1] Present address: Department of Mechanical Engineering, University of Urmia, Urmia, Iran.

[2] Present address: ARIS, 66 Banbury Road, Oxford OX2 6PR, United Kingdom.

Contributed by the International Gas Turbine Institute and presented at the 43rd International Gas Turbine and Aeroengine Congress and Exhibition, Stockholm, Sweden, June 2–5, 1998. Manuscript received by the International Gas Turbine Institute February 1998. Paper No. 98-GT-112. Associate Technical Editor: R. E. Kielb.

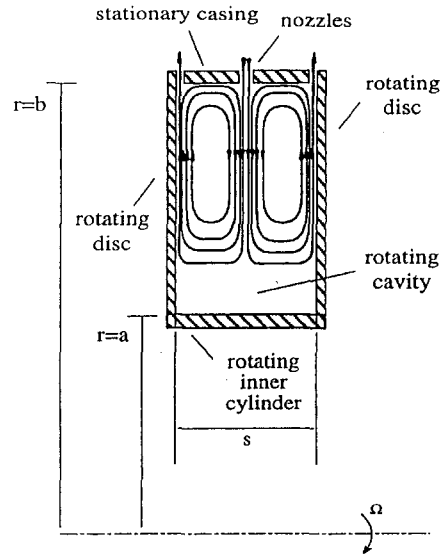

Fig. 1 Rotating cavity with a peripheral flow of cooling air

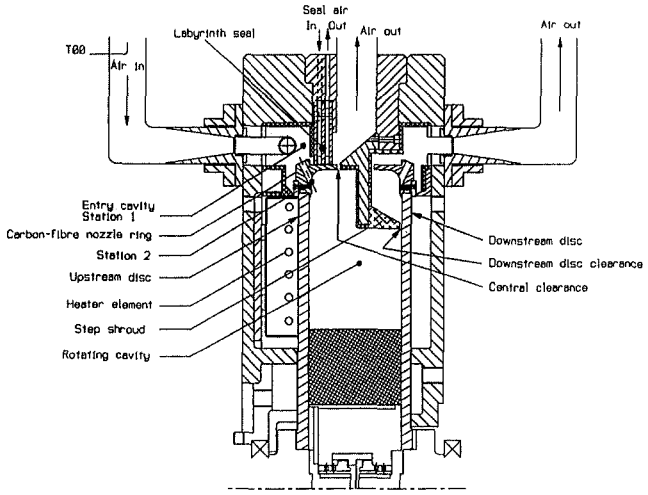

Fig. 2 Peripheral flow rig

20.3 mm diameter, the outlets of which were tangential to the nozzle ring. (The swirl reduced the rate of change of angular momentum of the air as it passed through the nozzles, and this consequently reduced the electrical power required to rotate the disk assembly.)

Air could leave the system through either the central clearance or the downstream clearance (see Fig. 2) between the stepped casing and the rotating discs. It was possible to control the ratio of the mass flow rate leaving the downstream clearance, $\dot{m}_d$, to that leaving the central clearance, $\dot{m}_c$ using valves in the two outlet pipes. A separate air supply and labyrinth seal on the outside of the upstream nozzle ring was used to prevent leakage between the inlet and the central outlet. For the experiments described below, $\dot{m}_d = \dot{m}_c = 0.5\ \dot{m}_i$.

2.2 Instrumentation. The front (cavity-side) surface of the heated upstream disk was coated with a fiber-glass "mat," 1 mm thick, in which were embedded ten thermocouples and ten fluxmeters. Signals from the rotating instrumentation were taken out through a silver/silver graphite slip ring unit, and the voltages were measured and recorded using a computer-controlled Solartron datalogger and digital voltmeter with a resolution of $\pm 1\ \mu v$.

For some of the earlier heat transfer tests in the series, the air temperature was measured in the inlet pipe upstream of the rig; in later tests, a total temperature probe was located in the stationary cavity surrounding the upstream nozzle ring (station 1 in Fig. 2). Owing to windage and heat transfer from the nozzle ring to the air in the stationary cavity, the air temperatures measured in the earlier tests had to be corrected. For all tests, the total temperature was also increased by the work done in increasing the angular momentum of the cooling air as it passed through the rotating nozzle ring from the stationary to the rotating cavity. These corrections for work and heat transfer to the cooling air, which are described by Quinn (1996), led to increased uncertainty in the reference air temperature used in the calculations of the Nusselt numbers.

The inlet and outlet flow rates were measured by orifice plates, manufactured to British Standards BS 1042, with a nominal uncertainty of ± 3 percent. By supplying sealing air to the labyrinth seal on the upstream nozzle ring, it was possible to reduce the difference between the inlet and outlet flow rates to around 0.5 percent.

The speed of the rotating-disk assembly was determined by means of an electromagnetic transducer and toothed wheel. The frequency of the oscillatory signal was measured, with an uncertainty of ± 1 rpm, by a timer-counter.

2.3 Range of Nondimensional Parameters. The nondimensional parameters considered in this study were the rotational Reynolds numbers, Re_ϕ, the nondimensional flow rate,

Nomenclature

a, b = inner, outer radius of disk
C_W = nondimensional mass flow rate $= \dot{m}_i/\mu b$
G = gap ratio $= s/b$
k = turbulent kinetic energy, thermal conductivity
$\dot{m}$ = mass flow rate
Nu = Nusselt number $= rq_s/k(T_s - T_{\mathrm{ref}})$
q_s = heat flux from disk to cooling air
r, ϕ, z = radial, tangential, and axial directions
Re_ϕ = rotational Reynolds number $= \rho\Omega b^2/\mu$
s = axial spacing between disks
T = temperature
u_τ = friction velocity $= \sqrt{\tau_w/\rho}$
V_r, V_ϕ, V_z = time-averaged velocities in (r, ϕ, z) directions
x = nondimensional radial coordinate $= r/b$
y = normal distance from wall
y^+ = nondimensional distance $= \rho u_\tau y/\mu$
ϵ = dissipation rate of turbulent kinetic energy
θ = angle of inlet nozzles to radial direction in $r-z$ plane
λ_T = turbulent flow parameter $= C_W/\mathrm{Re}_\phi^{0.8}$
μ = dynamic viscosity
ρ = density
τ_W = total wall shear stress
Ω = angular speed of disks

Subscripts

fd = free disk value
c = central clearance
d = downstream clearance
i = inlet value
s = disk surface
ref = reference value

C_W, the turbulent flow parameter, λ_T, and the local Nusselt number, Nu, all of which are defined in the nomenclature.

The turbulent flow parameter is particularly important for determining the flow structure in rotating cavities (see Owen and Rogers, 1995). It is related to the flow rate entrained by a rotating disk, and for a disk rotating in an infinite environment (the so-called free disk) the entrained flow rate, $C_{W,fd}$, can be estimated by

$$C_{W,fd} = 0.22\ \mathrm{Re}_\phi^{0.8} \tag{2.1}$$

so that

$$\lambda_{T,fd} = C_{W,fd}\,\mathrm{Re}_\phi^{-0.8} = 0.22 \tag{2.2}$$

For most air-cooled turbine disks, $\mathrm{Re}_\phi = 0\ (10^7)$ and $\lambda_T < \lambda_{T,fd}$; for the experiments described below a wide range of Re_ϕ and λ_T values was tested. Although the maximum value of Re_ϕ for the rig was around 3×10^6, which is lower than that in most engines, the flow structures are expected to be similar to those found at equivalent values of λ_T in the engine.

Values of Re_ϕ, C_W, and λ_T for the tests are given in Table 1. (It should be noted that, by convention, C_W and λ_T are negative for a radial inflow of cooling air, as occurs in the tests described here.) Also shown in Table 1 are the values of T_{ref}, corrected as described in Section 2.2, which were used in the Nusselt numbers.

The Nusselt number, Nu, was based on the heat flux, q_S, measured by the fluxmeters, the surface temperatures measured by the thermocouples, and the reference temperature based on the corrected total temperature of the inlet air. The measured heat flux included both convection to the air and radiation to the other surfaces in the rotating cavity, allowance for which was made in the computations described below.

3 Computational Model

The computational model used in this work is the same as that described by Gan et al. (1996) and Mirzaee et al. (1998) related to the rotating cavity with peripheral flow.

Table 1 Parameters used in experimental study

C_W	$Re_{\phi 1}$ x 10^{-6} λ_T T_{ref} (C)	$Re_{\phi 2}$ x 10^{-6} λ_T T_{ref} (C)	$Re_{\phi 3}$ x 10^{-6} λ_T T_{ref} (C)	$Re_{\phi 4}$ x 10^{-6} λ_T T_{ref} (C)
	0.48	1.01	1.97	3.89
-24000	-0.66	-0.38	-0.22	-0.12
	19.4	23.3	30.4	32.5
	0.38	0.76	1.53	3.01
-12000	-0.41	-0.23	-0.13	-0.078
	36.8	37.6	36.7	44.1
	0.46	0.91	1.84	3.62
-6000	-0.176	-0.1	-0.058	-0.034
	25.9	30.4	33.9	51.5
	0.4	0.79	1.58	3.07
-3000	-0.097	-0.056	-0.033	-0.019
	30.9	37.2	47.3	69.1
	0.37	0.73	1.47	3
-1500	-0.053	-0.03	-0.0174	-0.0098
	35	42.4	54.2	80.3

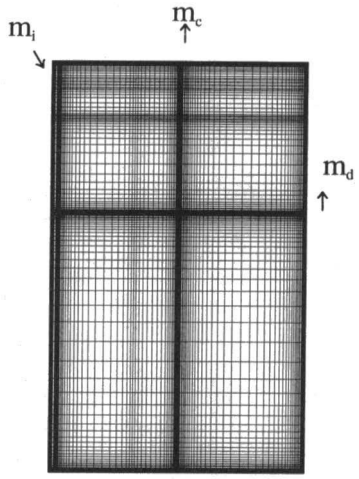

Fig. 3 Typical grid distribution (147 × 131 grid nodes in r–z plane)

In the work presented here, the stepped-shroud is represented by a stationary block in the computational model, using the blockage method described by Patankar (1980). Incompressible steady-state computations were carried out using an axisymmetric elliptic multigrid finite-volume solver for the discretized forms of the Reynolds-averaged Navier–Stokes and energy equations, incorporating the Launder–Sharma (1974) low-Reynolds-number $k-\epsilon$ turbulence model.

Computations were carried out with a 147 × 131 nonuniform grid in the $r-z$ plane, as shown in Fig. 3. A fine grid distribution was used near the boundaries so that $y^+ < 0.5$ for the near-wall grid. The inlet nozzles, which were inclined at an angle $\theta = 24$ deg to the radial direction in the $r-z$ plane, were modeled as an equivalent-area annular slot, and outlet boundaries were axial clearances which matched the clearances in the experimental rig.

The following boundary conditions were used:

(*i*) no-slip boundary conditions at solid surfaces;
(*ii*) at inlet, $V_r = -V_i \cos\theta$, $V_Z = V_i \sin\theta$ and $V_\phi = \Omega r$, where V_i is the magnitude of the velocity determined from the measured mass flow rate and the inlet area;
(*iii*) at outlet, V_r was uniform, $V_Z = 0$ and $\partial V_\phi/\partial r = 0$;
(*iv*) a polynominal fit to measured temperatures was used to provide the radial temperature distribution of the heated disk for each case, and the insulated inner cylinder and stationary surfaces were assumed to be adiabatic;
(*v*) The unheated steel disk was not insulated, and its temperature was not measured. The interior (cavity-side) surface temperature of this disk was estimated in the computations by calculating the heat flux through the disk, assuming that its exterior face behaved as a free disk (see Mirzaee et al., 1998).

The reference temperature for the Nusselt number was the corrected inlet total temperature in the rotating frame of reference, values of which are given in Table 1.

In the heat transfer computations, a surface-to-surface radiation model could be included, so that predictions of total Nusselt numbers (including both convective and radiative heat flux) could be compared directly with the measurements. A simplified cavity geometry was assumed for the radiation correction, with computed stepped shroud surface temperatures translated onto the "hidden" surfaces of the simple cavity. The radiation model is described in detail by Karabay (1996).

Three sets of computed Nusselt numbers are presented below:

(*a*) assuming the unheated disk to be adiabatic;

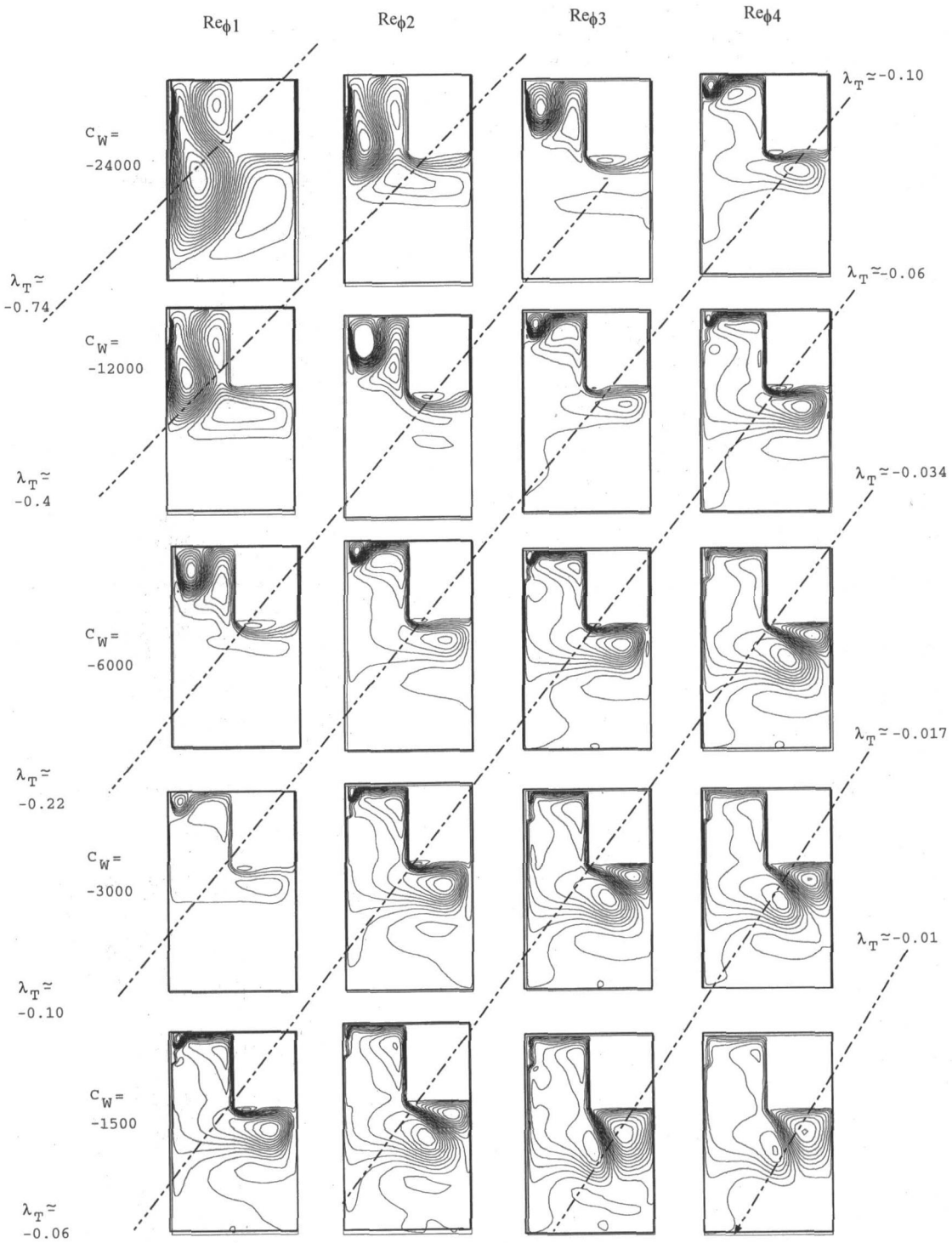

Fig. 4 Effect of Re_ϕ, C_w, and λ_T on computed streamlines

(*b*) assuming the unheated disk to be conducting, as outlined in (*v*) above;
(*c*) as in (*b*) but allowing for radiation from the heated disk.

It is considered that case (*c*) is the most appropriate one for comparisons with the measured Nusselt numbers.

4 Computed Flow Structure

Figure 4 shows the computed streamlines corresponding to the 20 cases shown in Table 1. The individual figures form a matrix corresponding to the Re_ϕ and C_W values, with the diagonals corresponding to approximately constant values of λ_T. Although the flow structure is complex, Fig. 5 shows a simplified picture, and the salient features are described below.

(*i*) For a given value of λ_T, the flow structures shown in Fig. 4 are very similar.
(*ii*) A simplified diagram of the flow structure for large values of $|\lambda_T|$ (for example, $\lambda_T = -0.4$) is shown in Fig. 5(*a*). There is radial inflow in the boundary layer on the upstream disk, radial inflow in the boundary layer on the radial surface of the stepped casing, and

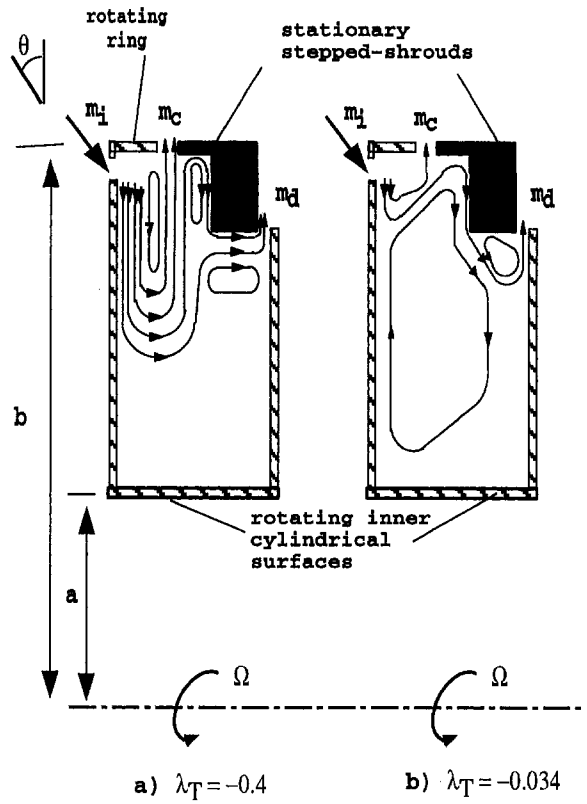

Fig. 5 Simplified diagram of flow structure

axial flow toward the downstream disk in the boundary layer on the axial surface of the casing. Half the flow that separates from the upstream disk flows radially out through the central clearance; the other half splits into two streams, each feeding one of the two boundary layers on the casing, before flowing out through the downstream clearance.

(*iii*) A simplified diagram for small values of $|\lambda_T|$ (for example, $\lambda_T = -0.034$) is shown in Fig. 5(*b*). In this case, where rotational effects are stronger and flow effects weaker, the radial inflow in the boundary layer on the upstream disk is restricted to the larger radii, and there is radial outflow over the rest of the disk surface. In addition, the radial inflow on the radial face of the stepped casing separates at the corner and forms a free shear layer before leaving through the downstream clearance; consequently, the axial flow in the boundary layer on the axial face of the casing is toward the upstream disk, the reverse to that in the large $|\lambda_T|$ case. The recirculation regions are therefore different for large and small $|\lambda_T|$.

(*iv*) At intermediate values of λ_T (for example, $\lambda_T = -0.06$), the flow shows features intermediate between these two cases.

Figure 6 shows the computed effect of λ_T on the axial distribution of $V_r/\Omega r$ and $V_\phi/\Omega r$ for various values of x. The $V_r/\Omega r$ plots show that, at the larger values of $|\lambda_T|$ and x, there is radial inflow in the boundary layer on the upstream disc ($z/s = 0$); at the smaller values of $|\lambda_T|$ and x, there is radial outflow in the boundary layer. The main recirculation occurs in the outer part of the cavity, $x > 0.75$, and the strength increases as $|\lambda_T|$ increases.

Figure 6 also shows that the magnitude of $V_\phi/\Omega r$ tends to increase as $|\lambda_T|$ increases. For $|\lambda_T| = 0.4$, $V_\phi/\Omega r$ increases as x decreases (for $x > 0.75$) in the region of radial inflow near the upstream disk. In this region, the angular momentum of the radial inflow tends to be conserved, creating free-vortex behavior. For the smaller values of $|\lambda_T|$ and x, there are only small variations of $V_\phi/\Omega r$ with either x or z/s. As is usual with rotating flows, radial inflow occurs in the boundary layers on the rotating disks where $V_\phi/\Omega r > 1$, and outflow occurs where $V_\phi/\Omega r < 1$.

5 Comparison Between Computations and Measurements

Figures 7 to 9 show the effect of Re_ϕ on the temperatures and Nusselt numbers for $C_W = -6000$, $-12{,}000$, and $-24{,}000$ respectively. The measured and fitted temperatures refer to the heated disk, and these temperatures were used as boundary conditions for the computations.

As stated in Section 3, as the temperatures of the unheated disk were not measured, it was necessary to make assumptions: these are referred to as the "adiabatic-disk assumption" and the "conducting-disk assumption." The Nusselt numbers for the heated disk were computed using the assumptions for the unheated disk; in addition, for the conducting-disk assumption, the computed Nusselt numbers were corrected to allow for radiation from the heated disk to the other surfaces in the cavity. There are, therefore, three curves of computed Nusselt numbers for each set of measurements.

Figure 7 shows the results for $C_W = -6000$ and $4.17 \times 10^5 < \mathrm{Re}_\phi < 3.28 \times 10^6$. Referring to the temperatures, it can be seen that the measured temperature of the heated disk is nearly uniform with T_S around 95°C. The adiabatic assumption produces a discontinuity in temperature on the unheated disk at $x \cong 0.82$, which is the location of the edge of the stepped casing. As expected, the conducting-disk assumption produces a lower computed temperature, and the temperature difference between the two assumptions increases as $|\lambda_T|$ decreases. The conducting-disk assumption with the radiation correction produces computed Nusselt numbers (referred to below as the "corrected Nusselt numbers") that agree reasonably well with the measured values in Fig. 7. The adiabatic assumption produces computed Nusselt numbers that are significantly lower than all the

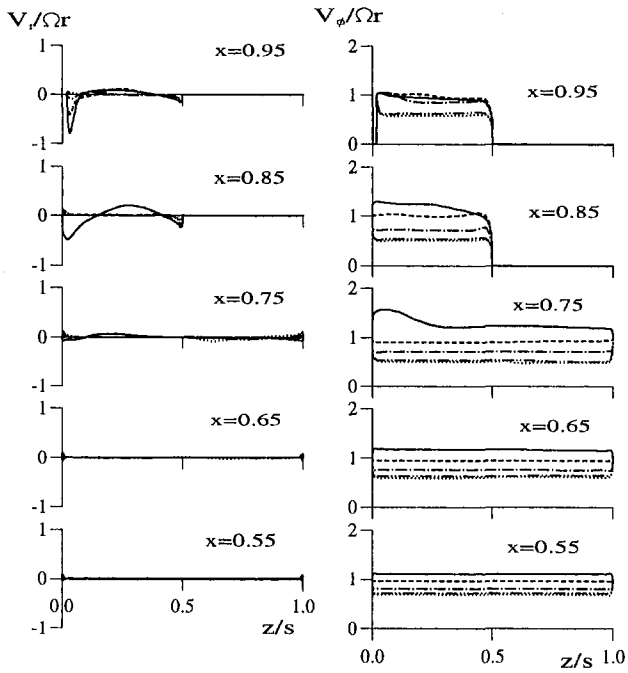

Fig. 6 Computed effect of λ_T on velocity distributions: — $\lambda_T = -0.4$; - - - $\lambda_T = -0.22$; — · — $\lambda_T = -0.10$; — · · — $\lambda_T = -0.034$; . . . $\lambda_T = -0.01$

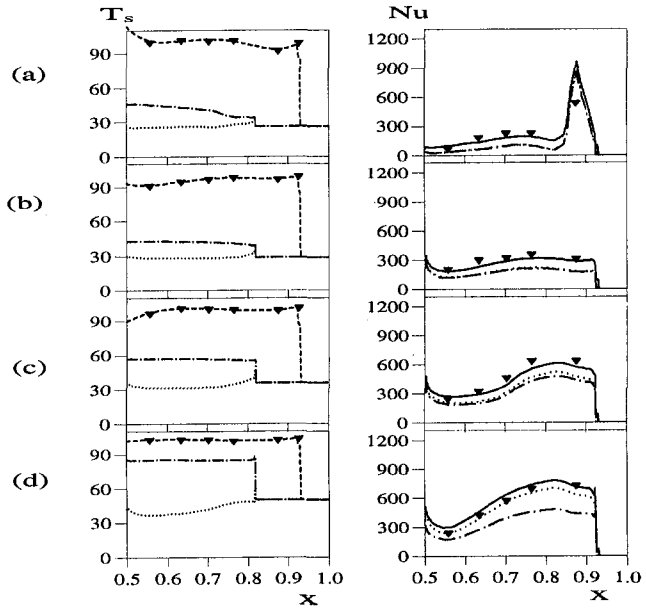

Fig. 7 Comparison between computed and measured temperatures and Nusselt numbers for $C_W = -6000$:

(*a*) $Re_\phi = 4.17 \times 10^5$, $\lambda_T = -0.1912$
(*b*) $Re_\phi = 8.30 \times 10^5$, $\lambda_T = -0.1103$
(*c*) $Re_\phi = 1.64 \times 10^6$, $\lambda_T = -0.063$
(*d*) $Re_\phi = 3.28 \times 10^6$, $\lambda_T = -0.036$

▼ Measured temperatures and Nusselt numbers on heated disk, - - - - Fitted temperature on heated disk, — · — Temperatures on unheated disc and Nusselt numbers on heated disk, computed using adiabatic-disk assumption, ... Temperatures on unheated disk and Nusselt numbers on heated disk, computed using conducting-disk assumption, — Nusselt numbers on heated disk computed using conducting-disk assumption with radiation correction

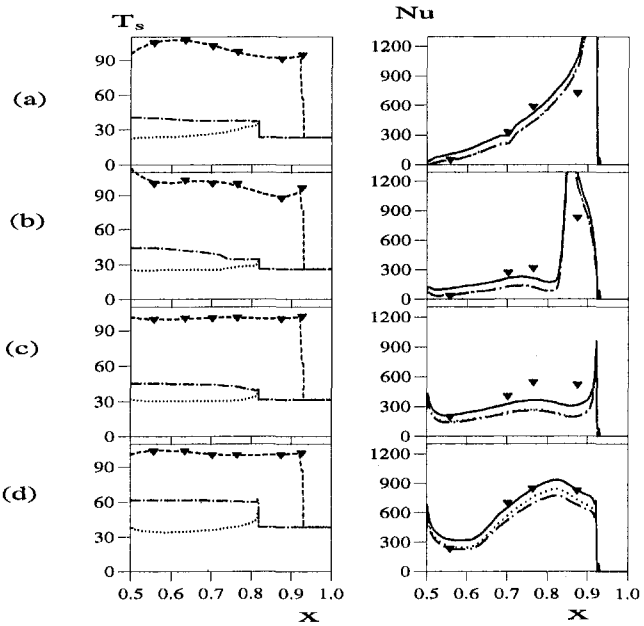

Fig. 8 Comparison between computed and measured temperatures and Nusselt numbers for $C_W = -12000$:

(*a*) $Re_\phi = 3.92 \times 10^5$, $\lambda_T = -0.401$
(*b*) $Re_\phi = 7.78 \times 10^5$, $\lambda_T = -0.232$
(*c*) $Re_\phi = 1.53 \times 10^6$, $\lambda_T = -0.135$
(*d*) $Re_\phi = 3.02 \times 10^6$, $\lambda_T = -0.07$

(For legend see Fig. 7)

measurements, and the difference increases as Re_ϕ increases. As with many other experiments involving rotating disks, radiation can be significant.

It is worth commenting on the distributions of Nu in Fig. 7. In Fig. 7(a), the peak around $x \cong 0.9$ is associated with the point where the radial outflow in the boundary layer on the heated disk meets the radial inflow, as discussed above. The computed peak Nusselt number significantly overestimates the measured value; this is also the case for all conditions where the "meeting point" occurs in the region where measurements were made. In Fig. 7(b, c, d), this point occurs radially outward of the heated section of the disk and, consequently, there is radial outflow in the boundary layer over the heated section. For this outflowing region, Nu increases as Re_ϕ increases.

Figure 8 shows the results for $C_W = -12000$. For this case, there is a larger region of inflow over the heated disk, with sharp peaks in Nu where the radial inflow and outflow meet. Despite the complex nature of the flow structure, the "corrected Nusselt numbers" produce many of the features seen in the measured values.

The Nusselt numbers in Fig. 9, for $C_W = -24{,}000$, show an even more peaky distribution in regions where the radial inflow and outflow meet on the heated disk.

As the flow structure depends principally on λ_T, as shown in Section 4, it is useful to present the Nusselt numbers in groups with constant values of λ_T. This is done in Fig. 10 for $\lambda_T \cong -0.22$, -0.10, -0.06, and -0.034. The computations are the "corrected" values (with the conducting-disk assumption and the radiation correction).

Figure 10(a), for $\lambda_T \cong -0.22$, shows the peaky distribution associated with combined radial inflow and outflow in the boundary layers on the heated disk. For the smaller values of λ_T in Figs. 10(b, c, d), the majority of the results show the behavior associated with radial outflow in the boundary layer. The exception is the case for $Re_\phi = 3.43 \times 10^6$ and $C_W = -24000$ in Fig. 10(b), where the computations show a sharp peak near the outer radius of the heated disk.

For a given value of λ_T, both the computations and experiments show the same qualitative behavior for Nu; the distribu-

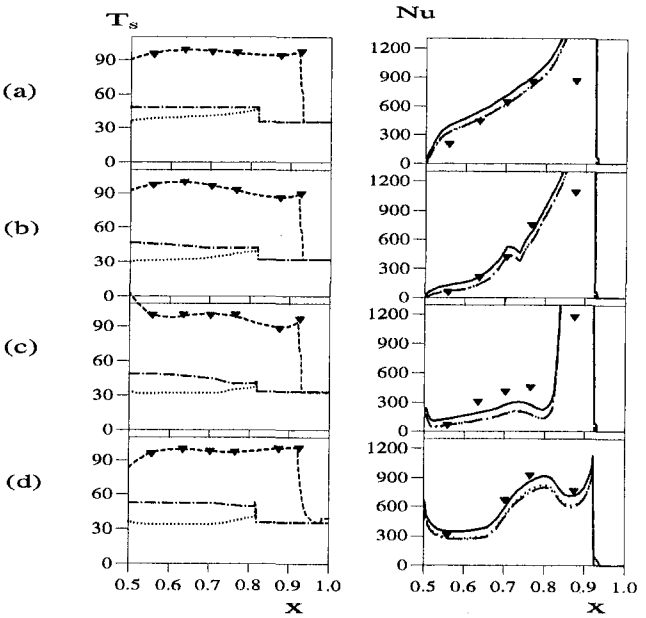

Fig. 9 Comparison between computed and measured temperatures and Nusselt numbers for $C_W = -24000$:

(*a*) $Re_\phi = 4.34 \times 10^5$, $\lambda_T = -0.742$
(*b*) $Re_\phi = 8.77 \times 10^5$, $\lambda_T = -0.422$
(*c*) $Re_\phi = 1.74 \times 10^6$, $\lambda_T = -0.242$
(*d*) $Re_\phi = 3.43 \times 10^6$, $\lambda_T = -0.141$

(For legend see Fig. 7)

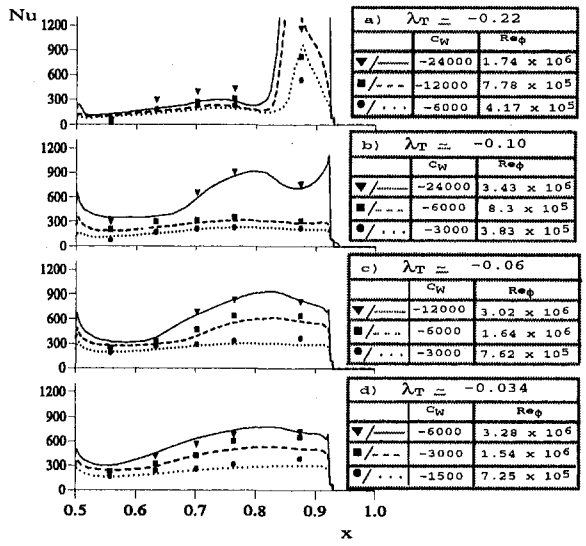

Fig. 10 Effect of C_W, Re_ϕ, and λ_T on computed and measured Nusselt numbers. (Symbols represent measured values; lines represent computed values)

tions are similar, and Nu increases as Re_ϕ increases. Considering the experimental and computational uncertainties, and in view of the complexity of the flow structure, the agreement between the measured and computed values is mainly good.

6 Conclusions

(*i*) The computations show that, although complex, the flow structure depends principally on the magnitude of the turbulent flow parameter, λ_T.

(*ii*) The cooling air injected at the periphery of the upstream heated disk creates a region of radial inflow in the boundary layer on this disk, the extent of which increases as $|\lambda_T|$ increases.

(*iii*) At the smaller values of $|\lambda_T|$, the computations show that radial outflow occurs over most of the surface of the upstream disk.

(*iv*) The computations and measurements both show a peak in Nu on the upstream disk in the region where the computed radial inflow and outflow meet, but the computations significantly overestimate the peak value.

(*v*) For a given value of λ_T, the computed and measured Nusselt numbers show similar distributions, and the magnitude of Nu increases as Re_ϕ increases.

(*vi*) Considering the computational and experimental uncertainties, and the complexity of the flow structure, the agreement between the computed Nusselt numbers (corrected for conduction and radiation effects) and measured values is mainly good.

As no velocity measurements were made, it is not possible to comment on the accuracy of the computed flow structure. However, the agreement between the computed and measured Nusselt numbers suggest that the main features of the flow have been reproduced by the computations.

Acknowledgments

The authors wish to thank BMW-Rolls-Royce GmbH, the UK Engineering and Physical Sciences Research Council, and the Defence Research Agency for funding the research described in this paper.

References

Gan, X., Mirzaee, I., Owen, J.M., Rees, D.A.S. and Wilson, M., 1996, "Flow in a rotating cavity with a peripheral inlet and outlet of cooling air," ASME Paper No. 96-GT-309.

Karabay, H., 1996, "Radiation heat transfer in a single cavity," Internal report No 60/96, School of Mech Eng., Univ. of Bath, United Kingdom.

Launder, B.E., and Sharma, B.I., 1974, "Application of the energy dissipation model of turbulence to flow near a spinning disc," *Letters in Heat and Mass Transfer,* Vol. 1, pp. 131–138.

Mirzaee, I., Gan, X., Wilson, M., and Owen, J.M., 1998, "Heat transfer in a rotating cavity with a peripheral inflow and outflow of cooling air," ASME JOURNAL OF TURBOMACHINERY, Vol. 120, pp. 818–823.

Owen, J.M., and Rogers, R.H., 1989, *Flow and heat transfer in rotating-disc systems, Vol. 1: Rotor-stator systems,* Research Studies Press, Taunton; Wiley, New York.

Owen, J.M., and Rogers, R.H., 1995, *Flow and heat transfer in rotating-disc systems, Vol. 2: Rotating Cavities,* Research Studies Press, Taunton; Wiley, New York.

Patankar, S.V., 1980, *Numerical Heat Transfer and Fluid Flow,* Hemisphere, New York.

Quinn, P.A., 1996, "Experimental study of a rotating cavity with peripheral flow. Report 6: Heat transfer measurements with a stationary step shroud," Report No 77/96, School of Mech. Eng., Univ. of Bath, United Kingdom.

Wilson, M., Chen, J.X., and Owen, J. M., 1996, "Computation of flow and heat transfer in rotating-disc systems," *Trans IMechE 3rd Int. Conf. on Computers in Reciprocating Engines and Gas Turbines,* pp. 41–50.

An Experimental Study on the Relationship Between Velocity Fluctuations and Heat Transfer in a Turbulent Air Flow

M. J. Denninger[1]

A. M. Anderson
email: andersoa@union.edu

Department of Mechanical Engineering,
Union College,
Schenectady, NY 12302

The work presented here is the first reported study to test the general correlation for turbulent heat transfer proposed by Maciejewski and Anderson (1996). A turbulent pipe flow apparatus was built for heat transfer and fluid studies. Tests were performed for a range of Reynolds numbers from 27,000 to 90,000. The heated wall temperature, adiabatic temperature, the wall heat flux, and the maximum velocity fluctuations were measured at each Reynolds number. The nondimensional groups recommended by Maciejewski and Anderson were formed and compared to the correlation. The results verify the correlation with agreement to within ±7 percent (as per Fig. 11). This study has important implications for the study of heat transfer in a wide range of fields, including the gas turbine industry. The development of a geometry independent correlation will lead to faster turn-around times and improved engine design.

Introduction

One of the most persistent and difficult problems in the gas turbine industry is the prediction of heat transfer to turbine blades and vanes. Current heat transfer theory cannot accurately predict the heat transfer to the first-stage blades of a newly designed gas turbine under all engine conditions. Most turbulent heat transfer correlations are restricted to the specific geometry for which they were developed because they are usually based on a length-based Nusselt number and a length-based Reynolds number. Testing geometrically similar engines is the only way to generate accurate correlations for gas turbine heat transfer prediction. The hope of constructing a general correlation for turbulent heat transfer rests on the possibility that surface convective heat transfer rates in turbulent flows can be characterized in purely local terms.

Recently, Maciejewski and Anderson (1996) developed a geometry-independent correlation for turbulent flow from studies of turbulent flow in air, water, and FC-77, for internal flows, external flows, and flows with high levels of free-stream turbulence. They proposed a new nondimensionalization technique and found that they could predict wall temperature in terms of the adiabatic temperature, the wall heat flux, the maximum streamwise turbulent fluctuations, and the fluid properties (without reference to the flow geometry) to within ±12 percent for the cases studied. To develop the correlation, they made some assumptions about the adiabatic temperature rise for the external flows and about the maximum turbulent fluctuations for the internal flows. This was necessary because none of the existing data sets contained all of the necessary information. The work presented here is the first to test the correlation proposed by Maciejewski and Anderson (1996) by measuring all of the required parameters.

Review of Existing Turbulence Models. The motivation for this work is to generalize existing methods for solving turbulent heat transfer problems. Current methods for solving turbulent heat transfer include empirical models for the Nusselt number and friction factor, and semi-empirical models that solve the time-averaged momentum and energy equations using empirical inputs to model the turbulent shear stress and turbulent heat transfer terms.

Semi-Empirical Models. The time-averaged momentum equation for turbulent boundary layer flow with constant density and negligible body forces is:

$$\bar{u}\frac{\partial \bar{u}}{\partial x} + \bar{v}\frac{\partial \bar{v}}{\partial y} - \frac{\partial}{\partial x}\left[\bar{v}\frac{\partial \bar{u}}{\partial y} - \overline{u'v'}\right] + \frac{1}{\rho}\frac{d\bar{P}}{dx} = 0 \quad (1)$$

$\overline{u'v'}$ is the turbulent shear stress and represents the "closure problem" in turbulent heat transfer. The turbulent shear stress is usually modeled by an algebraic or differential equation. One of the simplest models assumes that the turbulent shear stress is proportional to the mean velocity gradient:

$$\overline{u'v'} = -\epsilon_m \frac{\partial \bar{u}}{\partial y} \quad (2)$$

where ϵ_m is the eddy diffusivity for momentum and is related to the mixing length l as follows:

$$\epsilon_m = l^2 \frac{\partial \bar{u}}{\partial y} \quad (3)$$

The Prandtl mixing length theory proposes that close to the wall, l scales on the distance from the wall, and in the outer region of the boundary layer l scales on the momentum boundary layer thickness. Using empirical models for l and further assumptions about the shape of the velocity profile, one can derive an approximate but closed-form relation between skin friction and Reynolds number (see Kays and Crawford, 1980):

$$\frac{C_f}{2} = 0.0287\ \mathrm{Re}_x^{-0.2} \quad (4)$$

The time-averaged energy equation for turbulent boundary layer flow is:

[1] Currently at Raytheon Electronic Systems, Mechanical Engineering Lab, Sudbury, MA.

Contributed by the International Gas Turbine Institute and presented at the 43rd International Gas Turbine and Aeroengine Congress and Exhibition, Stockholm, Sweden, June 2–5, 1998. Manuscript received by the International Gas Turbine Institute February 1998. Paper No. 98-GT-108. Associate Technical Editor: R. E. Kielb.

$$\bar{u}\frac{\partial \bar{t}}{\partial x} + \bar{v}\frac{\partial \bar{t}}{\partial y} = \frac{\partial}{\partial y}\left(\alpha\frac{\partial \bar{t}}{\partial y} - \overline{\nu' t'}\right) \quad (5)$$

where $\overline{\nu' t'}$ is the turbulent heat flux. Similar to the momentum problem, the turbulent heat transfer problem can be related to the temperature gradient:

$$\overline{\nu' t'} = \epsilon_h \frac{\partial \bar{t}}{\partial y} \quad (6)$$

where ϵ_h is the eddy diffusivity for heat. Using the turbulent Prandtl number, $\mathrm{Pr}_t = \epsilon_m/\epsilon_h \cong 0.85$, the value for ϵ_h can be evaluated given ϵ_m. This allows for an approximate solution of Eq. (5), which yields (see Kays and Crawford, 1980):

$$\mathrm{St}\ \mathrm{Pr}^{0.4} = 0.0287\ \mathrm{Re}_x^{-0.2} \quad (7)$$

Equations (4) and (7) agree with experimental data for constant velocity and surface temperature, but the mixing length model breaks down if the flow changes physical nature. The eddy viscosity can become zero in regions of zero velocity gradients, which poses a problem because it is not physically realistic. Better models, such as the κ–ϵ and the algebraic stress model have been developed; however, these require simultaneous solution of a set of equations and don't offer a closed-form solution that is easily used by a designer.

Empirical Models. Another class of models is of the experimental variety in which the data from heat transfer experiments are plotted and correlations in the form of St, Nu = f(Re, Pr) result. These correlations exist for a variety of geometries, Prandtl numbers, and Reynolds numbers and provide a simple method for calculating heat transfer.

Among the many empirical models are that of Dittus and Boelter (1930) for fully developed turbulent flow in a smooth circular pipe:

$$\mathrm{Nu} = 0.023\ \mathrm{Re}^{4/5}\ \mathrm{Pr}^{n} \quad (8)$$

where $n = 0.4$ for heating and 0.3 for cooling. The experimental conditions are a Prandtl number range of 0.7 to 160, Reynolds number greater than 10,000, and a length-to-diameter ratio greater than 10.

Sieder and Tate (1936) modeled the effect of property variations and found that

$$\mathrm{Nu} = 0.027\ \mathrm{Re}^{4/5}\ \mathrm{Pr}^{1/3}\left[\frac{\mu}{\mu_s}\right]^{0.14} \quad (9)$$

μ is the viscosity evaluated at the free-stream temperature and μ_s is the viscosity evaluated at the surface temperature. The experimental conditions are a Prandtl number range of 0.7 to 16,700, Reynolds number greater than 10,000, and a pipe length-to-diameter ratio greater than 10.

Petukhov et al. (1970) recommended:

$$\mathrm{Nu} = \frac{(f/8)\ \mathrm{Re}\ \mathrm{Pr}}{\left(1.07 + 12.7\left(\frac{f}{8}\right)^{1/2}(\mathrm{Pr}^{2/3} - 1)\right)} \quad (10)$$

where the friction factor, f, can be obtained from the Moody (Nikuradse) diagram. This experimental conditions are a Prandtl number range of 0.5 to 2000, and a Reynolds number range of 10^4 to 5×10^6.

All of these correlations are for fully developed turbulent flow in a smooth circular pipe and are found to agree reasonably well with experimental data. Many correlations exist for this type of flow and still others for noncircular pipes, channel flow, and external flow in a variety of configurations. For specialized applications, such as flow over a turbine blade or flow over an airfoil, one must develop one's own correlations using similar techniques.

The empirical and semi-empirical solution methods have shortcomings. Solving the momentum and energy equations for turbulent flow requires an iterative solution to the temperature field and carries some assumptions about the shape of the velocity profile (specifically, the law of the wall). In complex geometries or adverse conditions this may not hold. In addition, the computation time can be extensive. The correlations of the form Nu = f (Re, Pr) are established by experimental data from specific configurations. If this differs from the geometry for which it is being applied, the results may not be acceptable. The lack of generality in the existing methods has created the motivation for the development of a general correlation.

Development of a General Correlation

Most turbulent heat transfer studies rely on a traditional nondimensionalization method, which leads to the development of such nondimensional variables as St, Nu, Re, and Pr. Recent work by Maciejewski and Anderson (1996) used an innovative approach to dimensional analysis to establish the elements of a general correlation for turbulent heat transfer in incompressible flows, which is independent of the geometry of the flow and independent of the thermal boundary conditions imposed on the flow.

The development of the Maciejewski/Anderson correlation is based on three assumptions: (1) the dimensional equivalence of the units of temperature and energy; (2) the existence of a single local measure of the turbulence, which incorporates the effects of geometry; and (3) the existence of a single local reference temperature, which incorporates the effects of thermal boundary conditions.

Assumption (1) is contrary to the position typically adopted by heat transfer texts although texts devoted to dimensional analysis either require (Sedov, 1959) or accept it (Bridgman, 1931). Adoption of this position leads to the formulation of a set of dimensionless variables for turbulent heat transfer that

Nomenclature

C_p = specific heat, J/kg K or 1/kg
c_f = skin friction coefficient
f = friction factor
k = conductivity, W/m K or 1/ms
l = mixing length
Nu = Nusselt number
Pr = Prandtl number
q'' = wall heat flux, W/m^2
Re = Reynolds number
St = Stanton number
T_w = wall temperature, °C or J
T_{ad} = adiabatic wall temperature, °C or J
U^* = reference velocity, m/s
$\bar{u}$ = mean component of turbulent velocity, m/s
u' = fluctuating component of turbulent velocity, m/s
u^+ = non-dimensional mean velocity = $\bar{u}/u_w$
u'^+ = non-dimensional turbulent velocity = u'/u_w
$u'_{\max}$ = maximum turbulent fluctuations, m/s
u_w = wall velocity = $\sqrt{V^2 f/8}$, m/s
V = pipe mean velocity, m/s
ϵ_h = eddy diffusivity for heat
ϵ_m = eddy diffusivity for momentum
ν = kinematic viscosity, m^2/s
μ = viscosity, Pa-s
ρ = density, kg/m^3
Π_0 = dimensionless driving potential
Π_1 = dimensionless surface heat flux
Π_2 = dimensionless velocity fluctuations
Π_3 = Prandtl number

do not require the use of a geometric or fluid length scale. Assumption (2) was addressed by Maciejewski and Moffat (1992a, b) who showed that the local value of the surface heat flux may be directly determined by the maximum local value of the turbulent velocity fluctuations, $u'_{\max}$. Assumption (3) was addressed by Anderson and Moffat (1992a, b) who showed that the local driving potential for heat transfer, which accounts for the effects of upstream thermal boundary conditions, is the difference between the actual local surface temperature, T_w and the local adiabatic surface temperature, T_{ad}.

Maciejewski and Anderson (1996) assumed that a relationship of the following form exists:

$$q''_w = f(u'_{\max}, \Delta T_{w,ad}, \rho, C_p, k, \mu) \tag{11}$$

Following Panton (1984), Callen (1985), and others, they further assumed that temperature and energy are dimensionally equivalent. (In this system, ΔT is expressed in J, C_p is expressed in kg^{-1}, and k is expressed in $\mathrm{m}^{-1}\mathrm{s}^{-1}$. The Boltzmann constant, $k_B = 1.38 \times 10^{-23}$ J/K, is used to convert Kelvins to Joules for the purpose of evaluating ΔT, C_p, and k.) The relation between the variables can be expressed nondimensionally as follows:

$$\Pi_0 = f(\Pi_1, \Pi_2, \Pi_3) \tag{12}$$

where:

$$\Pi_0 \equiv \frac{q''_w}{\rho U^{*3}} \quad \Pi_1 \equiv \frac{C_p(T_w - T_{ad})}{U^{*2}}$$

$$\Pi_2 \equiv \frac{u'_{\max}}{U^*} \quad \Pi_3 \equiv \frac{\mu C_p}{k} \tag{13}$$

and:

$$U^* \equiv \frac{k}{(\rho C_p)^{2/3}} \tag{14}$$

Π_0 may be interpreted as the nondimensional surface heat flux, Π_1 as the nondimensional driving potential for heat transfer (temperature difference), Π_2 as the nondimensional level of the turbulent fluctuations, and Π_3 as the nondimensional fluid viscosity (also recognized as the Prandtl number). The variables ρ, C_p, and k serve as the basis variables for the purpose of this nondimensionalization. The combination $U^* = k/(\rho C_p)^{2/3}$ has dimensions of velocity and serves as a reference velocity. Fluid properties are evaluated at the film temperature, $T_f = (T_w + T_{ad})/2$.

Maciejewski and Anderson (1996) used the following five data sets to develop the correlation:

1 Maciejewski and Moffat (1992a, b) —a study of boundary layer heat transfer in the presence of very high levels of free-stream turbulence (i.e., local free-stream turbulence levels between 20 and 60 percent of the local free-stream mean velocity). The study was conducted in air on a flat heat transfer surface placed in the margin of a turbulent free jet.

2 Hollingsworth and Moffat (1989) —a study of boundary layer heat transfer in the absence of free-stream turbulence conducted on both flat and concave heat transfer surfaces placed in a water channel.

3&4 Anderson and Moffat (1992a, b; 1990) —studies in air conducted in rectangular channels with roughness elements on one wall. The 1992 studies employ a dense array of flat elements and the 1990 study employs a sparse array of cubical elements.

5 Garimella and Schlitz (1992) [see also Schlitz (1992)] —studies conducted in rectangular channels with roughness elements on one wall using FC77 as a coolant. They employed an array of extremely flat elements.

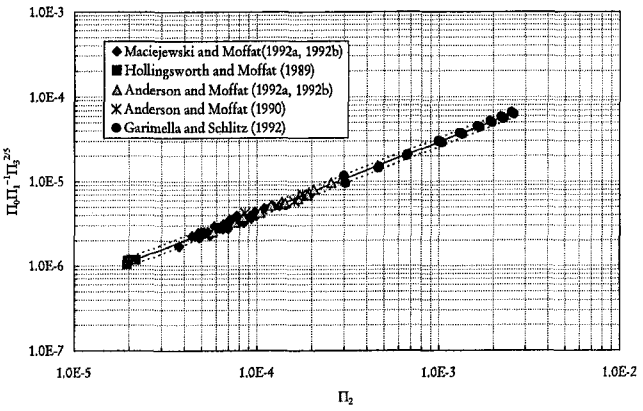

Fig. 1 General correlation

The resulting correlation developed by Maciejewski and Anderson is:

$$\Pi_0 = 0.0092\Pi_1\Pi_2^{5/6}\Pi_3^{-2/5} \tag{15}$$

The data and the correlation are shown in Fig. 1. (The solid line represents the correlation and the dashed lines are ±12 percent.) The correlation is limited to incompressible flows over the range of variables shown. The data sets used to generate the correlation represent a diverse range of experiments for which to test the hypothesis of Maciejewski and Anderson (1996). However, there were shortcomings to these data sets that prevent a clear verification of this correlation. The external flow data sets measured the maximum turbulent fluctuations, the wall heat flux, and the mean temperature of the flow but did not measure the adiabatic temperature. This was estimated using the mean and wall temperature data. The internal flow studies measured the adiabatic temperature and the wall heat flux but did not measure the maximum turbulent fluctuations. These values were inferred from the pressure drop in the test section. The study presented here includes direct measurement of the maximum turbulent fluctuations, the wall heat flux, and the adiabatic temperature.

Description of Experimental Facility

A schematic of the wind tunnel is shown in Fig. 2. The tunnel operates in suction mode. Air enters through a large filtered plenum into a 10.2 cm ID (4″) PVC supply tube. The supply tube is connected to a 30.5 cm (12″) long 10.2 to 5.1 cm (4 to 2″) diffuser, which decreases the inner tube diameter to the test section diameter. The test section is 1.8 m (6′) long and is

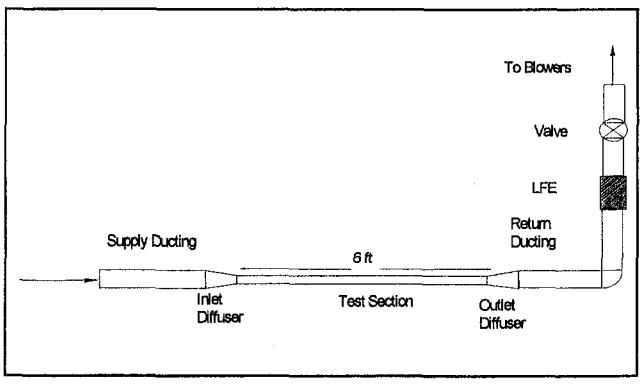

Fig. 2 Schematic of wind tunnel

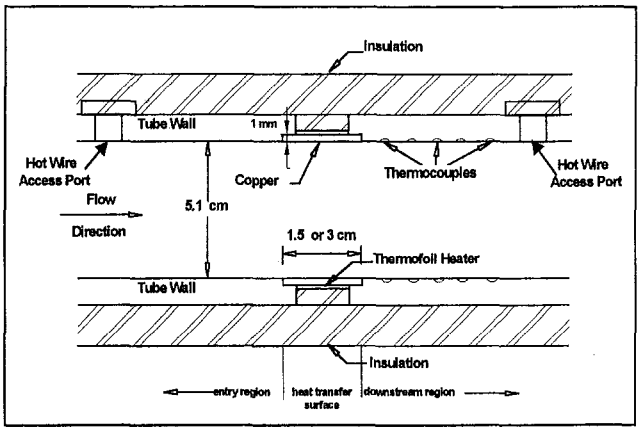

Fig. 3 Schematic of test section

constructed from 5.1 cm (2″) ID cast acrylic tubing. A 30.5 cm (12″) long 5.1 to 10.2 cm (2 to 4″) diameter diffuser joins the test section to the return duct flow (10.2 cm ID PVC tube). A laminar flow element (LFE) is mounted downstream of the test section for measurement of channel flow rate and a valve is used to control the flow rate. The return duct is connected to two blowers, which supply the air flow.

The test section is shown in Fig. 3. It consists of an entry region, a heat transfer surface, and a downstream region. The entry region is 88 cm long, which allows for a length-to-diameter ratio of 17.4 to ensure fully developed flow at the heat transfer surface. The heat transfer surface consists of a 5.1 cm (2″) ID, 1 mm (0.040″) thick copper cylinder with an etched thermofoil heater glued around the outside diameter. The surface fits between the two acrylic tubes that form the entry and downstream regions. Tests were run for both a 3 and a 1.5 cm long (in the flow direction) heat transfer surface. The downstream region is 88 cm long and is instrumented with thermocouples for downstream temperature measurement. Hot wire access ports are located up and downstream of the heat transfer surface. Pressure taps are located 1 m apart for measurement of channel pressure drop.

Surface temperatures are measured on the heat transfer surface, on the entry region wall, and on the downstream wall by calibrated 36 gage type-K thermocouples. The inlet bulk temperature (which is also the adiabatic temperature for this study) was measured using three thermocouples placed around the center of the inlet flow approximately 1 m upstream of the heat transfer surface.

Velocity measurements are made using a Dantec model 56C17 constant temperature hot-wire anemometer with a miniature boundary layer probe (Dantec model P14) mounted on a Unislide computer controlled traversing system. The hot-wire output is fed to a Keithly DAS800 A/D card mounted in a desktop PC. Data were acquired at 100 Hz, with 2000 samples taken at each point. There are six access ports in the test section (three upstream and three downstream of the heat transfer surface).

Experimental Procedure. The heat transfer and velocity data were acquired separately. Velocity profiles were acquired for range of Reynolds numbers between 27,000 and 90,000. For each test the valve was set and the flow rate was measured with the laminar flow element. The test section pressure drop was measured and compared to predicted values. The hot-wire calibration was checked against a pitot probe before each traverse and found to agree within 1.3 percent on average. At each point the computer recorded the hot-wire position, the average velocity of 2000 readings at that point, and the turbulent fluctuations based on the rms value using 2000 readings. Each profile was then integrated over the pipe flow area to determine the flow rate and compared to the laminar flow element reading. The two agreed within 1.4 percent on average.

Temperatures were acquired for both the 1.5 and 3 cm heat transfer surface. The flow rate was set to that of a corresponding velocity profile and the power to the heater was set to achieve a 20°C temperature rise at the copper surface. Temperatures were monitored until steady state was reached and then recorded for all thermocouple locations.

Data Reduction. The maximum turbulent fluctuations were found by direct examination of the velocity profiles. All profiles presented here were measured at the upstream port location. Centerline turbulence levels ranged from 1.2 percent at Re = 90,000 to 2.5 percent at Re = 27,000. The adiabatic temperature for this configuration is the measured inlet temperature so its measurement does not require any additional tests (see Anderson and Moffat, 1990, for further explanation). The wall temperature was measured by the embedded thermocouples in the acrylic and copper sections. Fluid properties were evaluated at the film temperature. The value for the heat flux was calculated as the input power minus the conductive losses due to lead-wire conduction, and axial and radial conduction through the tube.

Lead-wire losses were calculated using a simple one-dimensional model and were typically less than 0.1 percent of the input power. The tube conduction losses were calculated using a finite element model of the test section. The model inputs were the experimentally determined steady-state temperature of the copper inner and outer surface, the downstream wall temperatures, the outer tube temperatures, and the input power minus the lead-wire losses. The tube conduction heat losses were found to be 6–10 percent of the input power for the 3 cm heater and 10–15 percent of the input power for the 1.5 cm heater.

Uncertainty Analysis. An *N*th-order uncertainty analysis was performed to determine the uncertainty on the two main calculated quantities, the wall heat flux and the maximum fluctuating velocity. The standard single sample uncertainty analysis as recommended by Kline and McClintock (1953) and extended by Moffat (1982) was used. All uncertainties are quoted at 20:1 odds. The uncertainty in adiabatic temperature rise was estimated as ±0.15°C (0.7 percent). The uncertainty in the fluctuating velocity was based on the Chi-square variable for 2000 readings and was found to be approximately ±3 percent. The largest uncertainty was in the estimation of the wall heat flux due to the uncertainty in the tube conduction losses. This value was determined by perturbing the finite element program inputs and is estimated at ±50 percent, which yields an uncertainty in the wall heat flux of 3 to 8 percent.

Experimental Results

Aerodynamic Studies. Wall friction factors, f, were measured for Reynolds numbers from 20,000 to 90,000. The results are plotted in Fig. 4 and show excellent agreement (for Re > 30,000) with a correlation for turbulent pipe flow. Uncertainty in the friction factor ranged from 1 to 5 percent and error bars are shown on the plot. The measured friction factor values for Re < 30,000 are lower than the predicted value, which may indicate that the flow is not yet fully turbulent.

The structure of the flow was verified by making velocity traverses across the test section over the range of Reynolds numbers. Figure 5 plots the mean turbulent velocity versus distance from the wall in wall coordinates where:

$$u^+ = \frac{\bar{u}}{u_w} \quad \text{and} \quad u_w = \sqrt{\frac{f}{8}\,V^2} \tag{16}$$

$$y^+ = \frac{y u_w}{\nu} \tag{17}$$

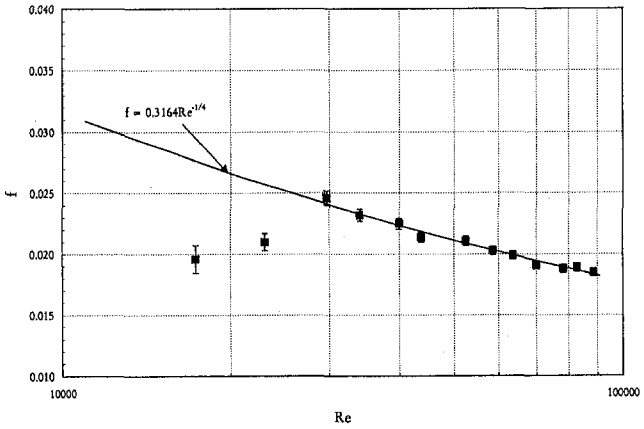

Fig. 4 Friction factor versus Reynolds number

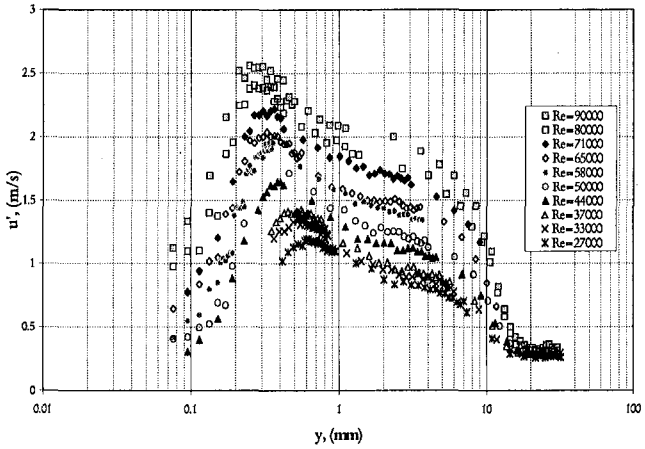

Fig. 7 Fluctuating velocity profile, u' versus y

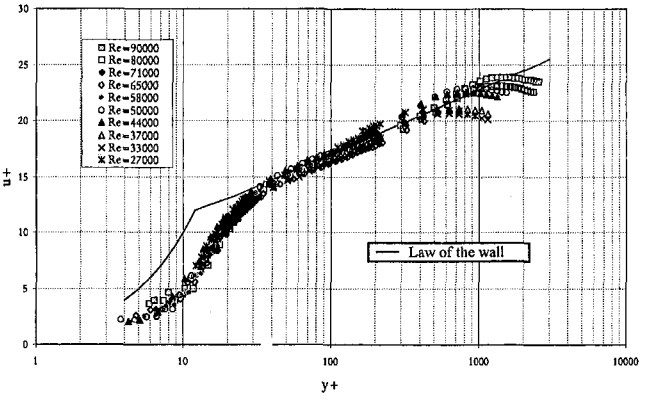

Fig. 5 Mean velocity profile plotted in wall coordinates

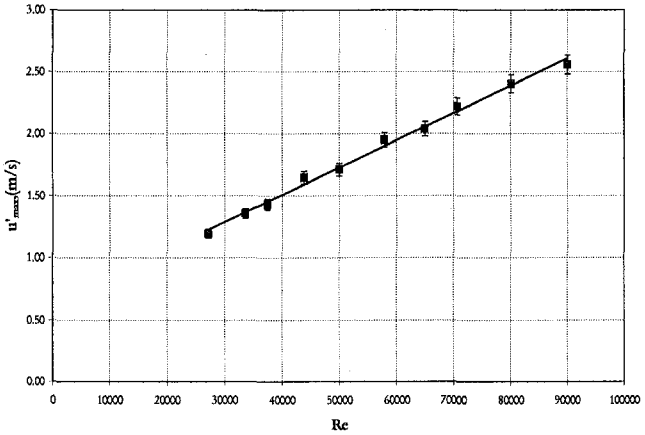

Fig. 8 Maximum velocity fluctuations versus Re

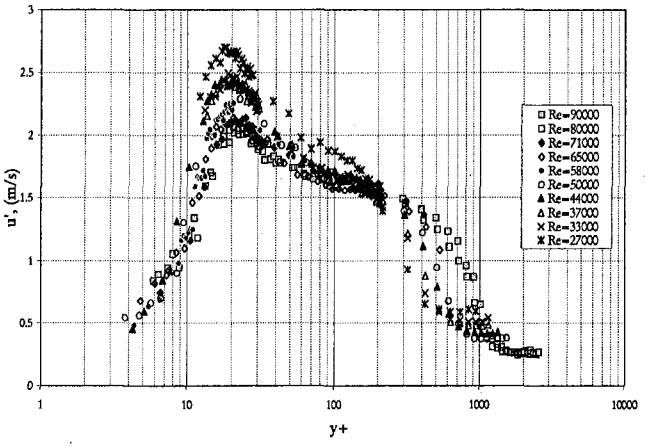

Fig. 6 Fluctuating velocities in wall coordinates

u_w is the friction velocity, ν is the kinematic viscosity, y is the distance from the wall and V is the mean velocity. The profiles collapse well in the log region and confirm that the flow is turbulent.

Figure 6 plots the nondimensional velocity fluctuations in wall coordinates, where:

$$u'^{+} = \frac{u'}{u_w} \tag{18}$$

u'^{+} peaks between $y^{+} = 10$ and 20, which agrees well with turbulent boundary layer data (Hinze, 1975). The maximum value decreases from about 2.7 at a Reynolds number of 27,000 to 2.0 at a Reynolds number of 90,000.

Figure 7 plots u' versus y for all cases tested. In this case, the maximum value of u' increases from about 1.2 m/s at Re = 27,000 to 2.6 m/s at Re = 90,000. The peak location moves closer to the wall as the Reynolds number increases. Figure 8 plots u'_{max}, as determined by observation of the profiles, versus Reynolds number. For the range of flows studied the relationship is fairly linear as shown in the figure. All data values are listed in Table 1 (1.5 cm heater) and Table 2 (3 cm heater).

Heat Transfer Data. Figure 9 plots the average heat transfer coefficient (at the heat transfer surface) versus the wall temperature rise for a temperature rise from 5 to 50°C. The plot verifies the data reduction scheme, showing that the values are independent of temperature rise. The uncertainty in the adiabatic heat transfer coefficient is about 7 percent for this Reynolds number as shown.

Figure 10 plots the heat transfer coefficient versus Reynolds number for the 1.5 and 3 cm heaters. For the range tested h increases fairly linearly with Re. The data are also compared with values predicted by Eq. (7) for fully developed turbulent pipe flow. As expected the experimental data (which is in the thermal entry region of the pipe) is higher than the correlation for the fully developed region. Data values are listed in Tables 1 and 2.

Correlation Predictions. The nondimensional variables recommended by Maciejewski and Anderson (1996) were formulated as shown in Tables 1 and 2. Figure 11 plots the new

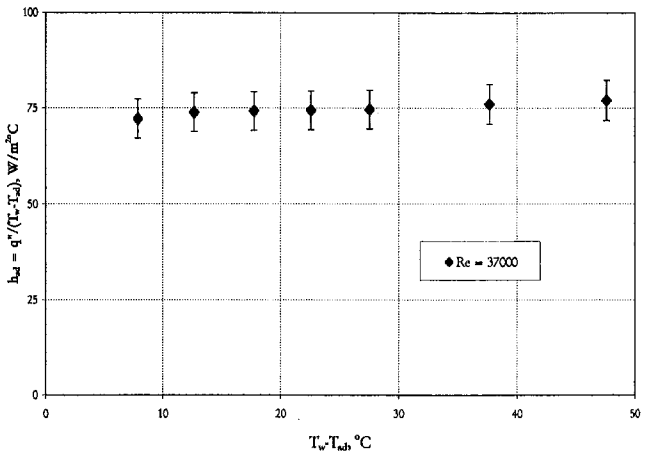

Fig. 9 Heat transfer coefficient versus temperature rise

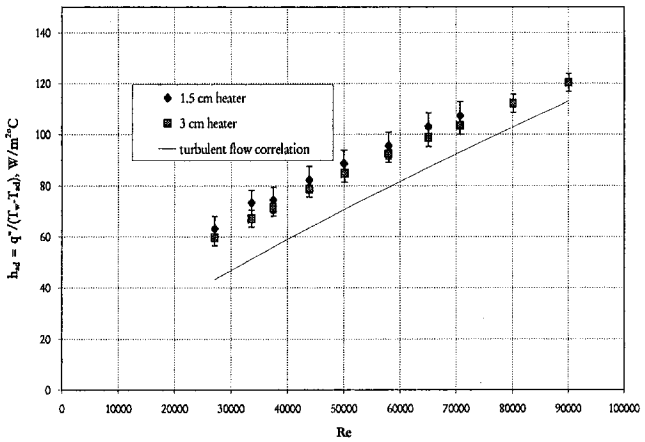

Fig. 10 Heat transfer coefficient versus Re

Table 1 1.5 cm heater data

Re	u'max (m/s)	T_{ad} (°C)	T_w (°C)	q"wall (W/m^2)	Π_0 x 10^9	Π_1 x 10^4	Π_2 x 10^4	Π_3
27104	1.19	22.6	45.4	1442.6	1.22	2.25	1.18	0.71
33618	1.36	24.5	45.1	1510.1	1.27	2.02	1.34	0.71
37441	1.43	24.6	45.2	1532.1	1.29	2.02	1.41	0.71
43820	1.65	22.6	45.2	1859.6	1.58	2.24	1.63	0.71
50000	1.71	24.7	45.1	1809.1	1.52	2.00	1.69	0.71
57897	1.95	24.6	45.1	1960.1	1.65	2.01	1.93	0.71
64984	2.04	22.9	45.4	2320.2	1.97	2.22	2.02	0.71
70687	2.22	24.8	45.1	2178.9	1.83	1.99	2.19	0.71

data as Π_2 versus $\Pi_0\Pi_1^{-1}\Pi_3^{2/5}$. The solid line is the Maciejewski/Anderson correlation and the dashed lines are ±12 percent. The 1.5 cm heater data appear to lie on top of the correlation, while the 3 cm data are slightly below. Comparing each to the correlation, the 1.5 cm data agree within a standard error of 3 percent and the 3 cm data agree within a standard error of 7 percent. Figure 12 plots the same data along with all the other data examined by Maciejewski and Anderson (1996).

Discussion

There are four elements of a general method for predicting turbulent heat transfer: (1) a method for predicting the local surface heat flux, q''_w, in terms of the local variables u'_{max}, $T_w - T_{ad}$, ρ, C_p, μ, and k, (2) a method for estimating u'_{max}, (3) a method for estimating $T_w - T_{ad}$, and (4) a method for estimating ρ, C_p, μ, and k.

The foundation for the first of these elements was proposed by the work of Maciejewski and Anderson (1996) and confirmed by this work.

Table 2 3 cm heater data

Re	u'max (m/s)	T_{ad} (°C)	T_w (°C)	q"wall (W/m^2)	Π_0 x 10^9	Π_1 x 10^4	Π_2 x 10^4	Π_3
27104	1.19	24.8	45.1	1211.8	1.02	1.99	1.18	0.71
33618	1.36	24.8	45.1	1363.6	1.15	1.99	1.34	0.71
37441	1.43	24.8	44.8	1428.3	1.20	1.96	1.41	0.71
43820	1.65	24.9	45.2	1599.8	1.34	1.99	1.63	0.71
50000	1.71	24.7	45.3	1745.3	1.46	2.02	1.69	0.71
57897	1.95	24.8	45	1867.2	1.57	1.98	1.93	0.71
64984	2.04	24.8	45	1995	1.68	1.98	2.01	0.71
70687	2.22	24.8	45.2	2110.1	1.77	2.00E	2.19E	0.71
80137	2.40	24.8	45	2264.9	1.90	1.98E	2.37E	0.71
90060	2.56	25	45.3	2442.5	2.05	1.99E	2.52E	0.71

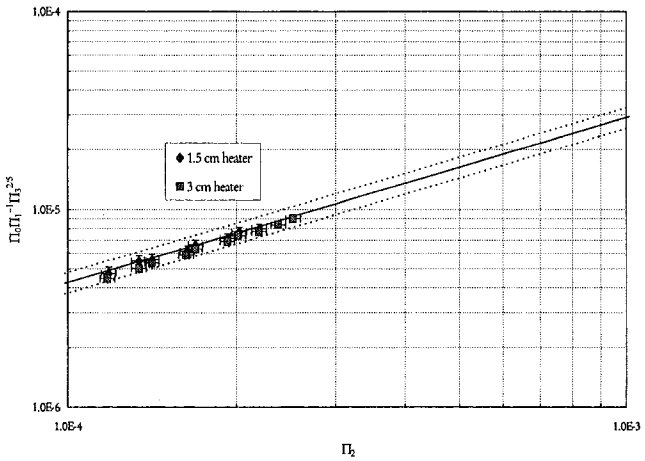

Fig. 11 Data in Maciejewski/Anderson variables

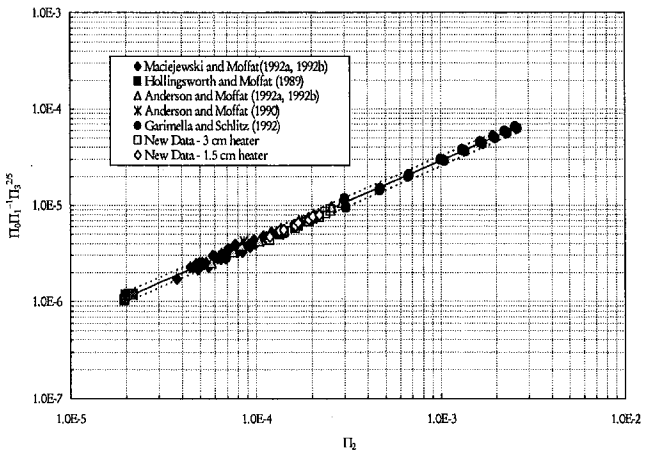

Fig. 12 Maciejewski/Anderson correlation

This study has not addressed element 2. Estimation of u'_{max} is nontrivial and it is essential to the proposed method for evaluating turbulent heat transfer. However, this falls within the domain of turbulence simulation and turbulence modeling. (Existing $k-\epsilon$ models could be used to estimate u'_{max}.) Or it can follow the work of Anderson and Moffat (1992a, b) who developed a method for estimating u'_{max} based on the channel pressure drop.

The third element is a method for estimating the local value of T_{ad}. (Once T_{ad} is determined, ρ, C_p, μ, and k can be evaluated via thermodynamic equations of state.) The estimation of T_{ad} can be conducted within the framework of linear mathematics, i.e., superposition. In flows that exhibit a clear marching direction, the superposition method can be applied to calculate the adiabatic temperature. In a recirculating flow, the value of the adiabatic temperature will approach the value of the bulk-mean temperature due to strong thermal mixing. An estimate of the bulk mean temperature may suffice for use in the correlation.

If these elements of a general method for predicting turbulent heat transfer can be established, then a general method for predicting turbulent heat transfer might consist of the following sequence of steps:

1 Use an existing technique in turbulence simulation or in turbulence modeling to estimate u'_{max} throughout the domain of the analysis in question.
2 Use the superposition method to evaluate T_{ad} at the first "point" along the boundary of the domain of the analysis.
3 Use the general correlation for turbulent heat transfer to evaluate q''_w (given T_w) or T_w (given q''_w) at the first "point" along the boundary of the domain of the analysis.
4 "March" along the boundary of the domain of the analysis, applying step (ii) and step (iii) at each "point" along the boundary.

Conclusion

This correlation verifies that turbulent heat flux can be predicted by purely local variables, independent of the global geometry of the flow and of the thermal boundary conditions. The level of the turbulent velocity fluctuations characterizes the flow boundary conditions, while the adiabatic temperature characterizes the thermal boundary conditions.

This work is also part of the development of a general method for solving turbulent flow heat transfer. The motivation for this work was to test the Maciejewski/Anderson correlation using a facility that would directly measure the wall temperature, the adiabatic temperature, the wall heat flux, and the maximum turbulent velocity fluctuations. The results presented here confirm the Maciejewski/Anderson correlation for an internal turbulent pipe flow of air. Although only a small range of the correlation has been tested, the fact that it lies directly on the correlation validates the original range of flows tested. Further work should look at extending the range tested under a variety of turbulent flow conditions.

Acknowledgments

The authors wish to acknowledge support from the Union College Faculty Research Fund and the help of Mr. Bryan Roy on this project.

References

Anderson, A. M., and Moffat, R. J., 1990, "Convective Heat Transfer From Arrays of Modules With Non-uniform Heating: Experiments and Models," Rept No. HMT-43, Department of Mechanical Engineering, Stanford University, Stanford, CA.

Anderson, A. M., and Moffat, R. J., 1992a, "The Adiabatic Heat Transfer Coefficient and the Superposition Kernel Function: Part 1—Data for Arrays of Flat Packs for Different Flow Conditions," ASME *Journal of Electronic Packaging,* Vol. 114, pp. 14–21.

Anderson, A. M., and Moffat, R. J., 1992b, "The Adiabatic Heat Transfer Coefficient and the Superposition Kernel Function: Part 2—Modeling Flat Pack Data as a Function of Channel Turbulence," ASME *Journal of Electronic Packaging,* Vol. 114, pp. 22–28.

Bridgman, P. W., 1931, *Dimensional Analysis,* Yale University Press, New Haven, CT.

Callen, H. B., 1985, *Thermodynamics and an Introduction to Thermostatistics,* 2nd ed., Wiley, New York.

Dittus, F. W., and Boelter, L. M. K., 1930, *Publications in Engineering,* University of California, Berkeley, Vol. 2, pp. 443.

Garimella, S. V., and Schlitz, D. J., 1992, "Enhanced Internal Cooling of Turbine Blades Using Large Scale Roughness Elements," *Fundamentals and Applied Heat Transfer Research for Gas Turbine Engines,* ASME HTD-Vol 226, pp. 9–15.

Garimella, S. V., and Schlitz, D. J., 1993, "Reducing Inter-Chip Temperature Differences in Computers Using Vortex Generators in Forced Convection," ASME *Journal of Electronic Packaging,* Vol. 115, pp. 410–415.

Hinze, J. O., 1975, *Turbulence,* McGraw-Hill, New York.

Hollingsworth, D. K., and Moffat, R. J., 1989, "Measurement and Prediction of the Turbulent Thermal Boundary Layer in Water on Flat and Concave Surfaces," Rept. No. HMT-41, Department of Mechanical Engineering, Stanford University, Stanford, CA.

Kays, W. M., and Crawford, M. E., 1980, *Convective Heat and Mass Transfer,* McGraw-Hill, New York.

Kline, S. J., and McClintock, F. A., 1953, "Describing Uncertainties in Single Sample Experiments," *Mechanical Engineering,* Jan., pp. 3–8.

Maciejewski, P. K., and Moffat, R. J., 1992a, "Heat Transfer With Very High Free-Stream Turbulence: Part I—Experimental Data," ASME *Journal of Heat Transfer,* Vol. 114, pp. 827–833.

Maciejewski, P. K., and Moffat, R. J., 1992b, "Heat Transfer With Very High Free-Stream Turbulence: Part II—Analysis of Results," ASME *Journal of Heat Transfer,* Vol 114, No 4, p 834–839.

Maciejewski, P. K., and Anderson, A. M., 1996, "Elements of a General Correlation for Turbulent Heat Transfer," ASME *Journal of Heat Transfer,* Vol. 118, pp. 287–293.

Moffat, R. J., 1982, "Contributions to the Theory of Single Sample Uncertainty Analysis," ASME *Journal of Fluids Engineering,* Vol. 104, pp. 250–260.

Panton, R. L., 1984, *Incompressible Flow,* Wiley, New York.

Petukhov, B. S., et al., 1970, *Advances in Heat Transfer,* Vol. 6, Academic Press, New York.

Schlitz, D. J., 1992, "Localized Enhancement of Heat Transfer From an Array of Heat Sources in Forced Convection," MS Thesis, Department of Mechanical Engineering, University of Wisconsin—Milwaukee, 1992.

Sedov, L. I., 1959, *Similarity and Dimensional Methods in Mechanics,* Academic Press, New York.

Sieder, E. N., and Tate, G. E., 1936, *Ind. Eng. Chem.,* Vol. 28, p. 1429.

Development of a Centrifugal Compressor With a Variable Geometry Split-Ring Pipe Diffuser

J. W. Salvage
Principal Staff Engineer
United Technologies,
Carrier Corporation,
Carrier Parkway, TR-4,
P.O. Box 4808
Syracuse, NY 13221

Higher noise levels resulted when a compressor was scaled to larger capacity. The machine's sound pressure level was relieved by increasing the distance between the impeller blade tip and diffuser leading edge. However, the part-load surge line deteriorated severely as a consequence. A variable geometry pipe diffuser solved this problem, permitting operation at stringent off-design conditions. The addition of a variable diffuser permits compressor selection very near its most efficient full-load operating point, without regard for limitations normally imposed by part-load requirements. The principal lessons learned during aerodynamic design refinement include (a) how performance and surge depend upon positioning the variable inlet guide vanes and variable diffuser, and (b) how to define simultaneous variation of inlet guide vanes and diffuser for specific operational objectives. Generally, each operating point requires a unique setting of the variable components to achieve maximum efficiency. However, linked movement is shown to yield both a satisfactory surge line and improved performance for most applications when compared to a compressor without the variable geometry pipe diffuser.

Introduction

Variable geometry in turbomachinery is mainly applied for range enhancement. However, when two components are independently variable (e.g., speed and inlet guide vanes (IGVs) or IGVs and diffuser vanes), optimizing part-load efficiency is usually possible as well.

Although the present work pertains to a variable pipe diffuser in a centrifugal compressor with variable IGVs, other investigators' accomplishments with vaned diffusers are relevant. Diffuser geometry is usually varied in one of two ways, variable vane stagger or variable wall position. Simon et al. (1987) studied variable IGVs with "adjustable" vaned diffusers, meaning that the vane stagger was changed by partial compressor disassembly. They showed that (a) although it is possible to maintain high surge pressure ratio to low flows by closing the diffuser with constant IGV setting, this leads to only local efficiency improvement; and (b) the full potential for improvement requires the ability to freely select combinations of IGV-diffuser settings.

Harada (1996) changed diffuser vane stagger from outside the compressor in response to conditions within the compressor. Pressure differences across the vane leading edge were sensed to indicate flow incidence. Diffuser vane stagger was controlled using the pressure difference for flows above 60 percent of design flow. Below 60 percent, stagger controlled diffuser wall static pressure fluctuation. Wide range was demonstrated, but optimized efficiency was not the objective.

The effect of variable wall position is exemplified by Comey et al. (1985). The diffuser passage area was altered by axially translating one diffuser endwall. Wall movement was also accomplished from outside the compressor for this work. The primary challenge was sealing the vanes as they protruded through the opposite wall. A two-point reduction in stage efficiency and more than 50 percent reduction in surge margin was attributed to vane-end leakage. Furthermore, a 2 percent reduction in work accompanied implementation of variable diffuser geometry. Fairing of the vaneless diffuser lead-in resulted in extra full-load dump loss at the impeller trailing edge. As the diffuser wall was closed, the impeller exit velocity diagram was changed such that work input increased less than normal with flow reduction. At design speed with axial IGVs, closing the diffuser led to an additional 15 percent flow reduction without surge for a pressure ratio near 7. Similarly, at 60 percent of design speed near a pressure ratio of 3, diffuser closure resulted in a 20 percent flow reduction before surge.

Sishtla (1996) reported test results for three configurations that varied only the vaned diffuser throat area rather than the full diffuser's channel width. Such configurations were also shown capable of maintaining satisfactorily high head to low flows, achieving nearly linear surge lines from the fully open geometry to settings that achieved as little as 15 percent head reduction for 80 percent flow reduction.

Two concepts of variable geometry pipe diffusers were described by Salvage (1996): the split-ring diffuser (SRD) and the recirculation diffuser. Prototype test results suggested both concepts could effectively enhance surge margin for compressors that already use variable IGVs. Leakage effects remained a major concern. Both efficiency loss and surge margin reduction resulted when variable geometry was implemented, even for the diffuser fully open. Development of the SRD is described below. It was deemed more cost effective and easier to develop than the recirculation diffuser.

The particular compressor application considered here is a chiller system (see Appendix) of a size typically used to air condition buildings. Such systems frequently have severe operating requirements, often entailing maintenance of high pressure ratio from the design point to 10 percent of the design flow.

The compressor approximates a simple aerodynamic scale of smaller compressors with fixed-geometry pipe diffusers already in service. Experience indicated a potential for unacceptable

Contributed by the International Gas Turbine Institute and presented at the International Gas Turbine and Aeroengine Congress and Exhibition, Stockholm, Sweden, June 2–5, 1998. Manuscript received by the ASME Headquarters April 1, 1998. Paper No. 98-GT-7. Associate Technical Editor: R. Kielb.

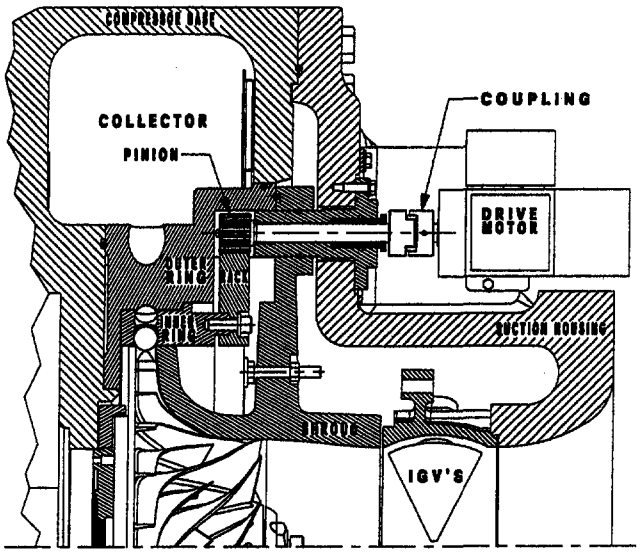

Fig. 1 Compressor cross section

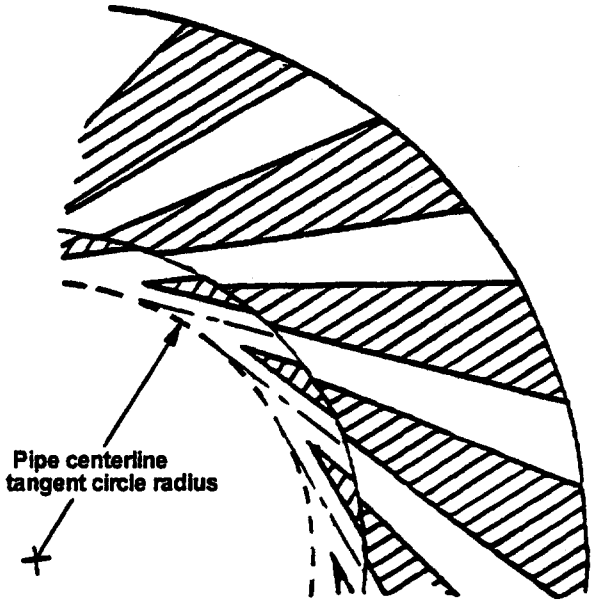

Fig. 2 Cross section of the split-ring diffuser

noise levels with the larger machine. The means to control the noise (namely, increasing the distance between the impeller blade tip and the diffuser leading edge) was known to be effective. However, increasing impeller-diffuser spacing was also known to adversely affect part-load surge margin by increasing flow blockage due to added diffusion between the impeller and the diffuser throat. Fortunately, increasing impeller-diffuser spacing was accompanied by improved full-load efficiency as shown below.

Although each point has a unique IGV/SRD combination yielding maximum efficiency, directly coupling IGV and SRD movement will be seen to yield both a surge line satisfying most applications and significantly improved part-load performance when compared to a fixed diffuser and variable IGVs. Coupled IGV/SRD movement reduces system control complexity. For most applications, the efficiency difference is small between the best attainable with independent IGV/SRD control and that obtained with linked IGVs and SRD.

Description of the Compressors

The compressor used in this investigation is composed of a set of seven uncambered IGVs, a backswept impeller, a pipe diffuser, and a constant cross-sectional-area collector. The compressor cross section is shown in Fig. 1.

The pipe diffuser geometry is defined by a short constant-area throat section, followed by a length of 4 deg divergence and then a second divergence of 8 deg. The SRD is characterized by a cylindrical cut that divides the normally continuous ring of pipes into a tangentially movable inner ring and a fixed outer ring. The means to actuate the SRD inner ring is illustrated in Fig. 1. A cross section of the SRD is shown in Fig. 2. Compressor geometry is summarized in Table 1.

Test results are discussed for both fixed (i.e., nonvariable) and variable pipe diffuser configurations. Fixed diffusers do not have the "split-radius to tangent-circle-radius ratio" defined in Table 1. The variable diffuser may either be adjustable, meaning the inner ring's tangential position can be changed only by partial disassembly, or "actuatable," meaning the inner ring can be moved by electric motor driven from outside the compressor.

Peak efficiency operating conditions of flow and head parameters are provided in Table 2.

Test Description

Compressor configurations were tested in a complete refrigeration system using HFC134a as the working fluid. The system is composed of evaporator, compressor, condenser, subcooler, and throttle valve. The compressor is driven by a constant-speed hermetic motor. The system and its fundamental operational requirements, as well as experimental and data reduction details specifically for this study, are described in the Appendix.

Accuracy of compressor performance measurements is within ±1.5 percent for flow coefficient, ±0.5 percent for the head coefficients and ±0.8 percent for efficiency (see Appendix).

Effect of Impeller-Diffuser Spacing

The variation of head coefficient, H/U_{tip}^2, versus a flow coefficient, $Q_0/(U_{\text{tip}}D_{ls}^2)$, is shown in Fig. 3 for three fixed-diffuser configurations that differ only by the impeller blade tip diame-

Nomenclature

a = sonic velocity
c_p = specific heat at constant pressure
D = diameter
H = head rise
h = enthalpy
m = mass flow rate
p = pressure
Q = volume flow rate
t = temperature
U = impeller tangential velocity
v = specific volume
ρ = density

Subscripts

avg = average
cond = condenser
evap = evaporator
f = liquid state
p = polytropic
rim = impeller hub flowpath exit
sc = subcooler
tc = tangent circle of pipe diffuser centerlines
tip = impeller blade tip
w = water
0 = inlet stagnation conditions
l = inlet
ls = impeller inlet edge-of-blade
2 = discharge

Table 1 Summary of compressor geometry

Compressor	A	B	C	C' [1]	D	E	F	G
Impeller geometry								
Impeller rim radius [in, (m)]	8.305 (0.2109)	8.305 (0.2109)	8.305 (0.2109)	8.305 (0.2109)	8.305 (0.2109)	8.305 (0.2109)	8.305 (0.2109)	6.091 (0.1547)
Impeller inlet-hub to rim radius ratio	0.2577	0.2577	0.2577	0.2577	0.2577	0.2577	0.2577	0.2778
Inlet hub to edge-of-blade (eob) radius ratio	0.4662	0.4662	0.4662	0.4662	0.4662	0.4662	0.4662	0.4872
Inlet eob blade angle with respect to meridional	62.12°	62.12°	62.12°	62.12°	62.12°	62.12°	62.12°	60.38°
Number of blades, splitters	11, 11	11, 11	11, 11	11, 11	11, 11	11, 11	11, 11	11, 11
Impeller blade-tip to rim radius ratio	1.0000	0.9750	0.9500	0.9500	0.9250	0.9007	0.9007	0.9750
Exit blade angle with respect to meridional	51.01°	50.94°	50.79°	50.79°	50.57°	50.28°	50.28°	50.10°
Impeller exit blade-height to rim-radius ratio	0.0990	0.1014	0.1037	0.1037	0.1062	0.1087	0.1087	0.1019
Average exit blade-thickness to blade-height ratio	0.1211	0.1187	0.1168	0.1168	0.1153	0.1142	0.1142	0.1208
"Cold"-clearance to blade-height ratio	0.0389	0.0380	0.0371	0.0371	0.0363	0.0355	0.0355	0.0402
Pipe diffuser geometry								
Number of pipes	18	18	18	18	18	18	18	20
Tangent-circle to impeller-rim radius ratio	1.0500	1.0500	1.0500	1.0500	1.0500	1.0500	1.0500	1.0000
Split-radius to tangent-circle-radius ratio	N/A	N/A	N/A	1.1057	1.1057	1.1057	1.1437	1.2617
"Full" rotation of inner ring	N/A	N/A	N/A	7.50°	7.50°	7.50°	9.543°	8.168°
Minimum percent of throat area open	N/A	N/A	N/A	27.8%	27.8%	27.8%	13.3%	4.4%
Throat-diameter to impeller-rim-radius ratio	0.1103	0.1103	0.1103	0.1103	0.1103	0.1103	0.1103	0.1141
Throat-length to diffuser-exit-radius ratio	0.0151	0.0151	0.0151	0.0151	0.0151	0.0151	0.0151	0.0151
Initial divergence angle	4°	4°	4°	4°	4°	4°	4°	4°
Initial divergence length / (diffuser exit radius)	0.1209	0.1209	0.1209	0.1209	0.1209	0.1209	0.1209	0.1209
Second divergence angle	8°	8°	8°	8°	8°	8°	8°	8°
Exit to tangent-circle radius ratio	1.7001	1.7001	1.7001	1.7001	1.7001	1.7001	1.7001	1.9242
Overall area ratio	4.15	4.15	4.15	4.15	4.15	4.15	4.15	5.20
Collector								
Cross sectional area / (diffuser exit radius)^2	0.3604	0.3604	0.3604	0.3604	0.3604	0.3604	0.3604	0.3390

[1] Probes were installed just upstream of the impeller leading edge for this configuration, adding abnormal loss.

ter. As the IGV position is changed for each configuration, the head coefficient at surge first decreases rapidly, then tends to flatten with reduced flow rate. The head level for points identified as "critical to setting part-load operating limit" decreases as the blade tip diameter decreases or, equivalently, as spacing is increased between the impeller blade tip and the diffuser leading edge. The identified points are deemed critical because the operating line must pass below them. This implies, for example, that compressor *C* must be selected for lower full-load head rise than compressor *A* or *B*. Such a selection point is generally farther from peak compressor efficiency.

Changes in average sound pressure level are shown in Fig. 4 for each axial-IGV surge point of the configurations in Fig. 3. Similar sound measurements are shown for the same impeller with smaller blade tip diameters employing the SRD. The method of ARI Standard 575 (1994) was used to derive averages. Although data were acquired in a factory environment, the dominant sound source is tonal at blade passing frequencies and their harmonics. These range from 1.5 k to 6 k Hz while background factory noise is in the frequency range below 150 Hz with at least 10 dB lower sound levels. Fig. 4 shows that the noise reduction rate, initially about 0.7 dB per percent of blade diameter reduction, tends to diminish with increased spacing.

The effect of impeller-diffuser spacing on compressor peak efficiency is given in Fig. 5. The three fixed-diffuser configurations (the same as used in Fig. 3) indicate a significant benefit for this particular compressor design. The extra spacing likely provides more uniform conditions into the pipe diffuser despite potential adverse frictional effects. However, the data trend indicates diminishing efficiency advantage for more spacing. (See the next section for discussion of the variable diffuser configurations, also shown in Fig. 5.)

Thus, increasing impeller-diffuser spacing is an extremely effective means to reduce compressor sound level for the present compressor design. However, part-load surge lines markedly deteriorate. The surge line of compressor *C*, Fig. 3, is unacceptable for a chiller system because the full-load head is limited to relatively low values, well away from peak efficiency, to avoid part-load surge. Hence, variable diffuser geometry was required when other sound suppression methods proved far less effective than increasing the impeller-diffuser spacing.

Table 2 Compressor operating conditions at peak efficiency

Compressor	A	B	C	C' [1]	D	E	F	G
Flow coefficient, $Q_0/(U_{tip}\,D_{tip}^2)$	0.0502	0.0525	0.0539	0.0500	0.0522	0.0508	0.0524	0.0570
Polytropic head coefficient, H_p/U_{tip}^2	0.5960	0.5885	0.6058	0.5775	0.6014	0.5967	0.5918	0.5601
Wheel Mach number, U_{tip}/a_0	1.38	1.35	1.31	1.31	1.28	1.24	1.24	1.24
Impeller wheel speed [rpm]	9237	9237	9237	9237	9237	9237	9237	11678
Inlet volume flow, Q_0 [cfm (m^3/sec)]	3856 (1.820)	3723 (1.757)	3559 (1.680)	3298 (1.557)	3179 (1.500)	2854 (1.347)	2933 (1.384)	2028 (0.958)
Impeller inlet edge-of-blade relative Mach number	0.854	0.854	0.854	0.854	0.854	0.854	0.854	0.820
Overall pressure ratio	3.220	3.081	2.963	2.818	2.787	2.628	2.602	2.463

[1] Probes were installed just upstream of the impeller leading edge for this configuration, adding abnormal loss.

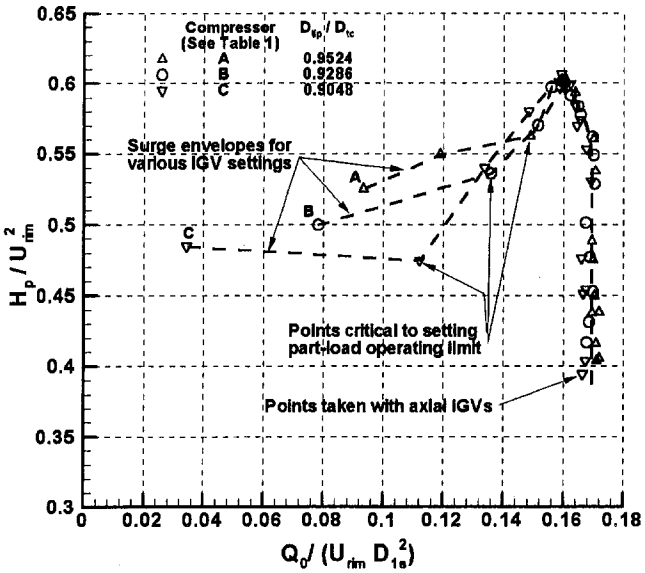

Fig. 3 Head versus flow for three compressors of different impeller-diffuser spacing

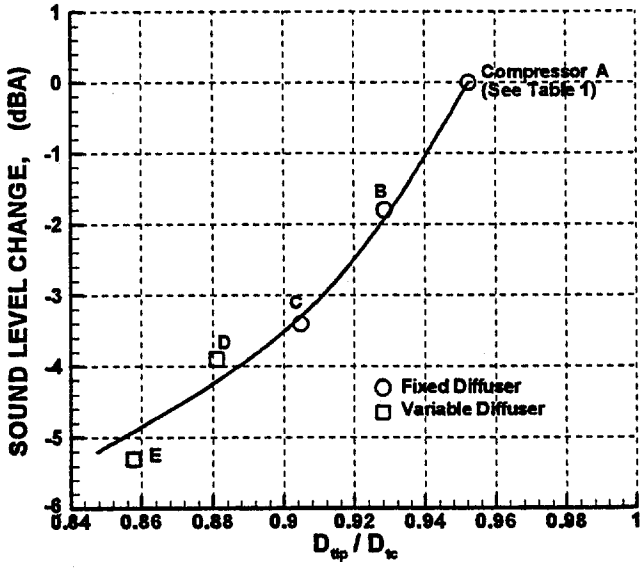

Fig. 4 Effect of impeller-diffuser spacing on emitted sound pressure level

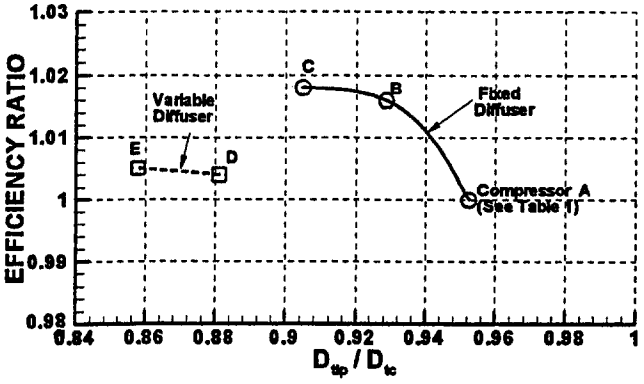

Fig. 5 Effect of impeller-diffuser spacing on compressor efficiency

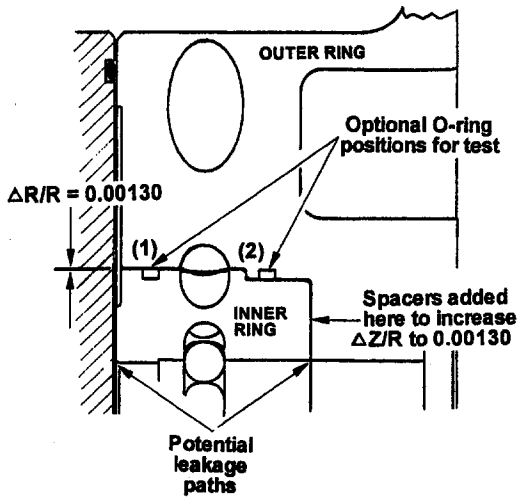

Fig. 6 Cross section of the adjustable split-ring diffuser

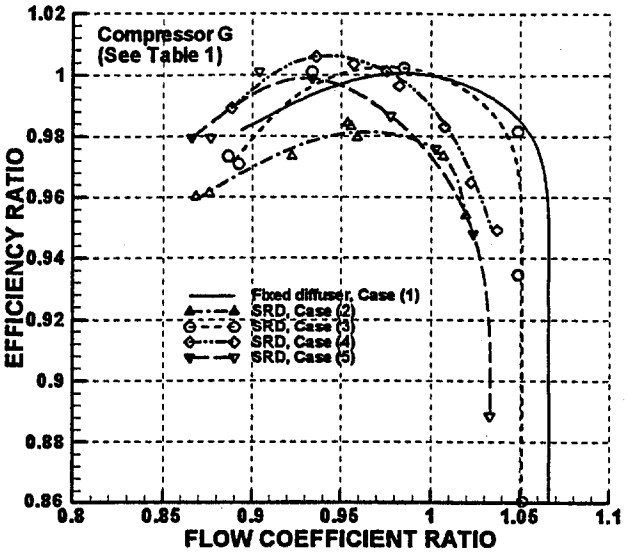

Fig. 7 Variation of efficiency with flow for the adjustable split-ring diffuser as influenced by leakage

Effect of Flow Leakage

Experience, as well as open literature, has suggested that leakage flows hinder application of the SRD. A special adjustable SRD was used with compressor *G*, Table 1, to evaluate leakage effects as well as to confirm and expand previous work. A cross section is shown in Fig. 6. The following leakage paths were provided (1): passage-to-passage and (2) vents to impeller exit. Passage-to-passage leakage elimination was not practical for the present application. Suitable placement of O-rings and clearance between parts was used to investigate vents to impeller exit. Indeed, a suitable design (see Fig. 1) hinders flow through one leakage path.

Variation of efficiency with flow coefficient, nondimensionalized by values at peak efficiency for the fixed diffuser, is shown in Fig. 7 for the following five configurations, all with axial IGVs: (1) Fixed diffuser (no flowpath leakage); (2) Without O-rings (implying maximum leakage); (3) Both O-rings in place (only passage-to-passage leakage allowed); (4) One O-ring (position 1, Fig. 6), tight metal-to-metal axial contact of inner and outer ring; and (5) One O-ring (position 1, Fig. 6), axial (and radial) clearance to radius ratio of 0.00130 between inner and outer ring. The following is observed from Fig.

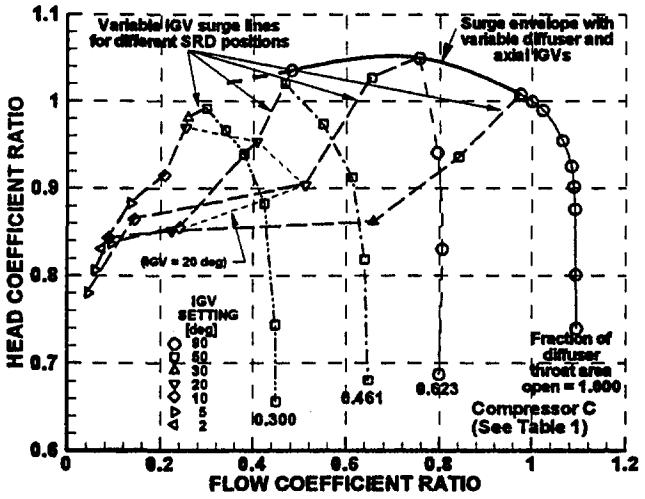

Fig. 8 Variation of head versus flow for the actuatable split-ring diffuser

7: (a) Any leakage reduces the compressor's maximum flow due to recirculation effects; (b) The full effect of leakage on efficiency is about 2 percent for the configurations studied here, comparing configurations (1) and (2); (c) Efficiency degradation is probably small if passage-to-passage leakage is the only source, comparing configurations (1), (3), (4), where efficiency measurement uncertainty is about ±0.8 percent; and (d) Flowpath leakage to impeller exit may be controlled to about 0.5 percent for a leakage rate represented by a clearance-to-radius ratio of 0.00130, comparing configurations (4) and (5).

The measured efficiency is shown in Fig. 5 for two configurations of the final SRD design. The two configurations differ from each other only in the amount of impeller-diffuser spacing. Although data accuracy should be considered, one conclusion from Fig. 5 is that an efficiency penalty of about 1.3 percent results from using the SRD instead of a fixed diffuser. On the other hand, the efficiency resulting from increased impeller-diffuser spacing when the SRD is used (case D or E) is about the same as the alternative fixed diffuser (case A) that has unacceptably high noise.

Tests of the adjustable SRD configuration also showed that the part-load surge line was not affected by flow leakage.

Variable Geometry

Head coefficient is plotted in Fig. 8 versus flow coefficient, each nondimensionalized by values at peak efficiency for the configuration with fully open diffuser and axial IGVs. Diffuser and IGV positions are varied for the results shown. Compressor *C′*, Table 1, was used and had an externally actuatable SRD.

Two $\frac{3}{8}$ inch (9.5 mm) diameter cylinders were mounted 90 deg apart, extending from the casing flow path to near the compressor centerline, normal to the axis of rotation and just upstream of the impeller. Although the cylinders contained special instrumentation not directly involved with the present discussion, the extensive data taken during that investigation provided means to assess effects of variable geometry on compressor performance. Abnormally high losses certainly result from the cylinders' presence. However, since all data in Fig. 8 were collected with the cylinders present, normalizing the data eliminates any influence on efficiency variation with IGV and SRD position.

The test procedure involved setting the SRD and determining head-versus-flow relationships while varying the IGVs. The SRD was then reset more closed, and IGV variation was repeated. Figure 8 shows the vane line for an axial IGV setting and the location of surge at other IGV positions for each discrete SRD setting. Figure 9, discussed below, shows all of the data taken. The following is noted:

1 Figures 8 and 9 illustrate "snapshots" of compressor performance with variable geometry. Any point to the left of data for an axial IGV setting with fully open diffuser and under the surge envelope identified in Fig. 8 can be achieved by at least one combination of the SRD and IGVs.
2 Surge occurred at high head levels as the diffuser inner ring was rotated toward closure with the IGV settings more open; i.e., at 90 deg and 50 deg settings. The maximum head level achieved is more than the intended application requires. In fact, when the IGVs are axially aligned, surge flow could be reduced more than 50 percent through SRD movement only.
3 Below the 30 deg IGV setting (see Fig. 8 for a line illustrating variation for the 20 deg IGV setting), closing the SRD can increase flow as well as head at surge. (Although not shown here for simplicity, choke flow decreases monotonically with diffuser closure, as would be expected.)
4 The points at low IGV settings tend to define an ultimate lower bound for surge that may not depend on the diffuser position. Admittedly, this observation is difficult to defend because data accuracy is questionable in this region.
5 The highest surge line is achieved when only the SRD is varied while the IGVs are axially aligned. The lowest surge line occurs when only the IGVs are varied with the SRD fully open, similar to a fixed diffuser configuration. Thus, various surge lines may be "designed" between these extremes by simultaneous IGV/SRD movement.

Sufficient data was taken for the four configurations of Fig. 8 to construct contours of constant efficiency. These are shown in the four parts of Fig. 9. Peak efficiency for the fully open SRD is seen to occur at surge for the axial IGV setting. This point was also used for reference to construct three approximate operating lines as examples for chiller applications (see Appendix). These lines model compressor requirements imposed by the chiller system when the condenser inlet water temperature changes during a cooling season. For example, the line labeled "2.5 deg/10%" implies a 2.5°F (1.39°C) reduction in condenser inlet water temperature for each 10 percent of load reduction. Note, the three lines are copied to each part of Fig. 9.

It is seen that employing the variable SRD will allow selection of a compressor at its most efficient full-load point and still accommodate severe off-design operating conditions.

Effect of Optimization Choices. Various compressor operating assumptions can be evaluated using Fig. 9. Efficiency can be determined along any operating line as a function of flow while retaining association with geometric variables. Examples are shown in the four parts of Fig. 10. Results for the 2.5 deg/10 percent line are shown in Fig. 10(*a*). Note that curves describing constant diffuser settings extend to the lowest experimental flows. Results for the 0.5 deg/10 percent line are shown in Fig. 10(*b*). Results for the 0 deg/10 percent line are shown in Fig. 10(*c*) where the occurrence of surge terminates the low-flow values of curves describing constant diffuser settings.

The combinations of diffuser and IGV settings that yield maximum efficiency are identified as the locus of points describing the upper bound of efficiency in the first three parts of Fig. 10. For example, in Fig. 10(*a*) the maximum efficiency attained on the 2.5 deg/10 percent line can be compared with the efficiency variation for the fully open diffuser, representing the fixed diffuser. This illustrates the magnitude of the advantage for variable diffuser geometry combined with variable IGVs. The compressor power savings is about 7.3 percent at a flow coefficient ratio of 0.5.

Using the applicable part of Fig. 9, it is possible to identify the approximate IGV and diffuser settings that yield maxi-

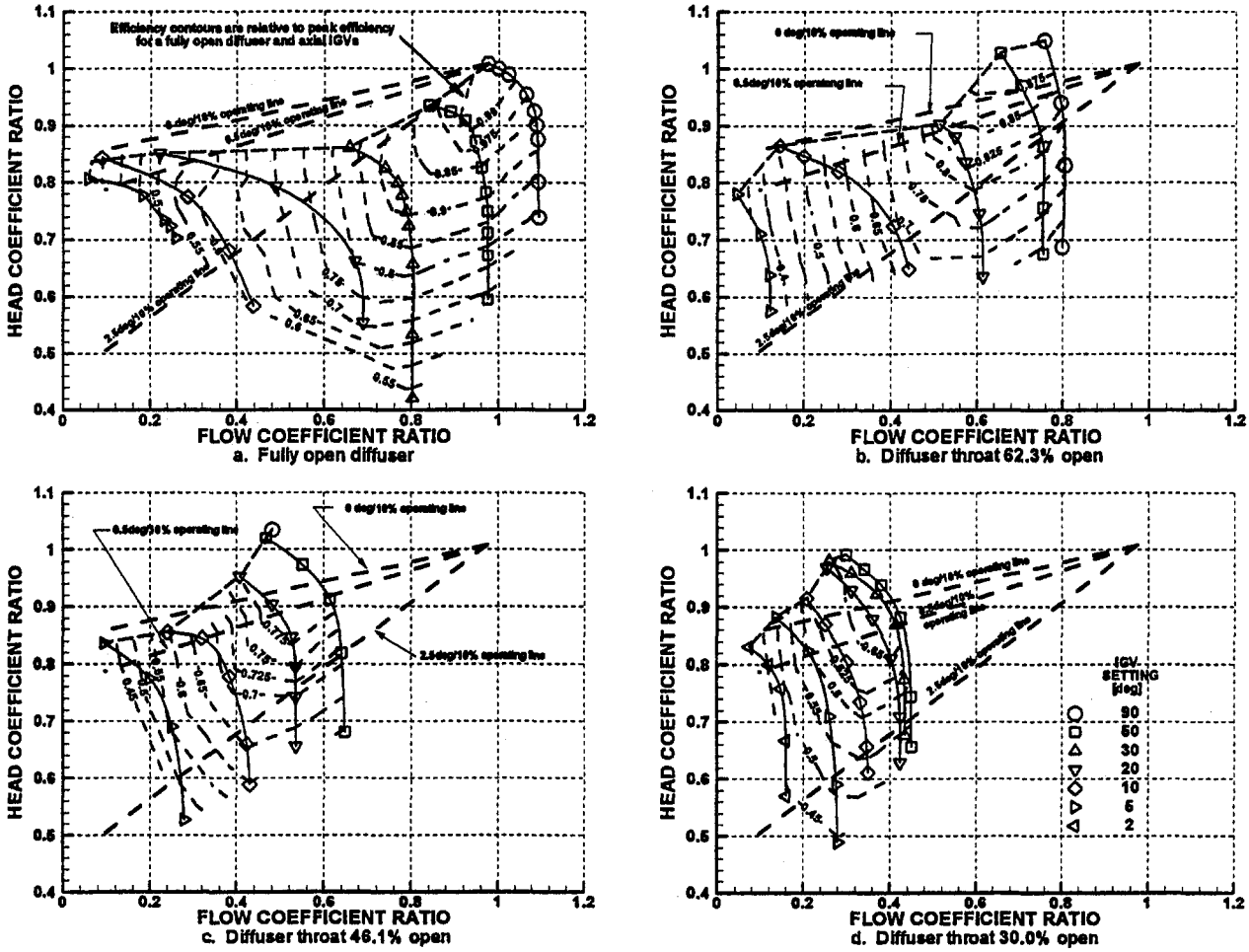

Fig. 9 Efficiency contours for various settings of the split-ring diffuser

mum efficiency in Figs. 10(b) and 10(c). These combinations are identified by curves in Fig. 10(d) and depict the efficiency occurring along the 2.5 deg/10 percent line when performance is optimized for the higher operating lines. Differences between curves illustrate the progressively severe penalty paid for optimizing a compressor to higher operating lines. For example, using IGV/SRD settings resulting from optimization on the 0 deg/10 percent line will produce efficiencies on the 2.5 deg/10 percent line that are nearly the same as a fixed diffuser. Furthermore, there is a compressor power reduction of only about 3 percent if the IGV/SRD settings resulting from optimization on the 0.5 deg/10 percent line are used when compared to the optimum for the 2.5 deg/10 percent line. However, surge margin on the 2.5 deg/10 percent line would then be far greater.

Surge will usually limit compressor operation on a high operating line if performance is optimized for a lower line; and, as just discussed, reduced performance is likely on a low operating line when performance is optimized for a high line. The 0.5 deg/10 percent line is a reasonable compromise for chiller applications. This load line satisfies all but the most stringent application requirements, and a compressor with variable IGVs and SRD that is optimized for the 0.5 deg/10 percent line performs better on the low operating line than the equivalent compressor with fixed diffuser.

When variable-component movement is directly coupled, performance optimization can still be established for one operating line. Selection of the operating line for optimization offers a chance to choose between competing objectives, namely, high efficiency and broad range.

Determination of the Actuation Schedule. The two variable geometry components, IGVs and SRD, are directly linked in the present application. Thus, movement of one implies a corresponding, preselected movement of the other, greatly simplifying system control. This section details how movements are chosen.

Simultaneous IGV-SRD movement is defined to produce optimum performance along the 0.5 deg/10 percent operating line. The following illustrates a simple process that adequately satisfies this basic objective, regardless of the operating line chosen for optimization:

1 Define the value of flow and head at surge for axial IGVs and a fully open diffuser. This point becomes the basis for the "optimum" operating line. Although efficiency is usually close to its maximum value at this condition, the point is chosen because it represents the compressor's maximum head capability for an easily definable geometric configuration.
2 Define the IGV and SRD positions required to achieve "optimum" performance at a number of different positions along the operating line. For the present work, 75 percent and 50 percent of the full load point defined in (1) are used. Explicitly how this is done is described below.
3 Define surge points for various IGV settings (usually between 5 deg and 20 deg from fully closed IGV position)

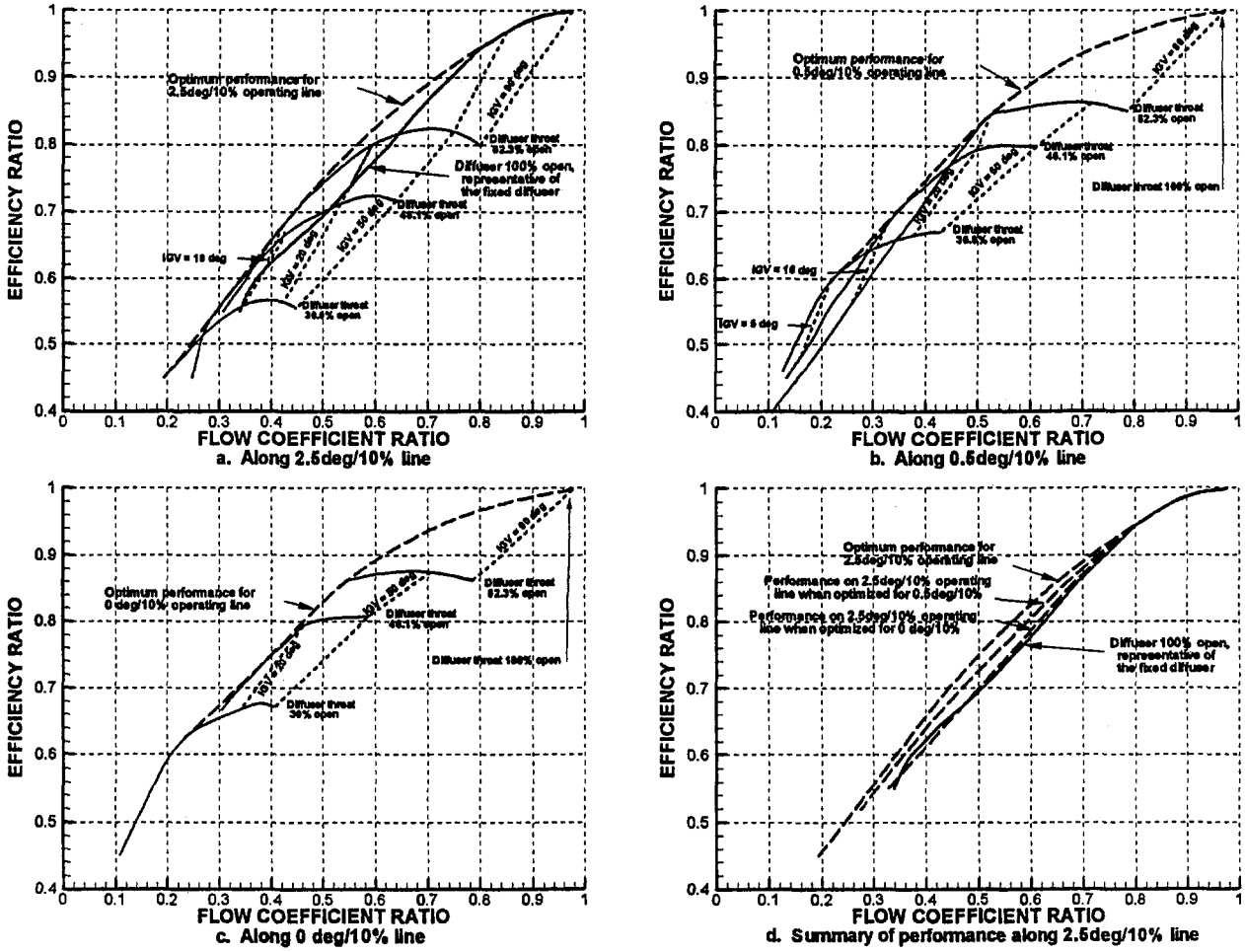

Fig. 10 Efficiency variation along assumed operating lines

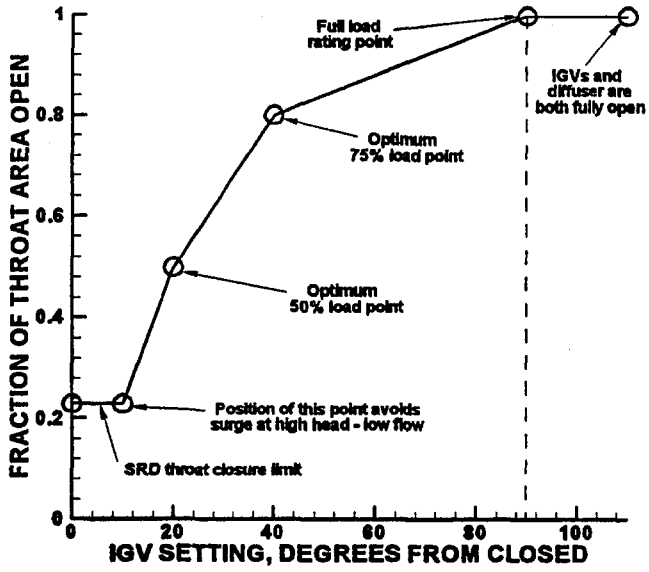

Fig. 11 Schematic of the IGV-SRD movement algorithm

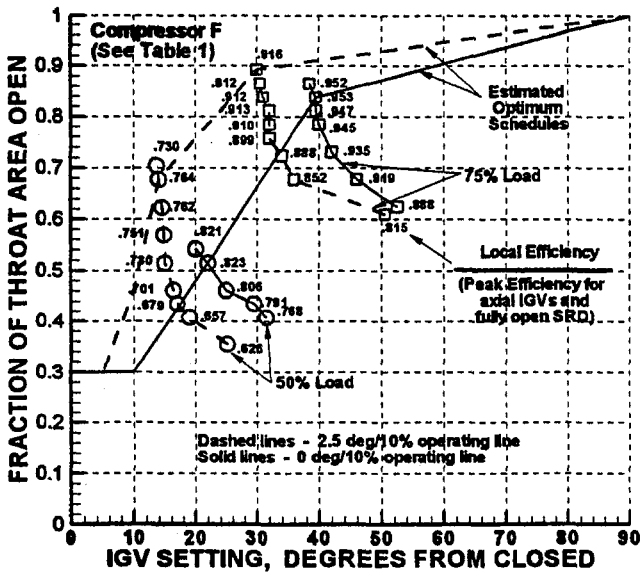

Fig. 12 Results measured during an optimization process

for the fully closed SRD. The intersection of the line described by the points defined in (2) with the curve describing surge establishes the maximum IGV setting required when the SRD is fully closed. A schematic of the control curve is shown in Fig. 11.

The following method identifies optimum performance at selected positions along the operating line (see examples in Fig. 12):

1 With the IGVs and SRD in "open" positions, close the SRD until the desired load fraction is achieved. Record any

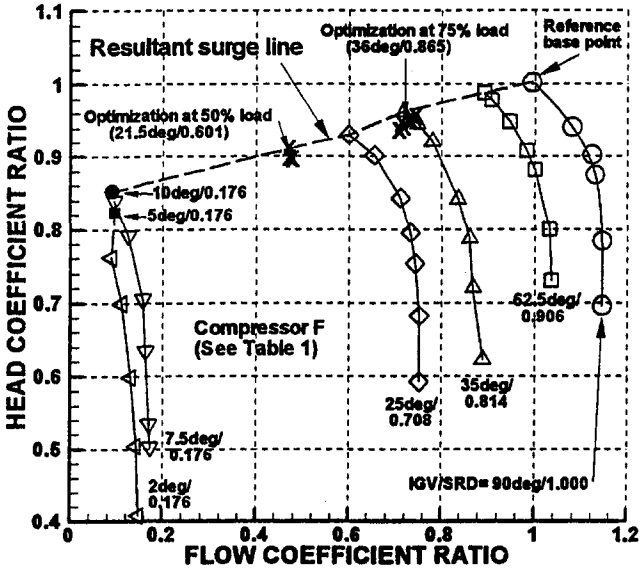

Fig. 13 An example operating envelope established through optimization for the 0.5 deg/10 percent operating line

values important to the optimization process (e.g., compressor efficiency, noise levels, vibration characteristics, bearing temperatures, etc.). As seen in Fig. 8, the open IGV setting yields the highest head the compressor can produce for a given diffuser setting.

2 Partially open the SRD by 5 deg or 10 deg. Close the IGVs until the desired load fraction is achieved, and record any values important to optimization. Continue the process of opening the diffuser and closing the IGVs until one of the following occurs: (a) efficiency has decreased from a maximum value, or (b) the compressor surges.

3 The IGV and diffuser settings can be refined as desired.

Compressor surge often terminates the search for optimum performance. Selection of the correspondence between IGV and SRD settings establishes the compressor's surge line. The designer's final choice is how close to surge to operate the compressor.

An example of the operating envelope established by this process is shown in Fig. 13 for optimum conditions along the 0.5 deg/10 percent-operating line for compressor *F*, Table 1. Points taken during an optimization process, similar to those shown in Fig. 12, are identified. The final settings for this example are such that 3 percent pipe diffuser throat area change will move a point on the 0.5 deg/10 percent-operating line into surge.

Conclusions

The development of a centrifugal compressor with a variable geometry pipe diffuser is described as a means for solving problems of high noise generation and poor surge margin. The principal lessons learned from experiments refining the variable geometry pipe diffuser's aerodynamic design include the following:

1 Increasing the impeller blade trailing edge distance from the diffuser leading edge was extremely effective in reducing compressor noise level for the present compressor design. Sound pressure was initially reduced at a rate of about 0.7 dB for each percent increase in impeller-diffuser spacing.

2 Surge margin markedly deteriorates with increased impeller-diffuser spacing.

3 When the SRD is used, a compressor may be selected at its most efficient full-load point and still accommodate severe off-design operating conditions.

4 The present study examined consequences of directly linking movement of the variable IGVs and SRD. Movement of one requires a corresponding, preselected movement of the other greatly simplifying system control. In this case, performance optimization can still be established for any one operating line. Selection of which operating line to "optimize" offers a chance to temper competing part-load objectives; namely, high efficiency and broad operating range.

5 A simple method is described to define the geometric conditions that establish optimum performance for discrete compressor operating points. Although only two points are actually optimized for the present application, the method is not limited by this.

6 The correspondence between IGV and SRD settings establishes the proximity of a compressor's surge line to the optimized operating line. The two are usually close simply because efficiency peaks near surge.

7 Flow leakage is controllable for the SRD design with a likely lower limit of about 0.5 percent loss in efficiency when compared to a fixed diffuser.

8 In many cases, independent control of IGV and SRD settings has diminishing benefit when a suitable compromise can be found that allows linked movement of variable components.

Acknowledgments

The author is grateful to Carrier Corporation for permission to publish this paper, particularly to Dr. Joost Brasz for continued encouragement and to Mr. Steve Meloling for his assistance. The following individuals are commended for their competence, patience, and persistence in gathering data related to this project: Messrs. Domiter, Grimaldi, House, King, Lee, Lewis, Liberty, Longway, Miller, and Phelps.

References

ARI Standard 550, 1990, *Standard for Centrifugal or Rotary Screw Water-Chilling Packages,* Air-Conditioning and Refrigeration Institute, Arlington, Va.

ARI Standard 575, 1994, *Standard for Method of Measuring Machinery Sound Within an Equipment Space,* Air-Conditioning and Refrigeration Institute, Arlington, VA.

Comey, D., Miccio, J., Palmreuter, E., and Waterman, W., 1985, "Variable Cycle Technology Propulsion System Program, Volume I, Variable Geometry Diffuser, Part II—Industry Version," AFWAL-TR-84-2090, Vol. I, Pt. II Wright-Patterson Airforce Base, OH.

Harada, Hideomi, 1996, "Study of a Surge-Free Centrifugal Compressor With Automatically Variable Inlet and Diffusser Vanes," ASME Paper No. 96-GT-153.

Simon, H., Wellman, T., and Monk, T., 1987, "Improvements in Performance Characteristics of Single-Stage and Multistage Centrifugal Compressors by Simultaneous Adjustment of Inlet Guide Vanes and Diffuser Vanes," ASME JOURNAL OF TURBOMACHINERY, Vol. 109, No. 1, pp. 41–7.

Salvage, J. W., 1996, "Variable Geometry Pipe Diffusers," ASME JOURNAL OF TURBOMACHINERY, Vol. 119, No. 4, pp. 831–8.

Schenck, Jr., H., 1961, *Theories of Engineering Experimentation,* McGraw-Hill, Inc., New York.

Sishtla, V., 1996, "Performance of Centrifugal Compressors With Variable Vaned Diffuser," *Proceedings, 1996 International Compressor Engineering Conference at Purdue,* W. Soedel, ed., Vol. II, Purdue Univ., West Lafayette, IN, pp. 767–773.

APPENDIX

Description of a Chiller System

The system components and vapor compression cycle are illustrated in Fig. 14. The system used in this investigation is composed of evaporator, compressor, condenser, subcooler, and a float-type throttle valve. The cycle benefit of subcooling is produced by flashing condenser liquid through an orifice into a series condenser. The compressor operates between refrigerant

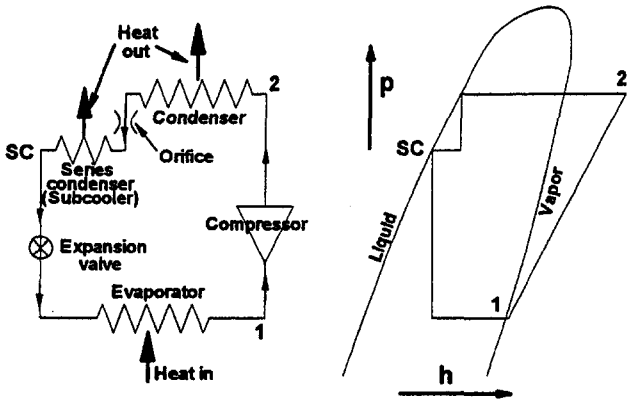

Fig. 14 Schematic diagram of the components and cycle for a chiller system

vapor states imposed by the evaporator and condenser. The evaporator's function is to deliver chilled water at constant temperature, normally at 44°F (6.7°C) for air conditioning. The condenser transfers heat from the isolated refrigerant system to some external medium. For water-cooled systems, this medium is water that circulates through a cooling tower and the condenser. Thus, condenser pressure is controlled by the cooling tower's return water temperature, dependent upon the time of day and the day of the year. A typical condenser design inlet water temperature is 86°F (30°C).

Chiller system "load" is essentially a measure of required evaporator heat exchange. As building occupancy or outside ambient temperature decreases, the building's return water temperature decreases. Therefore, the evaporator requires less exchange of heat to achieve the desired outlet water temperature.

Because buildings vary in design, ARI Standard 550 (1990) provides a consistent basis for system performance comparison at both design and off-design operation. The condenser inlet water temperature change with cooling load, 2.5°F (1.39°C) per 10 percent load reduction, was derived to represent a year's cooling cycle for a typical building in Atlanta. In terms of compressor parameters, the ARI unloading rate may be approximately represented by a line from design conditions to 50 percent of design head at 10 percent of design flow.

Requirements naturally vary for other regions of the world. In the Asia–Pacific area, for example, ambient temperatures are more constant throughout the year so that 0 deg-condenser unloading is commonly prescribed. Although there will always be a difference between refrigerant and water temperatures in a heat exchanger, reasonably-sized modern designs allow refrigerant-water temperature differences of 1 or 2°F (0.5 to 1°C) at full load. This significantly reduces required full-load compressor pressure ratio or power. As cooling load is reduced, water-refrigerant temperature difference tends toward zero for constant heat exchanger water flow rates. Thus, when heat exchangers are efficiently designed, refrigerant water temperature differences that occur with load reduction are usually small (but not negligible) compared to the overall evaporator-to-condenser temperature difference. The 0 deg-condenser unloading required for the Asia–Pacific area can be approximated by a line from design conditions to 85 percent of design head at 10 percent of design flow.

Data Reduction and Measurement Uncertainty. Measured pressures include evaporator, condenser, and series condenser (subcooler) saturation pressures. Pressure measurement uncertainty is about ±0.5 psi (±3.4 kPa) for this study.

Measured temperatures include subcooler leaving-saturated-refrigerant-liquid, subcooler leaving-water temperature, compressor suction temperature (an average of four readings measured in the pipe just upstream of the compressor), and compressor discharge temperature (an average of 2 readings measured in the pipe just downstream of the compressor). Refrigerant charge is specially adjusted to achieve 2° to 4° F (approximately 1° to 2° C) temperature rise between evaporator saturation temperature and compressor suction temperature to prevent liquid from entering the compressor. Temperatures are measured by copper-constantine thermocouples, and measurement uncertainty is ±0.2° F (±0.1° C).

Evaporator and condenser water flow inlet-to-outlet temperature differences are measured by thermopile. When compared to differences between independently measured inlet and outlet water temperatures, the thermopile measurement uncertainty is seen to be less than ±0.05° F (±0.03° C).

Evaporator and condenser water flows are measured by flow meters. Measurement uncertainty is ±0.5 percent of the indicated reading.

Power meter readings are recorded, as well as the current and voltage drawn by the motor.

Mass Flow Rate. The mass flow rate, m, is given by

$$m = [Q_w \quad \Delta t_w \quad c_p(t_{wavg}) \quad \rho(t_{wavg})]/(h_2 - h_{fsc}),$$

where Q_w is condenser water volume flow rate, where Δt_w is condenser water temperature rise, where $c_p(t_{wavg})$ and $\rho(t_{wavg})$ are, respectively, liquid specific heat at constant pressure and liquid density evaluated at bulk water temperature where h_2 is compressor discharge enthalpy, a function of p_{cond} and compressor discharge temperature, and where h_{fsc} is subcooler saturated liquid enthalpy, a function of subcooler leaving-refrigerant pressure.

Flow coefficient is defined as $mv_{0l}/(a_{0l}D_{tip}^2)$ where v_{0l} and a_{0l} are, respectively, specific volume and acoustic velocity evaluated from p_{evap} and compressor suction temperature. For a perfect gas, this parameter is a function of Mach number only. Another version of flow coefficient may be defined by substituting impeller tip speed for a_{0l}.

Uncertainty analysis (e.g., Schenck, 1961) suggests that measurement of the water flow temperature difference is most critical to mass flow rate determination, followed by the water flow rate itself. The flow coefficient measurement uncertainty is equally dependent upon flow and inlet pressure uncertainties, with inlet temperature being a much smaller contribution. The uncertainty of flow coefficient is approximately ±1.5 percent.

Input Head, or Compressor Input Work. The compressor input work is given by the difference between compressor discharge and inlet enthalpies, h_2-h_1, where h_1 is a function of p_{evap} and compressor suction temperature, and h_2 is a function of p_{cond} and compressor discharge temperature.

An input head coefficient is defined by dividing this enthalpy difference by the square of a suitable velocity, such as inlet acoustic velocity, a_{0l}, or impeller tip speed.

Pressure and temperature uncertainty contributions are nearly equivalent. Compressor input head coefficient measurement uncertainty is approximately ±0.7 percent.

Polytropic Head. A reversible polytropic process is used to evaluate the reversible work done by the compressor. The following equation defines polytropic head:

$$H_p = \ln (p_{cond}/p_{evap})(p_{cond}v_2 - p_{evap}v_{0l})/\ln [p_{cond}v_2/(p_{evap}v_{0l})],$$

where v_2 is the compressor discharge specific volume, a function of p_{cond} and compressor discharge temperature.

A polytropic head coefficient can be defined by dividing the polytropic head by the square of a suitable velocity such as a_{0l} or impeller tip speed.

Pressure uncertainty is the most critical for determination of polytropic head. The polytropic head coefficient measurement uncertainty is approximately ±0.5 percent.

Efficiency. Polytropic efficiency results from dividing the polytropic head, H_p, by the compressor input work, h_2-h_1.

Uncertainty analysis using results above for polytropic head and compressor input work suggests that measurement uncertainty of efficiency is approximately ±0.8 percent.

Other Important Measurements. Compressor shaft power, deduced from power meter readings less calculated hermetic motor electrical loss and estimated mechanical loss, is compared to gas power deduced from compressor thermodynamic measurements. "Power balances" within 3 percent are considered acceptable. Energy (heat) exchanged in the evaporator is added to energy consumed by the motor and compared with energy exchanged within the condenser. "Energy balances" within 1 percent are considered acceptable.

G. L. Arnulfi

P. Giannattasio

University of Udine,
Dipartimento di Energetica e Macchine,
Udine, Italy

C. Giusto

A. F. Massardo
Mem. ASME

University of Genova,
Istituto di Macchine e Sistemi Energetici,
Genova, Italy

D. Micheli
University of Trieste,
Dipartimento di Energetica,
Trieste, Italy

P. Pinamonti
University of Udine,
Dipartimento di Energetica e Macchine,
Udine, Italy

Multistage Centrifugal Compressor Surge Analysis: Part I—Experimental Investigation

This paper reports an experimental investigation on centrifugal compressor surge. The compression system consists of a four-stage blower with vaned diffusers and a large plenum discharging into the atmosphere through a throttle valve. Measurements of unsteady pressure and flow rate in the plant, and of instantaneous velocity in the diffusers of the first and fourth compressor stage, are performed during deep surge, at several valve settings and three different rotation speeds. Additional tests have been carried out on a different system configuration, i.e., without plenum, in order to obtain the steady-state compressor characteristics and to collect reference data on stall in surge-free conditions. In this configuration, a fully developed rotating stall was detected in the compressor diffusers, while during surge it affects only a limited part of the surge cycle. The goal of the present experimental work was to get a deeper insight into unstable operating conditions of multistage centrifugal compressors and to validate a theoretical model of the system instability to be used for the design of dynamic control systems.

Introduction

Recently, much effort has been devoted to improving the performance of centrifugal compressors by using both numerical techniques and experimental investigations. Although higher efficiencies were obtained with improved aerodynamic design, the working range of the compressor, where the compression system operates in stable conditions, remains narrow. The surge inception line is commonly adopted as the limit of the stable operating range.

Surge is a dynamic phenomenon consisting of large-amplitude low-frequency oscillations of flow rate. It can occur in compression systems, involving at least a compressor, a resistance, and a volume of sufficiently high capacity, when the flow rate is lower than the design value. Operation during surge is unacceptable for industrial applications, since it can cause serious damage to the plant.

The existence of two different kinds of surge is well known:

- a slight oscillation without any net back-flow, with frequency close to the Helmholtz resonance of the system, i.e., "mild surge";
- a strong oscillation including complete breakdown and reverse flow through the compressor, with frequency substantially lower than the Helmoltz frequency, i.e., "deep surge."

Mild surge may occur in systems where the compressor operates near its instability limit, and it is recognized as a trigger of the deep surge inception. The deep surge is a damaging condition that must be avoided. Therefore, a deep understanding of the phenomenon is required to minimize its effects and to design proper control systems. In particular, experimental investigations on pressure and velocity fields and on flow-rate oscillations in the compression system are needed to attain a better understanding of flow instability and to validate theoretical models.

As far as industrial centrifugal compressors are concerned, several experimental works were carried out to investigate surge (e.g., Toyama et al., 1977; Abdelhamid et al., 1979; Hansen et al., 1981) and, more recently, to study the interaction between surge and rotating stall (Ribi and Gyarmathy, 1993; Jin et al., 1994). Furthermore, experiments were performed to investigate the influence of the impeller and diffuser geometry on system instability (Jin et al., 1994; Cyrus et al., 1995; Ribi and Gyarmathy, 1995). These works are concerned with high-pressure single-stage centrifugal compressors, with tip impeller diameter between 100 and 400 mm and rotation speed between 10,000 and 50,000 rpm. Usually, tests were carried out during surge inception, detecting mild surge and limiting the observation of deep surge to few consecutive cycles in order to avoid damage.

The present research considers a compression system based on a low-pressure multistage centrifugal compressor, suitable for operation in conditions of completely developed deep surge. This compressor offers the possibility of varying its configuration, so allowing the influence of the geometry on surge features to be investigated. Detailed measurements of pressure, flow rate, and instantaneous velocities in the compressor diffusers have been performed in order to understand the instability behavior in more detail and to collect experimental data to be used for validating the theoretical model of the compression system described in Part II of the present work (Arnulfi et al., 1999).

Experimental Procedure

Test Rig. Experiments have been carried out at the Laboratory of the Dipartimento di Energetica, University of Trieste,

Contributed by the International Gas Turbine Institute and presented at the 43rd International Gas Turbine and Aeroengine Congress and Exhibition, Stockholm, Sweden, June 2–5, 1998. Manuscript received by the International Gas Turbine Institute February 1998. Paper No. 98-GT-68. Associate Technical Editor: R. E. Kielb.

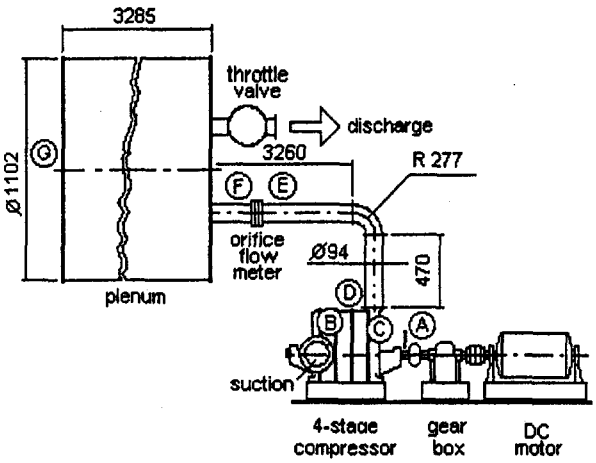

Fig. 1 Test rig

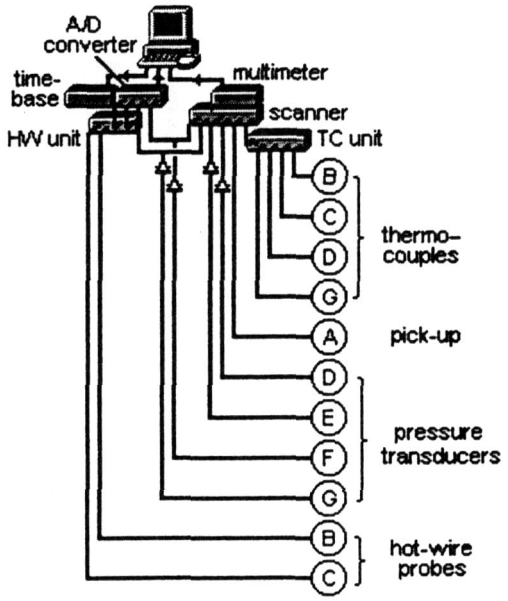

Fig. 2 Schematic of the instrumentation system

on a modular centrifugal blower plant (Fig. 1). Different configurations of this multistage compressor were investigated in previous works, by performing flow velocity measurements both in steady conditions (Arnulfi et al., 1995) and during rotating stall (Arnulfi et al., 1996).

In the present investigation, a blower configuration with four stages and vaned diffusers has been considered. All the stages have the same geometry; the shrouded impellers have 16 backswept blades (35 deg inlet angle and 67 deg outlet angle, both referred to the tangential direction, 160 mm inlet diameter, 465 mm outlet diameter, 23 mm inlet width, 8 mm outlet width); the vaned diffusers have parallel straight walls (470 mm inlet diameter, 570 mm outlet diameter, 10 mm axial width) and 27 straight blades (18 deg inlet angle and 40 deg outlet angle); the vaned return channels have eight curved blades.

The compressor is driven by a DC motor connected to a speed increasing gear. The blower operates in an open circuit: air enters a radial bellmouth inlet duct, flows through the blower, is fed to a cylindrical plenum by a connecting pipe, and is discharged into the atmosphere through a motorized throttle valve.

The plenum volume is 3.132 m^3, which is large enough to allow surge to arise with different configurations of the blower, namely, when varying the number of stages and the diffuser type. With the present blower configuration, deep surge occurs at stall inception at practically all rotor speeds.

Measuring Technique. Measurements were performed to determine both steady-state compressor characteristics and pressure and flow rate oscillations in the plant during surge. Furthermore, the instantaneous flow velocity was measured at the outlet of the first and last-stage diffusers, in order to investigate the interaction between surge and rotating stall. The instrumentation system is shown in Fig. 2, where the capital letters refer to the transducers location of Fig. 1. Pressures were measured by variable inductance transducers, temperature by type *K*-thermocouples, rotational speed by a magnetic pick-up.

The plenum pressure was measured by means of a single transducer mounted on the bottom lid, since the pressure can be considered as uniform throughout the volume at any time instant. It is due to plenum dimensions that are much smaller than the wavelength of an acoustic wave having a frequency on the order of that typically associated with surge.

The mass flow rate was measured by an orifice flow meter mounted in the pipe; such a measurement technique was preferred to the one proposed for unsteady flow measurements by Greitzer (1976) because the present plant allows the orifice flow meter to be properly located between compressor and plenum, while reducing the number of high-accuracy measure-

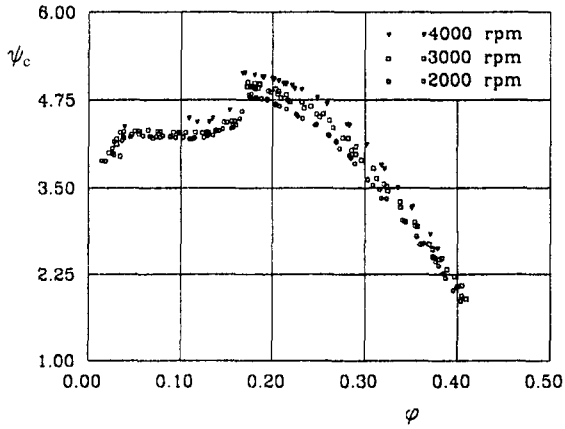

Fig. 3 Steady-state compressor characteristics

Nomenclature

A_i = inlet compressor area
C_1 = flow velocity in the first-stage diffuser
C_4 = flow velocity in the fourth-stage diffuser
f = frequency
f_H = Helmholtz frequency
$\dot{m}$ = mass flow rate
p_0 = ambient pressure
p_c = compressor delivery pressure
p_p = plenum pressure
t = time
T_H = Helmholtz period
U = impeller tip velocity
VAR = Valve Area Ratio
ρ_0 = air density at ambient conditions
$\varphi = \dot{m}/\rho_0 U A_i$ = flow coefficient
$\psi_c = 2(p_c - p_0)/\rho_0 U^2$ = compressor pressure coefficient
$\psi_p = 2(p_p - p_0)/\rho_0 U^2$ = plenum pressure coefficient

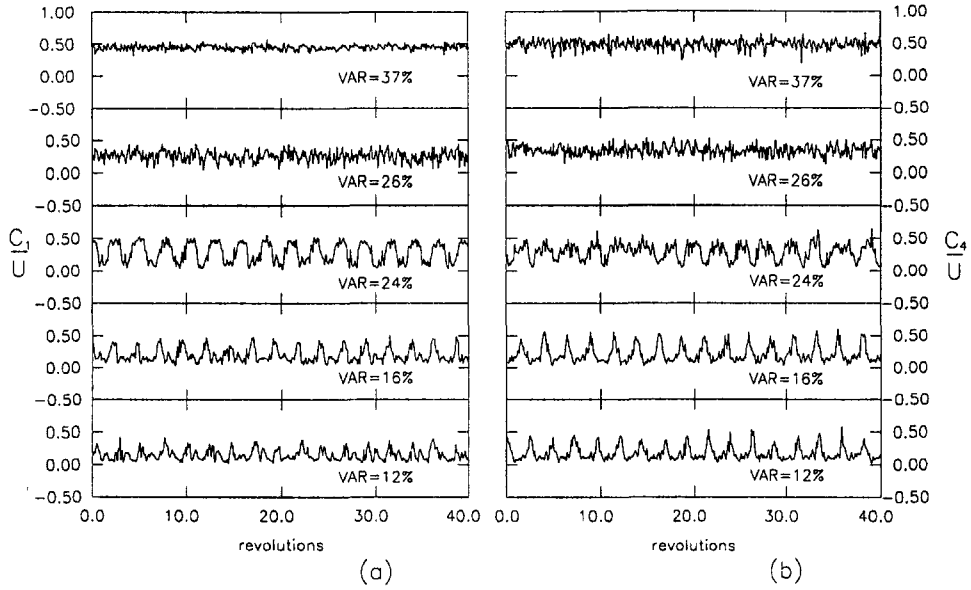

Fig. 4 Flow velocities in the diffusers of the first (*a*) and fourth (*b*) compressor stage at different valve settings and 3000 rpm

ments to be made. On the other hand, the use of an instrument suited for steady flow measurements was considered acceptable because of the slow dynamics of surge (few Hertz).

Velocity measurements were performed by means of two constant-temperature hot-wire Dantec anemometers, with single straight miniature probes (type 55P11, with tungsten wire of 5 μm diameter and 1.25 mm length). A stationary hot-wire technique was used to measure the intensity of the velocity vector in order to detect stall disturbances; the probes were located radially 8 mm upstream of the exit of the diffusers, in the middle of the blade-to-blade channel. Both probes had their wire oriented parallel to the rotor axis, i.e., normal to absolute velocity, the axial velocity being negligible due to the geometry of the diffusers.

The voltage signals of velocity, flow rate, and plenum pressure were sent to an A/D converter board, and the trigger signal was provided by a plug-in time-base card. Measurements were performed at a sampling rate of nine readings/revolution for almost 300 revolutions to detect stall and four readings/revolution for over 1000 revolutions to detect surge, which values appeared to provide a resolution suited to the frequency of the phenomena under investigation. As far as the other measurements are concerned, only average values were stored.

Operating Conditions. The tests were carried out at three compressor speeds, i.e., 2000, 3000, and 4000 rpm, and at different settings of the throttle valve, which were kept fixed during each test. Two different plant configurations, i.e., without and with plenum, were tested. In the former, the throttle valve was directly mounted at the exit of the compressor outlet pipe. Such a configuration was used to obtain the complete steady-state characteristics of the blower, surge being absent also at very low mass flow rates, and to measure flow velocity in the diffusers at conditions of fully developed rotating stall. On the contrary, the plant configuration, including the plenum, was employed to characterize the compression system operation during surge.

Experimental Results

Tests Without Plenum. The blower steady-state characteristics are shown in Fig. 3. The steep drop in pressure coefficient

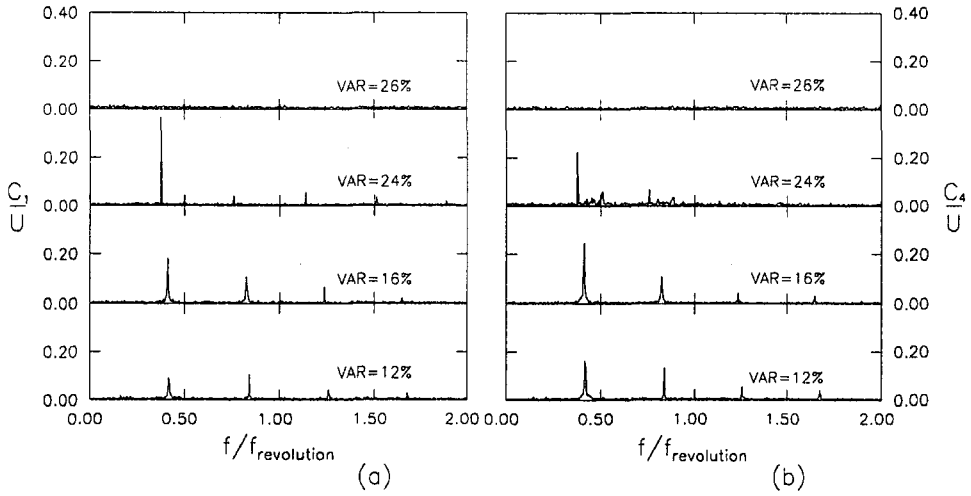

Fig. 5 Flow velocity spectra in the diffusers of the first (*a*) and fourth (*b*) compressor stage at different valve settings and 3000 rpm

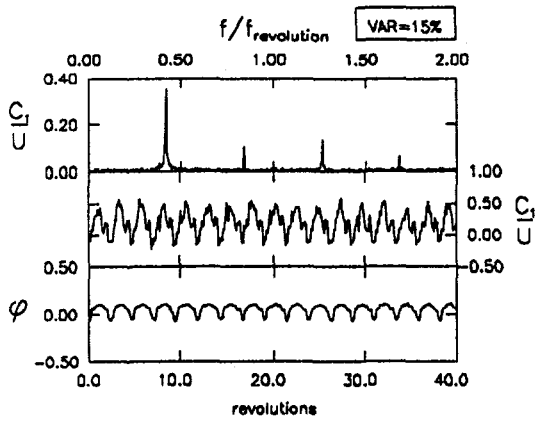

Fig. 6 Velocity spectrum and time history of velocity and flow coefficient in the diffuser of the first compressor stage, at 4000 rpm and VAR = 15 percent

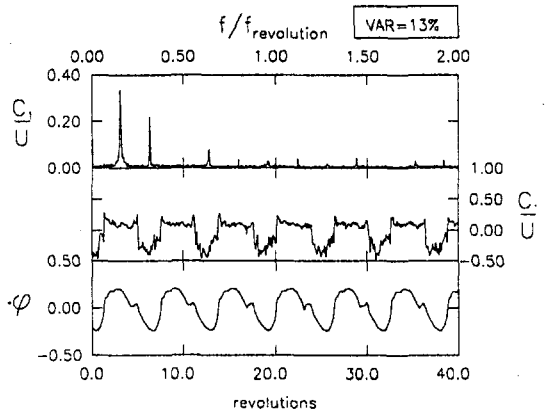

Fig. 7 Velocity spectrum and time history of velocity and flow coefficient in the diffuser of the first compressor stage, at 4000 rpm and VAR = 13 percent

suggests an abrupt stall inception at about $\varphi = 0.17$. The characteristic curves were obtained by means of a double sweep of the mass flow rate, both opening and closing the valve, in order to detect stall hysteresis, if any. An accurate evaluation near the stall limit showed no evidence of such a phenomenon.

Hereafter, the results of the hot-wire measurements are reported with reference to significant flow rate and compressor speed conditions. The different valve settings are expressed as Valve Area Ratio (VAR), i.e., the ratio of actual to maximum valve flow area.

Figure 4 shows the flow velocity in both diffusers during 40 consecutive revolutions, at 3000 rpm and different valve settings. The corresponding spectra, obtained by means of a FFT analysis, are plotted in Fig. 5 as a function of the ratio between the signal frequency and the impeller rotation frequency. Rotating stall is observed in both diffusers when VAR is 24 percent or lower. At this valve setting, the velocity signals in both diffusers appear to be quite sinusoidal, while new harmonics arise as the valve is closed. Figure 5 shows a stall frequency of about 20 Hz, which is 40 percent of the impeller rotation frequency. The same percentage value was found at the other compressor speeds. The present measurement technique, which employs a single probe, does not allow us to detect the number of stall cells, but previous tests on the same blower with different number of stages or vaneless diffusers always showed a single stall cell (Arnulfi et al., 1996).

At the highest rotational speed (4000 rpm) and low VAR values, surge was detected even in this plant configuration. Figures 6 and 7 show the time histories of velocity and flow coefficient together with velocity spectra at two different valve settings (VAR = 15 percent in Fig. 6 and VAR = 13 percent in Fig. 7). At VAR = 15 percent an oscillation at the stall frequency is observed in both velocity signal and flow coefficient trace, which also shows limited regions of reverse flow. At VAR = 13 percent, the oscillation frequency has fallen to 16 percent of the impeller rotation frequency and reverse flow is much more pronounced, so denoting the occurrence of surge instability.

It has to be pointed out that the present hot-wire technique allows only the magnitude of the flow velocity to be measured, not its direction. However, when a reverse flow occurs in the discharge pipe, it occurs also in the vaned diffusers, so that the sign of the velocity was changed according to the sign of the flow rate signal.

Tests With Plenum. By connecting the plenum to the discharge pipe, conditions of deep surge were observed at all the compressor speeds.

In Fig. 8 the surge cycles observed at 2000 rpm are shown for several valve settings in terms of plenum pressure coefficient ψ_p versus flow coefficient φ. In order to provide a clearer representation of the surge cycles, the signals have been filtered by cutting off frequencies higher than 30 Hz. In the same figure, the steady-state compressor characteristic referred to the plenum pressure is plotted for reference.

Figure 9 shows the time evolution of flow coefficient, plenum pressure coefficient and flow velocities in the first and fourth diffuser at the same conditions of Fig. 8. In these plots, time is nondimensionlized by using the Helmoltz period of the compression system. Surge oscillations are observed when VAR $\leq$ 26 percent, but at VAR values of 26 and 24 percent the phenomenon is not periodic, any reverse flow is absent, and the instability oscillations of the flow velocities are very small when compared with the flow rate and pressure ones. As it is demonstrated in Part II (Arnulfi et al., 1999), such conditions correspond to virtually stable operating points, the equilibrium steady-state flow coefficients being slightly greater than the stall limit value. However, a small perturbation is sufficient to cause a pronounced, but temporary, system instability. Such a situation occurs randomly and results in a nonperiodic behavior, rather than in a limit cycle. A similar phenomenon has been described by Lin (1996). When the valve is closed further on (VAR $\leq$ 20 percent), the system behavior becomes periodic, resulting in true surge cycles, and the velocity signals appear modulated at the same frequency as the flow rate oscillations. The limit cycles are typical of deep surge, since they exhibit two slow phases, which develop along both stable and negative branches of the compressor characteristic, and two much faster phases during which large changes in flow rate are observed at almost constant pressure. As the valve is closed, surge cycles shift to

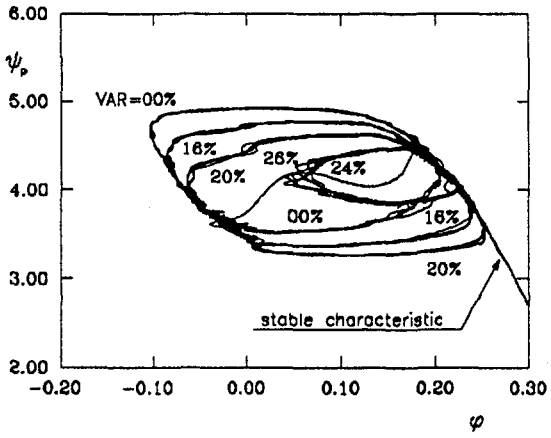

Fig. 8 Surge cycles at different valve settings and 2000 rpm

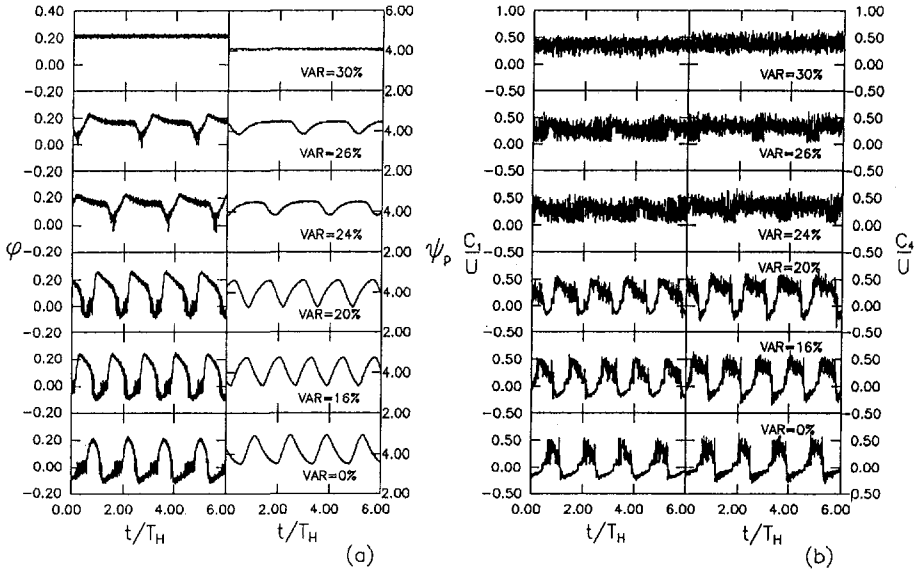

Fig. 9 Time histories of flow coefficient and plenum pressure coefficient (*a*), and of velocities in the diffusers of the first and fourth compressor stages (*b*), at different valve settings and 2000 rpm

higher pressures; at the same time the duration of the positive flow phase decreases while the length of the negative flow one increases. In fact, when the valve flow area is reduced, the storage of elastic potential energy into the plenum becomes faster, while the subsequent blow-down process mainly occurs as a reverse flow through the compressor rather than a positive flow through the valve. It results in an increased flow resistance when the plenum is emptying and, consequently, in a higher mean value of the cycle pressure.

At constant speed, the frequency of surge oscillations varies slightly with valve opening, a maximum value being reached at an intermediate throttle setting between surge inception and valve shut-off. Figure 10 shows the results obtained at 2000 rpm by means of a FFT analysis of the periodic signals reported in Fig. 9. A maximum surge frequency of 0.75 Hz, corresponding to 80 percent of the Helmoltz frequency, occurs at VAR = 16 percent, while it falls to about 0.70 Hz (74 percent of the Helmholtz frequency) when VAR is 0 or 20 percent. A similar behavior has been observed at higher compressor speeds. Figure 10 also shows that the flow rate, pressure, and velocity signals concerning the same valve setting contain the same number of harmonics of significant amplitude.

As far as the influence of the compressor speed is concerned, the surge frequency turns out to decrease when the speed is increased, as observed by Jin et al. (1994) in the case of a single-stage compressor. Figure 11 shows the velocity signals in the fourth diffuser and the corresponding spectra obtained at different speeds and VAR = 16 percent. The surge frequency turns out to decrease almost linearly from 80 percent of Helmholtz frequency at 2000 rpm to 54 percent at 4000 rpm.

The present hot-wire measurements confirm that rotating stall can occur during part of surge cycle. This is shown in Fig. 12, where the flow velocities in the fourth diffuser at 2000 rpm, already reported in Fig. 9, are plotted in a larger scale (time origins are not preserved) in order to point out stall oscillations. These latter are framed in the figure and are quite evident at VAR = 26 percent and VAR = 24 percent, which correspond to temporary instability conditions of the system rather than to real surge. However, stall oscillations are not always present because the "surgelike" cycle produces continuous changes in the flow features by moving the instantaneous working point through successive conditions of stability, stall inception, and full instability. Indeed, reference points A and B in Fig. 12, which denote the beginning and the end of the system instability, respectively, allow the rotating stall to be located over the whole cycle portion at decreasing pressure. When deep surge occurs, i.e., VAR $\leq$ 20 percent, stall is detected from the end of the reverse flow phase to an instant shortly before the stable branch of the compressor characteristic is reached, as already pointed out by Bammert and Mobarak (1976). Really, in deep surge conditions, Fig. 12 shows further velocity oscillations, which might have the stall frequency, occurring at 4 to 6 impeller revolutions after the surge line is crossed, some time before the flow reversal. In order to investigate on this matter, a FFT

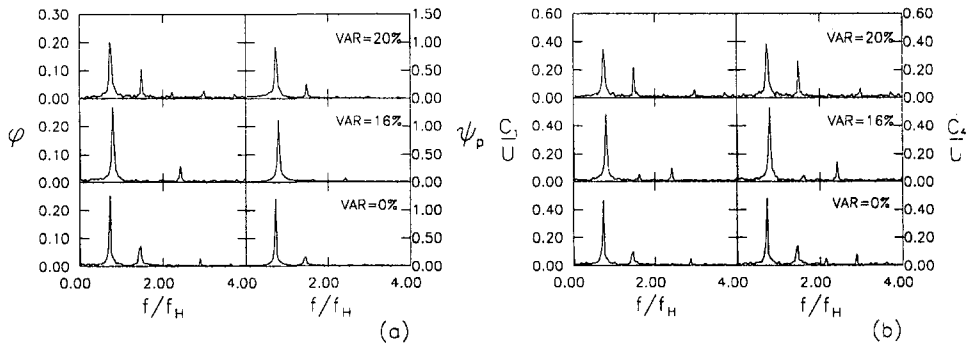

Fig. 10 Spectra of flow coefficient and plenum pressure coefficient (*a*), and of velocities in the diffusers of the first and fourth compressor stages (*b*), at different valve settings and 2000 rpm

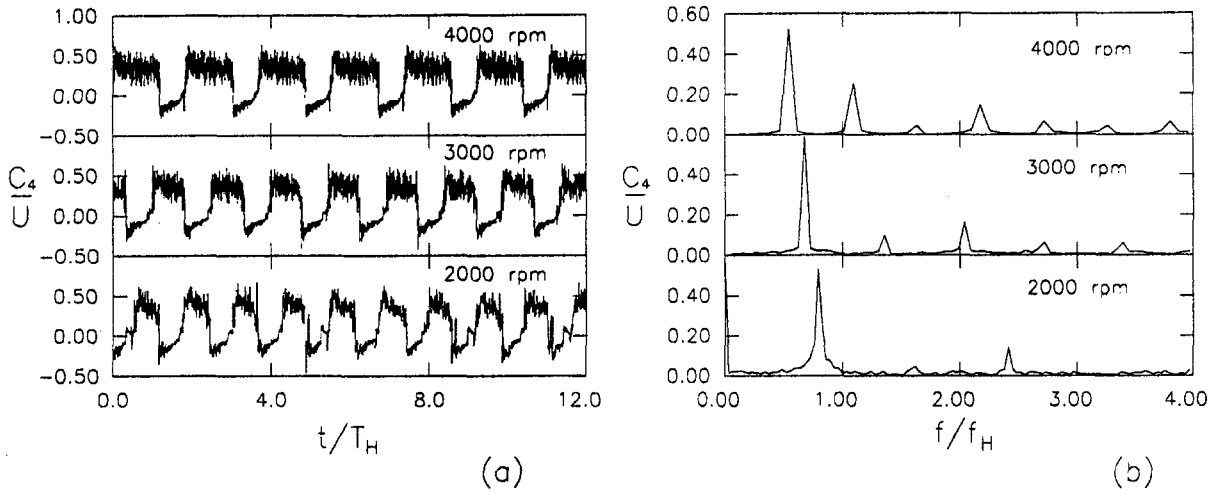

Fig. 11 Time history (*a*) and spectra (*b*) of flow velocity in the diffuser of the fourth compressor stage at VAR = 16 percent and different rotation speeds

analysis has been performed on windows of the flow velocity signals. Harmonics having a typical frequency of rotating stall were detected only on the low-pressure portion of the surge cycle. On the contrary, the little number of velocity oscillations and the large noise-to-signal ratio that characterize the inversion from positive to negative flow did not allow an accurate frequency analysis to be performed in this region and any conclusion to be drawn about the presence of rotating stall in the high-pressure side of the surge cycle. Figure 13 shows the results of the FFT analysis concerning the windows where rotating stall was detected. In part (*a*) of the figure the stalled portion of the deep surge cycle at VAR = 0 percent is marked, as an example, while in part (*b*) the velocity spectra show frequencies close to 40 percent of the impeller rotation frequency. This stall frequency turns out to be the same obtained by the tests without plenum, as also found by Greitzer (1976).

Conclusions

Detailed measurements in surge instability conditions were performed on a low-pressure compression system. The analysis of the flow rate and pressure measurements in the plant and of

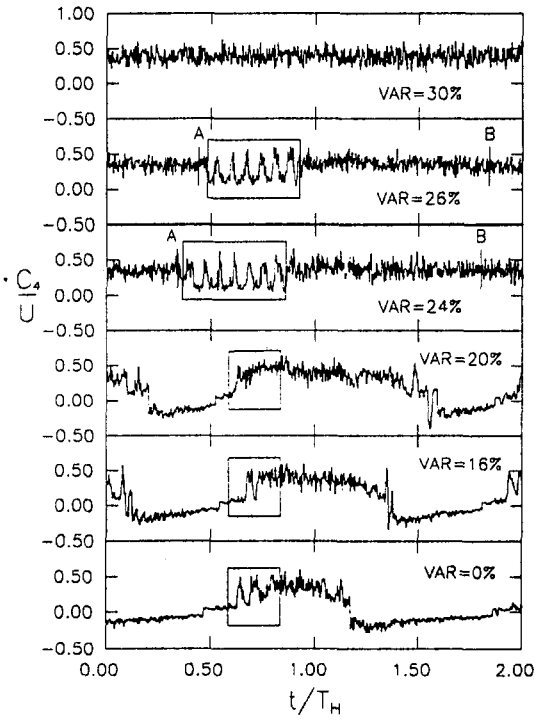

Fig. 12 Flow velocities in the diffuser of the fourth compressor stage during a surge cycle, at different valve settings and 2000 rpm. Frames point out stalled regions.

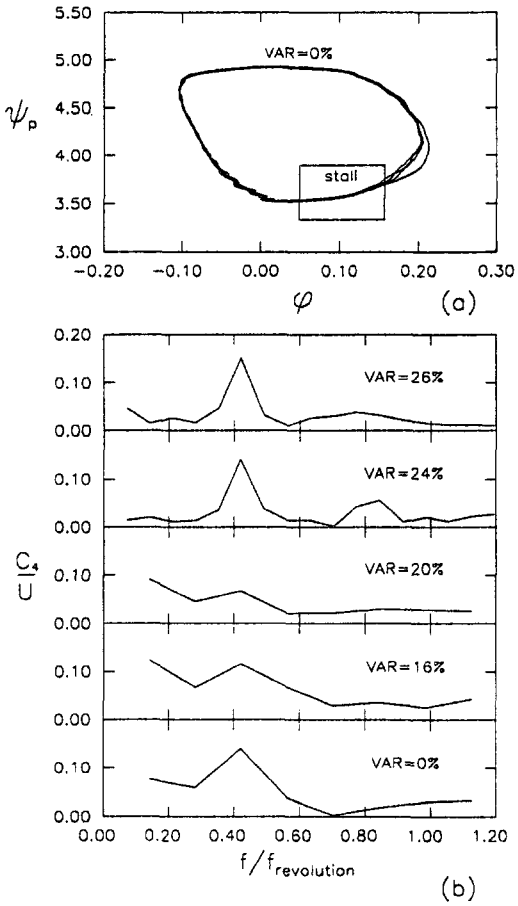

Fig. 13 Stalled portion of the surge cycle at VAR = 0 percent (*a*) and velocity spectra of the framed signals of Fig. 12(*b*)

the flow velocities signals in the diffusers of the multistage centrifugal compressor allowed the unsteady system behavior to be fully characterized.

Tests carried out on the plant configuration without plenum showed a high-frequency velocity oscillation in the diffusers due to rotating stall, while surge was detected only at the highest rotation speed. By connecting the compressor delivery pipe to a large plenum, typical low-frequency oscillations due to surge instability were observed at low flow rates and at all the tested compressor speeds. The surge features were examined in detail at different operating conditions of the compression system and significant differences in the measured values were observed when varying both valve setting and rotation speed. In particular, nonperiodic oscillations were detected when the steady-state equilibrium flow rate was set at a slightly higher value than the stall limit one. In addition, rotating stall was observed in the blower diffusers on the low-pressure portion of the surge cycle.

The aim of the present stage of the research was to get a deeper insight into surge instability of multistage centrifugal compressors and to obtain systematic experimental data for validating theoretical models of the compression system. These latter will be used to design both passive and active control systems capable of widening the stable operating range of the compressor through suppression of surge (Arnulfi et al., 1999).

Acknowledgments

The authors would like to thank MURST (Italian Research Ministry) for the financial support granted to this research.

References

Abdelhamid, A.N., Colwill, W.H., and Barrows, J.F., 1979, "Experimental Investigation of Unsteady Phenomena in Vaneless Radial Diffusers," ASME *Journal of Engineering for Power*, Vol. 101, pp. 52–60.

Arnulfi, G.L., Micheli, D., and Pinamonti, P., 1995, "Velocity Measurements Downstream of the Impellers in a Multistage Centrifugal Blower," ASME JOURNAL OF TURBOMACHINERY, Vol. 117, pp. 593–601.

Arnulfi, G.L., Micheli, D., and Pinamonti, P., 1996, "Experimental Investigation on Rotating Stall in a Centrifugal Blower With Two and Four Stages and Vaneless Diffusers," ASME Paper No. 96-GT-171.

Arnulfi, G.L., Giannattasio, P., Giusto, C., Massardo, A.F., Micheli, D., and Pinamonti, P., 1999, "Multistage Centrifugal Compressor Surge Analysis. Part II: Numerical Simulation and Dynamic Control Parameters Evaluation," ASME JOURNAL OF TURBOMACHINERY, Vol. 121, this issue, pp. 312–320.

Bammert, K., and Mobarak, A., 1976, in discussion of: Greitzer, E.M., "Surge and Rotating Stall in Axial Flow Compressors. Part II: Experimental Results and Comparison with Theory," ASME *Journal of Engineering for Power*, Vol. 98, pp. 213–215.

Cyrus, V., Sprinc, M., Paroubek, J., and Kyncl, J., 1995, "Nonsteady Flows in Centrifugal Compressor Stages With Low Flow Coefficient," VDI Berichte 1186, *Turbomachinery Fluid Dynamic and Thermodynamic Aspects Conference*, Erlangen (D), Mar., pp. 389–404.

Greitzer, E.M., 1976, "Surge and Rotating Stall in Axial Flow Compressors. Part I: Theoretical Compression System Model. Part II: Experimental Results and Comparison With Theory," ASME *Journal of Engineering for Power*, Vol. 98, pp. 190–217.

Hansen, K.E., Jorgensen, P., and Larsen, P.S., 1981, "Experimental and Theoretical Study of Surge in a Small Centrifugal Compressor," ASME Paper No. 81-FE-1.

Jin, D., Hasemann, H., Haupt, U., and Rautenberg, M., 1994, "The Flow Rotation Characteristics of a Centrifugal Compressor During Surge," ASME Paper No. 94-GT-154.

Lin, F., 1996, "On the Practical Stability and Its Application to Nonlinear Control of Surge," ASME Paper No. 96-GT-512.

Ribi, B., and Gyarmathy, G., 1993, "Impeller Stall as a Trigger for the Transition From Mild to Deep Surge in a Subsonic Centrifugal Compressor," ASME Paper No. 93-GT-234.

Ribi, B., and Gyarmathy, G., 1995, "The Behaviour of a Centrifugal Compressor Stage During Mild Surge," VDI Berichte 1186, *Turbomachinery Fluid Dynamic and Thermodynamic Aspects Conference*, Erlangen (D), Mar. pp. 341–356.

Toyama, K., Runstadler, P.W., Jr., and Dean, R.C., Jr., 1977, "An Experimental Study of Surge in Centrifugal Compressors," ASME *Journal of Fluids Engineering*, Vol. 99, pp. 115–131.

G. L. Arnulfi

P. Giannattasio

University of Udine,
Dipartimento di Energetica
e Macchine,
Udine, Italy

C. Giusto

A. F. Massardo
Mem. ASME

University of Genova,
Istituto di Macchine e
Sistemi Energetici,
Genova, Italy

D. Micheli
University of Trieste,
Dipartimento di Energetica,
Trieste, Italy

P. Pinamonti
University of Udine,
Dipartimento di Energetica
e Macchine,
Udine, Italy

Multistage Centrifugal Compressor Surge Analysis: Part II—Numerical Simulation and Dynamic Control Parameters Evaluation

This paper describes, from a theoretical point of view, the behavior of compression systems during surge and the effect of passive and active control devices on the instability limit of the system. A lumped parameter model is used to simulate the compression system described in Part I of this work (Arnulfi et al., 1999), based on an industrial multistage centrifugal compressor. A comparison with experimental results shows that the model is accurate enough to describe quantitatively all the features of the phenomenon. A movable wall control system is studied in order to suppress surge in the compressor. Passive and active control schemes are analyzed; they both address directly the dynamic behavior of the compression system to displace the surge line to lower flow rates. The influence of system geometry and compressor speed is investigated; the optimum values of the control parameters and the corresponding increase in the extent of the stable operating range are presented in the paper.

Introduction

To avoid surge, one commonly adopts a margin of safety between the surge line—the limit of stable operation—and the closest allowable operating point. However, this can prevent from operating in regions of maximum efficiency or pressure rise.

Methods have been developed to obtain a wider stable operating range by modifying the dynamic behavior of the compression system; this would allow compression operation in previously unusable, or even previously unstable, regions of the compressor map. In particular integrated tailored structure (passive control) and feedback control (active control) have been examined in depth. Active stabilization was demonstrated experimentally for high-speed centrifugal compressors by several investigations (Ffowcs Williams and Huang, 1989; Pinsley et al., 1991). These studies also showed that a lumped parameter model of the compression system is able to capture the essential dynamics of surge (Simon et al., 1993). In a similar way, much work was carried out to prevent surge by utilizing tailored structure (Gysling, 1989; Gysling et al., 1991). Both control systems were developed and utilized only for single-stage centrifugal compressors.

In the present paper, the mathematical model presented by Greitzer (1976) for a multistage axial compressor and widely utilized in literature for single-stage centrifugal compressors, with and without control, is applied to the compression system described in Part I of the present work (Arnulfi et al., 1999). It consists of an industrial low-pressure multistage centrifugal compressor, with vaned diffusers, connected to a large plenum and suitable for continuous operation in deep surge conditions, also at low rotation speeds.

Finally, models of active and passive control devices with a movable wall in the plenum, described in detail by Giusto (1997), are developed and applied to the present compression system. The influence of compression system geometry, rotation speed, and control parameters are discussed in depth.

Model of the Compression System

Governing Equations and Computational Procedure. A nonlinear lumped parameter model of the compression system (Fig. 1) was used, which is capable of detecting the occurrence of instability and of correctly reproducing the system unsteady behavior during surge. The model, which is similar to the one previously utilized for multistage axial compressors by Cinquetti and Massardo (1988), is derived from the one proposed by Greitzer (1976) and is based on the following assumptions: (*a*) the compressor is regarded as an actuator disk and its ducting is replaced by a constant area pipe of equivalent length; (*b*) inertial forces in the system are only associated with the dynamics of the fluid in the compressor duct; (*c*) the transient response of the compressor can be derived from its steady-state characteristic by introducing a proper time constant; (*d*) compressibility effects are confined to the gas contained in the plenum (the flow through the compressor and valve ducts is incompressible); (*e*) the pressure in the plenum is uniform throughout its volume at any time instant; (*f*) inertial forces due to the small mass of fluid in the throttle duct are negligible and the flow through the valve is quasi-steady.

Contributed by the International Gas Turbine Institute and presented at the 43rd International Gas Turbine and Aeroengine Congress and Exhibition, Stockholm, Sweden, June 2–5, 1998. Manuscript received by the International Gas Turbine Institute February 1998. Paper No. 98-GT-69. Associate Technical Editor: R. E. Kielb.

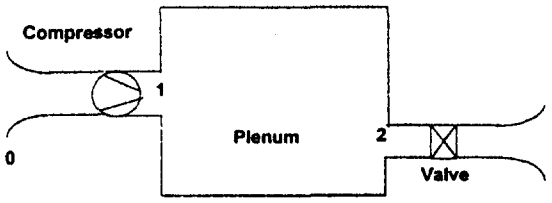

Fig. 1 Lumped parameter compression system without control

The length of the constant area pipe is computed by requiring that a given rate of change of mass flow produce the same unsteady pressure difference in the actual duct and in the equivalent one. It results in the following relation (Emmons et al., 1955):

$$\frac{L_c}{A_i} = \int_{\substack{\text{actual}\\ \text{ducting}}} \frac{ds}{A(s)} \tag{1}$$

The foregoing assumptions allow comparatively simple equations to be written, which describe the dynamics of the compression system:

$$\Delta p_c - (p_p - p_0) = \frac{L_c}{A_i}\frac{d\dot{m}_c}{dt} \tag{2}$$

$$\dot{m}_c - \dot{m}_t = \frac{V_p}{a_p^2}\frac{dp_p}{dt} \tag{3}$$

$$t_d \frac{d\Delta p_c}{dt} = \Delta p_{css} - \Delta p_c \tag{4}$$

$$p_p - p_0 = \frac{\dot{m}_t^2}{2\rho_0 A_t^2} \tag{5}$$

Equation (2) is the momentum conservation equation in the compressor ducting, Eq. (3) expresses mass conservation in the plenum, Eq. (4) is a first-order model of the transient response of the compressor and Eq. (5) represents the steady-state characteristic of the valve.

These equations are usefully nondimensionlized by:

$$\varphi = \frac{\dot{m}}{\rho_0 U A_i} \quad \psi = \frac{2\Delta p}{\rho_0 U^2} \quad \tau = \omega_H t = a_p\sqrt{\frac{A_i}{V_p L_c}}\, t$$

and the following set of equations is obtained:

$$\frac{d\varphi_c}{d\tau} = B(\psi_c - \psi_p) \tag{6}$$

$$\frac{d\psi_p}{d\tau} = \frac{(\varphi_c - \varphi_t)}{B} \tag{7}$$

$$\frac{d\psi_c}{d\tau} = \frac{(\psi_{css} - \psi_c)}{\tau_d} \tag{8}$$

$$\psi_p = \left(\frac{A_i}{A_t}\right)^2 \varphi_t^2 \tag{9}$$

Greitzer's parameter B in Eqs. (6) and (7) is defined as:

$$B = \frac{U}{2\omega_H L_c} = \frac{U}{2a_p}\sqrt{\frac{V_p}{A_i L_c}} \tag{10}$$

Greitzer (1976) showed that this parameter can be regarded as the ratio of pressure forces and inertial forces acting in the compressor duct, so playing a leading role in determining the dynamic behavior of the system. In particular he found that a critical value of B exists, beyond which surge instability occurs when the system is perturbed from the stall limit condition.

Term τ_d in Eq. (8) is the nondimensionlized time constant introduced to account for the delay in the compressor response during transient operation. According to Greitzer (1976), such a time lag is associated with the time needed for the full growth of a stall cell and it can be evaluated in terms of rotor revolutions N by means of the relation:

$$\tau_d = \frac{\pi D N}{2 L_c B} \tag{11}$$

Equations (6) to (9) were solved numerically for different values of B and different settings of the throttle valve (A_t), by means of a second-order accurate implicit scheme and a Newton–Raphson iterative procedure. The initial conditions were specified by imposing a small perturbation of the steady flow parameter, $\bar{\varphi}$, determined by the intersection of the compressor and valve characteristic curves.

Model Parameters. The model was employed for simulating unstable operating conditions of the compression system described by Arnulfi et al. (1999). It comprises a compressor, a plenum of sufficiently large volume, and a throttle valve directly mounted at the plenum exit.

The main input parameters of the model were the characteristic curves of the compressor and the values of A_i, L_c, V_p, D, and τ_d.

The steady-state compressor curves, i.e., $\psi_{css}(\varphi_c)$ at different speeds, were referred to the plenum pressure, instead of the compressor delivery pressure, because the model does not account for the pressure losses in the pipe connecting the compressor with the plenum. Obviously, the positive flow branch of the characteristic on the left of the uncontrolled surge line can only

Nomenclature

a = speed of sound
A = area
B = Greitzer's parameter
c = damping coefficient
D = impeller exit diameter
k = spring constant
K = gain
L_c = effective length
m = mass of the movable plenum wall
$\dot{m}$ = mass flow rate
M = U/a_p = tip Mach number based on plenum condition
N = rotor revolutions
p = pressure
q = wall displacement
Q = wall frequency parameter
s = curvilinear coordinate
t = time
U = impeller tip velocity
V = volume
W = wall aeroelastic coupling parameter
Δp = pressure rise
ζ = wall damping ratio parameter
η = nondimensional wall displacement
λ = eigenvalue
ρ = air density
τ = nondimensional time
υ = nondimensional wall velocity
φ = flow coefficient
ψ = pressure coefficient
ω = circular frequency

Subscripts

ap = auxiliary plenum
c = compressor
d = delay
H = Helmholtz
i = compressor inlet
opt = optimum
p = plenum
ss = steady state
t = throttle valve
w = movable wall
0 = ambient

Operators

$\delta(\ )$ = perturbation quantity
$\bar{\ }$ = time mean quantity

be measured without plenum, so that a proper correction was required. This latter was performed, at all flow rates, by means of a loss correlation obtained by comparing the measured pressures at the compressor exit and in the plenum during stable operation. The negative flow branch of the characteristic curve was determined by simply fitting the negative flow decreasing portion of the measured deep surge cycles. In fact, the slow blowdown process, which is typical of deep surge, is associated with negligible inertial forces in the compressor ducting, so that, under such conditions, the plenum pressure is very close to the steady-state compressor delivery pressure.

The characteristic area of the compressor duct, A_i, was taken as the compressor inlet area, being equal to 122.7 cm^2. The accurate evaluation of the equivalent duct length, L_c, by means of Eq. (1) was rather difficult, due to the complex geometry of the multistage compressor. Only a reasonable range of 10–14 m could be specified for this parameter, the exact value of which had to be determined by comparison of model predictions with experimental results. To completely specify parameter B at a given compressor speed, the values of plenum volume, V_p = 3.132 m^3, and of impeller external diameter, D = 465 mm, were provided as input data to the model. The value of time constant τ_d was computed by means of Eq. (11) on the basis of the number N of rotor revolutions needed for the development of a stall cell. The experimental results reported in Part I of the paper suggest that $N = 4$ should be a reasonable choice for the present compression system, so that all the operating conditions considered here were simulated by using such a value. The corresponding value of the time constant is imposed only when the compressor is operating on the stalled portion of the characteristic, namely, for flow coefficient greater than zero and less than the stall limit value. On the contrary, when reverse flow occurs or compressor is running on the unstalled branch of the characteristic, τ_d is set equal to a very small value, according to the fast compressor response observed when rotating stall is absent. This approach is slightly different from the one adopted by Greitzer (1976), where a time lag associated with stall is introduced also when the compressor is operating on the unstalled portion of the characteristic and the mass flow rate is increasing. The different choice is justified by the measurements performed on the present compression system, which show rotating stall cessation when the flow rate is increasing and the stall limit is crossed (Arnulfi et al., 1999).

Numerical Results—Model Validation. The model was validated by simulating all the experimental operating conditions of the compression system, which refer to compressor speeds of 2000, 3000, and 4000 rpm. The values of the throttle effective area, A_t, corresponding to the actual valve opening conditions were determined by computing the equilibrium steady-state flow parameter as the mean value of the measured flow parameters over a complete surge cycle, rather than by the less accurate *Valve Area Ratio* introduced in Part I of the paper. The correctness of such an approach was confirmed by numerical experiments, which showed that the net mass exiting the system during a simulated surge cycle is extremely close to the equilibrium steady-state mass flow rate multiplied by the cycle period.

Preliminary runs of the computer program were performed in order to compute the critical value of Greitzer's parameter B for the present compression system. At each compressor speed, the system was perturbed from the stall limit condition by varying the plenum volume in order to change B. The values of this parameter beyond which surge instability was detected turned out to be very close to $B = 0.06$ with only slight differences observed when changing the compressor speed. The actual values of B, corresponding to operation at 2000, 3000, and 4000 rpm, are 0.304, 0.457, and 0.608, respectively, so being much higher than the critical value. This justifies the deep surge character of all the instability conditions observed in the present work.

In the following, numerical results are reported for the most significant instability conditions observed in the present compression system and a comparison with the experimental values is performed. All the simulations were carried out by using the value L_c = 13.5 m for the length of the equivalent compressor duct, which was selected by pursuing the best fitting of the experimental values in a single operating condition of the compression system (2000 rpm, $\bar{\varphi} = 0.026$).

Figures 2 to 5 show the results obtained at the compressor speed of 2000 rpm, for some experimental valve opening conditions. Each figure comprises (a) a $\varphi-\psi$ plot of the computed and measured surge cycles, and (b) the corresponding diagrams of the compressor flow coefficient and the plenum pressure coefficient versus nondimensional time $\tau/2\pi$. For reference, the steady-state compressor characteristic is also reported in part (a) of each figure.

Figure 2 refers to the largest valve opening at which an oscillating behavior of the system is observed ($\bar{\varphi} = 0.173$). Figure 2(b) shows that the measured oscillations are nonperiodic, so that the closed orbit in Fig. 2(a) does not represent a surge limit cycle. As a matter of fact, in the present case the equilibrium steady-state flow coefficient turns out to be slightly greater than the stall limit value, so that the operating point is a stable one, being simply subjected to random perturbations. In fact, the numerical simulation correctly predicts the cycle shape resulting from a small disturbance, while providing a single oscillation before a permanent stability is recovered. Figures 3, 4, and 5 show the transient compression system behavior when $\bar{\varphi}$ is reduced to 0.114, 0.075, and 0.026, respectively. In all cases deep surge oscillations with regions of flow reversal are observed. Numerical results appear to reproduce quite well both shape and frequency of the measured pressure and the flow rate oscillations. In particular, the progressively faster filling and slower emptying of the plenum that occur when closing the valve are well captured, as well as the increase of the plenum pressure that results from the reduction in throttle area.

In Figs. 6 and 7 the model predictions are compared with the experimental results with reference to unstable system operations at 3000 and 4000 rpm, respectively. The results in these figures show a good prediction of the shape and the period of the surge oscillations. Only the maximum pressure in the plenum at 3000 rpm appears to be underestimated, which is common to all the other valve setting conditions at 3000 rpm. It might be due to an underestimation of the measured steady-state delivery pressure of the compressor near the stall limit.

The operating conditions of Figs. 3, 6, and 7 refer to almost the same valve setting, so that a meaningful comparison at varying speed can be established. As the compressor speed is increased from 2000 to 4000 rpm, parameter B grows proportionately, and the greater ratio of pressure forces and inertial forces in the system causes the surge oscillations to change their shape and period, as discussed by Greitzer (1976). In particular, the plenum pressure increases progressively and the surge cycle becomes more and more squarish due to the growing difference between the two time scales of motion that characterize deep surge (the long one associated with the slow increase or decrease in the plenum pressure, the shorter one concerning the very fast changes in mass flow rate that occur at almost constant pressure). Furthermore, the strong increase in the longer time scale of motion is responsible for the reduction in the frequency of surge oscillations that is observed when the compressor speed is increased. All these features of the transient system behavior appear to be well reproduced by the present model, which can be thus considered as a reliable basis for developing simulation models of surge control systems.

Passive and Active Control Systems

Surge could be prevented by damping flow oscillations when their amplitude is still low, as proposed by Epstein et al. (1989).

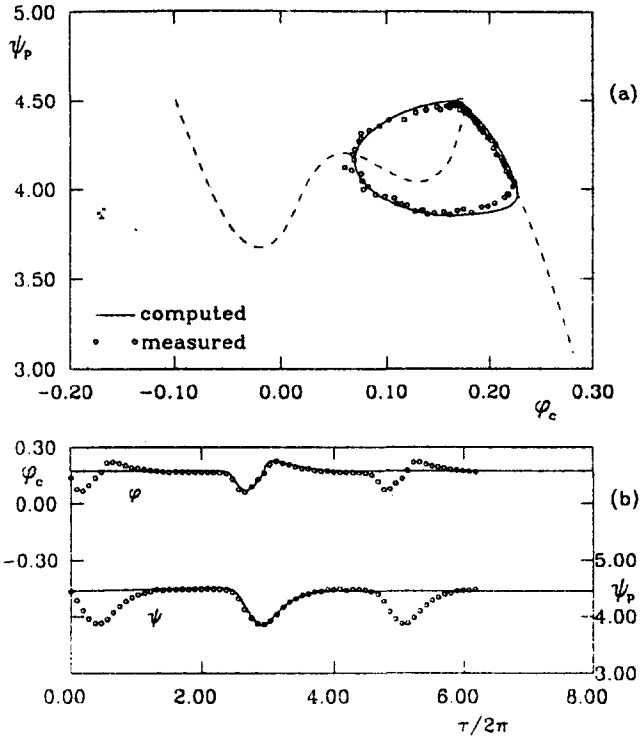

Fig. 2 Transient compression system behavior: 2000 rpm, $\bar{\varphi} = 0.173$

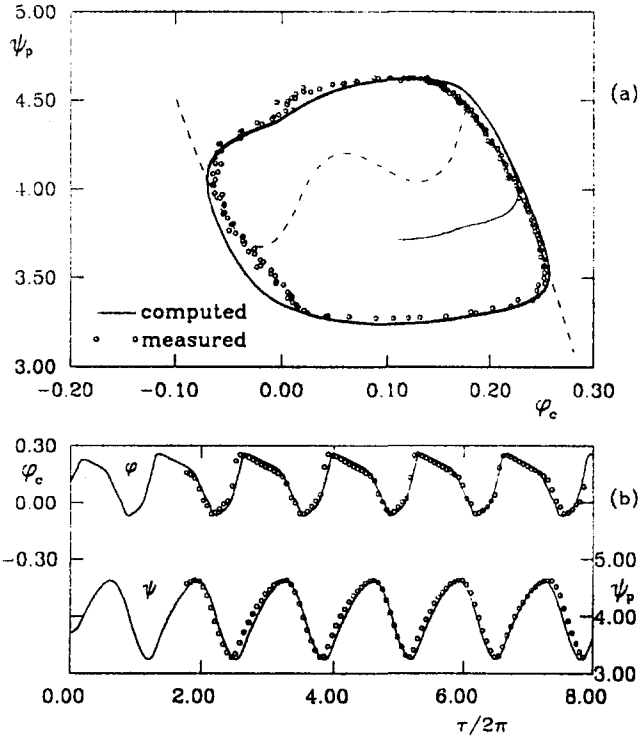

Fig. 3 Transient compression system behavior: 2000 rpm, $\bar{\varphi} = 0.114$

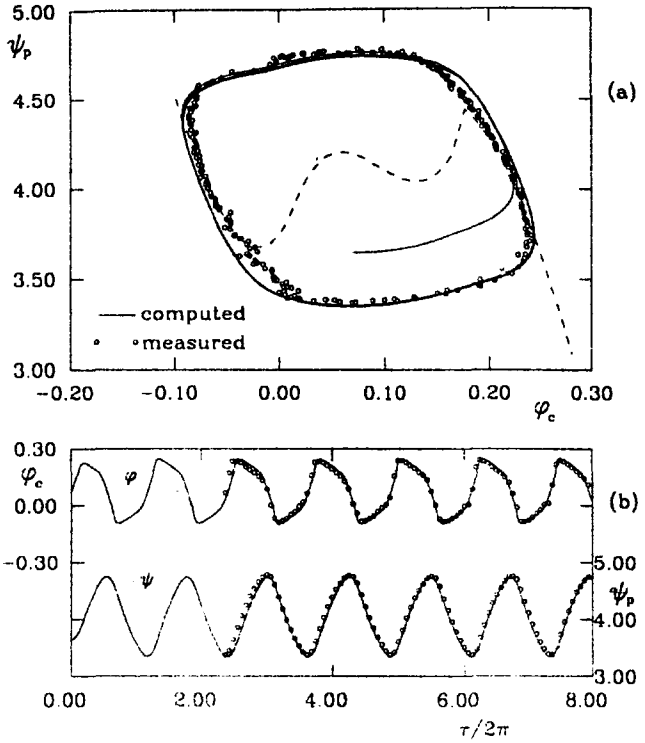

Fig. 4 Transient compression system behavior: 2000 rpm, $\bar{\varphi} = 0.075$

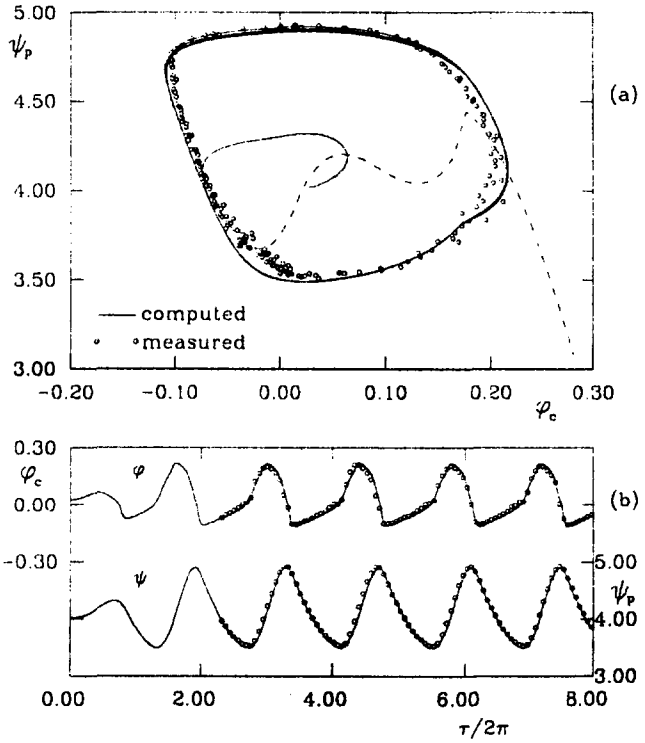

Fig. 5 Transient compression system behavior: 2000 rpm, $\bar{\varphi} = 0.026$

In this approach, the unsteady perturbations are directly affected and the flow parameters are virtually unaltered.

A movable plenum wall can be used for both passive and active control systems. If passive control is adopted, the movable wall acts as a mass-spring-damper system (Fig. 8) driven by the unsteady pressure perturbations in the plenum, so that its motion is directly coupled to the compression system dynamics. In the case of active (feedback) control (Fig. 9), the movable wall is the active element of the system, while the plenum pressure is the controlling parameter; really it is possible to define different *actuator–sensor* couples, as discussed by Simon et al. (1993).

To obtain the mathematical model of the compression system including active or passive control, Eqs. (2), (3), and (5) can

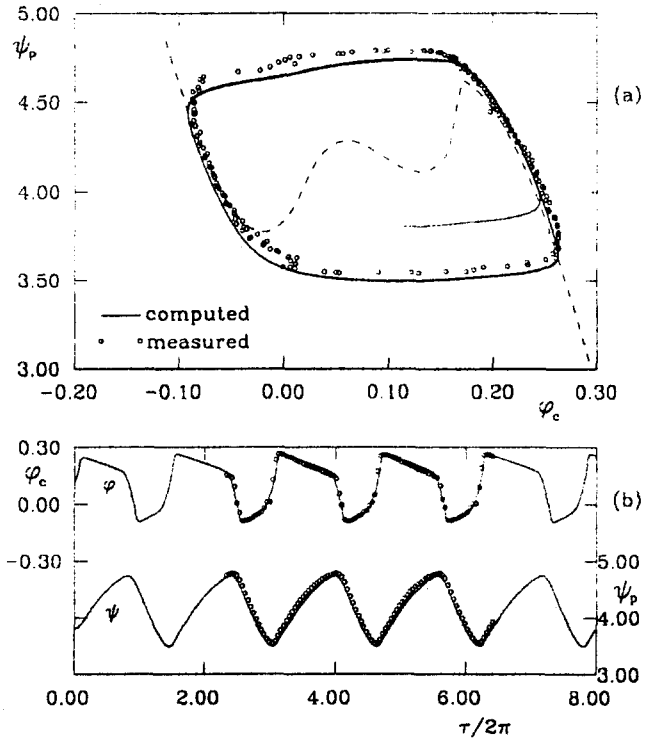

Fig. 6 Transient compression system behavior: 3000 rpm, $\bar{\varphi} = 0.117$

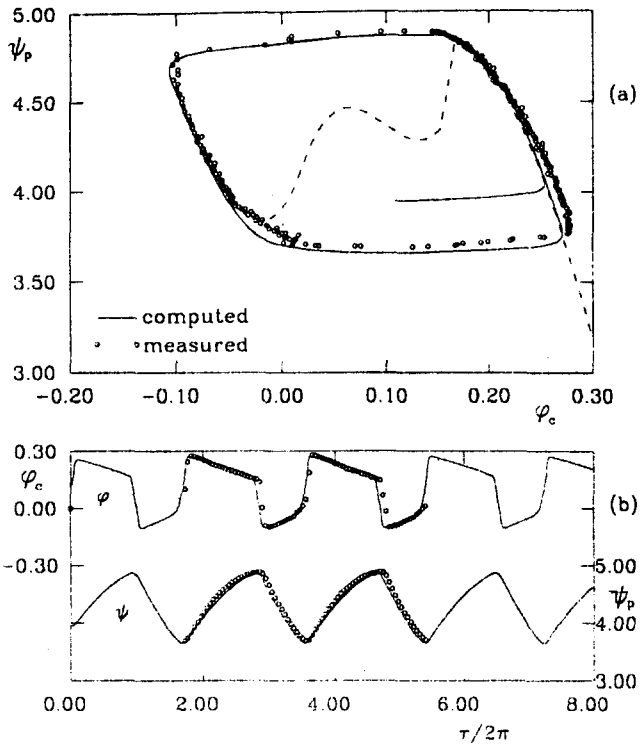

Fig. 7 Transient compression system behavior: 4000 rpm, $\bar{\varphi} = 0.113$

be used after some modification (Ffowcs Williams and Huang, 1989; Gysling, 1989). First of all, another equation must be considered, depending on the control system under investigation. Then, the equations can be linearized in a neighborhood of the equilibrium working point. In fact, the control device is aimed at avoiding surge inception, rather than to suppress completely developed surge, so that the small perturbation theory can be adopted (Pinsley, 1988).

If a passive control with movable wall is considered, the following linear equation is added to the existing set:

$$m\ddot{q} + c\dot{q} + kq = (p_p - p_{ap})A_w \tag{12}$$

In this case the movable wall is driven by the pressure fluctuations in the plenum, while its efficiency in dissipating unstable energy depends on the mass, spring, and damper characteristics, or rather on matching the dynamic characteristics of the control device with the fluid dynamics of the compression system (Gysling, 1989; Pinsley, 1988).

If the active control is employed, the control law of the actuator needs to be introduced in the mathematical model. The choice of this law depends on the particular actuator–sensor couple adopted (Simon et al., 1993). In the present work, a movable wall with a static pressure sensor in the plenum and a proportional control law were chosen, so that the equation to be included in the model is:

$$\delta v = \frac{d\delta\eta}{d\tau} = -K\delta\psi_p. \tag{13}$$

For the passive control system, the following stability matrix can be obtained and used to analyze the compression system stability (Gysling, 1989; Giusto and Massardo, 1996):

$$\left[\begin{array}{cc|cc} B\left(\dfrac{d\bar{\psi}_c}{d\bar{\varphi}}\right) - \lambda & -2B\dfrac{\bar{\psi}_p}{\bar{\varphi}} & 0 & 0 \\ \dfrac{\bar{\varphi}}{2B\bar{\psi}_p} & -\dfrac{\bar{\varphi}}{2B\bar{\psi}_p} - \lambda & 0 & -\dfrac{\bar{p}_p}{\rho_0}\dfrac{1}{M^2}\dfrac{\bar{\varphi}}{\bar{\psi}_p} \\ \hline 0 & 0 & -\lambda & 1 \\ 0 & 4WB^2\dfrac{\bar{\psi}_p}{\bar{\varphi}} & -\dfrac{\bar{p}_p}{\rho_0} - Q^2 & -2\zeta Q\sqrt{\dfrac{p_0\bar{p}_p}{p_p\rho_0}} - \lambda \end{array}\right] \times \begin{bmatrix} \delta\varphi_c \\ \delta\varphi_t \\ \delta\eta \\ \delta v \end{bmatrix} = \begin{bmatrix} 0 \\ 0 \\ 0 \\ 0 \end{bmatrix} \tag{14}$$

where the terms in the dotted line (2×2 matrix) represent the uncontrolled compression system and the control parameters W, ζ and Q are defined by Eqs. (16), (17), and (18), respectively.

For the active control the mathematical model is represented by the following set of equations (Giusto et al., 1997):

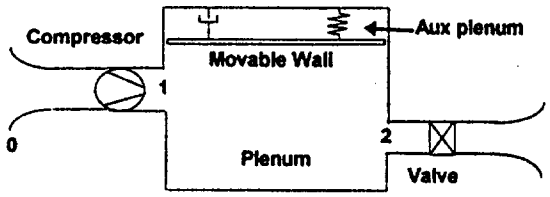

Fig. 8 Lumped parameter compression system with passive control

$$\left\{\begin{array}{l} \dfrac{d\delta\varphi_c}{d\tau} = B\left(\dfrac{d\psi_c}{d\varphi_c}\,\delta\varphi_c - \delta\psi_p\right) \\ \dfrac{d\delta\psi_p}{d\tau} = \dfrac{1}{B}\,\delta\varphi_c - \dfrac{1}{B\,\dfrac{d\psi_t}{d\varphi_t}}\,\delta\psi_p - \dfrac{2}{M^2}\dfrac{\rho_p}{\rho_0}\delta\upsilon \\ \hline \delta\upsilon = -K\delta\psi_p \end{array}\right. \tag{15}$$

where, as already stated for the passive control system, the terms included in the dotted line represent the compression system without control.

Control System Performance

The above-mentioned models were used to evaluate the effects of the active or passive control on the compression system described and tested in Part I of this work. The compressor characteristic curve was approximated by a cubic regression line based on the experimental data at 3000 rpm concerning the stable region without control. This curve was extrapolated to the normally unstable region in order to find new stable points when a control system is applied, as already discussed by Pinsley (1988).

The effect of the tailored structure–plenum wall–control on the compression system performance is shown in Fig. 10, where flow coefficient and wall displacement perturbations versus nondimensional time $\tau/2\pi$ are presented, at two different equilibrium flow rates. These results refer to the value of Greitzer's parameter B at 3000 rpm and to the optimum values of control parameters W, Q, and ζ (see next paragraph). At $\bar{\varphi} = 0.160$ the system is stable, while at $\bar{\varphi} = 0.153$ it operates in the unstable region. If passive control is introduced, the system behavior turns out to be stable under both conditions. It means that the control system, with carefully evaluated control parameters, does not negatively influence the stable point, while stabilizing performance at the previously unstable point, thanks to the suppression of surge.

A similar behavior is observed in Fig. 11 for the case of active control system. The control law used here is a simple proportional one, as suggested by Greitzer et al. (1992). The figure presents the flow rate coefficient, the pressure ratio coefficient and the wall velocity perturbations versus nondimensional time $\tau/2\pi$.

The results obtained for both control systems show that, when the active control is employed, the time needed for suppressing

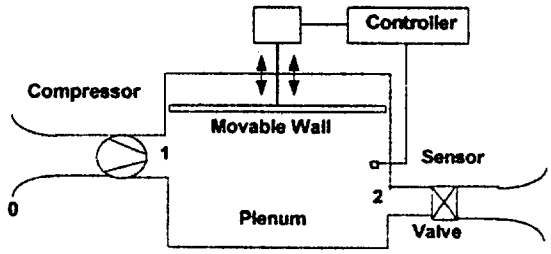

Fig. 9 Lumped parameter compression system with active control

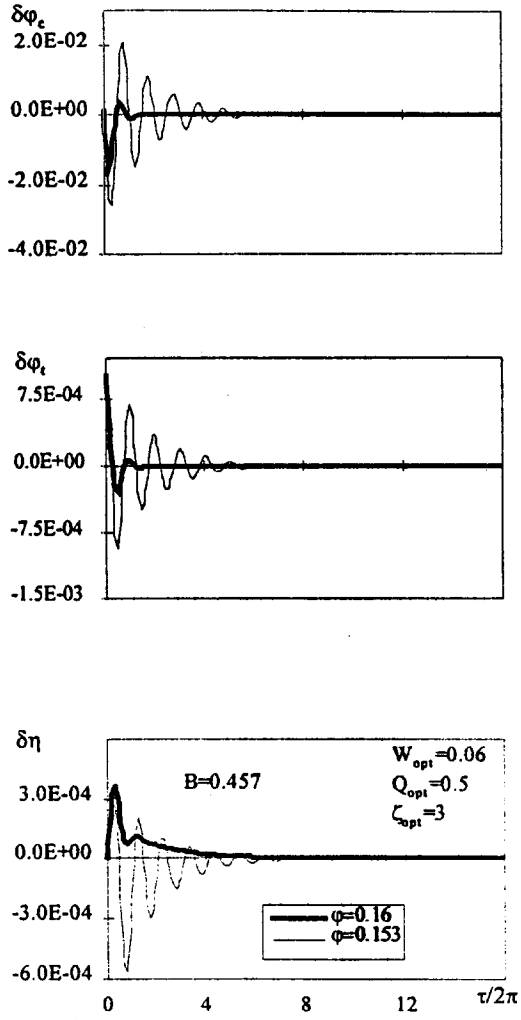

Fig. 10 Time-resolved flow rate coefficients and wall displacement perturbations when using passive control

flow rate oscillations is practically halved when compared with the passive control performance.

In the next section both control systems will be analyzed in depth, with special emphasis on the influence of the control parameters.

Parametric Analysis

Passive Control. The nondimensional control parameters concerning the movable wall in the plenum (see the stability matrix in Eq. (14)) are:

(a) aeroelastic coupling parameter

$$W = \frac{\rho_0 A_w^2 L_c^2}{m\bar{V}_p} \tag{16}$$

that determines the degree to which the wall responds to the pressure fluctuations in the plenum;

(b) critical damping ratio of the mass-spring-damper system

$$\zeta = \frac{c}{2m\omega_w}\cdot\sqrt{\frac{\bar{p}_p}{p_0}} \tag{17}$$

(c) ratio of natural frequencies of mass-spring-damper system and fixed wall compression system

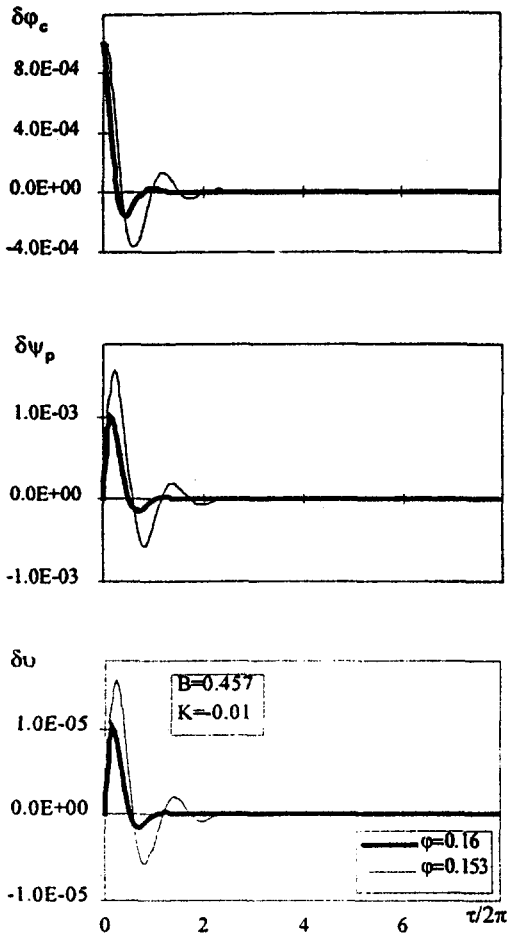

Fig. 11 Time-resolved flow rate coefficient, plenum pressure coefficient, and nondimensional wall velocity perturbations when using active control

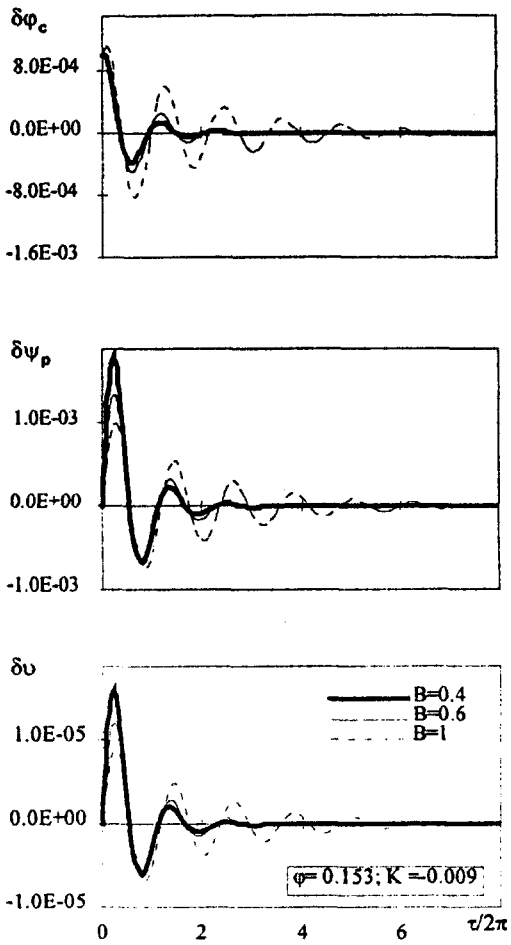

Fig. 13 Influence of B on flow coefficient, pressure coefficient, and nondimensional wall velocity perturbations when using active control

$$Q = \frac{\omega_w}{\omega_H} \cdot \sqrt{\frac{\rho_0}{\bar{p}_p}} \tag{18}$$

A parametric study was carried out, by using the code described by Giusto and Massardo (1996), in order to optimize the performance of the control system, that is, to maximize the compressor characteristic slope that allows a stable operating condition. Such an analysis showed that the movable wall performance is optimized, over the considered range of B (0.2–1.0), for the parameter values shown in Fig. 12.

If B is greater than 0.4, the control parameters are practically not influenced by the compression system geometry; in this case the optimum values of the movable wall parameters turned out to be $W = 0.06$, $Q = 0.5$, and $\zeta = 3$ and they were utilized to obtain the results shown in Fig. 10. For values of B lower than 0.4, parameter ζ shows a strong reduction while W and Q are practically constant.

It is noteworthy that, if the three control parameters are properly chosen, at high B values ($B > 0.4$) the dynamic response of the compression system is always the optimum one, even if the system geometry and/or the compressor speed are changed, provided that B remains greater than 0.4. For lower B values ($B < 0.4$), where ζ is greatly influenced by B, the optimum control system design parameters vary when changing geometry or compressor speed.

Active Control. The dynamic response of the compression system including active control was analyzed as described by Giusto et al. (1997). The influence of the most important parameters, B and K, was determined as shown in Figs. 13 and 14.

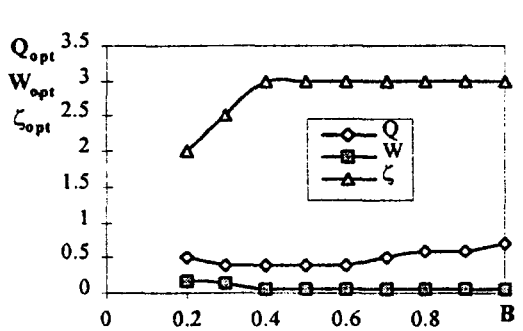

Fig. 12 Optimum values of passive control parameters

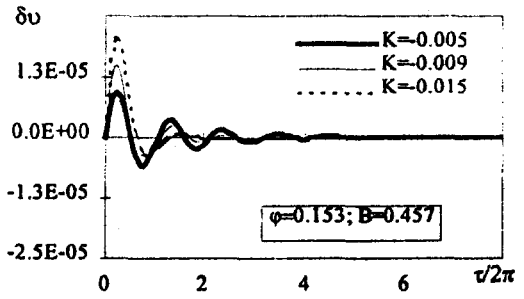

Fig. 14 Influence of K on nondimensional wall velocity perturbation

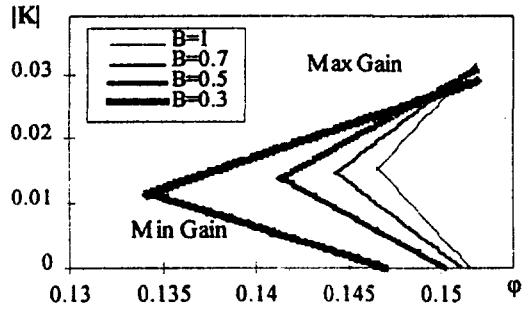

Fig. 15 Stability range of the compression system

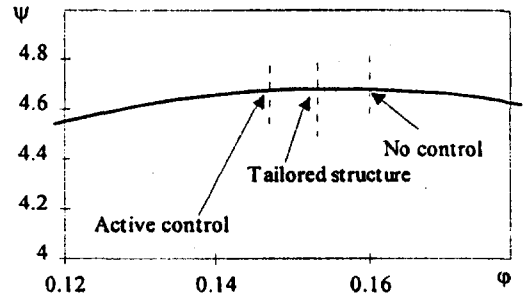

Fig. 17 Limit stable points without control, with tailored structure control, and with active control (W = 0.06; Q = 0.5; ζ = 3; K = −0.014)

In Fig. 13 the flow coefficient at the compressor exit, the plenum pressure coefficient and the nondimensional wall velocity are plotted versus nondimensional time $\tau/2\pi$. The analysis is presented for a flow coefficient value in the unstable region without control ($\bar{\varphi}$ = 0.153). The figure shows the influence of parameter B, at a fixed gain factor, the value of which, K = −0.009, was selected in order to obtain good performance within the whole considered range of B. Of course, the dynamic response is damped, but not so fast as shown in Fig. 11, where the K value was defined for the particular B value of 0.457. It can be observed that, when parameter B increases, the dynamic response of the system becomes more and more unstable and the time needed for recovering a stable operating condition increases.

As the influence of gain parameter K at a fixed B value is concerned, Fig. 14 shows, for the same $\bar{\varphi}$ value of Fig. 13, the need to choose the value of parameter K correctly (Giusto et al., 1997).

Taking into account the previous results, it is useful to plot the range of stability of the compression system in terms of gain parameter K versus flow coefficient $\bar{\varphi}$, at different values of B (Fig. 15). In this way, the simultaneous influence of the system characteristics (B and $\bar{\varphi}$) and the active control design parameter (K) can be pointed out. A limited range of K and B values exists where the system can be stabilized for a flow coefficient lower than the limit stable value without control ($\bar{\varphi}$ = 0.16); outside this field, the system cannot be stabilized in any case. It also appears that, when B increases, the controlled system is stabilized for higher flow rates, and the value of K corresponding to the minimum stable $\bar{\varphi}$ becomes practically constant (K = −0.014).

Control Systems Comparison. To obtain a better understanding of the control system performance, the maximum stable slope, $\delta\psi/\delta\varphi$, of the compressor characteristic curve is shown in Fig. 16 as a function of Greitzer's parameter B. The maximum stable slope for the compression system without control turns out to be practically zero, while the effect of both control systems under investigation is evident on the stability limit; the improvement of maximum stable slope values $\delta\psi/\delta\varphi$ is remarkable.

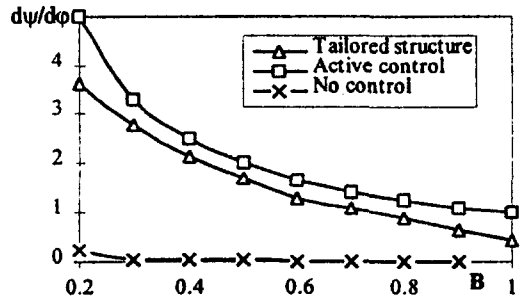

Fig. 16 Maximum stable slope when using passive or active control

As far as the influence of B is concerned, it can be observed that, when B increases, the minimum stable flow rate is closer and closer to that of the uncontrolled system, for both control techniques (mainly for passive control).

The best results were obtained when using active control, while a reduction in $\delta\psi/\delta\varphi$ of about 15 percent results for B = 0.457 if passive control is considered. Very high values of $\delta\psi/\delta\varphi$ are possible when the plenum volume is small and/or the compressor speed is low ($B < 0.4$). The results shown in Fig. 16 were obtained by using the optimum values of the control system parameters (Q, W, ζ or K) for each B value from 0.2 to 1.0.

Finally, Fig. 17 shows the limit stable points without control, with tailored structure control, and with active control, for the present compression system and B = 0.457. They were computed by using the optimum control parameter values resulting from Figs. 12 and 15.

Conclusions

A detailed study was carried out on surge behavior and on passive and active control devices in a compression system based on an industrial multistage centrifugal compressor.

The compression system without control was analyzed by means of a lumped parameter model, widely used in the literature for axial compressors and single stage centrifugal compressors. This model was validated by comparing the theoretical results with the experimental data presented in Part I of this work (Arnulfi et al., 1999).

Then, a simulation of the compression system including active or passive control devices was performed and the predicted behavior of the controlled system was presented and discussed.

In particular, the parametric analysis demonstrated the influence of the compression system geometry on the optimum values of the control parameters, and it showed that:

(*i*) if Greitzer's parameter B is high enough, the optimum values of passive control parameters do not depend on B; if B is lower, the value of the wall damping ratio parameter shows a large reduction;

(*ii*) when using the active control, a limited field of K and B values exists where the system can be stabilized; it also turns out that, when B decreases, the controlled system can be stabilized for lower flow rates;

(*iii*) the effect of both control systems on the stability limit is evident: the improvement in the maximum stable slope of the compressor characteristic curve is remarkable, especially when using active control.

In the present work, the reliability of a surge simulation model was demonstrated and interesting results were obtained by means of a theoretical analysis of the control devices. These results will be used to design control systems suitable for industrial applications, which will be tested on the experimental plant described in Part I of this work.

Acknowledgments

The authors would like to thank MURST (Italian Research Ministry) for the financial support granted to this research.

References

Arnulfi, G. L., Giannattasio, P., Giusto, C., Massardo, A. F., Micheli, D., and Pinamonti, P., 1999, "Multistage Centrifugal Compressor Surge Analysis: Part I—Experimental Investigation," ASME JOURNAL OF TURBOMACHINERY, Vol. 121, this issue, pp. 305–311.

Cinquetti, P., and Massardo, A. F., 1988, "Dynamic Behaviour Simulation of Axial Compressors" [in Italian], *43° Congresso Nazionale ATI,* Ancona (I), Vol. 2, Sept., pp. 143–156.

Emmons, H. W., Pearson, C. E., and Grant, H. P., 1955, *Trans. ASME,* Vol. 77, pp. 455–469.

Epstein, A. H., Ffowcs Williams, J. E., and Greitzer, E. M., 1989, "Active Suppression of Compressor Instabilities," *Journal of Propulsion and Power,* Vol. 5, pp. 204–211.

Ffowcs Williams, F. E., and Huang, X., 1989, "Active Stabilization of Compressor Surge," *Journal of Fluid Mechanics,* Vol. 204, pp. 245–262.

Giusto, C., and Massardo, A., 1996, "Passive Control Analysis and System Modelling of Dynamic Compressors" [in Italian], *Turbomacchine '96 Conference,* Genova (I), July, pp. 323–336.

Giusto, C., 1997, "Compressor System Control: Modelling and Experimental Analysis" [in Italian], Ph.D. Thesis, IMSE, University of Genova (I).

Giusto, C., Massardo, A., and Gandolfo, A., 1997, "Active Control Analysis and System Modelling of Dynamic Compressors" [in Italian], *52° Congresso Nazionale ATI,* Cernobbio (I), Sept., pp. 891–906.

Greitzer, E. M., 1976, "Surge and Rotating Stall in Axial Compressors. Part I: Theoretical Compression System Model. Part II: Experimental Results and Comparison With Theory," ASME *Journal of Engineering for Power,* Vol. 98, No. 2, pp. 190–217.

Greitzer, E. M., Epstein, A. H., Guenette, G. R., Gysling, D. L., Haynes, J., Hendricks, G. J., Paduano, J., Simon, J. S., and Valavani, L., 1992, "Dynamic Control of Aerodynamic Instabilities in Gas Turbine Engines," AGARD-LS-183.

Gysling, D. L., 1989, "Dynamic Control of Centrifugal Compressor Surge Using Tailored Structure," M.S., Thesis, MIT, Cambridge, MA.

Gysling, D. L., Dugundji, J., Greitzer, E. M., and Epstein, A. H., 1991, "Dynamic Control of Centrifugal Compressor Surge Using Tailored Structures," ASME JOURNAL OF TURBOMACHINERY, Vol. 113, pp. 710–722.

Huang, X. Y., 1988, "Active Control of Aerodynamics Instabilities," Ph.D. Thesis, MIT, Cambridge, MA.

Pinsley, J. E., 1988, "Active Control of Centrifugal Compressor Surge," M.S. Thesis, MIT, Cambridge, MA.

Pinsley, J. E., Guenette, G. R., Epstein, A. H., and Greitzer, E. M., 1991, "Active Stabilization of Centrifugal Compressor Surge," ASME JOURNAL OF TURBOMACHINERY, Vol. 113, pp. 723–732.

Simon, J. S., Valavani, L., Epstein, A. H., and Greitzer, E. M., 1993, "Evaluation of Approaches to Active Compressor Surge Stabilization," ASME JOURNAL OF TURBOMACHINERY, Vol. 115, pp. 57–67.

S. Damle

T. Dang

Department of Mechanical, Aerospace, and Manufacturing Engineering
Syracuse University,
Syracuse, NY 13244

J. Stringham

E. Razinsky

Solar Turbines, Inc.,
San Diego, CA 92186

Practical Use of Three-Dimensional Inverse Method for Compressor Blade Design

The practical utility of a three-dimensional inverse viscous method is demonstrated by carrying out a design modification of a first-stage rotor in an industrial compressor. In this design modification study, the goal is to improve the efficiency of the original blade while retaining its overall aerodynamic, structural, and manufacturing characteristics. By employing a simple modification to the blade pressure loading distribution (which is the prescribed flow quantity in this inverse method), the modified blade geometry is predicted to perform better than the original design over a wide range of operating points, including an improvement in choke margin.

1 Introduction

Turbomachine blade design systems usually employ a quasi-three-dimensional blade design module to generate the initial blading geometries (detailed design stage) after a mean-line performance calculation is completed (preliminary design stage). The quasi-three-dimensional blade design module typically consists of two steps: a flow-condition specification step for each blade row and a blade-geometry definition step. In the first step, a throughflow method with built-in loss correlations is used to select the radial work or flow-angle distribution (i.e., stagnation enthalpy rise or swirl) for each blade row so as to maximize the efficiency of the multistage machine. This search process is subjected to restrictions placed on the diffusion factor, blade stagger angle, surge margin, and structural integrity. The second step in the quasi-three-dimensional blade design module involves the use of families of standard profile shapes with correlated performance or quasi-three-dimensional blade-to-blade design methods (inverse or optimization techniques) to generate the blade geometries.

Although this family of quasi-three-dimensional blade design module has been a very useful design tool, it cannot accurately model many important features that are found to have profound effects on the performance of turbomachines. In particular, the highly three-dimensional and complex flowfield in the endwall regions (e.g., secondary flows and clearance effects) and three-dimensional multistage effects (e.g., in-coming streamwise vorticity and unsteady wakes) can only be modeled by quasi-three-dimensional methods through empirical correlations (e.g., losses and blockage associated with endwalls and clearances). Consequently, these quasi-three-dimensional methods are not always reliable, particularly for designs that are outside the region of validity of the correlations.

Following the current design practice closely, we have developed a full three-dimensional and viscous inverse method, which can readily be integrated into current blade design systems. In this proposed "improved" design system, we envision that the existing throughflow method would be retained to select the swirl distribution for each blade row and a "guessed" blade geometry. The proposed fully three-dimensional viscous inverse method is then employed to modify this "guessed" blade geometry to improve its aerodynamics performance. We note that the proposed three-dimensional inverse method allows for some controls over structural and manufacturing constraints.

2 Inverse Method

Existing two-dimensional and three-dimensional inverse methods are formulated with different choices of prescribed quantities. The two popular choices are (1) the pressure distributions along the blade upper- and lower-surfaces (Demeulenaere and Van den Braembussche, 1998; Giles and Drela, 1987), and (2) the blade pressure loading distribution (the difference in static pressure between the blade upper and lower surfaces), a stacking line (in the three-dimensional case), and the blade thickness distribution (Dang et al., 1997a; Novak and Haymann-Haber, 1983; Tan et al., 1984). Both approaches have advantages and disadvantages. The main issues of concern are the robustness of these formulations in three-dimensions (existence of solution for arbitrary prescribed quantities), and the compatibility of the method with existing design systems (relevance between the prescribed flow quantities and the throughflow solutions, and ease of incorporating structural requirements into the inverse method).

The primary prescribed quantities in the three-dimensional inverse method of Dang et al. (1997a) are the blade thickness distribution, the blade pressure loading distribution $\Delta p(r, z)$, and a stacking line. The computed geometric quantity is the three-dimensional blade camber surface. The design strategy employed in this inverse method is relatively compatible with many blade-generation procedures employed in industry. In many existing design systems, the blade profiles are generated using the following systematic geometric technique. The blade profile at a given spanwise station is constructed by superimposing a standard profile half-thickness shape (e.g., C4, T4, NACA 0015 base profiles) normal to and on either side of a camber line (usually a circular arc or a parabola). The camber leading- and trailing-edge angles are based on the throughflow solutions, flow-incidence selection, and blade-deviation angle correlations. These two-dimensional blade profiles are then stacked together along a predetermined stacking line (usually based on structural requirements) to form a three-dimensional blade profile.

Using the three-dimensional inverse method of Dang et al. (1997a), the designer would first select the blade thickness distributions at the computed spanwise stations and a stacking line, which is similar to the design strategy described above. Next, instead of generating the three-dimensional blade camber surface using standard camber surface shapes, the camber surface is now computed based on a prescribed blade pressure

Contributed by the International Gas Turbine Institute and presented at the 43rd International Gas Turbine and Aeroengine Congress and Exhibition, Stockholm, Sweden, June 2–5, 1998. Manuscript received by the International Gas Turbine Institute February 1998. Paper No. 98-GT-115. Associate Technical Editor: R. E. Kielb.

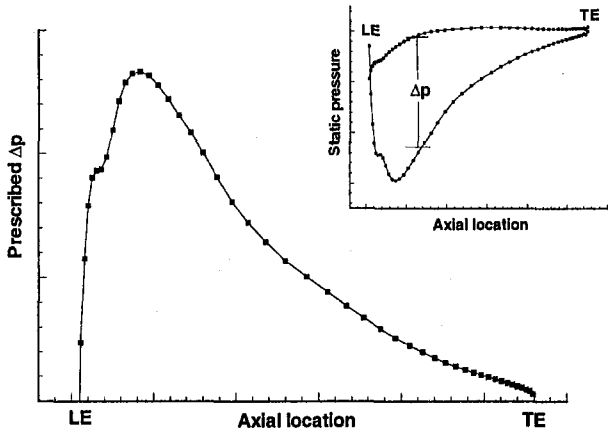

Fig. 1 Characteristics of prescribed blade pressure loading Δp

loading distribution. The shape of the prescribed blade pressure loading Δp (pressure difference between the blade pressure and suction surfaces) is characterized by the following properties (Fig. 1):

- The pressure loading must vanish at the blade leading and trailing edges.
- Flow incidence is imposed by forcing a "large" gradient in Δp near the blade leading-edge region. We note that with this three-dimensional inverse method, flow incidence is indirectly specified through the loading shape, and blade deviation angle is part of the solution.

The designer also must specify the magnitude of the prescribed Δp distribution. By considering the θ-momentum equation for a control volume coinciding with a streamtube between the blade leading and trailing edges, one can relate Δp to the tangential mass-averaged angular momentum per unit mass $r\bar{V}_\theta$ (Dang, 1995)

$$\int r\Delta p dA_\theta = \dot{m}[(r\bar{V}_\theta)_{TE} - (r\bar{V}_\theta)_{LE}] \tag{1}$$

where $\dot{m}$ is the mass flow rate within the streamtube. Consequently, the area under the $(r\Delta p)$ versus streamwise distance curve is approximately related to the local overall change in swirl across a blade row. We note that the right-hand side of Eq. (1) can be approximated using the throughflow solutions by assuming that the "blade" streamlines coincide with the meridional grid lines.

In the present three-dimensional inverse method, the equations of motion are solved using the robust finite-volume time-marching algorithm of Jameson et al. (1981). The viscous effect is modeled using the method proposed by Denton (1992) for turbulent flows. During this time-marching process, fluid is allowed to cross the blade surfaces, and a pressure-jump condition (i.e., the prescribed blade pressure loading Δp) is imposed across the blade surfaces. The flow-tangency condition along the blade surfaces is then used to calculate the correct blade geometry via an iteration process. The computer code employed in this study, called INV3D code, can run in both the "standard" analysis mode and the inverse mode. The readers are referred to the original papers and reports for the details of the method (Damle, 1998; Dang and Isgro, 1995; Dang et al., 1997a).

At the present time, we have demonstrated the use of this proposed three-dimensional inverse method to "modify" existing designs with the following strategy. First, aerodynamic improvements of the original blades are achieved by controlling the axial distributions of the blade pressure loading curves, keeping the radial distributions of flow variables (such as flow angles) at the blade inlet and outlet stations approximately the same (to retain blade-row matching in a multistage machine). The goals include: (1) reduction of adverse pressure gradients along the blade surfaces, and (2) control of the passage-shock position and strength. Second, the change in structural and manufacturing integrities of the blades are minimized by (1) keeping the blade tangential thickness distribution the same, and (2) choosing the blade stacking identical at an arbitrarily chosen axial location (so that the blade lean is not greatly modified).

In the study summarized by Dang et al. (1997b), we demonstrated the use of this inverse technique to redesign NASA Rotor 67 in the inviscid-flow limit. In this paper, we use a compressor blade designed by Solar Turbines for the DOE/ATS (Advanced Turbine Engine Systems) Program as a test case to evaluate the viscous-flow version of the INV3D code. This paper is organized as follows. In Section 3, we present the code-validation study, including a comparison of the viscous solutions predicted by the INV3D code and a Navier–Stokes code employed at Solar Turbines (Dawes, 1988). In section 4, we summarize the design modification study of this rotor using the inverse method. Finally, concluding remarks are given in section 5.

3 Code Verification

It was thought necessary first to evaluate/validate the INV3D code with an analysis code typically used by industry. Solar Turbines has come to trust the ability of their currently used Navier–Stokes analysis code developed by Dawes (1988). Thus we naturally chose the Dawes Navier–Stokes code for comparison with the INV3D.

The test case employed in this paper is the first-stage rotor of a compressor designed by Solar for the DOE/ATS program. This is a transonic rotor and so the ability of the viscous method to capture shock position and strength could be tested. The validation phase consists of two parts. First, we use only the analysis mode of the INV3D code to establish that we get the same predictions as the Dawes Navier–Stokes code. We note that the viscous method employed in the INV3D code was also checked against the Navier–Stokes code developed by Liu and Zheng (1996). In this investigation, we obtain both inviscid and viscous solutions to highlight the importance of the added viscous effect. Second, we used the pressure loadings obtained from the analysis solutions as input to the INV3D code running in the inverse mode to recover the original blade geometry.

Before we present the results from this validation study, we would like to note the differences in the two viscous codes. At this stage, the INV3D code doesn't handle tip clearance. Hence, both codes were used without tip clearance and with rotating hub and shroud. Both codes use wall functions to get the wall shear stress to avoid the use of excessively clustered meshes near solid boundaries. We also would like to note that while the Dawes Navier–Stokes code uses the Baldwin–Lomax turbulence model, the INV3D code uses a simple mixing length turbulence model similar to the method proposed by Denton (1992).

A sheared **H**-mesh with $104 \times 32 \times 32$ cells was used for all calculations. The grid has 48 cells in the axial direction between the blade leading and trailing edges, with the minimum mesh size on the order of 0.4 percent blade chord. A typical viscous calculation running in the analysis mode takes about 3 hours using a 533 MHz DEC Alpha workstation, while an inverse calculation typically takes about 30 percent more in computational time.

The viscous solutions were run with a viscosity corresponding to a Reynolds number of 0.8×10^6 (based on inlet velocity and blade chord at midspan). Both the INV3D code and the Dawes Navier–Stokes code were run at exactly the same inlet conditions and back pressure. We also ran the INV3D code in the inviscid mode at the same back pressure. The two parame-

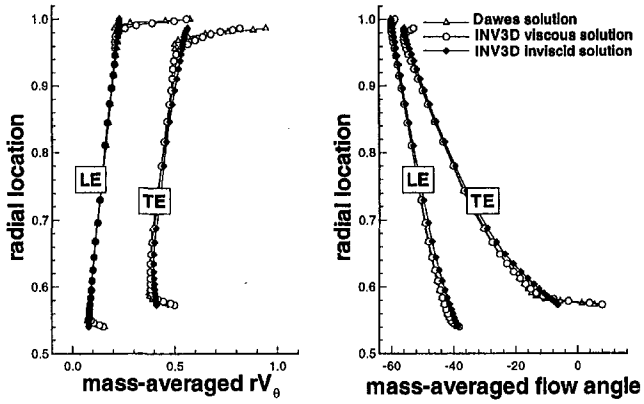

Fig. 2 Comparison of blade inlet/outlet flow distributions

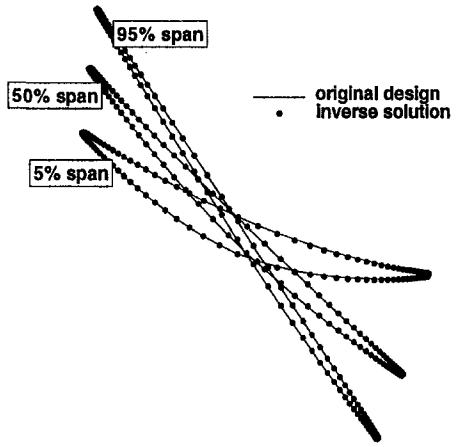

Fig. 4 Comparison of original blade geometries

ters of primary concern to the designers, the mass-averaged flow angle and the mass-averaged swirl $r\bar{V}_\theta$ (or work), were compared first. Figure 2 shows the comparison of the spanwise variation of these quantities at the leading- and trailing-edge stations. It can be seen that both the swirl and the flow angle distributions compare very well in qualitative shape as well as the actual numerical values. Thus the INV3D code did predict the same work input. It should be noted that the overturning of the flow within the boundary layers at the endwall regions were also well captured. In general the flow angles match within 1 deg in the main flow domain and within 2 deg in the boundary layers. Finally, we note that the inviscid solution matches relatively well with the viscous solutions except in the endwall regions.

Next, the surface static pressures predicted by the INV3D code are compared with those obtained using the DAWES code at the 5 and 95 percent span locations (endwall regions). Figure 3 (top curves) shows these comparisons, including the inviscid-flow solution. The figure shows that very good agreement is found between the two viscous methods. Furthermore, one can easily notice a big difference between the inviscid and the viscous solutions in the shock's position and strength. Thus, the necessity of going from inviscid to viscous calculations in the inverse method becomes evident, especially so in compressor designs in which shock waves are present and the adverse pressure gradients can cause boundary layers to grow (increasing blockage). Also shown in Fig. 3 are the resulting blade pressure loading distributions Δp (bottom curves). It is interesting to note that the areas under the pressure loading curves are nearly the same for the viscous and inviscid solutions, which is consistent with the agreements in the spanwise distributions of mass-averaged swirl $r\bar{V}_\theta$ shown in Fig. 2.

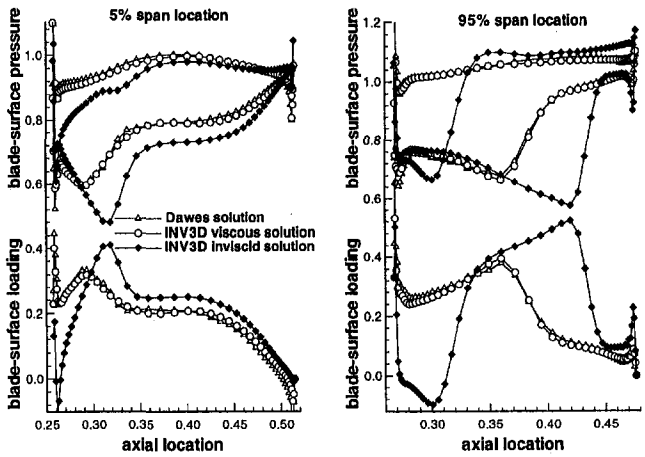

Fig. 3 Comparison of blade surface pressure distributions

The inverse mode of the INV3D code was tested next. The blade pressure loadings obtained from the analysis solution were input to the inverse mode, along with the thickness distribution and a stacking line. In this study, the coordinates of the original blade geometry at the leading edge are used as the prescribed stacking line to the inverse calculation. The blade geometry recovered by the INV3D code running in the inverse mode is shown in Fig. 4 (solid circle symbols) against the actual geometry of the original blade (solid line). It can be seen from this figure that the INV3D code reproduces the blade profile accurately. The flow solutions are also found to match exactly with the analysis and are not shown here for brevity.

4 Redesign of Rotor Blade

Next, we present a design modification study for this compressor rotor. The goal is to improve the efficiency of the blades while retaining the overall aerodynamic and structural/manufacturing characteristics of the blades. Specifically, to preserve the aerodynamic characteristics, we attempt to keep the work input to the modified rotor blade (as characterized by the radial distributions of $r\bar{V}_\theta$ at the blade leading- and trailing-edge locations) the same as the original design by applying Eq. (1) along the meridional grid lines. To minimize the change in the structural and manufacturing characteristics of the rotor, the blade tangential thickness distribution of the modified design is kept the same as the original design, and we arbitrarily choose the coordinates of the original blade geometry at the leading edge as the prescribed blade stacking line (the wrap angle at the leading edge for the two designs are identical). We note that the blade redesign study is carried out at the same back pressure as the analysis calculations for the original blade, resulting in a small difference in mass flow rate.

The blade-surface pressure distributions and the blade pressure loading distributions corresponding to the original blade design are summarized in Fig. 5 (hollow circle symbols) at four selected spanwise locations (5, 30, 70, and 95 percent span locations). We note that the incoming relative Mach number varies from 0.6 at the hub to 1.2 at the tip, corresponding to subsonic flow at the 5 and 30 percent span locations, and supersonic flow at the 70 and 95 percent span locations.

For the original design, examination of the blade-surface pressure distributions indicates that aerodynamic improvements can be made in the following areas:

- It is desirable to remove the suction peaks at the blade leading edge along the entire span. We note that these suction peaks also appear in the pressure loading curves.

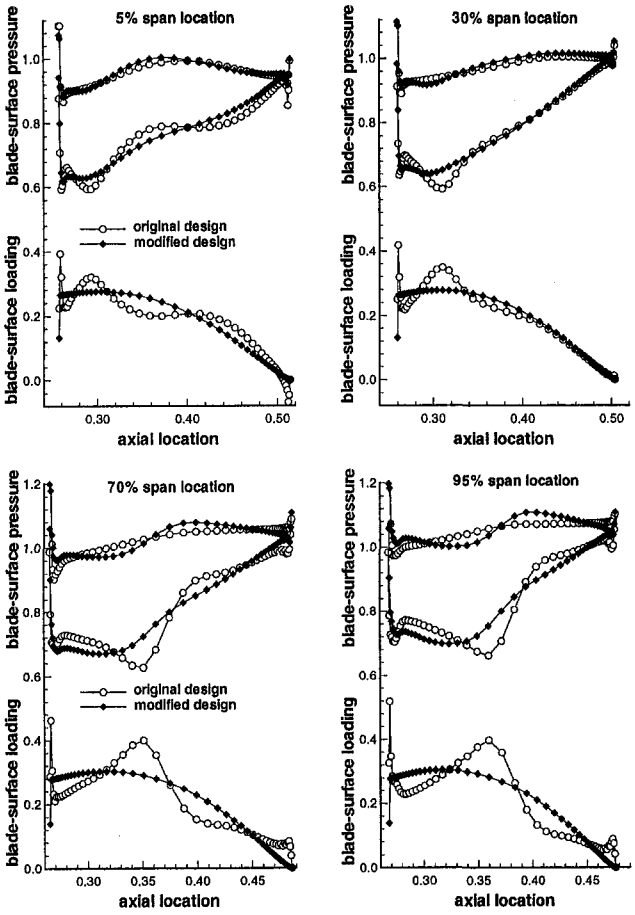

Fig. 5 Comparison of blade surface pressure distributions

- Near the hub region (5 and 30 percent span locations), the behavior of the pressure gradient in the first 30 percent chord could be improved. The figure shows the presence of a flow acceleration in the first 15 percent chord followed by a steep decceleration in the next 15 percent chord. We observe that these undesirable features in the blade-surface pressure distributions appear in the blade pressure loading distributions as "waviness."
- It is desirable to remove or weaken the shock waves appearing in the supersonic region (70 and 95 percent span locations). Here, we note that the shock waves seen in the blade-surface pressure distributions appear in the blade pressure loading as "discontinuities."

As a first attempt, it was thought that "smoothing" of the blade pressure loading would achieve the improvements mentioned above. This strategy was employed in the design modification study of Rotor 67 with excellent results (Dang et al., 1997b). Shown in Fig. 5 are the prescribed blade pressure loadings for the modified design (solid diamond symbols). We note that the prescribed blade pressure loadings of the modified design are roughly of the "quarter-cosine" type typically employed in throughflow codes (we note that the present method can handle arbitrary loading curves). They differ from those corresponding to the original blade design in the following ways. First, the suction peaks at the blade leading edge are removed. Second, the "waviness" characteristics in the first 30 percent chord in the subsonic section are replaced by a smooth distribution. Third, the discontinuities in the supersonic section corresponding to the shock locations are removed. Using the pressure loading distributions shown in Fig. 5, along with the blade thickness distribution and the blade stacking coordinates

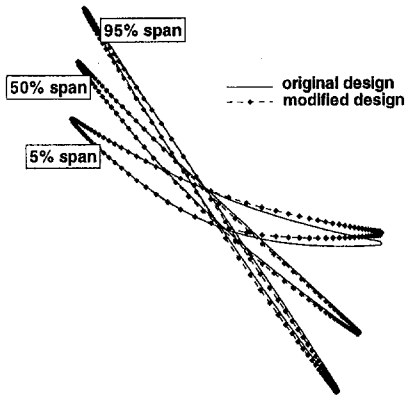

Fig. 6 Comparison of blade geometries

at the leading edge of the original blade design, the INV3D code running in the inverse mode produces the modified blade geometry shown in Fig. 6 (dashed line with solid diamond symbols). Also shown in the same figure is the geometry of the original blade (solid line). This figure indicates that the two geometries are not very much different, with the most noticeable differences in the two blade geometries found in the hub region, suggesting that the modified blade design would not affect the structural and manufacturing constraints (this needs to be verified using a structural analysis code, of course).

Shown in Fig. 5 are the blade-surface pressure distributions corresponding to the modified blade design (solid diamond symbol). At the 5 and 30 percent span locations, the figure clearly shows that the pressure distributions along the suction surface are improved. First, the suction peaks near the leading edge are removed. Second, the adverse pressure gradient on the suction surface in the first 30 percent chord are "milder" in the modified design. Near the tip region where the flow is supersonic (70 and 95 percent span locations), the figure shows that the shock waves on the suction surface are weakened dramatically in the modified blade, although the static pressure along the pressure surface is slightly worsened (this can possibly be improved by modifying the blade thickness distribution, which will be investigated in future work). Figure 7 shows comparisons of the static pressure contour between the original design and the modified design at the 95 percent span location. The figure shows the presence of a strong passage shock in both the original and modified designs. However, the figure shows that the passage shock weakens considerably as it impinges on the suction surface of the modified blade. A careful examination of

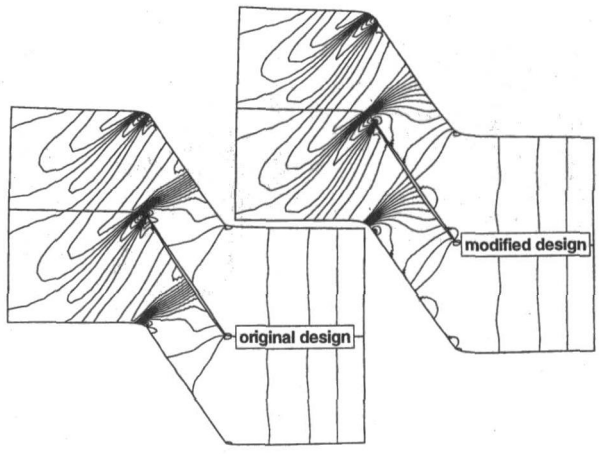

Fig. 7 Comparison of static pressure contour at 95 percent span location

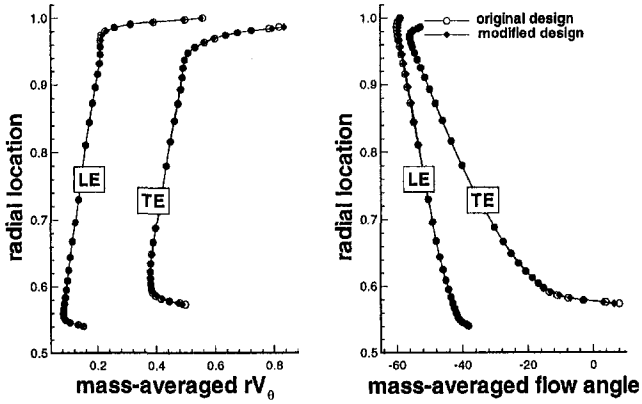

Fig. 8 Comparison of blade inlet/outlet flow distributions

the two blade geometries shown in Fig. 6 reveals that the presence of a slight reverse camber near the tip region in the modified design is responsible for this effect (Prince, 1980).

Figure 8 shows comparisons of the calculated spanwise distributions of mass-averaged $r\bar{V}_\theta$ and flow angle at the blade leading and trailing edges between the original blade design (hollow symbol) and the modified design (solid symbol). The figure clearly shows that application of Eq. (1) does result in the preservation of the work input to the rotor (although the overall mass-averaged values are slightly different). Also shown in this figure are the radial distributions of relative flow angle at the blade leading- and trailing-edge locations. The plot shows that the blade inflow and outflow angles are nearly unchanged, indicating that the modified design does not present matching problem with the neighboring blade rows.

Finally, a study is carried out to evaluate the performance of the modified blade at the off-design points. Figure 9 shows the comparisons of the compressor performance map between the original design and the modified design. The design mass flow rate relative to the flow range is indicated in the figure. These calculations, carried out using the INV3D code running in the viscous analysis mode, show that the two designs produce roughly the same pressure rise over the indicated flow range, with an improvement in adiabatic efficiency of nearly 1 percent. Moreover, the figure shows that the choke margin is improved in the modified design.

5 Conclusions

This paper summarizes our progress with a full three-dimensional viscous inverse method for turbomachine blade design. In the present inverse technique, the primary prescribed quantities are (1) the blade tangential thickness distribution, (2) the pressure loading distribution across the blade surfaces (the difference in static pressure across the blade surfaces), and (3) a blade stacking condition. The calculated quantity is the blade mean camber surface. The primary improvement of the present inverse method over existing inverse methods is that the flowfield is treated as fully three dimensional and viscous.

In this paper, we have demonstrated the use of this three-dimensional inverse method to refine an existing blade design, which is typical of compressor blades in industrial gas turbines. The blade considered is the first-stage rotor blade designed by Solar Turbines for the DOE/ATS program. By performing a very simple modification to the blade pressure loading distribution (i.e., "smoothing" it), while keeping the blade thickness distribution and the stacking coordinates (arbitrarily chosen at the leading edge) unchanged to preserve structural and manufacturing constraints, a modified blade geometry having better performance than the original blade design over a wide range of operating points was obtained. For the design example discussed in this paper, only one inverse calculation using the modified blade pressure loading shown in Fig. 5 was necessary to improve the blade design.

Currently, we are working on adding new capabilities into the three-dimensional inverse code to render it a more practical design tool. The improved three-dimensional viscous inverse method would include the following added capabilities: (1) tip-clearance effects, (2) inclusion of splitter blades, (3) a multistage capability similar to the APNASA code (Adamczyk et al., 1990), and (4) endwall flowpath cavities.

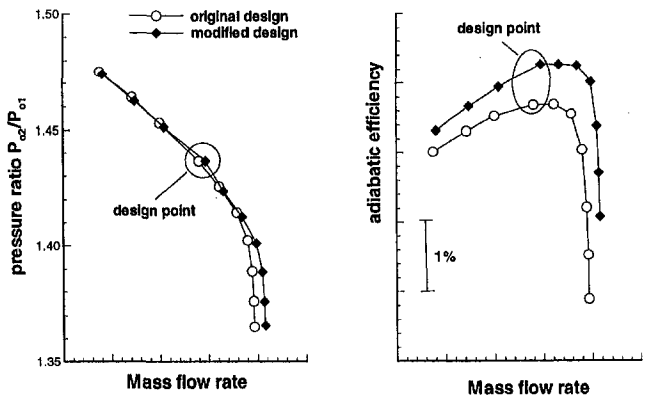

Fig. 9 Compressor performance map

Acknowledgments

This work is supported by DOE under the AGTSR program (Dr. Dan Fant, technical monitor). Technical assistance from T. C. Prince at Solar Turbines is acknowledged. The authors would like to thank Solar Turbines for providing internships to Mr. Sachin Damle during the summers of 1996 and 1997.

References

Adamczyk, J. J., Celestina, M. L., Beach, T. A., and Barnett, M., 1990, "Simulation of Three-Dimensional Viscous Flow Within a Multistage Turbine," ASME JOURNAL OF TURBOMACHINERY, Vol. 112, pp. 370–376.

Damle, S. V., 1998, "Fully Three-Dimensional and Viscous Inverse Method for Turbomachine Blade Design," Ph.D. dissertation, Department of Mechanical Engineering, Syracuse University.

Dang, T. Q., 1995, "Inverse Method for Turbomachine Blades Using Shock-Capturing Techniques," AIAA Paper No. 95-2465.

Dang, T., and Isgro, V., 1995, "Euler-Based Inverse Method for Turbomachine Blades: Part I—Two Dimensional Cascades," *AIAA Journal,* Vol. 33, No. 12.

Dang, T., Damle, S., and Qiu, X., 1997a, "Euler-Based Inverse Method for Turbomachine Blades: Part II—Three Dimensional Flows," submitted to *AIAA Journal.*

Dang, T., Nerurkar, A. C., and Reddy, D. R., 1997b, "Design Modification of Rotor 67 by 3D Inverse Method—Inviscid Flow Limit," ASME Paper No. 97-GT-484.

Dawes, W. N., 1988, "Development of a 3D Navier–Stokes Solver for Application to All Types of Turbomachinery," ASME Paper No. 86-GT-144.

Demeulenaere, A., and Van den Braembussche, R., 1998, "Three-Dimensional Inverse Method for Turbomachinery Blading Design," ASME JOURNAL OF TURBOMACHINERY, Vol. 120, pp. 247–255.

Denton, J. D., 1992, "The Calculation of Three-Dimensional Viscous Flow Through Multistage Turbomachines," ASME JOURNAL OF TURBOMACHINERY, Vol. 114, pp. 18–26.

Giles, M. B., and Drela, M., 1987, "Two-Dimensional Transonic Aerodynamic Design Method," *AIAA Journal,* Vol. 25, pp. 1199–1205.

Jameson, A., Schmidt, W., and Turkel, E., 1981, "Numerical Solution of the Euler Equations by Finite Volume Methods Using Runge–Kutta Time-Stepping Schemes," AIAA Paper No. 81-1259.

Liu, F., and Zheng, X., 1996, "A Strongly-Coupled Time-Marching Method for Solving the Navier–Stokes and $k-\omega$ Turbulence Model Equations With Multigrid," *Journal of Computational Physics,* Vol. 128, pp. 289–300.

Novak, R. A., and Haymann-Haber, X. X., 1983, "A Mixed-Flow Cascade Passage Design Procedure Based on a Power Series Expansion," ASME *Journal of Engineering for Gas Turbines and Power,* Vol. 105, pp. 231–242.

Prince, D. C., 1980, "Three-Dimensional Shock Structures for Transonic/Supersonic Compressor Rotors," *Journal of Aircraft,* Vol. 17, pp. 28–37.

Tan, C. S., Hawthorne, W. R., McCune, J. E., and Wang, C., 1984, "Theory of Blade Design for Large Deflections: Part II—Annular Cascades," ASME *Journal of Engineering for Gas Turbines and Power,* Vol. 106, pp. 354–365.

Turbomachinery Blade Design Using a Navier–Stokes Solver and Artificial Neural Network

S. Pierret

R. A. Van den Braembussche

Turbomachinery Department,
von Karman Institute for Fluid Dynamics,
Rhode-Saint-Genèse, Belgium

This paper describes a knowledge-based method for the automatic design of more efficient turbine blades. An Artificial Neural Network (ANN) is used to construct an approximate model (response surface) using a database containing Navier–Stokes solutions for all previous designs. This approximate model is used for the optimization, by means of Simulated Annealing (SA), of the blade geometry, which is then analyzed by a Navier–Stokes solver. This procedure results in a considerable speed-up of the design process by reducing both the interventions of the operator and the computational effort. It is also shown how such a method allows the design of more efficient blades while satisfying both the aerodynamic and mechanical constraints. The method has been applied to different types of two-dimensional turbine blades, of which three examples are presented in this paper.

Introduction

The main goal when designing turbines or compressors is to achieve light, compact, and highly efficient systems while reducing the cost and the duration of the design cycle in order to allow a rapid adaptation of the machines to the changing demands of the market.

The need to improve further the machine performance requires the use of three-dimensional Navier–Stokes solvers during the design process. These solvers, however, do not indicate what geometry modifications are required to improve the blade performance. The search for optimized blades must therefore be guided either by an experienced designer or by a numerical method. This often requires a large number of Navier–Stokes computations, to evaluate many different blade geometries, before reaching a good solution satisfying both the aerodynamic and the mechanical requirements. Although this procedure allows the design of very efficient blades, it is expensive in terms of computational and/or operator time. In order to keep the cost and the duration of the design process within reasonable limits, the design process must often be stopped as soon as an acceptable solution has been found without guarantee that it is also the optimum.

It is therefore important to reduce the number of Navier–Stokes computations needed to reach the optimum design. One way to speed up the design procedure is to use experience gained during previous designs for subsequent ones. However, the experienced designer may not always be available and/or may only have experience in a small number of turbine blade types.

The main objectives when developing the present method were: to guarantee optimum performance, to minimize the design time as well as the number of interventions of the designer, and to have an evolutionary method able to use knowledge acquired during previous designs.

This paper describes the design method for two-dimensional blade sections.

Description of the Two-Dimensional Design Method

The basic idea of the present method, of which a flow chart is shown in Fig. 1, is to accelerate the design of new blades using the knowledge acquired during previous designs of similar blades. The core of this knowledge-based design system is therefore a database containing the input and output of all previous Navier–Stokes solutions, i.e., the blade geometry ($\vec{G}$), the flow field boundary conditions (BC), and the blade performance ($\vec{P}$) characterized by the efficiency, the turning and the Mach number distribution on the suction and pressure sides.

Before starting the design of a new blade one has to specify the required performances (aerodynamic and mechanical), namely: inlet and outlet flow angles (β_1, β_2), the pressure ratio (P_2/P_{01}), the Reynolds number to axial chord ratio (Re/Cax), the blade cross-sectional area (Area), the trailing edge radius (R_{te}), the moments of inertia ($I_{\min}$ and $I_{\max}$) and the angle between $I_{\max}$ and the axial direction (alpha), etc.

The first step of the design consists of proposing a new optimized geometry that will have to be analyzed by the Navier–Stokes solver. One starts by scanning the database to select the sample that has a performance that is the closest to the required one. This geometry is then adapted, by means of an optimization procedure, to satisfy the required performance better. The last one uses a heuristic search procedure, called "simulated annealing," and an approximate model for the performance evaluation of the modified blade geometries. The approximate model used for this purpose is derived from the information contained in the database by means of an Artificial Neural Network (ANN). The latter is an interpolator, which builds the response surface by learning the relation between performance, boundary conditions, and geometry:

$$\vec{P} = \mathcal{N}(\vec{BC}, \vec{G}) \tag{1}$$

After mapping the database samples, the ANN is able to generalize, meaning that it can predict the performance of a new geometry, not present in the database.

During the second step, the new geometry, provided by the optimization, is evaluated by means of a Navier–Stokes solver.

After the Navier–Stokes calculation, the geometric parameters, the performance, and the boundary conditions of this new sample are added to the database.

Finally, if the target performance has not been reached, a new iteration is started. Each new blade definition however has to be preceded by the learning of the ANN using the new database. This one now contains a new geometry, closer to the requirements, which allows an improvement of the relationship $\mathcal{N}$.

Contributed by the International Gas Turbine Institute and presented at the 43rd International Gas Turbine and Aeroengine Congress and Exhibition, Stockholm, Sweden, June 2–5, 1998. Manuscript received by the International Gas Turbine Institute February 1998. Paper No. 98-GT-4. Associate Technical Editor: R. E. Kielb.

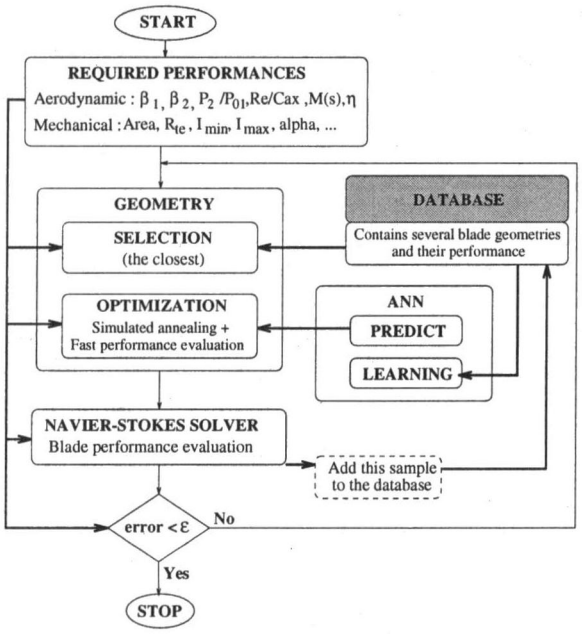

Fig. 1 General algorithm of the method

As the time for ANN learning is proportional to the number of training samples, it is sometimes of interest to build a sub-database (training database) containing only blade samples that are similar to the blade being designed. This "training database" is then used for the learning of the ANN.

The main components of this procedure will be discussed in more detail in the next sections.

The Two-Dimensional Navier–Stokes Solver (TRAF2D)

The Navier–Stokes solver used to predict the performance is the TRAF2D/3D solver developed by Arnone and Benvenuti (1994). The Reynolds-averaged Navier–Stokes equations are solved using finite volumes and a Runge–Kutta time integration scheme in conjunction with accelerating techniques such as local time stepping, residual smoothing, and Full-Approximation-Storage (FAS) multigrid. Two-dimensional computations are usually performed with 12,000 points requiring a memory of 3 MB and 6 minutes of computational time on an Alpha workstation (type 500/333).

Geometry Model

The blade is defined by a series of Bézier curves (Farin, 1993) connected into a closed contour in such a way as to ensure continuity at junction points.

A Bézier curve is specified by the coordinates of a series of points in space of which only the first and last lie on the curve they define. These points are known as the polygon points (or control points) of the curve, and the polyline constructed by connecting these polygon points with straight lines is known as the Bézier polygon of the curve. Bézier curves have three important properties: the degree of a Bézier curve, n, equals the number of polygon points -1, the tangents at the two end points are defined by the first and the last polygon lines, and the curvature radius at end points depends only on the position of the first three polygon points.

Bézier curves have been chosen because the poly-line formed by the polygon points mimics the Bézier curve and therefore allow an easy control of the curve. Although inflection points can occur with Bézier curves, they are far less frequent than with polynomials or other analytical functions.

One has preferred to use a series of Bézier curves (composite curves) instead of a single one because composite curves allow imposing the location, the tangent, and the curvature at key points on the blade surface, such as trailing edge location and the point on the suction side defining the throat. However, a special treatment at junction points is required to ensure the continuity, up to at least the second derivative. Although strict continuity of the third derivative is not necessary, the geometric model should, nevertheless, prevent large discontinuities in the slope of the curvature radius, which are often responsible for velocity peaks on the blade surface. The use of composite curves facilitates the geometric interpretation of the parameters defining the curve, allowing a better control of the geometry in order to avoid the generation of unrealistic blades.

This type of representation has been preferred to a point by point definition for three reasons: It ensures a very good continuity of the blade surface, the number of variables in the relation (1) is limited, and the parameters defining the geometry have a physical meaning that facilitates imposing limitations on their variations and therefore allows restricting the design space.

Parametric Blade Definition. Several models have been evaluated. The one presented hereafter turns out to be the one whose parameters have the best geometric interpretation avoiding the generation of unrealistic blades while having enough geometric flexibility to represent a large number of blade types. Moreover the velocity distributions obtained with this model are very smooth.

The blade geometry is specified by four key points linked by four curves. The four key points are fully defined by the following parameters: R_{te}, $\tilde{\beta}_2$, $\Delta\alpha$, δ_{te}, t, ϵ, Cax, λ (see Fig. 2). The key points 1 and 2 are linked by a Bézier curve defined by three additional polygon points whose location is function of: $\beta_{1\,\text{blade}}$, R_{le}, L_4, α_{ss}, L_1, and the tangent at point 2 (see Fig. 3). The key points 2 and 3 are linked using a Bézier curve defined by two additional polygon points. The last ones are located in such a way as to ensure the continuity up to the third derivative at

Nomenclature

alpha = angle between $I_{\min}$ and X
a, d = neural network calculated and imposed output
Cax = blade axial chord
Cp, Cv = specific heat coefficient
E = output error
F = transfer function
$I_{\min}$, $I_{\max}$ = minimum and maximum momentum of inertia of blade section
n = degree of a Bézier curve
NB = number of blades per row
P = static pressure
Re = Reynolds number = $\rho C_{ax}\sqrt{RT_{01}}/\mu_{01}$
t = pitch
W = connection weight
X, Y = abscissa and ordinate
β = relative flow angle
γ = learning rate
κ = momentum coefficient
ξ = loss coefficient
$\mathcal{N}$ = neural network relation
$\beta 1_{\text{blade}}$, λ, ϵ, $\tilde{\beta}2$, $\Delta\alpha$, δ_{te}, R_{te}, R_{te}, $L1$, $L3$, $L4$, α_{ss}, α_{ps} = blade parameters (see Figs. 3 and 4)

Subscripts

0 = stagnation conditions
1 = inlet of computational domain
2 = outlet of computational domain

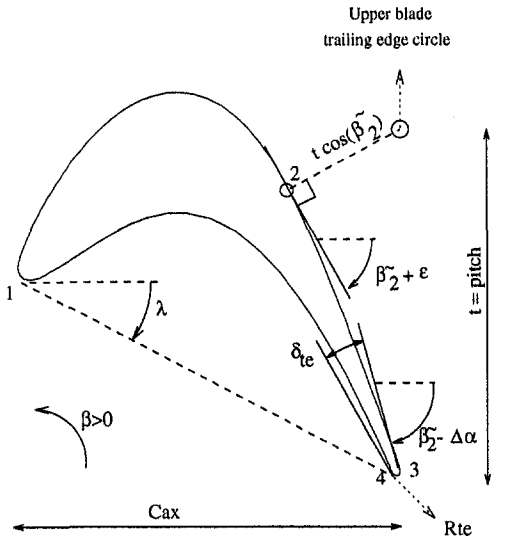

Fig. 2 Geometry model: basic parameters

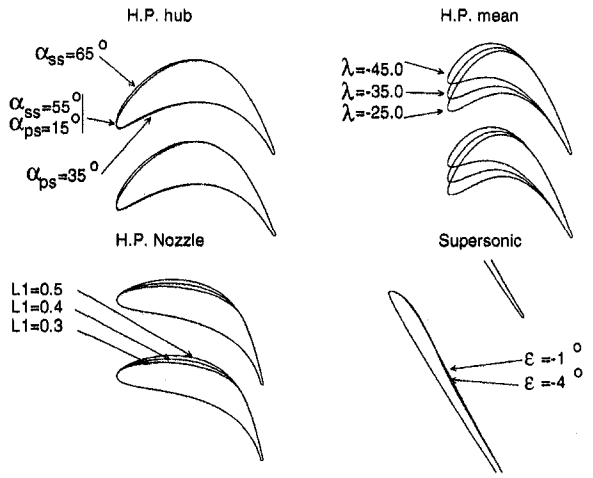

Fig. 4 Typical turbine blade geometries

point 2 and continuity up to the first derivative at point 3. A Bézier curve with three additional polygon points is used to define the pressure side in the same way as the first part of the suction side. This curve is fully defined by the parameters: $\beta_{1\,\text{blade}}$, R_{le}, L_4, α_{ps}, L_3, and the tangent at point 5. Using R_{le} and L_4 for both the suction and the pressure side guarantees the continuity of the curvature radius at the leading edge. The trailing edge is defined by a part of a circle whose radius R_{te} is specified. The two-dimensional blade geometry is thus fully defined by means of 15 parameters represented by $\vec{G}(n)$: $n = 1, 15$.

Examples. Figure 4 shows four types of turbine blade generated with this geometry model. For each blade, one parameter is changed and its influence on the blade shape is shown. This figure demonstrates that the method is capable of representing the various types of turbine blades encountered in industrial designs.

Artificial Neural Network

ANN are nonlinear models that can be trained to map functions with multiple inputs/outputs (Cichocki and Unbehauen, 1994). Although the initial goal of artificial neural network is to imitate some brain functions, they can also be thought of as a very powerful interpolator.

The goal when using ANN is to construct an approximation of (1) using the information contained in the database. An ANN (Fig. 5) is used here to relate performance (η, β_2, and the Mach number distribution given in 20 points on both blade sides ($\vec{M}(m)$: $m = 1, 40$)) to the geometric parameters and the aerodynamic boundary conditions. An ANN is composed of several elementary processing units called neurons or nodes. These nodes are organized in layers and joined with connections (synapses) of different intensity, called the connection weight (W) to form a parallel architecture. Each node performs two operations: The first is the summation of all the incoming signals and the second is the transformation of the signal by using a transfer function, very often defined by a sigmoidal function: $F(x) = 1/(1 + e^{(-x)})$. This function introduces power series (given implicitly in the form of an exponential term), which avoids making any hypotheses concerning the type of relationship between the input and the output variables. A network is generally composed of several layers: an input layer, zero, one or several hidden layers, and one output layer.

Trained ANN are able to generalize, which means that they give reasonable answers for input vectors that they have never seen. It is therefore possible to train an ANN on a representative set of input/output vectors without training the system on all possible cases.

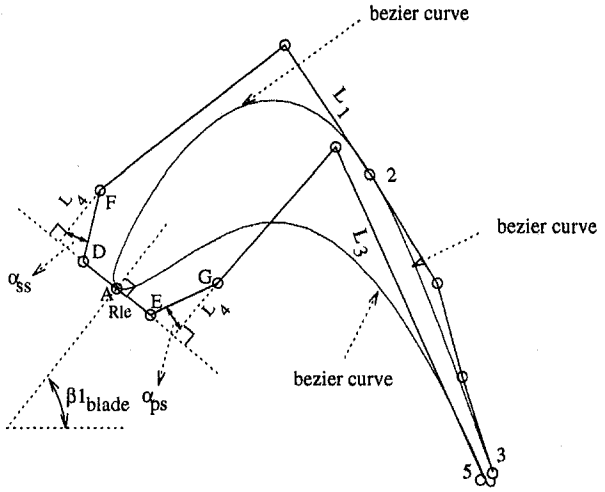

Fig. 3 Geometry model: Bézier curves

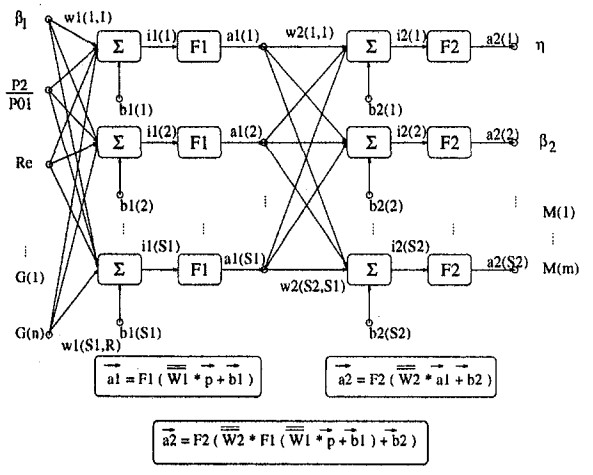

Fig. 5 A three-layer artificial neural network

Training by Back-Propagation of Errors. The learning process consists of adjusting the connection weights and the bias in order to make the calculated output vector ($\vec{a}$) coincide with the imposed output vector ($\vec{d}$).

When a vector is presented at the network input, the signal is propagated to the output layer. Generally, the output vector provided by the network does not correspond to the imposed output vector associated with the input vector.

The error (E) is defined by the summation of the square of the errors on each output node:

$$E = \frac{1}{2} \sum_{i=1}^{m+2} (d_i - a_i)^2 \quad (2)$$

This error is minimized by back-propagating the error to the network input. The back-propagation algorithm consists of finding better weight factors using the error (E) by adjusting each weight of the network proportionally and in the direction opposite to the error gradient with respect to this weight:

$$\Delta w_{ij} = -\gamma \frac{\partial E}{\partial w_{ij}}$$

where γ is a constant called the "learning rate," i is the node number, and j is the layer number.

To perform the learning process, a set of input/output vectors (training samples) must be available (database) that the network will learn to predict. All the training samples are presented sequentially until convergence of the error.

Speeding Up the Back-Propagation Learning Algorithm. The standard back-propagation training is characterized by a slow convergence. Numerous improvements of the standard back-propagation algorithm have been proposed in the literature and two of them are used here.

The first consists of modifying the weights, not only proportionally to the gradient of the error, but also proportionally to the change of weight of the previous iteration ($t-1$): $\kappa \Delta w^{t-1}$, where the momentum coefficient κ takes a value in the range [0, 1]. The purpose of this is to give the weight update a memory of its last update, providing a smoothing of the forces affecting the weight changes.

The second technique consists of adjusting the learning coefficient (γ), during the process of convergence, to fit the local shape of the error function better. The basic philosophy of learning rate adaptation is the following: If the gradient component has the same sign in two consecutive steps ($t-1$, t), the corresponding rate is increased and, if the gradient component alternates, the learning rate is decreased. One of the simplest and most efficient algorithms with locally adaptive learning rates has been proposed by Silva and Almeida (reported by Cichocki and Unbehauen, 1994). The algorithm employs batch back-propagation with momentum (κ):

$$\Delta w_{ij}^{(t)} = \gamma_{ij}^{(t)} \left(\frac{\partial E}{\partial w_{ij}} + \kappa \Delta w_{ij}^{(t-1)} \right)$$

Objective Function

A measure of the global performance of a blade geometry, with respect to the requirements, is needed at several steps in the design procedure: for the blade selection from the database, during the optimization process, and for the convergence check after the Navier–Stokes calculation.

Efficiency is only one of the many considerations among the design objectives. In addition, the mechanical constraints and the imposed outlet flow angle must also be satisfied. The general approach to this problem is to build an objective function (OF), which is the summation of penalty terms, in order to limit the violations of the constraints (Vanderplaats, 1984).

The introduction of an additional penalty term, based on the Mach number distribution, is justified by the three following arguments:

- The losses may have multiple local minima (several blades may have nearly the same losses) as well as large gradients (mainly occurring when the boundary layer transition suddenly jumps from near leading edge to near trailing edge).
- Blades are also supposed to perform well at off-design conditions. It is therefore important to introduce into the design some constraints on the Mach number distribution that ensure good performance of the blade over a wide range of operating conditions.
- Current Navier–Stokes solvers have some uncertainty in predicting the loss coefficient (mainly due to the uncertainties in turbulence and transition modeling).

The penalty on the velocity distribution is derived from the Mach number distribution in a limited number of points on the blade surface ($\vec{M}(m)$, $m = 1, 40$). The criteria on the Mach number distribution are then applied on the distribution, reconstructed using a cubic spline passing through these points. A high penalty is given to velocity distributions that are known not to be optimal.

There are four penalty terms on the Mach number distribution:

- Penalty if a minimum slope of the Mach number distribution on the suction side between the stagnation point and the throat point (point 2) is not reached.
- Penalty on the maximum Mach number on the suction side.
- Penalty based on the Pohlhausen parameter along the suction side in order to stay away from separation. (This type of penalty is very important in design because of the uncertainties in predicting separation with existing turbulence models.)
- Penalty based on the slope of the Mach number on the pressure side.

Finally the objective function is written as:

$$OF = P_{\text{Meca}} + P_{RP} + P_{\xi} + P_{\text{Mach}} = OF(\vec{P}, \vec{G}, \vec{BC}) \quad (3)$$

where P_{Meca} stands for the penalties on the mechanical constraints, P_{RP} stands for the penalties on the required performance, P_{ξ} stands for the penalties on the loss coefficient, and P_{Mach} stands for the penalties on the Mach number distribution.

It is also possible to use this method for the design of blades with an imposed Mach number distribution by adding, to the

Table 1 Mechanical and aerodynamic requirements

	Imposed	After 4 modif.
Inlet flow angle (β_1)	0.0^0	-
P_2/P_{01}	0.6629	-
Re/Cax (1/m)	$9.3\ 10^7$	-
$k = Cp/Cv$	1.287	-
Cax (m)	0.07615	-
NB (number of blades)	60	-
Blade radial location (m)	0.7781	-
Trailing edge radius (m)	$2.0\ 10^{-4}$	-
Area (m^2)	$1.73\ 10^{-4}$	$1.67\ 10^{-4}$
I_{min} (m^4)	$9.20\ 10^{-9}$	$8.74\ 10^{-9}$
I_{max} (m^4)	$1.07\ 10^{-8}$	$1.03\ 10^{-8}$
alpha	45.0^0	48^0
Outlet flow angle (β_2)	-73.4^0	-73.2^0
Loss coefficient (ξ)	0.0 %	1.54 %

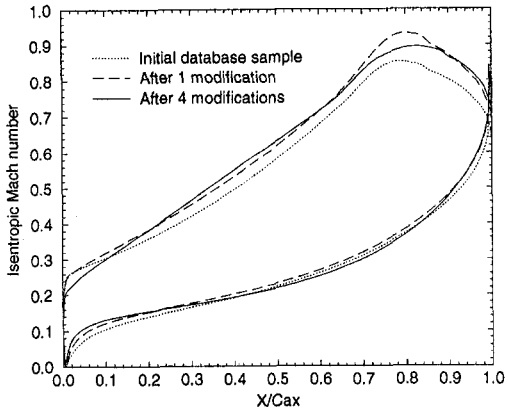

Fig. 6 Mach number distributions on the blade surface

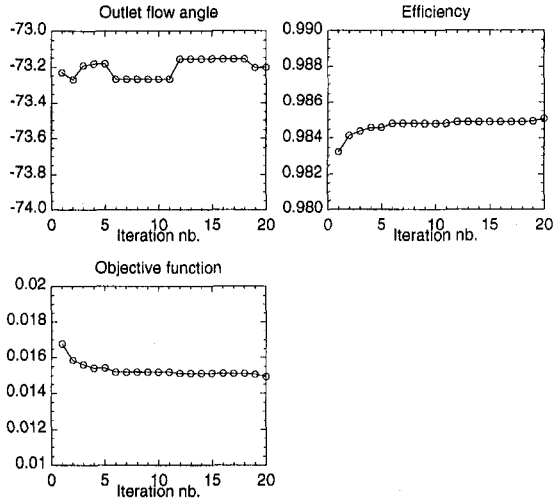

Fig. 8 Convergence histories

global objective function, a penalty term proportional to the difference between calculated and imposed Mach number distribution. This penalty is the summation of the square of the Mach number error along the blade surface.

Hence, depending on the type of design problem, we can minimize the losses or impose a Mach number distribution by switching on or off some penalty terms.

The development of the objective function is a delicate and long procedure. It may contain a lot of terms quantifying such design objectives as manufacturing constraints and cost.

Optimization

The goal of the optimization is to find the geometry that minimizes the objective function while evaluating the blade performance with the simplified model $\vec{P} = \mathcal{N}(\vec{BC}, \vec{G})$ obtained from ANN.

The choice of the optimization algorithm is mainly based on two considerations:

- the existence of many local optima in the design space may pose a problem for gradient type optimization methods.
- the efficiency of the optimization algorithm in terms of number of function evaluations is of far less importance when using a simplified prediction model than if a detailed Navier–Stokes computation was needed at each step of the optimization process.

For such optimization problems stochastic techniques offer a valid alternative to conventional gradient methods. Simulated Annealing (SA) algorithm, based on the analogy with the annealing of solids (van Laarhoven and Aarts, 1987), is such a method.

There is no real definition of what optimization based on simulated annealing really is. The only requirements are: Sufficient randomness must be inherent in the point selection process so that a wide field can be covered; more optimal points must be somewhat favored over less optimal points; and the degree of randomness must slowly decrease.

Results

This design procedure has been successfully tested on a large number of designs and will be illustrated here by three examples.

Design of a Reaction-Type Blade. The design requirements of this turbine blade are summarized in Table 1.

The design starts with a database containing 20 samples and an ANN with two layers and 10 nodes in the hidden layer. The computational time needed to train the ANN is less than 10 percent of the time needed by the Navier–Stokes solver.

The initial blade selected in the database, whose Mach number distribution and geometry are presented in Figs. 6 and 7, already has a good Mach number distribution. This is one advantage of the method, which uses as first guess a blade shape that has already been optimized under similar operating conditions. However, the pitch is slightly larger than the required one, the pressure ratio is smaller that the imposed one, and not all the mechanical constraints are respected.

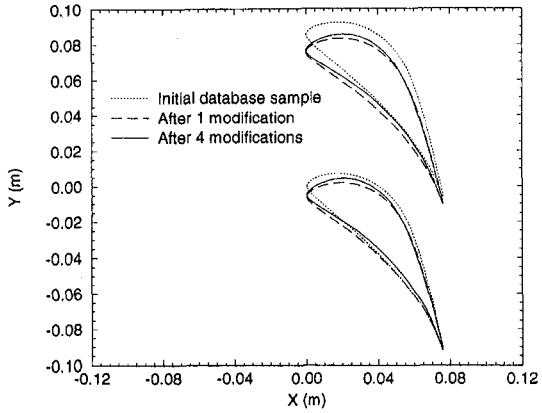

Fig. 7 Blade geometries

Table 2 Mechanical and aerodynamic requirements

	Imposed	After 7 modif.
Inlet flow angle (β_1)	55.0^o	-
P_2/P_{01}	0.7978	-
Re/Cax (1/m)	$9.3\ 10^7$	-
$k = Cp/Cv$	1.287	-
Cax (m)	0.03705	-
NB (number of blades)	192	-
Blade radial location (m)	0.708	-
Trailing edge radius (m)	$3.0\ 10^{-4}$	-
Area (m^2)	$3.10\ 10^{-4}$	$3.01\ 10^{-4}$
I_{min} (m^4)	$6.20\ 10^{-9}$	$6.30\ 10^{-9}$
I_{max} (m^4)	$2.70\ 10^{-8}$	$2.70\ 10^{-8}$
alpha	-	16^0
Outlet flow angle (β_2)	-68.9^0	-69.1^0
Loss coefficient (ξ)	0.0 %	3.86 %

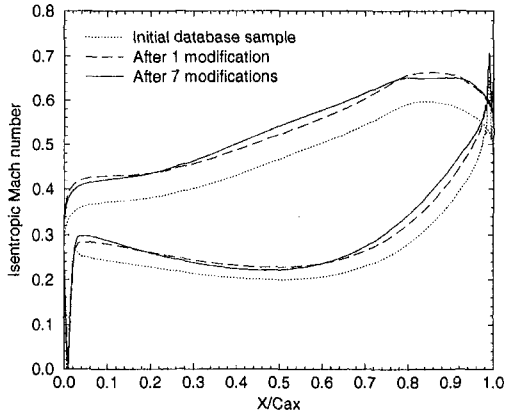

Fig. 9 Mach number distributions on the blade surface

Table 3 Mechanical and aerodynamic requirements

	Imposed	After 8 modif.
Inlet flow angle (β_1)	55.0°	-
P_2/P_{01}	0.8051	-
Re/Cax (1/m)	$7.0\ 10^7$	-
$k = Cp/Cv$	1.287	-
Cax (m)	0.03705	-
NB (number of blades)	192	-
Blade radial location (m)	0.708	-
Trailing edge radius (m)	$3.0\ 10^{-4}$	-
Area (m^2)	$3.10\ 10^{-4}$	$3.07\ 10^{-4}$
I_{min} (m^4)	$6.20\ 10^{-9}$	$5.97\ 10^{-9}$
I_{max} (m^4)	$2.70\ 10^{-8}$	$2.64\ 10^{-8}$
alpha	-	14^0
Outlet flow angle (β_2)	-68.9^0	-68.7^0
Loss coefficient (ξ)	-	4.23 %

This initial blade is then optimized by means of ANN and SA for the imposed requirements and analyzed by the Navier–Stokes solver. The result after the first modification and first Navier–Stokes solver is presented in Figs. 6 and 7. The Mach number distribution is smooth but the maximum value at $X/Cax = 0.8$ is quite large. It introduces an overly large diffusion on the rear part of the suction side.

Near-optimum performance has been obtained already after four modifications (four Navier–Stokes computations) (see Fig. 8). The main improvements on the Mach number distribution are on the suction side, close to the leading edge, and on the rear part of the suction side. The mechanical characteristics and the outlet flow angle are very close to the imposed values and the loss coefficient is low for this type of turbine blade (see Table 1). Continuing the iterations, after these four modifications, only minor improvements are found (Fig. 8).

Design of an Impulse-Type Blade. The design of impulse blades is usually very difficult because of the small pitch-to-axial-chord ratio, resulting in a strong interaction between the velocity distributions on the pressure and suction side and because of the small acceleration of the velocity from the leading edge to the trailing edge.

The design requirements of this second example are displayed in Table 2. This design started with a database containing 50 samples. The initial blade sample selected from the database has a slightly lower outlet isentropic Mach number (0.537 instead of 0.6 required) as well as a higher outlet flow angle than the required one (−70.1 deg instead of −68.9 deg).

A near-optimum solution is already obtained after seven modifications without any intervention of the operator. The suction side Mach number distribution increases almost linearly from the leading edge until the throat. The maximum Mach number on the suction side is only slightly higher than the outlet Mach number thus limiting the diffusion on the rear part of the blade (Figs. 9 and 10). The aerodynamic and mechanical requirements are satisfied within the imposed tolerances (see Table 2).

Design of an Impulse-Type Blade With an Imposed Mach Number Distribution. As mentioned previously, the method also allows defining a blade with a prescribed Mach number distribution on the suction and pressure side. The penalty term on the losses and the penalty on the Mach number criteria are replaced by a penalty expressing the difference between the required and the real Mach number distribution. The penalties on the outlet flow angle and on the mechanical requirements are unchanged.

The design requirements are displayed in Table 3.

To make sure that a solution exists, the Mach number distribution of an existing blade has been imposed as target distribution together with the corresponding outlet flow angle and mechanical constraints. Of course this existing blade is not stored in the database.

After eight modifications, an almost perfect agreement is obtained on both the suction and pressure side with only a discrepancy close to the leading edge on the pressure side (Fig. 11). The main reason for this discrepancy is the fact that the target Mach number distribution is not imposed in a sufficient number of points in the region $X/Cax < 0.1$. Figure 12 shows a good agreement between the blade, corresponding to the target velocity, and the redesigned one.

Conclusions

We have shown that, using the method presented in this paper, only a few Navier–Stokes computations are needed to

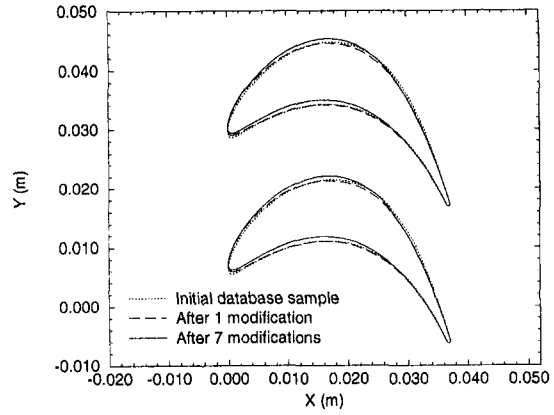

Fig. 10 Blade geometries

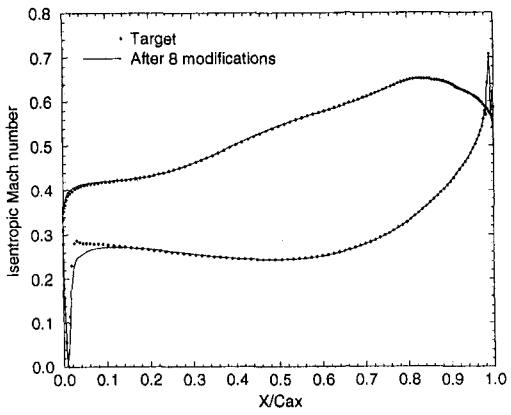

Fig. 11 Mach number distributions on the blade surface

define an optimized blade satisfying the aerodynamic and the mechanical requirements.

This design method allows the exploration of more design options in a given period of time than with traditional methods.

The efficiency of the method results from:

- the use of a robust geometry model, which avoids the generation of unrealistic blades but which nevertheless still has enough flexibility to reach a large number of blade types.
- the use of an artificial neural network and a database able to acquire experience from previous designs and efficiently use that experience from subsequent designs.
- A fully automated design procedure without operator intervention is possible mainly due to the development of an objective function, which translates the judgment of a specialized designer (concerning the quality and the reliability of the solution), and therefore the market demand, into a single number that can be handled by a computer.

The optimization algorithm, based on simulated annealing, guarantees that the system will not be trapped in a local minimum.

The method can be used with any Navier–Stokes solver.

Although this work has so far focused on two-dimensional turbine blades, the method can also be applied to the design of compressor blades.

This method can also be extended to the design of three-dimensional blades. The design can be realized in three steps:

- several two-dimensional sections are designed and then stacked and analyzed by a three-dimensional Navier–Stokes solver.
- the changes due to three-dimensional effects are then introduced as a correction to the two-dimensional requirements and the two-dimensional sections are redesigned.
- as soon as a database containing a sufficiently large number of three-dimensional computations is available, three-dimensional optimization is possible by extending the approximate model to the prediction of three-dimensional performances.

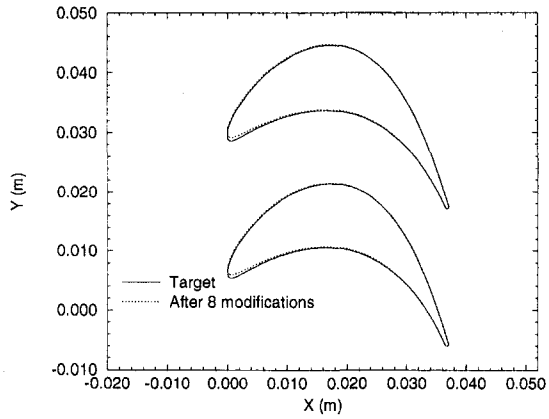

Fig. 12 Blade geometries

Acknowledgments

The first author is financially supported by the Belgian "Fonds pour la formation à la Recherche dans l'Industrie et l'Agriculture" (FRIA). The von Karman Institute acknowledges the computer support provided by Ansaldo Energia s.p.a. Thanks also to Dr. A. Arnone for making his solver available.

References

Arnone, A., and Benvenuti, E., 1994, "Three-Dimensional Navier–Stokes Analysis of a Two-Stage Gas Turbine," ASME Paper No. 94-GT-88.

Cichocki, A., and Unbehauen, R., 1994, *Neural Networks for Optimization and Signal Processing,* Wiley, New York.

Farin, G., 1993, *Curves and Surfaces for Computer Aided Geometric Design,* Academic Press, Inc.

Jou, W. H., Huffman, W. P., Young, D. P., Melvin, R. G., Bieterman, M. B., Hilmes, C. L., and Johnson, F. T., 1995, "Practical Considerations in Aerodynamic Design Optimization," AIAA-95-1730, pp. 950–960.

Pierret, S., 1997, "Turbomachinery Blade Design using a Navier–Stokes Solver and Artificial Neural Network," VKI Lecture Series 1997-05, Apr. 21–25.

Van Laarhoven, P. J. M., and Aarts, E. H. L., 1987, *Simulated Annealing: Theory and Applications,* Kluwer Academic Publishers.

Vanderplaats, G. N., 1984, *Numerical Optimization Techniques for Engineering Design,* McGraw-Hill, New York.

Effects of Periodic Wake Passing Upon Flat-Plate Boundary Layers Experiencing Favorable and Adverse Pressure Gradients

K. Funazaki

E. Koyabu

Department of Mechanical Engineering,
Iwate University,
Morioka, Japan

This paper deals with the investigation of wake-disturbed boundary layer on a flat-plate model with an elliptic leading edge. The wakes are generated by the transversely moving bars in front of the test model. The main focus of this paper is how the wake passage affects the transitional behavior of the boundary layer under the influence of favorable and adverse pressure gradients over the test surface. Detailed measurements of the boundary layer are conducted by the use of hot-wire anemometry. An ensemble-averaging technique is also employed in order to extract the periodic events associated with the wake passage from the acquired data. The previously observed dependence of wake-induced transition on the movement of the wake generating bar is confirmed. It is also found that the wake passage induces a significant change in the flow structure downstream of the flow acceleration region.

Introduction

A number of concerns have been raised about the unsteady-flow effect on the aerodynamic performance of rotor and/or stator cascades of axial turbomachines. For example, the deterioration in aerodynamic performance of a low-pressure turbine stage in commercial aero-engines, which is anticipated to occur when they operate under the cruise condition, could be reduced due to the existence of wake–blade interaction. Schulte and Hodson (1994, 1998a) found from the inspection of the steady and wake-affected pressure distributions on the blade suction surface that upstream blade wakes suppressed a separation bubble, which would otherwise have occurred on the suction surface and deteriorated the cascade performance. Funazaki et al. (1997c) conducted measurements of stagnation pressure distributions downstream of a linear cascade of turbine blades that was subjected to periodic wakes from the upstream moving bars, and identified a slight reduction in the loss associated with the blade wake. Similar to the study of Schulte and Hodson, they concluded from the flow visualization that a separation bubble on the blade suction surface was diminished due to the wake-blade interaction. Halstead et al. (1995a, b) investigated the wake–blade interaction phenomena in a large-scale compressor and turbine. Important studies related to separation bubble on a blade surface were also reported by several researchers (for example, Cumpsty et al., 1995; Gostelow et al., 1997).

Despite the above-mentioned studies, information is still lacking on the effects of free-stream turbulence and periodic wake passage upon the behavior of the separation bubble over a blade surface, which is important for the development of more efficient turbomachines. At the same time, such information is needed for verification of CFD codes as well as turbulence models that will be used in the aerodynamic design of turbomachines. This has driven the authors to start a research project that aims to gain quantitative data concerning the aerodynamic interaction between the separation bubble and incoming periodic wakes and/or free-stream turbulence. This paper describes the relevant fundamental studies employing a flat plate with an elliptic leading edge as a test model instead of a real turbine blade, in which the wake-affected boundary layer experiencing favorable and then adverse pressure gradient was investigated in detail. A focus was placed on how the periodic wake passage influenced the behavior of the boundary layer at the region where a separation bubble was likely to occur. A duct-contouring device was adopted to adjust the pressure gradient so that the pressure gradient of the turbine blade used by Funazaki et al. (1997c) was emulated over the test surface. A spoked-wheel type wake generator was employed to generate incoming wakes. This study also examined the effect of the rotation direction of the wake generator on the aerodynamic interaction between the wakes and the boundary layer similar to the previous studies (Funazaki et al., 1997a, b). Detailed hot-wire probe measurements were executed to obtain steady and wake-affected velocity data of the boundary layer.

Test Apparatus

Experimental Setup. Figure 1 shows a schematic layout of the test facility used in this study. The settling chamber and the contraction nozzle reduced free-stream turbulence from the blower down to about 0.8 percent. Incoming wakes were produced by a spoked-wheel type wake generator, which was located upstream of the test model. The wake generator consisted of a disk with 400 mm diameter and cylindrical bars of 5 mm diameter. Revolution number of the disk in the wake generator was counted by the optical tachometer. The wake generator was set so that each of the wake generating bars became parallel with the leading edge of the test model when it moved in front of the model. The fluctuation in revolution was also monitored and it was found to be less than 0.5 percent. Figure 2 shows the test model and the passage-contouring device attached on the top wall of the test duct, which was used to generate a specified pressure gradient on the surface of the test model. Also shown is the system for the boundary layer measurement. The test model made of acrylic resin was 1.075 m length and

Contributed by the International Gas Turbine Institute and presented at the 43rd International Gas Turbine and Aeroengine Congress and Exhibition, Stockholm, Sweden, June 2–5, 1998. Manuscript received by the International Gas Turbine Institute February 1998. Paper No. 98-GT-114. Associate Technical Editor: R. E. Kielb.

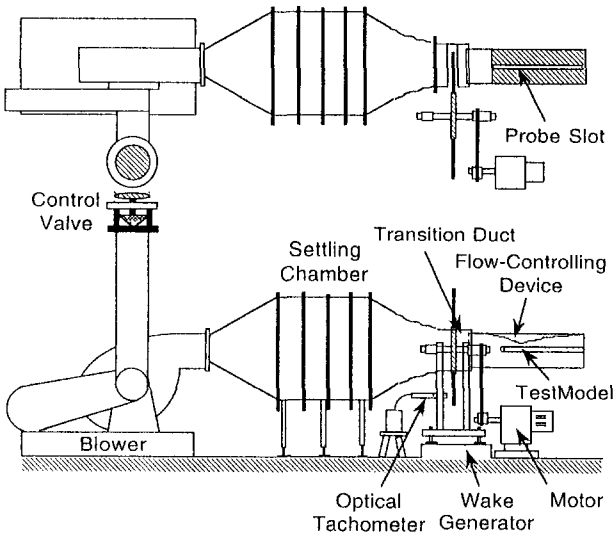

Fig. 1 Test apparatus

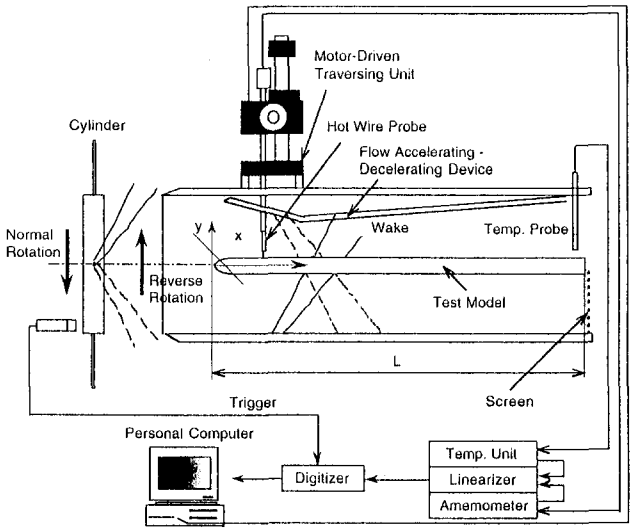

Fig. 2 Test model and the system for boundary layer measurement, with an explanatory illustration of wakes generated in the normal and reverse rotations

had a semi-elliptic leading edge with the long axis of 75 mm and the short axis of 15 mm, followed by a flat-plate afterbody. The width and thickness were 200 mm and 30 mm, respectively. Static pressure taps were provided on one side of the test model to measure the pressure distribution imposed on the test surface. Stainless steel foils covered the other side of the model to measure wake-affected heat transfer on the surface, which was not reported in this study. The passage-contouring device was adjusted so as to reproduce the pressure distribution similar to that on the suction surface of the turbine blade, which was investigated by Funazaki et al. (1997c). In order to avoid a biased inflow condition due to the asymmetric configuration of the test model with respect to the duct centerline, a screen was attached to the lower exit of the test duct. The mesh size of the screen was selected so that the aerodynamic stagnation line almost matched the mechanical stagnation line, which was confirmed by the oil-flow pattern near the leading edge of the test model. The contouring device was equipped with a slot along its centerline through which a hot-wire probe could be inserted into the main flow. The slot was securely plugged with several blocks to prevent the leakage from the slot.

Rotation direction of the disk in the wake generator was easily reversed, which changed the movement of the wake-generating bars relative to the test model, as designated "normal rotation" or "reverse rotation" in Fig. 2. Funazaki et al. (1997a, b) found through the previous studies that the relative movement of the bars and the associated fluid motion so-called negative jet seemed to have some effects on the transitional behavior of the wake-affected boundary layer. In those cases, however, since the leading edge of the test model used was sharp-edged, it could not be completely denied that the sharp-edged leading edge affected the transitional behavior of the boundary layer through the temporal fluctuation of the flow incidence associated with the wake passing. Therefore, the present study was anticipated to yield another evidence for the negative-jet effect upon the wake/boundary layer interaction.

Instrumentation and Data Processing. A single hot-wire probe was used to measure the boundary layer on the test model. A PC-controlled traversing unit placed the probe to the location to be measured with the precision ±0.01 mm. The probe was connected to a constant-temperature anemometer. By monitoring the free-stream temperature at the exit of the test section, T_∞, the temperature unit effectively compensated the temperature fluctuation of relatively low frequency during the long-running measurement. A/D conversion of the linearized signal of the probe was initiated with once-per-revolution signal from the optical tachometer, which guaranteed the application of the phase-locked averaging technique to the sampled data. The data

Nomenclature

d = diameter of the wake-generating bar
C_p = pressure coefficient
f = wake passing frequency
$\tilde{H}_{12}$ = shape factor
K = acceleration parameter
L = length of the test model
n = rotation per minute
n_b = number of wake-generating bars
p, P_0 = static pressure, stagnation pressure
Re = Reynolds number = $U_\infty L/\nu$
Re_x = local Reynolds number = $U_e(x)x/\nu$
S = Strouhal number
T = wake-passing period
$\tilde{T}u$ = ensemble-averaged turbulence intensity
T_∞ = free-stream temperature
t = time
$U_e(x)$ = free-stream velocity at the outer edge of the boundary layer
U_∞ = inlet velocity
$\tilde{v}$, v_k = ensemble-averaged velocity, sampled velocity data
x = streamwise coordinate
y = distance normal to the surface of the test model
δ_{99} = steady-state boundary layer thickness
$\tilde{\delta}$ = ensemble-averaged boundary layer thickness
$\tilde{\delta}_1$ = ensemble-averaged displacement thickness
$\tilde{\delta}_2$ = ensemble-averaged momentum thickness
$\tilde{\delta}_3$ = ensemble-averaged energy dissipation thickness
ν = kinematic viscosity
ρ = density

Superscript

$\sim$ = ensemble-averaged value

sampling rate was 50 kHz and each of the digitized time-history records contained 2048 words. Accordingly, phase-locked or ensemble-averaged velocity, $\tilde{v}$, was calculated from the acquired instantaneous velocity data, v_k ($k = 1, 2, \ldots, 100$) as follows:

$$\tilde{v}(x, y, t) = \frac{1}{N} \sum_{k=1}^{N} v_k(x, y, t) \tag{1}$$

Ensemble-averaged turbulence intensity was also defined by

$$\tilde{Tu}(x, y, t) = \frac{1}{U_e(x)} \sqrt{\frac{1}{N-1} \sum_{k=1}^{N} (v_k(x, y, t) - \tilde{v}(x, y, t))^2}, \tag{2}$$

where U_e was the local velocity determined from the static pressure measurements with the Bernoulli's equation. From the ensemble-averaged velocity, boundary layer integral characteristics such as displacement thickness were calculated using the following equations:

$$\tilde{\delta}_1(x, t) = \int_0^{\tilde{\delta}(x,t)} \left(1 - \frac{\tilde{v}(x, y, t)}{U_e(x)}\right) dy, \tag{3}$$

$$\tilde{\delta}_2(x, t) = \int_0^{\tilde{\delta}(x,t)} \left(1 - \frac{\tilde{v}(x, y, t)}{U_e(x)}\right) \frac{\tilde{v}(x, y, t)}{U_e(x)} dy. \tag{4}$$

$$\tilde{\delta}_3(x, t) = \int_0^{\tilde{\delta}(x,t)} \left(1 - \left(\frac{\tilde{v}(x, y, t)}{U_e(x)}\right)^2\right) \frac{\tilde{v}(x, y, t)}{U_e(x)} dy. \tag{5}$$

$\tilde{\delta}$ was an ensemble-averaged boundary layer thickness, which was the distance where the ensemble-averaged velocity reached the maximum among the data acquired at the same streamwise location. Shape factor was accordingly calculated by

$$\tilde{H}_{12}(x, t) = \tilde{\delta}_1(x, t)/\tilde{\delta}_2(x, t). \tag{6}$$

Uncertainty. Uncertainties of the inlet velocity and instantaneous velocity measured were about 2 and 3 percent. It followed the integral characteristics given by Eqs. (3), (4), and (5) contained uncertainties of about 6, 7, and 8 percent, respectively. The shape factor defined by Eq. (6) accordingly had more or less 10 percent uncertainty.

Results

Test Conditions. Wake-affected unsteady flow field around the test model was characterized by two non-dimensionalized number, i.e., Reynolds number Re, and Strouhal number S, defined by

$$\mathrm{Re} = \frac{U_\infty L}{\nu} \tag{7}$$

$$\mathrm{S} = \frac{fL}{U_\infty} = \frac{nn_b}{60} \frac{L}{U_\infty} \tag{8}$$

where U_∞ was inlet velocity and L was the length of the test model. In the present case U_∞ was 20 m/s, n was 1200 rpm and n_b was 2 and 3, corresponding to $\mathrm{Re} \cong 1.43 \times 10^6$ and S = 2.15 and 3.23, respectively. Inlet free-stream turbulence was about 0.8 percent.

Static Pressure Distribution. Figure 3 shows the pressure distribution on the suction surface of the turbine blade used by Funazaki et al. (1997c) and the measured static pressure distribution, with the calculated one by use of a potential flow analysis code based on BEM (Boundary Element Method) for comparison. Static pressure coefficient, C_p is calculated by

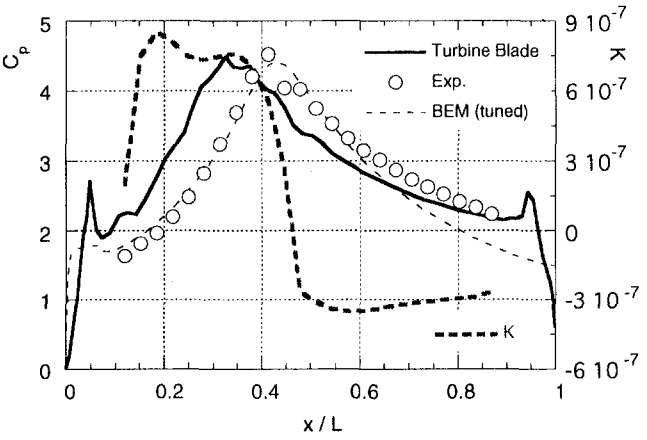

Fig. 3 Measured and calculated pressure distributions over the test surface, in comparison with the target pressure distribution on the turbine blade suction surface

$$C_p = \frac{P_0 - p}{1/2\rho U_\infty^2} = (U_e/U_\infty)^2. \tag{9}$$

Also shown is the corresponding acceleration parameter defined by the following equation:

$$K = \frac{\nu}{U_e^2} \frac{dU_e}{dx}. \tag{10}$$

It follows that the average acceleration parameter was about 0.8×10^{-6} before the deceleration. Although a slight difference in the peak position of the pressure distribution, which originated from the mechanical restriction of the passage-contouring device, was observed between the turbine blade and the present test model, the overall profiles of the pressure distributions were similar. Figure 3 also exhibits a small plateau just downstream of the peak value in the measured pressure distribution, implying the existence of a separation bubble.

Time-Resolved Behaviors of the Wake-Affected Boundary Layer

Raw Data. Figure 4 shows the raw signals of the velocity acquired at $y = 0.2$ mm for several measurement locations in the case of no wake condition. Although each of the measured points located relatively at the different location in the boundary layer, these figures clearly revealed some features of the transitional boundary layer experiencing favorable and then adverse gradients. Looking into the several velocity data obtained at the zone ranging from $x/L = 0.44$ to $x/L = 0.477$ (locations 3–7), a meaningful decrease in time-averaged velocity was observed at location 5 ($x/L = 0.486$). This almost matched the pressure data shown in Fig. 3, however, the boundary layer was so thin that it was quite difficult to confirm the existence of a possible separation bubble near that region from the measurement using a single hot-wire probe. Thereafter spike-like events occurred at location 8, indicating the initiation of the transition, followed by the abrupt completion of the transition. Figure 5 shows comparisons of the measured displacement and momentum thicknesses with the calculation using the boundary layer analysis code developed by Schmidt and Patankar (1991). This code, incorporated with the Lam–Bremhorst two-equation turbulence model, contains a limiting function that suppresses an excessive growth of the production term in the equation for the turbulence kinetic energy to avoid a rapid completion of transition. The calculated results agreed with the experimental data only in the acceleration region up to $x/L = 0.4$, prior to the onset of transition.

Figure 6 also exhibits the raw data of the wake-affected velocity in the case of S = 3.23. Two diagrams are shown for each

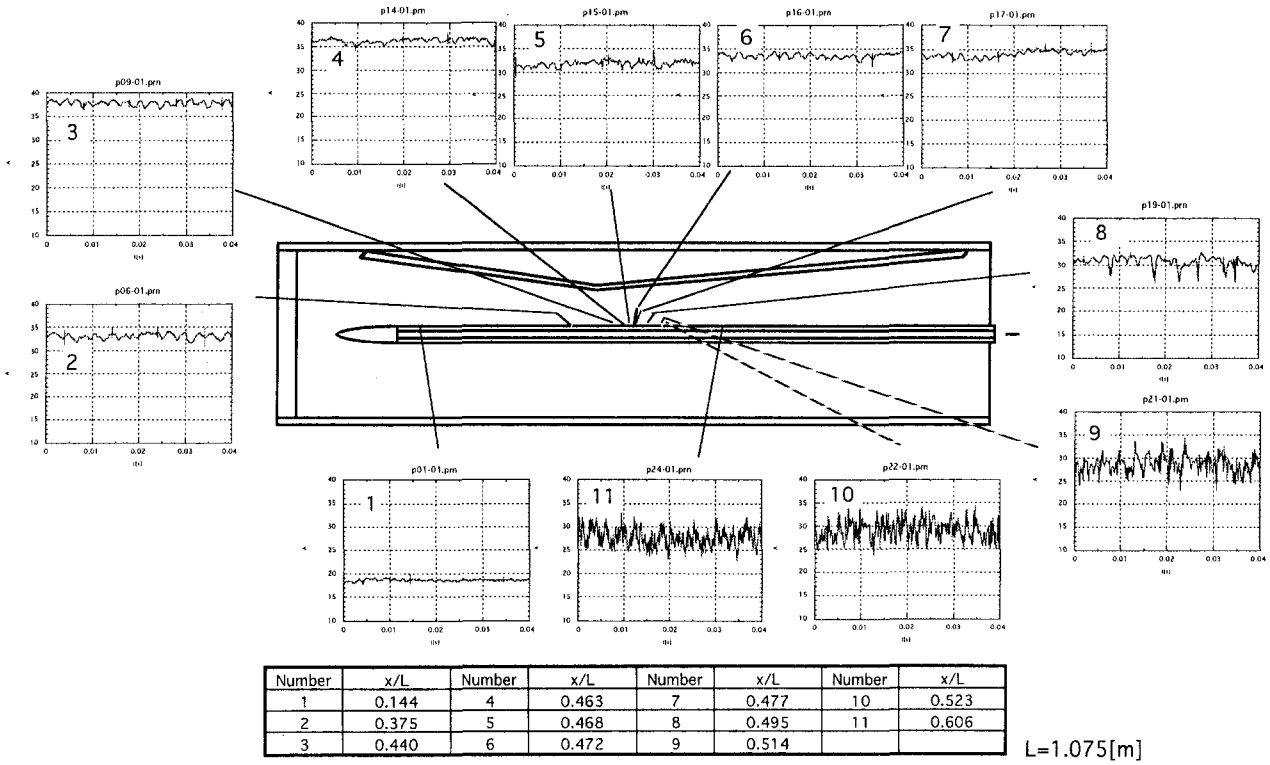

Number	x/L	Number	x/L	Number	x/L	Number	x/L
1	0.144	4	0.463	7	0.477	10	0.523
2	0.375	5	0.468	8	0.495	11	0.606
3	0.440	6	0.472	9	0.514		

L=1.075[m]

Fig. 4 Raw velocity signals measured at $y = 0.2 \times 10^{-3}$ m for several locations over the test model in the case of no wake condition, showing the transitional behavior of the boundary layer under the influence of the pressure gradient

of the measurement locations, where an upper and a lower diagrams present the data acquired in the normal and reverse rotation cases, respectively. As seen in the diagrams at location 1, the most upstream measurement point, the wake passages in the normal and the reverse rotation cases induced quite different events on the test surface. The detected velocity decreased during the wake passing in the normal rotation case, while the velocity in the reverse rotation exhibited a slight decrease followed by evident increase. This difference seems to be attributed to an effect of negative jet of the wake, which impinges on the test surface in the normal rotation and leave the test surface in the reverse rotation in a relative frame of reference moving with the free-stream. Enlargement of the highly fluctuating regions was observed from the data at locations 2, 3, and 4, indicating the progress in the wake-induced transition toward the downstream; however, the durations of those regions clearly differ between the normal and reverse rotation cases, as reported in the previous studies by Funazaki et al. (1997a, b). Close inspections of the data revealed that the highly fluctuating regions for the normal rotation case were likely to be accompanied by the significant decrease in velocity, while those regions for the reverse rotation showed only minor velocity decrease in the wake. In order to examine these phenomena from the viewpoint of the negative jet effect, the numerical study done by Valkov and Tan (1995) was reviewed, who analyzed the wake-disturbed flow field around a compressor cascade by use of a Navier–Stokes solver. Figure 7 shows the disturbance flow vectors around the compressor blade, which were obtained by subtracting the calculated unsteady flow field from the corresponding steady flow field at two different instants. Speaking of the relation of their results to the present study, wakes on the blade suction or pressure surface seemingly corresponded to ones in the reverse rotation case or the normal rotation case in terms of the relative motion of the fluid inside the wake against the surface of concern. However, one should keep in mind that the pressure distribution on the compressor blade was quite different from the present case, which affected the boundary layer thickness. It was found that incoming wakes were deformed by the stagnant flow at the leading edge, resulting in the appearance of accelerated flow region following the wake as expected from the negative jet theory (see Fig. 7(*b*)). In addition, the incoming wakes on the suction surface tended to migrate away from the suction surface. Therefore, one can conclude that the above-mentioned difference in the duration of the fluctuating region was mainly due to the effect of the wake migration from the suction surface. At location 8 spike-like events were no longer observed and the boundary layer thereafter reached the turbulent state rather abruptly. This observation implies that the wake-induced transition mode dominated the transition process as a whole, resulting in a fully turbulent state assisted by the adverse pressure gradient.

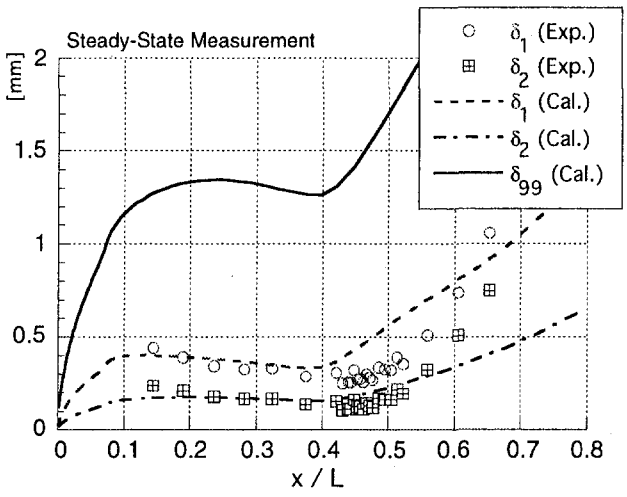

Fig. 5 Comparisons of displacement and momentum thicknesses between the measurement and the calculation

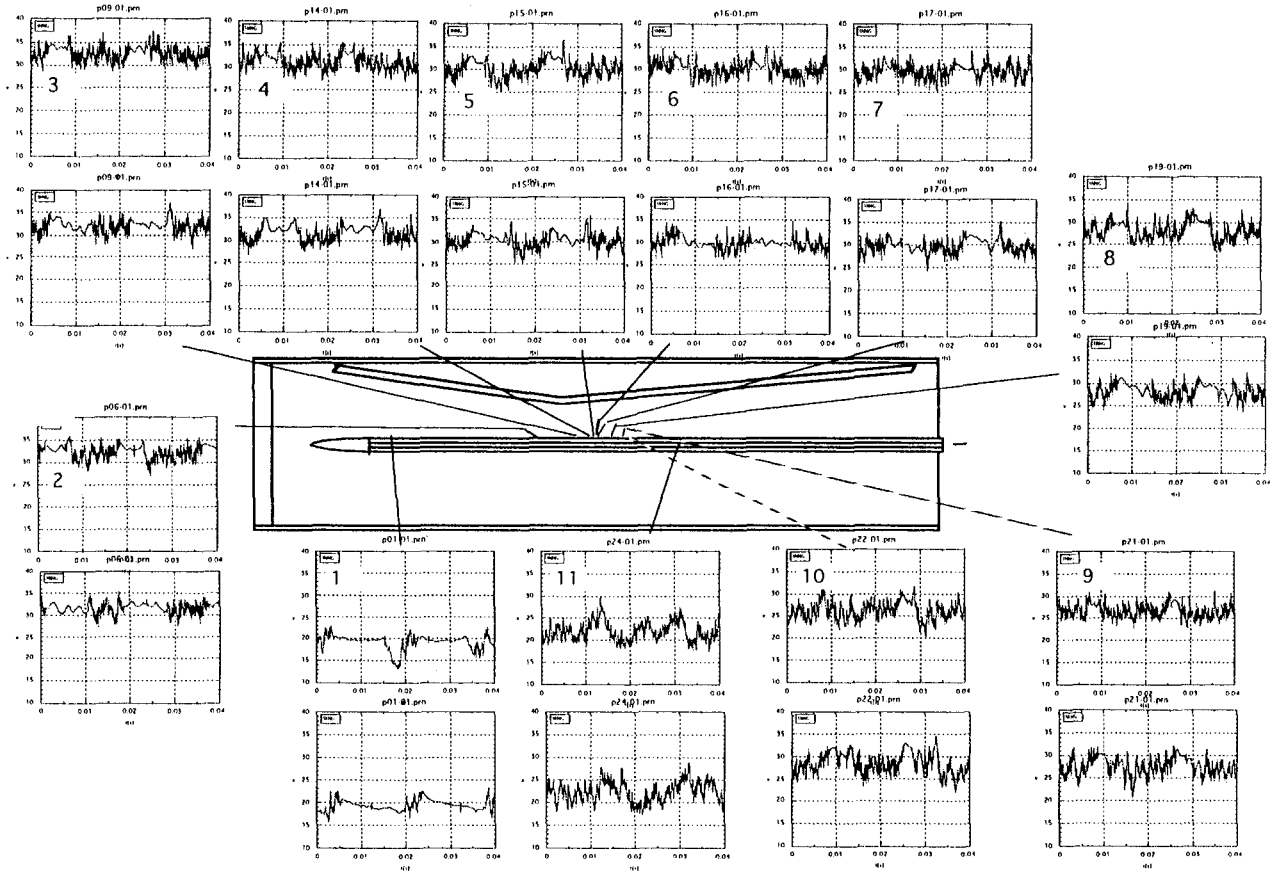

Fig. 6 Raw velocity signals measured at $y = 0.2 \times 10^{-3}$ m for several locations over the test model with the influence of the wake passing on the test surface (S = 3.23); where the upper and lower data of each of the graph columns were acquired in the normal and reverse rotation cases, respectively

Ensemble-Averaged Turbulence Intensity. For further investigation of the wake-affected boundary layer, ensemble-averaged turbulence intensity contours that represent bar-wakes interacting with the boundary layer are shown in Fig. 8. This figure represents some of the sequential snapshots during one wake-passing period T for the case of the normal rotation with S = 3.23. At the instant when one bar-wake, which was identifiable from its high turbulence intensity, reached the most upstream measuring position at $t/T \cong 0.0$, there was a clear evidence showing the appearance of wake-induced turbulence zone (turbulence patch) beneath the incoming wake. As the wake was convected downward, the leading edge of the induced turbulence patch moved almost along with the wake while the trailing edge of the patch lagged behind the wake, resulting in gradual expansion of the turbulence patch in the streamwise direction. Due to the effect of the flow acceleration, however, the height of the patch remained almost unchanged. In the instant when the leading edge of the patch reached the trailing edge of the foregoing turbulence patch ($t/T = 0.4$), another high turbulence region occurred at $x/L = 0.45$–0.5 (from location 4 to 7) designated "A," exhibiting quick growth in the y direction (normal to the wall) due to the effect of adverse pressure gradient. A plausible explanation on this event was a high rate of turbulence spot generation at the decelerating flow regime (Mayle, 1991). The other cause was the interaction between the bar-wake and a separation bubble, on which further investigations are needed.

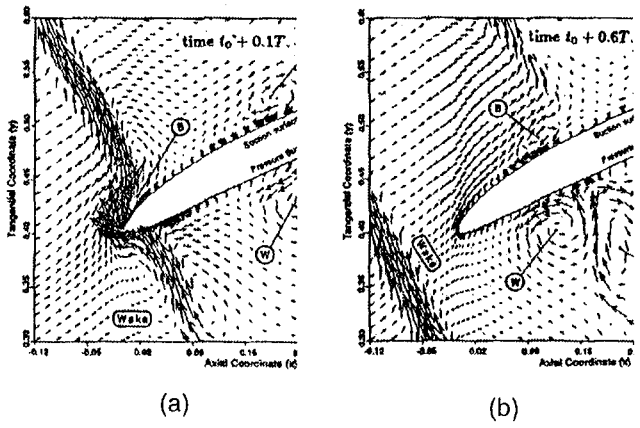

Fig. 7 Numerical calculations of wake–compressor blade interaction executed by Valkov and Tan (1995)

Figure 9 also shows the snapshots of the ensemble-averaged turbulence intensity contours for the reverse rotation with S = 3.23. As seen in the raw data of Fig. 5 or numerical calculation in Fig. 7, the incoming wake moved away from the test surface so that the wake width (or wake duration) became narrow compared to that of the normal rotation case. Since contributions from the wake turbulence to the turbulence patch were minimal, the streamwise extent of the turbulence patch was also relatively limited. At the moment when the wake passed over the zone $x/L = 0.45 - 0.5$, a highly turbulent region designated "B" appeared and grew likewise in the normal rotation case.

To enhance the understanding of the behaviors of the wake-induced turbulence patch observed in Figs. 8 and 9, the corresponding distance–time diagrams of the wake-induced turbulence contours measured at $y = 0.2$ mm are shown in Fig. 10 for the normal and reverse rotation cases. The turbulence patch exhibited a feature of evolution quite similar to the previous studies of

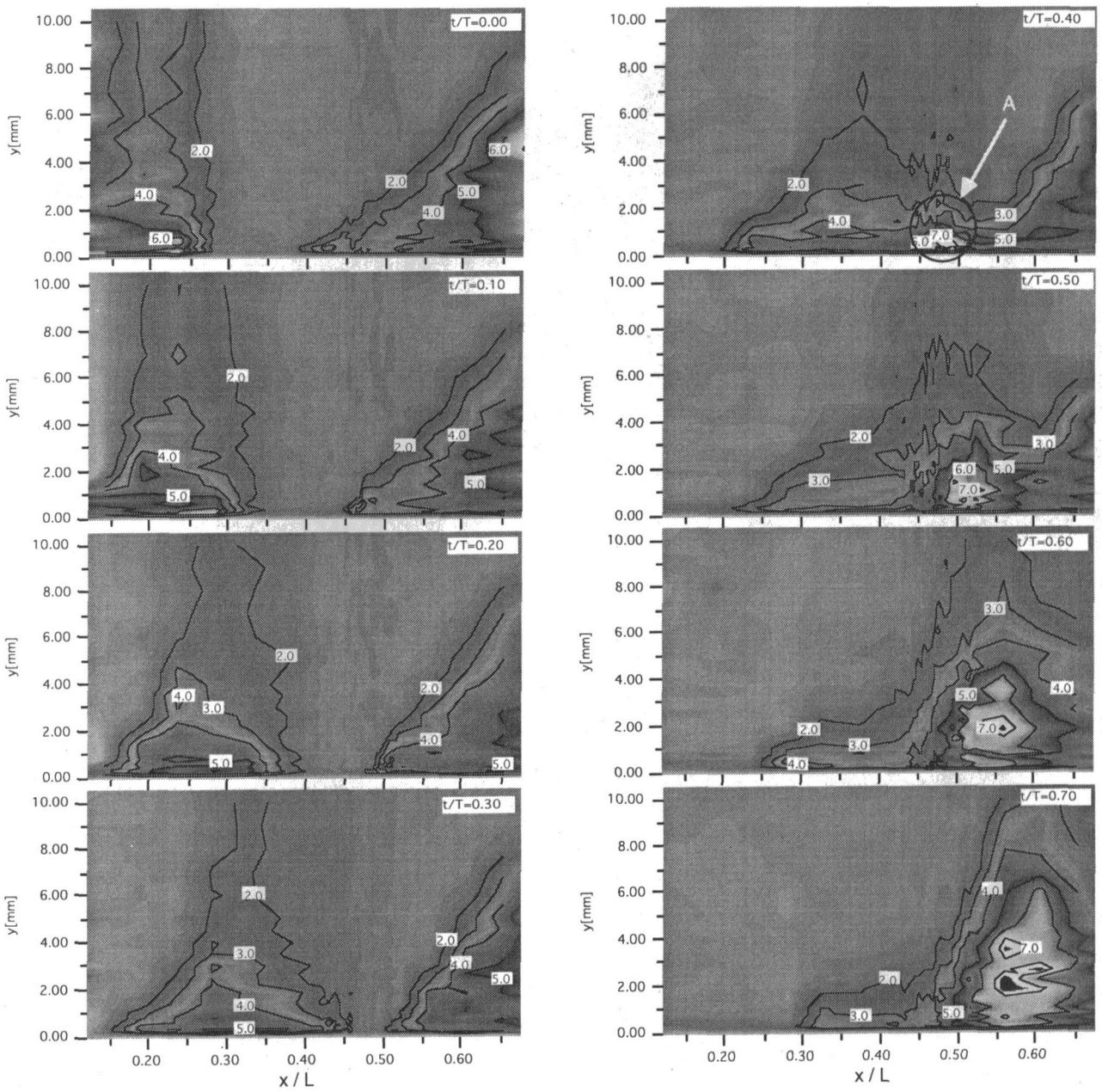

Fig. 8 Snapshots of the ensemble-averaged turbulence intensity contours of the wake-disturbed boundary layer experiencing favorable and adverse pressure gradients (S = 3.23/normal rotation)

Halstead et al. (1997a) or Funazaki et al. (1996b) in the acceleration region. A distinct difference in the timewise extent of the turbulence patch was again confirmed between the rotation cases. It was also evident that the transition process for the normal rotation case was dominated by the wake passage, while the inter-wake transition could be observed for the reverse rotation case. Recently much attention has been paid to the effect of calmed region on the separation bubble (Schulte and Hodson, 1998b, for example). In Fig. 10, however, the appearance of the calmed region was not clear, so that another contours of turbulence intensity were plotted for the lower Strouhal number case, S = 2.15, as shown in Fig. 11. Regions of relatively low turbulence intensity, marked with "C," occurred just behind the wake-induced turbulence patch and these could be regarded as calmed regions. The appearance of the low turbulence regions was also confirmed by comparing time–history records of turbulence intensity in the right-hand side of Fig. 11, which were measured at three different locations near the area "C."

Time-Averaged Shape Factor and Energy Dissipation Thickness. Figure 12 shows time-averaged shape factors for several unsteady flow conditions, which was defined by the integration of the ensemble-averaged shape factor over the wake-passing period as follows:

$$H_{12}(x) = \frac{1}{T}\int_0^T \tilde{H}_{12}(x, t)dt. \tag{11}$$

It is actually difficult to draw a general conclusion from this figure because of its large uncertainty, however, the following findings can be stated. First, the shape factor for no wake condition exhibited relatively high value over the zone ranging from $x/L = 0.4–0.5$, followed by sharp decrease indicating the onset of the boundary layer transition. This seems to be more evidence for the existence of the separation bubble that was mentioned above. Second, the wake-affected shape factor tended to decrease with the increase in Strouhal number, which was more

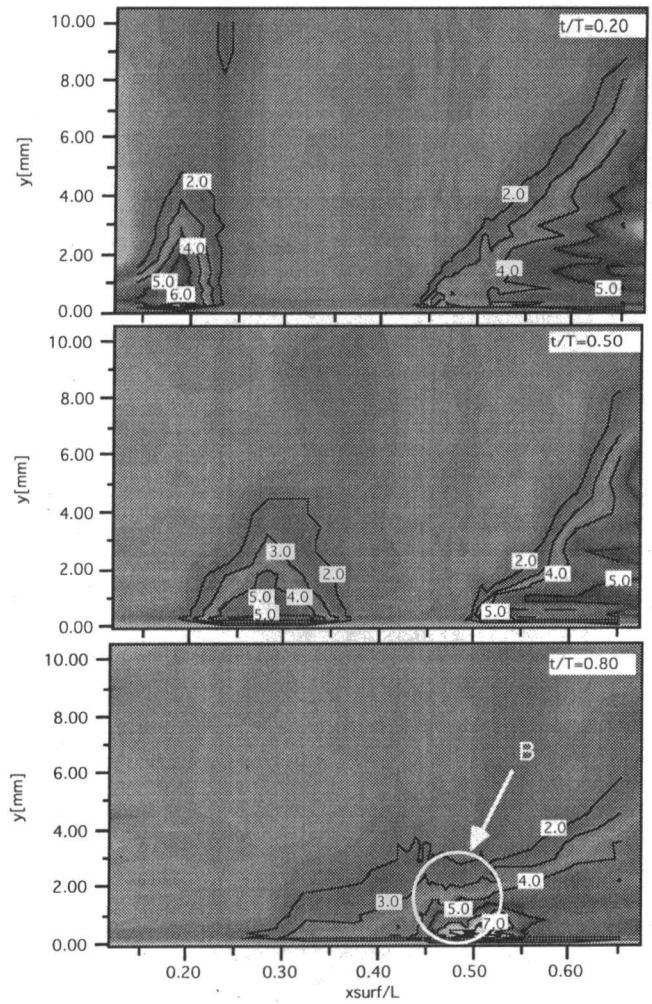

Fig. 9 Snapshots of the ensemble-averaged turbulence intensity contours of the wake-disturbed boundary layer (S = 3.23/reverse rotation)

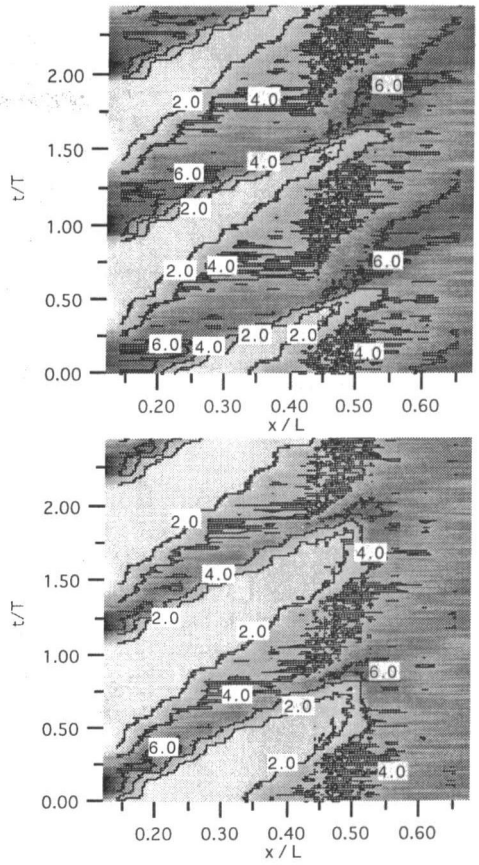

Fig. 10 Distance–time diagrams for ensemble-averaged turbulence intensity contours measured at y = 0.2 mm for S = 3.23 (upper: normal rotation/lower: reverse rotation)

pronounced in the normal rotation case for the same Strouhal number. Furthermore, the wake-affected shape factor for higher Strouhal number or normal rotation cases did not display any rise over the zone $x/L = 0.4–0.5$ in contrast with the no wake condition. This indicated that separation bubble was suppressed by the wake passage and the transition process was dominated by the aerodynamic interaction between the wake and the boundary layer experiencing the adverse pressure gradient.

Figure 12 shows time-averaged energy dissipation thickness distributions. As demonstrated by Denton (1993), energy dissipation thickness corresponds to entropy thickness or aerodynamic loss generation in the boundary layer. Although most of the measured data were of similar magnitude before $x/L = 0.4$, considerable differences were thereafter observed among the data. Despite some data scattering, a close inspection of this figure revealed that deviations of the wake-affected energy dissipation thickness from that of no wake condition gradually increased almost in a linear fashion along with x/L until the end of the flow acceleration. This corresponds to the behaviors of wake-induced turbulence regimes in the $x–t$ diagrams in Fig. 10, indicating little impact of the favorable pressure gradient upon the evolution of wake-induced turbulence patch. Significant increase in the energy dissipation thickness arose after $x/L > 0.4$, in particular for higher Strouhal number. No evidence could not be identified for loss reduction due to the wake passage.

As described earlier, the present study was motivated by the cascade test of Funazaki et al. (1997c). However, the present study could not fully reproduce the flow conditions of their previous study due to some mechanical restriction of the test facility. For example, free-stream turbulence intensity in the present study was slightly higher than that of the cascade test (about 0.5 percent). Furthermore, Reynolds number was much higher and the effect of curvature was ignored in this case. These differences were partly the reason for smaller separation bubble in this study than that in the cascade test, which seem-

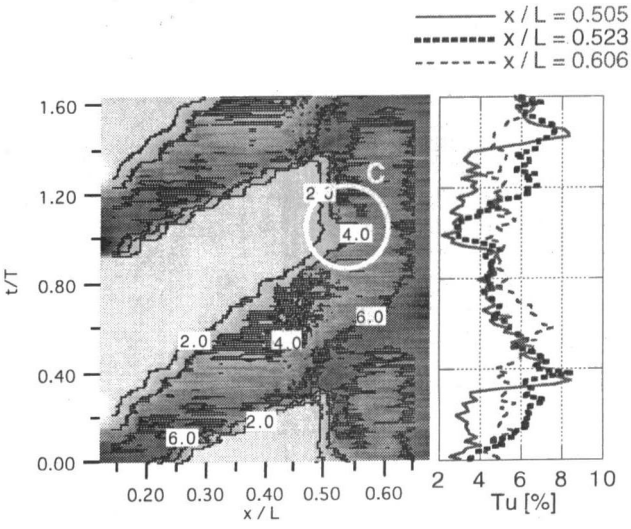

Fig. 11 Distance–time diagrams for ensemble-averaged turbulence intensity contours measured at y = 0.2 mm for S = 2.15 (normal rotation)

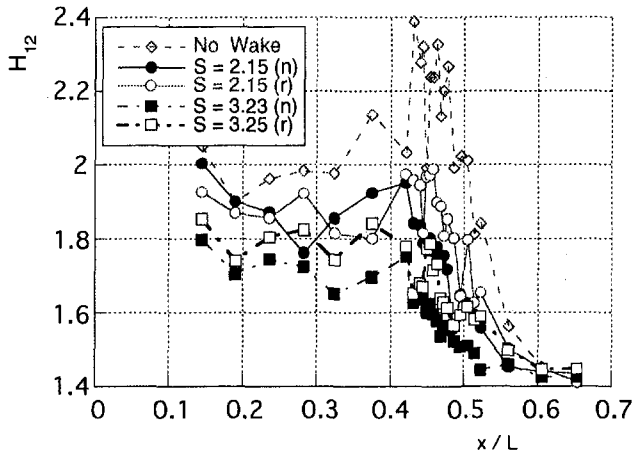

Fig. 12 Time-averaged shape factor

ingly led to less contribution of the separation bubble to the energy dissipation thickness, e.g., aerodynamic loss as seen in Fig. 13. This is consistent with the findings by Schulte and Hodson (1998a), in which they found that wake-induced loss reduction did not occur for relatively high Reynolds number flow. Lastly, the present authors believe that the relevant studies are still needed on loss generation in a boundary layer subjected to wake passage, focusing on Reynolds number effect.

Conclusions

The findings in this study can be itemized as follows:

1 From raw data and/or ensemble-averaged data of wake-disturbed velocity inside the boundary layer, a prominent difference was identified between the normal and reverse rotation likewise in the previous study using the sharp-edged flat plate. This was also confirmed by the distance–time diagrams of turbulence intensity.

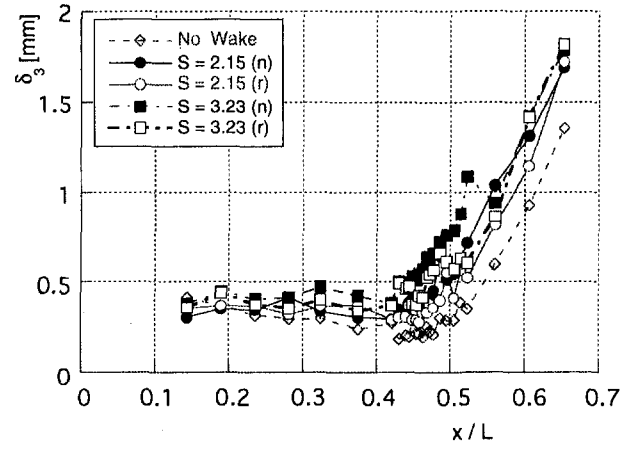

Fig. 13 Time-averaged energy dissipation thickness

2 Wake-induced turbulence patch exhibited an abrupt growth at the instance when its leading edge reached the decelerating flow region, and the boundary layer thereafter became fully turbulent suppressing the steady-state transition mode.

3 The appearance of calmed regions just behind the wake-induced turbulence patches was observed in the distance–time contours of turbulence intensity.

4 The time-averaged shape factor indicated that the separation bubble was suppressed by the wake passage and the transition process was dominated by the aerodynamic interaction between the wake and the boundary layer, in particular for high Strouhal number.

5 The time-averaged energy dissipation thickness linearly increased in the accelerating region on the test model.

6 No evidence could be identified for loss reduction due to the suppression of the separation bubble by the wake passage, partly because of the high-Reynolds-number flow in the present study.

Acknowledgments

The authors are greatly indebted to Mr. K. Sasaki of Technical Center of Iwate University in manufacturing the test facility.

References

Cumpsty, N. A., Dong, Y., and Li, Y. S., 1995, "Compressor Blade Boundary Layers in the Presence of Wakes," ASME Paper No. 95-GT-443.

Denton, J. D., 1993, "Loss Mechanisms in Turbomachines," ASME JOURNAL OF TURBOMACHINERY, Vol. 115, pp. 621–656.

Funazaki, K., Kitazawa, T., Koizumi, K., and Tanuma, T., 1997a, "Studies on Wake-Disturbed Boundary Layers Under the Influences of Favorable Pressure Gradient and Free-Stream Turbulence—Part I: Experimental Setup and Discussions on Transition Model," ASME Paper No. 97-GT-451.

Funazaki, K., Kitazawa, T., Koizumi, K., and Tanuma, T., 1997b, "Studies on Wake-Disturbed Boundary Layers Under the Influences of Favorable Pressure Gradient and Free-Stream Turbulence—Part II: Effect of Free-Stream Turbulence," ASME Paper No. 97-GT-452.

Funazaki, K., Sasaki, Y., and Tanuma, T., 1997c, "Experimental Studies on Unsteady Aerodynamic Loss of a High-Pressure Turbine Cascade," ASME Paper No. 97-GT-52.

Gostelow, J. P., Walker, G. J., Solomon, W. J., Hong, G., and Melwani, N., 1997, "Investigation of the Calmed Region Behind a Turbulent Spot," ASME JOURNAL OF TURBOMACHINERY, Vol. 119, pp. 802–809.

Halstead, D. E., Wisler, D. C., Okiishi, T. H., Walker, G. J., Hodson, H. P., and Shin, H. W., 1997a, "Boundary Layer Development in Axial Compressor and Turbines, Part 2 of 4: Compressors," ASME JOURNAL OF TURBOMACHINERY, Vol. 119, pp. 426–444.

Halstead, D. E., Wisler, D. C., Okiishi, T. H., Walker, G. J., Hodson, H. P., and Shin, H. W., 1997b, "Boundary Layer Development in Axial Compressor and Turbines, Part 3 of 4: LP Turbines," ASME JOURNAL OF TURBOMACHINERY, Vol. 119, pp. 225–237.

Mayle, R. E., 1991, "The Role of Laminar–Turbulent Transition in Gas Turbine Engines," ASME JOURNAL OF TURBOMACHINERY, Vol. 113, pp. 509–537.

Schmidt, R. C., and Patankar, S. V., 1991, "Simulating Boundary Layer Transition With Low-Reynolds-Number k–e Turbulence Models: Part 1—An Evaluating of Prediction Characteristics," ASME JOURNAL OF TURBOMACHINERY, Vol. 113, pp. 10–17.

Schulte, V., and Hodson, H. P., 1994, "Wake-Separation Bubble Interaction in Low Pressure Turbines," presented at the 30th AIAA/ASME/SAE/ASEE Joint Propulsion Conference.

Schulte, V., and Hodson, H. P., 1998a, "Unsteady Wake-Induced Boundary Layer Transition in High Lift Turbines," ASME JOURNAL OF TURBOMACHINERY, Vol. 120, pp. 28–35.

Schulte, V., and Hodson, H. P., 1998b, "Prediction of the Becalmed Region for LP Turbine Profile Design," ASME JOURNAL OF TURBOMACHINERY, Vol. 120, pp. 839–846.

Valkov, T., and Tan, C. S., 1995, "Control of the Unsteady Flow in a Stator Blade Row Interacting With Upstream Moving Wakes," ASME JOURNAL OF TURBOMACHINERY, Vol. 117, pp. 97–105.

I. H. Tuncer
Research Assistant Professor,
Department of Aeronautics,
Naval Postgraduate School,
Monterey, CA 93943
Mem. ASME

S. Weber
Development Engineer,
BMW Rolls-Royce GmbH,
AeroEngines,
Dahlewitz, Germany

W. Sanz
Associate Professor,
Institut für Turbomaschinen,
Graz Technical University,
Graz, Austria
Mem. ASME

Investigation of Periodic Boundary Conditions in Multipassage Cascade Flows Using Overset Grids

A Navier–Stokes solution method with overset grids is applied to unsteady multipassage cascade flows, and the unsteady blade loadings are compared against the single-passage solutions with the direct store interblade boundary condition. In the overset grid solutions, the multipassage domain is discretized with O-type grids around each blade and a rectangular background grid. Blade grids are allowed to move in time relative to the background grid, as prescribed by the oscillatory plunging motion. The overset grid method uses a simple, robust numerical algorithm to localize moving intergrid boundary points and to interpolate solution variables across grids. Computational results are presented for two and four-passage, subsonic and transonic flows through a turbine and a compressor cascade. The overset grid solutions over the multipassage periodic domains agree well with the single-passage solutions and the experimental data. It is concluded that the time linearization error introduced by the direct store approach is negligible in the range of flow conditions studied.

Introduction

The current trends in gas turbine design toward higher flow velocities and slender blades demand an accurate and detailed study of aeroelastic behavior of compressor and turbine blades. The prediction of blade flutter is critical in turbomachinery design and development, and considerable experimental and computational efforts are currently being made to determine flutter boundaries in highly loaded cascades with transonic and supersonic inflow (Ayer and Verdon, 1998; Grüber and Carstens, 1996; Försching, 1996; He, 1998). It is, therefore, of great interest to develop numerical methods to predict the unsteady aerodynamics of vibrating blades in cascade flows accurately.

Unsteady cascade flows as the blades undergo in and out-of-phase vibrations are currently being computed by solving the Euler and Navier–Stokes equations (Verdon, 1993). In the computation of out-of-phase cascade flows, the periodic boundary conditions are implemented either by discretizing the multipassage domain based on the Inter-Blade Phase Angle (IBPA) or by imposing temporal periodicity in a single-passage domain. The latter method is known as *direct store* (Erdos et al., 1977). Although the direct store method reduces the computational domain to a single blade passage, it in fact linearizes the periodic boundary condition in time. In addition, a periodic convergence may take a large number of periods to be computed on a single-passage domain, and a large storage may be required to store the periodic boundary information in time (Abhari and Giles, 1997).

In this work, a Navier–Stokes solver with an overset grid solution method is applied to compute out-of-phase, multipassage cascade flows (Fig. 1). The overset grid solution method has already been applied to steady and unsteady flows through an annular compressor blade (Tuncer, 1996; Tuncer and Sanz, 1997). We now attempt to compute multipassage flows through a turbine cascade, STC4, which has been investigated experimentally, and extensive data are available (Bölcs and Fransson, 1989), and to compare unsteady blade loadings and instantaneous flowfields with single blade passage solutions obtained with the direct store method and the experimental data.

In the single-passage solutions, the computational domain is discretized with a single deforming grid as shown in Fig. 2 (Weber et al., 1997; Peitch et al., 1994). Direct store boundary conditions are then applied to account for the phase shift between neighboring blade passages. The blade vibration is implemented by deforming the grid partially around the blade while keeping the periodic boundaries stationary. The flow variables at the periodic boundaries are stored as the blade vibration is imposed on the solution. The out-of-phase periodic boundary conditions based on the stored time history are applied until a convergent solution is obtained.

In the overset grid solution, the multiblade passage is discretized with a rectangular background grid and viscous grids around each blade, which are overset onto the background grid. The background grid covers the whole multipassage domain. Figure 1 shows a discretized two-passage domain over the STC4 turbine cascade. The blade grids are free to move with respect to the background grid, and a periodic vibratory motion with a phase shift is imposed on each blade independently. The main advantage of this approach lies in its versatility to resolve the multipassage computational domain with high-quality, mostly orthogonal subgrids, and in the application of simple periodic boundary conditions. Furthermore, it imposes almost no restriction on the vibratory motion of the blades. The implicit solution on the background grid also improves the time accuracy of the solution.

Overset Grid Solution Method

In the overset grid solution method, the computational domain is discretized with structured subgrids, which may overlay each other, as shown in Fig. 1. The Navier–Stokes equations are solved in each subgrid with the proper boundary conditions. In addition to the boundaries of the computational domain, subgrids may have intergrid boundaries with the neighboring subgrids and may also contain holes. Additional boundary conditions are therefore needed at the intergrid boundaries of a

Contributed by the International Gas Turbine Institute and presented at the 43rd International Gas Turbine and Aeroengine Congress and Exhibition, Stockholm, Sweden, June 2–5, 1998. Manuscript received by the International Gas Turbine Institute February 1998. Paper No. 98-GT-11. Associate Technical Editor: R. E. Kielb.

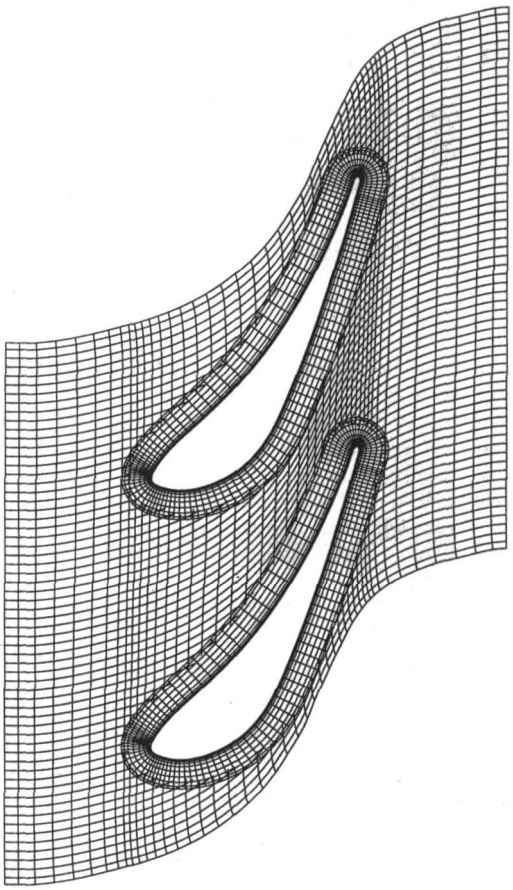

Fig. 1 Overset grids over the two-passage STC4 turbine blade. (Every other grid point is plotted.)

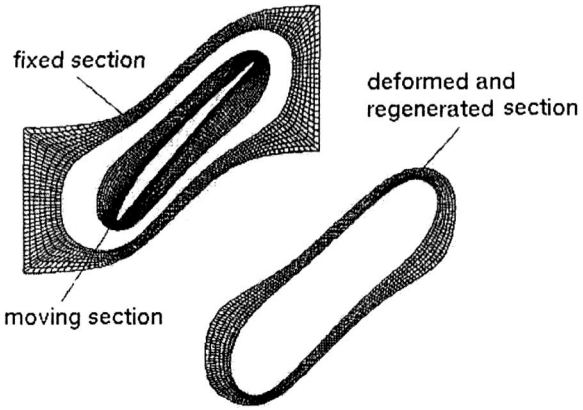

Fig. 2 Deforming grid structure for a typical single blade passage

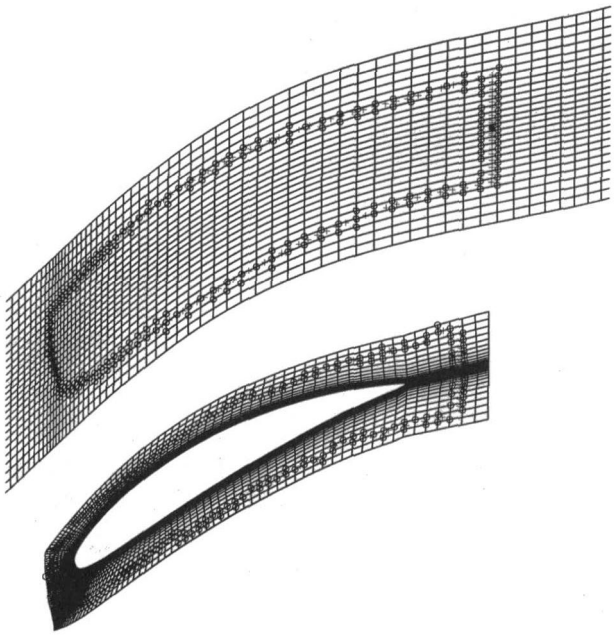

Fig. 3 Localization of the intergrid boundary points for a typical overset grid over a single blade passage

subgrid, and the hole points should be excluded from the integration of the Navier–Stokes equations.

In this study, the flow variables at the intergrid boundary points are interpolated from the neighboring donor grids. A boundary point localization method developed by Tuncer (1996) is used for the application of the intergrid boundary conditions. A boundary point is localized in a triangular stencil defined by (i, j), $(i, j \pm 1)$ and $(i \pm 1, j)$ grid points on the donor grid. The localization process is based on a directional search algorithm. The search direction follows the geometry gradients on the donor grid to minimize the distance between the boundary point and the current search location. The boundary point localization process also supplies the geometric interpolation weights at the boundary point in terms of the function values at the vertices of the triangular stencil. Thus, once the point is localized, the interpolation weights are readily available to interpolate flow variables at the boundary point from the donor grid.

Figure 3 shows the localized intergrid boundary points for a typical blade grid. The outer boundary points of the blade grid, denoted by +, are first localized on the background grid. This process defines the hole boundary points on the background grid. In the present study, the intergrid overlapping region is enlarged by extending the hole boundary points by one grid point inward in both the i and j directions. The extended hole boundary points are then similarly localized on the blade grid.

The boundary point localization and the interpolation of flow variables are performed at every time step as the blade grids move over the background grid, as specified by an unsteady motion. Since the boundary point localization process supplies the interpo-

Nomenclature

a = acoustic speed
A = maximum amplitude of the plunging motion
c = blade chord length
C_p = pressure coefficient = $(p - p_{in})/(P_0 - p_{in})$
C_p-dyn = dynamic pressure coefficient = $C_p/(A/c)$
exit = refers to outflow
f = frequency, Hz
h = amplitude of the plunging motion in time
in = refers to inflow
p = static pressure, Pa
P_0 = total pressure, Pa
t = time
T_0 = total temperature, K
α_{in} = inlet flow angle, deg
ϕ = interblade phase angle (IBPA)

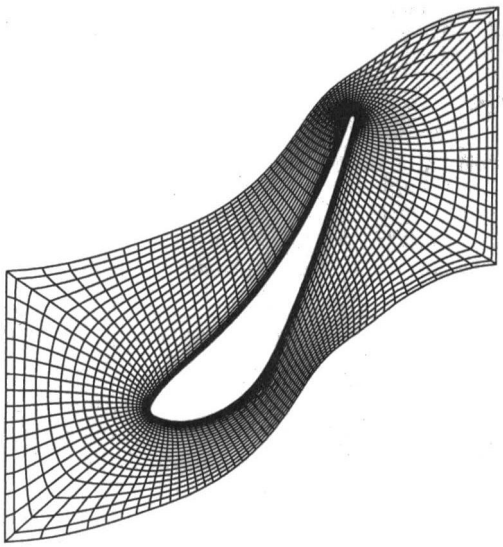

Fig. 4 Single passage grid used in direct store computations

lation weights, no interpolation data are stored. Flow variables at the intergrid boundary points are interpolated as an integral part of the localization process. The application of the intergrid boundary conditions is therefore quite robust and efficient.

Navier–Stokes Solver. An unsteady, implicit, thin-layer Navier–Stokes solver (Rai and Chakravarty, 1986; Ekaterinaris et al., 1994; Tuncer, 1996) with the third-order-accurate Osher's upwind biased flux difference splitting scheme is employed. The strong conservation-law form of the two-dimensional, thin-layer Navier–Stokes equations in a curvilinear coordinate system, (ξ, ζ), along the axial and circumferential direction, respectively, is given as follows:

$$\partial_t \hat{\mathbf{Q}} + \partial_\xi \hat{\mathbf{F}} + \partial_\zeta \hat{\mathbf{G}} = \mathrm{Re}^{-1} \partial_\zeta \hat{\mathbf{S}} \tag{1}$$

where $\hat{\mathbf{Q}}$ is the vector of conservative variables, $1/J(\rho, \rho u, \rho w, e)$, $\hat{\mathbf{F}}$ and $\hat{\mathbf{G}}$ are the inviscid flux vectors, and $\hat{\mathbf{S}}$ is the thin-layer approximation of the viscous fluxes in the ζ direction normal to the airfoil surface. The pressure is related to density and total energy through the equation of state for an ideal gas, $p = (\gamma - 1)[e - \rho(u^2 + w^2)/2]$.

The flowfield is assumed to be fully turbulent and the Baldwin–Lomax turbulence model is implemented only on the blade grids.

Boundary Conditions. In an unsteady cascade flow, vibration modes of blades with constant amplitude and constant interblade phase angle result in a pitchwise spatially periodic flow with a multipassage domain. Therefore, the number of passages depends on the interblade phase angle. An interblade phase angle of 0 deg (in-phase vibration) requires only one blade passage, phase angles of 180 and 90 deg (out-of-phase vibrations) two and four blade passages, respectively.

Numerical boundary conditions are applied at the inlet, exit, and periodic boundaries, and the blade surfaces. In overset grids, the conservative flow variables are interpolated from the neighboring subgrid at the intergrid boundaries at every time step.

At the inlet, total pressure, total temperature, and in-flow angle are given. At the outflow boundaries the exit static pressure is specified. The remaining flow variables are obtained using isentropic flow relations and the zero-order Riemann invariant extrapolation. Periodic boundary conditions are imposed by overlapping the interior solution at the lower and upper boundaries.

On the blade surfaces, the no-slip boundary condition is applied. The density and pressure gradients are set to zero on the

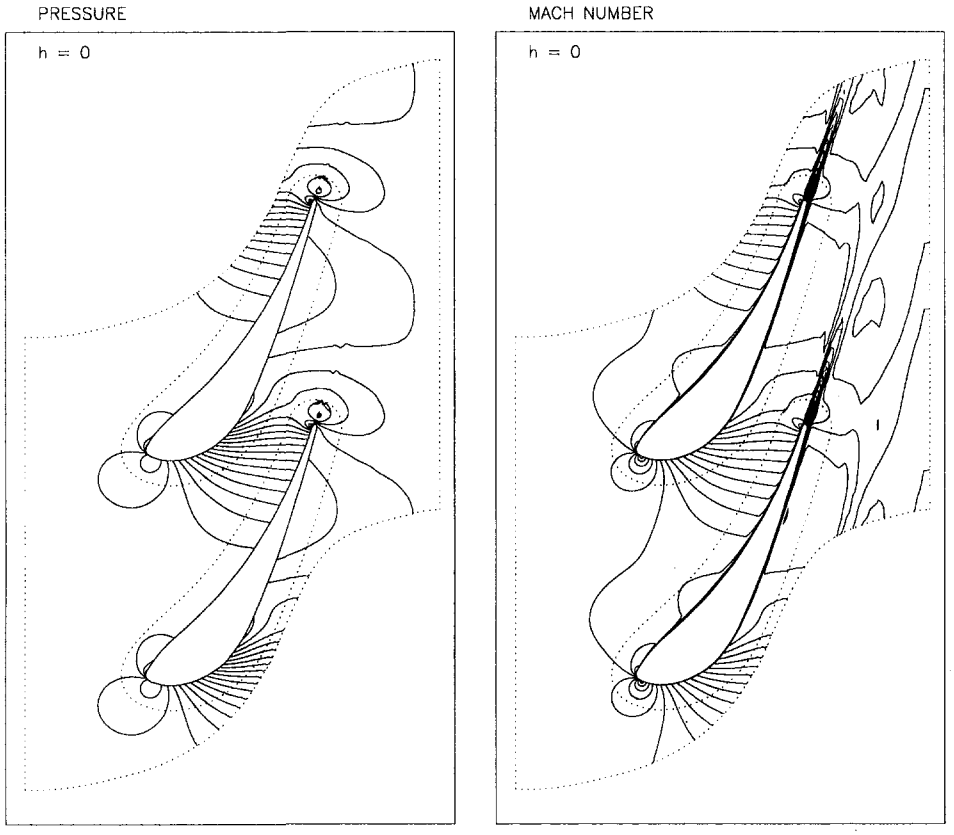

Fig. 5 Steady solution for STC No. 4 configuration, test case 6

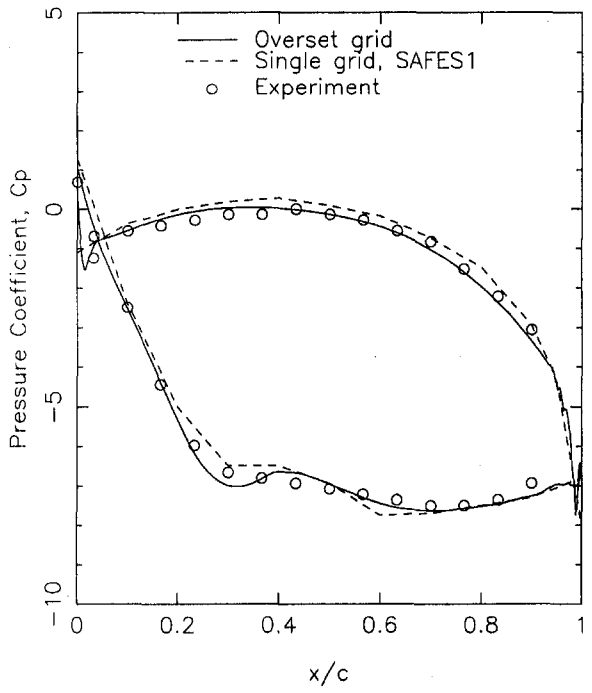

Fig. 6 Steady blade surface pressure distribution for STC No. 4 configuration, test case 6

blade surface and the surface fluid velocity is set equal to the blade plunge velocity. Since the formulation of the Navier–Stokes solver is based on an inertial frame of reference, the vibratory plunging motion of the blades is implemented by traversing the blade grid over the stationary background grid.

Numerical Implementation. The numerical integration in each computational grid is performed using an upwind biased, factorized, iterative, implicit, numerical scheme given by

$$
\begin{aligned}
&[I + h_\xi(\nabla_\xi^b \tilde{A}^+_{i,k} + \Delta_\xi^f \tilde{A}^-_{i,k})]^p \\
&\quad \times [I + h_\zeta(\nabla_\zeta^b \tilde{B}^+_{i,k} + \Delta_\zeta^f \tilde{B}^-_{i,k} - \mathrm{Re}^{-1}\delta_\zeta \tilde{M}_{i,k})]^p \\
&\quad \times (Q^{p+1}_{i,k} - Q^p_{i,k}) \\
&= -(Q^p_{i,k} - Q^n_{i,k}) \\
&\quad - h_\xi(\hat{F}^p_{i+1/2,k} - \hat{F}^p_{i-1/2,k}) \\
&\quad - h_\zeta(\hat{G}^p_{i,k+1/2} - \hat{G}^p_{i,k-1/2}) - \\
&\quad + \mathrm{Re}^{-1} h_\zeta(\hat{S}^p_{i,k+1/2} - \hat{S}^p_{i,k-1/2}) \\
&\quad + (1 - J^n_{i,k}/J^{n+1}_{i,k}) Q^p_{i,k} \qquad (2)
\end{aligned}
$$

In Eq. (2), $h_\xi = \Delta\tau/\Delta\xi$, etc., and $\tilde{A}^\pm = (\partial\tilde{F}/\partial\tilde{Q})$, etc., are the flux Jacobian matrices, J is the Jacobian of the curvilinear transformation, and Δ, ∇, and δ are the forward, the backward, and the central difference operators, respectively. The superscript n denotes the time step and p refers to Newton subiterations within each time step. $\hat{F}_{i+1/2,k}$ and $\hat{G}_{i,k+1/2}$ are numerical inviscid fluxes, which are evaluated using Osher's third-order-accurate upwinding scheme. The inviscid flux Jacobian matrices, $\tilde{A}$ and $\tilde{B}$, on the left-hand side are evaluated by the Steger–Warming flux-vector splitting. The viscous fluxes $\hat{S}_{i,k+1/2}$ are computed with second-order-accurate central differences. The last term on the right-hand side takes the grid deformation into account.

In overset grid solutions, the hole points in the background grid are accommodated by replacing the corresponding coefficient matrices by an identity matrix and by setting the right hand side to zero. This process essentially imposes no change in the flow variables for the hole grid points. One-sided differencing is used at the grid points next to the hole boundary points.

Results and Discussion

We computed unsteady flows through a turbine cascade referred as the Fourth Standard Configuration, STC No. 4 (Bölcs and Fransson, 1986), and through an annular compressor cascade (Schulz and Gallus, 1988). Unsteady solutions were initiated as the blades set into a plunging motion, $h(t)$, in the direction normal to its chord given by

$$h_n = A \sin(2\pi f t + (n-1)\phi)$$

where A is the amplitude, f is the frequency, ϕ is the interblade phase angle, and n refers to the blade number in the passage. In the present computations, $n = 1$ refers to the bottom blade. For all cases, the steady-state solutions were first computed at $t = 0$.

The single passage flows with the direct store interblade boundary conditions were computed by the SAFES1 Navier–Stokes solver developed at Institut für Strahlantriebe und Turboarbeitsmaschinen in Aachen, Germany (Weber et al., 1997). The single-grid version of the present solver was also employed in one of the cases studied.

The SAFES1 code is based on a node-centered finite volume formulation, and employs Roe's flux difference splitting scheme together with the MUSCL technique and van Albada's TVD flux limiter. It solves the implicit system of equations iteratively by using the standard Gauss Seidel or a red-black technique. It has a second-order accuracy in time. Linearization errors and the time accuracy may further be improved by Newton subiterations in each time step. It employs characteristic type boundary conditions at the inlet and the exit boundaries, no-slip condition on the blade surface, and the direct store type time-shifted boundary condition at the interblade boundaries. All the boundary conditions are linearized in time and implemented implicitly.

For out-of-phase, multipassage cascade flows, the direct store boundary condition assumes that all the blades undergo an identical oscillatory flow with a phase shift between neighboring passages, which is based on the interblade phase angle. The flow variables at the interblade boundaries are stored for each period of the computations, and are used in the next period to compute the time-shifted interblade boundary condition. The time-lagged application of the time-shifted boundary condition continues until a convergent solution is obtained.

STC No. 4, Case 6. For this test case, the out-of-phase unsteady motions of the blades are given by $\phi = 180$ deg, $f = 150$ Hz, $A = 0.0032c$. The inlet and the exit conditions are α_{in}

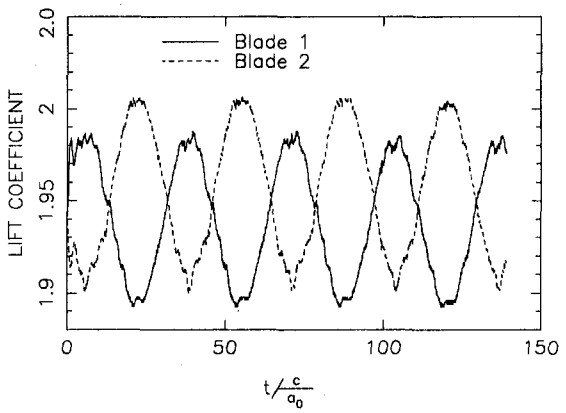

Fig. 7 Time history of the lift coefficient for STC No. 4 configuration, test case 6

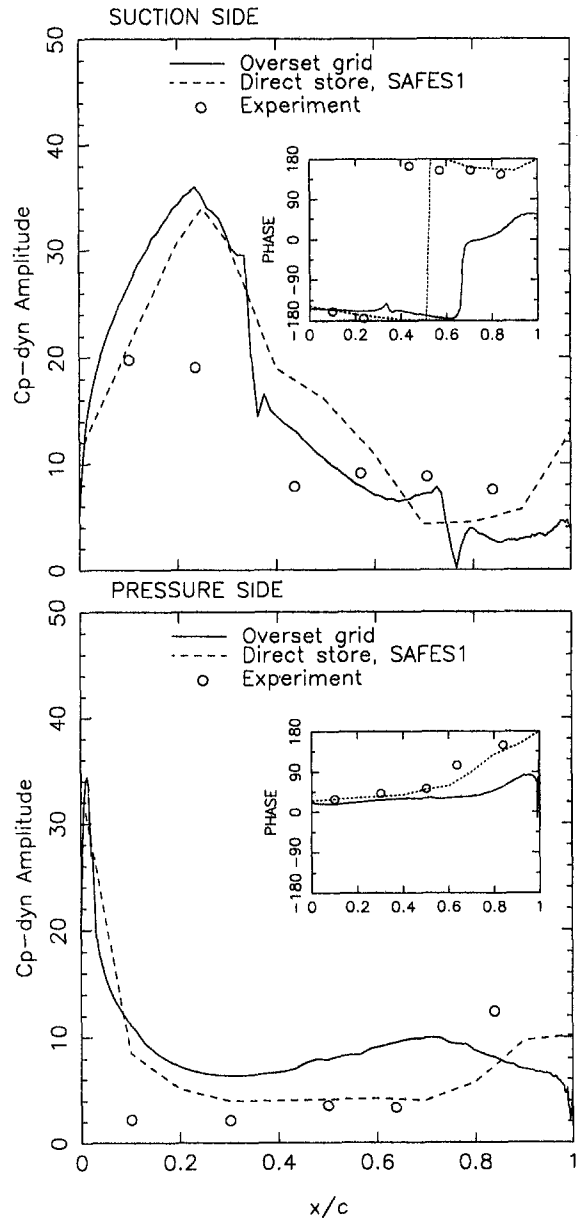

Fig. 8 First harmonic of the unsteady dynamic surface pressure distribution for STC No. 4 configuration, test case

= 50.0 deg, P_0 = 205800 Pa, T_0 = 330.1 K, and P_{exit} = 121,200 Pa.

The overset grids consist of two 266 × 25 size blade grids and a 91 × 123 size background grid as shown in Fig. 1. The grid distribution on the blade surface closely follows that of the single grid used in the SAFES1 computations (Fig. 4), which is of 281 × 33 size. The steady-state solution computed with the overset grids is given in Fig. 5. It is observed that the solution is periodic, and the flow variables have at least a second-order continuity across the intergrid boundaries. The computed surface pressure distribution, given in Fig. 6, also agrees quite well with the single grid SAFES1 prediction and the experimental data.

Next, the unsteady flow was computed as the out-of-phase unsteady motion of blades is introduced and the blade grids are set into the periodic plunging vibrations. The computations were carried out for more than three periods of the plunging motion. The time histories of the lift coefficients for the blades are shown in Fig. 7. It is noted that the periodic and out-of-phase blade loading is quickly attained after the first period. However, it appears that the blade loadings for blades 1 and 2 are not exactly the same as they are out of phase. The asymmetric blade loading may suggest that the overset grid solution captures a possible nonlinear behavior in the flowfield. This is in contrast to the assumption made in the direct store approach that each blade experiences exactly the same flowfield with a certain phase lag.

Figure 8 shows the amplitude and the phase distribution of the first harmonic of the dynamic surface pressure coefficient, C_p-dyn. The amplitude and the phase information are taken

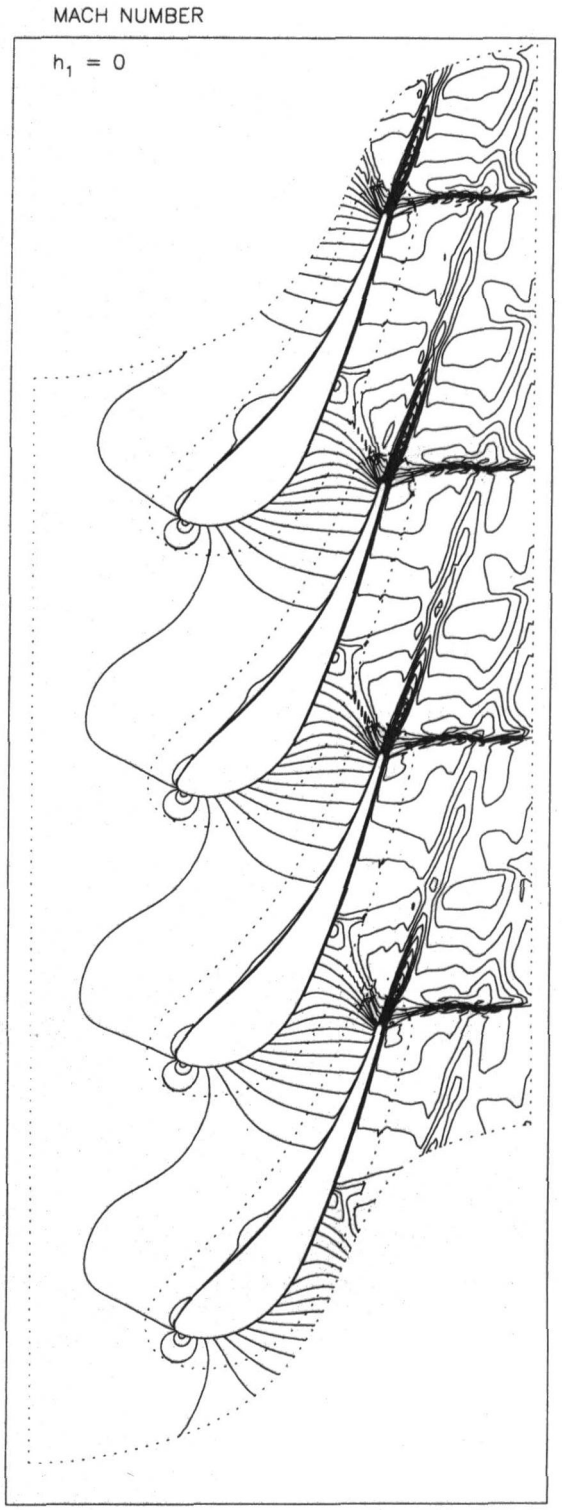

Fig. 9 Steady solution for STC No. 4 configuration, test case 5

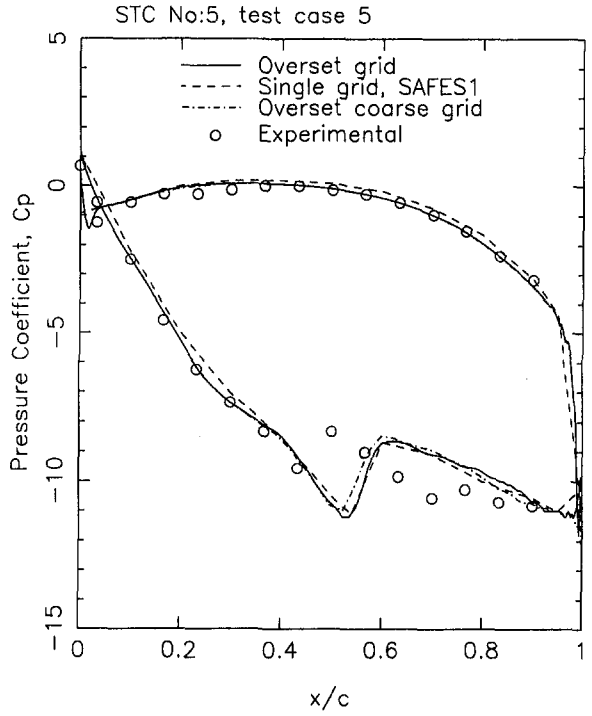

Fig. 10 Steady blade surface pressure distribution for STC No. 4 configuration, test case 5

from the third period of the solution, and they become almost time invariant after the second period of the computations. It should also be noted that the SAFES1 solution belongs to the tenth period of the single passage computations. Although the overset grid solution, in general, agrees reasonably well with the direct store solution of SAFES1 and the experimental data, the prediction of the phase relation downstream of the 60 percent chord diverges. The sudden phase shift on the suction side is also predicted by Abhari and Giles (1997) for the same configuration. We are currently looking into possible causes for this trend.

STC No. 4, Case 5. We next computed the four-passage, transonic cascade flow with $\phi = -90$ deg, $f = 150$ Hz, $A = 0.0030c$, $\alpha_{in} = 50.0$ deg, $P_0 = 219600$ Pa, $T_0 = 329.68$ K, and $P_{exit} = 91400$ Pa. The same grid structure was employed with an extended background grid. A coarser blade grid of 134 × 25 size where the number of grid points in the circumferential direction is reduced by one half was also used for a grid sensitivity study.

Figure 9 shows the steady-state solution in terms of Mach number distribution at $t = 0$. It should be noted that the blades are positioned in accordance with their phase shift. It is observed that in addition to the Mach number distribution, the shock location at the trailing edge is also captured without any discontinuity across the overset grids. The steady pressure distribution on blade 1 is given in Fig. 10. As seen, the overset grid and SAFES1 predictions again agree well. The coarse blade grid prediction also agrees very well with the baseline grid. However, the numerical solutions do not agree with the experimental data on the extension of the expansion fan and the position of the shock reflection on the suction side of the blade. This discrepancy may be attributed to the three-dimensional effects, the underestimation of the boundary layer thickness due to the lack of transition modeling, and a possible slight mismatch at the inlet and exit conditions. An in-depth study is needed for an attempt to understand the nature of the discrepancy.

Since the coarse grid solution resolves the pressure field as well as the finer grid, the coarse grid was employed in the unsteady flow solution. The unsteady flowfield was computed for more than three periods of the blade vibration. Figure 11 similarly shows the distribution of the amplitude and the phase of the first harmonic of the unsteady pressure coefficient on the blade 1 at the third period. It is noted that the overset grid solution produces a significantly better agreement with the experimental data on the suction surface. However, the phase relation on the pressure side lags both the experimental data and the SAFES1 prediction similar to the previous case.

Annular Compressor Blade. In an earlier study (Tuncer and Sanz, 1997) we computed an out-of-phase flow with $\phi = 180$ over an annular compressor blade (Schulz and Gallus, 1988) with overset and staggered grids. The staggered grid solution employed the present Navier–Stokes solver modified for deforming grids. Our computations showed that the two predictions agree well with each other. We now computed the same flowfield with direct store boundary conditions on the single-passage deforming grid. The flow conditions are $f = 500$ Hz, $A = 0.01c$, $\alpha_{in} = 43.85$ deg, $P_0 = 106{,}600$ Pa, $T_0 = 303.7$ K, and $P_{exit} = 101{,}900$ Pa.

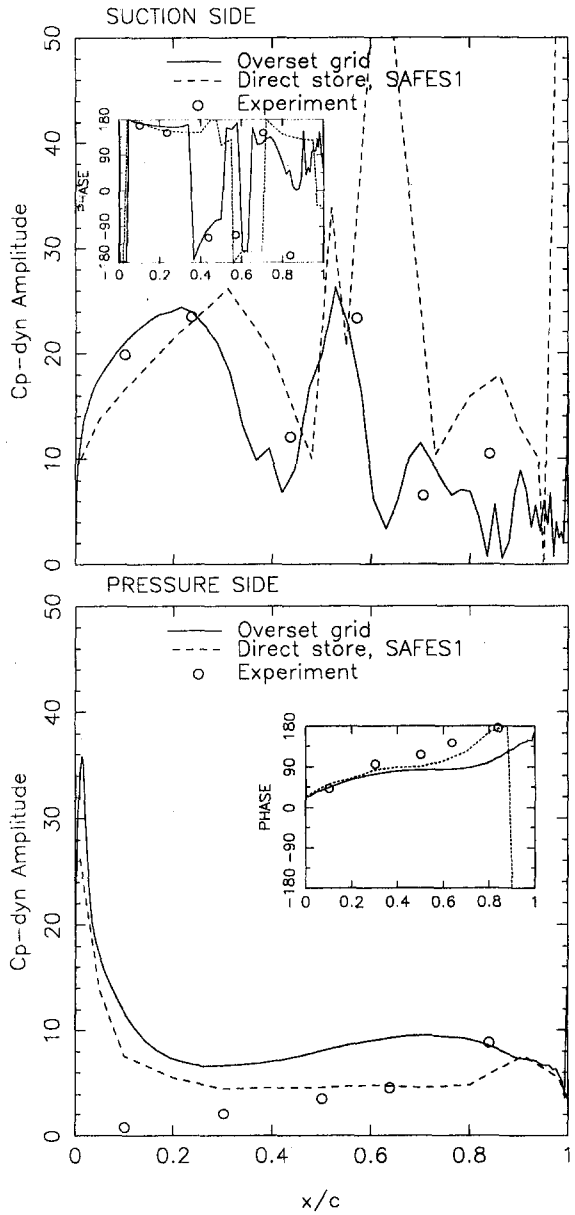

Fig. 11 First harmonic of the unsteady dynamic surface pressure distribution for STC No. 4 configuration, test case 5

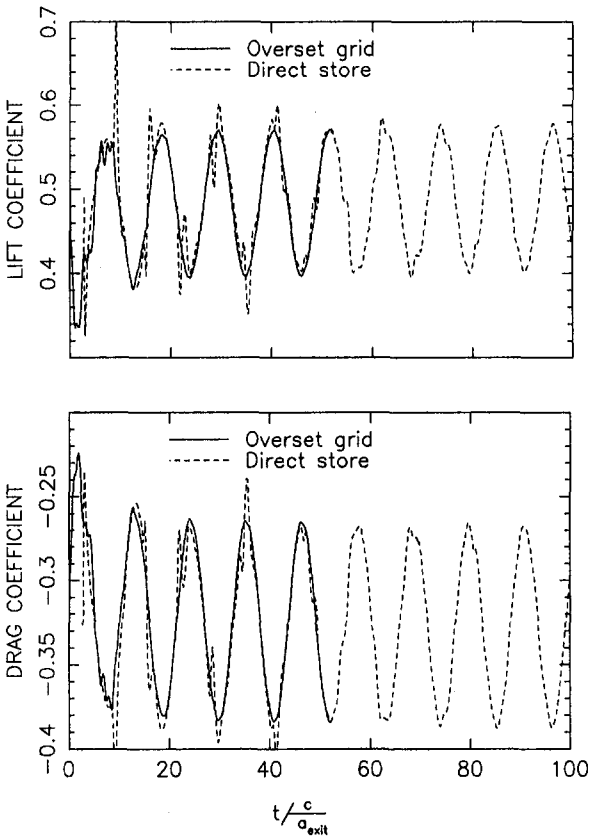

Fig. 12 Computed time histories of the blade loadings for a two-passage annular compressor cascade

Figure 12 shows the time histories of the lift and drag coefficients for blade 1. As seen, after the initial transition the direct store predictions tend to converge to the overset grid predictions. However, the periodic convergence takes more than twice the number of periods needed for the overset grid solution. It should be noted that the total number of grid points for the overset and the single grid domains are 7312 and 7421, respectively (Tuncer and Sanz, 1997). In addition, the application of the intergrid boundary conditions in overset grid solutions takes less than 1 percent of the total CPU per time step, and the implicit solution of two zones is more efficient than a single zone solution with the same number of total grid points. Therefore, the overset grid solutions, in general, have a higher computational efficiency in converging to a periodic solution.

Concluding Remarks

A Navier–Stokes solution method with overset grids has been applied to multipassage, subsonic and transonic cascade flows as the blades undergo out-of-phase vibrations. The computed unsteady blade loadings were, in general, found to be in good agreement with the single-passage solutions with direct store boundary conditions, and the experimental data. The single-passage solutions were obtained with the SAFES1 code, which is based on a finite volume formulation with an iterative solution algorithm, and with the modified version of the present solver.

Although the four-passage overset grid solution produced a better agreement with the experimental data, it appears that the error that may be introduced due to the time linearization of the interblade boundary conditions applied in the direct store method is not significant in the range of the flow conditions studied. However, the overset grid solution method is an alternative in the computation of multipassage cascade flows due to its simplicity in discretizing the flow domains, and in the application of the simple periodic boundary conditions. In addition, the overset grid solutions converge to a periodic blade loading much faster than the direct store solutions due to the discretization of the full periodic domain.

References

Abhari, R.S., and Giles, M., 1997, "A Navier–Stokes Analysis of Airfoils in Oscillating Transonic Cascades for the Prediction of Aerodynamic Damping," ASME JOURNAL OF TURBOMACHINERY, Vol. 119, pp. 77–84.

Ayer, T.C., and Verdon, J.M., 1998, "Validation of a Nonlinear Unsteady Aerodynamic Simulator for Vibrating Blade Rows," ASME JOURNAL OF TURBOMACHINERY, Vol. 120, pp. 112–121.

Bölcs, A., and Fransson, T.H., eds., 1996, "Aeroelasticity in Turbomachines—Comparison of Theoretical and Experimental Cascade Results," Communication de Laboratoire du Thermique Appliquée et de Turbomachines, No. 13, EPFL, Lausanne, Switzerland.

Ekaterinaris, J.A., Cricelli, A., and Platzer, M.F., 1994, "A Zonal Method for Unsteady Viscous, Compressible Airfoil Flows," *Journal of Fluids and Structures,* Vol. 8, pp. 107–123.

Erdos, J.I., Alzner, E.M., and McNally, W., 1977, "Numerical Solution of Periodic Transonic Flow Through a Fan Stage," *AIAA Journal,* Vol. 15, No. 11, pp. 123–149.

Försching, H., 1996, "A Parametric Study of Flutter Stability Characteristics of Turbomachine Cascades," ASME Paper No. 96-GT-260.

Grüber, B., and Carstens, V., 1996, "Computation of the Unsteady Transonic Flow in Harmonically Oscillating Turbine Cascades Taking Into Account Viscous Effects," ASME Paper No. 96-GT-338; ASME JOURNAL OF TURBOMACHINERY, Vol. 120, 1998, pp. 104–111.

He, L., 1998, "Unsteady Flow in Oscillating Turbine Cascades: Part 2—Computational Study," ASME JOURNAL OF TURBOMACHINERY, Vol. 120, pp. 269–275.

Peitch, D., Gallus, H.E., and Weber, S., 1994, "Computation of Unsteady Transonic 3-D Flow in Turbomachinery Bladings," *Proc. 7th International Symposium on Unsteady Aerodynamics and Aeroelasticity of Turbomachines,* Fukuoka, Japan, Sept. 25–29.

Rai, M.M., and Chakravarty, S.R., 1986, "An Implicit Form of the Osher Upwind Scheme," *AIAA Journal,* Vol. 24, No. 5, pp. 735–743.

Schulz, H.G., and Gallus, H.E., 1988, "Experimental Investigation of the Three-Dimensional Flow in an Annular Compressor Cascade," ASME JOURNAL OF TURBOMACHINERY, Vol. 110, pp. 467–478.

Tuncer, I.H., 1996, "A 2-D Navier–Stokes Solution Method With Overset Grids," ASME Paper No. 96-GT-400.

Tuncer, I.H., 1997, "A 2-D Unsteady Navier–Stokes Solution Method With Overset Moving Grids," *AIAA Journal,* Vol. 35, No. 3, pp. 471–476.

Tuncer, I.H., and Sanz, W., 1997, "Computation of Multi-Passage Cascade Flows With Overset and Deforming Grids," ASME Paper No. 97-GT-21.

Verdon, J.M., 1993, "Review of Unsteady Aerodynamic Methods for Turbomachinery Aeroelastic and Aeroacoustic Application," *AIAA Journal,* Vol. 31, No. 2, pp. 235–250.

Weber, S., Benetschik, H., Peitsch, D., and Gallus, H.E., 1997, "A Numerical Approach to Unstalled and Stalled Flutter Phenomena in Turbomachinery Cascades," ASME Paper No. 97-GT-102.

A Nonlinear Numerical Simulator for Three-Dimensional Flows Through Vibrating Blade Rows

H. A. Chuang[1]

J. M. Verdon

Aeromechanical, Chemical, and Fluid Systems,
United Technologies Research Center,
East Hartford, CT 06108

The three-dimensional, multistage, unsteady, turbomachinery analysis, TURBO, has been extended to predict the aeroelastic response of a blade row operating within a cylindrical annular duct. In particular, a blade vibration capability has been incorporated, so that the TURBO analysis can be applied over a solution domain that deforms with a vibratory blade motion. Also, unsteady far-field conditions have been implemented to render the computational inlet and exit boundaries transparent to outgoing unsteady disturbances and to allow for the prescription of incoming aerodynamic excitations. The modified TURBO analysis has been applied to predict unsteady subsonic and transonic flows. The intent is to validate this nonlinear analysis partially for blade flutter applications via numerical results for benchmark unsteady flows, and to demonstrate this analysis for a realistic fan rotor. For these purposes, we have considered unsteady subsonic flows through a three-dimensional version of the 10th Standard Cascade and unsteady transonic flows through the first-stage rotor of the NASA Lewis Rotor 67 fan. Some general correlations between aeromechanical stabilities and fan operating characteristics will be presented.

Introduction

The development of analyses to predict unsteady flows through turbomachinery blade rows has been motivated primarily by the need to predict the aeroelastic (flutter and forced vibration) and aeroacoustic (sound generation and propagation) characteristics of the blading. Accurate and efficient aerodynamic analyses are needed to determine the unsteady loads that act on the blades and the unsteady pressure responses that persist upstream and downstream of the blade row, for various sources of unsteady excitation. The latter include structural (blade) motions and aerodynamic disturbances at inlet and exit that carry energy toward the blade row.

The computational resources required to simulate nonlinear unsteady flows continue to prohibit the use of such simulations in detailed aeroelastic or aeroacoustic design studies. Thus, for the most part, the unsteady aerodynamic analyses that are being used in turbomachinery aeroelastic and aeroacoustic design prediction systems are based on linearized inviscid flow theory (Verdon, 1993), which has evolved to the point that three-dimensional, linearized, Euler analyses are currently being developed (Hall and Lorence, 1993; Montgomery and Verdon, 1997). Linearized viscous analyses are also now becoming available (Clark and Hall, 1995; Holmes et al., 1997). Linear analyses meet the needs of turbomachinery designers for efficient unsteady aerodynamic response predictions. However, of necessity, such analyses ignore potentially important physical features of unsteady flows, including the effects of moderate to large amplitude unsteady excitations and large-scale viscous separations.

Time-accurate, nonlinear, Euler and Reynolds-averaged Navier–Stokes analyses are therefore needed to understand and predict the relative importance of nonlinear and viscous effects on the unsteady flows associated with blade vibration and blade-row noise generation. Since the mid-1980's, a number of such analyses have been developed for turbomachinery configurations. These have been applied to predict unsteady flows through single blade rows due to prescribed blade vibrations (Huff and Reddy, 1989; Ayer and Verdon, 1998; Bahkhle et al., 1997), or to prescribed aerodynamic disturbances at the inflow or outflow boundaries (Giles, 1988; Dorney and Verdon, 1994), and unsteady flows through aerodynamically coupled blade rows (Rai, 1989; Janus and Whitfield, 1989).

The goals of the present effort have been to extend, demonstrate, and validate the TURBO analysis (Janus and Whitfield, 1989; Chen and Whitfield, 1993; Chuang and Verdon, 1998) for blade flutter applications. Earlier, Bakhle et al. (1997) added a moving blade capability to the TURBO code using an algebraic grid motion model. They applied one-dimensional, quasi-unsteady, far-field boundary conditions in all their calculations. In the present version of TURBO, an elliptic solver is used for computing the grid motion, and three-dimensional unsteady eigensolutions are applied in the far field. Thus, in the present version, an implicit, wave-split, finite-volume analysis is applied to predict the unsteady flow in the near field, and this analysis is coupled, at the computational inflow and outflow boundaries, to far-field eigensolutions for unsteady perturbations of fully developed, axisymmetric, mean flows.

The resulting analysis is used to perform parametric studies on unsteady flows through a three-dimensional version of the 10th Standard Cascade (Fransson and Verdon, 1993). In addition, it is applied to study unsteady flow through a transonic fan, the NASA Rotor 67 fan (Strazisar et al., 1989). We have considered inviscid unsteady subsonic and transonic flows excited by prescribed blade vibrations and, for validation purposes, we have compared the TURBO results for 10th Standard Cascade with those based on the two-dimensional, potential-based linearization, LINFLO (Verdon, 1993) and the three-dimensional, linearized Euler analysis, LINFLUX (Montgomery and Verdon, 1997). The predictions indicate that the current version of the three-dimensional TURBO analysis can provide useful and accurate unsteady aerodynamic response information for realistic turbomachinery configurations.

Unsteady Flow Through a Blade Row

We consider the flow, with negligible viscous and body forces, of a perfect gas with constant specific heat through a

[1] Present address: Pratt & Whitney, East Hartford, CT 06108.

Contributed by the International Gas Turbine Institute and presented at the 43rd International Gas Turbine and Aeroengine Congress and Exhibition, Stockholm, Sweden, June 2–5, 1998. Manuscript received by the International Gas Turbine Institute February 1998. Paper No. 98-GT-18. Associate Technical Editor: R. E. Kielb.

rotating and vibrating blade row that operates within a stationary annular duct. The duct is of infinite axial extent and has hub and duct radii, $r = r_H$ and $r = r_D$, respectively, and the blade row consists of N_B blades, which rotate about the duct axis at constant angular velocity $\Omega = \Omega e_\xi$. We assume that the flows far upstream and far downstream from the blading are at most small perturbations of fully developed, axisymmetric, steady background flows, and that in the absence of a vibratory motion, the blades are identical in shape, equally spaced around the rotor, and identical in orientation relative to the axisymmetric inlet flow.

We intend to resolve the unsteady flow numerically, in terms of curvilinear spatial coordinates, on a computational grid that rotates with the blade row and deforms with the vibratory blade motion. The vector $\mathscr{R}(\bar{\mathbf{x}}, t)$ describes the displacement of a moving field (grid) point, $\mathbf{x}$, relative to its reference or mean position, $\bar{\mathbf{x}}$, in the rotating frame. The displacement field, $\mathscr{R}$, is prescribed so that the solution domain deforms with the vibratory motions of the blades and is rigid far from the blade row.

For aeroelastic applications, we are usually interested in a restricted class of unsteady flows: those in which the unsteady fluctuations can be regarded as disturbances to a background flow that is steady in a blade-fixed, rotating reference frame. Moreover, the steady background flows at axial distances far upstream and far downstream from the blade row can be assumed to consist of at most a small steady perturbation from a fully developed, axisymmetric, steady flow. In the present study, we assume the time-dependent or unsteady fluctuations arise from prescribed vibratory blade motions. The interblade phase angle, σ, of this motion is given by $\sigma = 2\pi N_D/N_B$, where $|N_D|$, the number of nodal diameters, is the integral count of the number of times the vibrating disturbance pattern repeats around the wheel. The sign of N_D is determined by the direction of rotation of the disturbance pattern. If this pattern moves in the direction of blade rotation, then $N_D > 0$. We should note that the unsteady flow will be periodic over N_P blade passages, where $N_P = N_B/|N_D|$, $N_D \neq 0$.

Fluid Dynamic Governing Equations

In this discussion, all variables are dimensionless. To allow convenient comparisons between two-dimensional and three-dimensional solutions at midspan, the reference length used in the nondimensionalization is the blade chord at midspan; the reference density and flow speed are the inlet mean density and mean relative flow speed at midspan, respectively.

The field equations that govern the unsteady flow are determined from the conservation laws for mass, momentum, and energy, and the thermodynamic relations for a perfect gas. For turbomachinery configurations, these equations are usually cast in cylindrical coordinates, $\mathbf{x} = (r, \theta, \xi)$. However, it is convenient to solve these field equations in terms of body-fitted curvilinear spatial coordinates $(\alpha_1, \alpha_2, \alpha_3)$ and the time $\tau = t$, where the positive directions of α_1, α_2 and α_3 coordinate curves generally point in the streamwise, spanwise (hub-to-tip), and pitchwise directions. Thus, we arrive at the following form of the Euler equations:

$$\left.\frac{\partial \hat{\tilde{\mathbf{U}}}}{\partial \tau}\right|_{\alpha} + \frac{\partial}{\partial \alpha_j}\hat{\tilde{\mathbf{F}}}_j = \hat{\tilde{\mathbf{S}}}, \tag{1}$$

where

$$\hat{\tilde{\mathbf{U}}} = J^{-1}\tilde{\mathbf{U}}, \quad \hat{\tilde{\mathbf{F}}}_j = J^{-1}\left(\frac{\partial \alpha_j}{\partial t}\tilde{\mathbf{U}} + \frac{\partial \alpha_j}{\partial x_k}\tilde{\mathbf{F}}_k\right), \quad \hat{\tilde{\mathbf{S}}} = J^{-1}\tilde{\mathbf{S}} \tag{2}$$

and J is the Jacobian of the transformation $(\mathbf{x}, t) \rightarrow (\boldsymbol{\alpha}, \tau)$.

The state, $\tilde{\mathbf{U}}$, flux, $\tilde{\mathbf{F}}_j$, $j = 1, 2, 3$, and source term, $\tilde{\mathbf{S}}$, vectors in Eqs. (1) and (2) are given by

$$\tilde{\mathbf{U}} = \begin{bmatrix} \tilde{\rho} \\ \tilde{\rho}\tilde{\mathbf{V}}_{x_1} \\ \tilde{\rho}\tilde{\mathbf{V}}_{x_2} \\ \tilde{\rho}\tilde{\mathbf{V}}_{x_3} \\ \tilde{\rho}\tilde{E}_T \end{bmatrix}, \quad \tilde{\mathbf{F}}_j = \begin{bmatrix} \tilde{\rho}\tilde{\mathbf{V}}_{x_j} \\ \tilde{\rho}\tilde{\mathbf{V}}_{x_1}\tilde{\mathbf{V}}_{x_j} + \tilde{P}\delta_{1j} \\ \tilde{\rho}\tilde{\mathbf{V}}_{x_2}\tilde{\mathbf{V}}_{x_j} + \tilde{P}\delta_{2j} \\ \tilde{\rho}\tilde{\mathbf{V}}_{x_3}\tilde{\mathbf{V}}_{x_j} + \tilde{P}\delta_{3j} \\ \tilde{\rho}(\tilde{E}_T + \tilde{P}/\tilde{\rho})\tilde{\mathbf{V}}_{x_j} \end{bmatrix},$$

and

$$\tilde{\mathbf{S}} = \Omega \begin{bmatrix} 0 \\ 0 \\ \tilde{\rho}(2\tilde{V}_{x_3} + \Omega x_2) \\ -\tilde{\rho}(2\tilde{V}_{x_2} - \Omega x_3) \\ \tilde{\rho}\Omega(x_2\tilde{V}_{x_2} + x_3\tilde{V}_{x_3}) \end{bmatrix}, \tag{3}$$

where $\tilde{\rho}$, $\tilde{\mathbf{V}}$, $\tilde{E}_T = \tilde{E} + \tilde{V}^2/2$ and $\tilde{P} = (\gamma - 1)\tilde{\rho}(\tilde{E}_T - \tilde{V}^2/2)$ are the fluid density, relative velocity, relative specific total internal energy, and pressure, respectively, and γ is the specific heat ratio of the fluid.

Boundary Conditions. For turbomachinery applications, the field equations (1) must be supplemented by boundary conditions at blade surfaces and at duct walls, and periodicity and far-field conditions at the computational inflow and outflow boundaries. On the nth moving blade surface, $\mathscr{B}_n$, the Euler equations are solved subject to flow tangency conditions

$$(\tilde{\mathbf{V}}^{\text{abs}} - \boldsymbol{\Omega} \times \mathbf{r} - \dot{\mathscr{R}}_{\mathscr{B}_n}) \cdot \mathbf{n} = 0 \quad \text{for} \quad \mathbf{x} \in \mathscr{B}_n \tag{4a}$$

and, at the duct walls,

$$\tilde{\mathbf{V}}^{\text{abs}} \cdot \mathbf{n} = 0 \quad \text{for} \quad r = r_H, r_B \tag{4b}$$

The solution must also be subject to periodicity conditions, e.g., over N_P blade passages $\tilde{\mathbf{V}}(r, \theta + 2\pi N_P/N_B, \xi) = \mathbf{T}_{N_P}\tilde{\mathbf{V}}(r, \theta, \xi)$, where $\mathbf{T}_{N_P}$ rotates vectors through N_P passages.

Since transient unsteady aerodynamic behaviors are usually not of interest, a precise knowledge of the initial state of the fluid is not required. Temporally and circumferentially averaged values of the total temperature, the total pressure, and the flow angle are specified as functions of radius at the computational inflow boundary, and the temporally and circumferentially averaged pressure is specified at the outflow boundary, consistent with radial equilibrium. The unsteady fluctuations that carry energy away from the blade row must be determined as part of the nonlinear unsteady solution. A brief discussion of the far-field boundary conditions will be presented in the Far-Field Eigenanalyses section, below.

Displacement Field. The displacement field, $\mathscr{R}$, is assumed to vary harmonically with time, i.e., $\mathscr{R}(\bar{\mathbf{x}}, t) = \text{Re}\{\mathbf{R}(\bar{\mathbf{x}}) \exp(i\omega t)\}$. The complex amplitude of this field, $\mathbf{R}(\bar{\mathbf{x}})$, must be prescribed over the entire solution domain. In the present study, $\mathbf{R}$ is defined so that the solution domain deforms with the blade motion (i.e., $\mathbf{R} = \mathbf{R}_{B_n}$ for $\bar{\mathbf{x}} \in B_n$, where B_n is the mean position of the nth blade), slides along the hub and duct walls ($\mathbf{R} \cdot \mathbf{n} = \mathbf{0}$ for $\bar{r} = r_H, r_D$), and remains rigid far from the blade row ($\mathbf{R} \equiv \mathbf{0}$ for $\bar{\xi} \lesseqgtr \bar{\xi}_{\mp}$). In addition, $\mathbf{R}(\bar{\mathbf{x}})$ is prescribed along one blade-to-blade periodic boundary, such that it is continuous at the blade leading and trailing edges and decays exponentially away from the blade row. At the other periodic boundary, $\mathbf{R}$ is set so as to satisfy the periodicity condition.

In the near field, $\mathbf{R}(\bar{\mathbf{x}})$ is first determined along the hub and duct walls, and then, in the interior of the computational domain as solutions of Laplace's equation, $\nabla^2_{\bar{\mathbf{x}}}\mathbf{R} = \mathbf{0}$, in two dimensions. It is then determined in the interior of the computational domain as a solution of Laplace's equation in three dimensions, subject to Dirichlet boundary conditions, given above.

Finite-Volume Analysis

The near-field, finite-volume analysis is performed in a stationary reference frame, i.e., $\tilde{\mathbf{S}} = 0$ in the matrix equation (1).

A flux split, finite-volume analysis for nonlinear, inviscid, unsteady flows has been developed and implemented into the turbomachinery unsteady flow code, TURBO (Janus and Whitfield, 1989). This analysis was later modified for the prediction of viscous flows (Chen and Whitfield, 1993), and extended, under the present effort, for blade aeroelastic applications (Chuang and Verdon, 1998). TURBO is an implicit, multiblock, cell-centered, finite-volume code that can be used to predict three-dimensional, nonlinear, inviscid and viscous, steady and unsteady flows through and around blade rows. The fluid dynamic equations are solved in a stationary reference frame over a solution domain that rotates with the blade row and deforms with the vibratory blade motions. Additional information can be found in the references cited above.

The computational mesh used in TURBO is a sheared *H*-mesh, typically generated using either the IGB (Beach and Hoffman, 1992) or the TIGER (Soni and Shih, 1991) grid generation packages. A time-dependent coordinate transformation, $(\mathbf{x}, t) \rightarrow (\boldsymbol{\alpha}, \tau)$, where $\mathbf{x} = \bar{\mathbf{x}} + \mathscr{R}(\bar{\mathbf{x}}, t)$, from the rotating physical domain, in which the grid deforms with the blade motion, to a computational domain, in which the grid is stationary, uniform, and orthogonal, is applied to simplify the implementation of numerical differencing and flow boundary conditions.

Far-Field Eigenanalyses

Far-field solutions, based on reduced sets of governing equations, are applied to restrict axial extent of the near-field computational domain. These solutions ensure that outgoing disturbances, i.e., disturbances that travel away from the blade row, pass through the computational inflow and outflow boundaries without spurious reflections. Such reflections would contaminate the numerical solutions. To develop the far-field solutions, we first expand the unsteady-state vector, $\tilde{\mathbf{U}}$, into an asymptotic series of the form

$$\begin{aligned}\tilde{\mathbf{U}}[x, t] &= \mathbf{U}(\mathbf{x}) + \tilde{\mathbf{u}}(\mathbf{x}, t) + \ldots \\ &= \mathbf{U}(\mathbf{x}) + \mathrm{Re}\{\mathbf{u}(\mathbf{x}) \exp(i\omega t)\} + \ldots, \qquad (5)\end{aligned}$$

where the column vectors $\mathbf{U}(\mathbf{x})$ and $\tilde{\mathbf{u}}(\mathbf{x}, t)$ contain the conservation variables for the zeroth-order background flow, which is steady in the rotating frame, and a first-order unsteady perturbation, respectively, and the dots refer to higher order terms. The components of the vector $\mathbf{u}$ are the complex amplitudes of the first-order unsteady conservation variables, i.e., $\mathbf{u}^T = [\rho, \bar{\rho}v_r + \rho V_r, \bar{\rho}v_\theta + \rho V_\theta, \bar{\rho}v_\xi + \rho V_\xi, \bar{\rho}e_T + \rho E_T]$ where $\bar{\rho}$, $\mathbf{V}$, and E_T and ρ, $\mathbf{v}$, and e_T are the steady and the complex amplitudes of the first-order unsteady, primitive flow variables, respectively. Also, we assume that, far from the blade row, the mean or steady flow quantities are dependent only on radial position; i.e., $\bar{\rho} = \bar{\rho}(r)$, $P = P(r)$, etc., and that the radial component of the steady velocity is negligible; i.e., $\mathbf{V} = V_\theta(r)\mathbf{e}_\theta + V_\xi(r)\mathbf{e}_\xi$.

After substituting the foregoing series expansion into the nonlinear, time-dependent Euler equations and simplifying the equations, we find that the field equations, expressed in terms of rotating cylindrical coordinates (r, θ, ξ), governing first-order unsteady flow have the form

$$i\omega\mathbf{u} + r^{-1}\frac{\partial(r\mathbf{A}_2\mathbf{u})}{\partial r} + r^{-1}\mathbf{B}_2\frac{\partial\mathbf{u}}{\partial\theta} + \mathbf{C}_2\frac{\partial\mathbf{u}}{\partial\xi} - \mathbf{D}\mathbf{u} = 0, \qquad (6)$$

where $\mathbf{A}_2 = \partial\mathbf{F}_r/\partial\mathbf{U}|_{U_2=0}$, $\mathbf{B}_2 = \partial\mathbf{F}_\theta/\partial\mathbf{U}|_{U_2=0}$ and $\mathbf{C}_2 = \partial\mathbf{F}_\xi/\partial\mathbf{U}|_{U_2=0}$ are flux Jacobian matrices evaluated at $U_2 = \bar{\rho}V_r = 0$, $\mathbf{D} = \partial\mathbf{S}/\partial\mathbf{U}$ is the source-term Jacobian, and $\mathbf{F}_r$, $\mathbf{F}_\theta$ and $\mathbf{F}_\xi$ are the radial, tangential and axial fluxes.

For general, nonuniform steady background flows, approximate solutions to the linearized unsteady Eq. (6) can be constructed as a sum of convective and modal disturbances. By assuming the modal disturbances to have a Fourier series form, Eq. (6) yields an eigenvalue problem, which must be solved numerically. For a detailed description of the implementation of the far-field eigenanalysis of Eq. (6), we refer the reader to Montgomery and Verdon (1997). In the same paper, the near-field/far-field matching procedure is also described.

Numerical Results

Unsteady aerodynamic response predictions will be presented to demonstrate the current capabilities of the TURBO code. First, we will consider subsonic unsteady flows through a rotor, based on the Tenth Standard Cascade Configuration (Fransson and Verdon, 1993), which is referred to by Montgomery and Verdon (1997) as the 3D 10th Standard Cascade. Second, we will analyze the NASA Rotor 67 (Strazisar et al., 1989), which is a research transonic fan consisting of 22 blades.

We consider unsteady flows that are excited by prescribed single-degree-of-freedom, harmonic blade motions. The motions to be considered are pure rotations about axes at the blade midchords $(\mathbf{R}_B(\bar{\mathbf{x}}_B) = \alpha\mathbf{e}_r \times (\bar{\mathbf{x}}_B - \bar{\mathbf{x}}_P))$. The complex amplitude, α, of the torsional vibrations is assumed to be constant along the span; and $\bar{\mathbf{x}}_B - \bar{\mathbf{x}}_P$ is the distance, at constant radius, to the point, $\bar{\mathbf{x}}_B(r)$, on the mean or reference blade surface from the point, $\bar{\mathbf{x}}_P(r)$, at the mean position of the torsional axis.

These blade motions are termed subresonant if all fundamental acoustic response disturbances attenuate with increasing axial distance from the blade row; superresonant if such disturbances persist in the far upstream and far downstream flow regions and carry energy away from the blade row; and resonant if at least one acoustic response disturbance persists in either the far upstream or far downstream regions of the flow and carries energy along the blade row (Verdon, 1989b).

The TURBO analysis has been applied to predict unsteady surface pressure and the local (w_C) and global (W_C) work per cycle responses to the prescribed blade vibrations. The local and global works per cycle are determined from the relations

$$w_C(\mathbf{x}_{\mathscr{B}}) = -\omega^{-1}\int_{\phi}^{\phi+2\pi} P_{\mathscr{B}}\frac{\partial\mathscr{R}_B}{\partial t}\cdot\mathbf{n}_{\mathscr{B}}\,d(\omega t)$$

and

$$W_C = \oint_{\mathscr{B}} w_C(\mathbf{x}_{\mathscr{B}})\,dA_{\mathscr{B}}. \qquad (7)$$

In Eq. (7), $P_{\mathscr{B}}$ is the pressure acting at the point $\mathbf{x}_{\mathscr{B}}$ on the moving reference blade surface $\mathscr{B}$, $\mathscr{R}_B$ is the displacement of this point relative to its mean position in the rotating frame, $\mathbf{n}_{\mathscr{B}}$ is a unit vector normal to $\mathscr{B}$ and pointing into the fluid, and $dA_{\mathscr{B}}$ is a differential element of surface area.

In addition to the nonlinear TURBO results, for purposes of comparison, we will also present response predictions for the three-dimensional 10th Standard cascade based on the two-dimensional linearized analysis, LINFLO (Verdon, 1993) and three-dimensional linearized analysis, LINFLUX (Montgomery and Verdon, 1997). In LINFLO, the unsteady flow is regarded as a small perturbation of a nonuniform, potential, steady background flow. The full-potential analysis CASPOF (Caspar, 1983) has been used to provide the steady background flows for the LINFLO calculations. In LINFLUX, the unsteady flow is regarded as a small perturbation of a nonuniform, Euler, steady background flow. The TURBO analysis has been used to provide the steady background flows for the LINFLUX calculations.

The TURBO nonlinear steady-state solutions are determined, over a single extended blade passage, on an H-type grid. Since the TURBO code is written in terms of absolute-frame variables, the steady-state solutions for both numerical examples are obtained by marching the calculations in a time-accurate manner. These solutions are then used as inputs for both the unsteady TURBO computations as well as the linearized LINFLUX computations. The unsteady TURBO solutions are computed over

single or multiple blade passages, depending on the interblade phase angle.

Three-Dimensional 10th Standard Configuration. The three-dimensional Tenth Standard Cascade consists of 24 blades, which are twisted to reduce the variation in mean incidence due to blade rotation. The blades rotate within a cylindrical annular duct of inner radius $r_H = 3.395$ and outer radius $r_D = 4.244$. At midspan ($r = r_M$), the blades are staggered at $\Theta(r_M) = 45$ deg with a circumferential spacing, $G(r_M) = 2\pi r_M / N_B$, of unity, and the midspan blade section is a NACA 5506 airfoil, altered slightly (Verdon, 1989a) to have wedge-shaped trailing edges.

The mean blade chord lines are located at

$$r\theta = \xi \tan \Theta + nG(r), \quad 0 \le \xi \le \cos \Theta, \quad n = 0, \ldots, N_B - 1, \quad (8)$$

where

$$\frac{\tan \Theta(r)}{\tan \Theta(r_M)} = \frac{r}{r_M}. \quad (9)$$

The axial chord is constant, hence, the leading and trailing edge ξ and θ coordinates are constant along the entire span. The airfoil chord varies from 0.946 at the hub to 1.057 at the tip, because of twist, and the local thickness to chord ratio varies to maintain constant thickness. The cascade operates in a uniform axial inlet flow, which occurs at $M_{-\infty}^{abs} = 0.4015$, and rotates at an angular speed of $|\Omega| = 0.2145$. This three-dimensional configuration was chosen to match the subsonic Tenth Standard Configuration (Fransson and Verdon, 1993) at midspan, where the relative inlet Mach number, $M_{-\infty}$, is 0.7 and the relative inlet flow angle, $\Omega_{-\infty}$, is 55 deg.

The H-grid for the three-dimensional Tenth Standard Cascade, Fig. 1, consists of 141 axial, 41 tangential, and 11 radial surfaces (56,000 cells), and extends approximately one axial chord upstream and downstream from the blade row. This is identical to the grid used in the three-dimensional LINFLUX studies of Montgomery and Verdon (1997). Axial grid points are clustered near blade leading and trailing edges; circumferential grid points, near blade surfaces; and radial points are distributed uniformly. In particular, the normal and chordwise grid spacings at a blade leading edge are 0.02 and 0.10 percent of chord, respectively.

The axial extent of the grid was found to be sufficient for the mean flow field to reach axisymmetric steady states at the computational inflow and outflow boundaries. There are 81 axial points on the upper and lower blade surfaces, and 30 axial points on the upstream and downstream periodic boundaries. This distribution was found to be sufficient for the three-dimensional Tenth Standard Cascade calculations reported herein, with approximately 20 points per wave being applied to resolve the dominant acoustic waves.

The TURBO near-field, finite-volume solutions have been coupled to far-field acoustic eigensolutions, which have been determined on a radial grid consisting of 24 points clustered near the hub and duct walls. For the present calculations, any nearly convected disturbances that occur downstream of the blade row are simply convected numerically through the computational outflow boundary and into the far downstream region of the flow.

The three-dimensional Tenth Standard Cascade solutions, reported herein, were determined on an IBM-3CT Workstation. TURBO, "time-accurate," steady, subsonic, inviscid solutions required 780 CPU minutes per 1000 time steps and a minimum of 1500 to 2000 time steps to converge. The TURBO unsteady calculations were started from the steady solution, and performed using 500 time steps per cycle of blade motion and four Newton iterations per time step. For single-passage solutions, six to eight cycles of motion were needed to converge the nonlinear inviscid solutions to a periodic state. The subsonic inviscid calculations required 350 CPU minutes per blade passage per cycle of blade motion. The number of blade passages included in a nonlinear unsteady calculation depends upon the interblade phase angle. For example, if $\sigma = 60$ deg, six passages are needed.

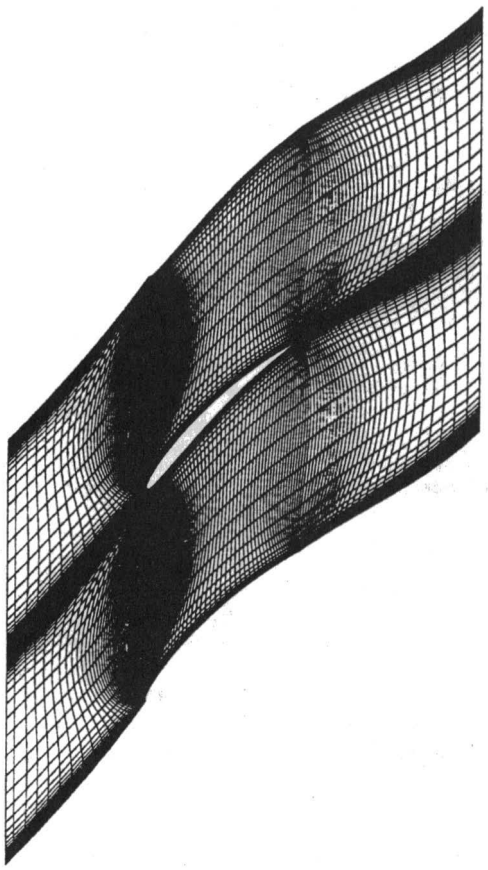

Fig. 1 TURBO computational grid at midspan for the three-dimensional 10th Standard Cascade

TURBO nonlinear steady and unsteady calculations require approximately 1350 μs/time step/cell with four subiterations. The memory requirement, using 32-bit arithmetic, is approximately 1.8 kilobytes/cell. This requirement is based on the option of using two blocks per blade passage and in-core storage for all variables.

Steady Flow. Predicted distributions of relative, steady, isentropic, surface, Mach number, based on local static pressure $[P(r, \theta, \xi)]$ and local, inlet, relative total pressure $[P_{T,-\infty}(r)]$, i.e.,

$$M = \left\{ \frac{2}{\gamma - 1} \left[\left(\frac{P_{T,-\infty}}{P} \right)^{(\gamma-1)/\gamma} - 1 \right] \right\}^{1/2}, \quad (10)$$

for the three-dimensional and two-dimensional, 10th Standard Cascades, are shown in Fig. 2. The inlet and exit, mean-flow quantities for the three-dimensional calculation are given in Fig. 3. For the CASPOF, full potential calculation, the relative inlet Mach number, $M_{-\infty} = 0.7$, and inlet flow angle, $\Omega_{-\infty} = 55$ deg, are prescribed and a Kutta condition is imposed at the blade trailing edges. For the TURBO calculation, the mean-flow, total pressure, total temperature, and inlet flow angle are specified at the computational inlet boundary, and the mean-flow static pressure at the hub is specified at the computational exit boundary, so that the relative inlet flow at midspan matches the two-dimensional conditions.

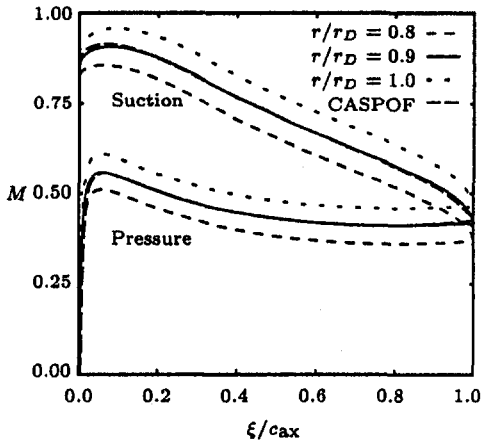

Fig. 2 Relative isentropic surface mach number distribution for the three-dimensional 10th Standard Cascade ($M^{abs}_{-\infty}$ = 0.4015, $|\Omega|$ = 0.2145)

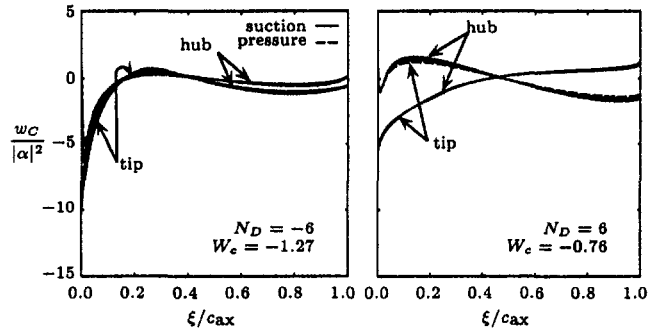

Fig. 4 Local work per cycle distributions at all spanwise stations and global works per cycle for the three-dimensional 10th Standard Cascade undergoing pure torsional vibrations about midchord at ω = 1 and $\sigma = \mp 90$ deg ($N_D = \mp 6$)

The TURBO steady-flow predictions at the hub, r/r_D = 0.8, midspan, r/r_D = 0.9, and tip, r/r_D = 1.0, given in Fig. 2, indicate that the Mach numbers on the blade suction and pressure surfaces show moderate variations with radius. Also, the three-dimensional TURBO predictions at midspan are in close agreement with the two-dimensional CASPOF predictions. In the three-dimensional TURBO solution, the flow is very close to Mach one in the tip region, along a blade suction surface just aft of the leading edge.

For the three-dimensional flow, the steady pressure (P = 1.4577), density ($\bar{\rho}$ = 1.0), and axial velocity (V_ξ = 0.5736) have constant values at inlet and the relative circumferential velocity, $V_\theta = -\Omega r$ varies linearly from 0.7283 at the hub to 0.9103 at the tip. At the computational exit boundary, the steady pressure, density, and axial velocity vary with radius (mean shear), and the circumferential velocity varies nonlinearly with radius (mean swirl). As indicated in Fig. 3, the steady blade loading causes increases in the pressure and density and decreases in the axial and circumferential velocities, especially the latter.

Blade Vibration. The three-dimensional TURBO and LINFLUX analyses and the two-dimensional LINFLO analysis have been applied to predict the unsteady aerodynamic responses of the three-dimensional and two-dimensional 10th Standard Cascades to pure bending and pure torsional blade vibrations at unit frequency. For a linearized analysis, the far-field conditions are determined based on the input mean flow before the unsteady computation begins. However, in the nonlinear TURBO analysis, a converged solution, which is steady in the rotating frame of reference, is used as the initial solution for an unsteady computation. Temporal Fourier decompositions of the flow quantities at inlet and exit are performed as the solution is marched in time. The temporal Fourier coefficients are updated N times per cycle, where N is a user input. The results in this paper have been determined using five updates per cycle. Thus, the far-field conditions are determined based on the most current temporal Fourier coefficients. Ideally, the zero-frequency, temporal Fourier coefficients should correspond to the initial mean flow. However, the back pressures used for all the unsteady TURBO calculations are the same as the back pressure used in the mean-flow calculation. As a result, the mean mass flow for different unsteady cases can differ by as much as 1 percent of the steady mass flow. One could maintain the same mean mass flow by adjusting the back pressure for each unsteady run, but this would be laborious and time consuming computationally.

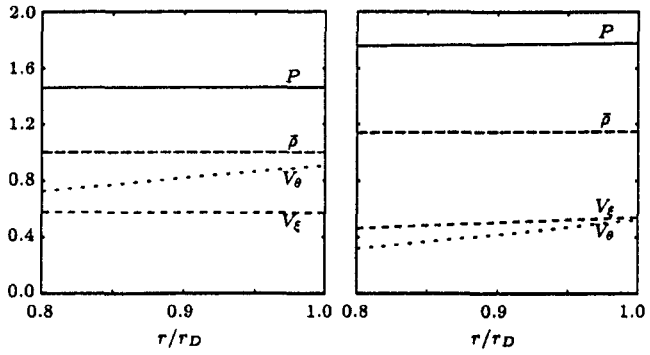

Fig. 3 Relative frame steady flow properties far upstream and far downstream of the three-dimensional 10th Standard Cascade ($M^{abs}_{-\infty}$ = 0.4015, $|\Omega|$ = 0.2145)

In the current three-dimensional TURBO analysis, two to three temporal harmonics are retained in the far-field solutions to minimize the reflection of outgoing transient higher harmonic waves back into the solution domain. Unfortunately, the initial impulsive blade motion appears to have generated anharmonic and higher harmonic waves. Some of these waves are reflected, and the reflections ultimately result in slight blade-to-blade variations in the work-per-cycle response. Therefore, for multipassage solutions, the local and global work-per-cycle predictions shown in this paper are the average of the corresponding values on each blade. In spite of these blade-to-blade variations, the higher harmonic terms are usually small compared to the first harmonic. Thus, the classification of sub- or superresonant unsteady motion is based on the propagation properties of the fundamental (i.e., first-harmonic) acoustic disturbances.

Local (w_C) and global (W_C) work-per-cycle predictions for the three-dimensional 10th Standard Cascade undergoing pure torsional at ω = 1 and $\sigma = \pm 90$ deg ($N_D = \pm 6$) are shown in Fig. 4, where the TURBO local response predictions are given at eleven spanwise stations from hub (r/r_D = 0.8) to tip (r/r_D = 1.0). These results indicate that the local work per cycle responses to the blade torsional vibrations do not vary significantly with radius. Since the multipassage TURBO solutions show slight blade-to-blade variations, the local work-per-cycle predictions shown in Fig. 4 are those on the reference blade, and the global work-per-cycle predictions are the averaged values.

The averaged local work-per-cycle predictions at midspan, as determined from the three-dimensional TURBO, LINFLUX and the two-dimensional LINFLO predictions, for the 10th Standard Cascade vibrating in torsion are shown in Fig. 5, for blade motions at unit frequency and at interblade phase angles, σ, of −90 deg, 0 deg, +90 deg, and +180 deg. The motions at σ = 0 and 90 deg are superresonant. For the in-phase motions at σ = 0 deg, propagating first-harmonic acoustic response disturbances, at (m, μ) = (0, 0), occur both upstream and down-

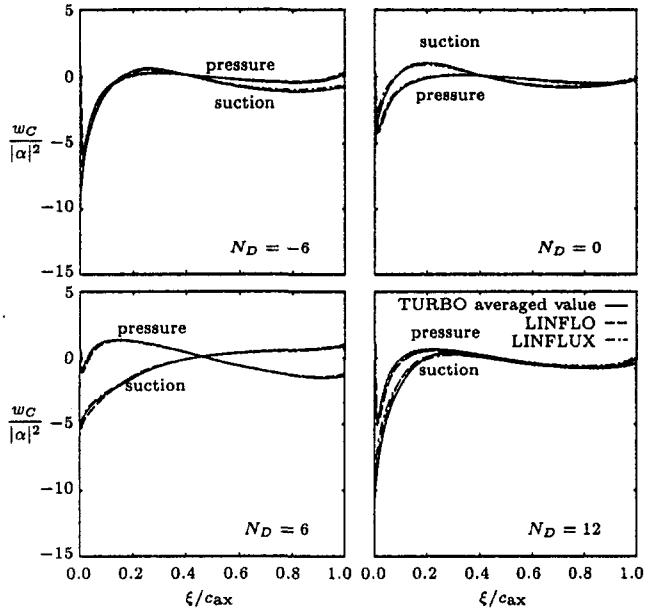

Fig. 5 Averaged local work per cycle distributions at midspan, as predicted using the three-dimensional TURBO and LINFLUX analyses, and the two-dimensional LINFLO analysis, for the 10th Standard Cascade undergoing torsional blade vibrations about midchord at $\omega = 1$

stream of the blade row. For the motions at $\sigma = 90$ deg, such a disturbance occurs only in the upstream region. For the (subresonant) motions at -90 deg and $\sigma = 180$ deg all acoustic response disturbances attenuate. The results in Fig. 5 show excellent agreement among the three codes.

Global work-per-cycle predictions for the two-dimensional and three-dimensional 10th Standard Cascade cascades undergoing prescribed blade vibrations are shown in Fig. 6, where results for the global work per cycle versus interblade phase angle are given for pure torsional vibrations about midchord at unit frequency. The three-dimensional TURBO results, indicated by the circular symbols in Fig. 6, have been determined for $N_D = -6, -4, 0, 4, 6, 8, 16$, and 18; the three-dimensional LINFLUX results, indicated by the square symbols, for $N_D = -6, -5, \ldots, 18$, and the two-dimensional LINFLO results, for $-90 \text{ deg} \leq \sigma \leq 270$ deg in increments of one degree. The two-dimensional work per cycle predictions are multiplied by the blade span, i.e., $r_D - r_H = 0.2r_D = 0.849$, to allow a convenient comparison between the three-dimensional TURBO and LINFLUX predictions, and the two-dimensional LINFLO predictions.

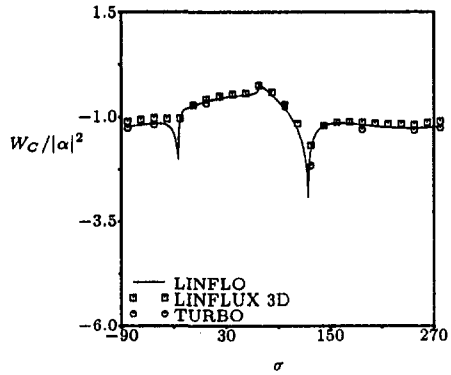

Fig. 6 Work per cycle versus interblade phase angle for the 10th Standard Cascade undergoing pure torsional vibrations about midchord at $\omega = 1$

The resonance or cut-off conditions for the two-dimensional configuration are $\sigma^-_{-\infty} = -26.93$ deg and $\sigma^+_{-\infty} = 117.12$ deg in the far upstream region and $\sigma^-_{+\infty} = -31.80$ deg and $\sigma^+_{+\infty} = 59.79$ deg in the far downstream region. The superresonant blade motions at $\omega = 1$ occur at interblade phase angles between these cut-off values and send a propagating wave into the upstream and/or downstream regions of the flow. The blade motions at $-90 \text{ deg} \leq \sigma < -31.80$ deg and $117.12 \text{ deg} < \sigma \leq 270$ deg are subresonant. The results in Fig. 6 indicate a very good agreement between the three-dimensional TURBO, the three-dimensional LINFLUX and the two-dimensional LINFLO global response predictions over the entire nodal diameter or interblade phase angle range of blade vibrations.

Next, we consider the acoustic properties far from the blade row. Predicted first- and second-harmonic axial eigenvalues and first-harmonic radial pressure modes, $p^R_{m\mu}(r)$, for three circumferential ($m = -1, 0, 1$) and two radial ($\mu = 0, 1$) modes are shown in Figs. 7–9. Here, the unsteady excitation occurs at $\omega = 1$ and $N_D = 6$ ($\sigma = 90$ deg). Because of mean blade loading, the steady inlet and exit conditions for the three-dimensional 10th Standard Cascade differ. As a result, the acoustic properties, $\chi_{m\mu}$ and $p^R_{m\mu}$, in the far-upstream region of the flow, differ from those in the far-downstream region. In particular, for an unsteady excitation at $\omega = 1$ and $\sigma = 90$ deg, the fundamental acoustic disturbances in the (0, 0) mode are of propagating type far upstream, but, of attenuating type far downstream. Note that the second-harmonic acoustic disturbances in the (0, 0) mode are of propagating type in both the upstream and downstream regions.

In the far-upstream region of the unsteady flow at $\omega = 1$ and $\sigma = 90$ deg, the propagating acoustic response disturbance has an axial wave number, κ_ξ, of 1.584 and the least damped or (0, 1) response disturbance has an attenuation constant, β, of 3.964. In the far-downstream region, $\beta = -1.077$ for the least-damped or (0, 0) response disturbance. These numbers agree favorably with those predicted by the two-dimensional LINFLO and three-dimensional LINFLUX analyses. For example, the LINFLO axial wave number, κ_ξ, is 1.603 and LINFLUX 1.583. Since the far-downstream mean flow is nonuniform, the axial

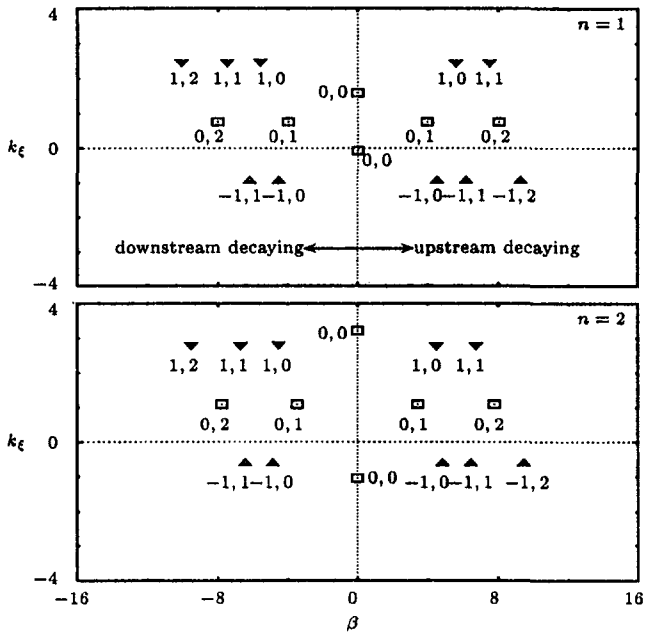

Fig. 7 Axial eigenvalues, $\chi = \beta + i\kappa_\xi$, at inlet for three circumferential ($m = -1, 0, 1$) and three radial ($\mu = 0, 1, 2$) modes of first- ($n = 1$) and second- ($n = 2$) harmonic acoustic disturbance for an unsteady flow at $\omega = 1.0$ and $N_D = 6$, through the three-dimensional 10th Standard Cascade

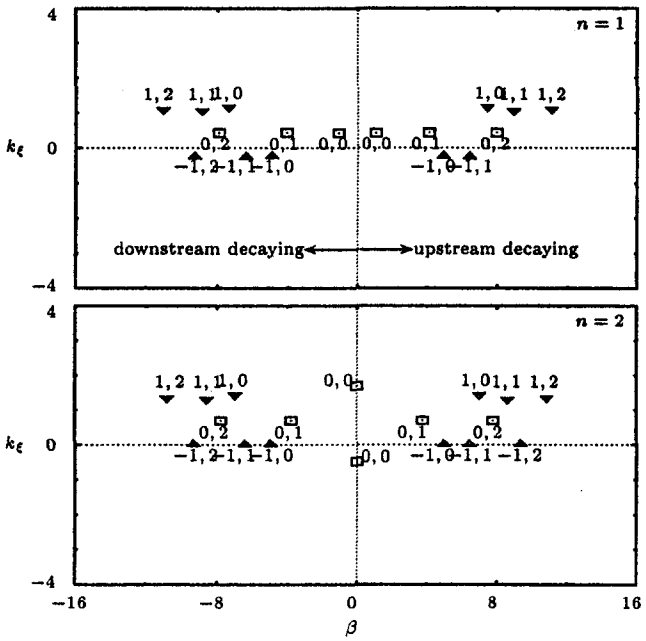

Fig. 8 Axial eigenvalues, $\chi = \beta + i\kappa_\xi$, at exit for three circumferential ($m = -1, 0, 1$) and three radial ($\mu = 0, 1, 2$) modes of first- ($n = 1$) and second- ($n = 2$) harmonic acoustic disturbance for an unsteady flow at $\omega = 1.0$ and $N_D = 6$, through the three-dimensional 10th Standard Cascade

wave numbers of the attenuating disturbances in a given circumferential mode vary with radial mode number, μ, as indicated in Fig. 8, particularly those for $m = 1$.

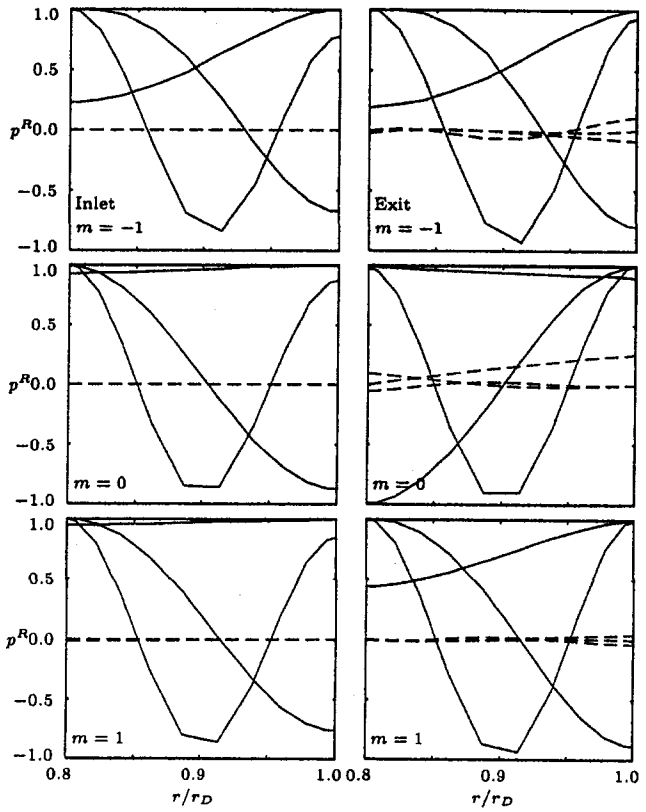

Fig. 9 First harmonic, radial pressure modes, $p^R_{m\mu}(r)$, $m = -1, 0, 1$, $\mu = 0, 1, 2$, at inlet and exit due to an acoustic excitation or response at $N_D = 6$ far upstream and for an acoustic response at $N_D = 6$ far downstream of the three-dimensional 10th Standard Cascade: (——) in-phase component; (– –) out-of-phase component of $p^R_{m\mu}(r)$

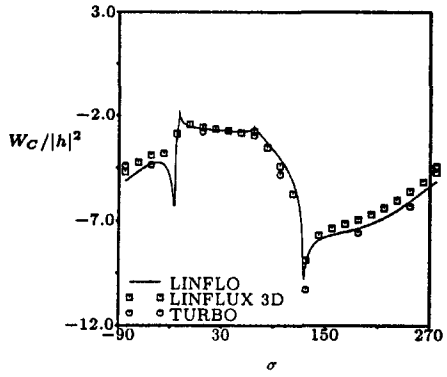

Fig. 10 Work per cycle versus interblade phase angle for the three-dimensional 10th Standard Cascade undergoing pure bending vibrations about midchord at $\omega = 1$

The radial eigenmodes for the pressures associated with the far upstream and far downstream acoustic responses for an unsteady excitation at $\omega = 1$ and $\sigma = 90$ deg are shown in Fig. 9. Although the inlet and exit mean-flow conditions differ, the upstream and downstream radial pressure modes are very similar, with the downstream modes showing a somewhat greater radial variations than their upstream counterparts. Note that the phase of a modal pressure disturbance is independent of radius for the uniform absolute mean flow at inlet, but the phase varies with radius for the mean flow with swirl and axial shear that exists in the far downstream region. Thus, the far-upstream, pressure modes, $p^R(r)$, are purely real, but the far-downstream modes have some imaginary or out-of-phase content.

The TURBO calculations for the subresonant $\sigma = -90$ deg and the superresonant $\sigma = 90$ deg blade motions reveal that, for the most part, the far-field acoustic responses are of small amplitude at the computational inflow and outflow boundaries. However, the superresonant torsional vibrations at $\sigma = 90$ deg produce an upstream propagating acoustic response disturbance that has an amplitude, a_A, of 1.352, and occurs at an axial wave number, κ_ξ, of 1.583. The corresponding LINFLO predictions are $a_A = 1.529$ and $\kappa_\xi = 1.603$.

In addition to the torsional motions considered above, we also performed TURBO calculations for the three-dimensional 10th Standard Cascade undergoing pure bending vibrations. We will briefly discuss the bending results without showing much detail here. The three-dimensional global work-per-cycle predictions agree very well with those from two-dimensional LINFLO and three-dimensional LINFLUX analyses; see Fig. 10. However, the superresonant TURBO results for $\sigma = 90$ deg are in poor agreement with the two-dimensional LINFLO results, but they are in reasonable agreement with the LINFLUX results. We have not established the reasons for the large discrepancies, but it was suggested by Montgomery and Verdon (1997) that we may not have adequate mesh resolution. We also have difficulties with the subresonant case at $\sigma = -90$ deg using TURBO, but have been unable to identify the cause. In addition, the bending solutions show noticeable blade-to-blade variations in the work-per-cycle predictions. We attribute these variations to the inability of the current far-field formulation to handle the anharmonic transient waves that are generated by the blade bending vibrations.

In summary, the TURBO local unsteady response for the three-dimensional 10th Standard Cascade, undergoing pure torsional vibrations at unit frequency, shows small variations with radius, as anticipated, and the results at midspan (Fig. 5), are in good very agreement with the two-dimensional LINFLO and three-dimensional LINFLUX predictions. The TURBO, LINFLUX, and LINFLO global work per cycle, W_C versus σ, predictions for torsional vibrations (Fig. 6) are also in very good agreement. We have obtained similar results for bending

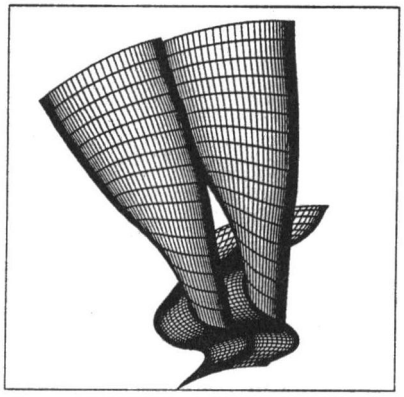

Fig. 11 TURBO computational grid for the NASA Rotor 67

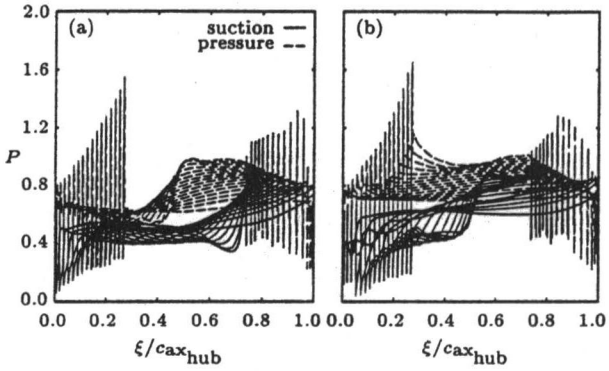

Fig. 12 Steady surface pressure distributions for the Rotor 67 fan (*a*) near the peak efficiency point, and (*b*) near stall

vibrations (Fig. 10). However, for selected bending modes, the results of the three analyses differ, and we are currently trying to identify the causes for these differences.

NASA Rotor 67. The NASA Rotor 67 is a research transonic fan with 22 blades. The tip diameter of the fan rotor varies from 51.4 cm at the leading edge to 48.5 cm at the trailing edge, and the hub-to-tip radius ratio varies from 0.375 to 0.478 from the inlet to exit (Strazisar et al., 1989). At the design point, the rotational speed of the rotor is 16,043 rpm. With an inlet axial Mach number of approximately 0.49, the tip speed at the designed rotation speed is 429 m/s, which corresponds to a tip relative Mach number of 1.38. Also, the mass flow rate at the design point is 33.25 kg/s and the pressure ratio is 1.63.

The purpose of the present numerical study is to demonstrate the capability of the TURBO code for analyzing the flutter characteristics of realistic transonic fans. Our goal is to obtain steady inviscid solutions at two throttle positions on the design speed line, one near peak efficiency and the other near stall. At each point, we will perform flutter analyses for torsional vibrations at two different nodal diameters.

The grid for the Rotor 67 (Fig. 11), consists of 121 axial, 33 tangential, and 17 radial surfaces (61,440 cells), and extends one axial chord, at midspan, upstream and downstream from the blade row. For the calculations, we assume that there is no clearance between the rotor blades and the outer duct wall. We have also idealized the endwalls such that near the computational inlet and exit boundaries, the inner and outer duct radii are constant. This is necessary because the three-dimensional far-field eigenanalysis assumes fully developed mean inlet and exit flows and, therefore, mean flows that do not vary with axial distance.

The computational grid consists of 65 axial points on the upper and lower blade surfaces, and 28 axial points on the upstream and downstream periodic boundaries. The grid is clustered near the leading and trailing edges, and near blade surfaces. The current version of the TIGER grid generation package (Soni and Shih, 1991) used for generating the Rotor 67 grid, does not have an elliptic grid smoother. Thus, the grid quality near the leading- and trailing-edge planes is relatively poor. Furthermore, we have not examined whether the selected grid has adequate resolution, especially in the axial direction, for the Rotor 67 flows being considered. The size of the grid was chosen such that unsteady calculations could be performed on a 128 MB workstation.

Steady Flow. Numerous researchers, e.g., Chima (1991) and Rhie et al. (1994) have performed numerical simulations of the NASA Rotor 67. These indicate that the flow field is very complicated and characterized by effects such as shock-boundary layer interaction, tip-leakage flow, unsteady vortex shedding, and flow separation with vortex roll up. Hence, we did not expect our inviscid TURBO solutions to agree well with the data. Surprisingly, the TURBO inviscid solutions show good qualitative agreement with the experimental data (Chuang and Verdon, 1998).

Figure 12 shows a carpet plot of the chordwise steady surface pressure distributions at 17 spanwise stations. The axial location is normalized by the axial chord at the hub. Due to blade twist, the normalized axial locations of the leading and trailing edges at the tip are approximately 0.25 and 0.75, respectively. At the near-peak-efficiency point, Fig. 12(*a*), in-passage shocks occur near the trailing edge on the suction surface. At the near-stall point, Fig. 12(*b*), the shocks move forward and ahead of the leading edges on the pressure surface.

The radial distributions of inlet and exit meanflow quantities for Rotor 67 operating near peak efficiency are shown in Fig. 13. At inlet, the relative circumferential velocity, $V_\theta = -\Omega r$ varies linearly from 0.436 at the hub to 1.263 at the tip. The steady static pressure (P), density ($\bar{\rho}$), and axial velocity (V_ξ) are nearly constant at inlet. At the computational exit boundary, the steady pressure, density, and axial velocity vary with radius (mean shear), and the circumferential velocity varies nonlinearly with radius (mean swirl). As indicated in Fig. 13, the steady blade loading causes increases in the pressure and density and decreases in the circumferential velocity. There is only a slight decrease in the axial velocity because this steady-flow point is not too far from the choke point.

Blade Vibration. For the flutter analysis, we have arbitrarily chosen a blade vibratory frequency of 1.19 times the rotation speed, or a reduced frequency of 0.54 (based on the midspan relative inlet velocity and blade chord), because we do not have any structural information for the blade. This frequency is probably representative of, or slightly higher than, the first mode frequency of a typical low-aspect-ratio fan. A torsional

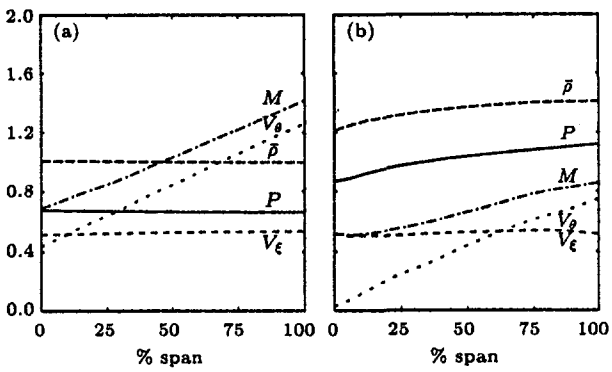

Fig. 13 Relative frame steady flow properties (*a*) far upstream and (*b*) far downstream of the NASA Rotor 67 fan ($M^{abs}_{-\infty} \approx 0.526$, $|\Omega| = 2.524$)

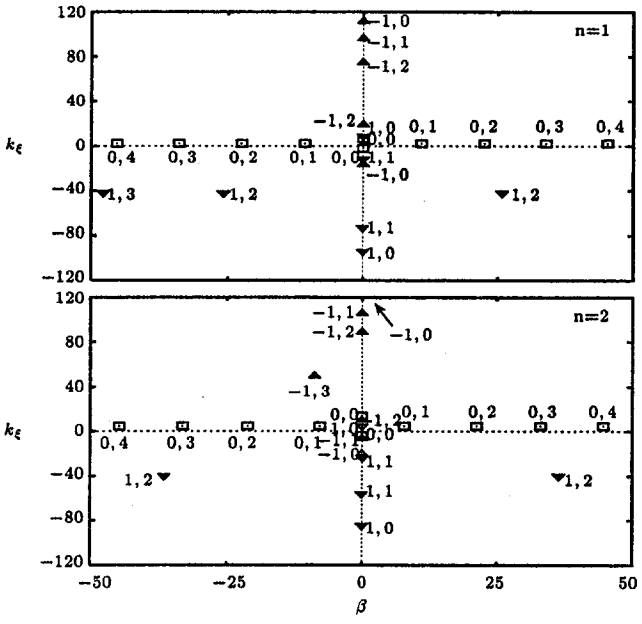

Fig. 14 Axial eigenvalues, $\chi = \beta + i\kappa_\xi$, at inlet for the first ($n = 1$) and second ($n = 2$) temporal harmonics, and three circumferential ($m = -1$, 0, 1) and five radial ($\mu = 0, 1, 2, 3, 4$) modes of acoustic disturbance in the far field of Rotor 67, for an unsteady flow at $\omega = 0.54$ and $N_D = 0$, and a meanflow condition near peak efficiency

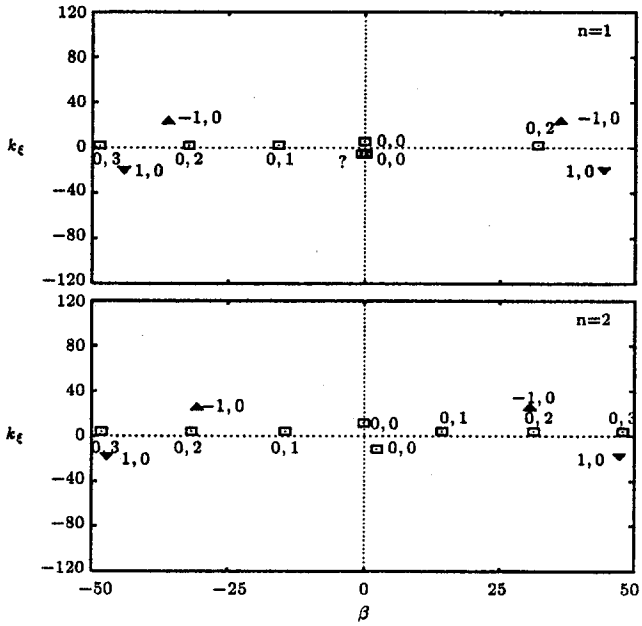

Fig. 15 Axial eigenvalues, $\chi = \beta + i\kappa_\xi$, at exit for the first ($n = 1$) and second ($n = 2$) temporal harmonics, and three circumferential ($m = -1$, 0, 1) and five radial ($\mu = 0, 1, 2, 3, 4$) modes of acoustic disturbance in the far field of Rotor 67, for an unsteady flow at $\omega = 0.54$ and $N_D = 0$, and a meanflow condition near peak efficiency

mode has been used in the flutter analysis of Rotor 67. As stated earlier, simple two-dimensional analytical mode shapes have been used because no detailed structural information is available. The TURBO code is actually capable of handling finite-element mode shapes, such as NASTRAN-generated modes.

The TURBO code was run for two nodal diameters, $N_D = 0$ and 11, at each of the meanflow conditions discussed above. At the near-peak efficiency point, the predicted first- and second-harmonic, axial eigenvalues, at inlet and exit, for the acoustic modes at $m = -1, 0, 1$, $\mu = 0, 1, 2$, and an unsteady excitation at $\omega = 0.54$ and $N_D = 0$ ($\sigma = 0$ deg) are shown in Figs. 14 and 15, respectively. As for the subsonic three-dimensional 10th Standard Cascade, the steady inlet and exit conditions differ due to mean blade loading. Thus, the acoustic properties, $\chi_{m\mu}$, in the far-upstream region of the flow differ from those in the far-downstream region. However, unlike the subsonic three-dimensional 10th Standard cascade, there are many propagating acoustic disturbances in the far-upstream region because the meanflow at inlet is supersonic in the blade-tip region.

Local and global work per cycle predictions for Rotor 67 undergoing pure torsional motions at $\omega = 0.54$ and $\sigma = 0$ and 180 deg ($N_D = 0$ and 11) at the two aforementioned meanflow conditions are shown in Fig. 16. The TURBO analysis shows the blade motion to be stable. Moreover, as indicated by the global work per cycle predictions, the stability margin is much greater at $N_D = 11$ than at $N_D = 0$. Also, the results for $N_D = 0$ show the margin to be greater near the stall point than near the peak efficiency point. A close examination of the local work per cycle distributions shows that unsteady forces around the in-passage shock play an important role in the stability of the blade motion. Near the peak efficiency point, the location of the in-passage shock in the outer portion of the blade is near the trailing edge on the suction surface and near midchord on the pressure surface. When $N_D = 0$, the unsteady forces ahead of the shock on both the pressure and suction surfaces extract energy from the blade motion. When the blade motion is out of phase, the unsteady forces on the pressure surface ahead of the shock are significantly more stabilizing than those for the $N_D = 0$ case, whereas the forces ahead of the shock on the suction surface are destabilizing. Near stall, the in-passage shock moves forward toward the leading edge on the pressure surface, and toward midchord on the suction surface. The unsteady forces on the pressure surface near the leading edge where the shock sits are extracting work from the blade; while the unsteady forces on the suction surface near the shock are stabilizing for $N_D = 0$ and destabilizing for $N_D = 11$.

In summary, we have presented numerical results for unsteady flows through the NASA Rotor 67. Our ultimate goal is to use the three-dimensional TURBO analysis to perform

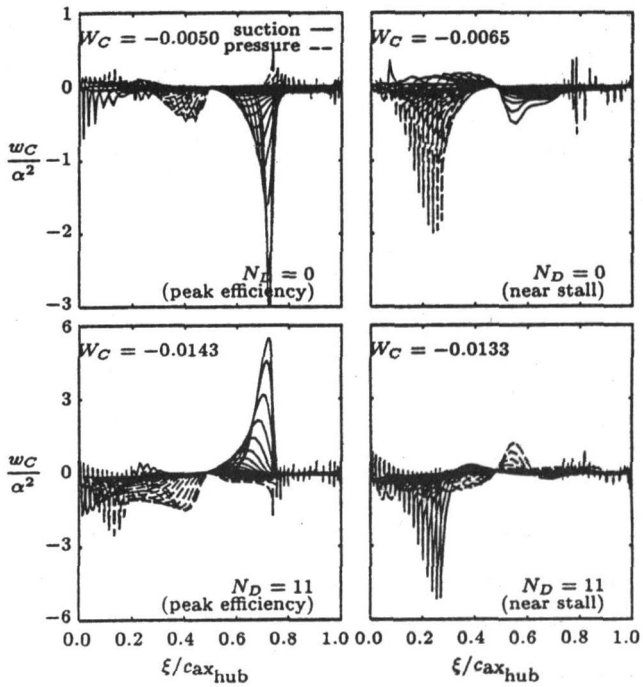

Fig. 16 Local work per cycle distributions and global works per cycle for the Rotor 67 fan undergoing pure torsional vibrations about midchord at $\omega = 0.54$ and $\sigma = 0$ and 180 deg ($N_D = 0$ and 11)

aeromechanical stability assessments of realistic turbomachinery fans. For the unsteady flows considered herein, the eigenanalyses have been used to determine the first two or three modal acoustic disturbances. Although, we have a reasonable understanding of the eigenanalysis for subsonic mean flows, such as those associated with the three-dimensional 10th Standard Cascade, we do not know how reliable the eigenanalysis is for supersonic flows. Sometimes, there are missing or superfluous modes, and we do not know whether these modes cause the solutions to deteriorate seriously.

Nevertheless, some interesting trends have been observed from the results of the TURBO unsteady analysis of Rotor 67 undergoing torsional vibrations. The analysis shows the torsional vibrations at $N_D = 0$ and $N_D = 11$ to be stable. Also, the blades are less stable at $N_D = 0$ than at $N_D = 11$. In addition, the torsional mode of vibration becomes slightly more stable as back pressure increases. These trends seem to agree with those observed for classical supersonic unstalled flutter, which is usually associated with a torsional mode.

Concluding Remarks

We have presented numerical results for three-dimensional unsteady flows using the TURBO analysis. These results pertain to flows in which the unsteady fluctuations are caused by prescribed blade vibrations. TURBO employs an implicit, flux-split, finite-volume scheme for solving the unsteady Euler equations in the near field, and numerical eigenanalyses for determining unsteady perturbations of fully developed, axisymmetric, swirling mean flows in the far upstream and far downstream regions. The numerical results indicate that the far-field eigenanalysis is capable of providing reasonable solutions for the axial eigenvalues and the radial pressure modes of the acoustic responses that can exist far upstream and far downstream of a blade row.

We have applied the TURBO analysis to predict unsteady subsonic flows through a simple turbomachinery configuration, i.e., a three-dimensional version of the 10th Standard Cascade. We have considered unsteady flows excited by prescribed blade vibrations that are highly two dimensional. For the three-dimensional 10th Standard Cascade, this allows us to compare and validate TURBO results against predictions based on previous two-dimensional analyses.

The numerical results indicate that the current version of the TURBO code is capable of providing accurate aerodynamic response information for unsteady subsonic flows. The numerical results indicate that the axial eigenvalues and radial eigenmodes of far-field acoustic disturbances can be accurately represented, and that the three-dimensional blade-surface, response predictions show reasonable radial trends. The three-dimensional nonlinear TURBO and linear LINFLUX results at blade midspan and the two-dimensional LINFLO results for the 10th Standard Cascade undergoing torsional vibrations are in good qualitative agreement.

We have also applied the TURBO analysis to predict unsteady flows through a realistic transonic fan, the NASA Rotor 67, undergoing torsional vibrations. Although some interesting trends have been observed from the TURBO results, we need to have a better understanding of the far-field eigensolutions for transonic flow applications.

To date, we have focused on demonstrating and validating the inviscid version of the TURBO code for subsonic flutter applications. In addition, we have applied the code, to predict flutter behaviors in transonic inviscid flows. The code needs further development and validation for transonic flows. Also, since viscous effects are expected to play an important role in the analysis of high-incidence flutter, a validation of the viscous capabilities of the TURBO code for unsteady applications should be carried out.

Acknowledgments

The research reported in this paper was supported under NASA Contract NAS3-26618. The authors are indebted to D. L. Huff, G. L. Stefko, and M. A. Bakhle for providing helpful assistance during the course of this effort.

References

Ayer, T. C., and Verdon, J. M., 1998, "Validation of a Nonlinear Unsteady Aerodynamic Simulator for Vibrating Blade Rows," ASME JOURNAL OF TURBOMACHINERY, Vol. 120, pp. 112–121.

Bahkhle, M. A., and Keith, T. G., Jr., 1997, "A 3D Euler/Navier–Stokes Aeroelastic Code for Propulsion Applications," AIAA Paper No. 97-2749.

Beach, T. A., and Hoffman, G., 1992, "IGB Grid: User's Manual (A Turbomachinery Grid Generation Code)," CR 189104, NASA.

Caspar, J. R., 1983, "Unconditionally Stable Calculation of Transonic Potential Flow Through Cascades Using an Adaptive Mesh for Shock Capture," ASME *Journal of Engineering for Power,* Vol. 105, pp. 504–513.

Chen, J. P., and Whitfield, D. L., 1993, "Navier–Stokes Calculations for the Unsteady Flowfield of Multi-stage Turbomachinery," AIAA Paper 93-0676.

Chima, R. V., 1991, "Viscous Three-Dimensional Calculations of Transonic Fan Performance," Technical Report TM-103800, NASA.

Chuang, H. A., and Verdon, J. M., 1998, "A Numerical Simulator for Three-Dimensional Flows Through Vibrating Blade Rows," CR 208511, NASA.

Clark, W. S., and Hall, K. C., 1995, "A Numerical Model of the Onset of Stall Flutter in Cascades," ASME Paper No. 95-GT-377.

Dorney, D. J., and Verdon, J. M., 1994, "Numerical Simulations of Unsteady Cascade Flows," ASME JOURNAL OF TURBOMACHINERY, Vol. 116, pp. 665–675.

Fransson, T. H., and Verdon, J. M., 1993, "Standard Configurations for Unsteady Flow Through Vibrating Axial-Flow Turbomachine Cascades," *Unsteady Aerodynamics, Aeroacoustics and Aeroelasticity of Turbomachines and Propellers,* H. M. Atassi, ed., Springer-Verlag, New York, pp. 859–889.

Giles, M. B., 1988, "Calculation of Unsteady Wake Rotor Interaction," *Journal of Propulsion and Power,* Vol. 4, No. 4, pp. 356–362.

Hall, K. C., and Lorence, C. B., 1993, "Calculation of Three-Dimensional Unsteady Flows in Turbomachinery Using the Linearized Harmonic Euler Equations," ASME JOURNAL OF TURBOMACHINERY, Vol. 115, pp. 800–809.

Holmes, D. G., Mitchell, B. E., and Lorence, C. B., 1998, "Three Dimensional Linearized Navier–Stokes Calculations for Flutter and Forced Response," *Unsteady Aerodynamics and Aeroelasticity of Turbomachines,* T. H. Fransson, ed., Kluwer Academic Publishers, pp. 211–224.

Huff, D. L., and Reddy, T. S. R., 1989, "Numerical Analysis of Supersonic Flow Through Oscillating Cascade Sections by Using a Deforming Grid," AIAA Paper No. 89-2805.

Janus, J. M., and Whitfield, D. L., 1989, "A Simple Time-Accurate Turbomachinery Algorithm With Numerical Solutions of an Uneven Blade Count Configuration," AIAA Paper No. 89-0206.

Montgomery, M. D., and Verdon, J. M., 1998, "A 3D Linearized Unsteady Euler Analysis for Turbomachinery Blade Rows, Part 1: Aerodynamic and Numerical Formulations; Part 2: Unsteady Aerodynamic Response Predictions," *Unsteady Aerodynamics and Aeroelasticity of Turbomachines,* T. H. Fransson, ed., Kluwer Academic Publishers, pp. 427–464.

Rai, M. M., 1989, "Three-Dimensional Navier–Stokes Simulations of Turbine Rotor–Stator Interaction; Part 1—Methodology, Part 2—Results," *AIAA Journal of Propulsion and Power,* Vol. 5, No. 3, pp. 305–319.

Rhie, C. M., Zacharias, R. M., Hobbs, D. E., Sarathy, K. P., Biederman, B. P., Lejambre, C. R., and Spear, D. A., 1994, "Advanced Transonic Fan Design Procedure Based on a Navier–Stokes Method," ASME JOURNAL OF TURBOMACHINERY, Vol. 116, pp. 291–297.

Soni, B. K., and Shih, M. H., 1991, "TIGER: Turbomachinery Interactive Grid Generation," *Proc. Third International Conference on Numerical Grid Generation in CFD,* Barcelona, Spain.

Strazisar, A. J., Wood, J. R., Hathaway, M. D., and Suder, K. L., 1989, "Laser Anemometer Measurements in a Transonic Axial-Flow Fan Rotor," Technical Report TP-2879, NASA.

Verdon, J. M., 1989a, "The Unsteady Aerodynamic Response to Arbitrary Modes of Blade Motion," *Journal of Fluids and Structures,* Vol. 3, No. 3, pp. 255–274.

Verdon, J. M., 1989b, "The Unsteady Flow in the Far Field of an Isolated Blade Row," *Journal of Fluids and Structures,* Vol. 3, No. 2, pp. 123–149.

Verdon, J. M., 1993, "Unsteady Aerodynamic Methods for Turbomachinery Aeroelastic and Aeroacoustic Applications," *AIAA Journal,* Vol. 31, No. 2, pp. 235–250.

Vortex Simulation of Rotor/Stator Interaction in Turbomachinery

M. Z. Chen

X. H. Wu

Division 404, Jet Propulsion Dept.,
Beijing University of Aeronautics
& Astronautics,
Beijing, 100083, People's Republic
of China

A new numerical method is presented in this paper to simulate rotor/stator interaction in turbomachinery by means of a vortex method based on a Lagrangian frame. The algorithm takes the result from steady solution as input, which gives an initial description of the unsteady disturbance flow field. To calculate the unsteady response to these disturbances, the Lagrangian vortex method is used to capture the convective process, and the deterministic vortex scheme to approximate the viscous diffusion process. The application of Baldwin–Lomax turbulence model in wakes is developed, to overcome difficulties such as the much higher calculated viscosity in the outer region than that in the boundary regions, and the difficulty in continuously tracing moving wake centerlines encountered when other numerical methods are used. Generally the agreement between the computational and experimental results is good. The sweeping characteristic of wakes, the influence of unsteadiness on incidence, and the decaying features of unsteady velocities and pressure are studied in the paper.

Introduction

It is well recognized that turbomachinery flow fields are inherently unsteady due to the relative motion between stationary and rotating blade rows. The purposes of studying this kind of unsteadiness are manifold, including understanding profoundly the real flow process, assessing the influences of commonly adopted time-averaged procedure on steady values, and probing into the influence of unsteadiness on mixing in turbomachines. As this unsteadiness causes unsteady gas-dynamic force to act on blades, obtaining this information will lay a foundation for gas–solid coupling unsteady computation to approach related problems, such as flutter. It is well known that the location and behavior of boundary layer transition significantly affect turbomachine performance, and the unsteadiness will affect the transition process. This shows another important role of the present study. From all mentioned above, one sees that simulation of this unsteadiness is of great importance in improving our knowledge of turbomachinery gas dynamics and thus raising our design level.

Due to the great importance of the problem, much research has been conducted, such as Erdos and Alzner (1977), Hodson (1985), Rai (1985), Giles (1990), Chen et al. (1985), and He (1990). These works have yielded useful and significant results that provide insight into the problem; however, there is much work to do to improve these methods and to deepen our understanding of the problem studied.

The vortex method presented in this paper is based on a Lagrangian frame. Fluid carrying continuously distributed vorticity is divided into many discrete vortex particles, which are traced in the Lagrangian manner. Strictly speaking, the vortex method adopted here is not a usual one; rather, it is a disturbance vortex method, i.e., for a single-stage compressor, if a relative steady solution of upstream rotor is known, and if an absolute steady solution of downstream stator is also known (these solutions can be easily obtained by the use of mature developed code, such as Denton's code), then the unsteady effects of rotor on stator can be worked out through the moving vortex particles

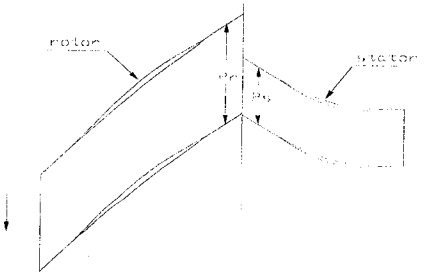

Fig. 1 A typical configuration of a single-stage compressor

in an absolute system. It is worth noting that using the vortex method to cope with the interaction problem is convenient. The authors' original idea for developing this method is based on the considerations that for modern transonic compressors, as pointed by Jung et al. (1996) for transonic turbines, if the velocity is sufficiently high at the interface between rotor and stator, then the effect of upstream unsteadiness on the downstream is much stronger than that of the downstream on the upstream. As the circulation distribution of vortex particles represents the circumferential nonuniformity of upstream flow, the unsteady mechanism can be described directly and conveniently by the process of vortex particles moving downstream.

The vortex method has been successfully used to simulate many unsteady flows, such as shear layer evolution, trailing vortex roll up, vortex shedding behind blunt bodies, and wake development. However, as far as we know, this method has not been applied to simulate rotor/stator interaction. In view of its

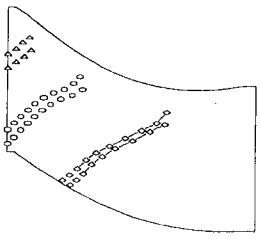

Fig. 2 Centerlines and half-band lines of wakes

Contributed by the International Gas Turbine Institute and presented at the 43rd International Gas Turbine and Aeroengine Congress and Exhibition, Stockholm, Sweden, June 2–5, 1998. Manuscript received by the International Gas Turbine Institute February 1998. Paper No. 98-GT-15. Associate Technical Editor: R. E. Kielb.

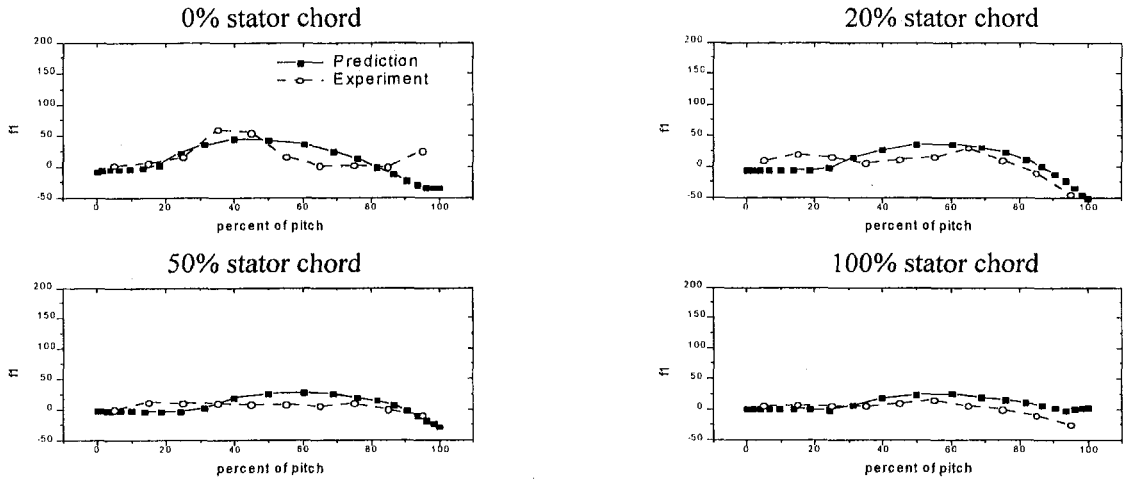

Fig. 3 Circumferential distribution of $\overline{u'v'}$ (m^2/s^2) for NASA-67 compressor

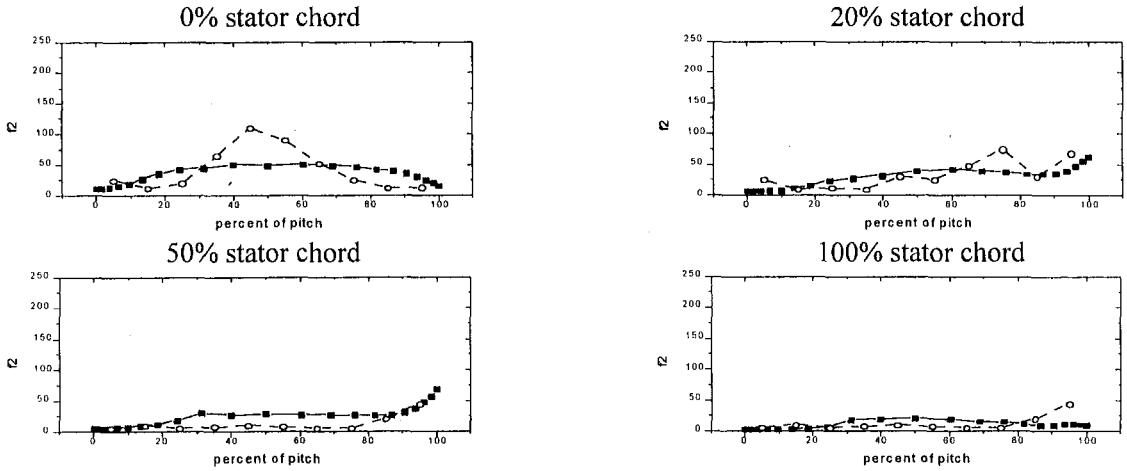

Fig. 4 Circumferential distribution of $\overline{u'^2}$ (m^2/s^2) for NASA-67 compressor

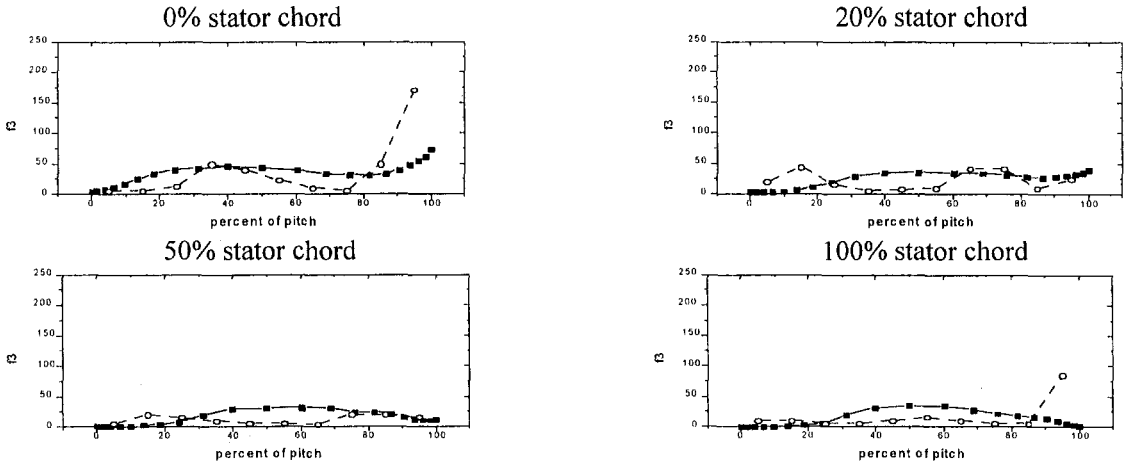

Fig. 5 Circumferential distribution of $\overline{v'^2}$ (m^2/s^2) for NASA-67 compressor

inherent advantages, we tried to explore its ability in dealing with the very complicated interaction problem. The results presented below are encouraging.

Analysis

Governing Equations. The vorticity dynamic equation for two-dimensional, viscous compressible flow is:

$$\frac{\partial \omega}{\partial t} + (V \cdot \nabla)\omega = -\omega(\nabla \cdot V) + \upsilon \nabla^2 \omega \qquad (1)$$

Now, divide a variable into two parts, i.e.,

$$q = \bar{Q} + q' \quad (q = \omega, V) \qquad (2)$$

where $\bar{Q} = 1/T \int_0^T q dt$, and T is a time period in a rotor/stator

Table 1 Airfoil mean section characteristics of a single-stage compressor

	Rotor	Stator
stage pressure ratio	1.66	
U_{tip} (m/s)	441.	0
blade number	23	40
chord length (m)	0.1432	0.08115
solidity	1.491	1.442
radius ratio	0.41	0.51
aspect ratio	1.8	2.4
inlet angle (deg)	43.24	47.28
outlet angle (deg)	41.63	0.

interaction problem. When the convergent solution is approached, the time-averaged value $\bar{Q}$ is no longer a function of time. q' is a disturbance variable. According to the definition given above, one sees that:

$$\int_0^T q'dt = 0 \tag{3}$$

Substituting ω and V of Eq. (2) by $\omega = \bar{\Omega} + \omega'$, $V = \bar{U} + u'$, respectively, one obtains:

$$\frac{\partial\bar{\Omega}}{\partial t} + \frac{\partial\omega'}{\partial t} + (\bar{U}\cdot\nabla)\bar{\Omega} + (\bar{U}\cdot\nabla)\omega' + (u'\cdot\nabla)\bar{\Omega} + (u'\cdot\nabla)\omega' = -\bar{\Omega}(\nabla\cdot\bar{U}) - \omega'(\nabla\cdot\bar{U}) - \bar{\Omega}(\nabla\cdot u') - \omega'(\nabla\cdot u') + v\nabla^2\bar{\Omega} + v\nabla^2\omega' \tag{4}$$

where $\bar{\Omega} = \nabla \times \bar{U}$ is time-averaged vorticity, and $\omega' = \nabla \times u'$ disturbance vorticity.

If the Mach number of time-averaged velocity is not very high, say, less than 2 or 3, then we can assume that the volume expansion corresponding to disturbance velocities is zero:

$$\nabla\cdot u' = 0 \tag{5}$$

When the Mach number increases and the circumferential nonuniformity increases, the error resulting from this assumption will increase. However, the benefit of employing this assumption in saving computer time is obvious. Further discussion about this assumption can be referred to Wu (1997). More importantly, the tenability of this method is not affected by whether or not this assumption is made.

According to the assumption, the third and the fourth terms on the right-hand side of Eq. (4) can be neglected.

Performing time-averaging operation to Eq. (4), and applying Eq. (3), one obtains:

$$(\bar{U}\cdot\nabla)\bar{\Omega} + \overline{(u'\cdot\nabla)\omega'} = -\bar{\Omega}(\nabla\cdot\bar{U}) + v\nabla^2\bar{\Omega} \tag{6}$$

Subtracting Eq. (6) from Eq. (4), applying Eq. (5) and the feature that any time-averaged quantity does not vary with time, we obtain the final equation for disturbance vorticity:

$$\frac{d\omega'}{dt} = -(u'\cdot\nabla)\bar{\Omega} - \omega'(\nabla\cdot\bar{U}) + \overline{(u'\cdot\nabla)\omega'} + v\nabla^2\omega' \tag{7}$$

where d/dt stands for material derivative. In the case of laminar flow, the viscosity is $v = v_l$, for turbulent flow $v = (v_l + v_t)$, the turbulent viscosity v_t, was predicted by the Baldwin–Lomax (1978) turbulence model.

The correlation term in the right-hand side of Eq. (7) $\overline{(u'\cdot\nabla)\omega'}$ stands for the time-averaged quantity of the production of the two disturbance variables. It can be obtained by storing this production at each time step and then performing a time-averaging operation.

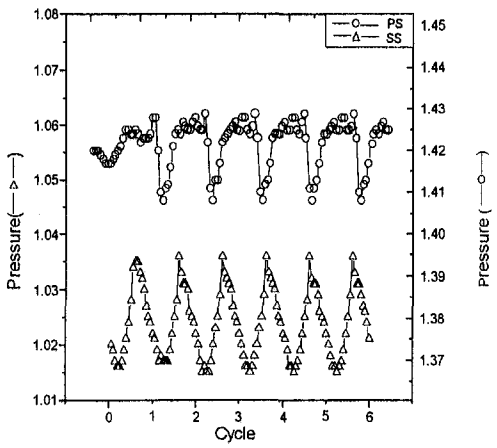

Fig. 6 Time history of pressure at 50 percent chord of stator

Initial and Boundary Conditions. The initial condition can be specified in a manner similar to that of Chen et al. (1985). We take a single-stage compressor as an example to describe the method (Fig. 1). At an initial time t_0, as we don't know the values of disturbance quantities inside the stator passage, we set them equal zero, except for that of upstream boundary of stator computation domain. As mentioned above, if the relative steady solution of rotor is known, which can be written as $\bar{Q}_R(\bar{x}, \lambda t)$, where $\bar{x}(x, y)$ stands for the coordinate of a point in the flow field, λ is the angular velocity of rotor, then the initial condition can be written as:

$$q'(x, y, t_0) = \begin{cases} \bar{Q}_R(x, y) - \bar{Q}_{(axi)}(x) & \bar{x} = \bar{x}_1 \\ 0 & \bar{x} \neq \bar{x}_1 \end{cases} \tag{8}$$

where $\bar{Q}_{(axi)}$ is the circumferential averaged value of $\bar{Q}_R$, and $\bar{x}_1$ is the coordinate of upstream boundary of stator computational domain.

On the solid wall, the no-penetration and no-slip conditions should be satisfied:

$$\bar{u}'\cdot n = 0 \tag{9}$$

$$\bar{u}'\cdot\tau = 0 \tag{10}$$

where n, τ are, respectively the normal and tangent unit vectors on the solid wall.

At upstream boundary, one can obtain the upstream boundary condition for disturbance variables at time t, according to the same idea as obtaining Eq. (8):

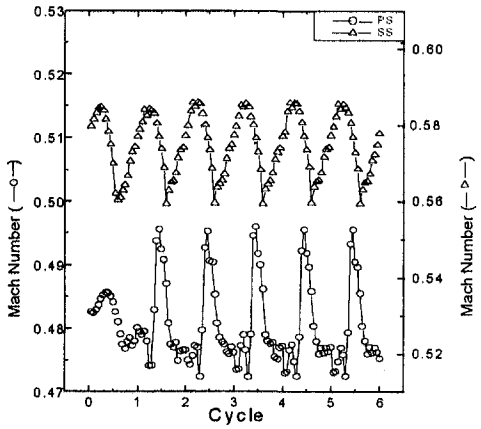

Fig. 7 Time history of Mach number at 50 percent chord of stator

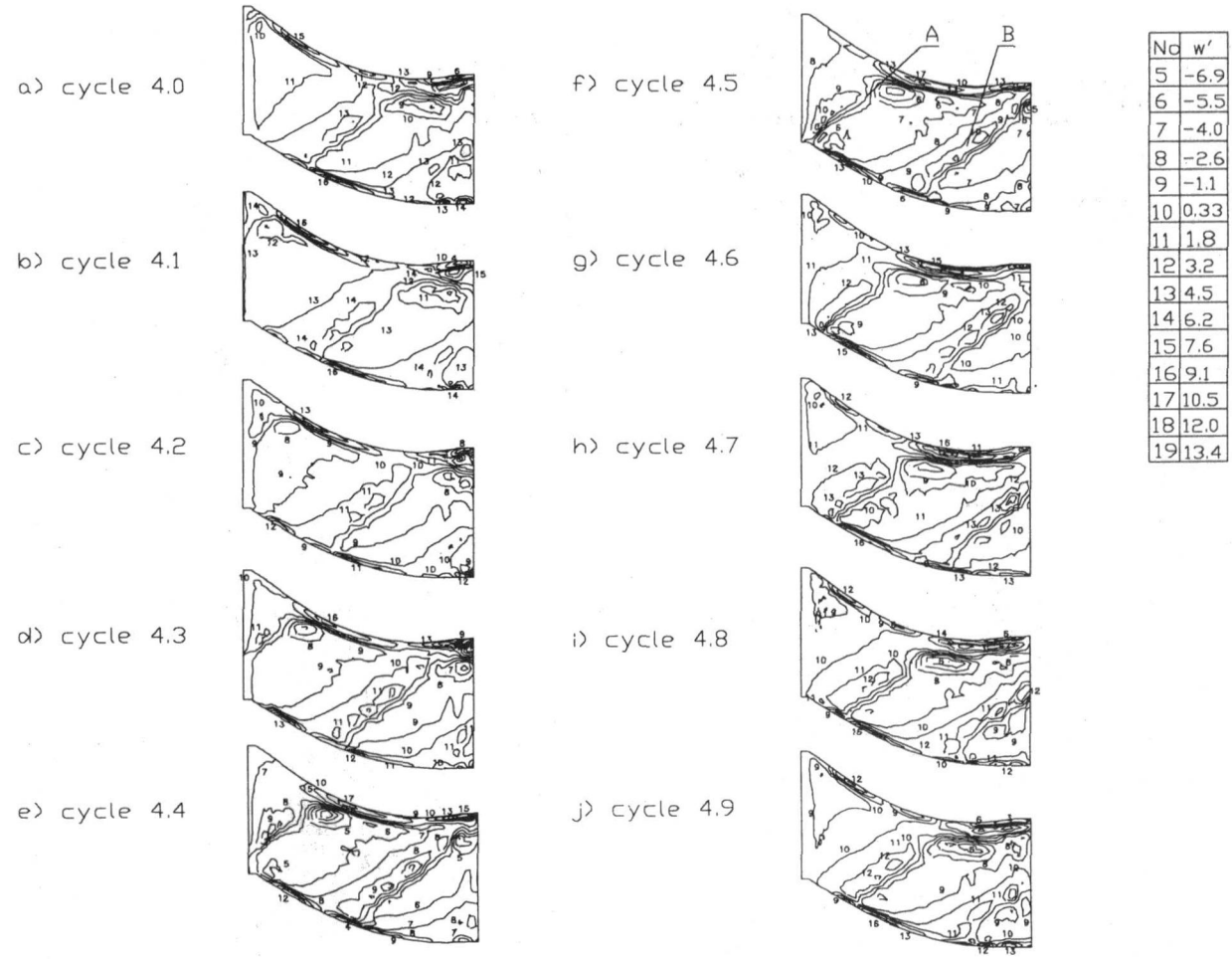

Fig. 8 Disturbance vorticity contours at different instants in one period

$$q'(x, y, t) = \bar{Q}_R(x, y - Wt) - \bar{Q}_{(axi)}(x) \qquad (11)$$

where $t = t_0 + k\Delta t$, $\Delta t = T/M$, time period, $T = P_r/W$, P_r is rotor blade spacing, W is the moving velocity of rotor blades, and M is the number of time steps in one period T.

On geometric boundaries in a single passage, if the rotor and stator have the same numbers of blades, the simple periodic condition holds:

$$q(x, y, t) = q(x, y + P_s, t) \qquad (12)$$

where P_s is the stator blade spacing. If the rotor spacing differs from that of stator (Fig. 1), one has to use the phase shift periodic boundary condition:

$$q(x, y, t) = q(x, y + P_s, t + \Delta T) \qquad (13)$$

where $\Delta T = (P_r - P_s)/W$.

As this boundary condition is rather complicated when the vortex method is used, we will not discuss it here in detail. Readers who are interested in this may refer to Wu (1997).

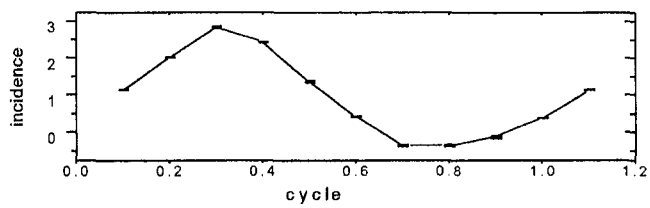

Fig. 9 Variation of disturbance incidence with time in one period

Turbulence Model. The Baldwin/Lomax turbulence model is used to calculate the turbulence viscosity coefficient, but this model is faced with two difficulties when it is used to compute unsteady rotor/stator interaction: One is the much higher computed viscosity in the outer region than in the boundary regions according to the original notation of Baldwin and Lomax model; the other is the difficulty in continuously tracing moving wake centerlines, which is often encountered by other numerical methods.

To overcome the first problem, we redefine y according to the method of Valkov and Tan (1995) as the smallest distance at which $F(y)$ meets the condition:

$$\left.\frac{dF}{dy}\right|_{y=y_{\min}} = 0 \qquad (14)$$

Based on this definition, the different effects of boundary layer and wakes can be distinguished.

In this paper, as the vortex method is a Lagrangian frame, which has the advantage to trace the trajectories of particles, so Baldwin–Lomax turbulence model can be conveniently used in the wakes. But $F(y)$ and u_{DIF} are defined as follows:

$$F(y) = y|\omega| \qquad (15)$$

$$u_{DIF} = (\sqrt{u^2 + v^2})_{\max} - (\sqrt{u^2 + v^2})_{\min} \qquad (16)$$

The center point of the wake moving into the inlet of stator computational domain at any time is defined as the point where the direction of disturbance vorticity changes. The centers of wakes transported in the stator passage at different times in a

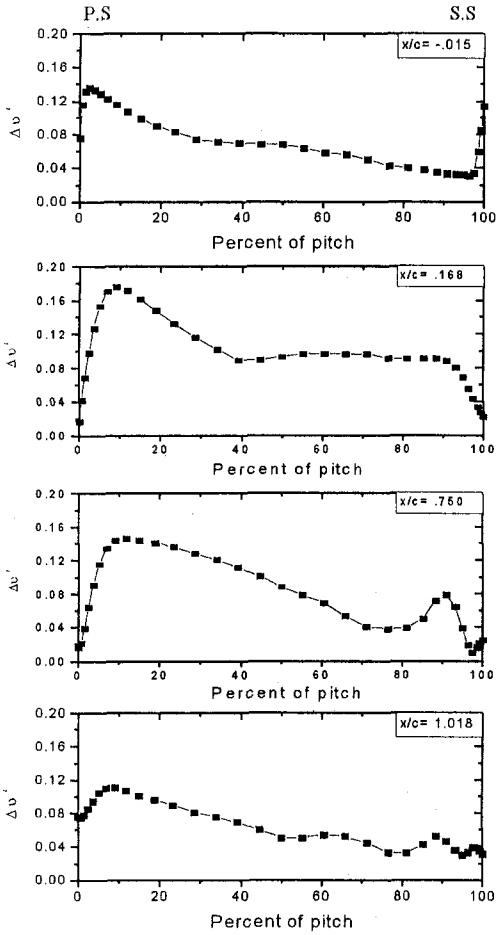

Fig. 10 First harmonic of the streamwise disturbance velocities

period are thus located. All the center points in one period form the centerline of wakes. Figure 2 shows three positions of wakes; for each position, the upper line is the centerline of the wake, the lower line is the half-band line of wake.

In the outer layer of the boundary, the total viscosity is:

$$\mu_{\text{tot}} = \mu_t + \mu_w \tag{17}$$

where μ_t is the turbulence viscosity coefficient of boundary layers, μ_w the eddy viscosity of wakes. In the inner layer of the boundary, the effect of wakes is relatively weak, so the wake viscosity is negligible.

Computation Procedure. The disturbance vorticity field can be represented by a set of discrete vortex particles:

$$\omega'(r, t) = \sum_{j=1}^{N} \Gamma_j' f_\sigma(r - x_j(t)) \tag{18}$$

where N is the number of vortex particles, r vector radius, $x_j(t)$ and Γ_j' the location and circulation of jth vortex at time t, respectively, $f_\sigma = 1/\sigma^2 f(r/\sigma)$, where σ is the radius of vortex particle, $f(r)$ shape function, in the present study, a Gauss core of second order is adopted, i.e., $f(r) = 1/\pi\, e^{-r^2}$.

The disturbance velocity field induced by the vortex particles is evaluated as follows:

$$\vec{u}_v'(r, t) = \sum_{j=1}^{N} \Gamma_j' K_\delta(r - x_j(t)) \tag{19}$$

where $K_\delta = K * f_\delta$, $K(r) = -(-y, x)/2\pi|r|^2$, and $*$ stands for convolution operator.

According to Batchelor (1967), the disturbance velocity associated with expansion rate H_m' is:

$$\vec{u}_e'(\vec{x}, t) = \frac{1}{2\pi} \int H_m' \frac{\vec{r}}{r^3}\, dS'(\vec{x}) \tag{20}$$

According to Eq. (5), the expansion rate of disturbance velocity $\nabla \cdot \vec{u}' = H_m' = 0$, so $\vec{u}_e' = 0$.

The disturbance velocity field consisting of $\vec{u}_e + \vec{u}_v'$ usually cannot meet the boundary condition, so a potential disturbance velocity is added to ensure a nonpenetrable condition on solid walls, i.e.,

$$(\vec{u}_e + \vec{u}_v') \cdot n = -\vec{u}_p' \cdot n \tag{21}$$

The potential disturbance velocity is the gradient of a potential function:

$$\nabla \phi(x) = \vec{u}_p' \tag{22}$$

and the potential function is the solution of Laplace equation:

$$\nabla^2 \phi = \frac{\partial^2 \phi}{\partial x^2} + \frac{\partial^2 \phi}{\partial y^2} = 0 \tag{23}$$

under the boundary condition of Eq. (21) on solid walls and unsteady boundary condition on geometric boundaries of Eq. (12) or Eq. (13).

After Δt, a vortex particle originally at $\vec{x}_1$ moves to $\vec{x}_2$, according to the relation:

$$\vec{x}_2 = \vec{x}_1 + (\vec{U} + \vec{u}')\Delta t \tag{24}$$

where the disturbance velocity $\vec{u}'(\vec{x}_1)$ is determined by the induced velocity and potential velocity at point $\vec{x}_1$.

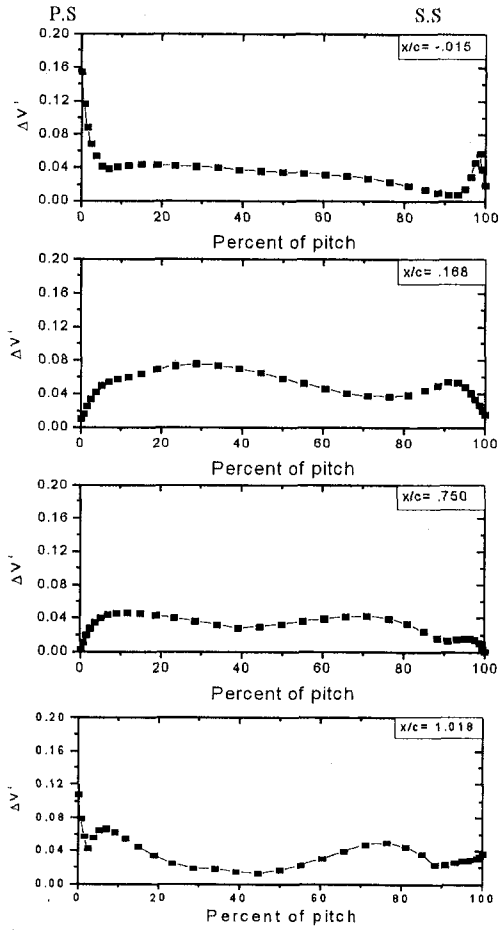

Fig. 11 First harmonic of the transverse disturbance velocities

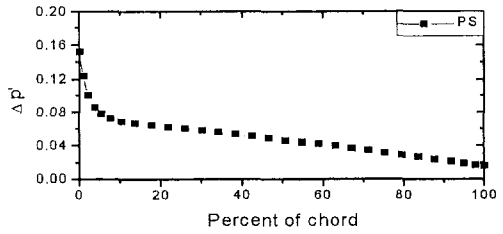

Fig. 12 First harmonic of unsteady pressure on pressure surface

The circulation variation of disturbance vorticity caused by convection and viscous process is prescribed as follows:

$$\Gamma_j'(t + \Delta t) = \Gamma_j'(t) + F[-u_j' \cdot \nabla \bar{\Gamma}_j - \Gamma_j'(\nabla \cdot \bar{U}_j) + \overline{(u_j' \cdot \nabla)\Gamma_j'} + \upsilon \nabla^2 \omega_j' \cdot S_j] \cdot \Delta t \quad (25)$$

where $F[\ ]$ stands for integration scheme, $\bar{\Gamma}$ time-averaged circulation, S_j a vortex element area. The correlation $\overline{(u' \cdot \nabla)\Gamma'}$ can be obtained through summing up $u' \cdot \nabla \Gamma'$ of each time step and then performing a time-averaging operation.

The contribution of viscous term to disturbance vorticity can be obtained by using the deterministic vortex method; see below.

Viscous Term. Under the research frame employed by the present paper, it is assumed that once a periodic convergent solution is reached, the trajectories of vortex particles remain unchanged from period to period. Therefore, it is not suitable to simulate viscous diffusion process by employing the random walk method. Instead, the deterministic vortex method is employed. Here the method proposed by Fishelov (1990) was used, and the operator on vorticity can be written in the discrete form:

$$\nabla^2 \omega' = \sum_{j=1}^{N} [\Delta f_b(\bar{x}_i - \bar{x}_j)] \Gamma_j'(t) \quad (26)$$

where $\Delta = \nabla^2$. This is our work form for the viscous term.

Vorticity Generation on Solid Walls. The no-slip condition on solid walls can be satisfied if a set of vortex sheets is generated on solid walls for every time step. The strength of the vortex sheet must meet the condition:

$$\Gamma' = \bar{u}' \cdot \tau \quad (27)$$

where $\bar{u}'$ stands for the sliding velocity on solid walls, τ a unit vector tangent to the solid wall. The vortex sheet is divided into several small elements. Once they enter the main flow region, they are converted into vortex particles, while keeping their vorticity strength unchanged.

Results and Discussion

To check the present method, we calculated the unsteady flows due to rotor/stator interaction in the first stage of NASA-67 compressor. The calculated results—unsteady velocity correlations $\overline{u'v'}$, $\overline{u'^2}$, $\overline{v'^2}$—are compared with experimental data (Hathaway, 1986) at four axial positions: 0, 20, 50, and 100 percent of chord, see Figs. 3, 4, and 5. These contours show that the prediction and experimental data are in general agreement, especially $\overline{u'v'}$ and $\overline{v'^2}$. Although $\overline{u'^2}$ is not very good near the stator leading edge, satisfactory agreement between the computational and experimental results at 20, 50, and 100 percent of chord is obtained. From the prediction we can conclude that the present method is reliable.

Based on the method, we calculate the unsteady flows in a high loading transonic compressor stage. The main features of the stage are listed on Table 1. The flow field on the stream surface at middle span was simulated. An H-type grids employed with the node number (47 + 43)*33, and 47, 43, represent axial grids of rotor and stator, respectively; 33, circumferential grid. The Reynolds number is 0.9×10^7 based on the stator chord length and stator inlet velocity. One time period is divided into 20 time steps.

To see the convergence history, Figs. 6 and 7 show the static pressure and Mach number contours, respectively, as a function of rotor blade passing cycle. The pressure is normalized with respect to the inlet steady total pressure. We see from the figures that after three cycles, the periodic repetition of pressure and Mach number contours appears from cycle to cycle, with the averaged relative error for total mesh points less than 3×10^{-2}.

To study the interaction of rotor wake with stator blades, Fig. 8 shows the disturbance vorticity contours at different time instants in a period. We see from the figures that when a wake is sweeping the stator blades, a complete wake is cut into several separate segments. So long as the vortex particles move into the stator passage, there appears to be a tendency that the particles are pushed toward the pressure surface of stator blades. There seem to be two processes during the particles moving downstream, i.e., (1) decentralization–centralization, Fig. 8(a–f), with two vorticity concentration areas formed (see A and B) at circle 4.5, the strengths of which are −2.6 and −1.1, respectively; (2) centralization–decentralization, Fig. 8(g–j), with vorticity concentration areas decentralized and broken near the exit of stator blades, where the pressure tends toward uniform distribution. The latter process indicates that as an interaction between wakes, vortices, and boundary layers, a strong mixing process occurs, resulting in a mixing of main flow with fluid carrying highly concentrated vorticity. This coincides with the observation of Kerrebrock and Mikolajczak (1970).

An important problem that concerns engineers a lot influence of unsteadiness on incidence. Figure 9 shows the variation of disturbance incidence with time in a period. The distribution is similar to a sine shape. The maximum disturbance is as high as 2.84 deg, while the minimum is −0.374 deg.

To study the decaying characteristic of unsteadiness, the amplitudes of the first harmonic of unsteady streamwise and transverse velocities at four axial location are shown in Figs. 10 and 11. The reference velocity is the steady velocity at the stator leading edge. The percent of the pitch is defined as 0 percent on the pressure side and 100 percent on the suction side. The percent of the chord is defined as 0 percent at leading edge and 100 percent at trailing edge. So $x/c = -0.015$ stands for a location of 1.5 percent axial chord upstream of stator; $x/c = 0.168$ and $x/c = 0.75$, two axial positions between the leading and the trailing edges; $x/c = 1.018$ represents a location of 1.8 percent axial chord downstream.

The maximum amplitude of streamwise disturbance velocity occurs at about 10 percent pitch near the pressure surface and the axial position $x/c = 0.168$, with magnitude as high as 18 percent of V_0. This is the result of the chopping of rotor wakes by the stator leading edge. Along the stator chord, the streamwise velocity decreases gradually. At $x/c = 0.75$, the amplitude is smaller than that at $x/c = 0.168$. At the position $x/c = 1.018$, the amplitude of streamwise disturbance velocity is the smallest of the four axial positions, where the disturbance velocity tends toward uniform distribution. The transverse disturbance velocity has the same characteristic as the streamwise one. But the

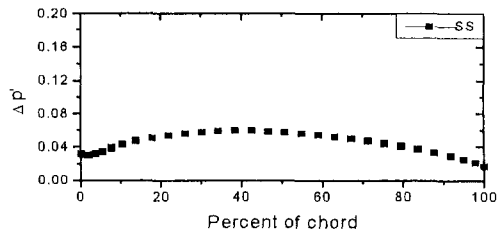

Fig. 13 First harmonic of unsteady pressure on suction surface

largest amplitude of the transverse velocity fluctuation is about 8 percent of V_0, occurring at 30 percent pitch near pressure surface and the axial position $x/c = 0.168$. From Figs. 10 and 11, we can see that the influences of unsteadiness are obvious near the leading edge of the stator blade and then decay rapidly along the stator chord. In addition, we can also see that the unsteadiness is stronger in the main flow region than near the pressure or suction surfaces. This is different from the turbulence fluctuation, which is much stronger in the boundary layer near solid surfaces.

The amplitude of the first harmonic of the unsteady pressure on the stator blade surface is shown in Figs. 12 and 13. The amplitude is normalized by the inlet steady total pressure. For this configuration, the unsteady pressure on the pressure surface decays along the stator chord. This effect is much more significant from leading edge to 10 percent of stator's axial chord. From this position to the trailing edge, the decaying trend becomes slower, and the minimum occurs at the trailing edge. The amplitude decays gently, on the suction surface of the stator blade. There is a little increase from the leading edge to 40 percent of chord, and the amplitude begins to decrease after this position. These decaying trends of unsteady pressure on solid walls agree with Ho and Lakshimnarayana (1996), who observed the decay of unsteady pressure.

Concluding Remarks

The unsteadiness caused by wakes and other vortices in turbomachinery is simulated by employing a Lagrangian-disturbance vortex method proposed in the present paper. The Baldwin–Lomax turbulence model is applied in boundary layer and wakes with some development to overcome the difficulties encountered when other numerical methods are used. Numerical results show that the predicted results are generally in good agreement with the experimental data. The calculated results also show that variety of unsteady flow phenomena, such as moving vortices, sweeping wakes, and decaying of unsteadiness can be well simulated with good convergence property.

Acknowledgments

Computation was supported by the State Key Lab. of Scientific and Engineering Computation. The authors wish to thank Dr. Li Ping Xu for his helpful suggestion.

References

Baldwin, B. S., and Lomax, H., 1978, "Thin Layer Approximation and Algebraic Model for Separated Turbulent Flows," AIAA Paper No. 78-257.

Batchelor, G. K., 1967, *An Introduction to Fluid Dynamics*, Cambridge University Press, Cambridge.

Chen, J. P., Celestina, M. L., and Adamczyk, J. J., 1988, "A New Procedure for Simulating Unsteady Flows Through Turbomachinery Blade Passages," ASME Paper No. 94-GT-151.

Chorin, A. J., 1973, "Numerical Study of Slightly Viscous Flow," *J. Fluid Mech.*, Vol. 57, pp. 785–796.

Erdos, J. I., and Alzner, E., 1977, "Numerical Solution of Periodic Transonic Flow through a Fan Stage," *AIAA J.*, Vol. 15, No. 11.

Fishelov, D., 1990, "A new vortex scheme for viscous flows," *J. Comp. Phys.*, Vol. 86, pp. 211–224.

Giles, M. B., 1990, "Stator/Rotor Interation in a Transonic Turbine," *J. Propulsion*, Vol. 6, No. 5, pp. 621–627.

Hathaway, M. D., 1986, "Unsteady Flows in a Single-Stage Transonic Axial-Flow Fan Stator Row," NASA-TM-88929.

He, L., 1990, "An Euler Solution for Unsteady Flows Around Oscillating Blades," ASME JOURNAL OF TURBOMACHINERY, Vol. 112, pp. 714–722.

Ho, Y.-H., and Lakshminarayana, B., 1996, "Computation of Three-Dimensional Steady and Unsteady Flow Through a Compressor Stage," ASME Paper No. 96-GT-70.

Hodson, H. P., 1985, "An Inviscid Blade-to-Blade Prediction of a Wake-Generated Unsteady Flow," ASME *Journal of Engineering for Gas Turbines and Power*, Vol. 107, pp. 337–344.

Kerrebrock, J. L., and Mikolajczak, A. A., 1970, "Intra-Stator Transport of Rotor Wakes and Its Effect on Compressor Performance," ASME Paper No. 70-GT-39.

Jung, A. R., Mayer, J. F., and Stetter, H., 1996, "Simulation of 3D-Unsteady Stator/Rotor Interaction in Turbomachinery Stages of Arbitrary Pitch Ratio," ASME Paper No. 96-GT-69.

Rai, M. M., 1985, "Navier–Stokes Simulations of Rotor–Stator interaction Using Patched and Overlaid Grids," AIAA Paper No. 85-1519.

Valkov, T., and Tan, C. S., 1995, "Control of the Unsteady Flow in a Stator Blade Row Interacting With Upstream Moving Wakes," ASME JOURNAL OF TURBOMACHINERY, Vol. 117, pp. 97–105.

Wu, X. H., 1997, "Numerical Simulation of Rotor-Stator Interaction in Turbomachinery by Use of a Lagrangian Vortex Method," Ph.D. thesis, Beijing University of Aeronautics and Astronautics, People's Republic of China.

Prediction and Measurement of Rotating Stall Cells in an Axial Compressor

H. M. Saxer-Felici

A. P. Saxer

A. Inderbitzin

G. Gyarmathy

Turbomachinery Laboratory,
Institute of Energy Technology,
Swiss Federal Institute of Technology,
8092 Zurich, Switzerland

This paper presents a parallel numerical and experimental study of rotating stall cells in an axial compressor. Based on previous theoretical and experimental studies stressing the importance of fluid inertia and momentum exchange mechanisms in rotating stall, a numerical simulation using the Euler equations is conducted. Unsteady two-dimensional solutions of rotating stall behavior are obtained in a one-stage low subsonic axial compressor. The structure and speed of propagation of one fully developed rotating stall cell together with its associated unsteady static pressure and throughflow field distributions are presented. The numerical capture of a stalled flow region starting from a stable high-flow operating point with an axisymmetric flow distribution and evolving at a reduced mass flow operating point into a rotating stall pattern is also discussed. The experimental data (flow visualization, time-averaged and unsteady row-by-row static pressure measurements) acquired in a four-stage water model of a subsonic axial compressor cover a complete characteristic line ranging from high mass flow in the stable regime to zero throughflow. Stall inception is presented together with clearly marked different operating zones within the unstable regime. For one operating point in the unstable regime, the speed of propagation of the cell as well as the static pressure spikes at the front and rear boundaries of the rotating stall cell are compared between computations, measurements, and an idealized theory based on momentum exchange between blade rows entering and leaving the stalled cell. In addition, the time evolution of the pressure trace at the rotor/stator interface is presented. This study seems to support the assumption that the cell structure and general mechanism of full-span rotating stall propagation are essentially governed by inertial effects and momentum exchange between the sound and stalled flow at the cell edges.

I Introduction

It is well known that the stability of any compression system is affected as the mass flow rate is reduced from its nominal value beyond the so-called limit of dynamic stability. Close to this operating point large-scale disturbances such as surge or/and rotating stall begin to appear in the compression system setting a performance boundary. Surge-like disturbances are primarily axisymmetric and involve variations in the mass flow through all the compression components. Rotating stall-like disturbances, on the other hand, show static pressure fields decaying away from the compressor and involve primarily circumferential flow distortions within the compressor itself. These produce a locally reduced throughflow in part of the compressor annulus while keeping the average mass flow and pressure rise fluctuations substantially below the levels encountered during surge. Rotating stall is characterized by cells of stalled fluid (with negative or nearly zero throughflow velocity) rotating around the annulus at a fraction of the rotor wheel speed.

The scope of this paper is twofold. First, to analyze the capability of a numerical procedure for unsteady inviscid flows to capture and sustain a physically meaningful fully developed rotating stall pattern. Second, to provide additional experimental data on rotating stall for a broad range of throughflows using a low-speed water model of a subsonic axial compressor.

Historically, the analysis of the flow field beyond the stability limit in axial compressors has been based mainly on experimental observations and studies (see, for example, Cumpsty, 1989). Also some approximate theoretical models derived from these observations are available, see for example the review of Longley (1994). Among them the model developed by Moore and Greitzer (1986) considers the stability of the whole compression system in which surge and rotating stall appear as eigenmodes.

While it is nowadays standard practice to use Computational Fluid Dynamics (CFD) tools to predict the flow within the stable operating range of a compressor, the CFD approach still needs to be established as a sound prediction method for operation in the unstable regime. To a lesser degree, rotating stall inception has been recently numerically investigated (Hendricks et al., 1997; He, 1997). Propagating stall in isolated linear cascades using vortex methods has been studied (see, for example, Speziale et al., 1986; Nishizawa and Takata, 1994), and stall behavior in a two-dimensional rotor–stator system has been reported by Outa et al. (1994). The latter study focused essentially on compressor performance and stall effect on blade loading.

In this frame of research, numerical solutions for the flow in a one-stage axial compressor are presented and compared with experimental data for operation in the rotating stall regime. This study focuses on full-span, fully developed rotating stall with the intent of providing more insight into the mechanism for the propagation of the rotating stall cell. This is achieved by analyzing the circumferential variations in static pressure and throughflow velocity produced by a single rotating stall cell. The CFD simulation presents a two-dimensional inviscid unsteady solution for a one-stage low subsonic axial compressor bearing similarity with any of the stages of the four-stage water model of a subsonic axial compressor (Hof et al., 1996). The use of the Euler equations for capturing and propagating rotating stall

Contributed by the International Gas Turbine Institute and presented at the 43rd International Gas Turbine and Aeroengine Congress and Exhibition, Stockholm, Sweden, June 2–5, 1998. Manuscript received by the International Gas Turbine Institute February 1998. Paper No. 98-GT-67. Associate Technical Editor: R. E. Kielb.

cells is prompted by previous experimental and theoretical studies (Cumpsty and Greitzer, 1982; Longley, 1994; Gyarmathy, 1996), which clearly indicate the crucial impact of fluid inertia and momentum exchange between the rotor and the stator rows for stall cell propagation. Furthermore, as shown in external and internal aerodynamics (Rizzi and Eriksson, 1984; Felici, 1992), the Euler equations allow the generation and capture of strong vortical flows as encountered during rotating stall. Because of the experimentally observed essentially axial-tangential nature of full-span rotating stall in low aspect ratio bladings, a two-dimensional numerical study is performed.

While the study of stall inception is of primary importance to control rotating stall and surge dynamically in order to extend the stable flow range of the compression system (see, for example, Garnier et al., 1991; Day, 1993; Gysling and Greitzer, 1994; Tryfonidis et al., 1995), there is still a need to understand the rotating stall dynamics as it often precedes surge. Hence, the intent here is rather to focus on the phenomenological understanding of rotating stall from a fluid dynamics point of view.

The water model permits an improved visualization compared to a similar air compressor, while retaining identical overall characteristic features. Compared to the air compressor, the water model presents a wider range of operation in the rotating stall regime without the appearance of surge, since no mass storage effects are present in this discharge system.

Based on specific parameters defining the stall cell such as cell width, speed of propagation, and static pressure spikes at the cell edges, a cross comparison between the CFD prediction, a theory based on momentum exchange between the rotor and stator rows as well as experimentally obtained stall patterns, is performed. The capture of the rotating stall pattern as part of the CFD solution by "jumping" from a stable operating point with an axisymmetric flow distribution and a constant throughflow to a reduced mass flow with a large circumferential disturbance traveling at reduced wheel speed is discussed. The analysis of stall inception is not an issue in this work.

Due to the absence of viscous and three-dimensional effects in the numerical simulation, emphasis is given to the general mechanism of stall cell propagation and overall cell structure while overlooking detailed flow features.

II Measurements in a Four-Stage Compressor Water Model

In an earlier investigation on centrifugal low-speed compressor rotating stall, a water model of the ETH Turbomachinery Laboratory single-stage centrifugal air compressor (using the principle of hydrodynamic analogy) has recently successfully been brought into operation (File et al., 1997). The aim was to study rotating stall through visualization (Gyarmathy et al., 1997). From the observed speed and structure of the single rotating stall cell, an idealized model for the propagation of a full-span rotating cell has been developed (Gyarmathy, 1996).

Based on this previous work, a water model of a nonexisting four-stage low-speed subsonic axial compressor has been constructed for studying stall patterns. In this section, the water model and the experimental results are presented, comprising the test rig facility, the compressor characteristics, the RS inception process, and the annulus blockage during RS for a broad range of throughflow coefficients. In addition, the first results of flow visualization are shown.

II.1 Experimental Facility. The closed-loop water circuit with the whole "compression" (i.e., discharge) system is shown in Fig. 1. The major components of the system are the axial compressor, the deaeration valve at the top, the throttle valve, and the Venturi tube for mass flow measurements. Downstream of the throttle valve and upstream of the compressor inlet, flow straighteners and a stagnation chamber ensure axial inlet flow into the compressor's IGV. Note that the loop does not provide for any elements allowing pneumatic storage effects, hence mild or deep surge in the compression system are excluded. Thus RS can be studied in the absence of these compressible effects.

The model, shown in Fig. 2, consists of a four-stage axial compressor built with variable inlet guide vanes and repeating

Nomenclature

Abbreviations

CFD = computational fluid dynamics
IGV = inlet guide vanes
RS = rotating stall
SLOR = successive line over-relaxation
stg = stagnation point

Symbols

A = apparent fluid inertia ratio, Eq. (4)
C = absolute velocity
c_x = axial velocity
ΔCp = pressure coefficient = $(p - \bar{p})/(1/2\bar{\rho}_1 U_2^2)$
ΔCp_{ref} = pressure coefficient = $(p - \bar{p}_{\text{sound flow}})/(1/2\bar{\rho}_1 U_2^2)$
h = static enthalpy
M = fluid mass contained in cascade channels
$\dot{m}$ = mass flow through surface S = $\int_S \rho(\vec{v} \cdot \vec{n}) dS$
$\dot{m}_n$ = normalized mass flow = $\dot{m}/\bar{\dot{m}}_1$
$\vec{n}$ = normal vector
p = static pressure
p_n = normalized static pressure = $p/(\frac{1}{2}\bar{\rho}_1 U_2^2)$
p^0 = stagnation pressure
S = surface
T^0 = stagnation temperature
T = rotor period
T_{RS} = rotating stall period
t = time
t_A = time at CFD occurrence of compact cell
t_B = time at CFD occurrence of diffused cell
t_C = time occurrence during stall generation
U_2 = rotational speed at Euler radius
V = volume
$\vec{v}$ = velocity vector
x_R = axial depth of rotor
x_S = axial depth of stator
α = flow angle in the absolute frame of reference, from axial
α_m = stator blade channel flow angle
β_m = rotor blade channel flow angle
λ_φ = blockage factor based on performance map, Eq. (2)
λ = blockage factor based on pressure trace, Eq. (1)
μ = fluid mass ratio, Eq. (5)
ρ = density
φ = flow coefficient = c_x/U_2, at Euler radius
ψ = stage pressure coefficient = $(h_3 - h_1)/U_2^2$ for air; = $(p_3 - p_1)/(\rho_1 U_2^2)$ for water
Ω_{RS} = stall cell speed of propagation ratio, Eq. (3)
ω_{RS} = angular speed of rotating stall cell
ω_R = angular speed of rotor

Subscripts

1 = inlet rotor
2 = exit rotor = inlet stator (= interface rotor/stator)
3 = exit rotor
1–2 = rotor domain
2–3 = stator domain
F = front boundary of stall cell
R = rear boundary of stall cell
n = normalized

Superscripts

$\bar{}$ = time-averaged value
^{0} = stagnation value

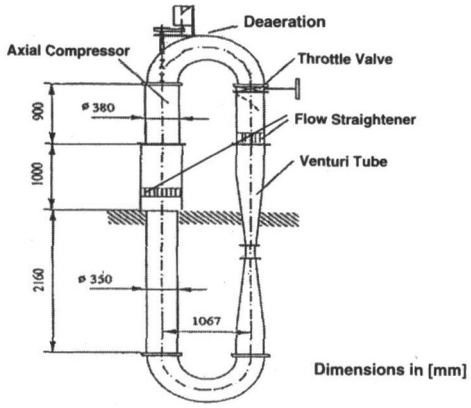

Fig. 1 Schematic of water model rig

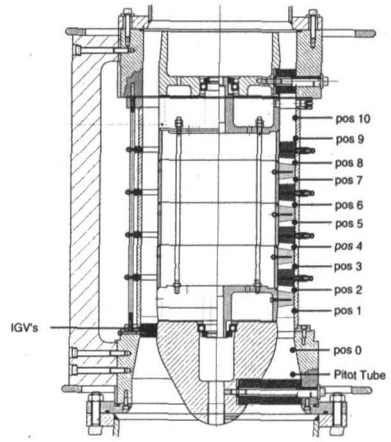

Fig. 3 Positions of measurements in axial compressor water model

stages. All nine rows comprise 30 blades each. The design values include a hub flow coefficient of 0.45, a midspan degree of reaction of 61 percent, and a midspan rotor speed of 2.1 m/s. The hub/tip radius ratio is 0.82 and the solidity of the stator and rotor is 1.39.

II.2 Instrumentation. Figure 3 presents a schematic of the four-stage axial compressor. Time-mean and unsteady static pressure measurements are taken at the compressor inlet, outlet, and in between the blade rows using static pressure tabs and fast-response pressure transducers (500 Hz), see markers 1–10 in Fig. 3. An additional tab is placed upstream of the IGV (marker 0). The reference total pressure for the compressor is obtained from three Pitot probes equally distributed over the circumference and located upstream of the IGV. The time-averaged pressures are obtained by measuring the pressure difference between the wall static taps and the reference inlet total pressure. Hydrostatic effects are compensated. In order to study the RS effects better, the blade passing frequency is filtered out in the measured static pressure history plots.

The flow visualizations are obtained by using polystyrene spheres with a diameter between 100 and 400 μm and a specific density of 1.05 kg/m^3. Photographs from a CCD video camera (CF 16/2) are processed by digitalization and imaging software.

II.3 Compressor Characteristic. In Fig. 4, the averaged characteristic of the four stages is shown for a rotor speed of 120 rpm. Due to incompressibility and negligible Reynolds number effects, the characteristic remains constant for different rotor speeds. Day et al. (1978) proposed dividing a stall characteristic into two categories. In "progressive stall," part-span stall is observed first, while in the "abrupt stall" characteristic full-span stall appears. The water model shows an abrupt behavior since after stall inception a full-span single cell RS is observed. The performance map for the entire range of flow coefficients can be structured into five different domains:

Region I includes the design point and is governed by stable flow from $\bar{\varphi} = 0.55$ to $\bar{\varphi} = 0.358$, the latter corresponding to the instability limit.

Region II ($\bar{\varphi} = 0.358$ to 0.31) covers the sudden jump to Region III when RS develops. No persistent operation is possible here. When the flow is increased to make RS disappear the jump is shifted to Region II*. A detailed description of such hysteresis is given by Day et al. (1978).

In Region III ($\bar{\varphi} = 0.31$ to 0.067) the compressor is operating in a single-cell full-span RS regime. The static enthalpy rise of the CFD solution for the single-stage compressor at RS conditions is also marked in Fig. 4. As expected, due to the two-dimensional inviscid nature of the CFD solution, the static enthalpy rise is higher than the measured data.

Region IV ($\bar{\varphi} = 0.067$ to 0.044) contains a second jump (and hysteresis) where the flow changes from RS operation to axisymmetric stall, in which a nearly 100 percent blockage of the annulus is observed.

Region V denotes an axisymmetric fully stalled flow over the entire annulus. This branch is similar to the unstalled characteristic branch, where the rise in static pressure is increasing when closing the throttle valve. Visualization of this flow indi-

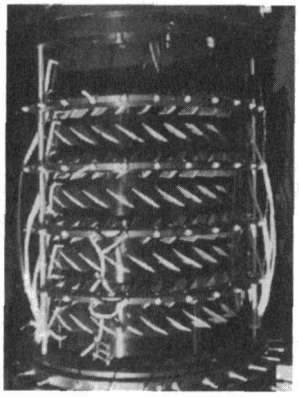

Fig. 2 Axial compressor water model (cylindrical rotor in transparent cylindrical casing)

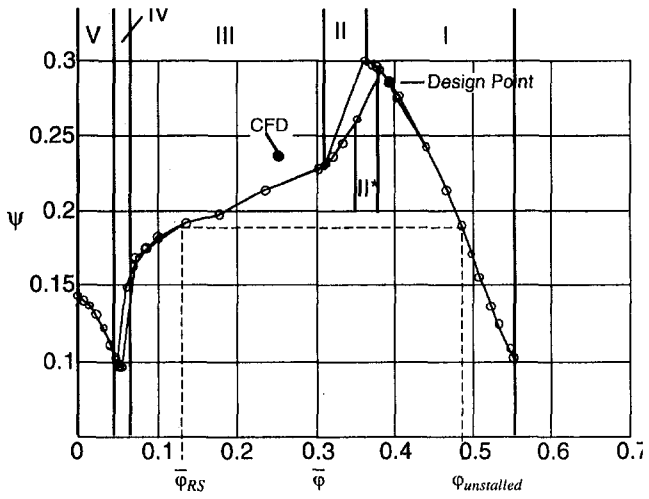

Fig. 4 Stage average performance map of four-stage axial compressor water model indicating five domains

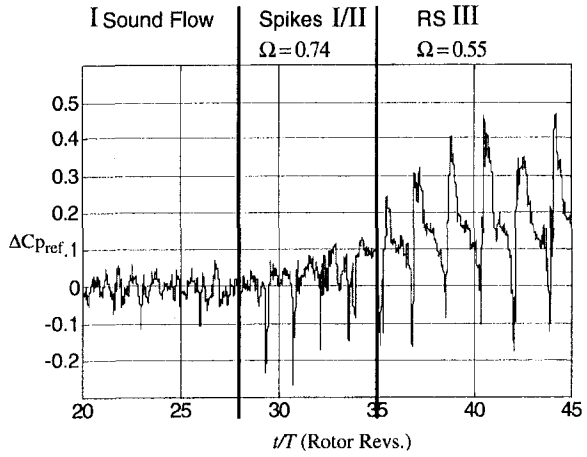

Fig. 5 Rotating stall inception with spike-type activity as measured by pressure transducer at position 6 in Fig. 3

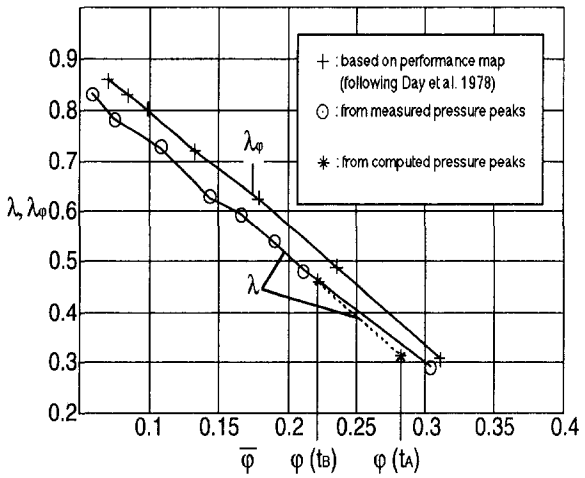

Fig. 6 Blockage factor as a function of flow coefficient

cates that the structure of the full-stall flow is similar in nature to the flow within the RS cell.

II.4 Rotating Stall Inception. Currently, rotating stall inception of an air compressor is divided into spike-type stall inception and stall inception due to modal activity, as discussed in Camp and Day (1998). The spike-type disturbances are characterized by sharp peaks in the history plot, which rotate with about 70 to 80 percent of rotor speed. Modal perturbations, on the other hand, revolve slowly up to 50 percent of rotor speed and appear as gentle waves. In Fig. 5 the history plot of the pressure transducer at position 5 during RS inception at a constant throttle valve position is shown. The roman numerals (I to III) correspond to the regions defined in Fig. 4. Prestall spikes propagating at about 74 percent of rotor speed are observed for about six rotor revolutions before the emergence of a fully developed full-span single cell RS propagating at 54 percent of rotor speed. Notice that the RS frequency varies from 53 to 56 percent of rotor speed in Region III.

The increase in time-averaged static pressure from sound flow to RS observed in Fig. 5 can be explained from the implementation of the data acquisition system. The reference pressure for the static pressure transducers is the environmental air pressure. The rise in pressure across the stages from positions 6 to 10 (Fig. 3) is subtracted from the geodesic height from position 6 up to the deaeration valve on top of the test rig. Consequently, the drop in pressure from sound to stall flow is measured as a pressure rise in Fig. 5 during RS inception.

II.5 Annulus Blockage. Day et al. (1978) presented a prediction of compressor performance. It is suggested that for abrupt stall characteristics a minimal blockage factor λ of 0.3 is necessary and that in case of lower blockage factors, i.e., higher throughflows, part-span stall would appear. This minimum blockage value at RS inception has then to be found in our water model, since no part-span stall has been observed. This is verified in Fig. 6 where the experimental blockage factor λ is plotted versus the flow coefficient. The blockage ranges from 0.3 at RS inception to 0.85 where full annulus stall is developed. The experimental blockage was obtained from the wall pressure traces as

$$\lambda = \frac{\text{time between suction peak and next pressure peak}}{\text{time between two suction peaks}} \quad (1)$$

As expected and described by Day et al. (1978), the blockage factor is a linear function of the flow coefficient. Following Day, it can also be calculated from the performance map as

$$\lambda_\varphi = \frac{\varphi_{\text{unstalled}} - \bar{\varphi}_{\text{RS}}}{\varphi_{\text{unstalled}}} \quad (2)$$

This correlation obtained from the characteristic in Fig. 4 is shown in Fig. 6 together with the measured data. Clearly the measured blockage of the annulus follows this model for Region III. In addition, the computed result is marked, and will be discussed later in Section IV. The shift between λ and λ_φ is due to the use of slightly different definitions.

II.6 Unsteady Static Pressure Measurements. The structure of the RS cell for two flow coefficient values as measured at two axial positions in the water model are discussed in this section. Measured time traces of casing wall static pressure in the interspace rotor/stator for high and low $\bar{\varphi}$ within Region III (Fig. 4) at positions 6 and 8 are shown in Figs. 7(*a*, *b*, *c*, and *d*), respectively. For $\bar{\varphi} = 0.31$, the pressure traces show a single RS cell propagating at 54 percent of rotor speed and blocking about 33 percent of the annulus. The cell front and rear boundaries are associated with low and high-pressure peaks, respectively. As explained in Section IV, these peaks mark the momentum exchange between the sound flow and the stagnant flow in the RS cell. Compared to the abrupt pressure change within the RS cell, a mild circumferential pressure gradient is present in the sound flow region.

At a low flow coefficient of $\bar{\varphi} = 0.075$, the cell covers 79 percent of the annulus and propagates at 55 percent of rotor speed. Within the small portion of sound flow remaining in the annulus, the static pressure gradient is large but nearly constant, while within the RS cell the pressure is increasing from the front to the rear boundaries.

The pressure distribution within the RS cell itself seems to depend on the size of the cell, i.e., on the flow coefficient. The RS cell structures in the different stages are similar in nature regarding the cell speed and blockage factor. An increase in the amplitude of the pressure spikes at the cell front and rear boundaries is observed from the first to the last stage.

III Numerical Procedure

The numerical procedure uses a multiblock grid generator MELLIP (Saxer-Felici, 1996) operating in conjunction with an unstructured flow solver called MULTI2 (Saxer, 1992).

III.1 Grid Generator and Flow Solver. MELLIP solves the Poisson equations in two dimensions in the axial-tangential plane for different spanwise locations (here at the Euler radius only). An iterative SLOR technique is applied on blocks of C and H grid types whose boundaries are allowed

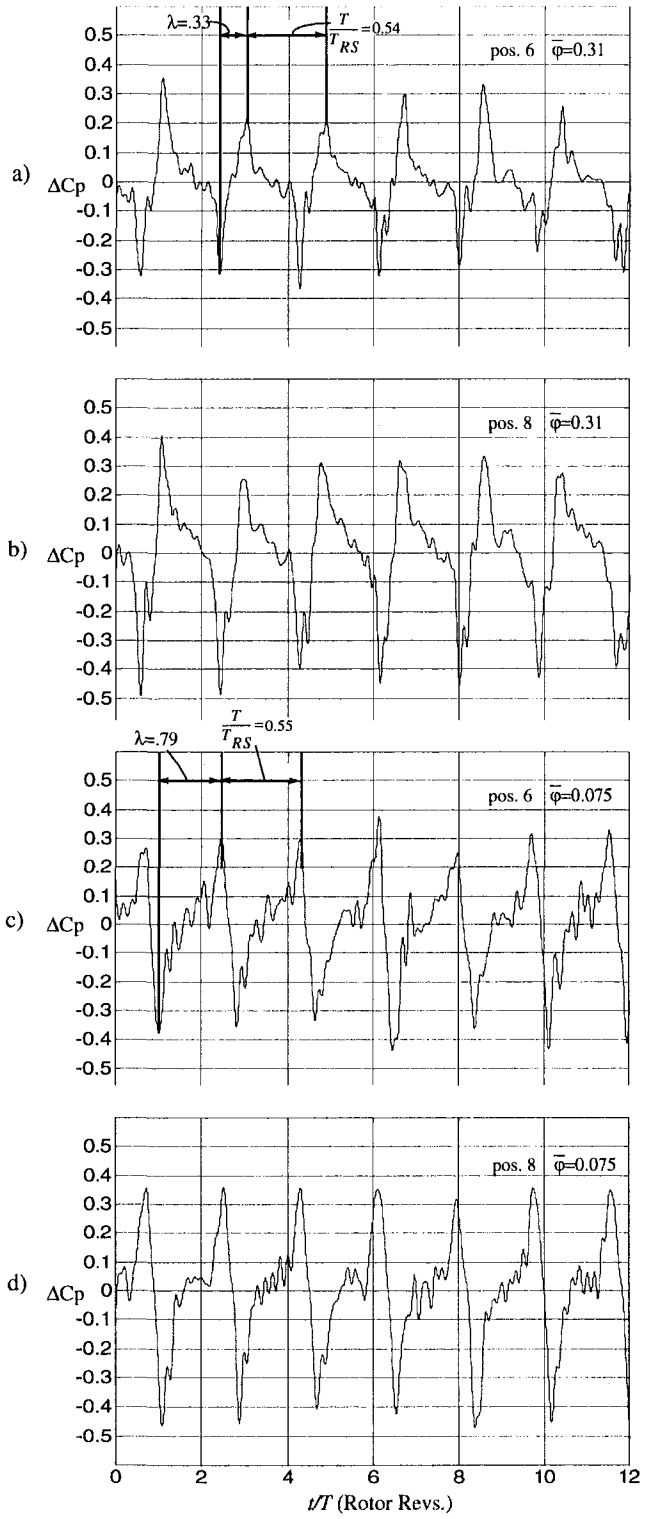

Fig. 7 Wall pressure trace between rotor and stator of: (*a*) stage 3 (position 6) during RS operation at $\bar{\varphi}$ = 0.31; (*b*) stage 4 (position 8) during RS operation at $\bar{\varphi}$ = 0.31; (*c*) stage 3 (position 6) during RS operation at $\bar{\varphi}$ = 0.075; (*d*) stage 4 (position 8) during RS operation at $\bar{\varphi}$ = 0.075

to move, resulting in an overall unstructured smooth grid. The source terms are calibrated to control spacing and orthogonality at the blade surfaces (Steger and Sorenson, 1979). MULTI2 solves the time-dependent Euler equations with an explicit, finite-volume, node-based Lax–Wendroff type algorithm (Ni, 1981), which has been extended to three-dimensional unstructured meshes and hexahedral cells (Saxer, 1992). For this particular study, the three-dimensional solver is used in two-dimensional mode in which three two-dimensional meshes are piled up to form a two-cell-height three-dimensional control volume. MULTI2 is capable of solving the time-dependent as well as the steady-state interaction in a rotor/stator configuration. A combined second- and fourth-difference numerical smoothing consistent with the second-order accuracy (both in space and time) of the discretization scheme is added to prevent high-frequency oscillations in the solution and to capture shock waves. The fourth-difference smoothing, an extension of the method proposed by Holmes and Connell (1989), ensures second-order accuracy in shock-free regions even on distorted grids, a desirable feature when studying the evolution of flow distortions or secondary flows. A nonlinear second-difference operator allows the procedure to capture shocks with an artificial bulk viscosity parameter tailored by the local flow divergence and Mach number in order to avoid large shock overshoots. Due to the low subsonic case studied here, the second-difference smoothing has been turned off.

III.2 Computational Domain and Boundary Conditions. In order to avoid excessive computational time, and in contrast to the experimental domain, the CFD work was performed on a single compressor stage. Also, the circumferential domain determined by the boundary conditions has been reduced to 15 blades (test rig compressor: 30 blades). Long inlet and exit domains were specified for enabling time-independent inlet and exit boundary conditions to be used despite the large blockage to be expected by rotating stall. The computational grid is presented in Fig. 8 with the location of the rotor inlet, rotor/stator interface, and stator exit (stations 1, 2, and 3, respectively). The block structure can be seen in a blow-up of the near-blade region. The blade disposition used in the simulation corresponds to a cut at the (rms) Euler radius of any of the repeating stages of the four-stage water model described in Section II and in Hof et al. (1996). The grid in domain 1 to 2 is fixed to the moving rotor blades and the Euler equations are solved in the relative frame of reference. In domain 2 to 3 the grid is stationary and absolute flow variables are used.

With respect to the overall goal of assessing the determining effects in the propagation of full-span rotating stall, the grid resolution, which is standard for an Euler simulation, seems adequate.

As described in detail by Saxer and Giles (1993) and Saxer (1992) nonreflecting boundary conditions are used. By adopting long inlet and exit farfields and by applying steady-state nonreflecting boundary conditions based on circumferentially averaged quantities at the inlet and the exit, any uncertainty in modeling the physically correct unsteadiness reaching the farfield boundaries should be minimized. At the rotor inlet, the average entropy (or stagnation pressure), stagnation temperature, and tangential flow angle are set in the absolute frame of reference and correspond to p_1^0 = 1 bar, T_1^0 = 300 K, $\bar{\alpha}_1$ = −31.3 deg. This is in contrast to calculations performed exclusively in the stable branch of the characteristic, where it is standard practice to set the rothalpy and relative flow angles at the rotor inlet. The circumferentially averaged conditions allow local flow adjustments due to potential effects. At the exit, the average static pressure is prescribed in order to reach the desired throughflow coefficient. At the rotor/stator interface, an unsteady numerically nonreflecting procedure based on the local characteristics variables ensures a physically consistent boundary condition (see Saxer, 1992), even in the presence of strong backflow.

A no mass flux condition is enforced at the pseudo hub and tip endwalls as well as on the stator and rotor blades. Also, the repeating, i.e., periodic condition is applied between the upper and lower boundaries of the multiple blade passages domain.

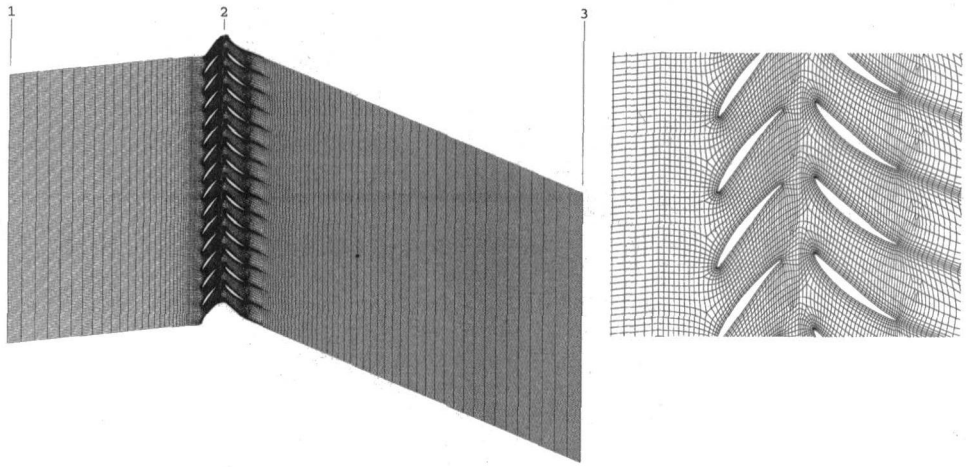

Fig. 8 Computational grid (15 channels, 3 mesh planes, 38475 nodes per mesh plane) with stations 1, 2, and 3 and blow-up of near-blade region

III.3 Validity of the Computational Solution. As MULTI2 has not been specifically designed for the low Mach number flows encountered in this study, i.e., inlet axial Mach number of 0.11 at stall conditions, its capability is additionally tested against an incompressible solution. Figure 9 shows the computed and analytical pressure coefficient distributions on the blade in the Gostelow cascade (Gostelow, 1984), where a conformal mapping transformation has been used to derive the two-dimensional analytic incompressible solution. The computed maximum Mach number is approximately 0.182, so that the compressibility effects are very small. The agreement is very good.

Another important issue is the time accuracy of the computed unsteady solution and its repeatability under stall conditions. The time traces of the inlet, rotor exit, stator inlet, and exit surface-integrated mass flows are shown in Fig. 10 for twelve rotor revolutions in the stall regime. For each station, a periodicity in mass flow fluctuations is observed. Notice that the rotor exit and stator inlet curves overlap, showing the conservation of mass across the interface. The blade passing frequency is also clearly visible. The phase shifts and amplitude differences are due to compressibility effects expressed by

$$\int_V \frac{\partial \rho}{\partial t}\, dV$$

This value is indicated on Fig. 10 for $V = V_{2\text{-}3}$ (computational volume from interface to stator exit). Inlet and exit mass flow fluctuations of about 15 percent of the mean value indicate significant surgelike pulsations superimposed upon the rotating stall phenomenon.

The instantaneous error in the continuity equation applied on the computational domain lies below 1 percent of the inlet mass flow.

III.4 Rotating Stall Generation. Two approaches have been tested to produce rotating stall starting from the axisymmetric unsteady solution in the unstalled branch of the characteristic. These are schematically depicted in Fig. 11. Both of them lead to the same rotating stall pattern at the same throughflow conditions.

As a starting point, the first technique uses the model of Day et al. (1978), which assumes that the axial velocity in the unstalled region is determined by the requirement for the unstalled section of the compressor to give the same pressure rise as in the stalled region. Then from the unstalled operating point, the rotor-relative inlet flow angle is abruptly increased to an average value corresponding to stall conditions. Once the stall process has developed, it is maintained by setting the inlet flow angle back to its constant absolute level, as given by the inlet guide vane. The second approach starts from the unstalled

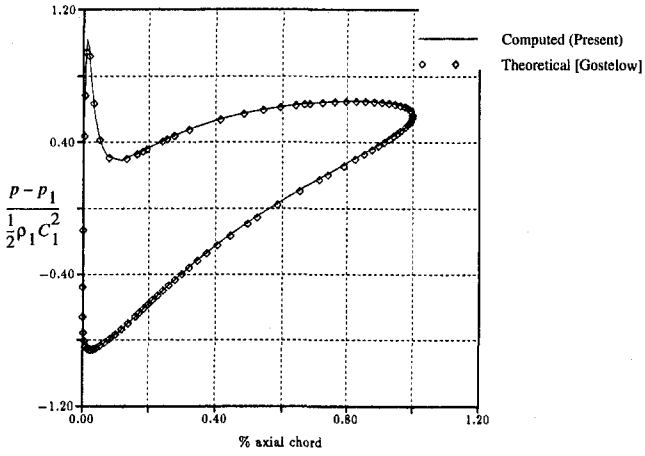

Fig. 9 Computed and analytical pressure coefficient distributions on the blade in the Gostelow cascade

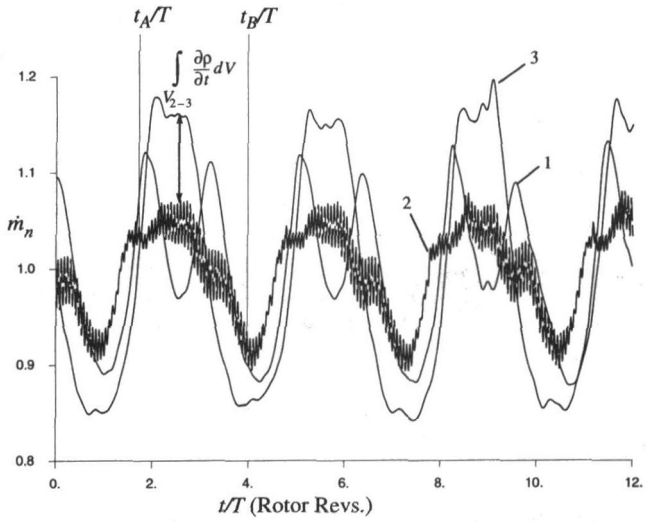

Fig. 10 Normalized mass flow iteration history during rotating stall, plotted for inlet (1), interface (2), and exit (3) surfaces

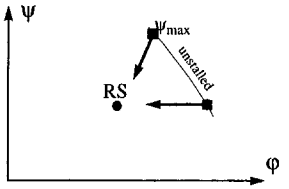

Fig. 11 Two ways of generating rotating stall (round symbol) from stable CFD solutions (squares)

branch near the peak of the characteristic. With the inlet conditions fixed by the absolute-frame stagnation conditions and flow angle, converged solutions are obtained when increasing the static pressure stepwise. When the instability limit is reached, the solution begins to show a breakdown of the static pressure rise (stronger rise of the inlet pressure than the step imposed in the exit pressure). The pressure fluctuations grow exponentially over the whole flow field. This is linked to the generation of several recirculation regions within the stator passages during the first 20 rotor revolutions. These zones will evolve later into a single rotating stall cell. In order to get a stable periodic unsteady solution, the exit pressure has to be manually reduced to an appropriate value. This value can be estimated from experimentally measured stage performance characteristics or from the first approach. As an example, Fig. 12 shows the static pressure time trace for the numerical probe #1 at the rotor/stator interface and illustrates the stall generation process in this second approach. The last upward step in exit pressure was taken at time $t/T = -10$, the manual reduction at $t/T = 10$.

In both approaches mentioned above, inviscid separated flow starts to develop in each of the stator passages on the suction side near the trailing edge. These recirculation regions grow then in each channel in a nonuniform way as can be seen in Fig. 13(a). A blow-up of a blade trailing edge with velocity vectors showing the recirculation zone is shown in Fig. 13(b). Once developed, the numerical unsteady behavior is quite periodical and computationally stable.

IV Analysis of Stall Flow

For the 15 blade passages shown in Fig. 8, the numerical solution presents a single stall cell at a throughflow coefficient $\bar{\varphi}$ of 0.25. The flow structure associated with the rotating stall is analyzed in this section by using unsteady static pressure and throughflow distributions as well as flow visualization. At the interface between rotor and stator, a comparison of numerical results with unsteady static pressure measurements at the same $\bar{\varphi}$ is shown. An estimate of the RS speed of propagation is conducted using the analytical model of Gyarmathy (1996) and compared to the experimental and numerical data.

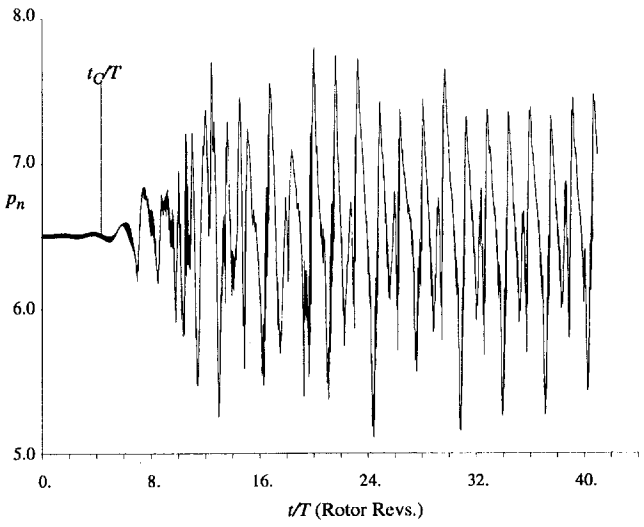

Fig. 12 Computed rotating stall generation history for probe #1 at rotor/stator interface (see Fig. 15 for probe location)

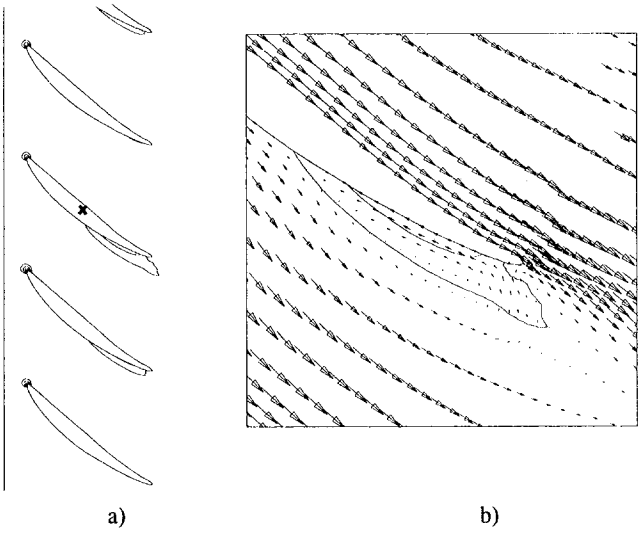

Fig. 13 (a) Isolines of axial velocity $c_x \leq 0$ in stator passages at time t_C, (b) blow-up of trailing-edge of blade × with velocity vectors

IV.1 RS Cell Structure. The unsteady axial velocity fields, the static pressure fields, and the instantaneous streamlines are shown in Figs. 14(a, b, c) for two times (t_A and t_B). This distinction is rendered necessary by the presence of significant nondamped mass flow fluctuations in the CFD solution. At time t_A the mass flow through the stage is high, at t_B it is low (see Fig. 10). The top fields of Fig. 14 show the instantaneous axial velocity contours (where $c_x \leq 0$) and the rotor/stator interface c_x profile over the periphery. The middle fields (b) display the static pressure. For visualization and interpretation purposes a frame of reference rotating with the calculated cell speed is used. Hence the RS cell appears to be stationary while the rotor row is moving downward and the stator row upward.

In the numerical solution a single cell is observed propagating at a fluctuating velocity ranging from 61 to 66 percent. Associated with this change in propagation speed is a change in the structure of the cell, which evolves from a diffused to a compact form and back with a frequency dictated by the surgelike fluctuations shown in Fig. 10.

At time t_A a compact RS cell is observed with strong backflow near its center and negative velocities of the order of the throughflow velocity. Larger regions of backflow are present in the rotor than in the stator, with a strong recirculation bubble forming ahead of the rotor (Fig. 14(c)). This deflects the rotor-relative incoming flow to the sides of the RS cell. Looking at the static pressure field one notices that viewed from the RS cell, a drop in pressure occurs at the front (bottom side) boundary of the cell, while a pressure maximum ends it. The width of the cell as defined by the circumferential extent between the front and rear boundary peaks in static pressure (see lines **F** and **R**) corresponds to 33 percent of the periphery. On the other hand, the circumferential static pressure remains nearly constant in the sound flow region (except of course variations due to blade potential effects). The center of the large vortical bubble is marked by a depression. The width of the RS cell can also be calculated from the peripheral distance formed by the bisection of the overall mean throughflow and the local axial flow distribution as shown on Fig. 14(a).

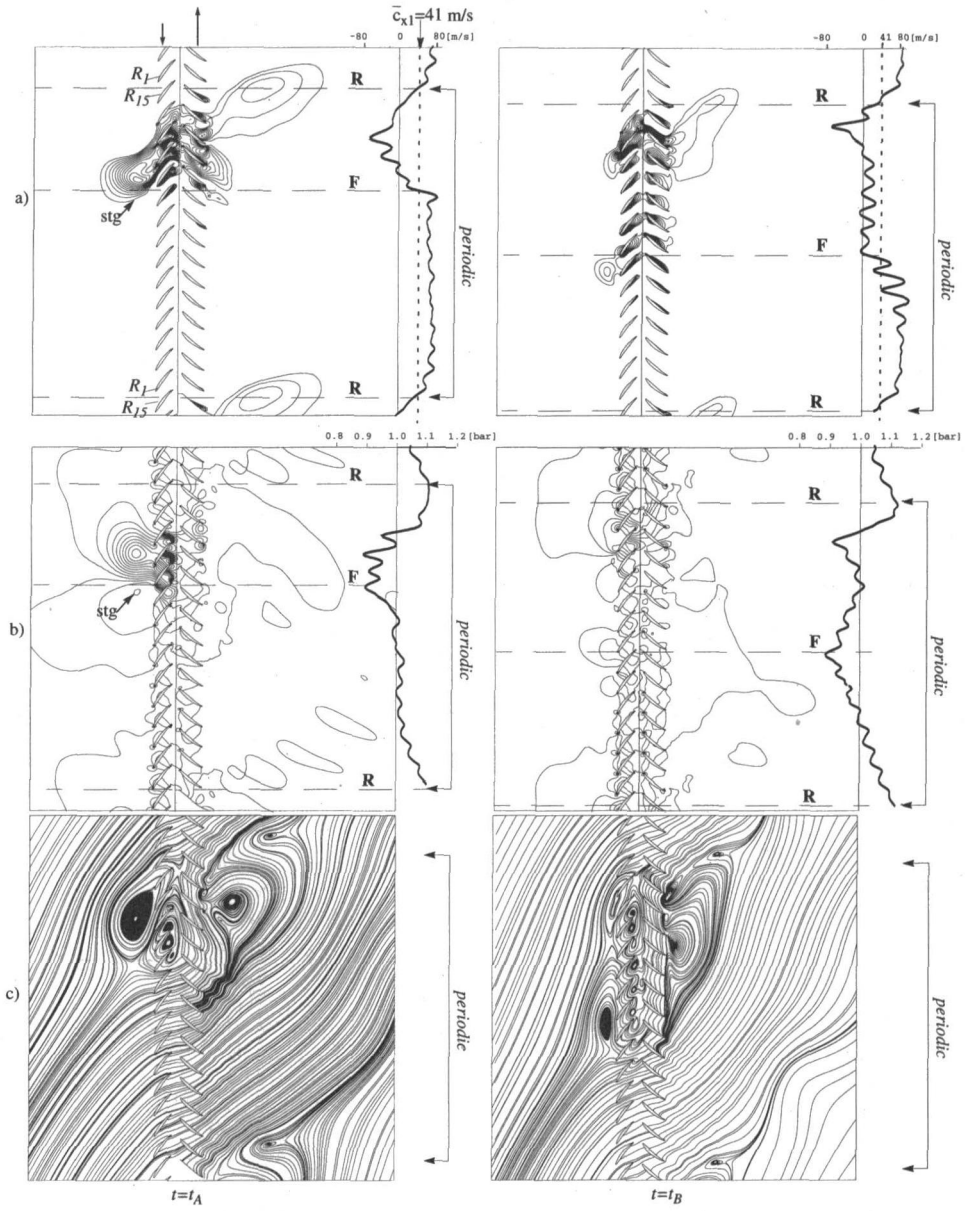

Fig. 14 (*a*) Contours of negative axial velocity, (*b*) static pressure contours, (*c*) instantaneous cell-frame streamlines, for times $t = t_A$ and $t = t_B$ (rotating stall frame of reference). For (*a*) profiles of axial velocity and for (*b*) profiles of static pressure along the rotor/stator interface are also shown ($\bar{\varphi} = 0.25$).

At time t_B a less compact, larger, RS cell is observed (Fig. 14(*c*)) with near zero throughflow. While the RS cell trailing edge is clearly marked by an abrupt change in static pressure, the cell leading edge is somewhat diffused, with smoother changes in static pressure. The sound flow presents a "ramp" distribution of static pressure along the circumference.

The unsteady static pressure recordings of five numerical probes located at the rotor/stator interface for twelve rotor revolutions are shown in Fig. 15 together with the fixed probes location. The times t_A and t_B corresponding to Fig. 14 are marked. A clear rotating stall pattern is observed with a speed of propagation (measured from peak-to-peak) of about 64 percent. The cell in its compact form seems to propagate slightly faster than in its diffused form. The evolution from diffused back to compact is marked by a "bump" in static pressure occurring between peaks. Its frequency is about half of the cell propagation speed and is linked to the overall mass flow pulsations present in the compression system, as seen in Fig. 10. In particular, a positive mass flow pulsation tends to render the cell more compact, while a negative pulsation tends to diffuse it. The blockage varies from 31 to 46 percent as measured in Fig. 14. The unsteady static pressure fluctuations ahead of the rotor are shown in Fig. 16. The pressure trace of probe #5, for example, is fairly constant except for one short pressure drop in each cell revolution. This drop in static pressure corresponds to the vortical bubble generated ahead of the rotor in Fig. 14(*c*).

IV.2 Comparison With Idealized Model. Gyarmathy (1996) derived a simple model to estimate the RS cell speed of propagation and the pressure spikes at the front and rear boundaries of the rotating stall cell. By considering the rotor and stator blade channels as one-dimensional counterrotating ducts exchanging momentum across the interspace, an expression for the Ω_{RS} ratio of RS cell speed to rotor speed is obtained in terms of geometric data. The model assumes an incompressible inviscid flow in a cascade of infinite number of blades and narrow channels without any diffusion. Viewed in the frame of

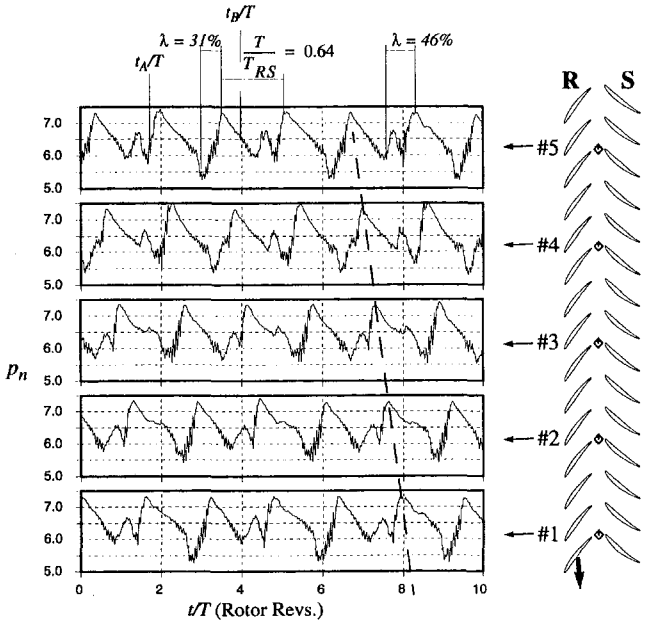

Fig. 15 Calculated normalized pressure history for 5 fixed probes placed along the rotor/stator interface ($\bar{\varphi} = 0.25$)

reference of the rotating stall cell, this process appears steady. At the front (lower) boundary of the cell, the stator channels containing high-velocity sound flow and the rotor channels with stalled flow steadily meet. The opposite effect takes place at the rear boundary, where stalled stator fluid emerging from the RS cell meets sound rotor fluid. The overall effect is a short-duration momentum exchange between the fluid masses transported by the two rows. The net result is a depression at the front boundary, where the stator fluid decelerates, while a static pressure peak is produced at the rear boundary where the rotor flow is decelerated. This general behavior is clearly seen in Fig. 14(a), where the front (**F**) and rear (**R**) boundaries of the RS cell are marked. The actual local pressure gradient and peaks depend on the abruptness of the momentum exchange. At the front boundary of the cell the driving mechanism is the transfer of the stator fluid momentum by suction. At the cell rear boundary, the transfer of the rotor fluid momentum toward the stator

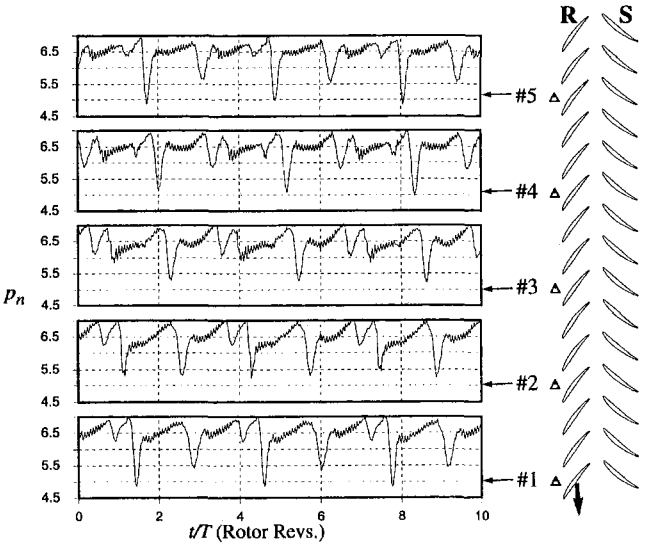

Fig. 16 Calculated normalized pressure history for five fixed probes placed upstream of the rotor ($\bar{\varphi} = 0.25$)

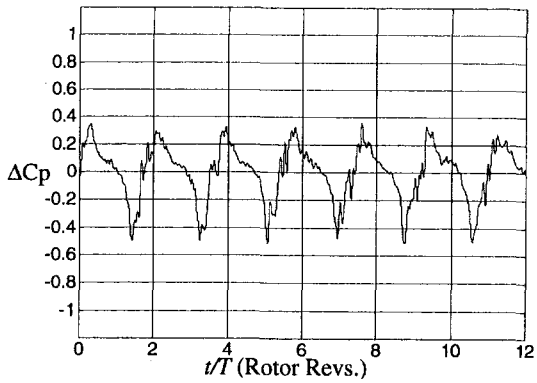

Fig. 17 Wall pressure trace between stage 4 rotor and stator (position 8) during rotating stall operation at $\bar{\varphi} = 0.25$

occurs through a jet-type effect. Hence, the rear boundary is defined by a steeper pressure gradient than the front boundary, as also seen in the numerical results in Fig. 14.

According to the analysis of the momentum exchange process at the cell boundaries, the following expression is found for the normalized RS cell speed of propagation:

$$\Omega_{RS} = \frac{\omega_{RS}}{\omega} = \frac{1}{1 + A} \tag{3}$$

where

$$A = \mu \frac{\sin^2 \beta_m}{\sin^2 \alpha_m}, \tag{4}$$

$$\mu = \frac{M_S}{M_R} \cong \frac{x_S}{x_R} \tag{5}$$

A represents the relative inertia of the fluid contained in the stator and rotor channels. μ is formed by the ratio of the circumferential mass entrained by the stator and rotor bladings, respectively. Here the blade channel flow angles α_m and β_m are approximated by the rotor and stator stagger angles (51.2 and 37.1 deg), respectively. According to this formula, the cell rotational speed is 56 percent of the rotor speed, which compares to 54 to 56 percent in the experiments and to 64 percent for the computed solution. A possible explanation for the higher value found in the CFD solution is given by the fact that in the computed solution, the actual mass entrained through the stall cell is larger on the rotor side than on the stator side; see Fig. 14. Thus μ in Eq. (5) is effectively reduced, bringing the corrected idealized model value to 65 percent for $\mu = 0.9$ (instead of $\mu = 1.3$).

IV.3 Comparison With Experimental Data. All measurements in the four-stage water model and the computations in the one-stage compressor at a given flow coefficient of $\bar{\varphi} = 0.25$ show a fully developed single RS cell. As seen in Fig. 6, the computed blockage closely complies with the experimental curve.

The normalized unsteady static pressure fluctuations measured at position 8 (i.e., in the rotor/stator interspace of the fourth stage) is shown in Fig. 17 for twelve rotor revolutions.

The shape of the pressure traces can be directly compared to the computed traces in Fig. 15, for example to that of probe #5 (or any other one). Apart from the slightly higher frequency of the CFD trace, the resemblance is conspicuous. For example, the abrupt pressure rise at the cell rear boundary is present both in the experimental and computed solution. This has also been observed by Cumpsty and Greitzer (1982). Also the more gentle static pressure decrease in the sound flow region is captured

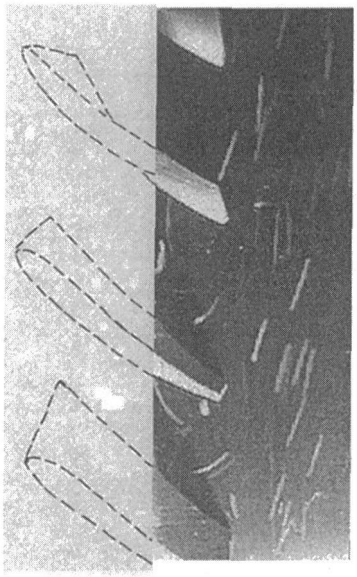

Fig. 18 Photograph of flow around stator trailing edge in stage 4 at $\bar{\varphi}$ = 0.25 (rotor speed of 60 rpm)

numerically. The absence of a flat plateau effect in the circumferential pressure distribution within the sound flow suggests that the RS cell acts as an obstruction like a cylindrical solid body placed in a potential flow producing a stagnation effect, which deflects the incoming flow, as originally postulated by Emmons et al. (1955). Hence, ahead of the RS cell (in the circumferential direction), the cascade operates at incidences lower than nominal values, while behind the RS cell trailing edge the incidence of the sound flow is larger; see Fig. 14(*c*). The pressure bump present before every second pressure peak may be the result of an interference between acoustic pressure waves and the stall cell. Some weak signals of "bump" effects are also present in the experimental data. However, the modulation of the RS phenomenon at $\Omega_{RS}/2$ frequency as observed in the (slightly compressible) CFD solution is absent in the water experiments.

The amplitude of the measured pressure spikes (from 0.3 to 0.5) seen in Fig. 17 closely corresponds to the idealized value of 0.45 estimated from the idealized model. The momentum exchange in the CFD solution is seen to be stronger (0.6 to 1).

A photograph of vortices formed near the trailing edge of the fourth-stage stator row is shown on Fig. 18 for $\bar{\varphi}$ = 0.25.

In Fig. 19 the computed instantaneous streamlines, viewed in the fixed stator frame of reference, are plotted at the same flow coefficient and times t_A and t_B. One should note that Fig. 19 shows the same flow domain as Fig. 14(*c*), however, the instantaneous streamlines are plotted in different frames of reference.

Stator trailing edge vortices, due to a slight back-flow pulse, clearly appear in the CFD solution. The stator vortices and the almost tangential flow motion behind the stator are also seen in the experiment (Fig. 18).

V Summary and Conclusions

A parallel numerical and experimental study of rotating stall in an axial compressor has been presented. The experimental work is based on measurements obtained in a four-stage water model of a subsonic compressor (repeating stages). The advantages of using the hydrodynamic analogy are:

- improved visualization capabilities due to low shaft speed;
- the possibility of studying RS for a broad range of throughflows from stall inception to zero throughflow without surge since no mass storage effects are present in the compression system.

The major experimental results are summarized as follows. From high to low flow coefficient ($0.55 > \bar{\varphi} > 0.067$) the water model presents a characteristic typical for low-speed axial compressors with an unstalled branch, a hysteresis, and a rotating stall branch. For $\bar{\varphi} < 0.067$, a second hysteresis is observed followed by a branch of negative slope near zero and at negative throughflow. In the rotating stall branch, a single fully developed full-span stall cell is observed. Its speed of propagation ranges from 54 to 56 percent of the shaft speed. Consistently with previous experimental data and Day's correlation for subsonic axial compressors, the blockage in the RS regime increases linearly from $\lambda = 0.3$ to $\lambda = 0.85$ with decreasing throughflow. Stall inception is of spike-type with prestall cells rotating at about 74 percent rotor speed. The shape of the pressure traces changes strongly as the blockage is increased.

The CFD simulation presents a two-dimensional inviscid unsteady solution in the RS regime for a single-stage air compressor geometrically similar to the water model. Two ways of numerically generating RS have been described and lead to the

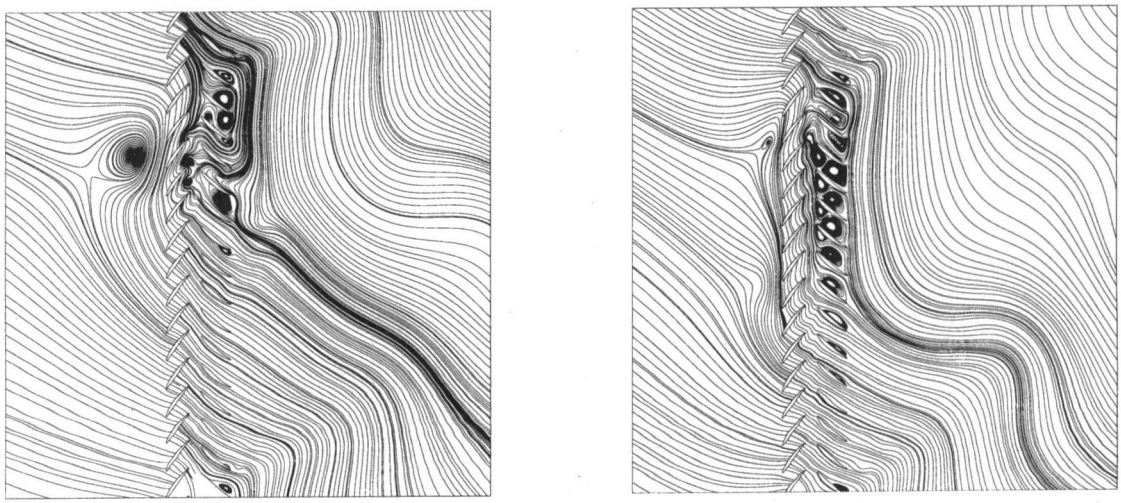

Fig. 19 Computed instantaneous streamlines shown in absolute frame of reference at times t_A and t_B and $\bar{\varphi}$ = 0.25

same RS pattern. A numerically sustainable stall flow solution that includes one fully developed RS cell has been presented. Due to periodic low-frequency mass flow pulsations associated with the axial length of the computational domain, the cell structure is not invariant in time. Its width (or blockage) varies periodically between 31 to 46 percent and its speed of propagation varies from 61 to 66 percent of the rotor speed. Viewing CFD results in the frame of reference of the RS cell is particularly interesting to gain insight in the problem.

The cell propagation speeds observed in the experiments and CFD can be explained with the help of an idealized theory based on momentum exchange between the rotor and stator rows at the RS cell front and rear boundaries.

Due to differences between experimental and simulated compression systems (# of stages and medium), a strict quantitative comparison is not appropriate. In spite of this, the computed RS pattern (cell propagation speed, blockage, circumferential static pressure distribution and blade-channel vortex formation) is consistent with the experimental data. Consequently it appears that the driving mechanisms for single cell full-span RS are essentially of two-dimensional inertial nature.

However, in order to substantiate the present approach further, future work ought to remove the simplifications assumed in the current CFD model (two-dimensional to three-dimensional, inviscid to viscous, single stage to multistage), thus revealing each contribution to the RS phenomenon.

Acknowledgments

The authors acknowledge the contribution of Mr. R. Haenggi and Mr. M. Fisler, who prepared and performed the preliminary rotating stall computations.

References

Camp, T. R., and Day, I. J., 1998, "A Study of Spike and Modal Stall Phenomena in a Low-Speed Axial Compressor," ASME JOURNAL OF TURBOMACHINERY, Vol. 120, pp. 393–401.

Cumpsty, N. A., and Greitzer, E. M., 1982, "A Simple Model for Compressor Stall Cell Propagation," ASME *Journal of Engineering for Power,* Vol. 104, pp. 170–176.

Cumpsty, N. A., 1989, *Compressor Aerodynamics,* Longman Scientific & Technical, UK, ISBN 0-470-21334-5.

Day, I. J., Greitzer, E. M., and Cumpsty, N. A., 1978, "Predictions of Compressor Performance in Rotating Stall," ASME *Journal of Engineering for Gas Turbines and Power,* Vol. 100, No. 1.

Day, I. J., 1993, "Stall Inception in Axial Flow Compressor," ASME JOURNAL OF TURBOMACHINERY, Vol. 115, pp. 1–9.

Emmons, H. W., Pearson, C. E., and Grant, H. P., 1955, "Compressor Surge and Stall Propagation," *Trans. ASME,* Vol. 79, pp. 455–469.

Felici, H. M., 1992, "A Coupled Eulerian/Lagrangian Method for the Solution of Three-Dimensional Vortical Flows," Ph.D. Thesis, Dept. Aeronautics & Astronautics, Massachusetts Institute of Technology, Cambridge, MA, USA, June, also GTL Report #211, MIT, Cambridge, MA, June.

File, G., Gyarmathy, G., and Staubli, T., 1997, "Water Model of a Single-Stage Centrifugal Compressor for Studying Rotating Stall," *Proc. 2nd European Turbomachinery Conference,* Antwerpen, Belgium.

Garnier, V. H., Epstein, A. H., and Greitzer, E. M., 1991, "Rotating Waves as Stall Inception Indication in Axial Compressors," ASME JOURNAL OF TURBOMACHINERY, Vol. 113, pp. 290–301.

Gostelow, J. P., 1984, *Cascade Aerodynamics,* Pergamon Press.

Gyarmathy, G., 1996, "Impeller-Diffuser Momentum Exchange During Rotating Stall," ASME Paper No. 96-WA/PID-6.

Gyarmathy, G., Inderbitzin, A., and Staubli, T., 1997, "Rotating Stall in Centrifugal Compressors," Video, Turbomachinery Laboratory of the Institute of Energy Technology, Swiss Federal Institute of Technology, Zurich.

Gysling, D. L., and Greitzer, E. M., 1994, "Dynamic Control of Rotating Stall in Axial Flow Compressors Using Aeromechanical Feedback," ASME Paper No. 94-GT-292.

He, L., 1997, "Computational Study of Rotating-Stall Inception in Axial Compressors," *AIAA Journal of Propulsion and Power,* Vol. 13, No. 1, pp. 31–38.

Hendricks, G. J., Sabnis, J. S., and Feulner, M. R., 1997, "Analysis of Instability Inception in High-Speed Multistage Axial Flow Compressors," ASME JOURNAL OF TURBOMACHINERY, Vol. 119, pp. 714–722.

Hof, A., Hauser, M., and Aeschlimann, B., 1996, "The 'Rheinfall' Water Model of an Axial Compressor: Design and Measurements" [in German], Semester-Project, Turbomachinery Laboratory of the Institute of Energy Technology, Swiss Federal Institute of Technology, Zurich.

Holmes, D. G., and Connell, S. D., 1989, "Solution of the 2-D Navier–Stokes Equations on Unstructured Adaptive Grids," AIAA Paper No. 89-1932-CP.

Longley, J. P., 1994, "A Review of Nonsteady Flow Models for Compressor Stability," ASME JOURNAL OF TURBOMACHINERY, Vol. 116, pp. 202–215.

Moore, F. K., and Greitzer, E. M., 1986, "A Theory of Post-Stall Transients in Axial Compression Systems, Parts I & II," ASME *Journal of Engineering for Gas Turbines and Power,* Vol. 108, pp. 68–97.

Ni, R.-H., 1981, "A Multiple Grid Scheme for Solving the Euler Equations," *AIAA Journal,* Vol. 20, No. 11, pp. 1565–1571.

Nishizawa, T., and Takata, H., 1994, "Numerical Study on Rotating Stall in Finite Pitch Cascades," ASME Paper No. 94-GT-258.

Outa, E., Kato, D., and Chiba, K., 1994, "A N-S Simulation of Stall Cell Behavior in a 2-D Compressor Rotor–Stator System at Various Loads," ASME Paper No. 94-GT-257.

Rizzi, A., and Eriksson, L.-E., 1984, "Computation of Flow Around Wings Based on the Euler Equations," *Journal of Fluid Mechanics,* Vol. 184, pp. 45–71.

Saxer, A. P., 1992, "A Numerical Analysis of 3-D Inviscid Stator/Rotor Interactions Using Non-reflecting Boundary Conditions," Ph.D. Thesis, Dept. Aeronautics & Astronautics, Massachusetts Institute of Technology, Cambridge, MA, USA, June; also GTL Report #209, MIT, Cambridge, MA, Mar.

Saxer, A. P., and Giles, M. B., 1993, "Quasi-Three-Dimensional Nonreflecting Boundary Conditions for Euler Equations Calculations," AIAA *Journal of Propulsion and Power,* Vol. 9, No. 2, pp. 263–271.

Saxer-Felici, H. M., 1996, "MELLIP: A Block-Structured Grid Generator for Turbomachinery Blading," Internal Report Turbomachinery Laboratory of the Institute of Energy Technology, Swiss Federal Institute of Technology, TN-LSM-96-02, Zurich.

Speziale, C. G., Sisto, F., and Jonnavithula, S., 1986, "Vortex Simulation of Propagating Stall in a Linear Cascade of Airfoils," ASME *Journal of Fluids Engineering,* Vol. 108, pp. 304–312.

Steger, J. L., and Sorenson, R. L., 1979, "Automatic Mesh-Point Clustering Near a Boundary in Grid Generation With Elliptic Partial Differential Equations," *Journal of Computational Physics,* Vol. 33, pp. 405–410.

Tryfonidis, M., Etchevers, O., Paduano, J. D., Epstein, A. H., and Hendricks, G. J., 1995, "Prestall Behavior of Several High-Speed Compressors," ASME JOURNAL OF TURBOMACHINERY, Vol. 117, No. 1, pp. 62–80.